

Ph.D. Thesis

SOLUTES AND CELLS

ASPECTS OF ADVECTION-DIFFUSION-REACTION PHENOMENA
IN BIOCHIPS

Søren Vedel

Supervisor: Henrik Bruus

Department of Micro- and Nanotechnology
Technical University of Denmark

13 August 2012

Solutes and cells

Aspects of advection-diffusion-reaction phenomena in biochips

Copyright © Søren Vedel 2012

Typeset using L^AT_EX, PGF and MATLAB

www.nanotech.dtu.dk/microfluidics

www.sorenvedel.com

*Til Emilie og Julie,
der har lært mig at holde meget mere livet*

Department of Micro- and Nanotechnology

Technical University of Denmark

Ørstedes Plads

Building 345 B

DK-2800 Kongens Lyngby

Denmark

+45 45 25 57 00

www.nanotech.dtu.dk

Abstract

The results in this thesis are part of the work carried out during the author’s doctoral studies. Funding for the project has been provided by the Programme Commission on Strategic Growth Technologies, the Danish Agency for Science, Technology and Innovation (grant no. 2106-08-0018 ‘ProCell’), and the overall title of the project is *Solutes and cells — aspects of advection-diffusion-reaction phenomena in biochips*. The work has consisted of several projects focusing on theory, and to some extent analysis of experimental data, with advection-diffusion-reaction phenomena of solutes as the recurring theme. Presented in this thesis is selected parts of the results obtained, which in some cases have also been published in peer-reviewed journals or presented at conferences and meetings, as listed in Sec. 1.2.

The studies of the distributions of solutes are motivated by microbiological phenomena in which cells quantitatively interpret the proximal concentration of specific solutes, and integrate this to achieve biological functions. In three specific examples, the author and co-workers have investigated different aspects of the influence of advection, diffusion and reaction on solute distributions, as well as the biological function that is achieved from these varying solute concentration fields. While the basic equations of solute transport have been known for one and a half century, the novelty of well-controlled high-resolution experimental data on the biological systems obtained from e.g. biochip microfluidics combined with the large variability between different biological systems means that many fundamental effects are yet to be revealed.

In the first subproject, we provide the first thorough theoretical description of the Taylor–Aris dispersion of solute concentration from the combined effects of time-dependent advection and diffusion. Combining Aris’s method of statistical moments with Fourier-expansion in time and expansion of all spatial dependencies in diffusion eigenmodes, we obtain closed-form expressions for the dispersion that apply to any constant channel cross-section of any initial distribution. These physically transparent expressions are given in terms of the fundamental processes of fluid velocity and solute diffusion causing the dispersion, which allow for both general and specific analyses. We identify a number of novel effects highlighted by different regimes of linear and non-linear response to any driving frequency, possible order-of-magnitude increases of the dispersion in certain regimes, and apparent transient anomalous diffusion, which are all shown to naturally arise from the competing physical processes of solute diffusion, momentum diffusion and local velocity variations.

In the second subproject, we study the influence of neighboring cells in shaping the

migration of the individual cell by a combined experimental and theoretical approach. Using highly controlled microfluidic cell to obtain culture high-resolution image data with subcellular resolution of migrating cells at various densities, we find strongly fluctuating instantaneous single-cell speeds but similar single-cell speed distributions and directional autocorrelation series among the cells. Furthermore, increasing density only influences the directionality and not the speed. To understand these findings, we analyze the membrane protrusions known as pseudopodia, that the cells use for generating locomotion. The statistics of these pseudopodia show that the cell only controls where these form, but not their behavior after formation. In addition, we find evidence of a cell-secreted chemical that also influences pseudopod formation, and pseudopod formation is therefore a diffusion-reaction process underlying cell migration. We further investigate these dependencies by formulating and using a conceptually simple physics-based model that emphasizes pseudopod-driven motility of the single cell and takes our experimental pseudopod statistics as input. Contrary to previous models aiming at investigating specific traits, ours correctly predict the vast majority of disparate migration features (speed, directionality and sampled space) for each cell in a population, and furthermore also correctly capture the dependencies on density. This shows that the varied single-cell behavior including the overall modulations imposed by density arise as a natural consequence of pseudopod-driven motility in a social context.

The final subproject concerns the combined effects of advection, diffusion and reaction of several solutes used by adipose-derived stem cells to make the decision to differentiate into terminal fat storing cells (adipocytes). Details of the signaling underlying the differentiation decision was investigated by combining microfluidic perfusion experiments with several different theoretical approaches. Contrary to current beliefs, we provide strong evidence that single-cell differentiation requires a signal secreted by all cells. Furthermore, a non-trivial secretion rate of this critical signaling species, combined with advection, diffusion and reaction results in complex responses as cell density and flow rate are varied. Since this work calls into question the basics of the differentiation procedure, many open questions have emerged for future studies.

Resumé

Resultaterne i nærværende afhandling er udarbejdet i løbet af forfatterens Ph.D.-studium. Ph.D.-projektet har været finansieret af Det Strategiske Forskningsråds Programkomite for Strategiske Vækstteknologier (bevilling nr. 2106-08-0018 ‘ProCell’), og den overordnede titel på Ph.D.-studiet har været *Signalstoffer og celler — aspekter af advektions-diffusions-reaktionsfænomener i biochips*. Arbejdet har bestået af flere projekter med fokus på teori, og i mindre grad analyse af eksperimentelt data, inden for advektions-diffusions-reaktionsfænomener af væskeopløste signalstoffer. I den foreliggende afhandling gennemgås udvalgte dele af resultaterne opnået under studiet. Dele af arbejdet er i løbet af studiet blevet publiceret i fagtidsskrifter, eller præsenteret ved konferencer, som uddybet i Sektion 1.2.

Studierne af væskeopløste signalstoffers fordelinger i tid og rum er motiveret af cellebiologiske fænomener, hvor celler kvantitativt registrerer koncentrationer af disse opløste stoffer i deres nærmiljø, og dernæst benytter dette til at ændre deres opførsel med henblik på at opnå specifikke biologiske funktioner. I dette Ph.D.-projekt har forfatteren og samarbejdspartnere, i tre specifikke eksempler, undersøgt hvorledes fordelingen af de opløste stoffer påvirkes af advektion, diffusion og kemisk reaktion, samt hvordan disse varierende fordelinger kan påvirke cellernes funktion. Selvom de grundliggende ligninger for advektion-diffusion-reaktionsdynamik er velkendte, har teknologien først for ganske nyligt tilladt høj-opløst og velkontrolleret data fra de biologiske systemer. Der er således endnu mange ukendte fundamentale biologiske processer og relationer, der venter på at blive opdaget og beskrevet.

I det første delprojekt analyseres den såkaldte Taylor–Aris spredning af et koncentrationsfelt, der opstår, når dette udsættes for en tidsafhængig strømning mens det diffunderer. Det teoretiske hovedresultat består af lukkede matematiske udtryk for denne spredning, der er gyldige for en vilkårlig geometri af kanalens tværsnit og en vilkårlig startfordeling af stoffet. Disse udtryk er fundet ved at kombinere Aris’ statistiske momenter for fordelingen af det opløste stof med Fourieropløsning i tid og tilsvarende udvikling af alle rumlige afhængigheder i diffusions-egenløsninger. Disse fysisk transparente matematiske resultater, der er udtryk i termer af de fundamentale fysiske processer, som definerer fænomenet — væskens hastighedsfordeling og diffusionen af stoffet — tillader både generelle analyser, samt behandling af specifikke tilfælde. Et antal nye fysiske effekter identificeres, hvoriblandt de mest bemærkelsesværdige er eksistensen af forskellige regimer af lineær og ikkelineær respons af spredningen på alle drivfrekvenser, størrelsesordensforøgelser af spredningen i visse regimer, og hvad der ved første øjekast ligner anormal

diffusion. Alle disse effekter vises at være naturlige følger af, at spredningen skyldes de konkurrerende fysiske processer bestående af stofdiffusion, diffusion af væskens impuls, samt lokale hastighedsvariationer.

I afhandlingens andet delprojekt analyseres indflydelsen af naboceller på bevægelsen af den individuelle celle, vha. både eksperimentelt og teoretisk arbejde. Det eksperimentelle data består af billeder af de bevægende celler ved forskellige celledensiteter, optaget med subcellulær opløsning i meget velkontrollerede mikrofluide celledyrkningsforsøg. Eksperimentelt er cellernes bevægelse karakteriseret ved store instantane hastighedsfluktuationer for den individuelle celle, mens hastighedsfordelingerne for alle celler i et givet forsøg er nominelt identiske. Samme overensstemmelse findes mellem de enkelte cellers retningsautokorrelationsfunktioner. Derudover findes det, at ændringer i celledensitet kun påvirker denne retningsautokorrelation, ikke hastigheden. Som et første skridt for at forstå disse effekter, analyseres herefter de såkaldte pseudopoder, der er fremspring langs cells ydre membran, som cellen benytter sig af, for at bevæge sig. Statistiske analyser af disse pseudopoder viser, at cellerne kun kan kontrollere hvor disse opstår, men ikke synes at kunne påvirke dem, når der er dannet. Der præsenteres desuden bevis for, at et stof udskilt af cellerne selv, også kan inducere dannelsen af pseudopoder i alle celler. En model baseret på simpel fysik introduceres for at undersøge alle disse observationer nærmere. Modellen postulerer, at cellernes bevægelse skyldes deres pseudopoder, og benytter derfor de eksperimentelt bestemte statistiske fordelinger for pseudopoderne som input. Modsat tidligere modeller, der har haft som mål at undersøge specifikke aspekter af cellebevægelsen, så som hastighedsfordelingen, forudsiger denne nye model de fleste fænomener i cellernes bevægelse (hastighed, retningsstabilitet og tilbagelagt afstand) for hver enkelt celle i populationen. Modellens forudsigelser for afhængigheden af disse parametre af celledensitet er også i god overensstemmelse med den eksperimentelle observationer. Dette illustrerer, at de observerede variationer i enkeltcelleopførsel, samt de overordnede ændringer påført af densitetsvariationer, alle er en naturlig konsekvens af pseudopod-medieret bevægelse i en social kontekst.

Afhandlingens tredje og sidste delprojekt omhandler de kombinerede effekter af advektion, diffusion og reaktion af adskillige opløste stoffer, som fedtvævsstamceller benytter sig af for at differentiere til fedtceller (adipocytter). Detaljerede undersøgelser af det signaleringsnetværk, disse celler benytter sig af for at opnå differentiation, foretoges både vha. mikrofluide perfusionsforsøg og adskillige teoretiske analyser. Dette arbejdes hovedresultat er identifikationen af et hidtil ukendt stof, der ikke desto mindre er det afgørende stof bag den enkelte celles beslutning om at differentiere. Det sandsynliggøres desuden, at dette stof udskilles af alle celler. Videre analyser indikerer tillige, at en ikke-trivial udskillelse af dette stof finder sted, hvorved en maksimal udskillelse findes under bestemte betingelser. Dette sidste delprojektet har ført til mange nye videnskabelige spørgsmål, idet hovedresultatet ændrer fundamentalt ved opfattelsen af, hvorledes differentiationen opnås.

Preface to the print edition

This printed edition is almost identical to the thesis submitted on 13 August 2012 for evaluation by a committee consisting of Associate Professor Kirstine Berg-Sørensen (DTU Physics, Denmark), Professor Frieder Mugele (University of Twente, The Netherlands) and Professor Pascal Silberzan (Institut Curie, France). Changes to the original manuscript included the present edition consist of a slightly rewritten general introduction in Chap. 1, updated lists of publications and corrections of typographical errors.

Upon the submission of the thesis for evaluation, the experimental collaborator of the work presented in Chap. 4 discovered that some of the presented data was void. It concerns the data in Fig. 4.13 on p. 106 labeled by $1/4(\text{DM}+\text{CM})$ from run 3 (upper right corner panel), which in fact has not been exposed to the stated conditions of $1/4(\text{DM}+\text{CM})$. These curves should therefore be disregarded. In doing so, most of the variations between the (now limited amount of) repeat experiments fall within the variations expected from finite statistics, but this error does not otherwise affect any of the conclusions presented in the manuscript. This erroneous data has therefore not been removed from the print edition in the interest of staying as close to the original manuscript as possible.

Søren Vedel
Department of Micro- and Nanotechnology
Technical University of Denmark
December 20, 2012

Preface

This thesis is submitted in partial fulfillment of the requirements for the degree of Doctor of Philosophy (Ph.D.) at the Technical University of Denmark. The work has been carried out within the Theoretical Microfluidics Group at the Department of Micro- and Nanotechnology (DTU Nanotech) at the Technical University of Denmark from April 2009 to August 2012, except for two research visits with Stephen R. Quake's group at Stanford University (February–August 2010 and a week in November 2010) and a short visit with Savaş Tay's research group at ETH Zürich in September 2011. The Ph.D. project has been supervised by Professor Henrik Bruus (DTU Nanotech and lately DTU Physics) and while abroad by Professor Stephen R. Quake.

It is my sincere pleasure to express my gratitude to Henrik Bruus for his outstanding and dedicated effort as supervisor and mentor; for giving me the freedom and encouragement to pursue my own ideas while also holding me accountable for their validity, and never accepting to leave the board before the dust has truly settled. I have benefitted greatly from his relentless teaching, our many inspiring discussions and his cheerful personality. I am also grateful to Stephen Quake for inviting me to visit with his lab and his equally inspiring supervision. Experiencing the daily life in his lab emphasized the benefits of cross-disciplinary research and taught me how physics and its methods form a strong tool for answering fundamental questions in biology. In addition, I have benefitted enormously from Savaş Tay's advice and collaboration which has been highly rewarding, and a great pleasure.

Finally, I would not have been without the loving support of Julie Brask, our daughter Emilie, and my family during the last three years. It is my hope that I have not scared you away with this three-month thesis hiatus.

Søren Vedel
Department of Micro- and Nanotechnology
Technical University of Denmark
13 August 2012

Table of Contents

List of Figures	xii
List of Tables	xiv
List of symbols	xvii
1 Introduction	1
1.1 Thesis outline	2
1.2 Publications	4
1.3 Supervision	5
2 Transient Taylor–Aris dispersion in time-dependent flows	7
2.1 Background	7
2.2 The physical model	9
2.2.1 The time-dependent velocity field	11
2.2.2 Physics of pulsatile flow	12
2.2.3 The advection-diffusion equation	13
2.2.4 Aris’s method of statistical moments	13
2.3 Mathematical solution of the dispersion problem	15
2.3.1 The zeroth axial moment and basis functions	16
2.3.2 The first axial moment and basis functions	17
2.3.3 Expressions for the effective diffusivity	18
2.4 Results for transverse uniform initial distribution	23
2.4.1 General aspects of dispersion and relaxation rates	23
2.4.2 Multiple-frequency flow in one-length-scale cross sections	24
2.4.3 Multiple-frequency flow in two-length-scale cross sections	31
2.5 Results for initial point concentrations	36
2.5.1 General observations for the dispersion of initial point concentrations	36
2.5.2 Flow fields and eigensolutions	37
2.5.3 Steady flows	38
2.5.4 Time-dependent flows	42
2.5.5 Implications for practical situations	43
2.6 Conclusions	44

3	Migration of cells in a social context	47
3.1	Background	48
3.1.1	Single-cell migration	48
3.1.2	Social cell migration	50
3.1.3	Open questions	51
3.2	Cells and experiments	51
3.2.1	Cell lines	51
3.2.2	Microfluidic cell culture experiments	52
3.3	Image analysis	53
3.3.1	Cell trajectories and velocities	53
3.3.2	Collision and pseudopod analyses	53
3.4	Experimental data analysis	55
3.4.1	Migration behavior at a fixed density	56
3.4.2	Dependence on cell density	61
3.4.3	Single-cell pseudopod statistics	63
3.4.4	Pseudopod formation biases	65
3.4.5	Tentative explanation	67
3.5	Modeling	68
3.5.1	Model cell	69
3.5.2	Pseudopod dynamics	71
3.5.3	Cell motion	74
3.5.4	Secretion of signaling molecules	75
3.5.5	Cell-cell contact	75
3.5.6	Initial conditions and sampling of model output	76
3.6	Comparisons with experimental data	77
3.7	Discussion	79
3.8	Conclusions and outlook	80
4	Differentiation of adipose-derived stem cells into adipocytes	81
4.1	Adipocyte background	82
4.1.1	What is a stem cell?	82
4.1.2	The central dogma of molecular biology	82
4.1.3	What it means to differentiate	83
4.1.4	Adipocytes	83
4.2	Cells, experiments and data	85
4.3	Image analysis tools	87
4.3.1	Vacuole detection	87
4.3.2	Vacuole cluster detection	89
4.3.3	Linking in time	91
4.3.4	Whole cell detection	91
4.3.5	Performance of the analysis tools	92
4.4	Validation of the experimental approach	92
4.4.1	Isotropic experimental conditions	92
4.4.2	Genetic markers validate image analysis and confirms signaling cascade	93

4.5	A cell-secreted signal is required for differentiation	95
4.5.1	Higher cell density leads to a higher fraction of differentiated cells . . .	95
4.5.2	Increasing the flow rate lowers the fraction of differentiated cells . . .	96
4.5.3	Increasing the level of cell-secreted chemicals: The effect of using conditioned medium	98
4.5.4	Evidence for the insufficiency of DM for differentiation	98
4.5.5	Intermediate summary	99
4.5.6	Secretion rate is independent of cell state	100
4.5.7	The secreted signal acts at the first level of the intracellular differ- entiation signaling pathway	102
4.5.8	Conceptual explanation of the differentiation	104
4.6	Detailed analysis reveals non-trivial secretion dynamics	105
4.6.1	Experimental evidence for non-trivial secretion: Lower levels of DM leads to higher fraction of differentiated cells	105
4.6.2	Continuum theory of supplied and secreted chemicals	107
4.6.3	Physical limits imposed on continuum theory by the experimental setup and results	107
4.6.4	The experimental results are inconsistent with normal reaction kinetics	109
4.6.5	The physics of chemoreception in perfusion flow	112
4.6.6	Particle-current-based reaction kinetics explains the experimental re- sults	114
4.6.7	Inferring single-cell conditions from population data	115
4.6.8	Details of fitting to population data	118
4.6.9	Results from fitting the single-cell model	119
4.6.10	A single hypothesis reconciles all results	120
4.7	Conclusions	121
4.8	Outlook	122
5	Conclusions and outlook	123
A	Mathematical and numerical details for Taylor–Aris dispersion	125
A.1	Detailed derivation of D_{eff} for transversely uniform initial solute distribution	125
A.2	Simplifying $\frac{1}{2} \frac{dM_2}{dt}$ for an initial point concentration	127
A.3	The long-time limit of $D_{\text{eff}}^{\text{point}}$ for steady flows	128
A.4	Short-time dispersion of an initially transverse uniform distribution	129
A.5	Numerics	129
A.5.1	Evaluation of the theoretical formulae	129
A.5.2	Brute-force numerics for transverse uniform initial distributions . . .	130
A.5.3	Brute-force numerics for initial point distributions	130
A.6	Pulsatile flow in a rectangular channel	131
B	Additional material for cell migration study	135
B.1	Summary of all experiments	135
B.2	Migration statistics of cells stimulated with tumor necrosis factor α (TNF α)	136

B.3	Additional data for dependence on cell density	137
B.4	No pseudopod formation-bias by positions existing pseudopodia	139
B.5	Numerical implementation of the developed cell migration model	141
C	Additional data for adipocyte stem cell differentiation	145
C.1	Additional genetic marker data	145
C.2	The irrelevance of fluid shear on stem cell behavior	148
C.3	Additional data for nearest neighbors and differentiation	149
C.4	Traditional biochemistry of ligand-receptor binding	153
D	Paper published in J. Micromech. Microeng.	155
E	Paper published in J. Fluid Mech.	167
F	Paper published in Proc. Natl. Acad. Sci. USA	197
	Bibliography	239

List of Figures

2.1	Schematic illustration of the Taylor–Aris dispersion phenomenon	8
2.2	The fluid velocity profile in pulsatile flow	12
2.3	$D_{\text{eff}}(t)$ in a tube exposed to single-frequency flow	26
2.4	$D_{\text{eff}}(t)$ in a tube exposed to multiple-frequency flows	29
2.5	$D_{\text{eff}}(t)$ in a rectangular channel exposed to multiple-frequency flows	34
2.6	$D_{\text{eff}}(t)$ for a peristaltic micropump	35
2.7	$D_{\text{eff}}^{\text{point}}(t)$ in steady flow	39
2.8	$D_{\text{eff}}^{\text{point}}(t)$ in unsteady flow	43
3.1	Basics of cell migration	48
3.2	Working principle of the automated pseudopod detection algorithm	54
3.3	Examples of cell migration trajectories	55
3.4	Cell direction of motion is random	56
3.5	Experimental migration statistics from a single experiment	57
3.6	Experimental example of migrating cells in contact	58
3.7	Dependence of experimental migration statistics on cell density	62
3.8	Experimental pseudopod statistics	64
3.9	Experimental evidence for pseudopod bias	66
3.10	Experimental determination of model parameters	69
3.11	Illustration of model cells	71
3.12	Chemotactic ability of model cells	73
3.13	Detailed comparison of model predictions with a single experiment	77
3.14	Density-dependence of model results compared to experiments	78
4.1	Basics of stem cell differentiation and adipocyte differentiation	82
4.2	Sketch of the microfluidic chip used	85
4.3	Example of data and image analysis proficiency	88
4.4	Details of vacuole cluster detection	89
4.5	Distributions of all cells and differentiated cells inside the chips	93
4.6	Temporal expression profiles of the six target genes	94
4.7	Φ as a function of time for experiments with CM and CM+DM	96
4.8	Experimental rebuttal of the necessity of cell-cell contact and the role of DM	97
4.9	Secretion is independent of cell state: evidence from cell-cell distances	101

4.10	Secretion is independent of cell state: evidence from cell numbers	102
4.11	Linear dependence between results to 1/4 DM and 1/4 DM + CM	103
4.12	Conceptual explanation of the differentiation process	105
4.13	Φ as a function of time for all experimental conditions	106
4.14	Steady-state concentration fields for stem cell differentiation	108
4.15	The concentration c_f of the cell-secreted chemical evaluated at the cells . .	110
4.16	Concentration f and particle-current J_f at the cells	114
4.17	Collapse of $\Phi(t)$ measurements according to a single-cell model	116
4.18	Hypothesized secretion-rate dependence on DM particle current	120
A.1	The pulsatile velocity field in a rectangular channel of $R = 5$	132
B.1	No effect of $\text{TNF}\alpha$ on cell migration	136
B.2	Whole-chamber cell trajectories at four different densities	137
B.3	Comparison of experimental speed distributions to Selmeczi <i>et al.</i>	138
B.4	Kurtosis $\kappa(C_i)$ of the distribution of C_i	138
B.5	Distributions of $\Delta\beta$ grouped based on the number of pseudopodia of the current cell	140
B.6	Flow diagram of the MATLAB implementation of the model	142
C.1	Supplementary data: temporal expression profiles of the six target genes . .	146
C.2	Independent experiments exhibit linear response to 1/4 DM and 1/4 DM + CM	147
C.3	Cellular shear stress	149
C.4	Additional data supporting state-independent secretion	150
C.5	Additional data supporting state-independent secretion	150
C.6	Additional data supporting state-independent secretion	151
C.7	Additional data supporting state-independent secretion	151
C.8	Additional data supporting state-independent secretion	152
C.9	Additional data supporting state-independent secretion	152

List of Tables

2.1	Dimensionless parameters of the peristaltic pump flow	35
2.2	\mathcal{M} for a power-law fluid	42
3.2	Model assumptions	70
3.3	Values assigned to model parameters.	76
4.1	List of the different experimental conditions and their abbreviations	86
B.1	Microfluidic experiments	135

List of symbols

Symbol	Description
$\nabla_{\perp} = \mathbf{e}_y \partial_y + \mathbf{e}_z \partial_z$	Cross-sectional part of the ∇ operator
$\langle \bullet $, and $ \bullet \rangle$	Bra of \bullet , and ket of \bullet
∂_{\bullet}	Partial derivative with respect to \bullet
$\langle \bullet \rangle$	Ensemble average of \bullet
$\bar{\bullet}$	Mean value of \bullet
$*$	Complex conjugation
\mathcal{A}	Cross-sectional area
a	Channel radius/half-height
Bi	Biot number
C	Directional autocorrelation
c	Concentration field of solute
c_p	p th axial moment of concentration
$\tilde{c}(x, \mathbf{r}_{\perp})$	Initial value for $c(x, \mathbf{r}_{\perp}, t)$
C_o	Characteristic concentration
D	Molecular diffusivity
D_{eff}	Effective diffusivity
$D_{\text{eff}}^{\text{avr}}$	Time-averaged effective diffusivity
$D_{\text{eff}}^{\text{point}}$	Effective diffusivity of a droplet
$D_{\text{eff}}^{\text{steady}}$	Effective diffusivity in steady flow
$D_{\text{eff}}^{\text{point steady}}$	Effective diffusivity of a droplet in steady flow
\bar{d}_{min}	Average minimum cell-cell distance
E	Expectation number
$\mathbf{e}_x, \mathbf{e}_y, \mathbf{e}_z$	Cartesian basis vectors
\mathbf{F}	Force
F_o	Force magnitude
\mathcal{F}_N	Coverage fraction of N cells
\mathfrak{f} , and \mathfrak{F}	Probability density and cumulative probability function
f_n	n th basis function
$G = k/g_{\text{crit}}$	Reduced reaction constant
g	Differentiation-determining intracellular solute

Continued on next page

Symbol	Description
g_{crit}	Critical activation level of g
I	Image intensity
I_{max}	Maximum intensity supported by image format
I_{rel}	Relative image intensity
J	Particle current
J_i	Bessel function, first kind of order i
K_{d}	Dissociation constant
k	Single-cell reaction constant
k_{ℓ}	Generalized wavenumber
\mathcal{L}	Channel length
L_{o}	Characteristic length
ℓ_{G}	Spatial extent of Gaussian kernel
ℓ_{sig}	Diffusive signaling distance against flow
\mathcal{M}	Maximum relative peak amplitude
M_p	p th full moment of concentration
m	Location parameter of GEV distribution
N_{m}	Number of model cell membrane points
N_{p}	Number of pseudopodia for a cell
N_{p}^{m}	Mode number of pseudopodia for a cell
\mathbf{n}	Surface normal vector
p	Pressure
\mathbf{p}	Probability
P_{o}	Characteristic pressure
$\text{Pé} = U_{\text{o}}L_{\text{o}}/D$	Péclet number
Q	Flow rate
$q_{j\ell}$	Generalized wavenumber
$R = w/a$	Channel aspect ratio
\mathbf{r}	Position vector
$\mathbf{r}_{\perp} = (y, z)$	Cross-sectional position vector
$\mathbf{r}_{\perp}^{\text{o}}$	Initial cross-sectional position of droplet
\bar{r}	Average cell radius
S	Secretion/reaction rate
$\text{Sc} = \nu/D$	Schmidt number
\mathcal{S}	Cell state variable
s	Scale parameter of GEV distribution
T_{o}	Characteristic time
t	Time
U_{o}	Characteristic velocity
u	Axial velocity component
\mathcal{V}	Volume
\mathbf{v}	Velocity
W	Decay rate of g

Continued on next page

Symbol	Description
w	Channel half-width
w_p	Pseudopod width
$Wo = \sqrt{L_o^2 \tilde{\omega}_o / \nu}$	Womersley number
\bar{x}	Solute center of mass
\mathbf{x}_c	Position of model cell center-of-mass
x, r, φ	Cylindrical coordinates
x, y, z	Cartesian coordinates
α_m, α_{ff}	Fluid momentum equilibration rate
α	Angle between pseudopod formation and direction of motion
Γ	Pre-factor
Γ_{cell}	Surface density of cells
γ	Cell friction coefficient
Δt_{samp}	Sampling interval
$\delta(x)$	Dirac delta function
$\delta_{n,m}$	Kronecker delta
ε_ℓ	ℓ th velocity component amplitude
ϵ	Cell collision distance
$\zeta(x)$	Riemann zeta function
η	Dynamic viscosity
$\Theta(x)$	Heaviside theta function
θ	Angle of pseudopod formation to nearest neighbor cell
κ	Kurtosis
λ_n	n th diffusion rate eigenvalue
μ_p	p th moment of conc. about the mean
ν	Kinematic viscosity of solvent
Ξ_n	Convexity of node n
ξ	Shape parameter of GEV distribution
$\xi_{i,n}$	n th root of Bessel function J_i
Π	Statistical weight
ρ	Radial distance from a cell
σ_G^2	Variance of Gaussian kernel
$\tau_0 = 2\pi/\omega_o$	Oscillation period
τ_c	Pseudopod contact time
τ_{lag}	Lag time
τ_p	Persistence time of directionality
τ_{pseud}	Pseudopod life time
Φ	Fraction of differentiated cells
ϕ	Weight factor for directional autocorrelation
$\chi_{\text{plate}}, \chi_{\text{rect}}$	Diffusivity enhancement
ψ_n	Outer angle of node n
Ω	Cross section
$\omega_o = Wo^2 Sc$	Base frequency, non-dimensionalized

Continued on next page

Symbol	Description
$\tilde{\omega}_0$	Base frequency, dimensionfull

Chapter 1

Introduction

Life is of an amazing complexity! It ranges across many forms, sizes and habitats, and routinely performs tasks such as autonomous behavior, reproduction and healing which apparently defy the normal laws of physics. However, all organisms consist of biological cells — or simply cells — which are the functional and structural unit of biology. Whether manifest as a single-celled organism such as a single bacterium, or consisting of the estimated 5×10^{10} cells making up the human body, all organisms are currently too complicated to be fully understood [73].

A uniting feature among all cells is that they sense and respond to their environment. Typically this information about the environment is carried by chemical species dissolved in the surrounding fluid. Under exposure of any such specific signal, the cell will *quantitatively* sense the concentration of the signal in its vicinity and respond equally quantitatively in a manner depending on the exact level of the sensed signal. These pre-programmed responses are (typically) mediated by a large number of intracellular reactions involving many interaction and reacting chemical species. The upshot is that the cellular behavior one observes does not simply reflect personality on the part of the cell but is instead a “deterministic” response in the sense that identical cells, which are additionally in the same state, will produce quantitatively similar responses to the same input.

Clearly, a high level of control of the near-cell environment is essential to unravel the logic underlying cellular responses and thereby make biology a truly quantitative science. Advances in engineering over the last twenty years have resulted in the field of microfluidics which have made experimentally accessible the sought-after high degree of control of the near-cell environment by exploiting the predictability of laminar flow. However, obtaining full control of the near-cell environment, i.e. completely controlling the signal to which the cells are subjected, requires detailed analysis of the involved physical processes to which the signaling molecules are exposed. These dissolved signaling molecules (also referred to as the solute) will diffuse, engage in chemical reactions and are advected¹ by the flow of the fluid (the solvent) into which they are dissolved, effects which together can lead to

¹This process is referred to by both of the etymologically identical words “advection” and “convection” in the literature. However, the word “convection” is used synonymously with “convection of heat” by the heat transport community, so the term “advection” will be used throughout this thesis to avoid confusion.

very complex signal distributions. In addition, cellular responses may also influence these signals — e.g. secretion of addition signals which interact with the supplied signal in the bulk — which complicate the situation further.

The deterministic nature of cellular responses and their hinging on interacting signaling molecules evolving in space and time means that the quantitative basis and indisputable laws of physics provide a good starting point for analyzing and interpreting quantitative data of cellular responses in order to answer fundamental problems in biology. Especially the physics credo of simple, transparent models capturing the essential features of a phenomenon using a limited number of unknown parameters have previously been applied with great success [132, 47, 115, 103, 68]. This contrasts the exhaustive models found in biology, see e.g. [114], that make detailed predictions for many different features but usually require a number of parameters which are not readily available and could suffer from omission of reactions not yet identified. The hope is that the lessons learned from the simple physics models reveal general features which eventually can be used to understand the complex reality of real life.

The studies in this thesis aim at understanding both the distribution of solute found under the influence of advection-diffusion-reaction dynamics, and also investigate how these distributions affect the cellular behavior using physics-based approaches. The work also details a personal journey of scientific interest going from the former to the latter. To complete this work, the author has interacted with a diverse set of scientists from engineering, experimental biology, theoretical and experimental physics. In addition, much of the work has involved the development and use of automated image analysis tools for extracting quantitative data for analysis and subsequent modeling. This combined experimental and theoretical approach have proven to form a strong tool for elucidating fundamental biological questions.

1.1 Thesis outline

The thesis consists of 5 chapters. Some of the work has already been published elsewhere, and the rest will appear, as listed in Sec. 1.2. A brief overview highlighting the contributions of the author of the present thesis will be given in the introduction to each chapter along with a list of relevant collaborators.

A list of the titles and a short outline of the subjects treated is given below.

- **Chapter 2 — Advection-diffusion: Transient Taylor–Aris dispersion in time-dependent flows.** In this chapter, we study theoretically the dispersion of a concentration field arising as a consequence of the combined effects of unsteady advection and diffusion. Starting from the well-known advection-diffusion equation, a general and closed-form mathematical solution for the so-called Taylor–Aris dispersion coefficient is obtained by combining Aris’s method of statistical moments with Fourier expansion in time and expansion of all spatial dependencies in diffusion eigenfunctions. Our theory extends previous results for single-frequency flows and its mathematical structure furthermore allows for physical interpretation contrary to previous theories. We identify a number of previously undiscovered effects, and show

that they fundamentally are all results of the competing physical processes of the diffusion of solute, diffusion of momentum and local velocity variations. The results have implications for the transport of nutrients, drugs, etc. in the blood stream as well as for mixing in many industrial applications.

- **Chapter 3 — Diffusion-reaction: Migration of cells in a social context.** This chapter presents a combined theoretical and experimental study on the influence of neighboring cells in shaping single-cell migration behavior. Using high-resolution image data with subcellular resolution of migration cells at various cell densities, we find that while single-cell speed fluctuates substantially during migration, single-cell speed distributions and directional autocorrelation series are surprisingly similar. Furthermore, increasing density only influences the directionality. Studying the statistics of the cell's migratory machinery — the force-generating membrane protrusions known as pseudopodia, which the cells use to transmit force to the substrate — we find that the cell cannot modulate these pseudopodia once they have formed, but can control where they form. Furthermore, we find evidence of a cell-secreted chemical that also influences pseudopod formation, which therefore becomes, in part, a diffusion-reaction process. To further investigate these effects, we develop a conceptually simple physics-based model that emphasizes pseudopod-driven motility of the single cell and takes the experimental pseudopod statistics as input. This model predicts the vast majority of the disparate migration features for the single cell, and furthermore also correctly predicts the dependence of these features on cell density. We therefore find that the varied single-cell behavior as well as the density-modulated behavior both arise as natural consequences of pseudopod-driven motility in a social context.
- **Chapter 4 — Advection-diffusion-reaction: Differentiation of adipose-derived stem cells into adipocytes.** In this chapter we study a problem of cell signaling using perfusion microfluidics and theoretical physics. Contrary to current beliefs, we find strong evidence that a previously unknown cell-secreted chemical is decisive in the commitment to the terminal adipocyte fate. This evidence is provided by non-trivial dependencies of single-cell differentiation on cell density, the addition of cell-secreted chemicals from parallel static batch experiments and perfusion flow rate. Furthermore, we find convincing evidence of non-trivial secretion of the purported chemical.
- **Chapter 5 — Conclusions and outlook.** We present general concluding remarks on our work and a discussion of the future directions of research which the author believe holds the most promise.

In addition to the thesis projects, the author has also worked on a final project during the doctoral studies concerning the use of pulsatile microfluidics as an analytical tool for analysis and application-specific optimization of microfluidic network topology. This work, which was initiated during the author's studies for the M.Sc. degree, has been omitted from the present thesis in the interest of space, and since it falls outside the scope of the

remaining parts. The results of the project were published in [140], which is included in Appendix D.

1.2 Publications

Published peer-reviewed papers

1. *Pulsatile microfluidics as an analytical tool for determining the dynamic characteristics of microfluidic systems*
Søren Vedel, Laurits Højgaard Olesen and Henrik Bruus
 Journal of Micromechanics and Microengineering **20**, 035026 1-11, 2010. Included in Appendix D.
2. *Transient Taylor–Aris dispersion for time-dependent flows in straight channels*
Søren Vedel and Henrik Bruus
 Journal of Fluid Mechanics **691**, 95-122, 2012. Included in Appendix E.
3. *Migration of cells in a social context*
Søren Vedel, Savaş Tay, Darius M. Johnston, Henrik Bruus and Stephen R. Quake
 Proceedings of the National Academy of Sciences of the USA (doi: 10.1073/pnas.1204291110).
 Included in Appendix F.

Papers under review

4. *Time-dependent Taylor–Aris dispersion of an initial point concentrations*
Søren Vedel, Emil Hovad and Henrik Bruus
sub judice for the Journal of Fluid Mechanics (submitted October 18, 2012).
5. *The role of paracrine and autocrine signaling in the early phase of adipogenic differentiation of adipose-derived stem cells*
 Mette Hemmingsen, **Søren Vedel**, Peder Skafte-Pedersen, David Sabourin, Philippe Collas, Henrik Bruus and Martin Dufva
sub judice for PLoS ONE (submitted December 18, 2012).

First-author conference proceedings

1. *Taylor–Aris dispersion of droplets (point concentrations)* by Søren Vedel, Emil Hovad and Henrik Bruus, Annual meeting of the APS Division of Fluid Dynamics, San Diego, CA, USA, Paper G6.00007, Bull. Am. Phys. Soc. **57**, 17, 2012.
2. *Cell migration in social context* by Søren Vedel, Savaş Tay, Darius M. Johnston, Henrik Bruus and Stephen R. Quake, Growth and Form: Pattern Formation in Biology, Aspen Center for Physics, Aspen, CO, USA, 2012.
3. *Motile behavior of cells in social context* by Søren Vedel, Savaş Tay, Darius M. Johnston, Henrik Bruus and Stephen R. Quake, Signals and Space: Spatio-Temporal Patterns in Simple Bio-Systems, Copenhagen, Denmark, 2011.

4. *Taylor–Aris dispersion in time-dependent laminar channel flows* by Søren Vedel and Henrik Bruus, Annual meeting of the APS Division of Fluid Dynamics, Long Beach, CA, USA, Paper EM.00001, Bull. Am. Phys. Soc. **55**, 16, 2010.
5. *Systems-level analysis of AC microfluidics and the problem of trapped gas bubbles* by Søren Vedel, Laurits Højgaard Olesen and Henrik Bruus, Annual meeting of the APS Division of Fluid Dynamics, Minneapolis, MN, USA, Paper LQ.00007, Bull. Am. Phys. Soc. **54**, 19, 2009.
6. *kHz microfluidics - An analytical tool for systems-level analysis in microfluidics* by Søren Vedel, Laurits Højgaard Olesen and Henrik Bruus, combined 1st Nordic Meeting in Physics and Annual Meeting of the Danish Physical Society, Kongens Lyngby, Denmark, 2009.

Invited seminars

1. *Cell migration in social context* by Søren Vedel, Savaş Tay, Darius M. Johnston, Henrik Bruus and Stephen R. Quake, Center for Models of Life at the Niels Bohr Institute (department of physics), University of Copenhagen, Denmark (January 19, 2012).
2. *Transient Taylor–Aris dispersion in time-dependent flows* by Søren Vedel and Henrik Bruus, Department of Mathematics, Technical University of Denmark (April 7, 2011).
3. *Transient Taylor–Aris dispersion in time-dependent flows* by Søren Vedel and Henrik Bruus, Department of Applied Mathematics, University of North Carolina, Chapel Hill (January 21, 2011).

1.3 Supervision

Main supervisor

Bubble removal by diffusion and porous flow by Jais Andreas Breusch Angel, 5 ECTS M.Sc. level special course, June 2009

Advection-reaction-diffusion studies in microfluidic biochips by Tobias Dirksen, 5 ECTS M.Sc. level special course, September 2010–January 2011

Co-supervisor

Characterization of microfluidic microchip for cancer research
B.Sc. thesis by Fatima AlZahra’a Alatraktchi, January–July 2011

Taylor dispersion in time dependent flow [70]
M.Sc. thesis by Emil Hovad, February–September 2011

Modeling of cell reactions and advection-diffusion processes in microfluidic biochips [91]
M.Sc. thesis by H. Kasper W. Lipsø, December 2011–July 2012

Chapter 2

Advection-diffusion: Transient Taylor–Aris dispersion in time-dependent flows

In this chapter we consider a problem of solute transport where the interplay of advection and diffusion results in increased solute dispersion. Although this so-called Taylor–Aris dispersion phenomenon has been studied for the last half century, a surprising lack of physical understanding of the roles of the basic processes remains. A general theory is developed in this chapter which includes the previously undescribed effects of unsteady flow and non-uniform initial solute distribution. This theory substantially extends all previous results, which are shown to be special cases, and the theory is used to shed light on these unknown phenomena.

The work presented in this chapter has been carried out by the author in collaboration with Henrik Bruus. The treatment of droplets of Sec. 2.5 was furthermore also done in collaboration with M.Sc. student Emil Hovad, whose research project the author co-supervised. The work in Secs. 2.2–2.4 on the general theory and its application to steady and unsteady flows for transverse uniform initial solute distributions has been published in [139], which can also be found in Appendix E. A second manuscript by the author, Emil Hovad and Henrik Bruus describing the results of droplet dispersion is under review for publication in the *Journal of Fluid Mechanics*.

2.1 Background

In his seminal work [129], G.I. Taylor clarified the basic physical principles for the dispersion of the concentration profiles of solutes in a steady Poiseuille flow which now bears his name. Contrary to the case without flow, where solute dispersion is due purely to molecular diffusion (Fig. 2.1(a)), the transverse speed variations from the solvent flow sets up transverse concentration gradients, and therefore by Fick’s law, net transverse diffusion (Fig. 2.1(b)). This enhances the transverse mixing and leads to increased axial dispersion (Fig. 2.1(c)). For a channel with a circular cross section of radius a , Taylor derived the now classical ex-

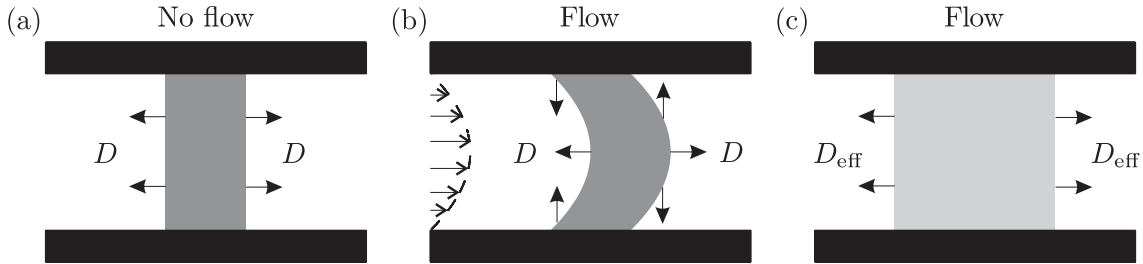


Figure 2.1: Schematic of the Taylor–Aris dispersion phenomenon. (a) Without flow, a strip of solute (gray) between channel walls (black) will be dispersed only due to molecular diffusion characterized by the diffusivity D . (b) Exposed to a flow, the solute will be stretched differently due to the variable flow speed, which sets up concentration gradients transverse to the flow direction. A diffusive flux results wherever concentration gradient arise, so molecular diffusion now acts both along, and transverse to, the direction of the flow. (c) The transverse diffusion combines with the flow to enhance the axial diffusion leading to an apparent “effective diffusivity” D_{eff} in the flow direction which exceeds the molecular diffusivity D .

pression for the effective diffusivity $D_{\text{eff}} = (1 + \text{Pé}^2/48)D$, where $\text{Pé} = aU_o/D$ is the Péclet number for the system measuring the relative effects of advection to diffusion, U_o being the average solvent flow speed and D the solute molecular diffusivity. Since the effect requires both advection and diffusion, one would in general expect a dependence on Pé as well as the cross-sectional geometry. Extensions of this so-called “shear-enhanced” dispersion to many different systems over the years for both solute and other advected properties such as heat have confirmed these expectations [48, 113, 33, 45, 137, 34, 61, 24, 60, 102, 27, 60, 142, 27], with the most noteworthy extension having been provided by Aris using the elegant method of statistical moments detailed below [10].

Despite the vast body of previous work on this subject, a number of surprisingly fundamental issues remain unresolved.

1. *The effect of an unsteady flow.* In many practical applications [122, 140] flows are unsteady and therefore typically generate more speed variations over time than their steady counterparts. That this can lead to increased mass transfer has long been recognized by the chemical engineering community, see e.g. [130, 95] for results on pulsating flow, yet most physical interpretations and quantitative aspects of these additional speed variations remain to be understood. This is highly surprising since the first mention of Taylor–Aris dispersion in time-dependent flows dates back to 1960 [11], and given the large volume of studies dedicated to steady flows. Time-dependent phenomena that have been studied are non-transient, single-frequency pulsating flows [67, 32, 145, 131, 72] and the first examples of transient-flow analysis of single-frequency flows by Mazumder and coworkers [99, 15]. These studies have focused more on the mathematics than the physics.

A wish to understand the effects of unsteady flows on the dispersion was the original motivation for this work. In an extension of the author’s research for the M.Sc. degree, an investigation of the dispersion from a time-varying peristaltic pump [122] led to the development of the theoretical framework presented in this chapter. The analysis of the pump is presented in Sec. 2.4.3.

2. *The effect of cross-sectional geometry.* It has been known for almost as long as Taylor’s original paper that the dispersion coefficient varies with the cross-section. However, why dispersion in channels with cross-sections of more than one length scale (such as the rectangle or the ellipse) can depend on either the short distance or the long [46, 4, 22] remains an open question.
3. *Dispersion of droplets and the dependence on initial distribution.* Almost all previous work has focused on the important special case of transverse uniform initial distribution of solute. Notable exceptions are a few studies of droplets (or initial point concentrations), which can be said to provide a logical next step, in addition to being no less important in neither practical nor theoretical regards (see e.g. [51]). The first mention of the problem focused on steady linear shear flow [53, 107], which was followed by work neglecting the confining walls for a time-oscillating linear shear flow [87] and steady Poiseuille flow in a circular cross-section [82], before Camassa *et al.* recently presented steady-flow solutions for both the parallel plates and circular cross-sections that did include the physical boundary conditions at the wall [27]. These few cases, which report of “anomalous” transient diffusion, provide a very limited physical insight to the effects particular to a non-uniformly transverse distribution such as an initial point concentration, and a general theoretical understanding of these matters is lacking.

In the following, we first derive the theoretical solution to the Taylor–Aris dispersion problem in any time-dependent flow with any initial solute distribution is presented. This solution is then used in the later parts of the chapter to investigate these fundamental questions.

2.2 The physical model

In the following we establish our physical model together with our notation and present the well-known method of moments for calculating the dispersion coefficient D_{eff} .

We consider a long, straight channel parallel to the x -axis, and assume that it is translational invariant along this axis with an arbitrary, but constant, cross section Ω . The coordinates in the transverse yz -plane are denoted $\mathbf{r}_\perp = (y, z)$, so that the full coordinates are written as $\mathbf{r} = (x, \mathbf{r}_\perp)$, and likewise for the gradient operator ∇ and the Laplace operator ∇^2 ,

$$\mathbf{r} = (x, \mathbf{r}_\perp), \quad \text{with} \quad \mathbf{r}_\perp = (y, z), \quad (2.1a)$$

$$\nabla = \mathbf{e}_x \partial_x + \nabla_\perp, \quad \text{with} \quad \nabla_\perp = \mathbf{e}_y \partial_y + \mathbf{e}_z \partial_z, \quad (2.1b)$$

$$\nabla^2 = \partial_x^2 + \nabla_\perp^2, \quad \text{with} \quad \nabla_\perp^2 = \partial_y^2 + \partial_z^2. \quad (2.1c)$$

The channel has length \mathcal{L} , cross-sectional area $\mathcal{A} = \int_\Omega d\mathbf{r}_\perp 1$, and volume $\mathcal{V} = \mathcal{L}\mathcal{A}$. Our analysis involves expansion of the spatial dependence of functions into linear combinations of suitably chosen basis functions. For notational convenience we shall therefore rely on a Hilbert-space representation using the compact Dirac bra-ket notation, employed more

often in quantum mechanics [43] than in fluid mechanics [25, 98, 97]. For any pair of functions $f(x, \mathbf{r}_\perp, t)$ and $g(x, \mathbf{r}_\perp, t)$ represented by the bra $\langle f|$ and the ket $|g\rangle$, the inner product $\langle f|g\rangle$ is defined by the following integral, where the asterisk indicates complex conjugation,

$$\langle f|g\rangle = \frac{1}{\mathcal{V}} \int_{-\frac{1}{2}\mathcal{L}}^{\frac{1}{2}\mathcal{L}} dx \int_{\Omega} d\mathbf{r}_\perp f^*(x, \mathbf{r}_\perp, t) g(x, \mathbf{r}_\perp, t), \quad (2.2)$$

This definition also includes the case, where the involved functions only depend on the transverse coordinates \mathbf{r}_\perp . For $f_\perp(\mathbf{r}_\perp, t)$ and $g_\perp(\mathbf{r}_\perp, t)$ we obtain

$$\langle f_\perp|g_\perp\rangle = \frac{1}{\mathcal{A}} \int_{\Omega} d\mathbf{r}_\perp f_\perp^*(\mathbf{r}_\perp, t) g_\perp(\mathbf{r}_\perp, t), \quad (2.3)$$

as the x -integration trivially gives unity. The inner product is linear

$$\langle f|A_1g_1 + A_2g_2\rangle = A_1\langle f|g_1\rangle + A_2\langle f|g_2\rangle, \quad (2.4)$$

and given the complex representation Eq. (2.10) of the real velocity field with $u_{-\ell} = u_\ell^*$, we shall often use that

$$\langle u_\ell|g\rangle = \langle g|u_\ell\rangle^* = \langle g^*|u_{-\ell}\rangle, \quad (2.5a)$$

$$\langle u_\ell e^{i\ell\omega_o t}|g\rangle = e^{-i\ell\omega_o t} \langle u_\ell|g\rangle. \quad (2.5b)$$

The bra-ket notation is particularly compact when working with basis function expansions. A set of functions $|f_n\rangle$, $n = 0, 1, 2, \dots$, is said to form an orthonormal basis when it fulfills the so-called completeness and orthonormal conditions given by

$$\sum_{n=0}^{\infty} |f_n\rangle\langle f_n| = 1, \quad \text{and} \quad \langle f_m|f_n\rangle = \delta_{m,n}, \quad (2.6)$$

respectively, where by the definition of the Kronecker delta $\delta_{m,n} = 1$ for $m = n$, and 0 for $m \neq n$. Any function $|g\rangle$ can formally be expressed by an expansion in this basis as

$$|g\rangle = \sum_{n=0}^{\infty} a_n |f_n\rangle, \quad (2.7a)$$

$$a_m = \langle f_m|g\rangle, \quad m = 0, 1, 2, \dots \quad (2.7b)$$

Here Eq. (2.7b) follows from multiplication of Eq. (2.7a) from the left by $\langle f_m|$ and using Eq. (2.6). We finally note that since the functions f and g in general depend on time, the inner product may also depend on time.

From now on we use dimensionless quantities defined in terms of the characteristic transverse length L_o , often the shortest distance a from the center line of the channel to the wall, the diffusion time T_o from the molecular diffusivity D of the solute, the advection velocity U_o from a scale U_{char} in the time-dependent flow, and the average solute concentration C_o of the solute concentration field $c(x, \mathbf{r}_\perp, t)$,

$$L_o = a, \quad T_o = \frac{L_o^2}{D}, \quad U_o = U_{\text{char}}, \quad C_o = \langle 1|c(x, \mathbf{r}_\perp, 0)\rangle. \quad (2.8)$$

The specific choice of U_{char} in Eq. (2.8) is not unique: for a steady flow it could be taken as the mean velocity; for a single-frequency oscillating flow as the RMS-velocity.

Denoting the base angular frequency of the solvent flow $\tilde{\omega}_o$ (rad/s), the system is characterized by three dimensionless numbers: the Péclet number Pé (the ratio of advection speed to mass diffusion speed), the Schmidt number Sc (the ratio of momentum diffusion speed to mass diffusion speed), and the Womersley number Wo (the square root of the ratio of oscillation speed at frequency $\tilde{\omega}_o$ to momentum diffusion speed for a Newtonian fluid of kinematic viscosity ν),

$$\text{Pé} = \frac{L_o U_o}{D}, \quad \text{Sc} = \frac{\nu}{D}, \quad \text{Wo} = \sqrt{\frac{L_o^2 \tilde{\omega}_o}{\nu}}. \quad (2.9)$$

For non-Newtonian fluids with an internal molecular stress relaxation time τ_{mol} , the Deborah number $\text{De} = \tau_{\text{mol}} \omega_o$ would appear, but this is not treated in the present work.

2.2.1 The time-dependent velocity field

We take the velocity field to be any axis-parallel channel flow $\mathbf{v} = u(\mathbf{r}_\perp, t) \mathbf{e}_x$, and represent $u(\mathbf{r}_\perp, t)$ by a standard Fourier series with components u_ℓ for each higher harmonic $\ell \omega_o$ (ℓ being an integer) in the dimensionless base frequency $\omega_o = \tilde{\omega}_o T_o = \text{Wo}^2 \text{Sc}$,

$$u(\mathbf{r}_\perp, t) = \sum_{\ell=-\infty}^{\infty} u_\ell(\mathbf{r}_\perp) e^{i\ell\omega_o t}, \quad (2.10)$$

where complex notation is introduced for the time with $i = \sqrt{-1}$. By demanding that $u_{-\ell}(\mathbf{r}_\perp) = u_\ell^*(\mathbf{r}_\perp)$, we ensure that the velocity field is real.

The fluid responds to changes in external conditions on a time scale which depends on its internal stress relaxation time, and whether fluid inertia dominates may be estimated by the product of the driving frequency $\tilde{\omega}_o$ and this internal time scale. For Newtonian fluids the stress relaxation time scale is given by the momentum diffusion time $1/\alpha_\Pi$, related to the momentum diffusion rate α_Π , which is derived from the momentum diffusion equation $\partial_t u = \text{Sc} \nabla_\perp^2 u$ and given by

$$\alpha_\Pi \propto \text{Sc} \quad (2.11)$$

with a geometry-dependent proportionality factor. The Schmidt number Sc appears since the time scale has been chosen to be the transverse mass diffusion time, and not the momentum diffusion time. Note that since $\alpha_\Pi \propto \text{Sc}$, the square of the Womersley number is proportional to the ratio of the dimensionless driving frequency ω_o and the momentum diffusion equilibration rate,

$$\text{Wo}^2 = \frac{\omega_o}{\text{Sc}} \propto \frac{\omega_o}{\alpha_\Pi}. \quad (2.12)$$

While we only require the existence of a Fourier series representation of the velocity field for the theory we develop below, expressions for the Fourier coefficients u_ℓ are needed for its application to practical problems. Unless explicitly stated otherwise, we will therefore restrict the practical applications to the incompressible Newtonian fluids of kinematic

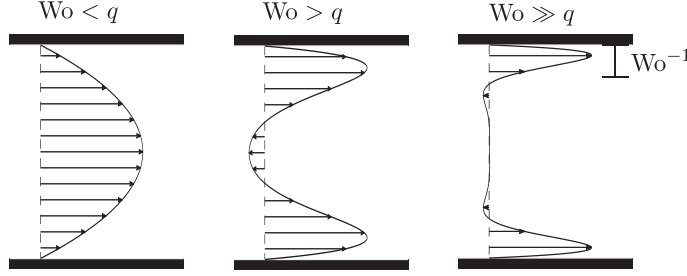


Figure 2.2: The changes in the velocity profile in pulsatile flow. The harmonically oscillating profile is the Poiseuille parabola as long as the Womersley number Wo measuring momentum diffusion time relative to the oscillation frequency $\tilde{\omega}_o$ is below a critical value q , where q is some number on the order unity which depends on the cross-sectional geometry through the momentum relaxation rate α_{fl} . When Wo exceeds q , momentum no longer has time to relax across the entire cross-section, and a boundary layer of width Wo^{-1} forms close to the wall. Furthermore, the fluid in the channel center oscillates out of phase with the boundary layer fluid. Naturally the width of the boundary layer decreases at higher Wo .

viscosity (or momentum diffusivity) ν in the laminar regime which are governed by the time-dependent Stokes equation,

$$\partial_t u(\mathbf{r}_{\perp}, t) = \text{Sc} \left[\nabla_{\perp}^2 u(\mathbf{r}_{\perp}, t) + \frac{1}{\mathcal{L}} \Delta p(t) \right]. \quad (2.13)$$

Here, $\Delta p(t)$ is the time-dependent pressure drop along the channel of length \mathcal{L} , resolved by the components $\varepsilon_{\ell} \Delta p e^{i\ell\omega_o t}$ (ε_{ℓ} is a dimensionless amplitude) with the dimensionless base frequency $\omega_o = Wo^2 \text{Sc}$, and the dimensionfull pressure has been normalized by the shear-induced pressure $P_o = \frac{\eta U_o}{L_o}$. The linearity of this equation allows us to solve the flow problem analytically and thereby obtain the Fourier coefficients u_{ℓ} and the momentum diffusion rate α_{fl} . The velocity components u_{ℓ} depend implicitly on α_{fl} through Wo by Eq. (2.12).

2.2.2 Physics of pulsatile flow

By representing the velocity field as a Fourier series, it is at this stage instructive to shortly describe the flow physics of each of the harmonically oscillating components in the series, while saving the mathematical details of solving Eq. (2.13) with a harmonically oscillating pressure difference Δp for later. A more thorough discussion of the physics of pulsatile flow was given in our paper [140], which is enclosed in Appendix D, so here follows a condensed discussion. The basic solution of pulsatile flow in a circular channel is due to Womersley [146].

In addition to the temporal oscillations of the fluid, its velocity profile varies depending on the relevance of fluid inertia, where this relevance is expressed by the Womersley number according to Eq. (2.12). Thus, at the limit of negligible inertia $Wo \lesssim q$, where q is some number on the order unity which depends on the cross-sectional geometry¹ through α_{fl} , the velocity profile is the Poiseuille parabola because momentum is in a quasi-steady state

¹For a circular channel we will show later that $q = \xi_{0,1}$, where $\xi_{i,n}$ is the n th root to the Bessel function of the first kind of order i , since $\alpha_{\text{fl}} = \text{Sc} \xi_{0,1}^2$.

at all times, see Fig. 2.2(a). In the inertially dominated regime $Wo \gtrsim q$ momentum no longer has time to relax the changes imparted by the oscillating pressure; momentum can no longer diffuse completely across the channel cross-section and relax the system to the Poiseuille parabola before the pressure changes again. Thus, a boundary layer close to the wall will form which contains the fluid that has reached a steady state, see Fig. 2.2(b) and (c). The fluid in this layer will remain in phase with the driving pressure exactly because it has relaxed, and width of this layer is about Wo^{-1} . The fluid in the channel center, which has not relaxed, will oscillate out of phase.

For cross-sections with two inherent length scales (e.g. rectangle or ellipse), these relaxation effects will occur for both length scales, but with different limiting values due to the different diffusion times in the two directions.

2.2.3 The advection-diffusion equation

The transport of the diffusive solute concentration c in the above-mentioned velocity field Eq. (2.10) is given by the dimensionless advection-diffusion equation,

$$\partial_t c(x, \mathbf{r}_\perp, t) + \text{Pé} u(\mathbf{r}_\perp, t) \partial_x c(x, \mathbf{r}_\perp, t) = (\partial_x^2 + \nabla_\perp^2) c(x, \mathbf{r}_\perp, t). \quad (2.14)$$

The corresponding boundary conditions are

$$\mathbf{n} \cdot \nabla_\perp c = 0, \text{ on all walls,} \quad (2.15a)$$

$$c(x, \mathbf{r}_\perp, 0) = \tilde{c}(x, \mathbf{r}_\perp), \quad (2.15b)$$

$$x^s \partial_x^q c \rightarrow 0, \text{ for } |x| \rightarrow \frac{\mathcal{L}}{2} \text{ and } s, q = 0, 1, 2, \dots, \quad (2.15c)$$

where \mathbf{n} is the surface normal and \tilde{c} is a given initial concentration field, and condition (2.15c) states that all spatial gradients in c as well as c itself vanish far away along the axis of the channel.

2.2.4 Aris's method of statistical moments

The great insight of Aris was to realize that the advection-diffusion problem can be rewritten as a series of equations for statistical moments of the solute distribution, which then can be solved sequentially [10]. More information about the distribution of c is added with each moment, however, the information contained in each moment remains valid no matter how many moments have been determined. In addition, some of the lower moments have direct physical interpretations.

Definition of the statistical moments

The p th axial moment $c_p(\mathbf{r}_\perp, t)$ of the solute concentration field $c(x, \mathbf{r}_\perp, t)$ and the associated full moment $M_p(t)$ are defined as

$$c_p(\mathbf{r}_\perp, t) = \frac{1}{\mathcal{L}} \int_{-\frac{1}{2}\mathcal{L}}^{\frac{1}{2}\mathcal{L}} dx x^p c(x, \mathbf{r}_\perp, t), \quad p = 0, 1, 2, \dots, \quad (2.16a)$$

$$M_p(t) = \langle x^p | c \rangle = \frac{1}{\mathcal{A}} \int_{\Omega} d\mathbf{r}_\perp c_p(\mathbf{r}_\perp, t), \quad p = 0, 1, 2, \dots \quad (2.16b)$$

The axial moments c_p correspond to the average of c along the length of the channel weighted by x^p , and the full moments M_p are the cross-sectional averages of c_p .

Taking the time derivative of Eqs. (2.16a) and (2.16b) and using the advection-diffusion equation (2.14), we obtain the recursive equations of motion for c_p and M_p ,

$$\partial_t c_p(\mathbf{r}_\perp, t) - \nabla_\perp^2 c_p(\mathbf{r}_\perp, t) = p(p-1)c_{p-2}(\mathbf{r}_\perp, t) + \text{Pé} u(\mathbf{r}_\perp, t) p c_{p-1}(\mathbf{r}_\perp, t), \quad p = 0, 1, 2, \dots, \quad (2.17a)$$

$$\frac{dM_p(t)}{dt} = p(p-1)\langle 1 | c_{p-2} \rangle + \text{Pé} p \langle u | c_{p-1} \rangle, \quad p = 0, 1, 2, \dots, \quad (2.17b)$$

with the boundary and initial conditions

$$\mathbf{n} \cdot \nabla_\perp c_p = 0, \text{ on all walls}, \quad (2.18a)$$

$$c_p(\mathbf{r}_\perp, t) < \infty, \quad (2.18b)$$

$$c_p(\mathbf{r}_\perp, 0) = \tilde{c}_p(\mathbf{r}_\perp), \quad (2.18c)$$

$$M_p(0) = \langle x^p | \tilde{c} \rangle. \quad (2.18d)$$

M_0 corresponds to the unit norm of c , while M_1 is the time-dependent axial center of mass \bar{x} of c ,

$$M_0 = \langle 1 | c \rangle = 1, \quad (2.19a)$$

$$M_1 = \langle x | c \rangle = \bar{x}(t). \quad (2.19b)$$

It is also useful to define the p th moment μ_p about the center of mass,

$$\mu_p(t) = \langle (x - \bar{x})^p | c \rangle, \quad (2.20)$$

and by the linearity, Eq. (2.4), we find for $p = 0, 1$ and 2 ,

$$\mu_0(t) = \langle 1 | c \rangle = 1, \quad (2.21a)$$

$$\mu_1(t) = \langle (x - \bar{x}) | c \rangle = 0, \quad (2.21b)$$

$$\mu_2(t) = \langle (x - \bar{x})^2 | c \rangle = M_2(t) - M_1(t)^2. \quad (2.21c)$$

In particular μ_2 is of key interest to this work, because it relates to the time-dependent spatial variance of the solute concentration and thus to the solute diffusivity D and the effective diffusivity D_{eff} . Other works have been concerned with the skewness μ_3 of the solute distribution [16, 27].

Effective diffusivity and statistical moments

For a vanishing velocity field, $u = 0$, the second moment μ_2 relates to the diffusivity D of the solute by $d\mu_2/dt = 2D$. Here we derive this result in dimensionless form, $d\mu_2/dt = 2$, using the bra-ket notation:

$$\frac{d\mu_2}{dt} = \langle (x - \bar{x})^2 | \partial_t c \rangle - 2 \langle (x - \bar{x}) | c \rangle \frac{d\bar{x}}{dt} = \langle (x - \bar{x})^2 | \nabla^2 c \rangle - 2\mu_1 \frac{d\bar{x}}{dt} = 2 \langle 1 | c \rangle = 2, \quad (2.22)$$

where in the last term we have integrated by parts twice and used the boundary conditions Eqs. (2.15a) and (2.15c). This corresponds to the well-known result for diffusion in one dimension, $(\Delta x)^2 = 2Dt$, with $\mu_2 \sim (\Delta x)^2$.

When the solvent velocity field u is nonzero the time-dependence of the variance is no longer linear. However, by a traditional generalization [10, 16, 11, 99, 32, 24, 27, 87] the dispersion or effective diffusivity $D_{\text{eff}}(t)$ is defined as the time-derivative of the axial variance $\mu_2(t)$

$$D_{\text{eff}}(t) = \frac{1}{2} \frac{d\mu_2}{dt} = \frac{1}{2} \frac{dM_2}{dt} - M_1 \frac{dM_1}{dt}, \quad (2.23)$$

Using this definition corresponds to describing the dispersion about the moving center-of-mass as a diffusion process, with all deviations from pure diffusion lumped into D_{eff} .

The main goal of this chapter is to solve Eq. (2.23) for general time-dependent flows in straight channels of arbitrary, constant cross-section, and to study how D_{eff} depends on the physical frequencies and relaxation rates of the systems.

Anomalous diffusion

To facilitate later discussions we make a small digression to introduce the terminology of what is in general referred to as “anomalous diffusion”. A normal diffusion process, characterized by a mean-squared displacement or variance proportional to time, arises whenever the motion is completely random. Any deviation from this t^s , $s = 1$ scaling signifies that the dispersion is no longer completely random, and is termed “anomalous”, with the terms “subdiffusive” and “superdiffusive” being used to describe dispersions which are slower ($s < 1$) and faster ($s > 1$), respectively, than pure diffusion. The special case ($s = 2$) corresponding to linear particle displacement with time is usually referred to as “ballistic”. It is in general recognized that the presence of external potentials leads to anomalous diffusion, see e.g. [49, 44]. In the Aris moment formulation, a purely diffusive motion about the center-of-mass results in $D_{\text{eff}} \propto t^0$, as shown in Eq. (2.22), while $D_{\text{eff}} \propto t$ corresponds to the ballistic regime.

2.3 Mathematical solution of the dispersion problem

The solution procedure of the problem was introduced by Barton [16] for steady flows and later extended to also include single-frequency harmonic pulsatile flows by Mukherjee and Mazumder [99]. The expressions presented in this section generalize their results to any given time-dependent flow. We derive them using the more compact bra-ket

formalism as follows: from Eq. (2.17a) with $p = 0$ and 1 we determine the axial moment $c_0(\mathbf{r}_\perp, t)$ and subsequently $c_1(\mathbf{r}_\perp, t)$. With these at hand, the full moment M_1 as well as the time derivatives $\frac{dM_1}{dt}$ and $\frac{dM_2}{dt}$ can be obtained from Eq. (2.17b) with $p = 1$ and 2, which then are fed into Eq. (2.23) to determine D_{eff} .

2.3.1 The zeroth axial moment and basis functions

We begin by analyzing the $p = 0$ axial moment equation (2.17a) for $c_0(\mathbf{r}_\perp, t)$,

$$(\partial_t - \nabla_\perp^2) |c_0(\mathbf{r}_\perp, t)\rangle = 0. \quad (2.24)$$

This moment fulfills the Neumann boundary condition

$$\mathbf{n} \cdot \nabla_\perp c_0 = 0, \text{ on all walls,} \quad (2.25)$$

and has the initial condition

$$c_0(\mathbf{r}_\perp, 0) = \tilde{c}_0(\mathbf{r}_\perp) = \int_{-\frac{1}{2}\mathcal{L}}^{\frac{1}{2}\mathcal{L}} dx \tilde{c}(x, \mathbf{r}_\perp). \quad (2.26)$$

Using separation of variables, the solution for $c_0(\mathbf{r}_\perp, t)$ can be written as the expansion

$$|c_0(\mathbf{r}_\perp, t)\rangle = \sum_{n=0}^{\infty} a_{0n} e^{-\lambda_n t} |f_n(\mathbf{r}_\perp)\rangle, \quad (2.27)$$

where the time-independent eigenfunctions $f_n(\mathbf{r}_\perp)$ with eigenvalues λ_n are defined by

$$(\lambda_n + \nabla_\perp^2) |f_n(\mathbf{r}_\perp)\rangle = 0, \quad n = 0, 1, 2, \dots, \quad (2.28a)$$

$$\mathbf{n} \cdot \nabla_\perp |f_n(\mathbf{r}_\perp)\rangle = 0, \text{ on all walls,} \quad (2.28b)$$

and form a complete orthonormal basis in the sense of Eq. (2.6). Note that the lowest $n = 0$ eigenvalue is zero, $\lambda_0 = 0$, with eigenfunction unity, $f_0(\mathbf{r}_\perp) = 1$, while for $n > 0$ the eigenvalues are positive, $\lambda_n > 0$. We remark that although the general advection-diffusion problem Eq. (2.14) is non-Hermitian, the reduced, transverse problem Eq. (2.28) is Hermitian, and we can take full advantage of the Dirac Hilbert-space formulation.

The expansion coefficients a_{0m} are found by multiplying Eq. (2.27) at $t = 0$ by $\langle f_m |$,

$$a_{0m} = \langle f_m | \tilde{c}_0 \rangle, \quad m = 0, 1, 2, \dots \quad (2.29)$$

For infinite time, all terms in Eq. (2.27) except $n = 0$ decay exponentially, and we obtain

$$|c_0(\mathbf{r}_\perp, \infty)\rangle = a_{00} |f_0(\mathbf{r}_\perp)\rangle = \langle 1 | \tilde{c}_0 \rangle |1\rangle = |1\rangle, \quad (2.30)$$

representing the state where, by diffusion, the solute concentration has spread out uniformly in space.

2.3.2 The first axial moment and basis functions

The $p = 1$ axial moment equation (2.17a) for $c_1(\mathbf{r}_\perp, t)$ is analyzed in a similar manner. Using that $c_0(\mathbf{r}_\perp, t)$ is now a known function, we have

$$(\partial_t - \nabla_\perp^2) |c_1(\mathbf{r}_\perp, t)\rangle = \text{Pé } u(\mathbf{r}_\perp, t) |c_0(\mathbf{r}_\perp, t)\rangle = \text{Pé } u(\mathbf{r}_\perp, t) \sum_{n=0}^{\infty} a_{0n} e^{-\lambda_n t} |f_n(\mathbf{r}_\perp)\rangle, \quad (2.31a)$$

where c_1 fulfills the Neumann boundary condition

$$\mathbf{n} \cdot \nabla_\perp c_1 = 0, \text{ on all walls,} \quad (2.31b)$$

and the initial condition

$$c_1(\mathbf{r}_\perp, 0) = \tilde{c}_1(\mathbf{r}_\perp) = \int_{-\frac{1}{2}\mathcal{L}}^{\frac{1}{2}\mathcal{L}} dx \, x \, \tilde{c}(x, \mathbf{r}_\perp). \quad (2.31c)$$

As pointed out by Barton [16], solving the inhomogeneous partial differential equation (2.31a) for c_1 requires some care regarding the null-space of the differential operator $(\partial_t - \nabla_\perp^2)$. Using the time Fourier expansion Eq. (2.10) of the velocity field $u(\mathbf{r}_\perp, t)$, we see that, due to the time-independent $\ell = 0$ component of u , the right-hand side of Eq. (2.31a) contains terms of the form $\text{Pé } a_{0n} u_0(\mathbf{r}_\perp) e^{-\lambda_n t} |f_n\rangle$, which have nonzero overlap with kets of the form $e^{-\lambda_n t} |f_n\rangle$. Noting that

$$(\partial_t - \nabla_\perp^2) [e^{-\lambda_n t} |f_n\rangle] = 0, \quad (2.32a)$$

$$(\partial_t - \nabla_\perp^2) [t e^{-\lambda_n t} |f_n\rangle] = e^{-\lambda_n t} |f_n\rangle, \quad (2.32b)$$

we thus expand $c_1(\mathbf{r}_\perp, t)$ in terms of both $e^{-\lambda_n t} |f_n\rangle$ and $t e^{-\lambda_n t} |f_n\rangle$, and seek solutions of $|c_1(\mathbf{r}_\perp, t)\rangle$ of the form

$$|c_1\rangle = \text{Pé} \sum_{n=0}^{\infty} \left[(\gamma_{1n} a_{0n} t + a_{1n}) |f_n\rangle + a_{0n} |\phi_n\rangle \right] e^{-\lambda_n t}, \quad (2.33)$$

where the unknown coefficients, γ_{1n} and a_{1n} , as well as the unknown time-dependent ket $|\phi_n(\mathbf{r}_\perp, t)\rangle$ are determined in the following. Inserting this trial expansion of $|c_1(\mathbf{r}_\perp, t)\rangle$ into the equation of motion (2.31a) leads to

$$(\partial_t - \nabla_\perp^2 - \lambda_n) |\phi_n(\mathbf{r}_\perp, t)\rangle = [u(\mathbf{r}_\perp, t) - \gamma_{1n}] |f_n(\mathbf{r}_\perp)\rangle. \quad (2.34)$$

The unknown ket $|\phi_n(\mathbf{r}_\perp, t)\rangle$ is now expanded in a Fourier series in time and a $|f_m(\mathbf{r}_\perp)\rangle$ series in space,

$$|\phi_n(\mathbf{r}_\perp, t)\rangle = \sum_{\ell=-\infty}^{\infty} \sum_{m=0}^{\infty} \beta_{mn}^\ell e^{i\ell\omega_o t} |f_m(\mathbf{r}_\perp)\rangle, \quad (2.35)$$

which upon insertion into Eq. (2.34) followed by multiplication by $\langle f_k|$ results in the following matrix equation for the coefficients β_{kn}^ℓ ,

$$(\lambda_k - \lambda_n + i\ell\omega_o) \beta_{kn}^\ell = \langle f_k | u_\ell | f_n \rangle - \gamma_{1n} \delta_{\ell,0} \delta_{k,n}. \quad (2.36)$$

Here, we see that the special case of the time-independent term $\ell = 0$, together with the diagonal term $k = n$, only allows a solution if we choose

$$\gamma_{1n} = \langle f_n | u_0(\mathbf{r}_\perp) | f_n \rangle, \quad (2.37)$$

while the β -coefficients are given by

$$\beta_{kn}^\ell = (1 - \delta_{\ell,0}\delta_{k,n}) \frac{\langle f_k | u_\ell(\mathbf{r}_\perp) | f_n \rangle}{\lambda_k - \lambda_n + i\ell\omega_o}. \quad (2.38)$$

Note that any value of β_{nn}^0 is allowed, so for convenience we set it to zero. Moreover, $\beta_{kn}^{-\ell} = (\beta_{kn}^\ell)^*$ ensures real values of the resulting fields.

Lastly, the coefficients a_{1n} are found using the initial condition (2.31c) in Eq. (2.33) at $t = 0$, multiplying by $\langle f_k |$, and finally exchanging the indices n and k ,

$$a_{1n} = \frac{1}{\text{Pé}} \langle f_n | \tilde{c}_1(\mathbf{r}_\perp) \rangle - \sum_{k=0}^{\infty} a_{0k} \sum_{l=-\infty}^{\infty} \beta_{nk}^\ell. \quad (2.39)$$

Collecting all terms, we write the formal solution as

$$|c_1(\mathbf{r}_\perp, t)\rangle = \text{Pé} \sum_{m=0}^{\infty} \sum_{n=0}^{\infty} \left[(a_{0n}\gamma_{1n}t + a_{1n})\delta_{n,m} + a_{0n} \left(\sum_{\ell=-\infty}^{\infty} \beta_{mn}^\ell e^{i\ell\omega_o t} \right) \right] e^{-\lambda_n t} |f_m\rangle. \quad (2.40)$$

2.3.3 Expressions for the effective diffusivity

The effective diffusivity $D_{\text{eff}} = \frac{1}{2} \frac{dM_2}{dt} - M_1 \frac{dM_1}{dt}$ can now be expressed in terms of a basis function expansion. The time derivative $\frac{dM_1}{dt} = \text{Pé} \langle u | c_0 \rangle$ of the full moment M_1 in Eq. (2.17b) becomes

$$\frac{dM_1}{dt} = \text{Pé} \sum_{n=0}^{\infty} \sum_{\ell=-\infty}^{\infty} a_{0n} \langle u_\ell | f_n \rangle e^{-(\lambda_n + i\ell\omega_o)t}, \quad (2.41a)$$

where we have used Eq. (2.5b) for the phase factor. By proper choice of the coordinate system, the initial centroid $\bar{x}(0)$ of the distribution is zero. This, combined with Eq. (2.19b), determines the initial value $M_1(0) = \bar{x}(0) = 0$, and time integration of Eq. (2.41a) gives

$$M_1 = \text{Pé} \sum_{n=0}^{\infty} \sum_{\ell=-\infty}^{\infty} a_{0n} \langle u_\ell | f_n \rangle \frac{1 - e^{-(\lambda_n + i\ell\omega_o)t}}{\lambda_n + i\ell\omega_o}. \quad (2.41b)$$

Here, the term $(n, \ell) = (0, 0)$ depends linearly on time because $\lim_{q \rightarrow 0} [(1 - e^{-qt})/q] = t$. Similarly, for the time derivative $\frac{1}{2} \frac{dM_2}{dt} = \langle 1 | c_0 \rangle + \text{Pé} \langle u | c_1 \rangle$ of the full moment M_2 , Eq. (2.17b), we obtain

$$\begin{aligned} \frac{1}{2} \frac{dM_2}{dt} &= 1 + \text{Pé}^2 \sum_{m=0}^{\infty} \sum_{n=0}^{\infty} \sum_{k=-\infty}^{\infty} \langle u_k | f_m \rangle e^{-(\lambda_n + ik\omega_o)t} \\ &\quad \times \left[(a_{0n}\gamma_{1n}t + a_{1n})\delta_{n,m} + a_{0n} \sum_{\ell=-\infty}^{\infty} \beta_{mn}^\ell e^{i\ell\omega_o t} \right]. \end{aligned} \quad (2.41c)$$

All expressions derived so far are explicitly real because of the pairwise summation of complex conjugate terms with index ℓ and $-\ell$. Furthermore, they apply to any initial solute distributions, such as the non-uniform distributions recently studied by [27], as well as any given velocity field, which can be represented by Eq. (2.10). Finally, we note that these equations clearly show that the term “shear dispersion” frequently used synonymously with Taylor–Aris dispersion is clearly misleading: the relevant feature is the *velocity variations* or equivalently *velocity gradients*, as these lead to the dispersion effect. While these gradients also impose a shear stress between the fluid layers of different velocity, this shear stress is not the cause of the dispersion.

Transverse uniform initial distribution of concentration

We now study the special case of an initial solute distribution \tilde{c} being uniform in the cross-sectional plane, a case of many practical applications, which has furthermore been the focus of most previously published studies. This introduces significant simplifications in D_{eff} , which otherwise depends on the channel cross-section, the flow profile u , and the initial solute distribution \tilde{c} through the coefficients u_ℓ , a_{0n} , a_{1n} , γ_{1n} , and β_{kn}^ℓ . Transverse uniformity leads to

$$|\tilde{c}_0\rangle = |1\rangle, \quad \text{and} \quad |\tilde{c}_1\rangle = 0, \quad (2.42)$$

and a_{0n} , β_{j0}^ℓ and a_{1n} therefore reduce to

$$a_{0n} = \delta_{n,0} \quad (2.43a)$$

$$\beta_{j0}^\ell = (1 - \delta_{\ell,0}\delta_{j,0}) \frac{\langle f_j | u_\ell \rangle}{\lambda_j + i\ell\omega_o}, \quad (2.43b)$$

$$a_{1n} = - \sum_{\ell=-\infty}^{\infty} (1 - \delta_{\ell,0}\delta_{n,0}) \frac{\langle f_n | u_\ell \rangle}{\lambda_n + i\ell\omega_o}, \quad (2.43c)$$

where $\langle f_j | u_\ell | f_0 \rangle = \langle f_j | u_\ell | 1 \rangle = \langle f_j | u_\ell \rangle$ has been used. Hence Eq. (2.41) becomes (see details in Appendix A.1)

$$\frac{dM_1}{dt} = \text{Pé} \sum_{k=-\infty}^{\infty} \langle u_k | 1 \rangle e^{-ik\omega_o t}, \quad (2.44a)$$

$$M_1 = \text{Pé} \sum_{\ell=-\infty}^{\infty} \langle u_\ell | 1 \rangle \frac{1 - e^{-i\ell\omega_o t}}{i\ell\omega_o} = \text{Pé} \left\{ \langle u_0 | 1 \rangle t + \sum_{\ell=-\infty}^{\infty} (1 - \delta_{\ell,0}) \langle 1 | u_\ell \rangle \frac{e^{i\ell\omega_o t} - 1}{i\ell\omega_o} \right\}, \quad (2.44b)$$

$$\begin{aligned} \frac{1}{2} \frac{dM_2}{dt} = 1 + \text{Pé}^2 \left\{ \sum_{\ell=-\infty}^{\infty} \langle u_\ell | 1 \rangle \langle u_0 | 1 \rangle t e^{-i\ell\omega_o t} + \sum_{m=0}^{\infty} \sum_{\ell=-\infty}^{\infty} \sum_{k=-\infty}^{\infty} \frac{\langle u_k | f_m \rangle \langle f_m | u_\ell \rangle}{\lambda_m + i\ell\omega_o} \right. \\ \left. \times (1 - \delta_{m,0}\delta_{\ell,0}) [e^{i\ell\omega_o t} - e^{-\lambda_m t}] e^{-ik\omega_o t} \right\}, \quad (2.44c) \end{aligned}$$

and after a final index change of m to n we arrive at

$$D_{\text{eff}}(t) = 1 + \text{Pe}^2 \sum_{n=1}^{\infty} \sum_{\ell=-\infty}^{\infty} \sum_{k=-\infty}^{\infty} \frac{\langle u_k | f_n \rangle \langle f_n | u_\ell \rangle}{\lambda_n + i\ell\omega_o} \left[e^{i(\ell-k)\omega_o t} - e^{-(\lambda_n + ik\omega_o)t} \right]. \quad (2.45)$$

This closed expression for the transient Taylor–Aris dispersion $D_{\text{eff}}(t)$ for any given time-dependent flow field $u(\mathbf{r}_\perp, t)$ in the case of complete transverse diffusion generalizes the previous steady and single-frequency results. The flow frequencies $\ell\omega_o$ and solute diffusion relaxation rates λ_n appears explicitly, while the momentum relaxation rates α_{fl} are implicit in $\langle f_n | u_\ell \rangle$.

The time-averaged diffusivity $D_{\text{eff}}^{\text{avr}}(t)$ over one oscillation period $\tau_0 = 2\pi/\omega_o$ is

$$D_{\text{eff}}^{\text{avr}}(t) = \frac{1}{\tau_0} \int_t^{t+\tau_0} D_{\text{eff}}(t) dt \quad (2.46a)$$

$$= 1 + \text{Pe}^2 \sum_{n=1}^{\infty} \sum_{\ell=-\infty}^{\infty} \sum_{k=-\infty}^{\infty} \frac{\langle u_k | f_n \rangle \langle f_n | u_\ell \rangle}{\lambda_n + i\ell\omega_o} \left[\delta_{\ell,k} - \frac{1 - e^{-\lambda_n \tau_0}}{(\lambda_n + ik\omega_o)\tau_0} e^{-(\lambda_n + ik\omega_o)t} \right], \quad (2.46b)$$

which in the long-time limit $t \gg 1/\lambda_1$ reduces to

$$D_{\text{eff}}^{\text{avr}}(\infty) = 1 + \text{Pe}^2 \sum_{n=1}^{\infty} \left[\frac{|\langle u_0 | f_n \rangle|^2}{\lambda_n} + \sum_{\ell=1}^{\infty} \frac{2\lambda_n |\langle u_\ell | f_n \rangle|^2}{\lambda_n^2 + \ell^2 \omega_o^2} \right]. \quad (2.47)$$

Note that the ℓ -sum only runs over positive integers and not as previously over all integers.

Finally, in the case of a steady flow given by

$$|u_\ell\rangle = \delta_{\ell,0} |u_0\rangle, \quad (2.48)$$

equation (2.45) for the effective diffusivity reduces to

$$D_{\text{eff}}^{\text{steady}}(t) = 1 + \text{Pe}^2 \sum_{n=1}^{\infty} \frac{|\langle u_0 | f_n \rangle|^2}{\lambda_n} (1 - e^{-\lambda_n t}), \quad (2.49)$$

and hence we recover the steady-flow, transient-solute result of Barton [16]. In the long-time limit $t \gg 1/\lambda_1$ this formally converges to the Taylor–Aris result

$$D_{\text{eff}}^{\text{steady}}(\infty) = 1 + \text{Pe}^2 \sum_{n=1}^{\infty} \frac{|\langle u_0 | f_n \rangle|^2}{\lambda_n}, \quad (2.50)$$

and will be referred to as the Taylor–Aris limit in the rest of the chapter. The independence of time of $D_{\text{eff}}^{\text{steady}}(\infty)$ illustrates that it behaves as a pure diffusion process in a reference frame moving with the center-of-mass.

Initial point concentration

We now turn our attention to an initial distribution of N_o solute molecules which are confined to a single point in space \mathbf{r}_o . The dimensionfull initial condition for the concentration is

$$\hat{c}(x, \mathbf{r}_\perp, 0) = N_o \delta(\mathbf{r} - \mathbf{r}_o), \quad (2.51)$$

where $\delta(\mathbf{x})$ is the three-dimensional Dirac delta function and $\mathbf{r}_o = (0, \mathbf{r}_\perp^o)$ ensures that the initial centroid of the distribution is zero as required for Eq. (2.41b). The initial point distribution is an idealized physical model of a droplet of solute and therefore has practical interest as a model of e.g. injected drugs into the blood stream [51] or injected additives into flows in industrial applications. Furthermore, the point distribution is the next logical step in building basic physical understanding of the dispersion phenomenon.

With the concentration scale (Eq. (2.8)),

$$C_o = \langle 1 | \hat{c}(x, \mathbf{r}_\perp, 0) \rangle = \langle 1 | N_o \delta(x) \delta(\mathbf{r}_\perp - \mathbf{r}_\perp^o) \rangle = \frac{N_o}{\mathcal{AL}}, \quad (2.52)$$

the non-dimensional initial concentration field is

$$\tilde{c}(x, \mathbf{r}_\perp) = \frac{\hat{c}(x, \mathbf{r}_\perp, 0)}{C_o} = \mathcal{AL} \delta(\mathbf{r} - \mathbf{r}_o), \quad (2.53)$$

so the initial conditions for the $p = 0$ and $p = 1$ axial moments are

$$|\tilde{c}_0\rangle = \frac{1}{\mathcal{L}} \int_{-\frac{\mathcal{L}}{2}}^{\frac{\mathcal{L}}{2}} dx x^0 \tilde{c}(\mathbf{r}) = \mathcal{A} \delta(\mathbf{r}_\perp - \mathbf{r}_\perp^o), \quad (2.54a)$$

$$|\tilde{c}_1\rangle = \frac{1}{\mathcal{L}} \int_{-\frac{\mathcal{L}}{2}}^{\frac{\mathcal{L}}{2}} dx x^1 \tilde{c}(\mathbf{r}) = 0. \quad (2.54b)$$

Contrary to the transversely uniform initial condition, $|\tilde{c}_0\rangle$ now depends on space; this will be shown to have a profound influence on the final result. With this spatial dependence the coefficients a_{0n} and a_{1n} become

$$a_{0n} = \langle f_n | \tilde{c}_0 \rangle = f_n(\mathbf{r}_\perp^o), \quad (2.55a)$$

$$a_{1n} = \frac{\langle f_n | \tilde{c}_1 \rangle}{\text{Pé}} - \sum_{m=0}^{\infty} a_{0m} \sum_{\ell=-\infty}^{\infty} \beta_{nm}^\ell = - \sum_{m=0}^{\infty} \sum_{\ell=-\infty}^{\infty} f_m(\mathbf{r}_\perp^o) \beta_{nm}^\ell. \quad (2.55b)$$

Using these simplifications, Eq. (2.41(a) and (b)) become

$$\frac{dM_1}{dt} = \text{Pé} \sum_{n=0}^{\infty} \sum_{\ell=-\infty}^{\infty} f_n(\mathbf{r}_{\perp}^o) \langle u_{\ell} | f_n \rangle e^{-(\lambda_n + i\ell\omega_o)t}, \quad (2.56a)$$

$$M_1 = \text{Pé} \sum_{n=0}^{\infty} \sum_{\ell=-\infty}^{\infty} f_n(\mathbf{r}_{\perp}^o) \langle u_{\ell} | f_n \rangle \frac{1 - e^{-(\lambda_n + i\ell\omega_o)t}}{\lambda_n + i\ell\omega_o}, \quad (2.56b)$$

$$M_1 \frac{dM_1}{dt} = \text{Pé}^2 \sum_{n=0}^{\infty} \sum_{m=0}^{\infty} \sum_{\ell=-\infty}^{\infty} \sum_{k=-\infty}^{\infty} f_n(\mathbf{r}_{\perp}^o) f_m(\mathbf{r}_{\perp}^o) \langle u_{\ell} | f_n \rangle \langle u_k | f_m \rangle \times \frac{1 - e^{-(\lambda_m + ik\omega_o)t}}{\lambda_m + ik\omega_o} e^{-(\lambda_n + i\ell\omega_o)t}, \quad (2.56c)$$

where as usual the factor $\frac{1 - e^{-(\lambda_m + ik\omega_o)t}}{\lambda_m + ik\omega_o}$ is understood as being equal to t for $(m, k) = (0, 0)$. Due to the spatial dependence of a_{0n} and a_{1n} we now have double sums in both M_1 and $\frac{dM_1}{dt}$ instead of the single sums found for the case of transverse uniform initial concentration.

The remaining term $\frac{1}{2} \frac{dM_2}{dt}$ from Eq. (2.41c) is,

$$\begin{aligned} \frac{1}{2} \frac{dM_2}{dt} &= 1 + \text{Pé}^2 \sum_{n=0}^{\infty} \sum_{m=0}^{\infty} \sum_{\ell=-\infty}^{\infty} \langle u_k | f_m \rangle e^{-(\lambda_n + ik\omega_o)t} \\ &\quad \times \left[\left(f_n(\mathbf{r}_{\perp}^o) \langle f_n | u_0 | f_n \rangle t - \sum_{q=0}^{\infty} \sum_{\ell=-\infty}^{\infty} f_q(\mathbf{r}_{\perp}^o) \beta_{nq}^{\ell} \right) \delta_{n,m} + \sum_{\ell=-\infty}^{\infty} f_n(\mathbf{r}_{\perp}^o) \beta_{mn}^{\ell} e^{i\ell\omega_o t} \right] \end{aligned} \quad (2.57a)$$

$$\begin{aligned} &= 1 + \text{Pé}^2 \sum_{n=0}^{\infty} \sum_{m=0}^{\infty} \sum_{\ell=-\infty}^{\infty} \sum_{k=-\infty}^{\infty} f_n(\mathbf{r}_{\perp}^o) \frac{\langle u_k | f_m \rangle \langle f_m | u_{\ell} | f_m \rangle}{\lambda_m - \lambda_n + i\ell\omega_o} \\ &\quad \times \left[e^{(\lambda_m - \lambda_n + i\ell\omega_o)t} - 1 \right] e^{-(\lambda_m + ik\omega_o)t}, \end{aligned} \quad (2.57b)$$

where again $\frac{e^{(\lambda_m - \lambda_n + i\ell\omega_o)t} - 1}{\lambda_m - \lambda_n + i\ell\omega_o}$ is understood as being equal to t for $(m, n, \ell) = (0, 0, 0)$. Details of going from Eq. (2.57a) to Eq. (2.57b) are given in Appendix A.2.

The effective diffusivity $D_{\text{eff}}^{\text{point}}$ for an initial point concentration is then found from Eqs. (2.56c) and (2.57b)

$$\begin{aligned} D_{\text{eff}}^{\text{point}} &= 1 + \text{Pé}^2 \sum_{n=0}^{\infty} \sum_{m=0}^{\infty} \sum_{\ell=-\infty}^{\infty} \sum_{k=-\infty}^{\infty} f_n(\mathbf{r}_{\perp}^o) \langle u_k | f_m \rangle \\ &\quad \times \left[\langle f_m | u_{\ell} | f_n \rangle \frac{e^{(\lambda_m - \lambda_n + i\ell\omega_o)t} - 1}{\lambda_m - \lambda_n + i\ell\omega_o} + f_m(\mathbf{r}_{\perp}^o) \langle u_{\ell} | f_n \rangle \frac{e^{-(\lambda_n + i\ell\omega_o)t} - 1}{\lambda_n + i\ell\omega_o} \right] e^{-(\lambda_m + ik\omega_o)t}. \end{aligned} \quad (2.58)$$

For the important special case of steady flow given by $|u_\ell\rangle = \delta_{\ell,0}|u_0\rangle$, this simplifies to

$$D_{\text{eff}}^{\text{point steady}} = 1 + \text{Pe}^2 \sum_{n=0}^{\infty} \sum_{m=0}^{\infty} f_n(\mathbf{r}_\perp^o) \langle u_0 | f_m \rangle \times \left[\langle f_m | u_0 | f_n \rangle \frac{e^{(\lambda_m - \lambda_n)t} - 1}{\lambda_m - \lambda_n} + f_m(\mathbf{r}_\perp^o) \langle u_0 | f_n \rangle \frac{e^{-\lambda_n t} - 1}{\lambda_n} \right] e^{-\lambda_m t}, \quad (2.59)$$

which in the long-time limit $t \gg 1/\lambda_1$ converges to the well-known result from transversely uniform initial distributions (see Appendix A.3 for details), Eq. (2.50),

$$D_{\text{eff}}^{\text{point steady}}(\infty) = 1 + \text{Pe}^2 \sum_{n=1}^{\infty} \frac{|\langle u_0 | f_n \rangle|^2}{\lambda_n}. \quad (2.60)$$

Hence, Eq. (2.60) confirms that an initial point concentration ultimately will fill the entire channel as time passes, just like we would expect on physical grounds. Only during the initial transient period which concludes on a time scale of $1/\lambda_1$ will the initial point concentration deviate from the transverse uniform case.

2.4 Results for transverse uniform initial distribution

2.4.1 General aspects of dispersion and relaxation rates

Our main result Eq. (2.45) implies directly that for all time-dependent flows the effective diffusivity depends on the velocity squared, $D_{\text{eff}} \propto \text{Pe}^2 \propto U_o^2$. However the specific form of D_{eff} depends on the magnitude of the amplitude $\|u_\ell\|$, of a given velocity component with frequency $\ell\omega_o$, relative to the amplitude $\|u_0\|$ of the steady component.

For small oscillation amplitudes $\|u_\ell\| \ll \|u_0\|$, the velocity field remains unidirectional, but its magnitude, and hence the velocity gradients, oscillates with frequency $\ell\omega_o$ around the steady value. Consequently, $D_{\text{eff}}(t)$ oscillates with frequency $\ell\omega_o$ around its time-averaged value $D_{\text{eff}}^{\text{avr}}(\infty)$. For sufficiently large amplitudes $\|u_\ell\| \gg \|u_0\|$ (the exact limit depends on the channel cross section geometry), the direction of the velocity field changes sign with frequency $2\ell\omega_o$. As a result, due to the terms with $k = -\ell$ in Eq. (2.46b), $D_{\text{eff}}(t)$ also oscillates with the double frequency $2\ell\omega_o$. Moreover, because this frequency-doubling ensures a non-zero, time-averaged effective diffusivity $D_{\text{eff}}^{\text{avr}} \propto \|u_\ell\|^2 \text{Pe}^2$, $D_{\text{eff}}^{\text{avr}}$ increases above $D_{\text{eff}}^{\text{steady}}$. This reflects that now $\|u_\ell\|U_o$ and not U_o should be chosen as U_{char} in Eq. (2.8), thus quantifying the observations made in the chemical engineering community that pulsating flows lead to increased mass transfer [130].

By definition, the variance of the solute distribution $\mu_2(t)$ is positive at all times, but this does not imply that the differential variance $D_{\text{eff}}(t) = \frac{1}{2} \frac{d\mu_2}{dt}$ also remains positive; in fact, negative values of $D_{\text{eff}}(t)$ are often encountered. In general, for short times $t \ll 1/\lambda_1, 1/(2\ell_{\text{max}}\omega_o)$, we find $D_{\text{eff}}(t) = 1 + t \text{Pe}^2 \sum_{n=1}^{\infty} |\langle f_n | u(0) \rangle|^2 > 0$, see Appendix A.4, while for steady flow oscillations of large amplitudes $\|u_\ell\| \gg \|u_0\|$ the transient contraction of the solute concentration field associated with each reversal of the

solvent flow direction leads to negative values of $D_{\text{eff}}(t)$. The cross-over point to negative values of $D_{\text{eff}}(t)$ depends on the relative amplitudes of all components of the velocity field, and is therefore not easily estimated in the general case. However, for the simple case of a single-frequency flow the cross-over point can be identified from Eq. (2.47). The time-averaged (positive) level is set by the diagonal terms $\ell = k$ for $-1, 0$, and 1 in the n -sum given by $|\langle u_0 | f_n \rangle|^2 / \lambda_n + |\langle u_1 | f_n \rangle|^2 2\lambda_n / (\lambda_n^2 + \omega_o^2)$, while the cross-terms $\ell = -k$ for -1 and 1 gives the oscillating terms $2\text{Re}[(\langle u_1 | f_n \rangle e^{i\omega_o t})^2 / (\lambda_1 + i\omega_o)]$. For the dominant $n = 1$ term at the intermediate frequency $\lambda_1 \ll \omega_o \lesssim \text{Sc}$, we can neglect λ_1 in the denominators, and since $\text{Wo} = \sqrt{\omega_o / \text{Sc}} \lesssim 1$ we have $\langle u_1 | f_n \rangle \approx \langle u_0 | f_n \rangle ||u_1|| / ||u_0||$, which results in $D_{\text{eff}} \propto 1 + 2 \frac{||u_1||^2}{||u_0||^2} \frac{\lambda_1}{\omega_o} \left[\frac{\lambda_1}{\omega_o} + \sin(2\omega_o t + 2\phi_0) \right]$, where the phase ϕ_0 is given by $\langle u_1 | f_n \rangle = |\langle u_1 | f_n \rangle| e^{i\phi_0}$. Negative values of $D_{\text{eff}}(t)$ are therefore expected for $||u_1|| > ||u_0|| \sqrt{\omega_o / (2\lambda_1)}$.

In the absence of a steady component in the velocity field, $u_0 = 0$, the frequency doubling is always present. Thus, for purely oscillating flows one finds a shear-enhanced dispersion above molecular diffusion, even though there is no net flow.

General conclusions for the shape dependence of D_{eff} may be obtained by applying random matrix theory [93] to the geometry-dependent inner product/eigenvalue expressions (2.45), (2.47), (2.49), (2.50), (2.58), (2.59) and (2.60) following the analysis of the shape-dependent quantum transport through quantum dots [26]. For a non-integrable system the values of the inner products in Eq. (2.49) can be regarded as a random distribution with an average of the order unity. We therefore expect the sum to be dominated by the lowest eigenvalues, for which $\lambda_n \propto 1/R^2$, where R is the aspect ratio of the characteristic length scales of the two cross section directions ($R \geq 1$), which for a rectangle is the wide “width” divided by the short “height”. Consequently $(D_{\text{eff}}^{\text{steady}} - 1) \propto \text{Pe}^2 R^2$, indicating that the dominating length scale no longer is the short “height” but the wide “width”. This is in agreement with the analysis of the shallow, slowly varying cross-sections studied previously [4, 46].

The effective diffusivity varies greatly depending on the system parameters. Below, we provide explicit estimates of the relaxation rates of the solute and fluid momentum in Newtonian fluids, by analyzing specific time-dependent systems of increasing complexity through the addition of more time scales to both motion of the solvent and diffusion of the solute. We interpret the results for D_{eff} in terms of the relaxation rates and the flow frequencies in agreement with the general considerations just outlined.

2.4.2 Multiple-frequency flow in one-length-scale cross sections

We begin by analyzing channel cross sections with only one inherent length scale, such as the circular tube or the infinite parallel-plate slit. Since these geometries are characterized by only one length scale, they have only one associated inherent time scale for each of the physical processes of solute diffusion and fluid momentum diffusion. All results presented in this section are computed for the circular cross section, but qualitatively they apply to other single-length cross sections. We consider a circular tube of unit radius (the radius being $a = L_o$ in dimensionfull coordinates) and calculate the velocity field from the Stokes

equation, Eq. (2.13). Using cylindrical coordinates and a generalized wavenumber k_ℓ , the velocity component u_ℓ fulfilling the boundary conditions $u|_{r=1} = 0$ and $\partial_r u|_{r=0} = 0$ is [146]

$$k_\ell = k_\ell(\text{Wo}) = \sqrt{-i\ell\text{Wo}^2} = \sqrt{-i\ell\omega_o/\text{Sc}}, \quad (2.61a)$$

$$|u_\ell\rangle = \varepsilon_\ell \frac{8}{k_\ell^2} \left[\frac{J_0(k_\ell r)}{J_0(k_\ell)} - 1 \right], \quad (2.61b)$$

where the steady-state Poiseuille solution is $u_0(r) = \lim_{\ell \rightarrow 0} u_\ell(r) = \varepsilon_0 2(1 - r^2)$. The velocity scale is taken to be the average steady state velocity $U_o = \Delta p a^2 / (8\eta\mathcal{L})$ for $\varepsilon_0 = 1$. The eigenfunctions and eigenvalues corresponding to Eq. (2.27) are

$$|f_n\rangle = \delta_{n,0} + (1 - \delta_{n,0}) \frac{J_0(\xi_{1,n} r)}{J_0(\xi_{1,n})}, \quad (2.62a)$$

$$\lambda_n = (1 - \delta_{n,0}) \xi_{1,n}^2, \quad (2.62b)$$

where $J_s(x)$ is the Bessel function of the first kind of order s , and $\xi_{s,n}$ is the n th root of $J_s(x)$. For cylindrical coordinates (axisymmetric case) $\langle f|g\rangle = \int_0^1 dr \, 2r f^*(r) g(r)$, so

$$\langle f_n|u_\ell\rangle = -\varepsilon_\ell \frac{16}{(\xi_{1,n}^2 - k_\ell^2)k_\ell} \frac{J_1(k_\ell)}{J_0(k_\ell)}, \quad \text{for } n > 0, \quad (2.63)$$

and $\langle f_n|u_0\rangle = \lim_{\ell \rightarrow 0} \langle f_n|u_\ell\rangle = -8/\xi_{1,n}^2$ for the steady term. Using these $\langle f_n|u_\ell\rangle$ in Eq. (2.45) allows us to calculate $D_{\text{eff}}(t)$ for an unsteady flow, and by inserting them in Eq. (2.49) we recover $D_{\text{eff}}^{\text{steady}}(t) = 1 + \text{Pé}^2 \left[\frac{1}{48} - \sum_{n=1}^{\infty} (64/\xi_{1,n}^6) \exp(-\xi_{1,n}^2 t) \right]$, the classic result for a transient solute concentration in a steady-flow obtained by Barton [16] that itself relaxes to the original result $D_{\text{eff}}(\infty) = 1 + \text{Pé}^2/48$ by Taylor [129].

The fluid momentum equilibration rate for the circular cross section is $\alpha_{\text{fl}} = \text{Sc} \xi_{0,1}^2$, so the generalized wavenumber $k_\ell = \sqrt{-i\ell\text{Wo}^2} = \xi_{0,1} \sqrt{-i\ell\omega_o/\alpha_{\text{fl}}}$ and the overlap integrals Eq. (2.63) depend explicitly on the fluid inertia through the ratio of the driving frequency ω_o to the fluid momentum equilibration rate α_{fl} . The velocity profile of this flow was presented previously in Fig. 2.2, p. 12, and we can now determine the limiting Wo of negligible inertia to $q = \xi_{0,1}$ as mentioned previously.

A steady-plus-one-frequency flow

We consider now the simple case of a steady flow of fixed amplitude $\varepsilon_0 = 1$ with the addition of one oscillating component of variable amplitude ε_1 . The dispersion in this particular flow has previously been studied to various levels of detail [11, 32, 99]. Our theory both recovers, quantifies, and provides insight to the underlying physical mechanisms encountered in these previous studies.

$D_{\text{eff}}(t)$ transiently builds towards a steady-oscillation level on the time scale $1/\lambda_1 = 1/\xi_{1,1}^2 = 0.068$, as seen in the example Fig. 2.3(a) (black line) for $\varepsilon_1 = 0.05$, $\text{Pé} = 20$, $\text{Sc} = 1000$, $\omega_o = 200$, and $\text{Wo} = \sqrt{\omega_o/\text{Sc}} = 0.447$. As expected from the general observations in

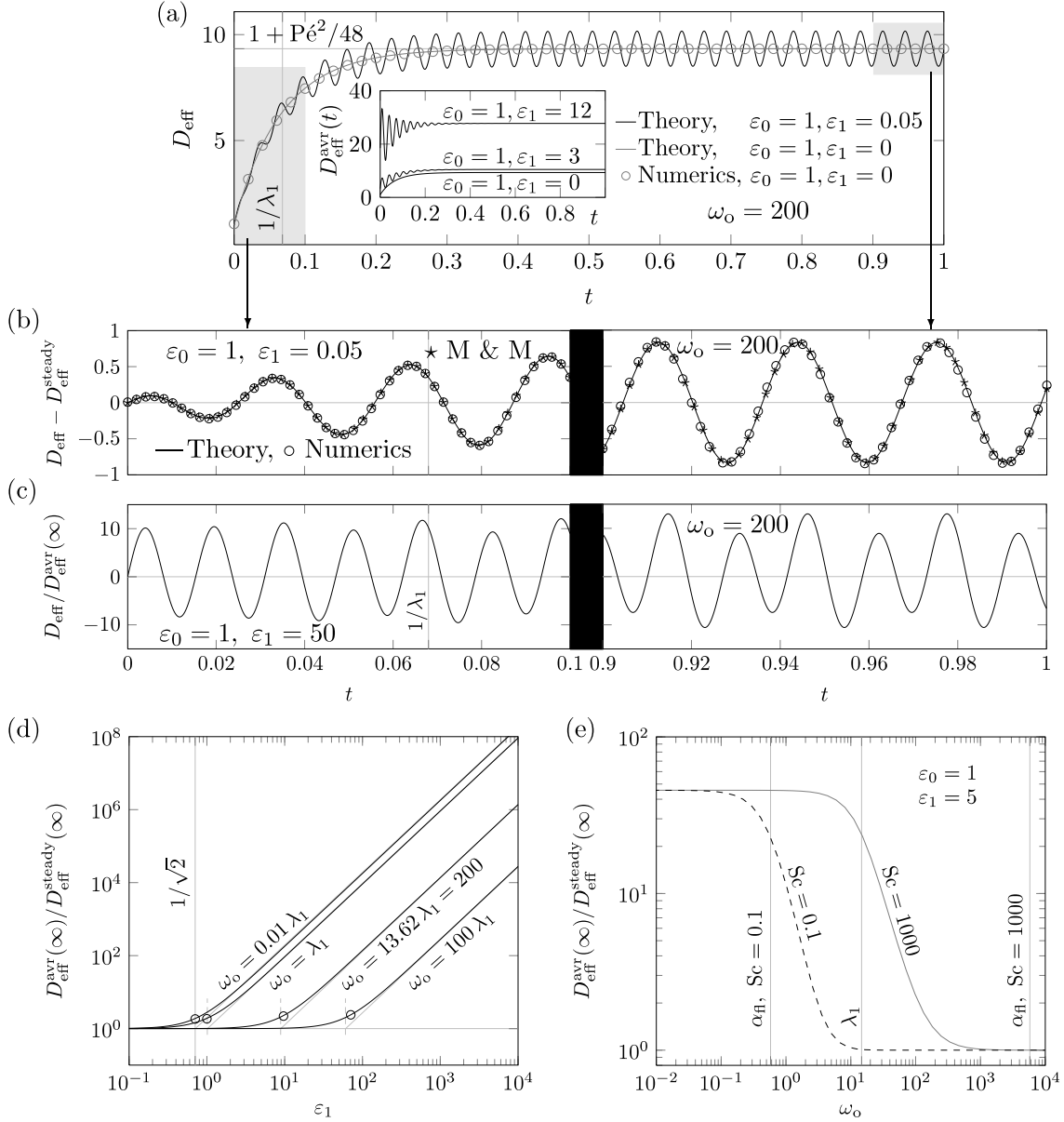


Figure 2.3: $D_{\text{eff}}(t)$ calculated by Eq. (2.45) in a tube of circular cross section for a harmonically oscillating flow of frequency ω_0 superimposed on a steady flow, $\text{Pé} = 20$. (a) $D_{\text{eff}}(t)$ for $\omega_0 = 200$, $\text{Wo} = 0.447$ and velocity amplitudes $\varepsilon_1 = 0.05 \ll \varepsilon_0 = 1$ (black line) oscillating around $D_{\text{eff}}^{\text{steady}}(t)$ determined by theory Eq. (2.49) (gray line), and by direct numerical simulation (gray circles). The inset shows $D_{\text{eff}}^{\text{avr}}(t)$ for $\varepsilon_1 = 0, 3$, and 12 , Eq. (2.46b). (b) Zoom-in on $D_{\text{eff}}(t)$ for the initial transient period $0 < t < 0.1$ (left) and the steady regime $0.9 < t < 1$ (right) showing agreement between our theory (black line), our numerics (circles), and the theory of Mukherjee and Mazumder (M & M) [99]. (c) Normalized effective diffusivity $D_{\text{eff}}(t)/D_{\text{eff}}^{\text{avr}}(\infty)$ showing frequency doubling; parameters as in panel (b) except now $\varepsilon_1 = 50$. (d) $D_{\text{eff}}^{\text{avr}}(\infty)/D_{\text{eff}}^{\text{steady}}(\infty)$, Eq. (2.65), versus ε_1 for four different frequencies ω_0 . The cross-over point ε_1^c (open circles) from the linear regime ($D_{\text{eff}}^{\text{avr}}/D_{\text{eff}}^{\text{steady}} \approx 1$) to the non-linear one ($D_{\text{eff}}^{\text{avr}}/D_{\text{eff}}^{\text{steady}} \propto \varepsilon_1^2$) increases for increasing ω_0 , as described by Eq. (2.66). (e) $D_{\text{eff}}^{\text{avr}}(\infty)/D_{\text{eff}}^{\text{steady}}(\infty)$ versus ω_0 for two fluids. For $\text{Sc} = 0.1$ (gas-like, dashed line) it decreases to 1 once $\omega_0 > \alpha_{\text{fl}}$ (solvent-momentum-diffusion limited), while for $\text{Sc} = 1000$ (water-like, gray line), it decreases to 1 when $\omega_0 > \lambda_1$ (solute-diffusion limited).

Sec. 2.4.1, $D_{\text{eff}}(t)$ oscillates around $D_{\text{eff}}^{\text{avr}}(t) \approx D_{\text{eff}}^{\text{steady}}(t)$ for $\varepsilon_1^2 \ll \varepsilon_0^2 = 1$ (gray line). The inset shows increasing $D_{\text{eff}}^{\text{avr}}(t)$ for growing oscillation amplitude, $\varepsilon_1 = 0, 3$, and 12 , where $D_{\text{eff}}^{\text{avr}}$ changes from following D_{eff} fairly closely at $\varepsilon_1 = 3$ to being substantially enhanced for $\varepsilon_1 = 12$. In Fig. 2.3(b) we zoom in on the two gray zones of panel (a) to show the excellent agreement between our theory for $D_{\text{eff}}(t) - D_{\text{eff}}^{\text{steady}}(t)$ (full line), numerics (circles, see Appendix A.5 for details), and the single-frequency theory of Mukherjee and Mazumder (stars) [99].

Extending the physical analysis provided by Mukherjee and Mazumder [99], we have augmented ε_1 by a factor 1000 to the value 50 in Fig. 2.3(c), and the normalized plot $D_{\text{eff}}(t)/D_{\text{eff}}^{\text{avr}}(\infty)$ illustrates that the oscillation-induced enhancement of $D_{\text{eff}}^{\text{avr}}(t)$ shown in the inset of panel (a) is accompanied by both a frequency doubling in, and negative values of, $D_{\text{eff}}(t)$ as discussed in Sec. 2.4.1. The onset of this non-linearity in the dispersion is further investigated in Fig. 2.3(d), where $D_{\text{eff}}^{\text{avr}}(\infty)/D_{\text{eff}}^{\text{steady}}(\infty)$ is plotted versus the oscillation amplitude ε_1 : A cross-over from the linear regime, where $D_{\text{eff}}^{\text{avr}}(\infty)/D_{\text{eff}}^{\text{steady}}(\infty) \approx 1$, to the non-linear regime, where $D_{\text{eff}}^{\text{avr}}(\infty)/D_{\text{eff}}^{\text{steady}}(\infty) \propto \varepsilon_1^2$, happens at a frequency-dependent critical value ε_1^c . We estimate ε_1^c in the low-frequency limit $\text{Wo} \lesssim \xi_{0,1} \approx 2.40$ from Eq. (2.47) using that in this case $\langle u_1 | f_n \rangle \approx \langle u_0 | f_n \rangle$, and since

$$\varepsilon_\ell = \delta_{\ell,0} + \varepsilon_1 (\delta_{\ell,-1} + \delta_{\ell,1}), \quad (2.64)$$

it follows that

$$D_{\text{eff}}^{\text{avr}}(\infty) \approx 1 + \text{Pé}^2 \sum_{n=1}^{\infty} \left[1 + \frac{2\varepsilon_1^2}{1 + (\omega_o/\lambda_n)^2} \right] \frac{|\langle u_0 | f_n \rangle|^2}{\lambda_n}. \quad (2.65)$$

Thus, the cross-over to period-doubled behavior (dominance of the ε_1^2 term) happens when ε_1 equals

$$\varepsilon_1^c = \frac{1}{\sqrt{2}} \sqrt{1 + \frac{\omega_o^2}{\lambda_1^2}} = \begin{cases} \frac{1}{\sqrt{2}}, & \text{for } \omega_o \ll \lambda_1, \\ \frac{\omega_o}{\sqrt{2} \lambda_1}, & \text{for } \omega_o \gg \lambda_1. \end{cases} \quad (2.66)$$

When $\omega_o \ll \lambda_1$, the solute fully equilibrates by diffusion (λ_1 is the solute diffusion equilibration rate) and thereby exploits all velocity gradients, so the cross-over to frequency-doubled behavior happens as soon as the amplitude of the sinusoidal part of the velocity field exceeds that of the steady component, i.e. at the RMS value $\varepsilon_1^c = 1/\sqrt{2}$ for $\varepsilon_0 = 1$. In contrast, for $\omega_o \gg \lambda_1$ the solute diffusion cannot fully follow the solvent oscillations, and only by increasing the amplitude significantly will the oscillation component contribute to D_{eff} , and as a consequence the cross-over amplitude scales as $\varepsilon_1^c \propto \omega_o/\lambda_1$. In Fig. 2.3(d) is shown that the estimates of Eq. (2.66) are correct. This result further agrees with, and quantifies, the observations of Chatwin and Watson [32, 145], but disagrees with Aris [11], who based on cases with $\varepsilon_1 \leq 1$ predicted that the pulsatile contribution to $D_{\text{eff}}^{\text{avr}}(\infty)$ is less than one percent, which is clearly incorrect for large values of ε_1 . For $\varepsilon_1 > \varepsilon_1^c$ we have $(D_{\text{eff}}^{\text{avr}} - 1) \propto \varepsilon_1^2 \text{Pé}^2$ signaling the change of characteristic velocity scale discussed in Sec. 2.4.1.

In addition to these limitations set by the equilibration of the solute, the dispersion may also be limited by fluid inertia, which similarly to the solute diffusion equilibration rate is characterized by a solvent-momentum equilibration rate α_{fl} . All time scales can be resolved by the solute when the driving frequency is much lower than the two equilibration rates, allowing time enough to establish the time-dependent velocity gradients and for the solute to diffuse in them, see Fig. 2.3(e). However, D_{eff} decreases if ω_o exceeds either of these equilibration rates.

The behavior of D_{eff} seems quantitatively similar whether the limiting factor is solute diffusion or solvent momentum diffusion, but the underlying physical mechanisms are different. For solute/solvent combinations which are limited by solute diffusion, $\lambda_1 \ll \alpha_{\text{fl}}$ (full gray line in Fig. 2.3(e)), the solute is constantly oscillating back and forth in addition to the steady motion as caused by the velocity field. This is still the case when $\omega_o > \lambda_1$, but here the solute only has time to diffuse by the gradients created by the steady velocity; new solute gradients are created by the oscillating part faster than the old gradients are smoothed out by diffusion. This corresponds to the case where the fluid is water.

In the other limit of solute/solvent configuration, $\alpha_{\text{fl}} \ll \lambda_1$, the limiting factor is the diffusion of fluid momentum (inertia): The fluid momentum does not have time to react to the pressure oscillations at the driving frequency, so the fluid will only be moved by the steady part of the pressure. Thus, only the steady velocity field will disperse the solute distribution, and $D_{\text{eff}}(\infty)$ becomes equal to $D_{\text{eff}}^{\text{steady}}(\infty)$ resulting in the dispersion of only the steady flow. This effect is seen in the dashed black line in Fig. 2.3(e), which corresponds to the case where channel radius is the same as for the water case above (thus keeping λ_1 fixed) but the fluid is air [40].

A steady-plus-two-frequencies flow

Through the driving pressure, we now add a second time scale to the flow so it consists of a steady component, and the two frequencies ω_o and $\tilde{\ell}\omega_o$, $\tilde{\ell}$ being an integer. The effects in D_{eff} of the previous subsection extend to the second frequency, and we continue to find good agreement between theory and numerics, see Fig. 2.4. We first take $\tilde{\ell} = 2$. As expected from the general observations in Sec. 2.4.1, $D_{\text{eff}}(t)$ oscillates around $D_{\text{eff}}^{\text{steady}}$ with the frequencies of the velocity field when the oscillation amplitudes ε_1 and ε_2 are sufficiently small (limits given below), see Fig. 2.4(a), while frequency-doubling and negative values appear when ε_1 and ε_2 become large, see Fig. 2.4(b). As for the single-frequency case, there is substantial increase of $D_{\text{eff}}^{\text{avr}}(\infty)/D_{\text{eff}}^{\text{steady}}(\infty)$ for large values of ε_1 and ε_2 and the cross-over to non-linearity for $\tilde{\ell} = 2$ may be predicted from simple estimates for $\text{Wo} \lesssim \xi_{0,1}$ as follows. Since

$$\varepsilon_{\ell} = \delta_{\ell,0} + \varepsilon_1(\delta_{\ell,-1} + \delta_{\ell,1}) + \varepsilon_2(\delta_{\ell,-2} + \delta_{\ell,2}), \quad (2.67)$$

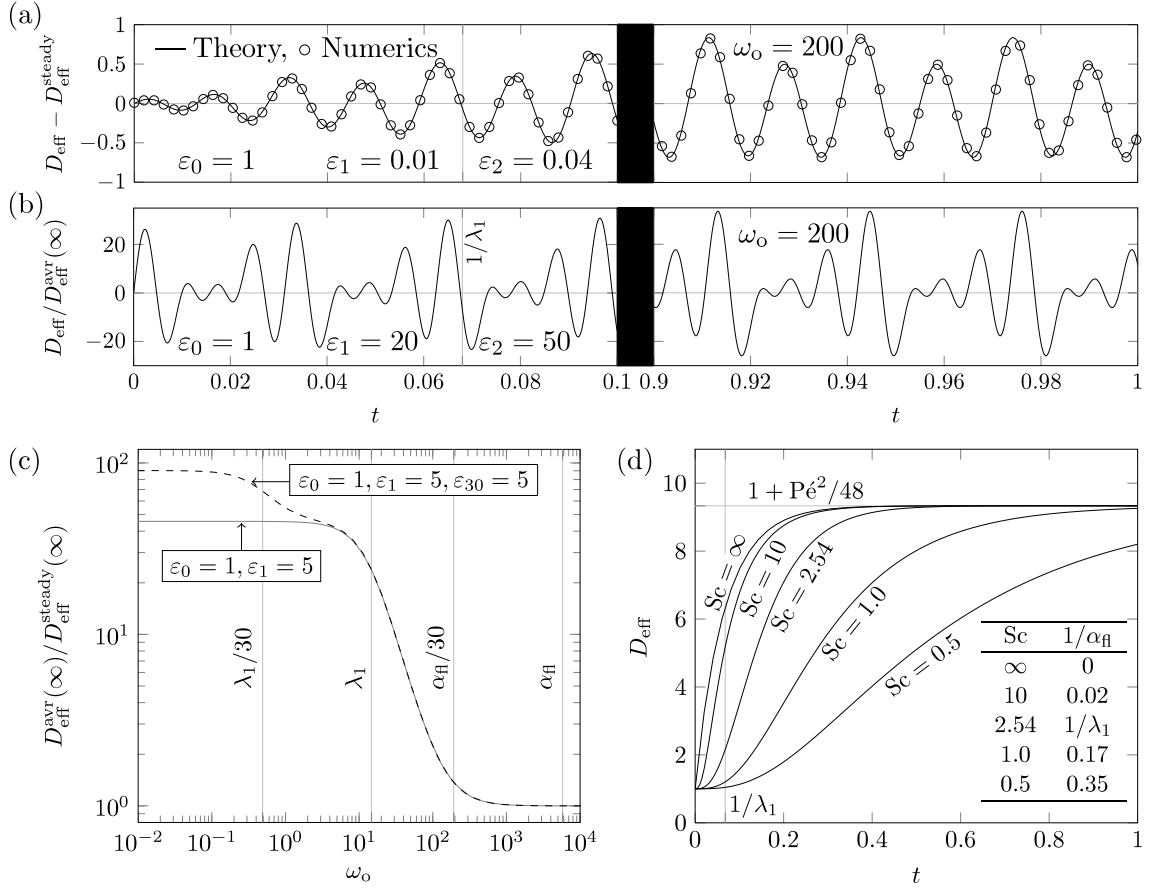


Figure 2.4: Calculated $D_{\text{eff}}(t)$ for a circular cross section as in Fig. 2.3, but with a second oscillating velocity component added. (a) $D_{\text{eff}}(t) - D_{\text{eff}}^{\text{steady}}(t)$ from Eq. (2.45) (black line) and numerics (circles) the transient period (left) and the steady regime (right) for small amplitudes, $\varepsilon_1 = 0.01$ and $\varepsilon_2 = 0.04$. (b) As in panel (a), but for large amplitudes, $\varepsilon_1 = 20$ and $\varepsilon_2 = 50$, showing frequency doubling for both ω_o and $2\omega_o$. (c) $D_{\text{eff}}^{\text{avr}}(\infty)/D_{\text{eff}}^{\text{steady}}(\infty)$ versus ω_o for $\text{Sc} = 10^3$ and $\varepsilon_0 = 1, \varepsilon_1 = \varepsilon_{30} = 5$ (dashed curve). For clarity $\ell = 30$ is used instead of $\ell = 2$ to better illustrate the effects of each frequency. $D_{\text{eff}}^{\text{avr}}(\infty)$ decreases in two steps as ω_o crosses $\lambda_1/30$ and λ_1 . The one-frequency case Fig. 2.3(e), $\text{Sc} = 10^3$ (gray curve), is shown for comparison. (d) Startup of tube flow from rest: Calculated $D_{\text{eff}}(t)$ versus time for $\text{Pé} = 20$. For $\text{Sc} \lesssim 1$ the dispersion saturates on the solvent acceleration time scale $1/\alpha_{\text{ff}} \approx 1/\text{Sc}$, while for $\text{Sc} \gg 1$ it saturates on the solute diffusion time $1/\lambda_1 = 1/\xi_{1,1}^2 \approx 0.07$. The Fourier series has $T = 5$ and contains 1000 terms.

we distinguish between the three regimes $\varepsilon_2 \ll 1$, $\varepsilon_1 \ll 1$ and $\varepsilon_1 = \varepsilon_2$. In the first case we trivially retrieve the result Eq. (2.66), while the second case similarly yields

$$\varepsilon_2^c = \frac{1}{\sqrt{2}} \sqrt{1 + \frac{4\omega_o^2}{\lambda_1^2}} = \begin{cases} \frac{1}{\sqrt{2}}, & \text{for } \omega_o \ll \lambda_1, \\ \frac{\sqrt{2}\omega_o}{\lambda_1}, & \text{for } \omega_o \gg \lambda_1. \end{cases} \quad (2.68)$$

Hence, the frequency doubling for each of the velocity field frequencies is independent, since a significant non-linear effect is found when either $\varepsilon_1 > \varepsilon_1^c$ or $\varepsilon_2 > \varepsilon_2^c$. In the third

case of $\varepsilon_1 = \varepsilon_2 = \varepsilon$, we find

$$\varepsilon^c = \frac{1}{\sqrt{2}} \sqrt{\frac{1 + \frac{5\omega_o^2}{\lambda_1^2} + \frac{4\omega_o^4}{\lambda_1^4}}{1 + \frac{5\omega_o^2}{\lambda_1^2}}} = \begin{cases} \frac{1}{\sqrt{2}}, & \text{for } \omega_o \ll \lambda_1, \\ \sqrt{\frac{2}{5}} \frac{\omega_o}{\lambda_1}, & \text{for } \omega_o \gg \lambda_1, \end{cases} \quad (2.69)$$

where the second threshold is slightly lower than for the single-frequency case Eq. (2.66).

Our understanding of the behavior of $D_{\text{eff}}^{\text{avr}}$ from the involved diffusion processes of fluid momentum and solute, presented in the previous section on single-frequency flow, applies to each of the frequencies of the flow. The addition of a second velocity frequency introduces more shear and hence more gradients to the concentration field and $D_{\text{eff}}^{\text{avr}}$ therefore increases even further when all velocity frequencies can be resolved, see dashed line in Fig. 2.4 (c), where solute diffusion is the limiting process ($\lambda_1 \ll \alpha_{\text{fl}}$) and where for clarity the second frequency is $30\omega_o$ instead of the $2\omega_o$. Two distinct decreases are found in this curve: the first is when the solute equilibration rate λ_1 surpasses $30\omega_o$, and the second when λ_1 increases past the base frequency. The decreases arise because the gradients created by $30\omega_o$ and ω_o , respectively, can no longer be exploited by the solute. When both frequencies can be resolved $D_{\text{eff}}^{\text{avr}}$ is almost a factor two greater than the single-frequency case of Fig. 2.3(e), here reproduced as the gray line, so the second velocity frequency leads to a large enhancement of D_{eff} . Had we chosen $\alpha_{\text{fl}} \ll \lambda_1$ in the figure, the same decreases would have been observed around $30\omega_o \approx \alpha_{\text{fl}}$ and $\omega_o \approx \alpha_{\text{fl}}$.

Unsteady, unidirectional flow: startup of Poiseuille flow

In the previous sections we found that fluid inertia limits the solute dispersion because the flow does not equilibrate to a steady state. To further investigate the inertial effects we consider solute in a circular channel where the solvent, after initially being at rest, suddenly at $t = 0$ begins to move due to an instantly applied pressure drop along the channel. The analytical solution of this startup of a Poiseuille flow is found in terms of a Fourier–Bessel expansion in the radial coordinate, where each term is multiplied by an exponential time decay of rate α_m [18],

$$u(r, t) = 2(r^2 - 1) - \sum_{m=1}^{\infty} \frac{16}{\xi_{0,m}^3} \frac{J_0(\xi_{0,m}r)}{J_1(\xi_{0,m})} e^{-\alpha_m t}, \quad (2.70a)$$

$$\alpha_m = \text{Sc } \xi_{0,m}^2, \text{ for } m = 1, 2, 3, \dots \quad (2.70b)$$

The smallest of these inertial decay rates, $\alpha_1 = \xi_{0,1}^2 \text{Sc} \approx 5.78 \text{Sc} = \alpha_{\text{fl}}$, sets the characteristic time of the acceleration $1/\alpha_{\text{fl}}$ as in Eq. (2.11) and in Sec. 2.4.2. To align this solution with the developed theory, the temporal functions are written as Fourier series with a base-period T much larger than the acceleration time, $T \gg 1/\alpha_{\text{fl}}$. Hence, the flow will reach a steady state significantly faster than the base-period T , and the approximation will be the

correct solution for $0 < t < T$. We obtain

$$u(r, t) = 2(1 - r^2) - \sum_{m=1}^{\infty} \sum_{\ell=-\infty}^{\infty} \frac{16J_0(\xi_{0,m}r)}{\xi_{0,m}^3 J_1(\xi_{0,m})} A_{\ell m} e^{i\ell\omega_o t}, \quad (2.71a)$$

$$A_{\ell m} = \frac{1 - e^{-\alpha_m T}}{\alpha_m T + i\ell 2\pi}, \quad (2.71b)$$

where $\omega_o = 2\pi/T$ so that $Wo = \sqrt{2\pi/(ScT)} = \xi_{0,1}\sqrt{2\pi/(\alpha_{\text{fl}}T)}$. The velocity scale is the same as for a steady flow in a circular tube, so the ℓ th velocity component $u_{\ell}(r)$ is

$$u_{\ell}(r) = 2(1 - r^2) \delta_{\ell,0} - \sum_{m=1}^{\infty} \frac{16 A_{\ell m} J_0(\xi_{0,m}r)}{\xi_{0,m}^3 J_1(\xi_{0,m})}. \quad (2.72)$$

Combining this with the eigenvalue solution of Eq. (2.62), we find for $n > 0$

$$\langle f_n | u_{\ell} \rangle = -\frac{8\delta_{\ell,0}}{\xi_{1,n}^2} - \sum_{m=1}^{\infty} \frac{32(1 - e^{-\alpha_m T})}{\xi_{0,m}^2 (\xi_{0,m}^2 - \xi_{1,n}^2) (\alpha_m T + i\ell 2\pi)}. \quad (2.73)$$

The two physical processes of fluid acceleration and solute dispersion happens on the two time scales $1/\alpha_{\text{fl}}$ and $1/\lambda_1$, respectively, but since fluid motion is required to generate the shear needed for the Taylor–Aris dispersion effect, the dispersion is limited by either the solute diffusion, or solvent inertia. In the first case ($\alpha_{\text{fl}} \gg \lambda_1$), the fluid reaches steady state much faster than the solute, and the dispersion therefore behaves as in the case of a steady flow. Since $\alpha_{\text{fl}} \propto Sc$ this can be thought of as having $Sc = \infty$, so the only transient behavior observed is that of the solute diffusion; this is the case for water. For the second case ($\alpha_{\text{fl}} \propto Sc \ll \lambda_1$) with slower momentum equilibration rates $0.1 < Sc < 10$ found in gases [40], the solute dispersion evolves in the slow increase of the velocity shear gradients, which now dominates the transient behavior, and $D_{\text{eff}}(t)$ is thus smaller than $D_{\text{eff}}^{\text{steady}}(t)$. These inertial effects are illustrated in Fig. 2.4(d), where dispersion co-evolves with the transient start-up of a Poiseuille flow in a straight tube at $P\acute{e} = 20$, and where the equilibration rates for solute mass diffusion and solvent momentum diffusion are equal for $Sc = \xi_{1,1}^2/\xi_{0,1}^2 = 2.54$. We take $T = 5$, and to diminish unphysical effects of the Gibbs phenomenon close to $t = 0$, we include 1000 terms in the Fourier series.

In conclusion, fluid inertia limits fluid shear and hence the solute dispersion. However, given the characteristic time scale $1/\alpha_{\text{fl}} \propto 1/Sc \ll 1/\lambda_1$, inertial effects only become important for Taylor–Aris dispersion in gasses.

2.4.3 Multiple-frequency flow in two-length-scale cross sections

We move on to consider the effects of adding a second length scale to the cross sectional geometry. We illustrate this case by use of the rectangle, but the presented findings hold quantitatively for other cross section with two length scales, e.g. the ellipse.

The rectangular cross section

We denote the height of the channel $2a$ and the width $2w$, with $w \geq a$ so that the aspect ratio $R = w/a$ satisfies $R \geq 1$. We take the characteristic length scale to be $L_o = a$, so $\text{Pé} = U_o a/D$ and $\text{Wo} = \sqrt{a^2 \tilde{\omega}_o / \nu}$, and in non-dimensional units we place the rectangular cross section such that $-R \leq y \leq R$ and $-1 \leq z \leq 1$. The analytical velocity field for the steady Poiseuille flow is well-known, see e.g. [25], and in analogy with Eq. (2.61b) by introducing a generalized wavenumber $q_{j\ell}$, the pulsatile velocity field is found by a trivial extension thereof (see Appendix A.6 for details),

$$q_{j\ell} = q_{j\ell}(\text{Wo}) = \sqrt{i4\text{Wo}^2\ell + j^2\pi^2}, \quad (2.74a)$$

$$|u_\ell\rangle = \varepsilon_\ell(1 + \delta_{\ell,0}) \frac{24}{\Gamma} \sum_{j,\text{odd}} \frac{1}{j\pi q_{j\ell}^2} \left[1 - \frac{\cosh\left(q_{j\ell} \frac{y}{2}\right)}{\cosh\left(q_{j\ell} \frac{R}{2}\right)} \right] \sin\left(j\pi \frac{z+1}{2}\right), \quad (2.74b)$$

where the pre-factor Γ and the velocity scale U_o (chosen as the cross-sectional average of the steady flow with $\varepsilon_0 = 1$) are given by

$$\Gamma = \Gamma(R) = 1 - \sum_{j,\text{odd}} \frac{1}{j^5} \frac{192}{\pi^5} \frac{1}{R} \tanh\left(j\pi \frac{R}{2}\right), \quad (2.75a)$$

$$U_o = \frac{\Delta p a^2 \Gamma}{3\eta \mathcal{L}}. \quad (2.75b)$$

The steady flow profile is retrieved from Eq. (2.74b) by the limit $u_0(y, z) = \lim_{\ell \rightarrow 0} u_\ell(y, z)$ using $q_{j0} = j\pi$. Similar to the circular cross section, the generalized wavenumber $q_{j\ell}$ depends explicitly on the fluid momentum equilibration rate $\alpha_{\text{ff}} = (1 + 1/R^2) \frac{\pi^2}{4} \text{Sc}$ since $q_{j\ell} = \pi \sqrt{i\ell(1 + \frac{1}{R^2}) \frac{\omega_o}{\alpha_{\text{ff}}} + j^2}$. The corresponding basis functions and eigenvalues are

$$|f_{nm}\rangle = \frac{2 \cos\left(n\pi \frac{y+R}{2R}\right) \cos\left(m\pi \frac{z+1}{2}\right)}{\sqrt{(1 + \delta_{n,0})(1 + \delta_{m,0})}}, \quad (2.76a)$$

$$\lambda_{nm} = \left(\frac{n\pi}{2R}\right)^2 + \left(\frac{m\pi}{2}\right)^2, \quad n, m = 0, 1, 2, \dots \quad (2.76b)$$

which satisfy the requirement $|f_{00}\rangle = 1$ with $\lambda_{00} = 0$. The single index n of Eq. (2.62) is here changed to the double index (n, m) , and $n = 0$ to $(n, m) = (0, 0)$. The inner products $\langle f_n | u_\ell \rangle$ of Eq. (2.45) become $\langle f_{nm} | u_\ell \rangle$ given by,

$$\langle f_{nm} | u_\ell \rangle = \begin{cases} \frac{\varepsilon_\ell(1 + \delta_{l,0})}{\sqrt{(1 + \delta_{n,0})(1 + \delta_{m,0})}} \frac{96R}{\Gamma\pi^2} \sum_{j,\text{odd}} \frac{q_{jl}R\delta_{n,0} - 2 \tanh\left(\frac{q_{jl}R}{2}\right)}{q_{jl}(j^2 - m^2)(n^2\pi^2 + q_{jl}^2 R^2)}, & n, m \text{ even}, \\ 0, & \text{otherwise,} \end{cases} \quad (2.77)$$

and sums $\sum_{n=1}^\infty = \sum_{n \neq 0}^\infty$ become $\sum_{\{n,m\} \neq \{0,0\}}^\infty$.

The two inherent length scales of this cross section introduce two diffusion times, one along each coordinate direction, and hence two solute equilibration rates,

$$\lambda_{20}(R) = \frac{\pi^2}{R^2} \text{ (width) } \quad \text{and} \quad \lambda_{02} = \pi^2 \text{ (height)}. \quad (2.78)$$

We have previously described how the behavior of D_{eff} can be understood in terms of the involved diffusion processes of fluid momentum and solute, and it follows directly that while this obviously extends to the present case, the presence of the additional time scales from the second geometric dimension introduces more structure: for each frequency in the fluid velocity field, the solute dispersion will increase if it has time to equilibrate along either of its transverse directions (i.e. if $\omega_o \lesssim \lambda_{20}$ or $\omega_o \lesssim \lambda_{02}$), with more dispersivity when the frequency allows equilibration along both directions. Thus, for a velocity field with two frequency scales there will be four critical frequencies: the two solute equilibration rates for each of the two fluid time scales. This is illustrated in Fig. 2.5(a) for the case of $\varepsilon_0 = \varepsilon_1 = \varepsilon_{30} = 1$ with $\text{Pé} = 20$ and $R = 100$, and for a solvent/solute composition such that the equilibration rate of the solvent momentum $\alpha_{\text{fl}} = (1 + 1/R^2)\frac{\pi^2}{4}\text{Sc}$ is much greater than those of the solute diffusion, λ_{20} and λ_{02} . As function of driving frequency ω_o , $D_{\text{eff}}^{\text{avr}}$ decreases in four steps: The first two and most significant drops happen near $\lambda_{20}/30$ and λ_{20} , where the diffusion across the width no longer can exploit the gradients of first the $30\omega_o$ -harmonic and then the ω_o -harmonic. The last two (minor) drops happen near $\lambda_{02}/30$ and finally λ_{02} , where the height-diffusion ceases to be able to follow the $30\omega_o$ -harmonic and lastly the ω_o -harmonic. The substantial increases in time-averaged dispersion found for the two-frequency-flow of the previous section is again found in this case: for low frequencies ω_o which allow complete solute equilibration, $D_{\text{eff}}^{\text{avr}}$ is almost a factor of two greater than when only the steady velocity contributes to the solute dispersion ($D_{\text{eff}}^{\text{avr}}(\infty) = 120.41$ at $\omega_o = 10^{-8}$ compared to $D_{\text{eff}}^{\text{avr}}(\infty) = 60.70$ at $\omega_o = 10^4$). For comparison we have also included the special case of $R = 1$, a one-length-scale cross section, where the two solute diffusion equilibration rates λ_{20} and λ_{02} are identical, and where we consequently find only two decreasing steps. We have also validated our theory against numerics for the case $R = 1$ (details given in Appendix A.5), and again find excellent agreement.

Since the solute equilibration rate λ_{20} depends on the aspect ratio R , Eq. (2.78), the same frequency ω_o and velocity component amplitudes ε_ℓ will give rise to different behaviors of D_{eff} in channels of different aspect ratios R . This is plotted in Fig. 2.5(b) for $\omega_o = 10^4$ and $\omega_o = 10^{-7}$ with the flow chosen as in (a) to be a two-frequency flow with amplitudes $\varepsilon_0 = \varepsilon_1 = \varepsilon_{30} = 1$. For reference we have also plotted the dependence of $D_{\text{eff}}^{\text{steady}}$ in the limit $R \rightarrow \infty$ where we retrieve the well-known result [45, 34] $D_{\text{eff}}^{\text{steady}}(\infty) = 1 + \chi_{\text{rect}}\text{Pé}^2$ with $\chi_{\text{rect}} = \frac{2}{105} + \frac{11532\zeta(5)^2}{\pi^{10}}$ where $\zeta(x) = \sum_{j=1}^{\infty} j^{-x}$ is the Riemann zeta function. For sufficiently fast oscillation, here $\omega_o = 10^4$ (lower black line), we have $\omega_o \gg \lambda_{02}$, and as in Fig. 2.4(b) this is too fast for the solute diffusion to follow, and we recover the steady-flow case (triangles) and $D_{\text{eff}}^{\text{avr}}(\infty) = D_{\text{eff}}^{\text{steady}}(\infty)$. Had we chosen larger oscillation amplitudes ε_ℓ the non-linear effect discussed in Sec. 2.4.1 would have set in and increased $D_{\text{eff}}^{\text{avr}}$. For the fixed slow oscillation frequency $\omega_o = 10^{-7}$ (top black line), $D_{\text{eff}}^{\text{avr}}$ initially increases with R , as the solute diffusion now is able to follow the fluid movement. However, due to

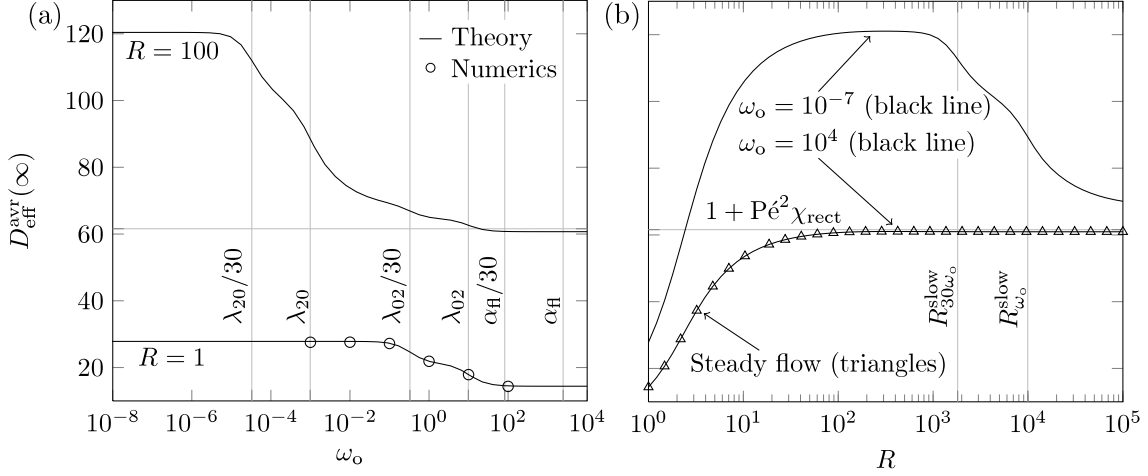


Figure 2.5: $D_{\text{eff}}^{\text{avr}}(\infty)$ for a two-frequency flow $\varepsilon_0 = \varepsilon_1 = \varepsilon_{30} = 1$ in rectangular channels of aspect ratio R . (a) $D_{\text{eff}}^{\text{avr}}(\infty)$ versus base frequency ω_o for $R = 1$ and $R = 100$ at $\text{Pe} = 20$, and with the agreement with numerics (circles) illustrated at $R = 1$ (details given in the Appendix). As ω_o increases $D_{\text{eff}}^{\text{avr}}$ decreases in four steps, namely when ω_o crosses $\lambda_{20}/30$, λ_{20} , $\lambda_{02}/30$, and λ_{02} (for $R = 100$). For $R = 1$ there are only two steps, namely when ω_o crosses $\lambda_{02}/30$ and λ_{02} this rate being the same for $R = 1$ and $R = 100$. (b) $D_{\text{eff}}^{\text{avr}}(\infty)$ versus R for fast oscillation ($\omega_o = 10^4$) and steady flow, both recovering the behavior of Fig. 2.3(a), and for slow oscillation ($\omega_o = 10^{-7}$), for which $D_{\text{eff}}^{\text{avr}}(\infty)$ reaches a maximum before decreasing in two steps at $\lambda_{20}(R) = 30 \times 10^{-7}$ and $\lambda_{20}(R) = 10^{-7}$, marked by the aspect ratios $R_{30\omega_o}^{\text{slow}}$ and $R_{\omega_o}^{\text{slow}}$, respectively.

the R -dependence of λ_{20} in Eq. (2.78), a point is reached beyond which $\lambda_{20}(R)/30 < \omega_o$, and $D_{\text{eff}}^{\text{avr}}$ decreases to a lower value. Later, when $\lambda_{20}(R)$ falls below ω_o , a second decrease occurs, after which $D_{\text{eff}}^{\text{avr}}$ settles at $D_{\text{eff}}^{\text{steady}}(\infty) = 1 + \chi_{\text{rect}} \text{Pe}^2$, since none of the added velocity gradients of the time-dependent velocity components contribute to $D_{\text{eff}}^{\text{avr}}$.

The highest value of $D_{\text{eff}}^{\text{avr}}$ achievable for a fixed velocity field with fixed frequency ω_o is found in a region with the upper limit set by $3\ell_{\text{max}}\omega_o \approx \lambda_{20} = \pi^2/R^2$, where ℓ_{max} is the maximum frequency component in the velocity field, and the lower limit is set by the value of R which ensures that the steady part of the velocity field reaches the maximum dispersion of $D_{\text{eff}}^{\text{steady}}(\infty) = 1 + \text{Pe}^2 \chi_{\text{rect}}$, $R \lesssim 100$.

Finally, a brief discussion is in order regarding the behavior of $D_{\text{eff}}^{\text{steady}}(\infty)$ in the limit $R \rightarrow \infty$. It is well-known that $\chi_{\text{rect}} = \frac{2}{105} + \frac{11532 \zeta(5)^2}{\pi^{10}} \approx 7.95 \chi_{\text{plate}}$ where $\chi_{\text{plate}} = 2/105$ is the coefficient for infinite parallel plates (no side walls) [45, 34], which might seem to contradict the general scaling of $(D_{\text{eff}} - 1) \propto \text{Pe}^2/R^2$ described in Sec. 2.4.1. However, the rectangular cross section is integrable, and the inner products $\langle f_{n0} | u_0 \rangle \propto 1/R$, because as function of the width coordinate y , u_0 is constant except for the ends covering a fraction $1/R$ of the width, while f_{n0} oscillates, see Eqs. (2.74b) and (2.76a). As a result, the factor R^2 from $1/\lambda_{nm}$ is canceled by the factor $1/R^2$ from the inner product, and $(D_{\text{eff}}^{\text{steady}} - 1) \propto \text{Pe}^2$, making the small height the dominant length scale. This explains why in $\chi_{\text{rect}} \approx \chi_{\text{plate}}$ instead of $\chi_{\text{rect}} \approx \chi_{\text{plate}} R^2$. Physically, the steady flow in high-aspect ratio rectangular channels is independent of the channel width except for boundary layers of width unity near the side walls, while it remains parabolic in the height. Compared to the infinite parallel

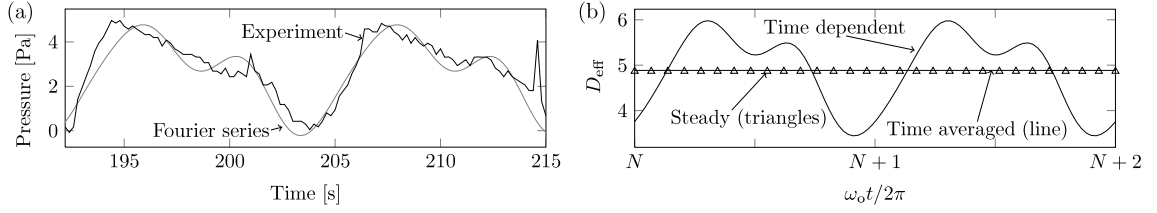


Figure 2.6: (a) Two periods of the measured time-dependent pressure delivered by the peristaltic pump (black) by [122] and of the approximate Fourier series ($|\ell| \leq 3$) used in the analysis (gray). (b) Calculated $D_{\text{eff}}(t)$ for the two cycles of the peristaltic pump following period $N = 10^4$ after the decay of all transients: the Fourier series (black), only the steady component (dashed), and the time-averaged Fourier series (gray).

plate channel, the side walls therefore increase both the mean velocity and the created gradients in the concentration field along the height, causing an increase of $D_{\text{eff}}(\infty)$, which none the less remains on the order of $D_{\text{eff}}(\infty)$ from the parallel plates. For channel cross sections which vary continuously along both cross section directions (e.g. elliptic), the characteristic length scale of velocity variations is of order R , resulting in shear along all of R and the scaling $(D_{\text{eff}}^{\text{steady}} - 1) \propto \text{Pe}^2 R^2$ as described in Sec. 2.4.1

Analysis of a peristaltic micropump

To illustrate the practical usefulness of the developed theory, we here shortly describe dispersion-limiting of a micropump. The pressure delivered by the novel 12-channel, eight-roller, peristaltic pump for microfluidics of [122] is pulsating with the operating base frequency $\tilde{\omega}_o = 0.52$ rad/s, as measured in a rectangular channel of $R = 2.67$ ($a = 75$ μm , $w = 200$ μm), and shown by the black line in Fig. 2.6(a). To analyze the influence of this time-dependent flow on the dispersion of a solute with typical molecular diffusivity $D = 10^{-9}$ m^2/s , we approximate the pressure by a Fourier series with $|\ell| \leq 3$ (gray line). The discrepancy between the approximation and the actual signal fluctuates faster than the highest harmonic and is not resolved by the solute. The velocity scale U_o is taken as the (dominating) steady component, and the dimensionless parameters of the system are listed in Table 2.1.

The pump is designed to have minimal dispersion, which follows from our theory: It is normally operated at $\omega_o = 2.94$, which is faster than the solute equilibration rate $\lambda_{20} = 1.39$ of the width, so only the diffusion in the height-direction with $\lambda_{02} = 9.87$ is resolved. Furthermore, because the square of all oscillation amplitudes are small, $|\varepsilon_\ell| < 0.12$, their contribution to D_{eff} is minute, and $D_{\text{eff}}^{\text{avr}}(\infty) = 1.004 D_{\text{eff}}^{\text{steady}}(\infty)$, see Fig. 2.6(b). The

Table 2.1: Dimensionless parameters of the flow generated by the peristaltic pump of [122], see Sec. 2.4.3.

R	2.67	ε_0	1.000	α_{fl}	2810
Pé	6.92	ε_1	$0.352 \exp(-2.19i)$	ω_o	2.94
Wo	0.05	ε_2	$0.203 \exp(-2.24i)$	λ_{20}	1.39
Sc	1000	ε_3	$0.059 \exp(+1.54i)$	λ_{02}	9.87

dispersion may be increased by running the pump at lower frequency, e.g. $D_{\text{eff}}^{\text{avr}}(\infty) = 1.17D_{\text{eff}}^{\text{steady}}(\infty)$ changing ω_o to $0.1\omega_o$, or with higher oscillation amplitudes, $D_{\text{eff}}^{\text{avr}}(\infty) = 1.39D_{\text{eff}}^{\text{steady}}(\infty)$ changing ε_ℓ to $10\varepsilon_\ell$ for $\ell \neq 0$. If these changes are made simultaneously, we find $D_{\text{eff}}^{\text{avr}}(\infty) = 2.76D_{\text{eff}}^{\text{steady}}(\infty)$.

2.5 Results for initial point concentrations

We provide here the first general study of the dispersion of initial point concentration, which will be shown to include the few previously published results as special cases. The illustrating special cases are limited to the circular tube and the parallel plates cross-sections, since we found in the previous section that two-dimensional channel cross-section geometries only deviate by having two inherent time scales.

The work presented in this section has been done by the author in collaboration with M.Sc. research thesis student Emil Hovad. The author did most of the analysis and calculations, all the numerical work and all interpretation presented in the following.

2.5.1 General observations for the dispersion of initial point concentrations

Many features of the behavior of $D_{\text{eff}}^{\text{point}}(t)$ are similar to the transverse uniform case, including the scaling with Pe^2 , the additivity of the response to the flow frequencies, the frequency-doubled response at $2\omega_o\ell$ to any flow frequency $\omega_o\ell$, the negative values of $D_{\text{eff}}^{\text{point}}$ at large amplitudes of the oscillating flow components, and the long-time behavior ($t \gg 1/\lambda_1$)²; consequently, only the transient period is of interest and will be studied in the following. Negative values of $D_{\text{eff}}^{\text{point}}$ has previously been shown for point releases in unbounded harmonically oscillating linear shear flows by [87], but are a general feature of all bounded flows according to the developed theory.

The explicit dependence on the initial release position through $f_n(\mathbf{r}_\perp^o)$ illustrates that $D_{\text{eff}}^{\text{point}}$ in general will vary with \mathbf{r}_\perp^o in any cross-section. Furthermore, and contrary to the case of transverse uniform distributions, the center-of-mass initially does not move with the channel mean speed but relaxes to it on the time scale $1/\lambda_1$, see Eq. (2.56b).

Equations (2.58) and (2.59), which are valid for any channel cross-section, explicitly confirms the hypothesis put forth by Latini and Bernoff [82] that transient anomalous diffusion (i.e. $D_{\text{eff}}^{\text{point}} \propto t^0$) is a hallmark of Taylor–Aris dispersion of point concentrations. However, the attention paid given to this hypothesis in e.g. [27] is somewhat strange given that “normal” transverse uniform initial distributions also exhibit a transient anomalous phase of $D_{\text{eff}} \propto t$ (these cases reach the Taylor–Aris limit as $1 - e^{-\lambda_n t}$), see Eq. (2.45). For a non-integrable cross-section both $f_m(\mathbf{r}_\perp^o) \langle u_0 | f_n \rangle$ and $\langle f_m | u_0 | f_n \rangle$ may be considered as a random distribution with an average on the order unity, so using short-time expansions

²This was shown explicitly for the special case of steady flow in Sec. 2.3.3 but of course holds for all flows (verified for a number of test cases by numerical investigations), as expected on physical grounds, once the solute has mixed completely in the transverse direction.

of the exponentials about $t = 0$ with $f_m(\mathbf{r}_\perp^\circ) \langle u_0 | f_n \rangle \approx \langle f_m | u_0 | f_n \rangle$ we find

$$D_{\text{eff}}^{\text{point}}(t) \approx 1 + \text{Péc}^2 \sum_{n=0}^{\infty} \sum_{m=0}^{\infty} f_n(\mathbf{r}_\perp^\circ) \langle u_0 | f_m \rangle \langle f_m | u_0 | f_n \rangle \lambda_m \left[\frac{1}{2} t^2 - \frac{\lambda_m + \lambda_n}{3} t^3 \right], \quad (2.79)$$

so in general $D_{\text{eff}}^{\text{point}} \propto t^2$ during the transient. This has been shown to be the case for simple linear shear flows by [53]. The additivity of the response to the flow frequencies ensures that $D_{\text{eff}}^{\text{point}}(t)$ in time-dependent flows will oscillate around these “anomalous” dispersions from only steady flow. We emphasize that this general scaling result is irrespective of the channel cross section and furthermore is not limited to pressure-driven flows.

2.5.2 Flow fields and eigensolutions

We give here the mathematical details of the flow fields and eigensolutions used in the remaining discussion of initial point concentrations.

The explicit dependence of the solutions Eqs. (2.58) and (2.59) on the initial position \mathbf{r}_\perp° must be included in the eigensolutions, which therefore depend on both transverse coordinates \mathbf{r}_\perp . The solution for the circular tube cross-section with coordinates $\mathbf{r}_\perp = (r, \phi)$ is,

$$|f_{nm}\rangle = \frac{1}{\sqrt{1 - \frac{n^2}{\xi_{m,n}^2}}} \frac{J_n(\xi_{m,n} r)}{J_n(\xi_{m,n})} e^{in\phi}, \quad (2.80a)$$

$$\lambda_{nm} = (1 - \delta_{n,0} \delta_{m,0}) \xi_{m,n}^2. \quad (2.80b)$$

The velocity field for the circular tube (Eq. (2.61b)) is independent of the azimuthal coordinate unlike these eigenfunctions. However, due to the separable form of the eigenfunctions, there is no contribution to the overlap integrals $\langle f_{nm} | u_\ell | f_{nm} \rangle$ and $\langle u_\ell | f_{nm} \rangle$ from the azimuthal coordinate. Hence, since all terms in Eqs. (2.58) and (2.59) are multiplied by $\langle u_\ell | f_{nm} \rangle$, and only the ϕ -independent $n = 0$ -terms from these overlap integrals contribute to the sums, all expressions are independent of the azimuthal coordinate ϕ in this cross-section. The latter of these overlap integrals are therefore identical to the solution for the transverse uniform case given in Eq. (2.63), and the former are computed using numerical integration.

For the parallel plates $-1 \leq z \leq 1$, the velocity field is

$$|u_\ell\rangle = \varepsilon_\ell \frac{3}{k_\ell^2} \left[\frac{\cos(k_\ell z)}{\cos(k_\ell)} - 1 \right], \quad (2.81)$$

where the generalized wavenumber $k_\ell = \sqrt{-i\ell\text{Wo}}$ is similar to the circular tube cross-section (see Eq. (2.61a)) and the velocity scale is $U_o = \Delta p a^2 / 3\eta\mathcal{L}$ where $2a$ is the channel height. This velocity field is independent of the width coordinate y . The eigenfunctions, however, must include the y -dependence to account for the initial position. To remedy this, one may introduce a set of fictitious walls at $y = \pm R$ experienced only by the concentration field, and then only study the obtained solution before the point concentration has time

to interact with the walls; the solution to this fictitious eigenvalue problem in a rectangle was given previously in Eq. (2.76). Fortunately, the eigenfunctions in Eq. (2.76a) separate in the two transverse coordinates, so again there is no dependence on the y -coordinate in the overlap integrals $\langle f_{nm}|u_\ell|f_{nm}\rangle$ and $\langle u_\ell|f_{nm}\rangle$, and all y -dependence in the sums is therefore removed (only terms of $n = 0$ are non-zero). The overlap integrals $\langle f_{0m}|u_\ell|f_{0m}\rangle$ are computed numerically and the other overlap integral is given by

$$\langle f_{nm}|u_\ell\rangle = \begin{cases} \varepsilon_\ell \frac{6\sqrt{2}(1+(-1)^m) \frac{1}{k_\ell} \tan(k_\ell) - \delta_{m,0}}{\sqrt{1+\delta_{m,0}}} \frac{1}{4k_\ell^2 - m^2\pi^2} & n = 0, \\ 0 & \text{otherwise.} \end{cases} \quad (2.82)$$

As before, the dependence on the initial position in the y -direction therefore drops out, and the result is independent of the positions of the fictitious walls (independent of R).

The rest of this section focuses on the features of D_{eff} particular to point concentrations, and we will focus only on the cases where all flow components have the same weight, $\varepsilon_\ell = 1$. Furthermore, the independence of the azimuthal and width coordinates allows us to set these to zero without any loss of generality.

2.5.3 Steady flows

Transient scaling with time

We start by considering dispersion in steady (time-independent) flows. Figure 2.7 illustrates the transient development of D_{eff} up to the Taylor–Aris limit for both a circular cross-section (panel (a)-(b)) with initial position $\mathbf{r}_\perp^\circ = (r_0, \phi_0)$ and a parallel plates cross-section (panel (c)) with $\mathbf{r}_\perp^\circ = (z_0, y_0)$. Following an initial period dominated by molecular diffusion ($D_{\text{eff}} \approx D \propto t^0$) is a transient period of $D_{\text{eff}} \propto t^s$ with the exponent $s = s(\mathbf{r}_\perp^\circ) \geq 2$ depending on the initial position \mathbf{r}_\perp° , before D_{eff} reaches the Taylor–Aris limit of complete transverse mixing with a diffusive spreading of $D_{\text{eff}} \propto t^0$. When the concentration is initially released on the channel centerline $\mathbf{r}_\perp^\circ = (0, 0)$ the solute spreads with $D_{\text{eff}} \propto t^3$ while off-center releases lead to $D_{\text{eff}} \propto t^2$. The scaling of $D_{\text{eff}} \propto t^3$ deviates from the general scaling of Sec. 2.5.1 because we here consider a real velocity field instead of a random one. The scaling behavior is identical for the two geometries, but the numerical values of both the limiting value of $D_{\text{eff}}^{\text{point steady}}$ and the transverse diffusive time scale $1/\lambda_1$ of course do depend on the specific geometry, as also shown previously for the transverse uniform case. In addition to this dependence of the temporal scaling on the initial position, the latter also affects the waiting time before the axial spreading increases past diffusion. It takes longer for solute released at the channel center to enhance its axial spreading than it does for off-center releases. These scalings are in agreement with both short-time studies ignoring the wall [53, 107, 82] as well as a study that employed a stochastic differential equation approach to specifically these two geometries including the wall [27]. Our general theory, whose predictions have also been confirmed by numerics (Fig. 2.7(b), see numerical details in Appendix A.5), therefore validate these previous results.

The temporal scalings can be understood from a simple physical model which captures and illustrates the essentials of the phenomenon. Consider a Poiseuille flow with a non-

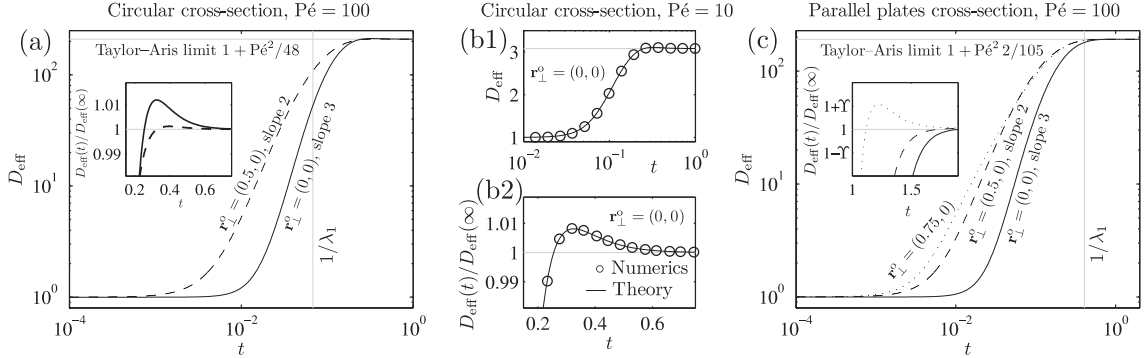


Figure 2.7: The effective diffusivity in steady flow in the circular and parallel plates cross-sections. The peaks in the effective diffusivity found just before it settles on the Taylor–Aris limit value are highlighted in the insets to panels (a) and (c), along with panel (b2). (a) The effective diffusivity in a circular cross-section at $\text{Pé} = 100$ with initial droplet position $\mathbf{r}_\perp^0 = (r_0, \phi_0)$ exhibits a maximum relative peak amplitude around 1 %. (b) Comparison of the theory (line) in the case of circular cross section with $\mathbf{r}_\perp^0 = (0, 0)$ at $\text{Pé} = 10$ to axisymmetric brute-force numerics (circles) confirms the existence of the peaks as well as the slope of the transient. (c) The parallel plate cross-section with $\mathbf{r}_\perp^0 = (z_0, y_0)$ has much lower relative peak amplitudes ($\Upsilon = 10^{-6}$) due to the markedly lower overall speed variations of the solute distribution since the solute diffusing in the y -direction does not move into different speeds.

dimensional velocity profile which scales as $u(r) \propto 1 - r^2$ for some suitably chosen transverse coordinate r , in which a point concentration is released at the position r_0 . The solute will begin to diffuse radially away from r_0 , and the evolving concentration field will be well approximated by a Gaussian for short times. This symmetric radial transport by diffusion will be on the order $\Delta r(t) \propto \sqrt{t}$, but as the solute diffuses radially it will experience a changing velocity field, so a molecule moving towards the center of the channel ($r_0 - \Delta r$) and a molecule moving away from the center ($r_0 + \Delta r$) will experience different axial displacements Δx_\pm during a time t . These axial displacements Δx_\pm may be estimated by inserting the positions $r_0 \pm \Delta r(t)$ into the aforementioned approximate velocity field $u(r) \propto 1 - r^2$ and integrating in time,

$$\Delta x_\pm = \int u(r_0 \pm \Delta r(t)) dt \propto (1 - r_0^2)t - \frac{1}{2}t^2 \mp \frac{4}{3}r_0 t^{3/2}. \quad (2.83)$$

With the center-of-mass of the solute being displaced axially as $\bar{x} \propto u(r_0)t$, the variance about this center-of-mass will scale as

$$\mu_2(t) = \langle (x - \bar{x})^2 | c \rangle \propto \frac{(\Delta x_- - \bar{x})^2 + (\Delta x_+ - \bar{x})^2}{2} = \frac{1}{4}t^4 + \frac{16}{9}r_0^2 t^3. \quad (2.84)$$

Hence, $D_{\text{eff}}^{\text{point}} \propto \frac{d\mu_2}{dt}$ will scale as $D_{\text{eff}}^{\text{point}} \propto t^2$ for short times except when the initial release point is at the channel center $r_0 = 0$, in which case $D_{\text{eff}}^{\text{point}} \propto t^3$. These scalings agree with the observations from Fig. 2.7. The transient expansion of the point concentration along the direction of the flow proportional to t^2 or t^3 is faster even than the “ballistic” dispersion of pure advection (i.e. $D_{\text{eff}}^{\text{point}} \propto t$). This is due to diffusion across streamlines from a region

of faster or slower flow speed. Furthermore, the differences in initial waiting time are a result of the fact that the initial speed variations experienced by solute diffusion at the channel center are small compared to the speed variations experienced off-center. A point concentration with centerline initial position will have to diffuse a greater distance to experience a substantial speed change which leads to the increase in $D_{\text{eff}}^{\text{point}}$ above unity.

The curve for $\mathbf{r}_{\perp}^o = (0.75, 0)$ in the parallel plates cross-section is observed to transition from an initial $D_{\text{eff}}^{\text{point}} \propto t^2$ -scaling to $D_{\text{eff}}^{\text{point}} \propto t$, seemingly violating the explanation just given. This is because the solute in this case quickly begins to interact with the wall, which limits the different speeds sampled by the transversely diffusing solute, an effect not included in the simple model. The reason for this deviation is that the channel wall is always felt, just as in the case of transverse uniform initial distribution (see Sec. 2.5.1); this limits the different speeds sampled by the solute since the diffusing front of solute cannot sample a greater speed variation, and sets the scaling to $D_{\text{eff}} \propto t$.

The transient in $D_{\text{eff}}^{\text{point}}$ is caused by the advective stretching of the solute, powered by the lateral diffusion. The axial dispersion during this phase is therefore caused by the variations in speed at different lateral positions, and not by diffusion, and it is consequently not expected to be diffusive (the latter characterized by $D_{\text{eff}}^{\text{steady}} \propto t^0$); the average motion during this phase is not random as it would be for diffusion. It is in general recognized that the presence of velocity fields leads to anomalous diffusion, exactly because the average motion is not random (see Sec. 2.2.4 and [49]). Furthermore, the cross-sectional averages used in Taylor–Aris dispersion theory (also for previous work on initial point concentrations [82, 27]) are not representative of an initial point concentration before it fills a substantial part of the channel (in the transverse direction), so the transient advective stretching of the point concentration is convoluted with the rest of the channel to produce what appears at a glance as physically counter-intuitive results. Hence, the “anomalous” diffusion found here is an artifact of the cross-sectional averages applied to an advection-dominated regime.

Peaks in the effective diffusivity

Contrary to the transverse uniform case, peaks in $D_{\text{eff}}^{\text{point}}$ exceeding the Taylor–Aris limit are observed in both geometries just prior to the relaxation to this limit, see insets in Fig. 2.7(a) and (c); the existence of the phenomenon has also been confirmed from brute-force numerics for a centerline initial position in a circular cross section at $\text{Pé} = 10$ in Fig. 2.7(b2). The existence of these peaks was first identified by M.Sc. student Emil Hovad during his research project [70]. Such peaks would not be expected in a dissipative process such as diffusion, but as discussed above, the transient is dominated by advection. This observation is key to understanding the phenomenon.

While the solute diffuses from the center to the channel walls on the time scale $1/\lambda_1$, the concentration field of an initial point release is not transversely uniform at this time, but remains concentrated towards the initial release position \mathbf{r}_{\perp}^o . Thus, while at the time $1/\lambda_1$ the Taylor–Aris effect of axial diffusion is occurring, the transversely non-uniform concentration field means that relatively more solute will diffuse transversely and outward from around the release point \mathbf{r}_{\perp}^o , and relatively less will diffuse from the wall towards \mathbf{r}_{\perp}^o .

Therefore, the amount of solute moving to higher speeds does not equal the amount of solute moving to lower speeds, which transiently results in an enhanced axial spreading exceeding the Taylor–Aris limit. $D_{\text{eff}}^{\text{point}}$ relaxes to this limit when the solute is distributed uniformly in the transverse direction whereby equal amounts of solute gain and lose the same speed changes, leading to a constant axial spreading, i.e. $D_{\text{eff}} \propto t^0$. Since the wall limits further diffusive movement of the solute, so particles at the wall only can diffuse towards the channel center thereby achieving higher speeds, the peaks can only occur when the solute has made first contact with the wall; this is when the transverse diffusion begins to dominate.

Furthermore, it follows that the largest peaks are found for the choices of r_{\perp}^0 that result in the solute distribution spreading into the largest speed differences. Thus, for the parallel plates (Fig. 2.7(b)) the largest effect is found when the solute is released close to one of the walls, while a center-line release in the circular tube (Fig. 2.7(a)) produces the largest effect in this geometry; the effect is also of greater magnitude in the circular channel since the speed variations are in two spatial dimensions contrary to the single-dimension speed variations in the parallel plates.

From this explanation it is clear that a velocity profile with larger radial speed variations should lead to even more pronounced peak amplitude. To investigate this further, we used the velocity profile of a Ostwald–de Waele power-law fluid of exponent q which has the rheological relationship $\tau = K (\partial u / \partial x)^q$ between shear stress τ and shear rate $\partial u / \partial x$ [101, 25]. We applied it only to the circular tube since the peaks are more pronounced here. In this geometry the non-dimensional velocity profile in pressure driven flow

$$u(r) = \frac{1 + 3q}{1 + q} \left[1 - r^{1+1/q} \right], \quad (2.85)$$

using the characteristic speed (Eq. (2.8))

$$U_o = \left(\frac{\Delta p}{\mathcal{L}K} \right)^{1/q} \frac{qa^2}{2^{1/q}(1 + 3q)}. \quad (2.86)$$

The case of $q = 1$ corresponds to a Newtonian fluid, $q < 1$ yields shear-thinning fluids (such as blood) and $q > 1$ corresponds to shear-thickening fluids which have more peaked velocity profiles than Newtonian fluids; the radial velocity profile becomes linear as q tends to infinity, $\lim_{q \rightarrow \infty} u(r) = 3(1 - r)$. Thus, by increasing q we achieved a velocity profile with greater speed variations across the tube radius. The increase of the maximum value of $D_{\text{eff}}^{\text{point}}$ from the Taylor–Aris limit is indeed found to increase with q to as much as 3.9 %, see Table 2.2 where we give the maximum relative peak amplitude \mathcal{M} ,

$$\mathcal{M} = \frac{\max_t \left\{ D_{\text{eff}}^{\text{point}}(t) \right\} - D_{\text{eff}}^{\text{point}}(\infty)}{D_{\text{eff}}^{\text{point}}(\infty)}. \quad (2.87)$$

To our belief, this is the first mention of such transient increases in dispersion past the Taylor–Aris limit in steady flows. As shown above, the effect is also confirmed from

Table 2.2: Maximum relative peak amplitude for a power-law fluid with exponent q . For $q > 1$ the velocity profile tends from the Poiseuille parabola of a Newtonian fluid at $q = 1$ to a linear peak at $q \rightarrow \infty$, while a sub-paraboloid velocity profile with an increasingly more flat mid-channel profile is found for $q < 1$. Hence, greater speed variations are experienced laterally for large q , leading to higher peak amplitudes. The velocity profile at the last entry of $q = 10^4$ is almost completely linear along the radial direction.

Exponent q	\mathcal{M}
10^{-1}	8.803×10^{-10}
10^0	1.201×10^{-2}
10^1	3.500×10^{-2}
10^2	3.886×10^{-2}
10^3	3.926×10^{-2}
10^4	3.930×10^{-2}
10^5	3.931×10^{-2}

numerics. The effect requires the presence of the channel walls which were neglected in [82], who therefore did not observe it. Interestingly, the effect was also not reported in [27], but their figures were small, and they did not verify their results with numerical computations.

2.5.4 Time-dependent flows

Our formula Eq. (2.58) describes the exact behavior of $D_{\text{eff}}^{\text{point}}$ for any time-dependent flow and any initial release position \mathbf{r}_{\perp}^0 . The behavior of $D_{\text{eff}}^{\text{point}}$ for time-dependent flows can in general be explained as a combination of the previous results on transverse uniform initial concentrations in any time-dependent flow, combined with the effects presented above (illustrated for steady flows) which are particular to point releases. Hence, a lengthy discussion of the evolution of $D_{\text{eff}}^{\text{point}}$ is not warranted, and we will therefore only briefly touch on this subject.

In harmonically oscillating (Womersley) flow, the maximum speed is at some times found in a boundary layer around the wall, and the fluid within this boundary layer will oscillate out of phase with the centerline fluid. The maximum value of the speed in this boundary layer is found at the diffusion distance from the wall set by the fluid oscillation frequency which in non-dimensional units is at the position $r = 1 - \text{Wo}^{-1}$ as discussed in Sec. 2.2.2. Thus, releasing the point concentration here will produce the same effect as releasing it at the center of the channel in steady Poiseuille flow; since this is the point where laterally diffusing solute will experience the greatest speed variations, the transient axial spreading is maximized at this release position. This is shown to be the case by the full line in Fig. 2.8(a) (computed for a circular tube), where furthermore the dashed and dotted lines are for a channel center and intermediate release points, respectively. Furthermore, the phase lag between the velocity of the center and the boundary layer of course means that a similar phase lag will be found between two droplets released in the center and within the boundary layer, respectively, as is also evident from Fig. 2.8(a).

The addition of a steady pressure gradient (of the same pressure amplitude) to the pulsating component yields an oscillating flow which is nonetheless always positive, and the position with the largest proximal speed variations is now no longer at $r = 1 - \text{Wo}^{-1}$ during the entire oscillation cycle; during the periods with a negative contribution from the

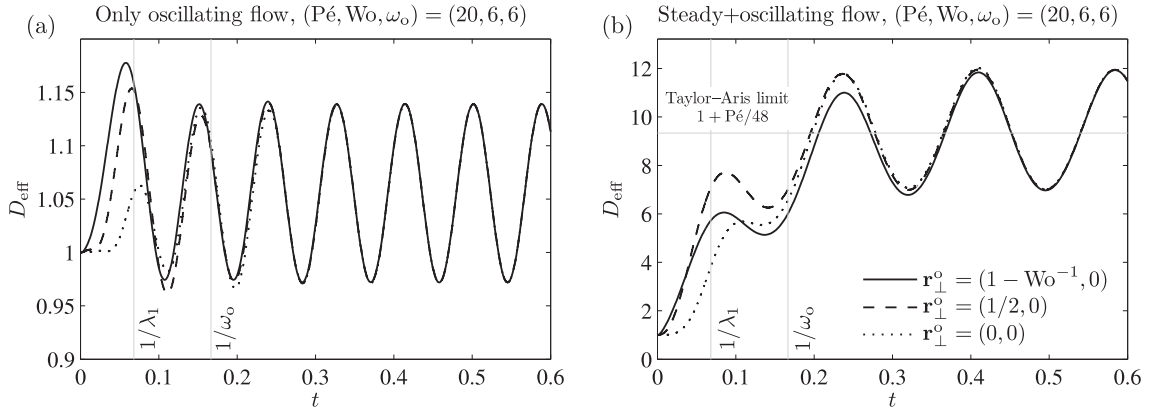


Figure 2.8: The effective diffusivity in unsteady flow at $(Pé, Wo, \omega_o) = (20, 6, 6)$ in the circular channel for a purely oscillating (Womersley) flow and a flow from combined steady and oscillating flow. Examples of the velocity profile of the purely oscillating flow was given in Fig. 2.2. Legend for both panels is given in (b). The information of the initial release point is erased as the solute mixes completely across the channel, and all release points follow the curve for $D_{\text{eff}}(t)$ for transverse uniform initial concentration. (a) The purely oscillating flow case exhibits a frequency-doubled response to the driving frequency ω_o . The largest transient axial spreading is experienced by the droplet released at the peak of the velocity boundary layer, at a distance Wo^{-1} from the wall, since this has the largest proximal speed variations. (b) Including a steady flow component to the flow of panel (a) results in a different response, since the velocity field now is changed. Since the contributions of each velocity frequency is additive, the largest transient axial spreading is now found by release points between the maximum of the steady flow component ($r = 0$) and the maximum of the oscillating flow component ($r = 1 - Wo^{-1}$). Notice that the solution oscillates around the Taylor–Aris limit for purely steady flow.

oscillating flow component in the near-wall boundary layer, the channel center speed will experience a positive contribution due to the transverse phase lag of the oscillating flow field. Hence, a position between the channel center ($r = 0$) and the boundary layer ($r = 1 - Wo^{-1}$) will have the largest time-averaged proximal speed variations over a cycle, and will consequently experience the most significant transient axial spreading. This can be seen in Fig. 2.8(b) for the position $\mathbf{r}_{\perp}^o = (1/2, 0)$ which is clearly dominating during the transient. In general, the release position of largest cycle-averaged proximal speed variations will have the most significant transient effects, even when more velocity frequencies are added. Naturally, this position shifts as more frequencies are added. Nonetheless, our formula Eq. (2.58) captures and contains all of these effects, and can be used to determine exactly where this “optimal” position is for any given flow, channel cross-section and \mathbf{r}_{\perp}^o .

2.5.5 Implications for practical situations

In addition to its scientific relevance, the transient persists long enough in physical systems that it has important implications for medical and industrial applications. Since it decays on a non-dimensional time scale of $1/\lambda_1$ which is typically on the order 10^{-1} (Eqs. (2.62b) and (2.76b)) and the normalization time scale is given by diffusion as L_o^2/D , decay of the transient for a solute with $D = 10^{-10} \text{ m}^2 \text{ s}^{-1}$ in 1000 s will only occur in channels with $L_o \leq 10^{-3} \text{ m}$; these time scales are long compared to the resting times for drug

delivery and many industrial applications, so the non-symmetric solute distributions and rapid spreading associated with the transient are present long enough that they cannot be ignored.

2.6 Conclusions

By combining Aris’s method of moments and Dirac’s bra-ket formalism, we have derived the compact, transparent, closed form (Eqs. (2.45) and (2.58)) for the transient Taylor–Aris dispersion, or effective diffusivity $D_{\text{eff}}(t)$, valid for any time-dependent flow of any initial solute distribution in a long, straight channel of arbitrary but constant cross section. For a general time-dependent flow, and as a function of system parameters, $D_{\text{eff}}(t)$ exhibits a rich and non-trivial structure due to the interplay between internal equilibration rates and external driving frequencies. Our main findings are

1. In general, the effective diffusivity is enhanced significantly by those parts of the time-dependent velocity field that have frequencies $\ell\omega_o$ lower than the fluid momentum diffusion rate α_{fl} and the solute diffusion rate λ_1 , in which case the dispersive effect has sufficient time to fully evolve. Furthermore, for Newtonian solvents in the cases of one-length-scale and steady-plus-one-frequency flow, one-length-scale and steady-plus-two-frequency flow, and two-length-scale and steady-plus-two-frequency flows, we have characterized the explicit suppression of the oscillatory enhancement of $D_{\text{eff}}^{\text{avr}}(\omega_o)$ each time a driving frequency $\ell\omega_o$ becomes larger than the internal diffusion relaxation rate λ_1 or the momentum relaxation rate α_{fl} . We found that this suppression is controlled by the solute mass diffusion in liquids and by the solvent momentum diffusion (or inertia) in gasses.
2. At oscillation amplitudes resulting in a net reversal of the flow $||u_{\ell}||$, a frequency-doubled response with negative values of $D_{\text{eff}}(t)$ occurs, contrary to the purely positive values of $D_{\text{eff}}(t)$ oscillating at the driving frequency found when the flow direction remains the same at all times. The frequency-doubling was found to arise due to the transient contraction of the dispersing solute associated with each flow reversal, while the frequency-doubling occurs because the reversal occurs twice per oscillation period.
3. Our formulation of D_{eff} in terms of inner products (overlap integrals) and eigenvalues facilitates general analyses in terms of random matrix theory. As an example of such an analysis we have sketched an explanation for the well-known fact that the relevant Péclet number for the Taylor–Aris dispersion in a channel of rectangular cross section involves the short height and not as expected on general grounds, the wide width. A similar general scaling argument was used to determine that the transient phase of $D_{\text{eff}}(t)$ for initial point concentrations scales as $D_{\text{eff}}^{\text{point}}(t) \propto t^2$ and not proportional to t as found for transverse uniform initial distributions.
4. For Newtonian solvents we have validated our theory by comparing it with the special cases of dispersion in steady flow and single-frequency pulsating flow treated in the literature, and by direct numerical simulations of single- and multiple-frequency flows.

5. We have derived the first general theory of dispersion of initial point distributions, which expressed a different temporal scaling than transverse uniform initial distributions during the transient. Analysis of this transient revealed that it is advection-dominated which causes the variations in scaling, and also accounts for the existence of transient peaks in $D_{\text{eff}}^{\text{point}}(t)$ exceeding the Taylor-Aris limit.

The work on initial point concentrations has exposed the limitations associated with the cross-sectional averages of the Taylor-Aris framework. While these can always be computed, their relevance for non-uniform initial distributions is less obvious and $D_{\text{eff}}(t)$ is in this case not simple to interpret. The physical effect of increased dispersion due to velocity variations will still likely be present for these initial distributions, but a new mathematical framework must be developed to describe it properly. We therefore do not find it appropriate to conduct any further analyses of non-uniform initial distributions with the framework developed in this chapter.

One obvious remaining open question is the effect of axially varying channel cross-sections. However, analyzing these cases would require modifications of the developed framework except for those cases which may be treated as small perturbations to otherwise fixed geometries.

Chapter 3

Diffusion-reaction: Migration of cells in a social context

In multicellular organisms and complex ecosystems, cells migrate in a social context. This is essential for the basic processes of life ranging from the migration of cells to form the specialized compartments (e.g. organs) in the developing embryo [55], over the collective migration leading to wound healing [84], to the migration of monocytes to infected cells during immunoresponse, and unregulated migration leads to disease including cancer metastasis [55]. In spite of more than half a decade of research [2, 3] the migratory behavior of cells in a social context remains as one of the major unresolved problems in biology according to *Science* [1]. Clearly, understanding of both single-cell migration at the cellular and sub-cellular level as well as characterization of cell-cell interactions are required to tackle this highly complex phenomenon.

In this chapter we study the social migration of fibroblast cells from the connective tissue of the skin of mice. These cells from a higher, multicellular organism “crawl” across surfaces, but do not form two or three dimensional structures¹. The work has been done in collaboration with Savaş Tay, Darius M. Johnston, Henrik Bruus and Stephen R. Quake during and after a six month visit to Stephen R. Quake’s lab at Stanford University’s Department of Bioengineering. The author did all data analysis, model development and implementation, while Savaş Tay and Darius M. Johnston carried out the experiments. A paper describing the main findings of this chapter has been published in the Proceedings of the National Academy of Sciences of the USA, which can also be found in Appendix F, p. 197.

¹Contrary to tissue cells from multicellular organisms such as mammals, bacteria — which are unicellular organisms — locomote by swimming rather than “crawling” on surfaces. A host of interesting and highly relevant social phenomena also occur for bacteria [62, 104], which however are mediated primarily by hydrodynamic interactions instead of cellular decisions.

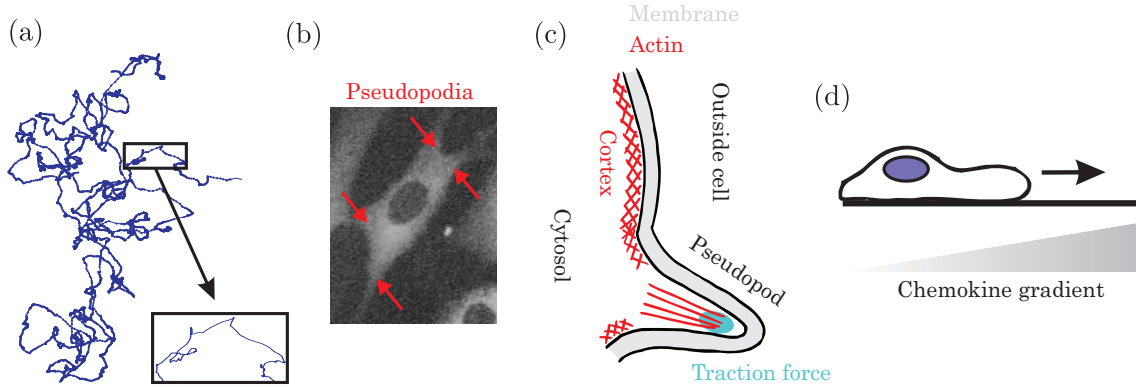


Figure 3.1: (a) Example of a persistent random walk characterized by random walk on long distances but directed motion on short length scales. (b) Picture showing the pseudopodia of a cell. (c) Schematic of the actin cortex found around the inside of the cell membrane, and how this is thought to be modulated inside pseudopodia. (d) In chemotaxis, cells move along a concentration gradient of specific signaling molecules known as chemokines.

3.1 Background

To set the stage for this work on social cell migration, we present here the relevant basics of cell migration and cellular interactions.

3.1.1 Single-cell migration

Whole-cell migration of isolated cells

Isolated, non-interacting cells have been found to exhibit a stereotypical migratory behavior that on short times maintain a given direction, but on long times becomes random. These basic features are shared across many different cell types, but the details may vary [57, 117, 90]. Typically, the motion of the cell may be described by Newtonian mechanics with one or more stochastically fluctuating forces, of which the simplest form is the so-called “persistent random walk” (or Ornstein–Uhlenbeck process) [136] which is characterized by a single Gaussian noise term and a single time-scale describing the cross-over from Newtonian (persistent) to random motion². Figure 3.1(a) illustrates the trajectory of a particle undergoing persistent random walk. The success of these models in describing the motion is undeniable, but their formulation lends little insight to the causes of the motion. A large body of work has therefore taken the opposite approach of seeking fundamental understanding of the involved subcellular processes.

Biomechanics of single-cell locomotion

Experiments have revealed that cells transmit traction force to the substrate almost exclusively in membrane protrusions known as pseudopodia, see examples in Fig. 3.1(b) [12, 100]. Within these pseudopodia the cell transiently forms linkages with the substrate

²Readers acquainted with stochastic processes will recognize this as the so-called Langevin approach.

as shown schematically in Fig. 3.1(c), and the cell then pulls itself towards these linkage sites, i.e. towards the pseudopodia. The force applied by each pseudopod was found to vary by about a factor of 2 in the few cases presented by Munevar *et al.* who measured the cellular traction force with subcellular resolution [100].

Cells contain several polymer networks jointly referred to as the “cytoskeleton” which are used among other things to maintain cell shape, actively transport macromolecules, conduct cell division, and also transmit force to the substrate. These polymers are available as oligomers in the cell’s plasma (the cytosol) and can dynamically polymerize to form long polymer chains. The cells control the nucleation, stabilization and degradation of these polymers to dynamically perform different tasks. Of special interest in pseudopod formation is the actin cytoskeleton, which is found in a cross-linked sheet around the inside of the cell membrane known as the cortex [5] (Fig. 3.1(c)). Upon proper stimulation, the actin is thought to break away from the cross-linked sheet to form a unidirectional protrusion away from the cell nucleus and thereby form the pseudopodium (Fig. 3.1(c)) [50, 135, 83]. It is also this actin sheet which attaches to specific molecules that link to the substrate surface across the cell membrane in these pseudopodia [5]. Finally, the cell pulls itself towards these linkage sites by connecting a second cytoskeleton — the microtubules, which emanate radially outward from an organelle known as the centrosome typically positioned close to the nucleus — to the actin, and actively pull on these attached microtubule filaments using motor molecules [50, 135]. Understanding the molecular intricacies involved in these processes is a matter of intense research [83, 50, 150]. Furthermore, modeling efforts and theoretical understanding incorporating these molecular findings at various levels of detail with reasonable agreement with experiments have been presented, e.g. [12, 42, 75, 116], but only for isolated cells, and in some cases containing many unknown biochemical parameters [120].

Chemotaxis: directed cell migration

Exposed to gradients of specific chemical signals known as chemokines, several cell types move along the steepest gradient, a phenomenon known as “chemotaxis” (Fig. 3.1(d)). It has been found that cells can sense and reliably move along very shallow relative gradients $(\Delta c/\Delta x)/c_0$ on the order of $10^{-3} \mu\text{m}^{-1}$ [94], and that the response becomes increasingly reliable at steeper gradients before it saturates at some level. It remains unknown how this is achieved on the pseudopod level: one study found random pseudopod formation but ordered retraction of lateral pseudopods in shallow gradients [7], while another study found biased pseudopod formation in the direction of the gradient [12].

Contact inhibition of locomotion

Colliding cells of several kinds including fibroblasts are known to repel each other upon collision, in a process known as contact inhibition of locomotion [2]. The collapse is thought to be achieved by locally depolymerizing the actin cytoskeleton [29]. Hence, if a pseudopod of one cell comes into contact with another cell, the local depolymerization of the actin skeleton will lead to cessation of the local force since the microtubules have no linkage to

pull on.

3.1.2 Social cell migration

While being the ultimate goal, social cell migration has attracted substantially less attention, presumably due to the increased level of complexity, the large amount of unknowns at the single-cell and sub-single-cell levels, as well as the inherent variations found between cell types. Most previous work has focused on either mechanically interlinked sheet-forming cell types such as endothelial and epithelial cells lining the blood vessels and surfaces of intra-body structures, respectively, or strongly polarized and aligning cell types.

Mechanically interlinked cell types

Migration of cells that form strong mechanical couplings with their neighbors are dominated by strong cell-cell cross-correlations, and bands of cells migrating together have been observed away from boundaries for several different cell types [143, 8]. Madin-Darby canine kidney epithelial cells have been found to transmit forces to each other through both the mechanical cell-cell linkages and by deforming the substrate, which leads to density-dependent spatial correlations between neighboring cells and a general dependence of the collective movement on the substrate stress field [9, 134, 8, 127]. At the boundaries, the cell sheet forms multicellular finger-like protrusions consisting of several aligned cells migrating together, furthermore linked together by an intracellular actin belt extending from cell to cell [105, 106]; the sheet follows behind these fingers and thereby moves into the previously uncovered area non-uniformly. The sheet is not pulled by the leader cells [134], but the cooperative stress coupling leads to the build-up of a wave of mechanical stress that slowly propagates through the monolayer and helps direct the migration towards the open boundary [118]. While these migratory behaviors are markedly different than isolated-cell migration, the exact role of the cell-cell linkages in shaping the collective migration remains unclear.

Strongly aligning cells

The collective behavior of strongly polarized and aligning cell types such as keratocytes (cells from nail and hair) has been observed to transition from no apparent collective motion at low cell densities to alignment of all cells as the density is increased [126]. This flocking behavior, where the population moves in a certain direction without it being stipulated by a leader, is found at many organismic length scales from cells over swarming insects [148] to birds [14] and to pedestrians in heavy traffic [68]. Theoretically, the phenomenon is captured by simple single-agent models obeying Newtonian mechanics combined with an additional random force term and strong alignment of the direction of motion of agents within the vicinity of each other; the simplest and most transparent of these is the Vicsek model where the cellular interaction is achieved by essentially a simplified Lennard–Jones potential [141], but several extensions have been proposed, e.g. [126, 147]. From a physics point of view, these studies revealed that ordered and directional macroscopic motion of active agents can arise in the absence of an external potential, and this response appears

to be largely independent of the details of the agents. Thus, while no direct linkages exist between the cells, the strong alignment induces multicellular behavior.

3.1.3 Open questions

While the large body of work referenced here have provided great amounts of insight, a number of fundamental questions remain unresolved.

1. *Migration of non-interlinked cells in a social context.* The migration of non-interlinked cells in a social context has not been addressed with single-cell resolution. In addition to providing fundamental insight into the interactions coordinating cell migration by both direct observation and by contrasting previous results of mechanically inter-linked cells, non-interlinked social cell migration also provides the first suitable experimental model for the role of the environment in shaping the biologically relevant single-cell migration scenarios of immunoresponse and cancer metastasis.
2. *How does the social context modulate pseudopodia dynamics?* The dependence of pseudopodia dynamics on being in a social context has apparently never been investigated. Thus, whether it changes, and the implications of being close to neighboring cells remain unexplored.
3. *The role of local alignment in emergent collective phenomena.* Flocking has only been observed in strongly aligned cells, so using cells with a lower propensity for local alignment will shed light on the role of local alignment in flocking. In addition to investigating some of the basics of this interesting non-equilibrium phenomenon, this could also further elucidate immunoresponse and the migration of cancer stem cells to form new metastases.

The combined theoretical and experimental work on the social migration of fibroblasts presented in this chapter has implications for all three questions.

3.2 Cells and experiments

3.2.1 Cell lines

High-resolution imaging data of both cell positions and pseudopodia was obtained using cells expressing different fluorescent fusion proteins in the nuclei (green) and cytosols (red), see Fig. 3.3(a). Specifically, we used p65^{-/-} mouse fibroblast (NIH 3T3) cells expressing the cytosolic fluorescent fusion protein p65-DsRed (red) as well as the nuclear marker H2B-GFP (green). Newly thawed cells were used for each experiment to prevent 3T3 cell re-transformation and to minimize heterogeneity. These cells form neither two-dimensional sheets, three-dimensional structures nor are they highly polarized, and their single-cell migratory behavior is established [12, 7, 94].

3.2.2 Microfluidic cell culture experiments

The experiments were conducted in an automated microfluidic cell culture platform containing 96 independently controlled and isolated chambers on each polymethylsiloxane (PDMS) based chip [63]. These 40 nanoliter chamber (1.12 mm by 0.9 mm by 40 μm) mimic physiological conditions more plausibly than traditional cell culture environments where concentrations of e.g. secreted signaling molecules are diluted into large volumes of surrounding fluid.

Cells were seeded at densities from 4,000–40,000 cells cm^{-2} ($\sim 40 - 400$ cells per chamber) into the microfluidic chambers, and were cultured for one day to reach 15-100% confluence before experiments. The external conditions were set to standard culture conditions (5% CO_2 and 37 $^\circ\text{C}$ external temperature) and maintained at this level. We made sure that cells were healthy, motile and proliferating before experiments. To conduct an experiment, we replaced the chamber volume at time $t = 0$, sealed the chamber using the microfluidic membrane valves, and imaged the cells at a constant rate Δt_{samp} either every 4 or 6 min in both GFP and DsRed fluorescence channels for 5 to 6 hours. The cells remained in the same media during the entire experiment. All cell densities were tested in parallel chambers, up to 24 different microfluidic chambers at a time, see Table B.1 in Appendix B, p. 135. To avoid edge effects, we focused on a region of $\sim 500 \mu\text{m} \times 700 \mu\text{m}$ in the center of the chamber which contained a population consisting of between 36 and 246 cells (corresponding to an average minimum nucleus-nucleus distance \bar{d}_{min} in the range $\sim 1\text{-}3$ cell diameters). We furthermore only used the first 200 min of the experimental data in all analyses to ensure nutritional deprivation was not a factor.

We varied the cell density by precisely controlling the cell counts in each chamber during automated seeding prior to experimentation. The cell counts were recorded at every time point during experiments by taking pictures and counting the number of GFP positive nuclei. This produced a well-controlled cell density in the chambers during the entire experimental duration. Since we only considered a region away from the chamber walls in the analysis, the number of cells in this region varies between chambers of purportedly identical density. Nevertheless, the number of cells in each picture is counted using the nuclear GFP signal and thus the numbers are exact. Therefore, instead of binning the data based on expected seeding density, we instead report the density-dependence of the data based on the average minimum cell-cell distance of all cells in a chamber over the entire experiment, \bar{d}_{min} .

Upon completing the trajectory analyses of the non-stimulated cells, we compared these results to cells of the same cell line exposed to the inflammatory signaling molecule tumor necrosis factor (TNF)- α in otherwise identical experimental conditions. We observed no difference in motility characteristics between non-stimulated cells and cells exposed to TNF α in the range 0.005 ng mL^{-1} to 100 ng mL^{-1} , see Appendix B.2. Since we furthermore did not observe any variation in pseudopod statistics between the two populations we included the cells exposed to TNF α in the analysis.

In total we analyzed the motility of 8566 cells at various densities in 79 different chambers using five different chips, producing a very comprehensive data set consisting of hundreds of thousands of data points. Each density was repeated at least once (each experiment

on different chips) and the majority repeated several times, see Table B.1. Small variations in \bar{d}_{\min} between otherwise identical chambers are due to the finite number of cells present in each chamber. We have presented the data according to the measured \bar{d}_{\min} rather than binning, since the actual nearest-neighbor distance will be shown to be important.

3.3 Image analysis

Automated algorithms were used to analyze the large experimental data set in order to minimize human bias and errors.

Cell positions and outlines were obtained automatically at each time step from the fluorescent images using previously published [128] custom MATLAB software courtesy of the Covert lab (<http://covertlab.stanford.edu/>) at the Department of Bioengineering at Stanford University. In short, the software detects the nuclei and cytosols using intensity thresholding combined with a number of filtering and segmentation steps. All cell tracking was manually checked to eliminate mistakes by the automated analysis.

3.3.1 Cell trajectories and velocities

The nucleus centroid $\mathbf{x}^i(t_j) = (x^i, y^i)_{t_j}$ was used as the position of cell i at time $t_j = j \Delta t_{\text{samp}}$, $j = 0, 1, 2, \dots$, so displacements $\Delta \mathbf{x}^i(t_j)$ and velocities $\mathbf{v}^i(t_j)$ were computed as

$$\Delta \mathbf{x}^i(t_j) = \mathbf{x}^i(t_{j+1}) - \mathbf{x}^i(t_j) \quad \text{and} \quad \mathbf{v}^i(t_j) = \frac{\Delta \mathbf{x}^i(t_j)}{\Delta t_{\text{samp}}}. \quad (3.1)$$

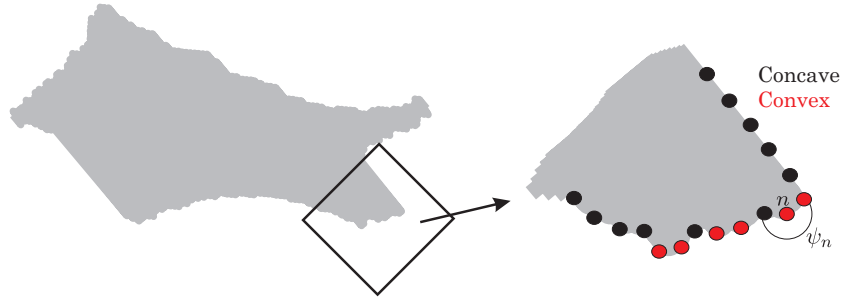
The experimental noise in determining cellular position was estimated to ~ 20 nm following the arguments in [90], with less than 0.2% of all recorded steps being below this limit (mean displacement between images was ~ 25 times this limit). These small displacements were found dispersed between larger, admissible displacements for individual cells, with no correlation in time. The directional autocorrelation series (detailed in Sec. 3.4.1) of the cells that occasionally recorded displacements close to the level of positional noise did not show significant deviations from cells with only admissible displacements, taken from the same chambers, so we concluded that all cell trajectories could be used without corrupting the conclusions.

3.3.2 Collision and pseudopod analyses

Collisions

Cell outline coordinates were obtained from each image as the boundary of the cytosolic (p65-DsRed) region of each cell. Contact was defined as two pixels belonging to separate cells being within a distance of 2 pixel from each other. Since this can occur over larger regions, neighboring outline pixels in contact with the same cell were grouped into regions and linked in time using custom algorithms. The times of contact $t_j, j, \dots, j + N$ for each of these contact regions were stored, and the contact time was obtained as $t_{j+N} - t_{j-1}$. Only contacts starting after the first image and contacts ceasing prior to the last image in each series were used, to ensure the entire lifetime of the contact was imaged.

Figure 3.2: Working principle of the automated pseudopod detection algorithm. The convexity boundary node n is determined from Eq. (3.2) using the outer angle ψ_n , and neighboring regions of convex nodes are grouped to pseudopodia. Nodes (filled circles) are color-coded to separate convex (red) from concave (black).



Pseudopodia

Pseudopodia were detected from the cell outlines using a custom MATLAB implementation of the automated algorithm suggested by Bosgraaf and van Haastert [23], with small modifications.

A pseudopod is an outward extension of the cell boundary, so following and edge-preserving smoothing step that removes pixelation noise, the algorithm determines the convexity of each node of each cell using the outer angle ψ_n of node n of the line segments pointing from the node to its two neighbors, see Fig. 3.2. Since $\psi_n = 180^\circ$ for all nodes of a spherical cell discretized by infinitely many nodes, the convexity of node n may be extracted from the outer angle by subtracting 180° . However, only a limited number of nodes N are used in discretizing, so $\psi_n > 180^\circ$ for a spherical cell; this is corrected by subtracting $360^\circ/N$ because the chain of N nodes forms a closed polygon. Thus, the convexity Ξ_n of node n defined by

$$\Xi_n = \psi_n - \frac{360^\circ}{N} - 180^\circ, \quad (3.2)$$

and $\Xi_n > 0^\circ$ indicates convex (outward) while $\Xi_n < 0^\circ$ indicates concave (inward) deflection from the outline. Regions of convexity (neighboring points with $\Xi_n > 0^\circ$) were for each cell linked in time, and the tip of the region was at each time step identified as the center node.

Pseudopodia were detected from these convexity regions by requiring (i) at least 2 neighboring convex nodes, (ii) cumulative convexity exceeding 10° , and (iii) mean convexity gradient exceeding $4^\circ \mu\text{m}^{-1}$. These requirements assure that the detected pseudopodia indeed are significant membrane protrusions and filter away noise from single aberrant boundary pixels. Single concave nodes were allowed in a convex region, and one time step of slight concavity of a region was allowed if the same pseudopod existed both before and after the concave time point. 154 analyzed cells were manually checked to assure the absence of algorithm-introduced bias.

Pseudopodia protrude and exert force for a period of time, before they collapse while providing little force. We computed the nucleus-tip distance between successive time steps,

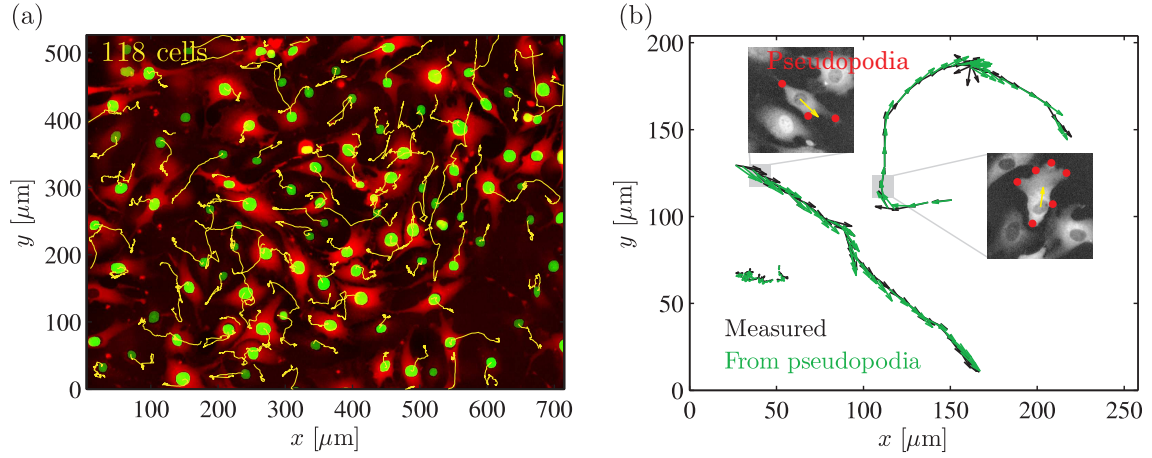


Figure 3.3: Trajectories of the cells generated during the first 200 min of an experiment. (a) trajectories (yellow) displayed on top of the fluorescence image illustrating the different fusion proteins used for the cytosols (red) and nuclei (green). (b) Trajectories can be nominally straight, curve, or display little apparent directionality. The vectorial sum of the pseudopodia of the cell (marked by red in insets) predicts the observed movement, since each pseudopod applies nominally the same force, see Sec. 3.1.1.

and included only growing (increasing distance) or stagnant (constant distance) pseudopodia in our analyses. Due to the sampling time of $\Delta t_{\text{samp}} \approx 5$ min, some pseudopodia were present in only one image. Cell collisions locally cause the pseudopodia to retract, so we neglected all pseudopodia arising or dying at the times of collision.

3.4 Experimental data analysis

All cells are observed to move at all cell densities, see examples in Fig. 3.3(a) and B.2 in Appendix B.3, p. 137. Furthermore, this movement exhibits no overall preferred direction of motion, which can be seen from Fig. 3.4 where in panel (a) we plot the distribution of angles between horizontal and all cellular displacements of all cells in an experiment, while panel (b) shows the full trajectories with the initial positions subtracted of all cells from the same experiment.

Turning our attention to the migration of the single cell, there is large diversity with negligible average cross-correlation in the migratory behavior of the cells at the same density (Fig. 3.3(a)). Some cells move along almost straight lines, other follow curved paths and yet other traverse very short distances with little apparent directionality (see examples in Fig. 3.3(b)). This continuum of different migratory behaviors, which is very different from the previously described stereotyped single-cell behavior found for isolated cells, suggests that there is a strong effect of the social context on the migration of the individual, even in the absence of cell-cell linkages. To fully understand this effect including whether it is due to inherent cell-cell motility variations or is an emergent group property, we quantified all aspects of the migration.

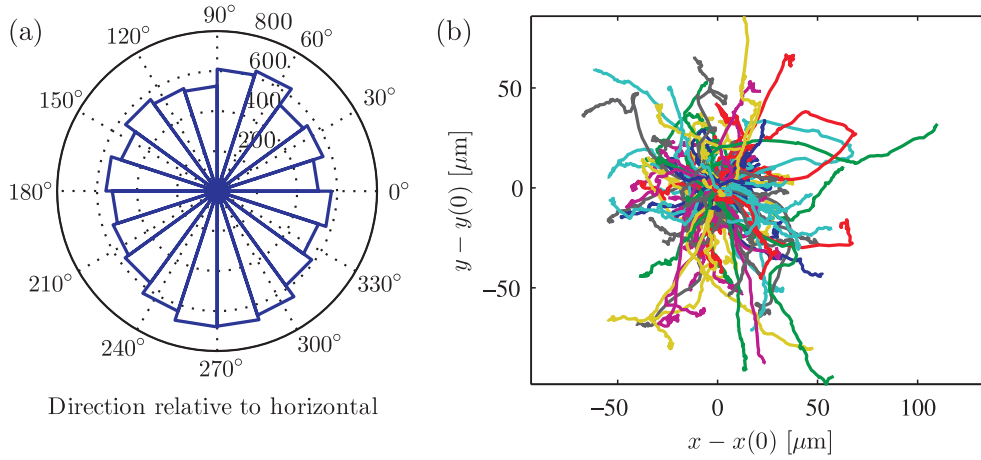


Figure 3.4: The cell direction of motion is random, here illustrated by two different means for a single experiment. (a) Histogram of the instantaneous angle of motion relative to horizontal and (b) all trajectories shifted to the same starting position (initial position $\mathbf{x}(t=0)$ has been subtracted, each trajectory is randomly given one of ten different colors) both confirm the absence of a preferred average direction of motion, within the limits of finite statistics.

3.4.1 Migration behavior at a fixed density

We first focus on an experiment at intermediate cell density ($\bar{d}_{\min} = 91.1 \mu\text{m}$) to present the key measures before considering how these depend on density in the following Sec. 3.4.2. Table 3.1 on p. 60 lists all investigations and observations.

Cell speed

The speed of the individual cell is observed to fluctuate substantially as a function of time as shown for four representative individual cells in Fig. 3.5(a) inset. Furthermore, the speed distribution of the individual cells during an experiment are similar, which can be seen from the color-coded histogram in Fig. 3.5(a) going from dark colors at low counts to light colors at high counts. These distributions all favor speeds around $0.25 \mu\text{m min}^{-1}$ yet most also have few speed measurements at $\sim 1.0 \mu\text{m min}^{-1}$. The average single-cell distribution from an experiment shows that this is caused by the existence of a distinct non-Gaussian tail (Fig. 3.5(b)). Such non-Gaussian tails in cellular speed distributions have previously been shown to be a general feature for several different non-sheet-forming motile cells [39].

The central limit theorem states that data from a large number of independent and identically distributed random variables will be distributed according to the normal distribution. If the random variables are not independent and/or identically distributed, the result is not a Gaussian distribution. Hence, the existence of similar non-Gaussian single-cell speed distributions suggests by the central limit theorem that each cell does not have an inherent velocity scale although the speeds follow the same distribution, but rather, that cell speed is a dependent variable. The simultaneous observations of fluctuating speed and similar single-cell speed distributions are consistent with cell speed being the result of

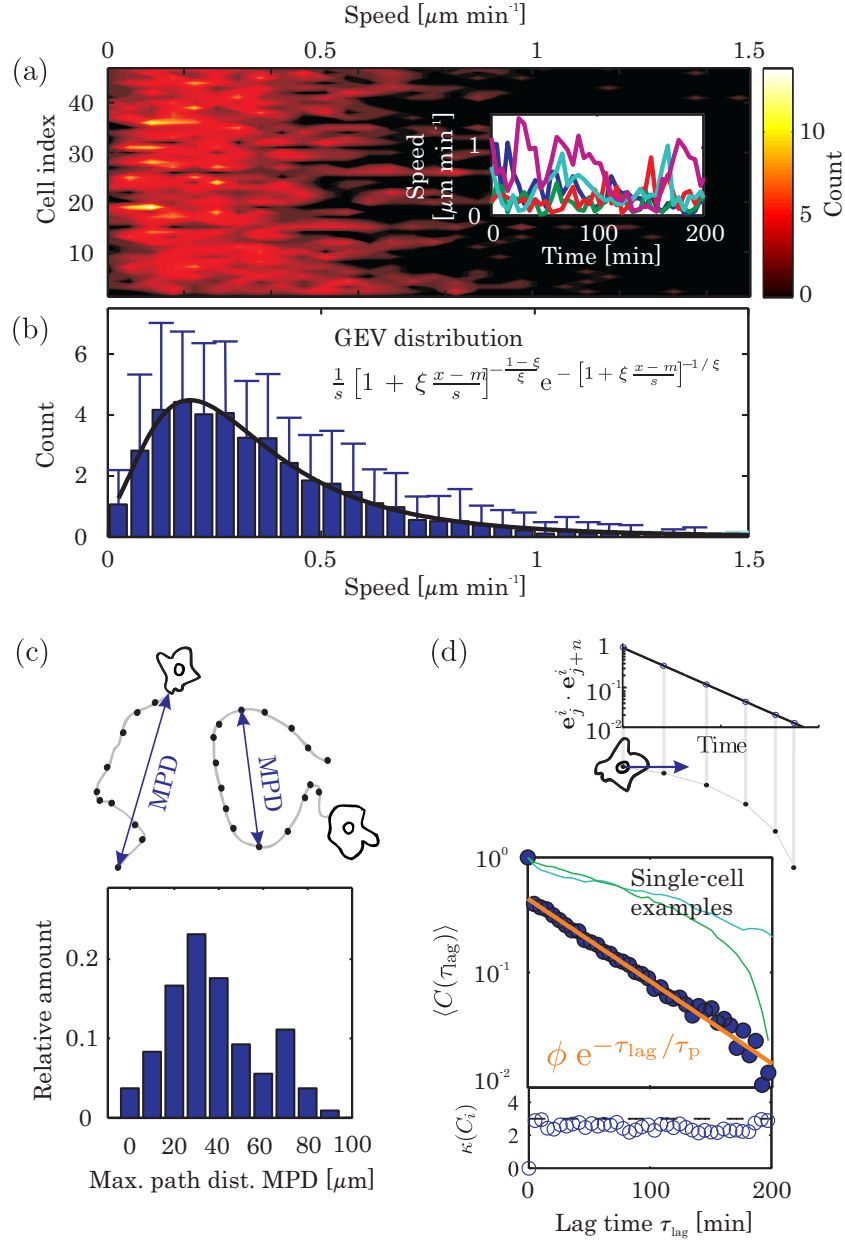


Figure 3.5: Experimental observations of cell migration. (a) Single-cell speed distribution, with inset showing speed vs. time for four single cells. (b) Average single-cell speed distribution (blue, with errorbars indicating standard deviation) is well fitted by a generalized extreme value (GEV) distribution characterized by the location parameter m , the scale parameter s and the shape parameter ξ , Eq. (3.3). (c) Population distribution of single-cell maximum path distance (MPD). (d) Chamber-average directional autocorrelation (blue circles) and fit (orange line) in the top panel. Also shown are single-cell autocorrelations from two sample cells moving nominally straight (lines). Kurtosis $\kappa(C_i)$ of the distribution of single-cell directional autocorrelation functions C_i computed at each lag time are given in the bottom panel. This kurtosis is everywhere close to the value 3 of the normal distribution and indicated by the dashed black line, so outliers only nominally affect the mean. The chamber-mean autocorrelation $\langle C(\tau_{\text{lag}}) \rangle$ in the top panel is therefore a representative measure of single-cell directionality.

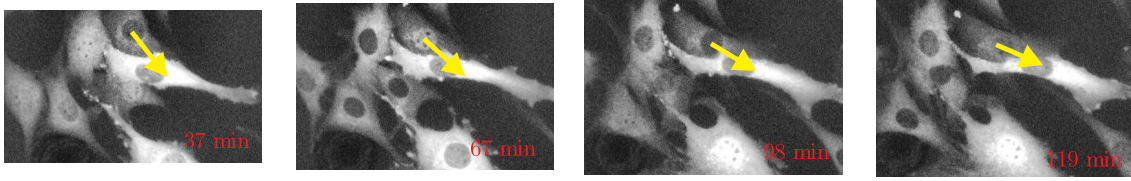


Figure 3.6: Example of a cell which continues to migrate into the same cell for a sustained period of time. The direction of displacement of the cell between this image and the next is indicated by the yellow arrow.

pseudopodia-driven locomotion with transient pseudopodia: Each time a new pseudopod forms, the cell speed is changed, causing the observed fluctuations (Fig. 3.5(a) inset), while the fact that pseudopodia “drive” the cell means that cell speed is a dependent variable.

In general, the speed distribution is well fitted at all densities by the probability density function of the generalized extreme value distribution (GEV), given by

$$f_{\text{GEV}}(x) = \frac{1}{s} \left[1 + \xi \frac{x - m}{s} \right]^{-\frac{1-\xi}{\xi}} e^{-[1 + \xi \frac{x - m}{s}]^{-1/\xi}}, \quad (3.3)$$

as shown in Fig. 3.5(b). This distribution is characterized by three parameters: the location m related to the position of the apex, the scale parameter s related to the width of the lobe, and the shape ξ related to the shape of the tail. This distribution forms a natural parametrization of the speed distribution at all cell densities; the reasons for this fit have not been further examined. To achieve the best fits, the logarithm of the experimental data was fitted to the logarithm of Eq. (3.3), which ensures that the distribution tail is well captured.

Single-cell sampled space: the maximum path distance

To quantify the variations in total space sampled by the individuals we introduce the “maximum path distance” (MPD), defined as the maximum distance between any two points on the trajectory of the individual cell. This measure, which is equivalent to the span dimension of polymer physics [144], displayed large variations across the population: for the present experiment we find MPD in the range 5-90 μm , see Fig. 3.5(c). Large and small MPD values thus correspond to cells moving nominally straight and cells that displace themselves small distances, respectively. MPD is therefore also non-trivially related to variations in single-cell trajectory curvature, although it is not a measure thereof.

Single-cell directionality

The observed variations in trajectories could be caused by a relative lack of collisions, however, we observed cells moving nominally straight even though they were in direct contact with other cells as well as cells without direct contact with other cells displaying little long-term directionality see Fig. 3.6. This indicates that collisions are not solely responsible for the variations in migratory behavior. While this could seem to contradict the repelling

of colliding cells in contact inhibition of locomotion, it will be shown later that this phenomenon does occur, but that whole-cell motion is a result of several competing processes. To further investigate this single-cell directionality, we compute the directional autocorrelation of the cellular trajectories using the unit vectors in the direction of instantaneous velocity. For cell i at the lag τ_{lag} this directional autocorrelation is given by

$$C_i(\tau_{\text{lag}}) = \langle \mathbf{e}^i(t + \tau_{\text{lag}}) \cdot \mathbf{e}^i(t) \rangle, \quad (3.4)$$

where $\mathbf{e}^i(t + \tau_{\text{lag}})$ and $\mathbf{e}^i(t)$ are the unit vectors in the direction of motion of cell i (e.g. $\mathbf{e}^i(t) = \mathbf{v}^i(t)/|\mathbf{v}^i(t)|$) at times $t + \tau_{\text{lag}}$ and t , and the brackets denote average over all times. Since we do not have infinite time series, we approximate Eq. (3.4) for a time series of N measurements by the unbiased estimate

$$C_i(\tau_{\text{lag}}) \approx H_i(n) = \begin{cases} \frac{1}{N-n} \sum_{j=1}^{N-n-1} \mathbf{e}_{j+n}^i \cdot \mathbf{e}_j^i & n \geq 0 \\ H_i(-n) & n < 0 \end{cases}. \quad (3.5)$$

where \mathbf{e}_{j+n}^i and \mathbf{e}_j^i are evaluated at times $(j+n)\Delta t_{\text{samp}}$ and $j\Delta t_{\text{samp}}$, respectively, and $\tau_{\text{lag}} = n\Delta t_{\text{samp}}$.

The directional autocorrelation describes the average alignment of the direction of motion of the same cell over time, and therefore measures the persistence of the direction of motion. Using the unit vectors in the direction of instantaneous velocity as opposed to the velocity vectors themselves removes any bias from the fluctuating speed and sets the range from 0 (no correlation) to 1 (complete correlation).

To investigate whether the chamber-average directional autocorrelation $\langle C(\tau_{\text{lag}}) \rangle$ well represents the individual C_i we computed the kurtosis $\kappa(C_i)$ of the distribution of C_i at each lag time. The kurtosis measures the influence of the outliers in defining the mean, and we use for reference the kurtosis of the normal distribution $\kappa = 3$. We find that the kurtosis of the distribution of single-cell directional autocorrelations is well described by the mean, since it is everywhere close to 3, see lower panel in Fig. 3.5(d) where the dashed line indicates $\kappa = 3$ of the normal distribution. This indicates that outliers only nominally affect the mean, and thus, that $\langle C(\tau_{\text{lag}}) \rangle$ is a representative measure.

This chamber-mean directional autocorrelation shows that the instantaneous step taken by each cell is positively correlated with the previous steps, see Fig. 3.5(d). The first sharp drop-off between the first and second time points occurs because changes in directionality are measured only every 4-6 min, and the rest of the data is well described by a decaying exponential $\phi e^{-\tau_{\text{lag}}/\tau_p}$. Here, the persistence time of directionality τ_p and the weight ϕ (varying from 0 to 1) describes respectively the time for the average cell to randomize its direction and the extent of directional motion in the chamber, with higher values of ϕ indicating a larger fraction of directionality persistent cells. For the present experiment we found $\phi = 0.38$ and $\tau_p = 56$ min.

Table 3.1: Summary of all experimental observations and model predictions.

	Experimental observations	
Pseudopodia	Cells dynamically form these protrusions which apply traction force to the substrate	Fig. 3.3(b)
Pseudopod life times	Distributed with a mean of 11.8 min.	Fig. 3.8(a)
Pseudopod life time and direction of motion	Same life time distributions found whether pseudopodia form along or against the current direction of motion	Fig. 3.8(b)
Single-cell number of pseudopodia	Nominally constant over time for the individual cell, but variations among the cells	Fig. 3.8(c) and (d)
Directional pseudopod bias	Pseudopodia formation is biased in the current direction of motion	Fig. 3.9(a)
Local pseudopod formation bias by other pseudopodia through pseudopod splitting	No evidence that this is dominating although we do observe it	Fig. B.5
Chemokine bias	Neighbor cells induce pseudopod formation by secreting a pseudopod-inducing chemical (chemokine)	Fig. 3.9(c)
Preferred direction of motion	No preferred direction of motion of the cells in a chamber	Fig. 3.4
Cell-cell collisions	Colliding cells transiently adhere to each other before the touching pseudopodia collapse, in a process known as contact inhibition of locomotion.	Fig. 3.8(e)
Single-cell speed	Fluctuating, but with similar distributions among cells indicating that all cells move. The average distribution is well fitted by a GEV distribution. Very similar across densities	Fig. 3.5(a) and (b), and Fig. 3.7(b)
Single-cell trajectories	Some are almost straight, other curl, yet other exhibit little apparent directionality. Fraction of cells moving nominally straight decays at higher density	Figs. 3.3, 3.7(a), 3.7(d) and Fig. B.2
Single-cell directionality	Chamber-average directional autocorrelation (which well represents the individual) decays exponentially ($\phi e^{-\tau_{\text{lag}}/\tau_p}$) on a time scale of $\tau_p = 50 \pm 11$ min. The weight factor ϕ decays at higher densities since a smaller fraction of cells move nominally straight	Figs. 3.5(d), 3.7(c) and 3.7(d)

Continued on next page

Cells moving nominally straight during whole experiment	Present at all densities	Figs. 3.7(a) and B.2, and Eq. (3.6)
Model predictions		
Single-cell speed	Fluctuating with similar distributions among cells and all cells moving. Average model speed distribution quantitatively reproduces experiment	Figs. 3.13(b), 3.13(c) and 3.14(b)
Single-cell trajectories	Some are almost straight, other curl, yet other exhibit little apparent directionality. MPD distribution is in quantitative agreement with experiment, but fraction of cells moving nominally straight is lower	Figs. 3.13(a) and (d)
Single-cell directionality	Chamber-average well represents the individual, and this average agrees with experiment	Figs. 3.13(e) and 3.14(a)
Effect of density	Model quantitatively captures the experimental findings across densities	Fig. 3.14

3.4.2 Dependence on cell density

Varying the cell density, we continue to observe straight-moving cells at all densities even though each cell at intermediate and high densities experience many collisions, see Fig. 3.7(a) with full chamber trajectories corresponding to this image given in Fig. B.2 in Appendix B.3, p. 137. The existence of straight-moving cells at all densities is a feature of the cells' social (interaction) dynamics, not just a mere coincidence, which can be seen from the coverage fraction \mathcal{F}_N of total cell surface area of N cells each of area \mathcal{A}_c to total chamber area \mathcal{A}_t ,

$$\mathcal{F}_N = \frac{N \mathcal{A}_c}{\mathcal{A}_t}. \quad (3.6)$$

The total area of investigation is $\mathcal{A}_t = 500 \text{ } \mu\text{m} \times 700 \text{ } \mu\text{m} = 3.5 \times 10^{-7} \text{ m}^2$, while the projected surface area of one cell ($\sim 20 \text{ } \mu\text{m}$ radius) is $\mathcal{A}_c = \pi \times (20 \text{ } \mu\text{m})^2 = 1.2 \times 10^{-9} \text{ m}^2$. Since we have between 36 and 246 cells in the chambers, the coverage fraction varies from 0.12 (36 cells) to 0.84 (246 cells), while $\mathcal{F}_N = 0.67$ is found for 100 cells. The fraction of available space for the cells to move on is at any instant $1 - \mathcal{F}_N$, which is therefore is low in most experiments. Since furthermore all the cells move and each experiment lasts for several hundred minutes, it is very unlikely by pure chance to find the straight paths as simply just a consequence of a relative lack of collisions.

The chamber-mean directional autocorrelation remains a representative measure of single-cell behavior across densities (see Fig. B.4), so we continue to study $\langle C(\tau_{\text{lag}}) \rangle$. The fraction of directionally persistent cells decreases at higher densities, but the persistence time of the individual cells remains essentially constant. This is illustrated by the decrease

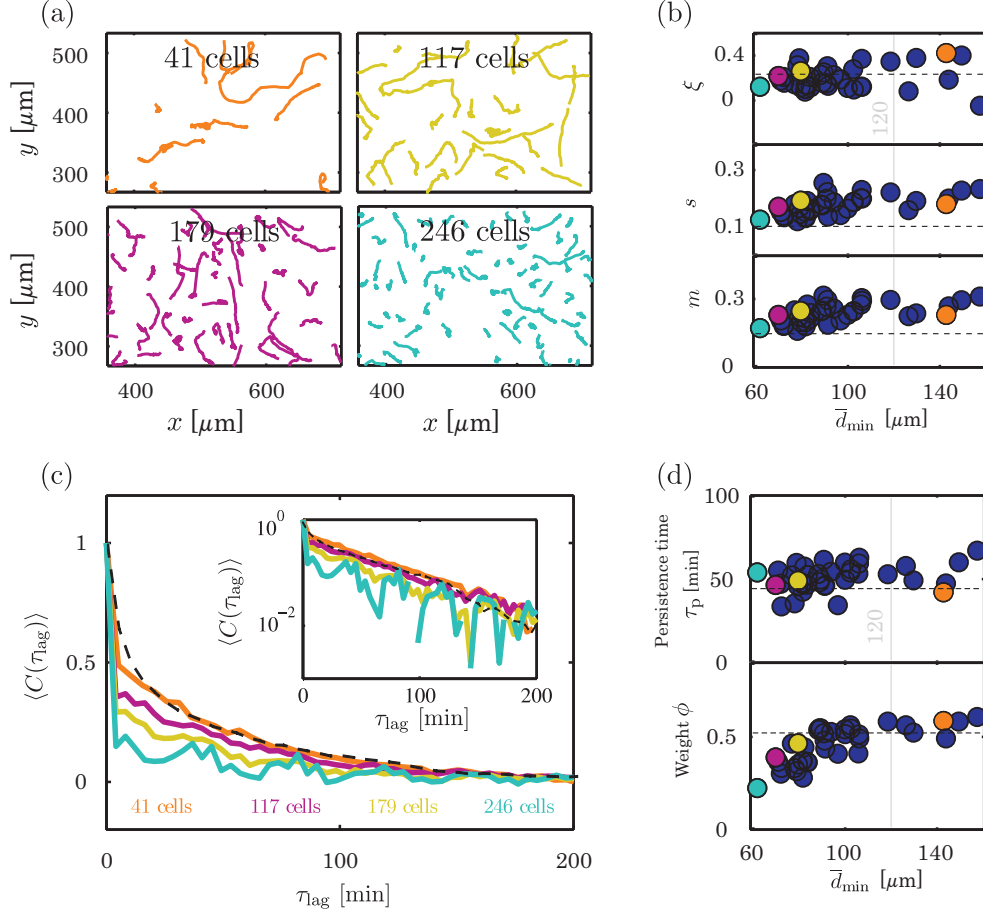


Figure 3.7: Effect of cell density on collective cellular migration, with dashed lines in (b)-(d) indicating results for isolated cells extracted from Ref. [117] (see also Fig. B.3 in Appendix B.3). (a) Examples of trajectories (see trajectories all trajectories for these experiments in Fig. B.2). The color-coding from (a) is re-used in the other panels to indicate how these four representative experiments score on the statistical measures. (b) Location m , scale s and shape ξ from least squares fits of average single-cell speed distributions to the GEV distribution Eq. (3.3) remain constant across densities. (c) Average directional autocorrelations $\langle C(\tau_{\text{lag}}) \rangle$ of the four experiments in (a) all follow the same exponential decay. (d) Weight ϕ and persistence time τ_p from least squares fits of average directional autocorrelations to $\phi e^{-\tau_{\text{lag}}/\tau_p}$ as a function of the average minimum nucleus-nucleus distance \bar{d}_{\min} in the chamber showing that persistence time τ_p is not affected by the changing density while the weight factor ϕ decreases due to higher collision rate.

of the weight ϕ and the constancy of persistence time of directionality τ_p in Fig. 3.7(c) and (d). Furthermore, the average single-cell speed distribution is also independent of density, see Fig. 3.7(b) where we plot the distribution of the three parameters m , s and ξ from fits to the GEV distribution (see sample fit in Fig. 3.5(b)).

Both our measurements of speed distribution and the low-density limit of the directional autocorrelation agree with previous results for human fibroblasts [117] (the latter indicated by dashed lines in Fig. 3.7(b), (c) and (d); see also Fig. B.3 in Appendix B.3). These findings indicate that the observed directionality does not depend on the fluctuating speed of the single cell, and the small variations in τ_p both within and across densities suggests that the directional persistence of motion, unlike cell speed and trajectory, is an inherent property of the cell's motility apparatus (i.e. internal polarization). Furthermore, the convergence of all our statistical measures to the level of isolated cells at $\bar{d}_{\min} \approx 120 \mu\text{m}$ determines the critical density where the social context becomes important.

3.4.3 Single-cell pseudopod statistics

We first verified that the cell migration in the social context is also mediated by pseudopodia, the force-generating protrusions. In Fig. 3.3(b) we plot the measured displacement vectors of three cells (black) and the displacements predicted from the vectorial sum of the pseudopod positions, where the latter well predicts the displacements since the force applied by each pseudopod is nominally the same [100], as previously mentioned. To further probe the origin of the diverse cellular migratory behavior described above, we therefore next investigated their pseudopodia.

Pseudopod behavior and life times

A pseudopodium grows for a period of time before retracting into the cell, thereby ending the local force it applied. To quantify the time each pseudopod exerted a force, we measured the pseudopod life times up to retraction, as previously described. To avoid bias in this analysis, we first manually tracked pseudopod life times of ~ 40 cells which did not collide and found no pseudopodia existing for more than 80 min. Next, using the automated analysis, we then obtained pseudopod life times from 154 cells across densities which each went at least 80 min without colliding: within the collision-free interval we measured the life times of all pseudopodia starting at each time step. Pseudopod life times were found to vary significantly, but with a mean life time of $\langle \tau_{\text{pseud}} \rangle = 11.8$ min and no dependence on density, see Fig. 3.8(a). The apparently exponential distribution of pseudopod life times could hint at an underlying Poisson process, but this has not been examined further. Furthermore, by computing the angles of pseudopod formation $\Delta\alpha$ in relation to the direction of motion, we found that pseudopod life times were unaffected by where it forms, see Fig. 3.8(b). These angles were computed between the current vectorial displacement $\Delta\mathbf{x}^i(t_j)$ (see Eq. (3.1)) and the vector connecting the nucleus and the pseudopod tip.

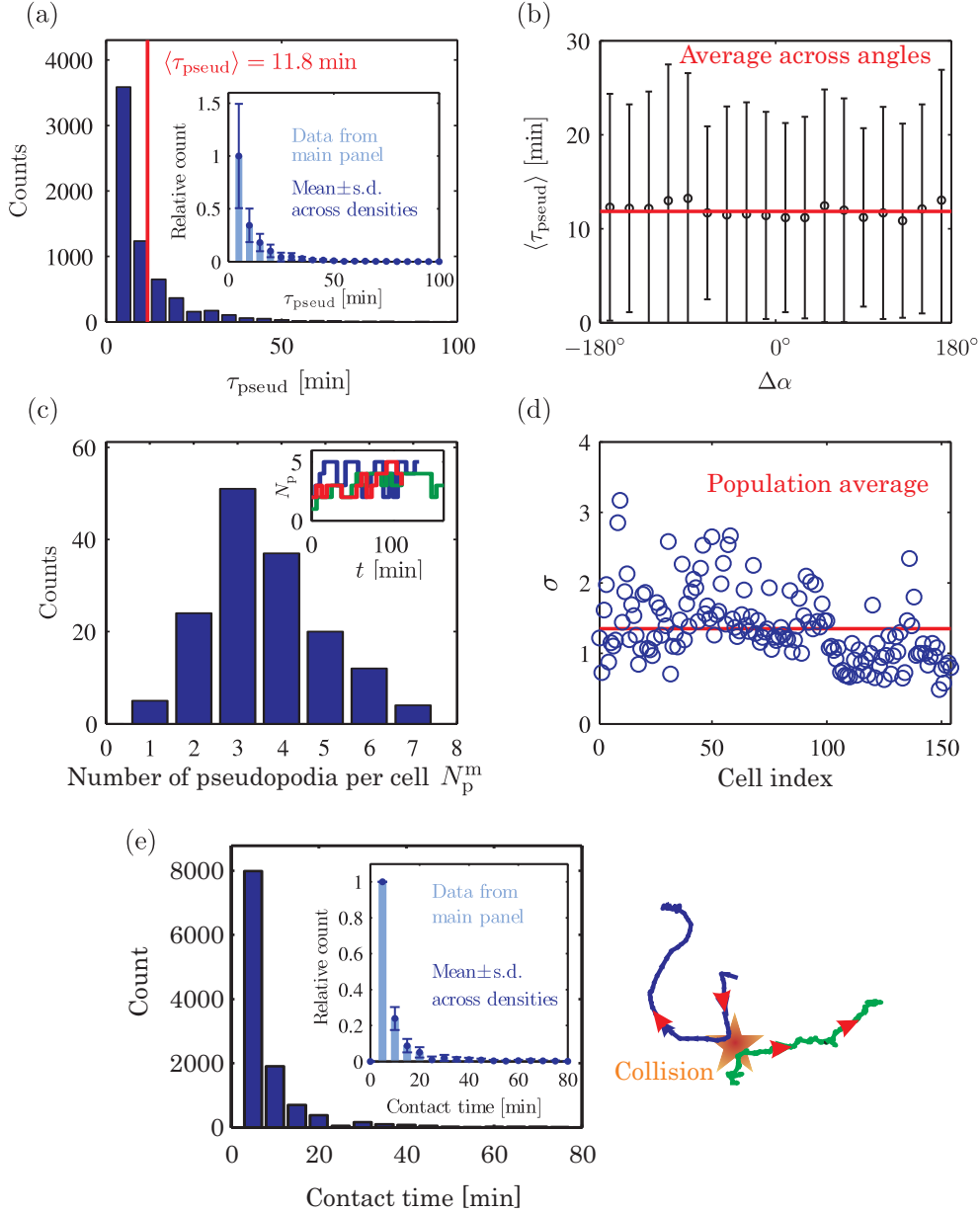


Figure 3.8: Single-cell pseudopod statistics. (a) Pseudopod life times with red line indicating mean of $\langle \tau_{\text{pseud}} \rangle = 11.8$ min, and the inset showing the independence of these life times on density by plotting the normalized distribution from the main panel along with the mean \pm s.d. based on 8 independent experiments across densities. (b) Pseudopod life times as function of the angle $\Delta\alpha$ between the position of pseudopod formation and the current direction of motion. Red line indicates the mean life time for all pseudopodia (it is the same red line as in (a)). (c) Number of pseudopodia per cell is roughly conserved over time. Inset shows single-cell number of pseudopodia versus time and main panel gives the distribution of single-cell mode numbers N_p^m over time of pseudopodia. (d) The standard deviation σ , see Eq. (3.7), of the instantaneous number of pseudopodia about the mode number of pseudopodia N_p^m , computed for each cell, shows that the mode number is a representative measure of the cell's number of pseudopodia. The red line gives the average for all cells in the figure which is 1.35. (e) Time periods of contact for colliding cell pairs (combined for all densities) is heavily dominated by short times. Inset shows independence of collision times with density by plotting the normalized distribution from the main panel along with mean \pm s.d. based on 34 independent experiments across densities. Also shown is the actual trajectories of two colliding cells (blue and green), with red arrows indicating direction of motion.

Single-cell pseudopod number is a conserved quantity

The instantaneous number of pseudopodia N_p for each cell shows small variation during the experiments, see inset to Fig. 3.8(c) where we plot the single-cell number of pseudopodia as a function of time for three representative cells. To quantify the variations about the mode number N_p^m (the integer number most often occurring) we define the standard variation about the mode number,

$$\sigma \equiv \sqrt{\frac{1}{n-1} \sum_{i=1}^n (N_p^i - N_p^m)^2}, \quad (3.7)$$

where N_p^i is the number of pseudopodia of the single cell at measurement time point i . This measure is similar to the standard deviation, but while the latter is computed with reference to the mean, our measure is computed with reference to the mode number. We show in Fig. 3.8(d) that for all cells the standard variation about the cell-specific mode number over time is small, with a mean variation of $\langle \sigma \rangle = 1.35$ for the 154 cells presented in the figure, signifying only small fluctuations³ about N_p^m . For each cell we therefore take N_p^m as the representative single-cell number of pseudopodia. The distribution of these mode numbers varies between 1 and 7, see Fig. 3.8(c).

Pseudopod collisions

Colliding pseudopodia of different cells transiently remain in contact before they collapse and thereby exhibit contact inhibition of locomotion [2, 29]. The distribution of contact times is strongly dominated by short times, as shown in Fig. 3.8(e) and furthermore also exhibits no dependence of density Fig. 3.8(e) inset. This independence of cell density suggests that pseudopod collapse is a basic cellular process dominated by inherent intracellular subprocesses.

We do not observe retraction of non-pseudopodial parts of the cells upon contact with other cells, and here only see effects of excluded volume. This explains why cells in contact can still move in the same direction, as shown previously in Fig. 3.6.

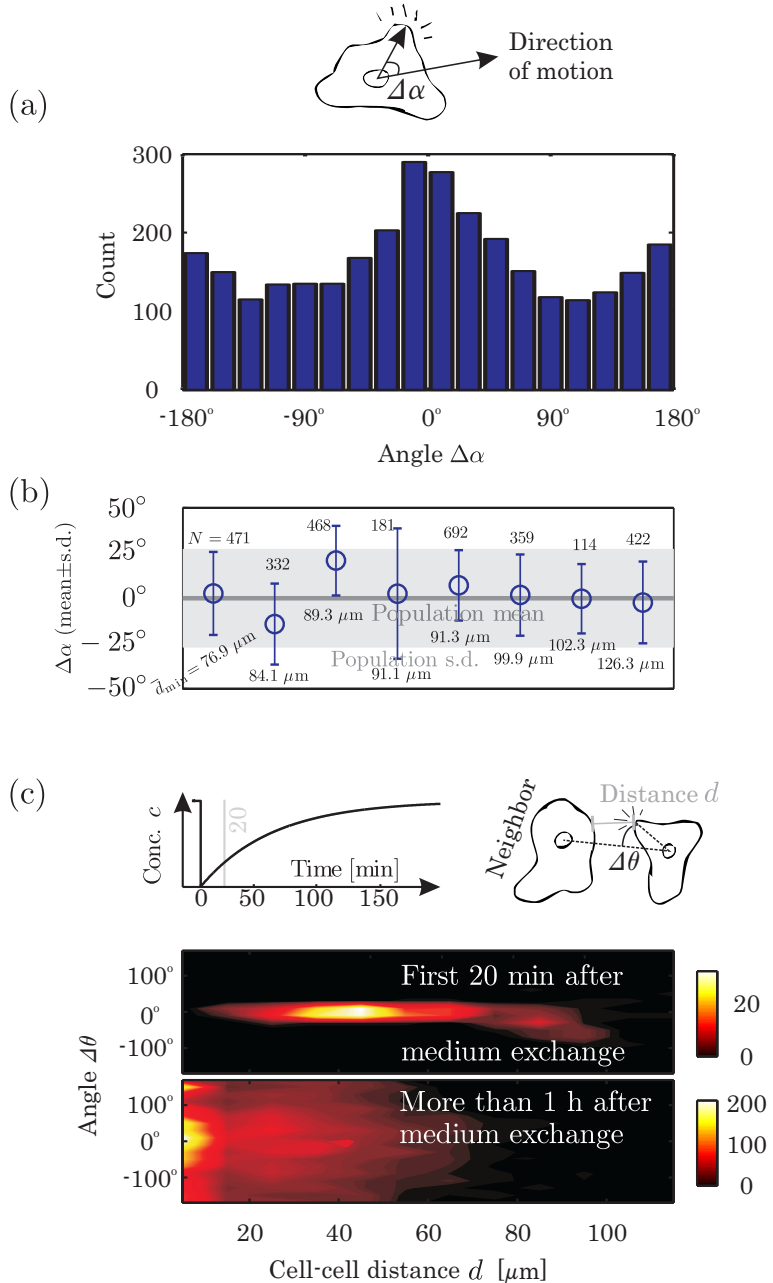
3.4.4 Pseudopod formation biases

Since pseudopodia provide the forces leading to cell locomotion, their sites of formation are decisive for both speed and directionality, yet how formation depend on internal and external factors is still debated [7, 12, 138]. Certainly, pseudopod formation and/or positions cannot be random since the persistence time of directionality $\tau_p = 49.6 \pm 11.1$ min (Fig. 3.7(d)) exceeds the mean pseudopod life time $\langle \tau_{\text{pseud}} \rangle = 11.8$ min (Fig. 3.8(a)). However, preferential collapse of lateral pseudopodia is not observed (Fig. 3.8(b)), nor do we find any dominant⁴ effect of branching of existing pseudopodia into two new pseudopodia (see Appendix B.4) which has otherwise been reported for isolated cells moving in shallow chemokine gradients [7].

³This apparent conservation of number of pseudopodia is presumably due to a limited, and roughly constant, amount of the intracellular actin used by the cells to form the pseudopodia.

⁴We do observe branching, but not at a significant rate compared to the other biases presented here.

Figure 3.9: Experimental evidence for biased pseudopod formation. (a) Pseudopod formation angle $\Delta\alpha$ with the current direction of motion (combined across densities) shows a clear preference of pseudopod formation in the current direction of motion, although pseudopodia are observed to form at all angles. A symmetric distribution favoring small angles is found at all densities which at all densities is well fitted by a Gaussian plus a constant baseline. (b) The findings in (a) are independent of cell density, as evidenced here by plotting mean \pm s.d. of the Gaussian term for each of the 8 independent experiments used for this analysis. The density-compiled data from (a) of $\Delta\alpha = 0 \pm 27^\circ$ are given by the gray region. The chamber density (expressed in terms of \bar{d}_{\min}) and the number of investigated pseudopodia N are also listed for each data point. (c) Position and angle of pseudopod formation $\Delta\theta$ in relation to the nearest neighbor cell. At time $t = 0$, the entire volume of the microfluidic chamber is replaced with fresh media, effectively removing any chemokine background and allowing new chemokine gradients to be established (see schematic in figure inset). The cells overwhelmingly move to the nearest neighbor during the first 20 min after media replacement but only mildly so (and only when the nearest neighbor is very close) after 60 min, indicating that secreted chemokines induce pseudopod formation.



Further investigations indicated that pseudopod formation is dominated by two independent biases by (i) the current direction of motion (Fig. 3.9(a)) and (ii) chemicals (chemokine) secreted by the cells, (Fig. 3.9(c)).

Bias by the current direction of motion

Evidence for pseudopod formation-bias by the current direction of motion was found by computing the angle $\Delta\alpha$ between the current cellular direction of motion and the position of pseudopod formation (Fig. 3.9(a)). We previously showed in Fig. 3.8(b) that the life time of the pseudopod as a function of this angle, but we do find a significant influence of $\Delta\alpha$ on the formation of new pseudopodia. The distribution of pseudopod formation angles relative to the current direction of motion in Fig. 3.9(a) displayed a clear bias for the present direction of motion. Furthermore, this effect is independent of cell density, see Fig. 3.9(b). On the molecular level, this is probably mediated by an internal polarization of key molecules [77].

Bias by secreted chemokine(s)

The existence of cell-secreted, pseudopod-inducing chemicals was found by studying the influence of neighbor cells in biasing pseudopod formation: in Fig. 3.9(c) we plot histograms of the number of pseudopodia as a function of the angle $\Delta\theta$ between the position of formation relative to the nucleus-nucleus line and the distance d to the nearest neighbor (dark color: low count, light color: high count). Pseudopodia formed exclusively towards the nearest neighbor cell during the first 20 min after medium replacement (Fig. 3.9(c) top panel), but much less so when the analysis is redone starting 60 min after replacement (except when the neighbor is very close; lower panel). This is most likely caused by one or several secreted chemokine(s), as evidenced by the decrease of the response at later times, except very close to neighbors, and corroborated by the fact that most chemokine molecules have diffusivities on the order $10^{-10} \text{ m}^2 \text{ s}^{-1}$ which sets the time scale for chamber filling to ~ 40 min. In other words, the secreted chemokines will have saturated the chamber by 40 minutes, effectively reducing chemokine gradient depths and the signal-to-noise ratio of chemokine receptor activity. The notion of a cell-secreted chemokine bias is furthermore supported by previous studies showing that these cells exhibit chemotaxis, e.g. [7, 12], and also themselves secrete several known chemokines, e.g. [128]. Moreover, the constant base level of pseudopod formation observed in our investigation of directional bias (Fig. 3.9(a)) further illustrates the existence of an additional and independent pseudopod formation biasing system.

3.4.5 Tentative explanation

The observations presented here indicate that the motile apparatus of the individual cell is centered around maintaining a certain direction through an internally controlled pseudopod formation bias (polarization). Being in a social context introduces a second mechanism based on chemokine-mediated biasing, similar to a previous report for *Dictyostelium* cells [112], as well as a higher frequency of pseudopod formation due to collisions. Once a

pseudopod forms, it appears the cell loses control over its fate, as the pseudopod seems to be following pre-determined programs of growth and pulling followed by collapse without force. In this view, the diverse single-cell migratory behaviors would arise as a physical consequence of pseudopod-mediated locomotion in a social context with fluctuating near-cell environment. Social cell migration can therefore be viewed as a reaction-diffusion problem at the pseudopod level where the cells react with a cell-secreted chemical to form their pseudopodia, although the consequence of the reactions are somewhat different from normal chemical reactions.

3.5 Modeling

To investigate whether these observed traffic rules on the individual cell level indeed do cause the very varied collective motion we observe, we formulated an agent-based mathematical model using the simplest physically reasonable assumptions for the motion of the individual cell based on three types of input: *(i)* our own pseudopod observations, *(ii)* previous experimental studies on chemotaxis of isolated cells, and *(iii)* Newton's second law of particle motion. This model, which can be considered as an extension of the Vicsek model [141, 126, 147], not only exploits known cellular biophysics of pseudopod-driven motility in a direct and intuitive way contrary to the abstract thermodynamic ensemble averages of cellular Potts-type models [64, 125], but also enables handling of the few hundreds of cells per experiments — a mesoscale not suitable for continuum modeling [110, 79, 17].

To investigate whether pseudopodia-mediated locomotion in a fluctuating near-cell environment explains our experimental cell migration observations, the model is centered on the behavior of the pseudopods of the single cell, with whole-cell migration given by its pseudopodia, and biased formation of new pseudopodia that are allowed to arise anywhere along the cell's membrane. An analytically solvable model was not identified, so a numerical implementation based on these premises and points *(i)*-*(iii)* above was developed. In short, model cells are two-dimensional idealizations consisting of a set of N_m points discretizing the cell membrane, which are connected through a center-of-mass. The motion of this center-of-mass is taken as the motion of the cell, with the membrane points each being allowed to move in relation to the center-of-mass in response to pseudopod formation or collapse, cell-cell contact, etc., as detailed in the following. The model furthermore assumes that each cell secretes chemokines, which all other cells react to. Cellular force transduction is achieved by forming pseudopodia through membrane point activation, and these form preferentially in regions of high chemokine concentration and in the current direction of motion; the former is achieved by biasing the probability of formation with the local chemokine concentration.

The model contains a list of parameters, which in most cases are determined directly from the experimental data or the literature; all parameters are summarized in Table 3.3. The simplest reasonable approach has been applied (Table 3.2 lists all assumptions underlying the model), yet, due to the pseudopod-centered formulation, the model is inevitably more complex and contains more parameters than some of the previously presented models neglecting the pseudopodia. Thus, while such simpler whole-cell theoretical models

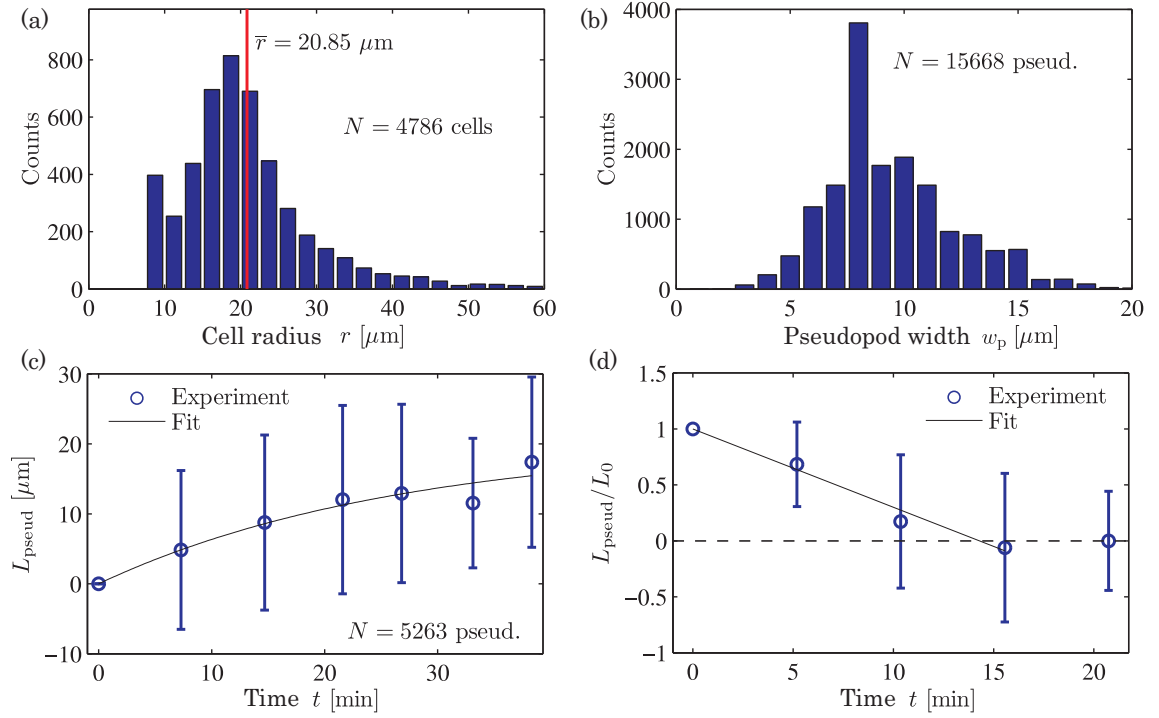


Figure 3.10: Experimental determination of model parameters. (a) Cell radius is computed as the average distance between the nucleus and the cell outline. (b) Pseudopod width has been measured at the base of the protrusion. (c) Pseudopod growth obtained from 5263 pseudopodia is approximated by an exponential function (Eq. (3.9)). (d) Pseudopod collapse following cessation of a pseudopod from either age or contact with other cells occurs at a constant rate depending on the initial length. Pseudopodia do not collapse between the second to last and final data points (at $t = 16$ min and $t = 22$ min).

have been presented in the past with the objective of investigating certain traits of the collective migration phenomena [141, 126, 39, 110, 79, 64, 147] none of these models are able to simultaneously account for a wide variety of the migration data such as ours, and our model thus provides one of the simplest ways of incorporating all of our observations in a physically transparent formulation. For comparison, a single-cell model of similar complexity coupling cell shape to speed due to Shao *et al.* consisting of three coupled partial differential equations and 14 parameters is only able to predict the trend found experimentally between these two variables [120, 119]; our model is able to predict a much larger part of the experimental data, while including cell-cell interactions, yet only using 13 parameters.

In the following the formulation of the numerical model is presented. Details of its implementation in MATLAB are given in Appendix B.5, p. 141.

3.5.1 Model cell

Each cell is modeled as a set of N_m points along the cell membrane, see Fig. 3.11, some being active and the rest passive. All N_m points are connected through a center-of-mass

Table 3.2: Model assumptions

–	Cell motion is quasi-static
–	The scale of secreted concentration is the same for all cells, c_0
–	All pseudopodia apply a force of the same magnitude, F_o
–	All collisions last the same time, τ_c
–	Chemokine activation of membrane points is biased by a Hill function of the relative concentration. This function is the same for all membrane points and all cells.
–	All cells have the same friction parameter γ
–	All pseudopodia grow and collapse according to the same relations, Eqs. (3.9) and (3.11)
–	All cells are circular with the same radius \bar{r}
–	Each cell has a fixed number of pseudopods at each time, but different cells have different numbers

with position \mathbf{x}_c . In a given time step, a number of the points are active and move outwards from the otherwise circular cell to form pseudopodia⁵.

The number of membrane points per cell N_m is taken as the cell circumference divided by twice the pseudopod width (by extending a membrane point, the base pseudopod width in the model is roughly twice the distance between two membrane points),

$$N_m = \frac{2\pi r}{2w_p}. \quad (3.8)$$

Using the experimental mean radius $\bar{r} = 20.9 \mu\text{m}$ (Fig. 3.10(a)) and pseudopod width $w_p = 8 \mu\text{m}$ (Fig. 3.10(b))⁶ we find $N_m \approx 36$. If two neighboring points are activated at the same time, the width of the pseudopod becomes larger and the force in this direction increases in agreement with experimental results [12].

To account for the experimental observation of conserved single-cell number of pseudopodia (Fig. 3.8(c)), each model cell is assumed to have a constant number of pseudopodia N_p , and a pseudopod cannot form before an old one stops due to either age or contact with another cell (detailed below)⁷. Each model cell is assigned a random number of pseudopodia N_p ranging from 1 to 7 which does not change. We found no difference whether each cell is assigned N_p according to the distribution shown in Fig. 3.8(c) or from a uniform distribution, so we used the latter for all presented results to limit the number of variables.

Experimental studies of isolated migrating cells have revealed that they have a protrusion opposite the direction of motion in addition to their pseudopodia. This protrusion known as the uropod, is pulled towards the cell center by intracellular myosin, while applying less traction force than pseudopodia [83]. Contrary to these findings, most cells

⁵The real cells are obviously not circular, but as time passes, the formation and collapse of pseudopodia make the model cell shape a dynamic and dependent entity, in agreement with experimental observation.

⁶This agrees with the report of pseudopod width of $\sim 5 \mu\text{m}$ in [12].

⁷However, since it takes some time for a former pseudopod to retract back into the cell, there will be times where the model cell will appear to have more pseudopodia than N_p ; likewise, cells which often collide with other cells will at some instances appear to have fewer pseudopodia.

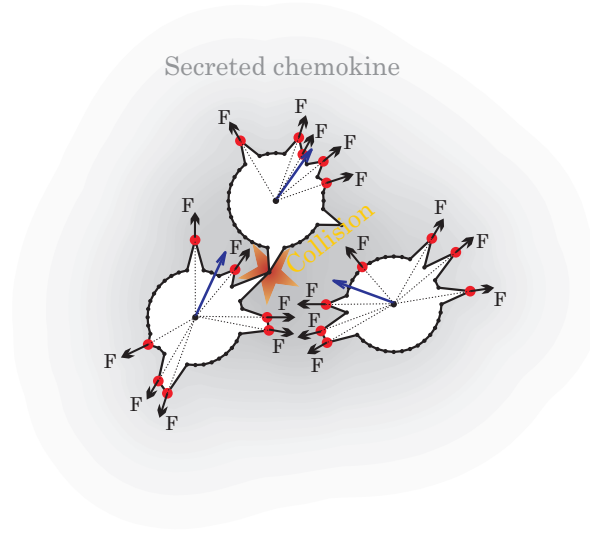


Figure 3.11: Illustration of model cells. Each cell consists of a number of membrane points (black dots) connected through the cell's center-of-mass (black dot in center) that dynamically and stochastically activate in response to their own history and the environment. Active membrane points (red dots) move outwards while each exerting a force \mathbf{F} radially away from the center-of-mass, and each cell moves by the resultant force from its pseudopodia. Furthermore, each cell secretes a pseudopod-inducing chemical (chemokine) whose concentration is indicated by the grayscale background. Touching pseudopodia of colliding cells transiently remain in contact prior to collapse.

in our experiments did not exhibit an observable morphological polarity as they formed pseudopodia in almost any direction, and consequently uropodia could rarely be unambiguously identified. In addition, the dynamics of uropod formation and maintenance for a cell which is constantly changing direction of motion is not well understood, and fibroblasts in particular have lower levels of uropodial myosin compared to e.g. *Dictyostelium* cells [123]. In the experimental observations on which we base our model we therefore neglected cell uropodia, and all experimentally observed protrusions were treated as pseudopodia. Due to the comparatively small traction forces applied by the uropodia and their low numbers, this is a reasonable first approximation, and the good agreement between model and experiment given below further justify these assumptions.

3.5.2 Pseudopod dynamics

Life of a pseudopod

Each pseudopod in the model (activated membrane point) is upon formation assigned a life time drawn from the distribution given in Fig. 3.8(a), and a new point is only activated when an existing pseudopod exceeds its assigned life time.

Following collision of a pseudopod with another cell, it is observed that a new pseudopod does not form at the position of the old pseudopod immediately after the release. This is in line with biochemical investigations which indicate that contact inhibition of locomotion is caused by a local inhibition of actin polymerization in the region of contact [29]. This is implemented in the model by including a resting time τ_{rest} following the release of the collided points, where said point cannot be reactivated. Following the data, we pick $\tau_{\text{rest}} = 5.5$ min, the mean time difference between two frames.

Protrusion

For each activated point, pseudopod protrusion is modeled by moving the point radially outward. We followed the tip of 5263 pseudopodia experimentally to obtain data on the growth of the pseudopodia, see Fig. 3.10(c). Using the mean of the experimental data for simplicity (and thereby ignoring the large variations) the pseudopod length $L_{\text{pseud}}(t)$ as a function of time can be approximated by

$$L_{\text{pseud}}(t) = L_0 \left(1 - e^{-t/\tau_{\text{pseud}}^{\text{growth}}} \right), \quad (3.9)$$

with $L_0 = 26.7 \mu\text{m}$ and $\tau_{\text{pseud}}^{\text{growth}} = 20.2 \text{ min}$.

The mathematical formulation for the protrusion of an activated point at position \mathbf{x}_i at a time t during the growth of the pseudopod is

$$\mathbf{x}_i + L_{\text{pseud}}(t) \frac{\mathbf{x}_i + \mathbf{x}_c}{|\mathbf{x}_i + \mathbf{x}_c|}, \quad (3.10)$$

where \mathbf{x}_c as previously is the position of the cell center.

Collapse

Pseudopodia collapse back into the cell after the prescribed pseudopod life time has passed or following ended collision⁸. The data given in Fig. 3.10(d) shows that the collapse rate depends on pseudopod length, since the normalized pseudopod length may be fitted by

$$\frac{L_{\text{pseud}}(t)}{L_0} = -K t, \quad (3.11)$$

with collapse rate $K = 0.07 \text{ min}^{-1}$. Hence, in the model each collapsing membrane point does so an amount $K L_0 \Delta t$ per time step, where L_0 is the full length of the pseudopod from Eq. (3.9) and Δt is the duration of the time step. Similar to pseudopod extension, collapse of a point occurs along the direction from the nucleus to the point. As shown in Fig. 3.10(d), the average pseudopod has completely retracted after $\sim 16 \text{ min}$, and therefore does not retract any further; hence the second to last and last data points have about the same length. The fit presented by Eq. (3.11) only applies until the pseudopod has collapsed, so in the model we retract pseudopodia only until they reach the radius \bar{r} of the unperturbed cell.

Pseudopod force

Each pseudopod (active membrane point) is assigned a force of magnitude F_o along the direction from the cell center to the activated point i (see Fig. 3.11)

$$\mathbf{F}_i = F_o \frac{\mathbf{x}_i + \mathbf{x}_c}{|\mathbf{x}_i + \mathbf{x}_c|}, \quad (3.12)$$

⁸Biophysically this collapse occurs since the cell-substrate adhesion is broken and the cell degrades the polymerized actin, so pseudopod retraction is caused by the elastic force of the membrane.

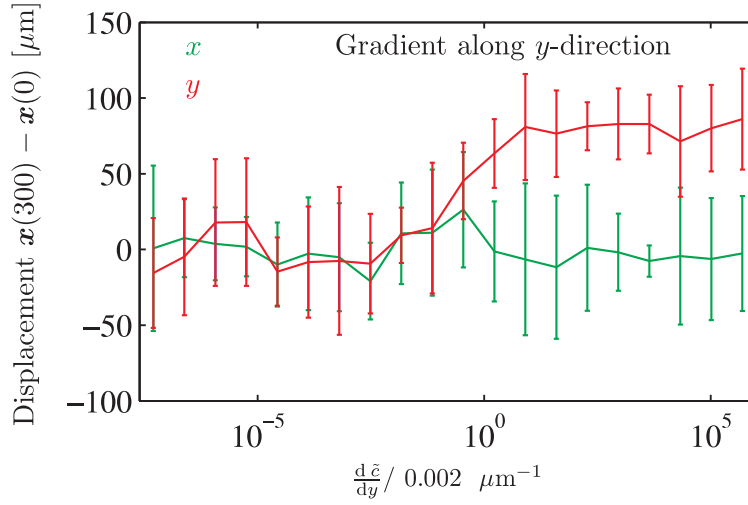


Figure 3.12: Chemotactic ability of model cells. Average displacement in 300 min simulation for different relative gradients (the gradient is applied only in the y direction) illustrate that model cells reliably respond to gradients above $0.002 \mu m^{-1}$, as experimentally observed by Melvin *et al.* [94]. The simulation was repeated 20 times for a single cell at each gradient level and errorbars indicate standard deviation.

where as in Eq. (3.10) \mathbf{x}_i is the position of the i th point and \mathbf{x}_c is the position of the cell center. The point force at the base of each pseudopod is estimated to $F_o \approx 1.1 \times 10^{-7}$ N from Munevar *et al.* [100] who showed experimentally that traction forces can be well approximated by point forces at the pseudopodia in NIH 3T3 fibroblasts. The direction of the force is justified by noting that the intracellular pulling force is thought to be mediated by the microtubules that emanate an organelle found right in front of the nucleus [5, 135].

Pseudopod formation bias

A new membrane point is activated after an already active point exceeds its life time or collides with another cell. The stochastic selection of this new point i is biased by secreted chemokine with factor Π_i^c and the current direction of motion with factor Π_i^d , so the probability that this point is activated out of the total N_m points of the cell is

$$p_i = \frac{\Pi_i^c + \Pi_i^d}{\sum_{i=1}^{N_m} (\Pi_i^c + \Pi_i^d)}. \quad (3.13)$$

A biased stochastic activation was used due to the low number of involved intra- and extracellular signaling molecules (at typical extracellular chemokine concentrations in the nanomolar range [56, 66] there are large relative fluctuations of as much as 100 % [80]).

The directional bias is determined from a fit to the experimental data in Fig. 3.9(a) using the angle $\Delta\alpha$ between the current direction of motion and the line connecting the center-of-mass \mathbf{x}_c and the current membrane point. A Gaussian fit to the normalized experimental data $\Pi_i^d = \Pi_0^d + \Pi_1^d e^{\frac{-\Delta\alpha^2}{2a^2}}$ with mean 0° , standard deviation $a = 29.7^\circ$, and amplitudes $\Pi_0^d = 0.04$ and $\Pi_1^d = 0.05$ was used.

Our experimental observations only imply the existence of a pseudopod formation bias by cell-secreted chemokines, not the exact form. To implement this crucial feature in the model, we therefore used previously published results on single-cell chemotaxis. Firstly, the results of Arriemerlou and Meyer implied that pseudopods are more likely to form in

the regions of higher chemokine concentration [12]. Secondly, the previously mentioned results from single-cell experiments on NIH 3T3 fibroblasts by Melvin *et al.* had revealed that relative concentration gradients $(\Delta c/\Delta x)/c_0$ of $0.002 \mu\text{m}^{-1}$ are required for unambiguous chemotactic response, and that the response saturates at higher concentrations, while relative concentrations lower than the aforementioned limit do not produce reliable chemotaxis [94]. Furthermore, it has been demonstrated that the local gradient across the cell relative to the average concentration of the cell is the decisive parameter [56]. All this points to a sigmoidal activation function based on local relative chemokine concentration. We use a Hill function based on the local relative chemokine concentration of the cell at membrane point i , c_i/\bar{c} , where $\bar{c} = \sum_{i=1}^{N_m} c_i/N_m$ is the instantaneous average concentration experienced by the cell, as sigmoidal functions of this type are ubiquitous in biochemical signaling activation including gradient sensing in bacterial chemotaxis [89]. The biasing function is

$$\Pi_i^c = \frac{\left(\frac{c_i}{\bar{c}}\right)^h}{1 + \left(\frac{c_i}{\bar{c}}\right)^h}, \quad (3.14)$$

where h is the Hill coefficient.

Running our model for isolated cells, we found we could reproduce the experimental results of [94] using $h = 50$ in Eq. (3.14), see Fig. 3.12 where each data point represents the average over 20 single-cell simulations each run for 300 min at each concentration. Biochemically, the Hill coefficient h is an expression of cooperativity among the chemical receptors mediating the chemotactic signal, with the coefficient corresponding to the number of cooperating receptors, and it has been shown that improved gradient sensing is achieved by increasing the cooperativity [71]. While the value $h = 50$ used in the model is unrealistically high — the reference value is $h \approx 3$ found for haemoglobin [124] — Hill coefficients of ~ 10 have been reported for bacterial chemotaxis [89], and Hill-like behavior with apparent Hill coefficients of $h \approx 42$ have furthermore been demonstrated to arise from more complex interlinked signaling networks in the maturation of *Xenopus laevis* oocytes [52]. Due to the overall agreement of the model and the lack of data for further investigation, this issue has not been probed in detail.

3.5.3 Cell motion

Each model cell is moved by the resultant force from its pseudopodia. Due to the time-scales and small masses involved, cell inertia is negligible and the following relationship is postulated

$$\sum_i \mathbf{F}_i = \gamma \mathbf{v}, \quad (3.15)$$

where γ is the same constant for all cells, \mathbf{F}_i is the force of pseudopod i and \mathbf{v} is the velocity of the cell. The displacement of the model cell center $\Delta \mathbf{x}$ is then given by

$$\Delta \mathbf{x} = \mathbf{v} \Delta t, \quad (3.16)$$

where Δt is the time step. It has been shown in the literature that NIH 3T3 fibroblasts move along the direction of the resulting traction force [100], which essentially is the postulate of Eqs. (3.15) and (3.16).

Physically, γ accounts for the Stokes drag from the fluid and the cell friction force with the substrate, which also scales linearly with the velocity. It is related to the energy dissipated by the making and breaking of cell-substrate chemical bonds as the cell moves. Contrary to measurements of the strength of these bonds, the friction is rarely determined experimentally, and the irregularity, softness and general ignorance of the significant molecular contributors of the cell attachment during migration makes first-principles theoretical analysis difficult. γ is the same for all cells in the model (also across densities) and is fitted from the ensemble average of the velocity distribution data at the value $\gamma = 39.0 \text{ kg s}^{-1}$, which compares reasonably well with an estimated friction coefficient of $\gamma \approx 29 \text{ kg s}^{-1}$ extracted from Munevar *et al.* [100] but is larger than $\gamma \approx 1 \text{ kg s}^{-1}$ given by an order-of-magnitude estimate of the friction per unit cell surface area of $10^9 \text{ kg s}^{-1} \text{ m}^{-2}$ by Larripa and Mogilner⁹ [81]. For comparison, these numbers are many orders of magnitude greater than the viscous Stokes friction with the medium

$$\gamma_{\text{Stokes}} = 6\pi\eta r \quad (3.17)$$

of $\gamma_{\text{Stokes}} \approx 4 \times 10^{-7} \text{ kg s}^{-1}$, where $\eta = 1.002 \times 10^{-3} \text{ Pa s}$ is the viscosity of the liquid (assumed to be water) and $r \approx 20 \text{ }\mu\text{m}$ is the cell radius (Table 3.3). This is not surprising since the molecular interactions with liquid molecules is weaker than the interactions with attaching polymers used by the cells.

3.5.4 Secretion of signaling molecules

To mediate the chemotactic response of Fig. 3.9(c), model cells secrete chemokines. We assume that each model cell secretes at a constant rate from the entire perimeter and the concentration field from each cell is thus approximated by the analytical solution for a constant source [25],

$$c(d) = c_0 \operatorname{erfc}\left(\frac{d}{\ell_{\text{diff}}}\right), \quad (3.18)$$

where $\operatorname{erfc}(x)$ is the complementary error function, d is the distance from an extracellular point to the cell membrane, c_0 is the concentration at the cell membrane (taken to be the same for all cells) and ℓ_{diff} is the length scale the concentration field decays on. Due to dilution and degradation, the effective signaling distance of a cell is estimated to 50 times the cell radius by Francis and Paulsson [54], and the length scale ℓ_{diff} is therefore taken to be 1/3 of the effective signaling distance of a cell of radius $r \sim 20 \text{ }\mu\text{m}$, i.e. $\ell_{\text{diff}} = 340 \text{ }\mu\text{m}$.

3.5.5 Cell-cell contact

The contact inhibition of locomotion is at the pseudopod level characterized by the time of contact τ_c (Fig. 3.8(e)). Aiming for simplicity we assume in the model that the force is applied until the contact stops. The contact time τ_c is — also for simplicity — taken as the

⁹The value by Larripa and Mogilner [81] was estimated from the reported work of others on endothelial cells and a multicellular *Dictyostelium* slug, so the apparent disagreement of our model with this estimate is not a major cause of concern.

Table 3.3: Values assigned to model parameters.

Parameter	Symbol	Value and unit	Source
Cell friction	γ	39.0 kg s^{-1}	Global fit
Pseudopod force	F_o	$1.1 \times 10^{-7} \text{ N}$	Extracted from Munevar <i>et al.</i> [100]
Number of membrane points per cell	N_m	36	Eq. 3.8 and Fig. 3.10(a)
Number of pseudopodia per cell	N_p	1 – 7	Fig. 3.8(c)
Full pseudopod length	L_0	$26.7 \text{ }\mu\text{m}$	Eq. (3.9) and Fig. 3.10(c)
Pseudopod collapse rate	K	0.07 min^{-1}	Eq. (3.11) and Fig. 3.10(d)
Hill coefficient	h	50	Fig. 3.12 and Melvin <i>et al.</i> [94]
Decay length scale of secreted chemokines	ℓ_{diff}	$340 \text{ }\mu\text{m}$	Fig. 3.10(a), combined with Francis and Palsson [54]
Cell radius	r	$20.9 \text{ }\mu\text{m}$	Fig. 3.10(a)
Collision tolerance distance	ϵ	$3 \text{ }\mu\text{m}$	Chosen to best capture the dynamics, no observable changes choosing ϵ in the range $1 \text{ }\mu\text{m} - 5 \text{ }\mu\text{m}$
Cell-cell contact time	τ_c	5.5 min	Fig. 3.10(e)
Time between successive activations of the same membrane point	τ_{rest}	5.5 min	Own data
Characteristic pseudopod growth time	$\tau_{\text{pseud}}^{\text{growth}}$	20.7 min	Eq. (3.9) and Fig. 3.10(c)

most frequent experimentally observed contact time of pseudopodia in contact with other cells from the data, which unfortunately is identical to the mean sampling time Δt_{samp} ,

$$\tau_c = 5.5 \text{ min.} \quad (3.19)$$

If an active membrane point comes within a distance ϵ of any point of any other cell (does not need to be an activated point) the two points are deemed to be in contact. This continues until a total of τ_c has passed whereafter the local force is stopped and the previously active membrane point becomes passive and therefore collapses. The exact value of ϵ does not influence the behavior of the model cells for the range $1 - 5 \text{ }\mu\text{m}$.

3.5.6 Initial conditions and sampling of model output

We initiate the model by seeding cells at a desired concentration, using either the known starting positions from an experiment or random placement. In the experiments we only track cells in the middle of the chamber, neglecting cells close to the wall. In the model

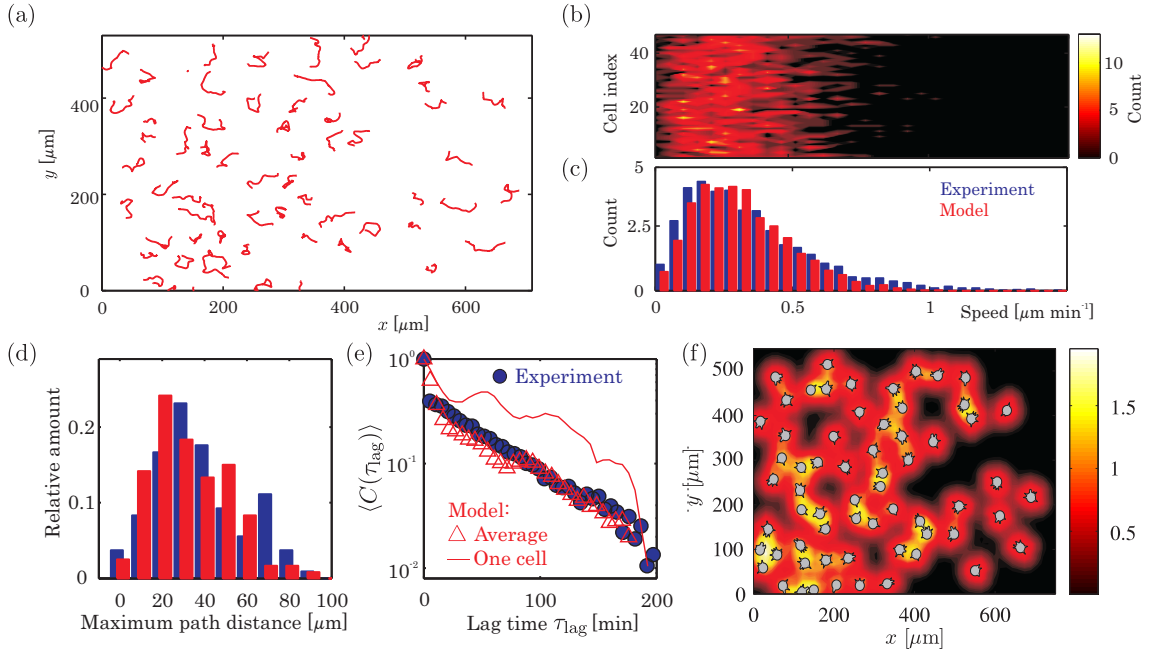


Figure 3.13: Detailed comparison of model predictions with a single experiment (model: red, experiments: blue). Experimental data is the same as in Fig. 3.5. (a) Example model trajectories in 200 min. (b) Single-cell speed distributions (compare to Fig. 3.5(a)). (c) Average single-cell speed distribution, showing excellent agreement with experiments. (d) Population distribution of maximum path distance. (e) Chamber-averaged directional autocorrelation and one single-cell autocorrelation from a cell moving nominally straight. (f) Example of model-predicted cell-secreted chemokine field with the cells indicated in gray.

we therefore include cells around the cells on interest (in a band of 4-5 cells) and include a density-specific background chemokine concentration representing the almost constant concentration field experienced by the cells, which together ensure that the correct boundary conditions are imposed on the tracked model cells. The simulation time step Δt must be smaller than all the model time scales. In addition, the time scale must also allow for colliding cells to be within ϵ of each other before the unphysical process of crossing into each other. To satisfy these criteria we have taken $\Delta t = 0.25$ min.

We store the positions of the model cells and the concentration field at each time step, yielding trajectories and concentration fields. For true comparison between model and experimental data, the model trajectories are sampled at the experimental sampling rate, and motility statistics are computed from these resampled data.

3.6 Comparisons with experimental data

The model results are summarized in Figs. 3.13 and 3.14 which demonstrate quantitative agreement with the experiments in terms of single-cell speeds (Fig. 3.13(b) and (c) and Fig. 3.14(b)), trajectories (Fig. 3.13(a) and (d)) and directionality (Fig. 3.13(e) and Fig. 3.14(a)), thereby verifying our experimentally-derived hypotheses of the role of the

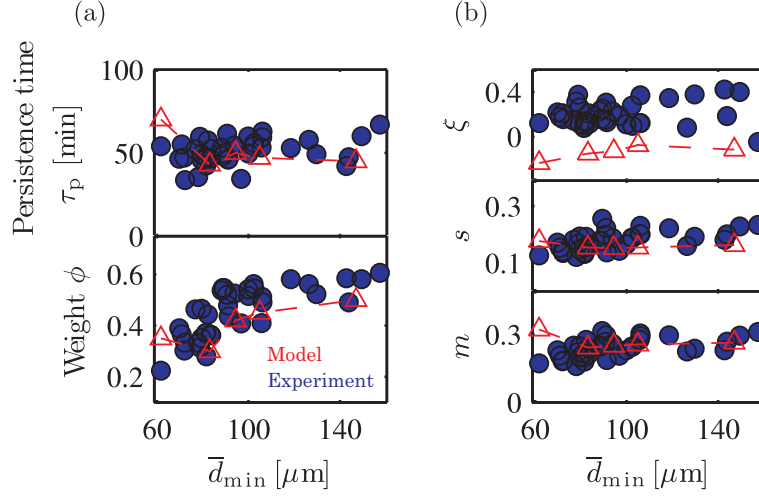


Figure 3.14: Model results across densities with red indicating model predictions and blue giving the experimental values (taken from Fig. 3.7(b) and (d)). (a) Weight ϕ and persistence time τ_p for the fit to $\phi e^{-\tau_{\text{lag}}/\tau_p}$ is in fair agreement across densities. Notably, the model captures the increase of the weight factor ϕ from ~ 0.3 to ~ 0.6 around $\bar{d}_{\min} = 120 \mu\text{m}$. (b) Location parameter m , scale parameter s and shape parameter ξ in fits of the chamber-averaged speed distribution to a GEV distribution, Eq. (3.3). The shape parameter ξ , describing the tail of the distribution, is not well captured by the model since it underpredicts this part of the speed distribution, which can be seen from the example in Fig. 3.13(c).

social interactions on motility. The model quantitatively reproduces across cell densities — with a single value of γ — that the individual cells have the same non-normal speed distribution (Fig. 3.14(b)) with an average that is statistically identical to the experimental average (non-parametric two-sample Kolmogorov-Smirnov test, $P > 0.4$ for all cases; $P = 0.91$ for the case shown in Fig. 3.13(c)), the exponentially decaying autocorrelation (Fig. 3.13(e) and Fig. 3.14(a)) including the changes in the weight factor ϕ indicating the importance of the social interactions, and both the shape and range of the distribution of maximum path distances (Fig. 3.13(d)). The model also predicts the existence of cells moving along almost straight lines for the entire experiment (see Fig. 3.13(a)) and the maximum path distance for these cells (largest single-cell measurements of maximum path distances are the same for model and experiment, Fig. 3.13(d)), but it does underpredict the ratio of these cells, as indicated by smaller tail of model predictions in Fig. 3.13(d). Although the model captures many features of our single-cell microscopy data, it falls short of perfectly reproducing the tail of the speed distribution (Fig. 3.13(c) and Fig. 3.14(b)) and the exact shape of the average directional autocorrelations (Fig. 3.13(e)). This indicates that directional persistence is likely achieved through a more complex machinery than is assumed in the model. An example of a model-predicted chemokine field is given in Fig. 3.13(f).

3.7 Discussion

The agreement of model predictions with experimental data for all the emergent properties presented in Figs. 3.13 and 3.14 suggests that the subprocesses included in the model govern the motility. We therefore arrive at the following explanations for our observations: the dynamically changing positions of pseudopodia cause large fluctuations in speed at all densities while directional persistence is achieved primarily by the directional bias of pseudopod formation but heavily influenced by both collisions and the secreted chemokine. The cells at low densities behave as isolated cells since they rarely collide and the nominally isotropic chemokine field therefore has little influence on the positions of new pseudopodia, while high collision rates at high densities leads to constant randomization of pseudopodia positions and low ϕ . At any density, straight moving cells execute this motile behavior because their lateral pseudopodia are more often suppressed by lateral collisions with other cells abruptly changing, large chemokine gradients; cells displaying little overall directionality constantly have their direction of motion cut off leading to many collisions; while curling cells experience few collisions and/or a clear and slowly moving chemokine bias. The observed continuum of different trajectories is therefore a direct consequence of the fluctuating near-cell environment, and is no more surprising than similar observations of very varied trajectories of many interacting bodies obeying Newtonian mechanics. The model thus provides the first comprehensible description of social cell migration that captures all the complexity formulated in terms of biophysically well-defined single-cell quantities, and furthermore illustrates how very complex biological behavior emerges from simple interaction rules.

Our cells, which neither align nor form persistent cell-cell linkages, maintain their single-cell behavior at increased densities although this behavior is modulated by stronger social interactions at higher densities. This is contrary to both mechanically interlinked and strongly aligning cell types which exhibit larger cross-correlations and emergent multicellular behavior at higher densities. This therefore highlights the role of local alignment in achieving coordinated multicellular behavior, and also illustrates that coordinated multicellular responses do not arise in all multicellular ensembles; this is just the well-known fact that coordinated response is not guaranteed at the multiagent level, such as e.g. human escape panic [68]. Furthermore, our results illustrate that chance and cell-cell interactions play large roles in determining where a cell moves in the social context, and therefore emphasize the need for additional guidance, if a particular cell is to migrate to a specific location. This rationalizes the need for cell-specific chemokines known to be recruiting monocytes during immunoresponse, and could also help explain why certain types of cancer has a propensity for metastasizing to specific tissues, e.g. the preference of prostate cancer to metastasize in the bones [5].

Contrary to several other cell types e.g. keratocytes [126], our 3T3 fibroblast cells do not exhibit large-scale multicellular organization such as flocking [141]. Fibroblasts deviate mainly from these flocking types by not having strong local alignment of the neighbors, and thereby illustrate the criticality of this feature in achieving flocking. We nonetheless hypothesize that the observed effects of the neighboring cells on single-cell migration is highly relevant at physiological conditions. Within a population, the high collision rate

continuously randomizes the directionality of the individual cells, so that on average there will always be cells moving away from the population. In the presence of an external signal, some of these boundary cells will be correctly aligned with this signal and will reliably move up the gradient, with the directional persistence providing the initial stabilization of the movement away from the population. This mechanism provides an isotropically sensitive and quickly responding direction sensor of the population to external signals, even though the single cell polarizations vary and single cell realignment with the external signal would occur on the time scale of directional persistence (τ_p). While this social effect is fundamentally different from flocking, it is another example of how nature achieves group level dynamics for biological function beyond the control of the individual by modulating noise at the level of the individual. The full understanding of the underpinnings, limits and consequences of such emerging population behavior remains to be investigated.

3.8 Conclusions and outlook

Our investigations of social cell migration for thousands of cells at different densities have revealed a diverse migratory behavior, which is largely controlled by the changing environment: While the single cell tries to maintain its current direction of motion through preferentially forming pseudopodia in this direction, secreted chemokine induce pseudopod formation while collisions lead to pseudopod collapse, resulting in much more complex migratory behaviors than reported for isolated cells, even in the absence of cell-cell variations. A simple model based on these observations quantitatively reproduces most migration behaviors across densities, including the existence of outliers, illustrating that these are the intercellular rules governing migration. In addition to their biological significance, our findings illustrate how complex biological behavior arises as a physical consequence of noisy single-cell behavior and interactions among the individuals, opens up for the derivation of continuum theory and illustrate the importance of single-cell data in understanding such behavior.

Our statistical results combined with the model could be used to derive a continuum theory of the collective migration. While the number of cells in our experiment (a few hundred) is typically too low for a continuum description, it would be of great interest to derive such a theory for future macroscale studies. Such continuum theories have successfully been applied to collective behavior of both swimming and migrating cells [110, 79, 17]. Our experimentally validated model could be used to derive a continuum theory of the collective migration, which we would expect to include pair correlations due to the importance of cell-cell interactions in shaping local dynamics, much like the Zimm theory of polymers in dilute solutions [44]. Specifically, obtaining a sound description of the “collision” term of the continuum theory based on the microscopic (subcellular) dynamics described here would not only contribute to the identification of the correct continuum model (in contrast to ad-hoc arguments and empirical data fitting), but would also lead to a deeper understanding of collective dynamics and perhaps yield new insight to rheology.

Chapter 4

Advection-diffusion-reaction: Differentiation of adipose-derived stem cells into adipocytes

In this chapter we turn our attention to the differentiation of stem cells into fat-storing adipocyte cells. The scientific and societal interests in understanding the genesis and growth of adipocytes are enormous, with potential applications ranging from regenerative medicine to potential solutions to the current obesity pandemic [37, 111]. Focusing on the mechanisms leading to differentiation, it will first be shown that differentiation is mediated by a previously unknown cell-secreted signal. Subsequent detailed analysis of the data combined with theoretical models reveal what appears to be non-trivial reaction kinetics. Furthermore, the dependence on a cell-secreted chemical implies that single-cell differentiation, like cell migration, is modulated by the social context, and thereby presents another example of coordinated multicellular response resulting from the interaction of ignorant individuals.

Below follows a personal account of this currently ongoing project, which has been done in collaboration with microbiologists Mette Hemmingsen and Martin Dufva of DTU Nanotech as well as Henrik Bruus. Due to the fixed duration of the doctoral studies in Denmark, not all aspects of this project are finalized. Hence, while we have no single, indisputable analysis explicitly illustrating our conclusions, a number of independent analyses of very different character all point to the same explanation. The author developed the image analysis tools, conducted all analyses of experimental data, developed all numerical models and developed all theoretical analyses presented in the following, while Mette Hemmingsen performed both cell culture and gene expression experiments. A manuscript covering the main findings of this chapter has been submitted for publication in PLoS ONE.

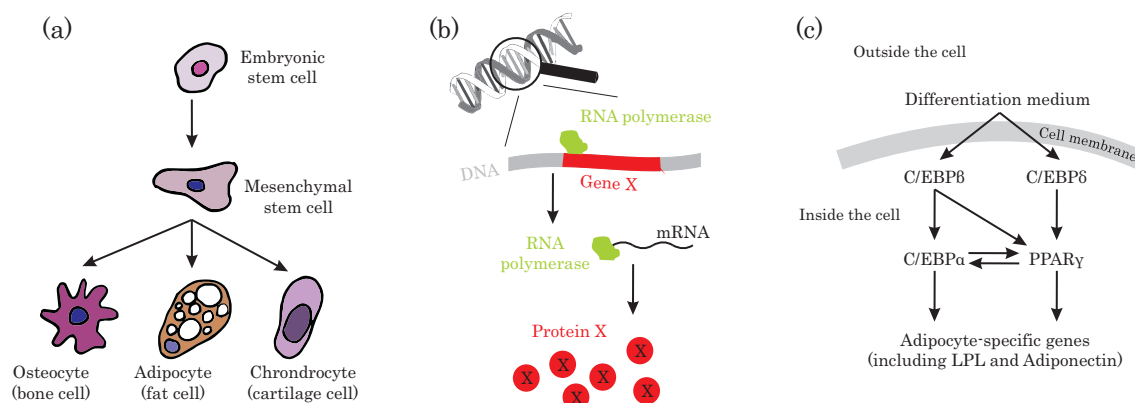


Figure 4.1: Stem cell differentiation basics, the central dogma of molecular biology and the core signaling network of adipocyte differentiation. (a) Specialization of cells is achieved through a number of differentiation steps, with each step resulting in increased specialization. Embryonic stem cells can differentiate into mesenchymal stem cells (among others), and mesenchymal stem cells can further differentiate into bone cells, cartilage cells and fat cells (adipocytes). (b) The central dogma of molecular biology posits that the genes of the DNA are “written” (transcribed) onto messenger RNA (mRNA) by specialized molecules known as RNA polymerases. The protein encoded by the gene is produced by the ribosomes from the information encoded onto the mRNA. (c) The core signaling network underlying adipocyte differentiation consists of three sequential layers of transcription factors which each are activated by the layer above. An arrow indicates that a transcription factor upregulates the expression of its target (the transcription factor the arrow points to).

4.1 Adipocyte background

4.1.1 What is a stem cell?

Most cells of multicellular organisms are specialized to perform particular functions — think of e.g. heart and bone — yet they all descend from the same fertilized egg cell. This specialization is achieved during development through a number of differentiation steps, with each step resulting in increased specialization, before the fully specialized state is reached. An example is shown in Fig. 4.1(a). Stem cells are able to divide, thereby sustaining or increasing the number cells in the organism. Since each differentiation is irreversible, some stem cells have the capacity to differentiate into many cell types while more specialized stem cells only can differentiate into a limited number of other cell types. The former are found in the early stages of the developing embryo, while the latter are found at later stages and in some cases throughout the lifetime of the organism. In the adult, these more specialized stem cells take care of repairing damaged tissue and maintain the natural turnover of regenerative organs such as blood or skin by replacing the dead cells with fresh operating cells. The reader is referred to textbooks such as [5] for more on stem cells.

4.1.2 The central dogma of molecular biology

Any cell, whether a stem cell or not, produces a host of proteins which perform many of the functions of the cell. These proteins are encoded by sequences on the cell’s DNA

known as a genes, which the cell copies onto a single-stranded DNA segment known as messenger RNA (or mRNA); the ribosomes then construct the protein encoded by the mRNA from individual amino acids (Fig. 4.1(b)). The process of DNA \rightarrow RNA \rightarrow protein is referred to as the “central dogma” of molecular biology following Francis Crick [36]. Some genes are produced at all times, while other are produced in response to external signals; examples of the former are “housekeeping” genes used to maintain the integrity of the cell (e.g. components of the cytoskeleton discussed in the previous chapter such as actin), while examples of the latter are e.g. external signals causing the cell to differentiate. Since proteins are only produced when the associated gene is “read”, any gene whose protein is produced by the cell is said to be “expressed” by the cell; there are typically many more genes on the DNA than what are being expressed at any instant. Molecules known as RNA polymerases perform the actual copying of DNA to RNA, in a process known as transcription (Fig. 4.1(b)). The activity of these RNA polymerases can be controlled by small molecules binding to the specific DNA sequences which can up- or down-regulate the RNA polymerase activity on this specific gene, i.e. control the expression of the gene. These small molecules are therefore known as “transcription factors”, and it is these molecules that are activated by external signals in the example of differentiation-signaling above [5].

In general, a gene and the protein it codes for are referred to by the same name. To distinguish between them, italics will be used to designate the gene while roman font will be used for the protein. Thus, the gene *SSH* encodes the protein SSH.

4.1.3 What it means to differentiate

When a cell differentiates, it expresses a new set of genes which endows it with new capabilities. Differentiation occurs in response to a number of signals which culminates in the expression of these new fate-specific genes. Furthermore, differentiation is an irreversible process with the irreversibility achieved by the continued expression of the fate-specific genes upon differentiation. On the molecular level, this is typically achieved by having at least one of the fate-specific genes act as a up-regulator of all fate-specific genes, so that once this gene is turned on, it ensures that all fate-specific genes remain turned on [6].

4.1.4 Adipocytes

Adipocytes are a particular cell type which has specialized in storing sugars (triglycerides) as fat, and are thought to be the main storage facility for the storage of excess energy derived from food intake [108]. They form the predominant part of what is known as adipose tissue which can be found on most individuals, but excessively in especially unfortunate individuals with certain dispositions. Adipocytes are derived from mesenchymal stem cells through differentiation (see Fig. 4.1(a)) after the latter first differentiate into a preadipocyte state. Mesenchymal stem cells are among the more specialized types of stem cells, but can in addition to adipocytes also differentiate into bone cells (osteoblasts) and cartilage cells (chondrocytes) [59]. Upon differentiation into adipocytes, these cells will store encountered excess triglycerides as fat in intracellular membrane-enclosed compartments known as vacuoles (see examples of vacuoles in Fig. 4.3(a)-(c)) [78]. These vacuoles

grow in both size and number as more fat is stored, until at some point the vacuoles start to merge, before finally only a single, large vacuole is found inside each cell [37].

Differentiation of the preadipocyte stem cells into adipocytes *in vitro* requires the presence of adipocyte differentiation medium (DM), which is normal medium with 15% fetal calf serum and four key reagents (0.5 mM isobutyl-methylxanthine, 10 mg mL⁻¹ insulin solution, 1 μM dexamethasone, and 0.2 mM indomethacin) that combine to activate the differentiation signaling [152]. Although the role of some of these reagents have been identified, it is in general not known how the differentiation is achieved. Supporting this is the fact that static flask experiments require around three weeks of constant exposure before differentiation occurs, which is very much longer than would be expected *in vivo*. This points to holes in the current understanding.

The critical intracellular molecular species mediating the differentiation have been identified from a large body of previous work. Even though many transcription factors have a role in adipogenesis [108, 74, 85], it is the expression during differentiation of $PPAR\gamma^1$, $C/EBP\alpha^2$ which leads to the expression of adipocyte-specific genes [86] Fig. 4.1(c). The activation of these adipocyte-specific (fate-specific) genes marks the full differentiation of the cells. Since $PPAR\gamma$ and $C/EBP\alpha$ are themselves activated by the transcription factors $C/EBP\delta$ and $C/EBP\beta$, the full differentiation requires the sequential activation of three levels/stages of genes, see Fig. 4.1(c) [28, 149]. A positive feedback between $PPAR\gamma$ and $C/EBP\alpha$ ensures the maintenance of the differentiated state [69], and furthermore explains why $PPAR\gamma$ has been observed to act as a master switch turning on the differentiation program [37]. However, the C/EBP genes along with $PPAR\gamma$ are also involved in other signaling networks which in some cases have profound influence on the differentiation; for instance, $Wnt10a$ from the ubiquitous Wnt -pathway is known to deactivate the $PPAR\gamma$ proteins by binding to them, which completely halts the differentiation program since no unbound transcription factors are available to activate the adipocyte-specific genes [30, 69].

Surprisingly little is known about how the four reagents of the differentiation medium activate the essential transcription factors of the differentiation pathway. Complicating matters further is previous evidence that cell density and shape also have a role in determining cell fate: confluence and a rounded cell shape have been found to be requisites for mesenchymal stem cell differentiation into adipocytes [65, 76, 92]. Especially the latter seems suspicious, and is more likely a reversal of cause and effect. Hence, whether the supplied reactants are sufficient for differentiation, only lead to the activation of certain signals which in the end cause the differentiation, or cause the differentiation through yet different means is unknown. Adipocyte tissue is highly involved in signaling and thus actively impacts the organism, leading to a systemic response to changing conditions [37, 58, 133]. Interestingly, the supplied reagent isobutyl-methylxanthine is known to lead to the secretion of several signals (including $Dkk1$) that inhibit Wnt [69, 30, 35]; since Wnt itself deactivates $PPAR\gamma$ and thereby halt the differentiation, inhibiting Wnt leads to increased differentiation. This indicates the role of isobutyl-methylxanthine, but does not explain the role of the remaining reactants, and also does not explain why the upstream genes

¹Full name: peroxisome proliferator-activated receptor γ .

²Full name: CCAAT/enhancer-binding protein α , where CCAAT is the abbreviation for cytidine-cytidine-adenosine-adenosine-thymidine.

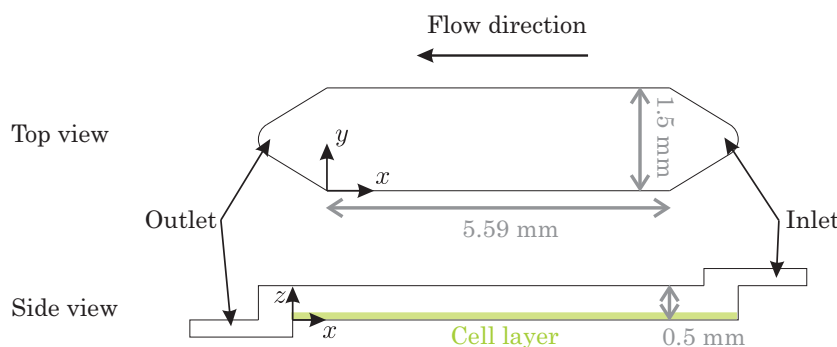


Figure 4.2: Sketch of the footprint of the microfluidic chip used for the experimental parts of this study, with perfusion flow going from right to left.

$C/EBP\delta$ and $C/EBP\beta$ must be activated for differentiation. This, along with the previously mentioned observations of strong dependence of differentiation on cell density [92] and the fact that increased differentiation has been observed in static culture when only half of the medium is replaced [69] led us to hypothesize the potential role of a cell-secreted chemical underlying the differentiation signaling, with the secretion being caused by the differentiation medium. This hypothesis gains further strength from a recent finding that stem cells similar to ours implanted in proximity to breast cancer are strongly affected by a tumor-secreted chemical, that perturbs the normal differentiation procedures and converts the stem cells to tumor cells [31]. Given the systemic nature of the mammalian energy storage system, and irrespectable of its exact functioning, it is of immense interest to understand the mechanisms underlying the differentiation processes at the single-cell level as well as the systemic response. The rest of this chapter details the investigations into the details of the signaling leading to differentiation.

4.2 Cells, experiments and data

The cells used were primary human mesenchymal stem cells obtained from liposuction, which were kindly donated from the Collas lab at the University of Oslo (www.collaslab.com). Such stem cells have previously been shown to have the adipocyte-differentiation capacity [151, 152]. Contrary to cell lines (such as the widely used 3T3-L1 cell line for adipocyte differentiation), these primary cells are much closer to the “real world”, and in addition are both abundantly available and raise no ethical concerns.

The experiments were conducted in the ProCell system, a generic PMMA³-based microfluidic perfusion system which allows for up to 16 parallel experiments to be conducted simultaneously with well-controlled external conditions (CO_2 and temperature) [121]. Varying the flow rate perturbs the fields of any cell-secreted chemicals, so perfusion experiments are well-suited for studying our hypothesis of a critical cell-secreted signal involved in the differentiation. Microfluidic perfusion cell culture has previously been used to identify cell-secreted chemicals involved in the differentiation of mouse embryonic stem cells [21].

Cells were plated onto the bottom of the chamber (see Fig. 4.2) and constantly perfused with fresh medium supplied at a flow rate Q . The cells were imaged with a regular interval

³PMMA: poly(methylmethacrylate).

Table 4.1: List of the different experimental conditions and their abbreviations

Abbreviation	Full name
CM	Conditioned medium (collected from static flask experiment)
DM	Adipocyte differentiation medium (normal medium with 15% fetal calf serum, 0.5 mM isobutyl-methylxanthine, 10 mg mL ⁻¹ insulin solution, 1 μM dexamethasone, and 0.2 mM indomethacin)
DM+CM	Normal DM mixed 1.5:1 with CM
1/4 DM	Normal DM diluted at 1:4 in normal medium
1/4 (DM+CM)	Normal DM+CM; the mixture is diluted at 1:4 in normal medium
1/4 DM+CM	1/4 DM mixed 1:1 with undiluted CM
Control	Normal growth medium without any reagents or fetal calf serum

(typically 1-2 day), and an experiment was run for up to the 22 day limit found to be the normal differentiation time in static flask experiments. To investigate the role of a cell-secreted chemical, experiments were conducted at up to four different densities Γ_{cell} in the range $\sim 0.3 \times 10^8 \text{ m}^{-2}$ to $\sim 3 \times 10^8 \text{ m}^{-2}$. Furthermore, since the amount of the purported secreted signaling molecules would increase in a high-density static culture experiment post differentiation, medium collected from parallel flask experiments with differentiated cells were also used in conjunction with normal differentiation medium. Thus, some experiments were exposed to only differentiation medium (DM), and other to DM and this conditioned (collected) medium (CM). Moreover, since the cells in these perfusion experiments could receive higher amounts of the reagents depending on cell reaction kinetics and chamber flow rate, the ratio of DM to CM and DM to normal medium have also been probed, as detailed in Table 4.1 which also lists the different experiments and their abbreviations.

The data from an experiment consists of a set of phase-contrast digital images. Since the field of view of the microscope is substantially smaller than the typical chamber footprint ($\sim 1.5 \text{ mm} \times 6 \text{ mm}$) raw phase contrast images were stitched together using the dedicated microscope software (Zeiss AxioVision[®]) prior to further image analysis. The stitched images maintain the high resolution of the individual images of $0.64 \text{ } \mu\text{m pixel}^{-1}$ and examples of these stitched images can be seen in Fig. 4.3(a)-(b). Lipid vacuoles show up as white beads in the images, while the cell outline and various intracellular structures show up as black lines (Fig. 4.3(c)). However, the cells congregate and occasionally lie over each other, and in these cases it is difficult to distinguish individual cells even for a trained observer.

In addition to the image data, the expression level of six key genes at different stages of the differentiation procedure were quantified using the Taqman[®] Probe-based real time polymerase chain reaction method (RT-PCR/qPCR). The probed genes are the transcription factors from *C/EBPδ* and *C/EBPβ* from the first stage of the intracellular signaling cascade (see Fig. 4.1(c)), *C/EBPα* and *PPARγ* from the second level of the cascade and finally two adipocyte-specific genes from the final stage of the signalling cascade (lipoprotein lipase (*LPL*) and *Adiponectin*), which are only active when the cell has differentiated

into an adipocyte. The method detects the amount of expression of the target genes by investigating the messenger RNA (which, as discussed in Section 4.1.2, is exactly the molecules which carry the information about which genes the cell is currently expressing) using gene-specific fluorescent probes. These probes become fluorescent only when bound to the corresponding mRNA segment, so the fluorescence intensity provides a quantitative measure of the gene expression level. The method was applied to the cumulative pool of mRNA harvested from an entire experiment and subsequently amplified using the PCR technique. The fluorescence levels of the six genes were normalized to the expression level of β -actin, a "housekeeping" gene involved in the actin cytoskeleton, that forms a natural reference since it by all accounts is unaffected by the differentiation procedure [13].

This is the first study of adipose-derived stem cells in a microfluidic perfusion system, so determining the experimental protocol was a major achievement by the experimental collaborator Mette Hemmingsen. This, combined with the three-week duration of each experiment and the initial bugs and failures inherent to the newly developed experimental platform have limited the number of successful experiments to only a handful, even though it has taken 1.5 year and a dedicated and diligent effort to generate this data. All available data is presented in what follows, although not all of it has been replicated.

4.3 Image analysis tools

One chamber contains up to $\sim 2,000$ cells, differentiated individual cells contain upwards of 100 vacuoles, and each chamber is typically imaged ~ 15 times during an experiment, so manual tracking would be cumbersome, slow and error prone. A set of image analysis tools were therefore developed to analyze and quantify the differentiation process. These consist of (i) vacuole detection, (ii) clustering of vacuole from the same cell and (iii) linking of these properties in time. All analysis tools were developed and implemented in MATLAB, exploiting the Image Processing Toolbox when appropriate. The image analysis algorithms store information about the positions and areas of each vacuole, group together the vacuoles from the same cell, and link these differentiated cells in time.

4.3.1 Vacuole detection

Prior to any analysis, image intensities were adjusted using MATLAB's built-in contrast-limited adaptive histogram equalization function `adapthisteq`, yielding a discrete intensity I defined in every pixel.

Vacuoles are nominally spherical objects which have much higher intensity than the background (Fig. 4.3) so they are most easily detected by converting the image to black-and-white (thereby obtaining a binary image), and grouping regions of neighboring white pixels to form individual vacuoles. The success of this method hinges critically on the choice of the threshold value separating black from white. Using a threshold of relative intensity of $I_{\text{rel}} = I/I_{\text{max}} = 0.9$, where I_{max} is the maximum intensity supported by the image format⁴, was found to provide a satisfactory estimate.

⁴For the 16-bit integer images recorded for this study the maximum pixel value is $I_{\text{max}} = 2^{16} - 1 = 65535$.

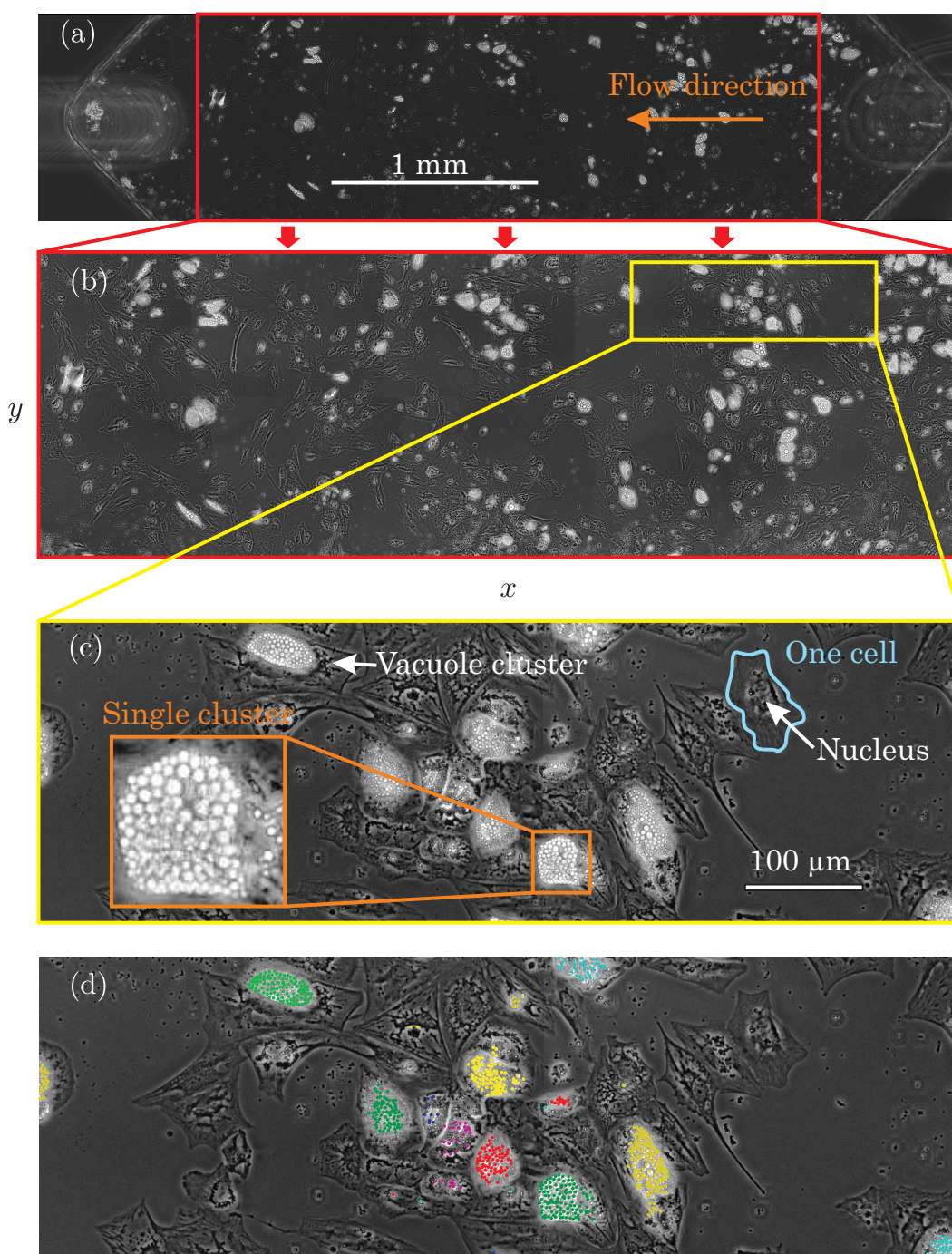


Figure 4.3: Sample data from day 14 of an experiment and illustration of image analysis algorithms. (a) Raw image of one chamber. The inlet and outlet are visible to the left and right of the romboïd chamber footprint (the inlet and outlet are marked by the shaded whitish circular marks stemming from the milling tool head). This image is stitched together of 16 individually obtained images. (b) Intensity-adjusted image showing only the chamber (no inlet and outlet) corresponding to the region marked by the red rectangle in panel (a). Individual cells are visible and differentiated cells have stored clusters of lipid vacuoles of varying sizes; these are the regions containing white, circular bead-like objects. (c) Zoom in on the region marked by the yellow rectangle in panel (b) illustrates the individual cells (one example is marked by light blue), where both the nucleus and other intracellular structures are visible. Note the difficulty in distinguishing individual cells when the intercellular distance is low. The inset of the orange rectangle displays a closer zoom on one vacuole cluster in a single cell with large variation in vacuole sizes. (d) Output of the image analysis algorithms displayed for the region shown in (c)). Each detected vacuole is marked by a colored dot with vacuoles grouped in the same cluster marked by the same color. Colors are reused due to a limited number of available colors in MATLAB.

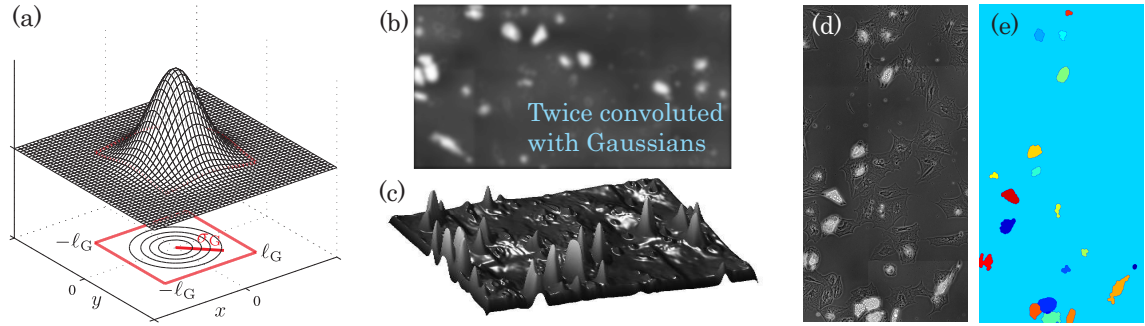


Figure 4.4: Details of vacuole cluster detection. (a) The Gaussian kernel with spatial extend ℓ_G and variance σ_G . (b) Excerpt of image after the two convolutions with Gaussians as described in the text. (c) A surface plot of (b). Taking the opposite sign of the pixel values (converting the hills to valleys), the individual vacuolar regions can be detected by a watershed transform. (d)-(e) The original image (d) and the result of the watershed transform procedure (e), rotated 90 ° clockwise compared to (b). Differently colored connected regions in (e) correspond to different regions (colors are reused in the panel due to their limited number).

In a subsequent control step, the regions of white pixels from the binary image were only accepted as vacuoles if they satisfied the following criteria: (i) the region exceeded 2 pixel, (ii) the region did not exceed 250 pixel (large vacuoles were found to be no larger than ~ 100 pixel), (iii) the ratio of the major axis to the minor axis of the region did not exceed 3 and (iv) the corresponding regions in the original image had an intensity gradient towards the edges. The axes are defined by the ellipse with the same normalized second central moment as the region, and are computed by MATLAB's `regionprops` command. The criteria filtered away regions too small, too large, too ellipsoidal or unlikely to be single vacuoles. Vacuoles are spherical so the apex was closer to the light source and the boundary regions consequently had lower intensity. The intensity gradient of each region was therefore used to ensure that the region was indeed spherical. Criterium (iv) was implemented by requiring the mean relative intensity gradient away from the region centroid $\langle \partial_{\mathbf{r}} I_{\text{rel}} \rangle$ be negative, $\langle \partial_{\mathbf{r}} I_{\text{rel}} \rangle < 0$. This gradient was approximated numerically for a region centered in (x_n, y_n) as

$$\begin{aligned} \langle \partial_{\mathbf{r}} I_{\text{rel}} \rangle &= \langle \nabla I_{\text{rel}} \cdot (\mathbf{e}_x + \mathbf{e}_y) \rangle_{\text{region}} \\ &\approx \sum_{i=-d, d} \frac{[I(x_{n-i}, y_n) - I(x_n, y_n)] + [I(x_n, y_{n-i}) - I(x_n, y_n)]}{2d I_{\text{max}}}, \end{aligned} \quad (4.1)$$

where d is the distance in units of pixel over which the gradient is approximated. d was taken as the aforementioned minor axis of each individual region. All regions satisfying these criteria were selected as individual vacuoles in the image, and their centroid position and region area (in unit of pixel) were stored.

4.3.2 Vacuole cluster detection

The vacuoles of the differentiated cells exhibit both individual-vacuole growth, increase in vacuole number and merging of vacuoles to large “supervacuoles” as time passes. Since

primarily the number of differentiated cells is of interest, vacuoles belonging to the same cell must be identified and clustered. Simple thresholding with a lower limit than for the individual vacuoles does not work by itself, firstly because the individual vacuoles are separated by regions of much lower intensity, and secondly, because at later times differentiated cells each containing many vacuoles tend to group together. Instead, a so-called “marker-based watershed segmentation” algorithm was developed to segment the detected vacuoles to the corresponding cells. This routine involves three steps: (i) detecting the vacuolar regions, (ii) picking the markers and (iii) segmenting the vacuolar regions based on the positions of these markers.

Thresholding can be used to detect all vacuolar regions, however only without any regard to which cell each region belongs. To do this, the low-intensity borders between the individual vacuoles were first smoothed out by convoluting the intensity-adjusted grayscale image twice with Gaussian kernels of different variance σ_G^2 and spatial extend ℓ_G , see Fig. 4.4(a) and (b). For a pixel at (x_n, y_n) the kernel was applied to the region of $-\ell_G + x_n \leq x_n \leq \ell_G + x_n$, $-\ell_G + y_n \leq y_n \leq \ell_G + y_n$. A first pass with a kernel of $(\sigma_G, \ell_G) = (\sqrt{200}, 5)$ pixel smeared out the vacuolar intensity and thereby increased the intensity of the intervacuolar spaces, while a second pass with a $(\sigma_G, \ell_G) = (\sqrt{150}, 50)$ pixel kernel resulted in high-intensity regions of roughly uniform intensity wherever groups of vacuoles are located. While the first pass would appear unnecessary, it was found to provide the initial smoothing which increases the performance of the entire algorithm. A black/white (binary) conversion of this smoothed image using the image-mean intensity for threshold then returned the vacuolar regions.

Following the convolution with Gaussian kernels, the regions of highest intensity correspond to the centers of each vacuole cluster, see Fig. 4.4(b). Estimates of each cell was therefore found by identifying the subregions of local intensity maxima in the convoluted image using MATLAB’s `imextendedmax` function (which suppresses any maxima lower than a threshold, which was picked to be 300). These maximum regions were then dilated using a circular structuring element with a 10 pixel radius; these dilated regions were used as the markers of the individual cells containing vacuoles.

Having identified markers for each of the differentiated cells, the vacuolar regions found previously only need to be segmented to the appropriate markers. This was achieved using the watershed transform, an image transform which distinguishes regions of different local intensity minima. The transform views grayscale values as differences in altitude, like hills and valleys in a landscape. Hence, just like a drop of water in a landscape will flow along a path of steepest descent before settling in a point of local minimum resulting in the emergence of different puddles or catchment basins in the rain, the watershed transform can be thought of as separating the grayscale image into regions corresponding to the different puddles. Thus, to segment the rest of the vacuolar regions into the correct regions corresponding to the previously determined markers, a value increasing monotonically towards the markers must be assigned to each point in the vacuolar regions. The distance of each point to the nearest edge of the vacuolar region was found to work satisfactorily. Figure 4.4(c) shows a surface representation of the distance transform applied to the vacuolar region resulting from a binary conversion of Fig. 4.4(b). Since the watershed transform identifies minima (puddles), the output from the distance transform was

inverted before applying the transform. Then, the marker regions were forced to be the local minima in the inverted distance transform (using the `imimposemin` function), which ensures that they indeed will “collect the water”. The segmentation was then achieved by computing the watershed transform. A label is assigned to each pixel in the entire image by the transform, with similar labels indicating that two points belong to the same group. A sample output of the segmentation is shown in Fig. 4.4(e) with the original image shown in the neighboring panel (d). Finally, vacuoles were grouped based on their label numbers.

4.3.3 Linking in time

The positions of differentiated cells were linked in time based on the metric distance between their positions in the two subsequent images. However, more cells differentiate over time, new clusters formed, and the vacuole detection algorithm also occasionally identified cellular debris despite its intentions. To account for these disturbances, variations in cluster size were included in the linking algorithm.

Starting with each cluster at time t_n , the algorithm first identified all clusters at time t_{n+1} whose centroid positions are within 200 pixel. Among these, the algorithm then requires that the change in cluster area (defined as area at time t_{n+1} divided by area at time t_n) does not vary more than 70 % between two frames. During the initial growth phase both single vacuoles and clusters increase their relative volume (and hence their projected surface area) substantially so the requirement of limited relative growth is too severe. Thus, clusters which have an absolute change in area of up to 50 pixel² are included even if they exceed the requirement of limited relative growth. The algorithm then picked the closest of the clusters which satisfy the growth criteria, before moving on to the next cluster at time t_n . The algorithm iteratively works to link clusters between two frames and thereby minimizes the overall distance between all linked clusters between the two regions. Thus, if two clusters at t_{n+1} both link to the same cluster at t_n , the closest of the clusters at t_{n+1} will be selected and the unpaired cluster at t_{n+1} will be linked to another cluster at t_n , should one such exist that satisfies the requirements and in addition is not closer to another cluster at t_{n+1} . This ensures that the highest number of linked clusters satisfying the requirements and lowers the overall error.

4.3.4 Whole cell detection

For normalization purposes, knowledge of the positions and areas of all cells in the chamber is important. Unfortunately, detection of the entire cell was very difficult in the images: the absence of fluorescent markers means that there is no tag associated with every cell — only differentiated cells have the easily-detectable vacuoles — and since the cells are very close, and in some cases overlap, even manually detecting the individual cells with certainty was difficult. Attempts to detect the cells automatically were in vain⁵, so a manual count

⁵These attempts have tried to identify the “halo” found around the outer membrane of the cells. While such halos are fairly easily detected on isolated cells, the close proximity to other cells severely limits the halo intensity and also introduces large variations around the cell membrane, typically including large regions with no detectable halo. The developed algorithms have employed both edge detection algorithms and thresholding using a lower level than for vacuole detection. Professor of Image Analysis Rasmus

of all cells in one image per experiment was used. The cell density was observed to decrease somewhat only between the time of plating and the first subsequent measurement point, so the manual count was performed at this second time point.

4.3.5 Performance of the analysis tools

All analysis have been performed on a 64 bit computer with 24 GB RAM, where complete analysis of a full experiment took about 20 h. Each of the stitched images were typically ~ 100 MB with each experiment consisting of 10 – 11 images.

The analysis tools were very good at detecting individual vacuoles and vacuolar regions, with an estimated error rate below 1 % independently of cell density and the size of the vacuoles. The error rate was found by comparison to manual counting in one low-density and one high-density experiment. However, correctly assigning the correct amounts of multicellular vacuolar regions to the individual cells posed some problems. Thus, while detecting the vacuoles in these regions was fairly easy, correctly segmenting the image proved difficult, mainly because the distance transform in some cases produced regions that did not agree with the actual cells. Comparison to manual counting of the differentiated cells on two separate experiments found success rates of 92 % and 89 %, respectively, i.e. an error of ~ 10 % on the amount of detected vacuolar regions. Since on average $1/4$ of all cells differentiate in the experiments (as will be shown below), this corresponds to an error on the fraction of differentiated cells of ~ 0.025 . In addition, the manual counting of all cells also carries an uncertainty, especially in regions with overlapping cells. These are most pronounced in high-density experiments, and carries an estimated error in this case of up to 10 %.

4.4 Validation of the experimental approach

4.4.1 Isotropic experimental conditions

The distribution of cells in the chamber was found to be isotropic at all experimental conditions. This is illustrated in Fig. 4.5 which shows histograms of the number of cells as function of position found in the chambers for the different densities in bins of size $250 \times 250 \mu\text{m}^2$. The spanwise variations are consistent with the counting error of finite statistics of N spanwise cells, \sqrt{N}/N . Thus, all cells in the chamber on average experiences the same degree of contact and proximity to other cells, so any intercellular signaling molecules will on average be present at the same rate for all cells. Doing the same analysis for the differentiated cells at days 5, 15 and 21 in an experiment exposed only to differentiation medium, we found a similar isotropy in the positions of the differentiated cells. These findings also hold for experiments exposed to differentiation medium combined

Larsen, Department of Informatics and Mathematical Modeling, Technical University of Denmark was consulted regarding this problem; he concluded that its level of difficulty made it appropriate for a M.Sc. thesis research project. No student was available to perform the research so no further work was done in this regard.

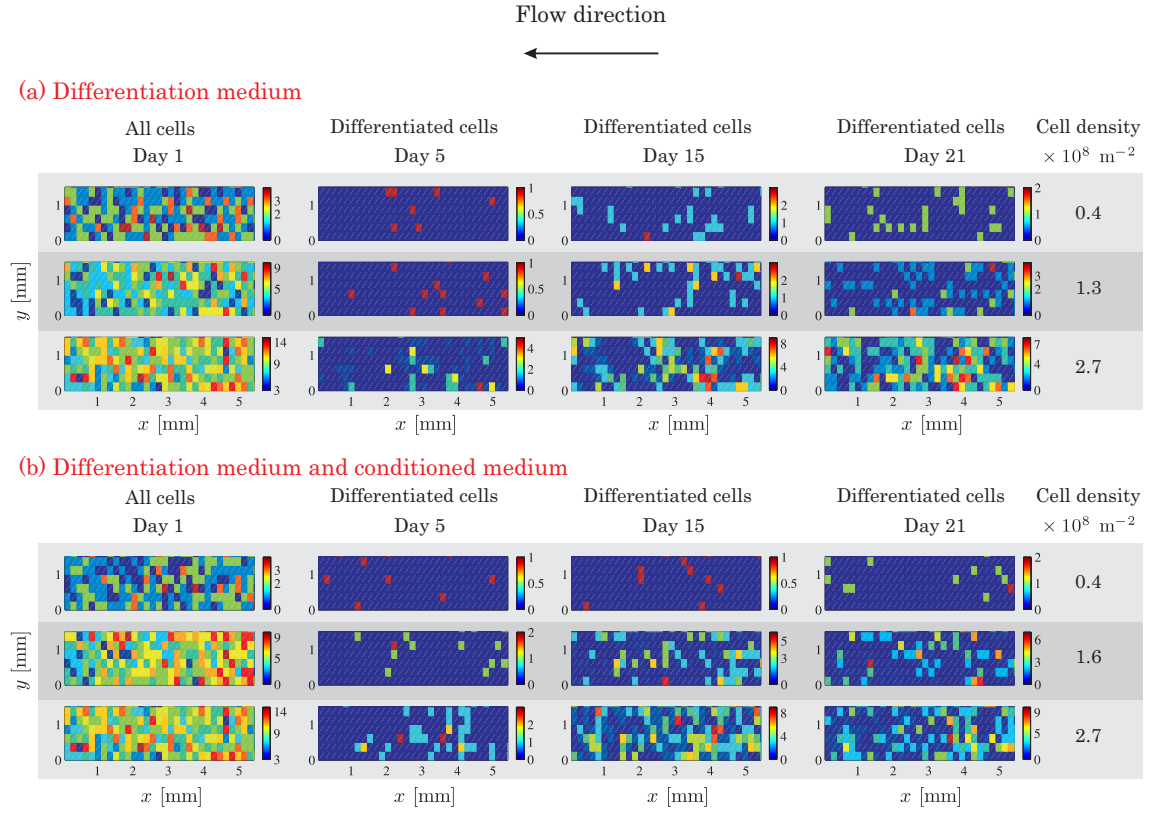


Figure 4.5: Histograms of the distributions of cells in the chambers, with color indicating the number of counts in bins of size $250 \times 250 \mu\text{m}^2$. The first column shows the positions of all cells, while the remaining columns display only differentiated cells. The perfusion flow is going from right to left in all cases as illustrated in the sketch of the experimental setup in Fig. 4.2. (a) An experiment exposed only to differentiation medium showing no dependence of lengthwise position in the chamber for both cellular positions and the positions of differentiated cells. (b) An experiment exposed to differentiation medium combined with conditioned medium, where again no dependence on lengthwise position is detected.

with conditioned medium (Fig. 4.5(b)). With the hypothesized role of a cell-secreted critical chemical in initiating the differentiation process in mind, these isotropies mean that chamber-averages are significant measures of the average single-cell behavior.

4.4.2 Genetic markers validate image analysis and confirms signaling cascade

Validation of the image analysis

The image analysis approach was verified by comparing to the temporal expression profiles of the six target genes involved in the differentiation pathway presented previously (Sec. 4.1.4 and Fig. 4.1) as the cells were exposed to 1/4 DM with and without CM. These specific experiments were used because they result in the most pronounced differentiation, as will be shown below. As shown by the results in Fig. 4.6 (and by the replicated results

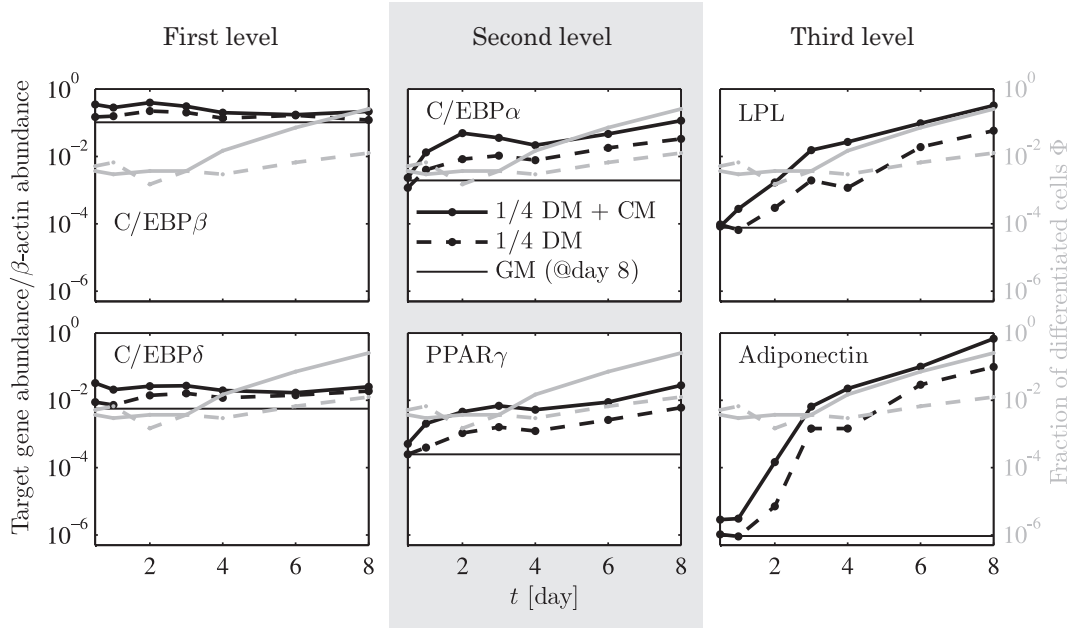


Figure 4.6: Temporal expression profiles (black) of the six target genes *C/EBPδ* and *C/EBPβ* (first level of signaling cascade, see Fig. 4.1), *PPARγ* and *C/EBPα* (second level) and the adipocyte-specific *LDL* and *Adiponectin* (third level) exposed to 1/4 DM (dashed black lines) and 1/4 DM + CM (full black lines). Also shown is the fraction of differentiated cells Φ (gray, same line styles). For reference, the expression level of the same genes from experiments exposed only to growth medium (and sampled only at the last day) is also included (thin black line). Differentiating cells express all these genes at elevated levels and in a temporal pattern consistent with the three levels of the differentiation signaling cascade (see Sec. 4.1.4). Furthermore, the optical detection is in agreement with the genetic data, although with a small delay time of ~ 1 day. See the results of an additional, repeat experiment in Fig. C.1 on p. 146 supporting these findings.

from an independent experiment in Fig. C.1, p. 146), the fraction of differentiated cells in a chamber Φ — computed from the image analysis results as the total amount of differentiated cells divided by the total amount of cells — was observed to steadily increase starting at day 3. Contrary to this, the expression level of the two genes *C/EBPδ* and *C/EBPβ* from the first level of the differentiation signaling cascade were high at all times following stimulation, while the genes of the second level (*C/EBPα* and *PPARγ*) and third level (*LDL* and *Adiponectin*) were found to build up over time. The initial relative abundance of the genes of the third level were ~ 2.5 orders of magnitude smaller than the second-level genes which emphasizes that these adipocyte-specific genes of the third level are turned on only in response to upregulation of *C/EBPα* and *PPARγ* of the second level. In all cases, the expression levels exceeded the results found from cells exposed only to normal growth medium, thereby indicating the significance of these genetic results.

The time scale of ~ 3 days before detection of differentiated cells from the image analysis is in agreement with this genetic data. Differentiated cells are only detected by the image analysis once they have stored enough fat to form a least one vacuole of at least 4 pixel² area, so it is not surprising to find a delay of ~ 1 day compared to the

expression profiles. This validates the use of the image analysis to detect and investigate the differentiation, and furthermore sets the delay time between when a cell is differentiated and when this can be detected visually. The experimental results presented in the rest of this chapter are obtained using the image analysis unless stated otherwise.

Confirmation of the three-level signaling cascade

This temporal gene expression data confirms the current belief presented already in Sec. 4.1.4 that a three-level signaling cascade is governing the differentiation process: the temporal buildup from essentially zero concentration of the adipocyte-specific genes (*LDL* and *Adiponectin*) in response to a temporal buildup of the genes at the second level (*C/EBP α* and *PPAR γ*), while the genes at the first level are activated much faster than the first measurement at 12 h [28, 149]. Furthermore, the time scales of these responses also agree with the current explanation: *C/EBP δ* and *C/EBP β* transcription factor proteins are already present in an inactive form prior to the onset of the differentiation program and are therefore quickly activated, *C/EBP α* and *PPAR γ* are synthesized in response to the activation of these proteins of the genes of the first level and build up on a time scale of many hours, while activation and production of the third level genes requires the build-up of significant amounts of active second-level gene products, which takes days.

4.5 A cell-secreted signal is required for differentiation

Contrary to the current understanding, our experimental data suggests that the decision to differentiate is mediate by a cell-secreted chemical, see Fig. 4.7. This conclusion is supported by several independent lines of evidence presented in the following. Such signaling systems where a cell-secreted signal is required are known as paracrine or autocrine signals, depending on whether the signal is secreted by the receiving cell (autocrine) or not (paracrine), and are in the adult organism used for e.g. tissue repair [5].

4.5.1 Higher cell density leads to a higher fraction of differentiated cells

We start by considering the experiments exposed to only normal differentiation medium (DM) at low flow rate ($Q = 33 \text{ nL min}^{-1}$). Figure 4.7(a) illustrates the fraction of differentiated cells Φ as a function of time for four different cell surface densities Γ_{cell} in the range $0.31\text{--}3.03 \times 10^8 \text{ m}^{-2}$. The cells at the highest density completely fill the chip footprint, and may even be lying on top of each other, while the mean free distance between cells at the lowest density is 3-4 cell diameters. Due to the isotropy of the positions of all cells as well as only differentiated cells (Fig. 4.5), Φ is an unambiguous measure of the differentiation.

The data in Fig. 4.7(a) shows a strong dependence of Φ on the cell density with two distinct features: (i) the value of Φ at the conclusion of the experiment is an increasing function of cell density Γ_{cell} , and (ii) the response time is a decreasing function of Γ_{cell} . Hence, the data clearly shows that a higher percentage of cells differentiate at higher cell densities. While Φ appears to be an essentially linearly increasing function of time for the two lowest densities, the two highest densities exhibit a different dynamics where Φ

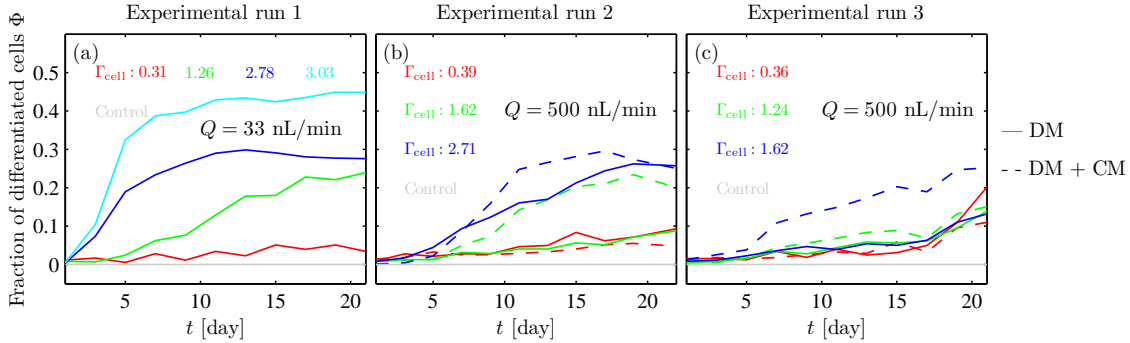


Figure 4.7: Fraction of differentiated cells Φ as a function of time for cells exposed to normal differentiation medium (DM) with (full lines) and without (dashed lines) conditioned medium (CM) containing cell-secreted chemical signals. Also shown is the result of a control experiment where the cells were exposed only to normal growth medium. Surface cell density Γ_{cell} is measured in units of 10^8 m^{-2} . The flow rate was varied between the first experimental run ($Q = 33 \text{ nL min}^{-1}$) to 500 nL min^{-1} in the two other runs.

initially increases before saturating at a nominally constant level after ~ 10 days. This time scale is different from the minimum 21 days reported from static culture experiments [151], but this discrepancy could be due to differences in the measure of differentiation used in the cited study. It is uncertain whether or not Φ at $\Gamma_{\text{cell}} = 1.26 \times 10^8 \text{ m}^{-2}$ would continue to grow following the conclusion of the experiment at day 21; in the interest of increasing the total experimental output it was decided not to probe this with additional (longer) experiments.

Contrary to the previous findings from static experiments mentioned in Sec. 4.1.4, differentiated cells not in direct contact with other cells are observed in our low-density experiment, see Fig. 4.8(a). This clearly illustrates that neither direct cell-cell contact nor cellular confluence are required for differentiation.

Taken together, these observations indicate a strong dependence of Φ on cell density which nonetheless is independent of direct cell-cell contact. A likely explanation is that a cell-secreted chemical is required for the differentiation. Furthermore, the increased levels of Φ at high cell density is inconsistent with the differentiation-inducing chemical being already in the differentiation medium; were the differentiation induced directly by components of DM, we would expect either similar Φ at all cell densities, or in the case of limited supply of the active DM components, lower Φ levels at higher cell densities. This is inconsistent with our observations.

4.5.2 Increasing the flow rate lowers the fraction of differentiated cells

Turning up the flow rate from $Q = 33 \text{ nL min}^{-1}$ (Fig. 4.7(a)) by a factor ~ 15 to $Q = 500 \text{ nL min}^{-1}$ has noticeable effects on the fraction of differentiated cells Φ , see full lines in Fig. 4.7(b)-(c) which show two sets of replicated experiments at this high flow rate. While this large increase in fluid speed leads to increased shear experienced by the cells, this shear nonetheless remains two orders of magnitude lower than the limiting value of changing cellular behavior (see Appendix C.2). Compared to the results from the low flow

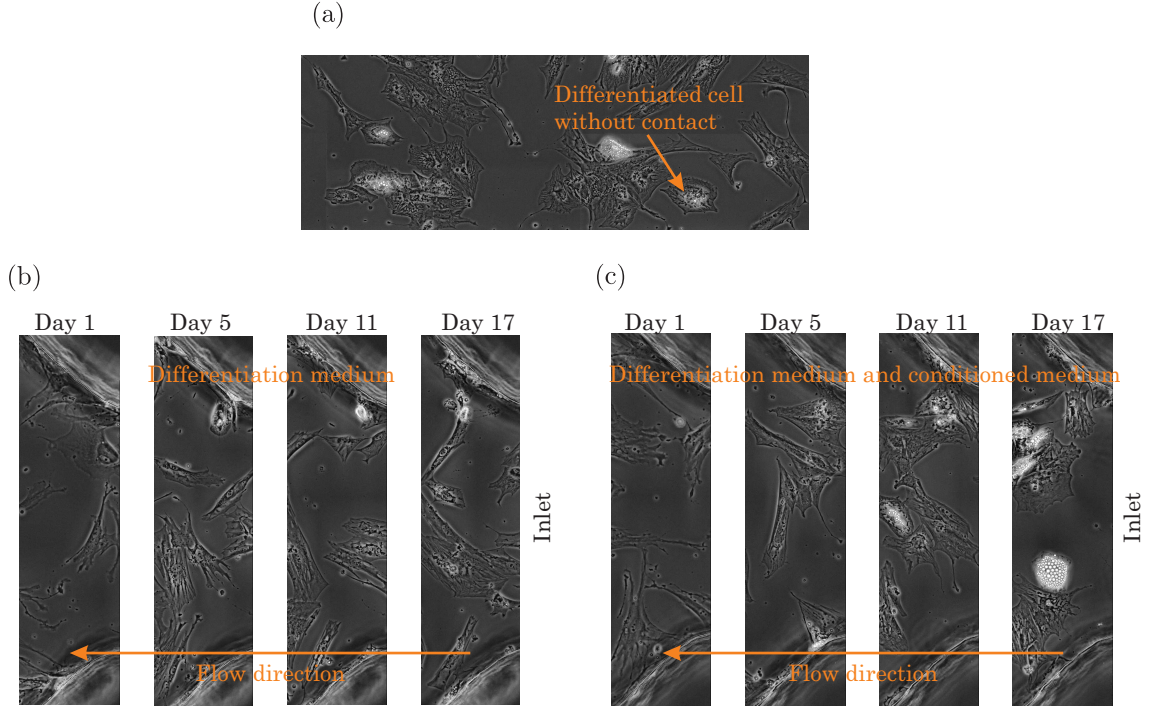


Figure 4.8: Experimental rebuttal of the previous notions that direct cell-cell contact is required for differentiation (a), and that differentiation is initiated by the differentiation medium (b)-(c). (a) A newly differentiated cell which is not in direct contact with other cells. (b) Small segment of the chamber close to the inlet (which is at the right in all figures) for an experiment stimulated only with differentiation medium at low cell density ($\Gamma_{\text{cell}} = 0.4 \times 10^8 \text{ m}^{-2}$) shows no differentiated cells at the very inlet, even though these cells receive more differentiation medium than cells in the chamber. (c) Differentiating cells are found close to the inlet when conditioned medium is supplied in addition to the differentiation medium.

rate in panel (a), Φ grows more slowly for all densities in this higher flow rate. Furthermore, while the responses at the low densities $\Gamma_{\text{cell}} \approx 0.35 \times 10^8 \text{ m}^{-2}$ is generally unaffected by the change in flow rate, Φ at intermediate densities ($1.24 - 1.62 \times 10^8 \text{ m}^{-2}$) is much lower for the high flow rate than for the low; in fact, Φ is of similar magnitude at the high flow rate for all cell densities in the range $0.36 - 1.62 \times 10^8 \text{ m}^{-2}$. Contrary to this, Φ reaches the same value at the conclusion of the experiment for both high and low flow rates at the medium high cell density (compare blue lines from runs 1 and 2, Fig. 4.7(a)-(b)). In spite of attempts to the contrary, the highest density in run 3 (blue line) was lower than in the two other runs ($\Gamma_{\text{cell}} = 1.62 \times 10^8 \text{ m}^{-2}$ compared to $\Gamma_{\text{cell}} \approx 2.7 \times 10^8 \text{ m}^{-2}$; the cells attached at a lower rate due to unknown reasons), so the comparable result at $\Gamma_{\text{cell}} = 2.71 \times 10^8 \text{ m}^{-2}$ in run 2 has unfortunately not been repeated. Nevertheless, the result of increasing the flow rate is that Φ grows much slower at all densities, remains close to 0 at all times for the low cell densities, is decreased substantially for intermediate cell densities, and reaches the same level but in longer time at high density. Such a pronounced effect of flow rate which nonetheless maintains the isotropic conditions in the chamber shown previously (Fig. 4.5), yet does not impart enough shear to stress to affect the cells, is inconsistent with differentiation being

caused by the differentiation medium, but points to a cell-secreted chemical being required for differentiation.

4.5.3 Increasing the level of cell-secreted chemicals: The effect of using conditioned medium

To further investigate the role of cell-secreted signals in the initiation of the differentiation pathway, a series of parallel experiments were conducted using “conditioned” medium (CM) containing cell-secreted signals in combination with the normal differentiation medium (detailed in Sec. 4.2). Supplying the cells in the microfluidic system with a 1.5:1 mixture of DM and CM (abbreviated DM+CM, see Table 4.1) increases the level of cell-secreted chemicals while maintaining roughly the same concentration of the reagents of the differentiation medium. However, the level of cell-secreted signaling molecules in CM is unknown.

The results of these experiments are given by the dashed lines in Fig. 4.7(b)-(c) which are to be compared to the full lines presenting the results of DM alone with the same color coding. The fraction of differentiated cells Φ is observed to increase by the addition of CM for cell densities above $\Gamma_{\text{cell}} = 1.24 \times 10^8 \text{ m}^{-2}$, while the response is the same for lower densities. The timing of the response is not affected by the addition of CM.

This general trend of increasing Φ at higher densities resulting from increased concentration of cell-secreted chemicals further supports the notion that a cell-secreted chemical is necessary for the differentiation. Furthermore, the fact that no effect of CM is found at low densities strongly indicate that a certain threshold concentration of the cell-secreted chemical must be exceeded for the differentiation to occur.

4.5.4 Evidence for the insufficiency of DM for differentiation

Cells at the very inlet only experience the differentiation medium, but do so at a higher rate than cells further downstream in the chamber. These cells can therefore be used to investigate whether DM alone is sufficient for differentiation.

The absence of upstream cells close to the inlet ensures that the only source of cell-secreted chemicals is the neighbors. Due to the combined effects of advection and diffusion, each secreting cell can only interact with cells close to itself, as the perfusion flow will otherwise transport the solute downstream. Since diffusion dominates at small length scales and advection at large there is an effective signaling distance ℓ_{sig} orthogonal to the flow direction (along the chamber cross-section), which can be estimated from the steady state advection-diffusion equation for the secreted solute f . ℓ_{sig} is the length scale where advection and diffusion become equal, i.e. the length scale which sets the Péclet number to unity, so

$$\ell_{\text{sig}} = \frac{D_f}{U_o}, \quad (4.2)$$

where D_f is the diffusivity of f . The cell-secreted chemical cannot diffuse further transverse distances than ℓ_{sig} because it is washed away by the flow.

The speed U_o will be largest furthest away from the walls due to the paraboloid velocity profile, so the limiting values of ℓ_{sig} are determined in the following using both the

speed at the channel centerline and the speed one cell diameter d from the wall. Both are evaluated at an estimated cell height of 10 μm above the channel floor. Using the highest flow rate of $Q = 500 \text{ nL min}^{-1}$ (which ensures that the cells receive the largest amount of reagents per unit time), the speed U_o for the two cases is found from the analytical solution to the Navier–Stokes equation in a rectangular channel [25] of cross-section $(h, w) = (500 \text{ } \mu\text{m}, 500 \text{ } \mu\text{m})$. Expressed in terms of the channel-average speed $\bar{U} = Q/(h \times w) = 3.33 \times 10^{-5} \text{ m s}^{-1}$, the speed at the cells along the centerline is $0.19 \times \bar{U}$ while the speed one cell diameter from the wall is $0.05 \times \bar{U}$. Therefore, the signaling distance is found to be

$$\ell_{\text{sig}} = \begin{cases} 32 \text{ } \mu\text{m} & \text{at centerline} \\ 120 \text{ } \mu\text{m} & \text{close to wall} \end{cases} \quad (4.3)$$

under the assumption that the secreted molecules are cytokines and therefore have a molecular size of $\sim 20 \text{ kDa}$ which sets $D_f \approx 2 \times 10^{-10} \text{ m}^2 \text{ s}^{-1}$ [54]. This equation reveals that ℓ_{sig} is at least 1.5 cell radii ($d \approx 20 \text{ } \mu\text{m}$), so cells separated by less than ℓ_{sig} can communicate by a secreted chemical. In all cases, the perfusion time d/U_o of medium exchange around the cells is fast (3.2 s to 12.7 s), at least as fast as anywhere in the chamber (where the perfusion time varies from 12.3 s at the centerline to 68.2 s one cell radius from the wall), illustrating that cells in the inlet do receive more DM than cells in the chamber.

While no cells, not even those in the lowest density experiments, were close to being separated by more than ℓ_{sig} , no differentiating cells were found in the inlet at either normal DM or DM diluted by a factor of four (1/4 DM), see sample time series in Fig. 4.8(b). In fact, no differentiated cells were found even for the low flow rate $Q = 33 \text{ nL min}^{-1}$ with normal DM where ℓ_{sig} increases by a factor of ~ 15 . In all cases, differentiating cells were found further downstream, and when CM was supplied in addition to DM as shown in the sample time series in Fig. 4.8(c). This clearly indicates that DM is insufficient for differentiation and further suggests that the presence of a continuous high concentration of some ligand is required for differentiation. However, it should be emphasized that at the last sampling time (~ 22 days), some cells in high-density regions close to the inlet hint at the storage of the first vacuoles, yet, since differentiation is always achieved much faster in the chamber (first differentiated cells are typically found after 3 – 5 days), these hints of early stages of differentiation in inlet-proximal cells is not likely to have been caused by DM. While this analysis does not definitively exclude DM as a potential source of the differentiation chemical, it does establish that any such effect is not the prime source of the chemical.

4.5.5 Intermediate summary

The four analyses just presented have indicated that a cell-secreted chemical, and not the reagents of the differentiation medium, are used by the cells to make the differentiation decision. However, spontaneous differentiation is not observed in the absence of the differentiation medium as indicated by the controls in Fig. 4.7, so the cells only secrete this required chemical in response to DM. Moreover, the data presented here does not indicate whether the decision to differentiate is based solely on this secreted chemical or on a combination with differentiation-medium-reagents.

Since the decision to differentiate depends on the concentration of the cell-secreted chemical and therefore on the cell density, this differentiation is a systemic response: it cannot be achieved by any single cell but it emerges from the collective single-cell responses. Just like the flocking phenomenon of collective migration [14, 38, 126], adipocyte stem cell differentiation is another instance where single-cell fate is heavily influenced by being in a multicellular environment.

4.5.6 Secretion rate is independent of cell state

The cell enters a new state upon differentiation where a new set of genes is expressed. Therefore, changing state from undifferentiated to differentiated could conceivably impact the secretion rate of the differentiation-inducing chemical. Two independent analyses, presented in the following, both reached the conclusion that this is not the case.

The first analysis starts by at each time step identifying the positions of all previously differentiated cells, and then detects the distance of each newly differentiated cell to the nearest previously differentiated cell, see Fig. 4.9 which shows the result for an experiment exposed to DM at $Q = 500 \text{ nL min}^{-1}$ at $\Gamma_{\text{cell}} = 2.71 \times 10^8 \text{ m}^{-2}$. At all times, the distribution of these nearest distances between newly and previously differentiated cells (blue bars in the figure) is skewed towards larger distances than the distribution of nearest neighbor distances of all cells (red line). This indicates that the newly differentiated cells are not the nearest neighbor cells to already differentiated cells, which would otherwise be expected to be the case, if differentiated cells secrete the differentiation-inducing signal at a higher rate than undifferentiated cells. Thus, this analysis indicates that all cells secrete at the same rate independently of their state. This result is independent of whether the flow rate is high ($Q = 500 \text{ nL min}^{-1}$) or low ($Q = 33 \text{ nL min}^{-1}$) and whether or not only differentiation medium or differentiation medium combined with conditioned medium is used to stimulate the cells (see Figs. C.4, C.6 and C.8 in Appendix C.3). Since presumably the cells secrete this differentiation-inducing chemical in response to the differentiation medium at all times, cells downstream from a previously differentiated cell would receive more of the chemical than those upstream. To correct for this, only newly differentiated cells upstream of already differentiated cells were used in Fig. 4.9, however, including all cells do not change the conclusions of this analysis (see Figs. C.4 and C.6 in Appendix C.3).

A second and independent analysis of the data was conducted to ensure the validity of the hypothesis that all cells secrete at the same rate. This analysis detected all newly differentiated cells n_i within a radius of ρ from any previously differentiated cell i (total amount of newly differentiated cells at a time point is N), and compared to the expected number $E(n)$ of newly differentiated cells within ρ from random placement of all newly differentiated cells in the entire chamber. The interrogation radius ρ must be picked large enough that a substantial amount of cells is present, yet small enough to avoid significant resampling of the data. In the results presented in the following, $\rho = 200 \text{ }\mu\text{m}$ has been used; in confluent conditions this corresponds to ~ 10 cell diameters, yet only at high densities and large times is resampling an issue. To avoid this resampling, the last time step has been excluded from all analysis. As shown in Fig. 4.10, the average amount of differentiated cells $\langle n_i \rangle_i$ do not exceed the expectation $E(n)$ when taking the standard

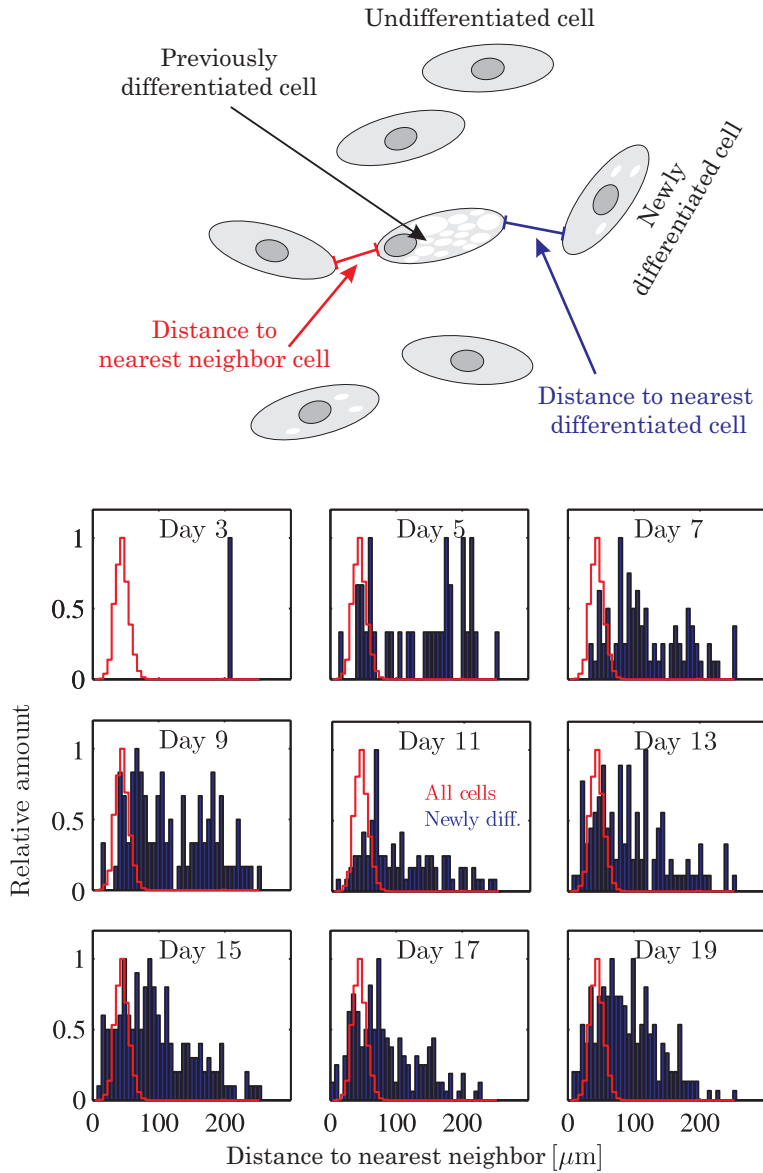


Figure 4.9: Distributions of the average distances between newly differentiated cells and the closest already differentiated cell (blue), compared to the average distance between all nearest neighbor cells (red) for data at the density $2.7 \times 10^8 \text{ cell m}^{-2}$ exposed to differentiation medium at $Q = 500 \text{ nL min}^{-1}$. Each plot in each panel is normalized by its largest value to ease comparison. The distributions of distances between newly differentiated cells and previously differentiated cells are skewed towards larger distances than the distribution of nearest neighbor distances. This indicates that the newly differentiated cells are not the nearest neighbors to already differentiated cells, which would be expected if differentiated cells secrete the critical chemical at a higher rate. This illustrates that all cells (both differentiated and undifferentiated) do secrete the differentiation factor.

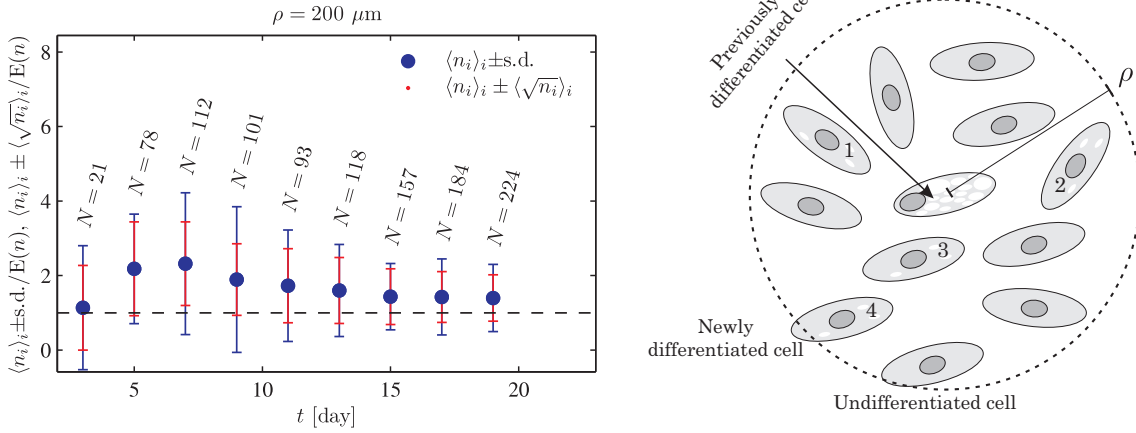


Figure 4.10: Average number $\langle n \rangle$ of newly differentiated cells within a radius of $\rho = 200 \mu\text{m}$ from each previously differentiated cell normalized by the amount $E(n)$ expected from random placement of all newly differentiated cells in the whole chamber ($n = 4$ in the schematic). N indicates the total number of newly differentiated cells detected in the present image. The blue errorbars indicate the standard deviation of the number of newly differentiated cells within the radii of the previously differentiated cells, while the red errorbars illustrate the average counting error due to finite statistics (see text for details). The average amount of newly differentiated cells within the interrogation regions of previously differentiated cells is in agreement what one would expect from random placement, which suggests that there is no enhanced secretion of the critical factor by differentiated cells. This confirms the conclusion from Fig. 4.9.

deviation of the n_i into account. The conclusion is the same when only considering the mean counting error $\langle \sqrt{n_i} \rangle$ (red errorbars) averaged over all previously differentiated cells at any given time point. Hence, the amount of differentiated cells within the radius ρ of already differentiated cells is what one would expect from random placement of these newly differentiated cells. Similar to the first analysis, the results in the figure are discounting any newly differentiated cells placed downstream of the previously differentiated cell, but the results do also not change when including all newly differentiated cells in the analysis, and they furthermore do not change when the cells are also stimulated by CM (see Figs. C.5, C.7 and C.9 in Appendix C.3).

These results, taken together with the first (independent) analysis, indicate that the secretion rate of the critical chemical is independent of the cell state.

4.5.7 The secreted signal acts at the first level of the intracellular differentiation signaling pathway

Comparing the expression levels to 1/4 DM and 1/4 DM+CM across genes indicates how the cells respond to the increased level of the differentiation-inducing cell-secreted chemical in the 1/4 DM+CM experiment. By plotting the expression time series of the response to 1/4 DM against the response to 1/4 DM+CM (such as those from Fig. 4.6), the same linear dependence is found for each of the genes, see Fig. 4.11 and details in Fig. C.2, p. 147. The colors in Fig. 4.11 correspond to the different genes while different markers correspond to different and independent experiments: circles (o) and plusses (+) are from

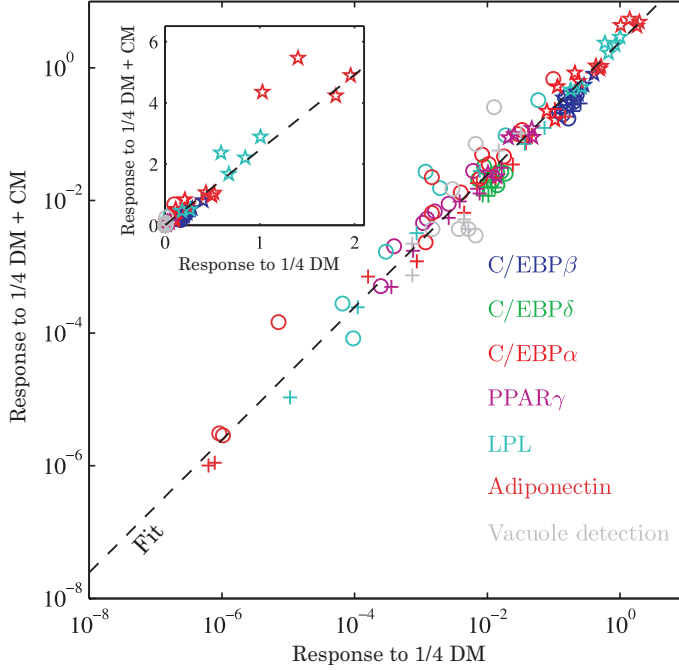


Figure 4.11: Relative gene expression abundance (normalized by β -actin expression level) for cells exposed to 1/4 DM and 1/4 DM + CM for five independent sets of experiments all follow the same linear relationship $\text{Response to 1/4 DM + CM} = a \times (\text{Response to 1/4 DM})$. These include experiments for the first 8 days of stimulation at the same density (\circ and $+$) and three sets of experiments at different densities analyzed after 21 days of stimulation (\star). The dashed black line indicates a representative fit ($R^2 = 0.97$) to this linear relationship with $a = 2.46$. The linear relationship indicates that genes from all three levels of the differentiation signaling cascade are perturbed similarly by the addition of CM containing cell-secreted signals, and therefore suggests that these signals activate the genes at the first level of the cascade, $C/EBP\delta$ and $C/EBP\beta$. Also shown is the fraction of differentiated cells (gray) obtained from the image analysis, which follow the same trend. Figure C.2 in Appendix C.1 shows the results from the individual experiments.

the first eight days at fixed densities, while pentagrams (\star) are for separate experiments at day 21 at low, medium and high densities. The linear dependence is even reproduced when plotting against each other the fraction of differentiated cells Φ obtained from the image analysis, which emphasizes the universality of the relationship.

The dashed black line indicates a fitted linear scaling $\text{Response to 1/4 DM + CM} = a \times (\text{Response to 1/4 DM})$ between the data from experiments exposed to 1/4 DM and 1/4 DM+CM across all genes (but excluding image analysis data), with the scaling parameter $a = 2.46$. The fit was done to the logarithm of the raw data to minimize bias, and the coefficient of determination of the fit of $R^2 = 0.97$ indicates that the fit is representative of the data.

The linear relation between the responses at different concentration levels of the differentiation-inducing cell-secreted signal indicates that this signal must be acting at the first level of the three-level signaling cascade leading to differentiation. This is evident since genes from all three levels follow the same linear scaling when the concentration of differentiation-inducing cell-secreted chemical is increased (Fig. 4.11); had the chemical been acting at an intermediate level, the scaling would have been different for unaffected and affected levels, which is contrary to our observations. Thus, the differentiation-inducing cell-secreted chemical activates the first-level genes $C/EBP\delta$ and $C/EBP\beta$ which then lead to the differentiation through the normal pathway.

Comparison to previously found cell-secreted signals

It has previously been found that the supply of the differentiation medium leads to secretion of several signals (among these Dkk1) that inhibit the Wnt signalling pathway, where activation of this latter suppresses differentiation as previously mentioned [30, 35]. Hence, it is already established that these cell-secreted chemicals affect the differentiation, since unsuppressed Wnt-signaling will otherwise inhibit the activation of the differentiation-critical gene *PPAR γ* (see Fig. 4.1).

However, our data strongly suggests by two independent lines of reasoning that a new and hitherto unknown signal is required to initiate the differentiation process. First, the linear relation between the responses from experiments exposed to 1/4 DM and 1/4 DM+CM across all genes at all levels of the signaling cascade rule out the Wnt-inhibiting signals. Were these signals the dominating secreted factors, then they would only affect *PPAR γ* , *C/EBP α* (due to the positive feedback between this and *PPAR γ*) as well as the downstream adipocyte-specific genes *LDL* and *Adiponectin*, but leave *C/EBP δ* and *C/EBP β* unaffected. We would therefore expect different scalings between the unaffected genes (*C/EBP δ* and *C/EBP β*) and the affected genes (*PPAR γ* , *C/EBP α* , *LDL* and *Adiponectin*) which is clearly not the case. Second, the addition of CM at low cell densities $\Gamma_{\text{cell}} \approx 0.4 \times 10^8 \text{ m}^{-2}$ does not affect the fraction of differentiated cells Φ contrary to the findings at higher cell densities, as shown in Fig. 4.7. This is contrary to the expected increased Φ upon the addition of CM at any cell density if CM mainly consisted of Wnt-inhibiting factors. Furthermore, the fact that all cells secrete f at the same rate independently of their state also suggests that it acts early in the differentiation process (prior to 12 h) when no differentiated cells are present.

Hence, an additional cell-secreted chemical acting at the first level of the differentiation pathway is required to initiate the differentiation process, and this signal operates in addition to any Wnt-pathway-modulating secreted chemicals. Furthermore, this illustrates that the differentiation medium acts along at least two independent signaling pathways (Wnt and the differentiation cascade) to achieve the differentiation.

4.5.8 Conceptual explanation of the differentiation

The experimental findings suggest the following explanation of the results, summarized in Fig. 4.12. The cells secrete a differentiation-inducing chemical f which is required for the differentiation, and which furthermore initiates the differentiation by acting at the first level of the signaling cascade. This chemical is secreted only in response to critical components of the differentiation medium DM, and is secreted at the same rate S by all cells independently of their state (differentiated or not). Hints of a maximal secretion rate at some concentration of the differentiation medium could indicate that differentiation is the product of competing processes each depending on different critical components; these speculations are yet to be verified.

Differentiation does not require cell-cell contact and is furthermore limited by this cell-secreted signal, with an increase of the fraction of differentiated cells resulting from an increase in the concentration level. Once differentiated, the cells will start to form lipid-

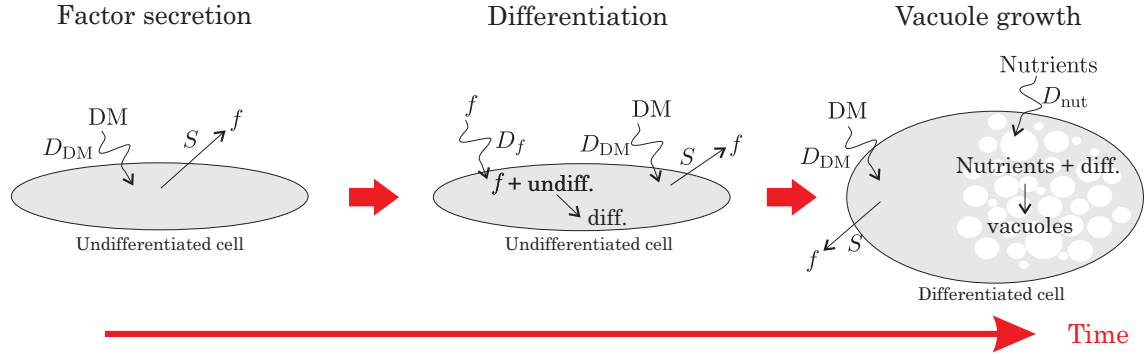


Figure 4.12: Conceptual explanation of the differentiation process. Each cell secretes a critical differentiation-inducing chemical f in response to the differentiation medium DM. This signal is required to initiate the differentiation signaling pathway. Once differentiated, a cell will begin to form lipid-filled vacuoles, whose production are likely limited by the availability of nutrients.

filled vacuoles at a rate which presumably depends, among other things, on the amount of available nutrients and time (the latter due to finite rates of sugar uptake).

4.6 Detailed analysis reveals non-trivial secretion dynamics

The proposed explanation hinges critically on the purported secretion of a differentiation-inducing signal whose identity remains unknown. To verify that this hypothesis is consistent, the remaining parts of this chapter is devoted to further experiments and physical investigations of the extracellular distribution of secreted signal and the level sensed by the cells. The errors of the experimental values of Φ mean that direct comparison between theory and experiment is too much to ask; yet, the trends of the experimental data should be captured by the theories. Furthermore, the proposed theoretical methods seem to provide the best means of progress since it is very difficult to obtain strong experimental data with single-cell resolution.

4.6.1 Experimental evidence for non-trivial secretion: Lower levels of DM leads to higher fraction of differentiated cells

The concentrations of DM and CM were varied experimentally as described in Table 4.1. The results, shown in Fig. 4.13, consistently finds increasing fraction of differentiated cells Φ when DM is lowered and CM is increased.

We focus first on the effect of using a solely lower DM concentration, see dashed lines in the middle column of Fig. 4.13; the full lines are the results of using only DM in normal concentration (these lines are the same as the full lines in the left column, where the latter contains the data from Fig. 4.7). The fraction of differentiated cells Φ is found to increase upon lowering the concentration of DM, except for the lowest cell density, where the results of $1/4$ DM are indistinguishable from normal DM. Moreover, the variations in

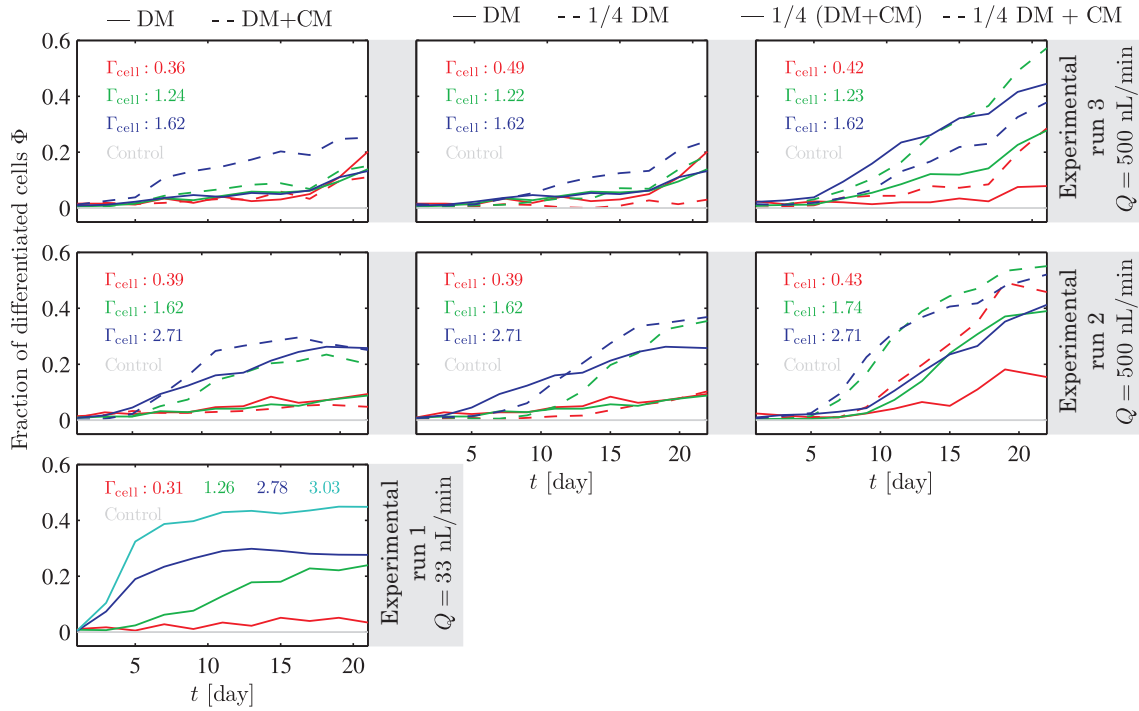


Figure 4.13: Fraction of differentiated cells Φ as a function of time for all experimental conditions listed in Table 4.1. Cell density is measured in units of 10^8 m^{-2} . The flow rate was $Q = 33 \text{ nL min}^{-1}$ in run 1 but 500 nL min^{-1} in the two other runs. The left column recapitulates the data from Fig. 4.7 for completeness. Furthermore, the full lines in the middle column are the response to only DM from the left column. In general, higher values of Φ are found when DM is diluted and the ratio of CM to DM is increased.

Φ at $\Gamma_{\text{cell}} = 1.62 \times 10^8 \text{ m}^{-2}$ between runs 2 and 3 exceed the counting error⁶ for this lower concentration of DM, but both runs do produce significant increases of Φ compared to normal DM. These observations suggest that an increased secretion results when the level of the differentiation medium is lowered.

Adding a small amount of CM to the lowered concentration of DM is achieved in the experiments with $1/4 (\text{DM} + \text{CM})$, where the concentration of added cell-secreted chemicals obviously is only a fourth of normal CM. As shown by the full lines in the right column of Fig. 4.13, a large increase in Φ is observed for all but the lowest cell densities (red lines, $\Gamma_{\text{cell}} \approx 0.4 \times 10^8 \text{ m}^{-2}$), and interestingly, the response for the medium density (green line in run 2 (replicated by blue line in run 3), $\Gamma_{\text{cell}} \approx 1.7 \times 10^8 \text{ m}^{-2}$) is indistinguishable from the medium high density response (blue line in run 2, $\Gamma_{\text{cell}} = 2.7 \times 10^8 \text{ m}^{-2}$). These observations are consistent with the interpretation of a higher secretion rate at $1/4 \text{ DM}$, combined with a low background level of the secreted chemical caused by the addition of $1/4 \text{ CM}$.

Maintaining the concentration of DM at one fourth, but now using the full concentration of CM, further increases Φ across all cell densities. Remarkably, this occurs even for the

⁶The counting error signifying the expected variation between repeat experiments varies from $\sim 6 \%$ at the lowest density experiments with ~ 300 cells to $\sim 2 \%$ at the highest density cases of ~ 2700 cells.

lowest cell density which has remained unaffected by all other combinations of CM and DM. The responses in run 2 at $\Gamma_{\text{cell}} = 1.62 \times 10^8 \text{ m}^{-2}$ (green) and $\Gamma_{\text{cell}} = 2.71 \times 10^8 \text{ m}^{-2}$ (blue) are very similar which was also the case for 1/4 (DM + CM), however, the result at $\Gamma_{\text{cell}} = 1.62 \times 10^8 \text{ m}^{-2}$ in run 3 (blue) is markedly different. Thus, whether the similarity between the results at intermediate and medium high densities in run 2 are experimental artifacts or holds against the test of replicated experiments remains unknown. However, taking together all these experimental observations suggests a higher secretion rate at lower DM levels.

4.6.2 Continuum theory of supplied and secreted chemicals

The differentiation medium DM and the secreted chemical f are subjects to advective and diffusive transport in the chamber, and are therefore appropriately described by continuum theory. The obvious dependence on the flow rate found experimentally is most easily studied by normalizing with the advection time L_o/U_o instead of the diffusion time L_o^2/D used in Chapter 2 (Eq. (2.8)), where U_o is taken as the average speed in the chamber. Ignoring for simplicity the specifics of the inlet and outlet, and non-dimensionalizing length scales by the chamber height, we consider in what follows a two-dimensional rectangular chamber of $0 \leq z \leq 1$ and $0 \leq x \leq 12$, to which inlet and outlet of length 6 and height 1 have been added to avoid any inlet-derived disturbances of the results (see the actual chamber in Fig. 4.2). The non-dimensional concentration c_i of solute i therefore obeys the non-dimensional advection-diffusion equation

$$\partial_t c_i + \mathbf{v} \cdot \nabla c_i = \frac{1}{\text{Pé}_i} \nabla^2 c_i, \quad (4.4)$$

where Pé_i is the Péclet number of solute i (as in Eq. (2.9)). The boundary conditions are

$$\text{Wall with cells: } -\mathbf{n} \cdot \nabla c_i = \text{Bi}_i R_i(c_i, c_j, \dots), \quad (4.5a)$$

$$\text{All other walls and outlet: } \mathbf{n} \cdot \nabla c_i = 0. \quad (4.5b)$$

where $R_i(c_i, c_j, \dots)$ is a reaction term and Bi_i is the Biot number of the solute measuring the ratio of diffusion time to reaction time, with low values of Bi corresponding to a regime dominated by diffusion. The exact expression for Bi naturally depends on the kinetics of the reaction, but for a simple first-order reaction $c_1 \rightarrow c_2$ with rate constant k it becomes kL_o/D . The inlet boundary conditions are

$$c_i = c_i^{\text{init}} \quad (4.6)$$

where c_i^{init} is some value.

4.6.3 Physical limits imposed on continuum theory by the experimental setup and results

The experimental system together with the experimental findings provide a number of constraints on the involved physical processes that can be used to further elucidate the role and workings of the unidentified secreted signal f . These constraints are listed here.

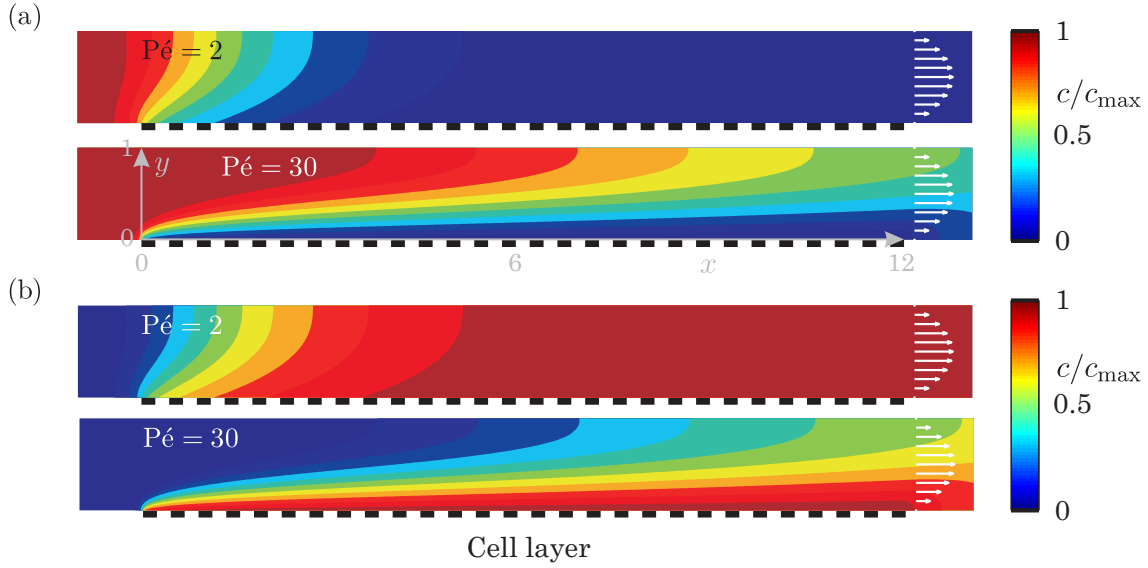


Figure 4.14: Steady state concentration fields in the microfluidic system normalized by their maximum value, with flow going from left to right. The non-dimensional coordinate system is indicated in gray in the lower panel in (a). (a) Steady-state concentration fields of a chemical reacting with the cells (indicated by the dashed black line) at the two experimentally relevant Péclet numbers of $Pé = 2$ and 30. The solute is supplied at the inlet. A concentration boundary layer forms since the reaction is diffusion-limited as evidenced by $Pé > 1$. (b) Distribution of a cell-secreted chemical with a similar molecular size as the supplied chemical exhibits the same boundary layers.

Moderate Péclet numbers assures the formation of a concentration boundary layer around the cells

The average speeds \bar{U} at the two flow rates were $\bar{U} = 7.33 \times 10^{-7}$ at $Q = 33 \text{ nL min}^{-1}$ and $\bar{U} = 1.11 \times 10^{-5}$ at $Q = 500 \text{ nL min}^{-1}$ using $\bar{U} = Q/(h \times w)$ with $h = 500 \text{ }\mu\text{m}$ and $w = 1500 \text{ }\mu\text{m}$. Combined with an estimated diffusivity of about $2 \times 10^{-10} \text{ m}^2 \text{ s}^{-1}$ [54] and the channel height $h = 500 \text{ }\mu\text{m}$ used for the non-dimensionalization, the Péclet number is $Pé \approx 2$ at $Q = 33 \text{ nL min}^{-1}$ and $Pé \approx 30$ at $Q = 500 \text{ nL min}^{-1}$. This implies that the transport of the solute will be dominated by advection, and furthermore, that the cells on the bottom of the chamber will not have access to all solute supplied at the inlet; the solute entering the chamber close to the ceiling will not have the time to diffuse down to the cells at the bottom. A boundary layer signifying the interaction distance of the cells will therefore form above the chamber bottom. This boundary layer can be seen in Fig. 4.14(a), which displays a numerical solution of the advection-diffusion equation Eq. (4.4) for a supplied solute reacting with the cell layer, where the latter is indicated by the thick, dashed black line. The equation was solved in the steady state using COMSOL MULTIPHYSICS version 3.5a. The concentration is normalized to the inlet concentration in the figures. The exact values of c depend on the chemical kinetics, but the shape and extension of the boundary layer is independent of these kinetics. Furthermore, since the secreted signal f is likely a cytokine and therefore also has a diffusivity of about $2 \times 10^{-10} \text{ m}^2 \text{ s}^{-1}$, its distribution will also be characterized by similar boundary layers, see

Fig. 4.14(b).

The formation of the boundary layer depends on the value of the Péclet number, which in turn depends on the unknown diffusivity of the solute. However, at its lowest value physically possible of $D \sim 2 \times 10^{-9} \text{ m}^2 \text{ s}^{-1}$ we still find $\text{Pé} \approx 0.2 - 3$ for the flow rates used, so a boundary layer will always form at the highest flow rate.

Steady-state extracellular conditions

The extracellular conditions are dominated by the perfusion flow, which relaxes on time scales that are several orders of magnitude lower than the ~ 21 days it takes to complete each experiment.

- *Stokes flow:* Fluid inertia is completely negligible at even the high flow rate, since the Reynolds number $Re = \bar{U}h/\nu$ is much below unity: $Re = 3.7 \times 10^{-4}$ at the low flow rate and $Re = 5.6 \times 10^{-3}$ at the high flow rate using the parameters of the previous subsection and assuming that the fluid is water. The flow therefore reaches a steady state on the order of milliseconds, and the flow is furthermore completely laminar [25]. This justifies ignoring the details at the inlet and outlet.
- *Concentration fields:* The solute concentration fields interact with the cells and the reaction time therefore depends on the reaction kinetics. In addition, the moderate Péclet numbers assure that there will be a small contribution from Taylor–Aris dispersion in the steady-state concentration fields. The Taylor–Aris relaxation rate can be used to estimate the time scale on which the solute concentration fields settles into the steady state. This time scale is ~ 300 s, using the longest of the relaxation rates in a rectangular channel (the transverse) of $R^2/\pi^2 \times h^2/4D$ (see Eq. (2.78)). This time scale is also much lower than any biologically relevant time scales, so only the steady state is relevant.

Response is limited by the cell-secreted signal

The response is limited by the availability of the cell-secreted chemical f since a larger fraction of cells differentiate when the amount of f is increased. This is not to say that additional signals are not necessary for the initiation of the differentiation signaling pathways, but any such additional signals are present at high enough levels that their availability do not limit the differentiation.

4.6.4 The experimental results are inconsistent with normal reaction kinetics

The spatially isotropic experimental results indicate that the cellular response to the cell-secreted chemical is the same anywhere along the chamber, even when varying the flow rate. Since fluid shear is very unlikely to affect the cells (Appendix C.2), the observed variations in Φ must be caused by physical transport processes of advection and diffusion coupled with the secretion of f from the cells. Hence, independently of the exact form of

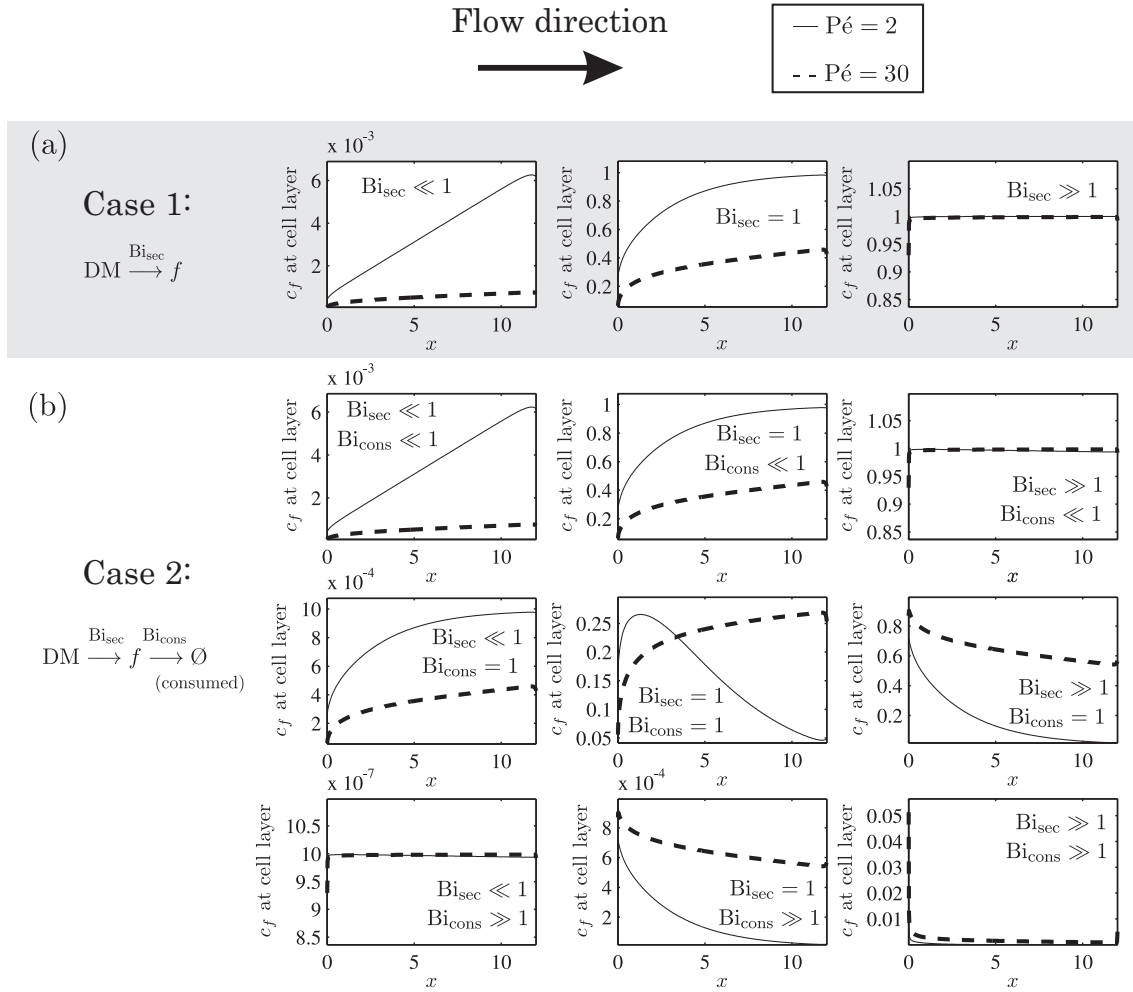


Figure 4.15: The concentration c_f of the cell-secreted chemical evaluated at the bottom of the chamber where the cells reside, plotted as a function of non-dimensional chamber length x . Each subpanel contains results for $\text{Pé} = 2$ (full line) and $\text{Pé} = 30$ (dashed), and each panel corresponds to one of the kinetic schemes presented in Sec. 4.6.4 as summarized to the left. None of the results are consistent with the experimental observations of lengthwise isotropic differentiation and notable variation between low and high Pé .

the reaction term in Eq. (4.5), the advection-diffusion-reaction equations can be used to investigate the criteria which guarantee such behavior.

We assume in the following that the decision to differentiate is made based on the concentration c_f of a cell-secreted chemical f , so we will be concerned only with c_f evaluated along the chamber floor. Such concentration-dependent kinetics is known as the law of mass action and are typically found in biochemistry [5, 124]. Even though the exact chemical kinetics are unknown, requiring that the results are consistent with the experimental findings and furthermore internally consistent will be used in the following to exclude normal law-of-mass-action-kinetics. These consistencies stipulate that any variations along

the cells at a particular value of $Pé$ must be substantially lower than the variation between the concentration of c_f at the low and high flow rate. Otherwise, we would expect either similar experimental results at the two flow rates, or observable variations along the lengthwise direction of the chamber, which are both inconsistent with the experimental observations in Figs. 4.5 and 4.7.

The Péclet number is varied from the low ($Pé = 2$) to the high flow rate ($Pé = 30$), while all possible combinations of simple and plausible reaction schemes are investigated. Therefore, the Biot numbers of the various reaction schemes are kept as free parameters. The model includes two non-dimensional concentration fields: the supplied differentiation medium, whose concentration is denoted c_{DM} and the cell-secreted chemical with concentration c_f . These both obey the advection-diffusion equation in the bulk, and are coupled through a chemical reaction at the cells. This chemical reaction models the secretion of f by the cells in response to DM. The equations are

$$\partial_t c_f + \mathbf{v} \cdot \nabla c_f = \frac{1}{Pé_f} \nabla^2 c_f \quad \text{with} \quad -\mathbf{n} \cdot \nabla c_f|_{\text{cells}} = R_f(c_f, c_{DM}, \dots), \quad (4.7a)$$

$$\partial_t c_{DM} + \mathbf{v} \cdot \nabla c_{DM} = \frac{1}{Pé_{DM}} \nabla^2 c_{DM} \quad \text{with} \quad -\mathbf{n} \cdot \nabla c_{DM}|_{\text{cells}} = -R_{DM}(c_f, c_{DM}, \dots), \quad (4.7b)$$

and the inlet conditions are $c_f^{\text{init}} = 0$ and $c_{DM}^{\text{init}} = 1$. DM is not the full differentiation medium, but the critical parts of the latter which purportedly cause the cells to secrete f . The equations are solved numerically in the steady state using COMSOL MULTIPHYSICS version 3.5a.

Case 1: The simple scheme

We move along according to Occam's Razor and therefore start with the simplest reaction scheme imaginable, namely that DM is converted to f by the cells in a first-order reaction with dimensionfull rate S_{sec} . This models that DM is both sensed and consumed by the cells, and that secretion is proportional to the consumed amount of DM. The reaction terms in Eq. (4.7) are

$$R_{DM} = \text{Bi}_{\text{sec}} c_{DM} \quad \text{and} \quad R_f = \text{Bi}_{\text{sec}} B c_{DM}. \quad (4.8)$$

where $\text{Bi}_{\text{sec}} = S_{\text{sec}} L_o / D$ is the the Biot number of the consumption. This is not a traditional chemical reaction between two species where stoichiometry dictates the relation between the numbers of input and output molecules, and we must therefore allow each cell to secrete a number of f molecules that differs from the number of consumed DM molecules. The non-dimensional factor B measures this conversion ratio of DM molecules to f molecules, but will for simplicity be taken to be unity in the following. This simplification only shifts the level of f , not the dynamics.

The dependence on c_{DM} means that the availability of this chemical limits the dynamics, see the results in Fig. 4.15(a). When $\text{Bi}_{\text{sec}} \ll 1$ almost none of the DM is used by the individual cell, so c_{DM} -availability does not limit the response, and the result is therefore that the cell-secreted chemical f builds up downstream. At the other limit of $\text{Bi}_{\text{sec}} \gg 1$ any

available c_{DM} will be converted to f , leading to a nominally constant level of c_f along the cells. However, increasing the flow rate does not alter the level of c_f much, and the c_f -level variations are inconsistent with the experimental observations. At intermediate levels of $Bi_{sec} = 1$, there are noticeable variations in c_f along the cells for the two different flow rates, however, the downstream variations in c_f overlap significantly with the variations between low and high flow rate. Hence, this kinetic scheme is inconsistent with the experimental observations, and must be excluded.

Case 2: The full scheme

The most complex reaction scheme consistent with the experimental conditions, which is nonetheless kept to first-order kinetics, assumes that DM is being converted to f by the cells, who both secreted and consume the latter. The chemical reactions are therefore $DM \rightarrow f$ with rate S_{sec} and $f \rightarrow \emptyset$ with rate S_{cons} , where \emptyset indicates that f is consumed. The corresponding reaction terms to Eq. (4.7) are

$$R_{DM} = Bi_{sec}c_{DM} \quad \text{and} \quad R_f = Bi_{sec}Bc_{DM} - Bi_{cons}c_f. \quad (4.9)$$

where $Bi_{sec} = S_{sec}L_o/D$ and $Bi_{cons} = S_{cons}L_o/D$.

Each of the two reactions — consumption of DM or consumption of f — can limit the response. Allowing each Biot number to be either small, large or unity, a total of $3^2 = 9$ different combinations exist. Figure 4.15(b) clearly illustrates that none of these satisfy the requirements stipulated by the experiments, so we will not go into the details of the underlying physics. However, it must be concluded that even this most elaborate reaction scheme cannot explain the experimental observations. Fundamental solute transport combined with chemical law-of-mass-action kinetics appears to be unable to reproduce the experimental findings.

4.6.5 The physics of chemoreception in perfusion flow

The experimental results are evidently inconsistent with the traditional law-of-mass-action chemical kinetics usually assumed in biochemistry. The basic premise of law-of-mass-action kinetics is that the probability that a molecule is present at a specific location is proportional to its concentration. However, in a perfusion flow the current of arriving molecules also depends on the flow due to advection. The effects of the perfusion flow on the physics of cellular chemosensing is therefore revisited to look for a possible explanation which is consistent with our experimental results.

Using a very simple model in the spirit of Berg and Purcell [19], we suppose the cellular sensing system consists of a number of independent receptors, and ignore for simplicity any cross-correlations between these. Consider a single such receptor on a cell that can bind molecules of a particular species (the ligand), but can bind only one such molecule at a time. The cell is immersed in a medium which in addition to the cell also contains a concentration of the molecular species. The cell can only infer the external concentration from the bound receptors, and must therefore infer these external conditions from the current J of impinging molecules on its receptors. The probability that a molecule will

bind to a free receptor in the interval dt is given by the number of molecules arriving at the receptor during the interval, $J dt$, and the probability q that a molecule binds, once it is at the receptor. The probability of binding is therefore

$$p_b = qJ dt. \quad (4.10)$$

Since the receptor-ligand complex is a thermal system, the ligand can be spontaneously released due to thermal fluctuations. The probability that this happens in the interval dt is denoted dt/τ_b , where τ_b is the average time a molecule stays bound to the receptor. Denoting by \bar{p} the average binding probability, the receptor is on average bound with probability \bar{p} and free with probability $1 - \bar{p}$. The average binding probability \bar{p} is therefore the weighted sum of the probability of binding minus the probability of release, with the weights provided by the probabilities that the receptor is free or bound, respectively. The following equation therefore describes the time rate-of-change of \bar{p}

$$\partial_t \bar{p} = (1 - \bar{p})qJ - \frac{\bar{p}}{\tau_b} \quad (4.11)$$

Solving this equation in the steady state yields

$$\bar{p} = (1 - \bar{p})qJ\tau_b \quad \text{or} \quad \bar{p} = \frac{qJ\tau_b}{1 + qJ\tau_b}. \quad (4.12)$$

This result shows that the particle current of ligand molecules to the receptor determines its binding probability, and not concentration as usually reported [5, 6, 20]. Since the cell infers the external conditions from its occupied receptors, a higher binding probability corresponds to an increasing response.

Diffusive limit

In the limit of zero flow velocity, the current J is given only by diffusion and Eq. (4.12) reduces to the Michaelis–Menten probability $\bar{p} = c/(K_d + c)$ that is well known from biochemistry (see Eq. (C.7) in appendix C.4, p. 153). Assuming for simplicity that the cell is a sphere of radius a , and that the receptor is a small spherical patch of radius s on the surface of the cell, the current J from only diffusive transport is in the steady state given by $J_{\text{diff}} = 4Dsc_\infty$, where D is the diffusivity of the solute and c_∞ is the solute concentration in the medium far away from the cell (which is assumed to be constant and controlled by the experimenter) [19]. Equation 4.12 in this case becomes

$$\bar{p} = \frac{c_\infty}{\frac{1}{4qDs\tau_b} + c_\infty}, \quad (4.13)$$

which is identical to the Michaelis–Menten case with $K_d = (4qDs\tau_b)^{-1}$. The measurable dependence on concentration found in biochemistry is thus retrieved in the zero-flow limit, as must be the case.

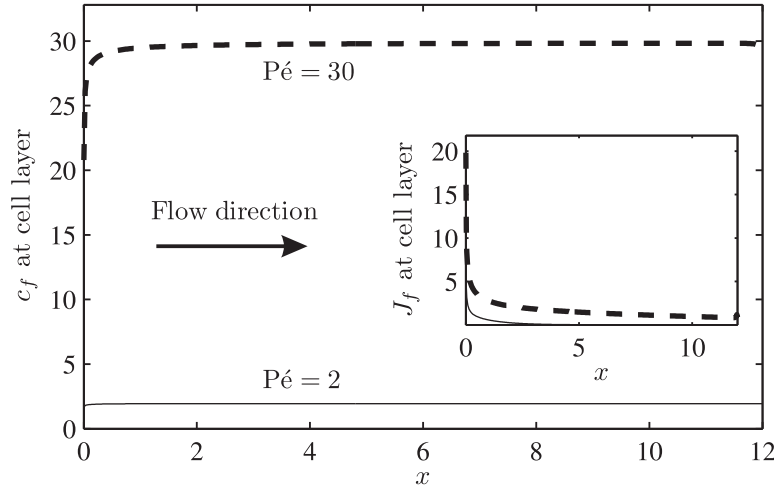


Figure 4.16: Concentration of f at along the cells under the assumption that secretion is proportional to the particle-current J_{DM} of DM received by the cells. For the present example $Bi_{sec} = 10^{-3}$ and $K_{sec} = 10^2$. The inset shows the corresponding particle-current J_f of f to the cells.

Perfusion experiments

In a perfusion experiment, the current J will have contributions from the flow in addition to the purely diffusive current J_{diff} above. While the exact form of the current is difficult to calculate analytically, it is obvious from Eq. (4.12) that the binding probability increases with the current. Thus, one expects higher binding probability at the same concentration in a perfusion experiment, and therefore a higher response than in a static experiment.

4.6.6 Particle-current-based reaction kinetics explains the experimental results

Applying the theory of particle-current-dependent secretion above to the stem cells, we consequently assume that secretion of f depends on the particle current J_{DM} of impinging DM particles. DM particles bound to a receptor can be either released after some time or consumed (internalized). As a simplifying assumption, this removal of DM particles is considered to occur at a constant rate S_{sec} . The reaction terms in Eq. (4.7) therefore become

$$R_{DM} = Bi_{sec}c_{DM} \quad \text{and} \quad R_f = K_{sec}J_{DM}, \quad (4.14)$$

where $Bi_{sec} = S_{sec}L_o/D$, K_{sec} is a non-dimensional secretion rate, $J_{DM} = \int_{\partial\Omega} \mathbf{n} \cdot \mathbf{j} \, dA$ is the non-dimensionalized particle current to a cell, $\mathbf{j} = -\nabla c_{DM}/Pé_{DM} + \mathbf{v}c_{DM}$ is the total non-dimensional DM flux, and the integral is taken over the surface area of a cell. Furthermore, only the diffusive contribution to \mathbf{j} exists at the cells since there is no flow in the vertical direction. However, the advection ensures that more molecules per unit time can diffuse to the cell which increases the flux.

The concentration c_f at the cell layer is plotted in Fig. 4.16 for the two relevant Péclet numbers. This results satisfies both the criteria imposed by the experimental results:

nominally constant c_f level along the lengthwise chamber direction, and large variation between the c_f level at the two flow rates. Hence, this simplest kinetic scheme integrating the developed theory satisfies both the criteria, and by Occam's Razor must therefore be accepted as a full description.

The arguments presented in the previous section that biological signaling in perfusion flow depends on the particle current and not the concentration should apply to any signaling system, including the detection of f leading to the differentiation. According to this theory, we would therefore expect that differentiation depends on the current J_f of f instead of the concentration. However, as shown by the example in the inset to Fig. 4.16, none of the reaction schemes produced distributions of J_f along the cell layer that satisfied both small variations along the cells for each value of $Pé$, and noticeable variations between J_f for the two values of $Pé$. It is at the time of this writing not understood why current-based sensing should only apply to the secretion and not to the differentiation signaling, and time has not allowed for resolving this discrepancy. Whether this means that the current-based sensing presented in Sec. 4.6.5 is too simple to account for the differentiation signaling or if this theory suffers from fundamental flaws therefore remains unresolved. We move along assuming that this is a minor issue, which does not fundamentally corrupt the results.

A higher level of c_f is observed at the high $Pé$ in Fig. 4.16. This is in contrast to the experimental results of Sec. 4.5 where a lower fraction of differentiated cells were observed at high $Pé$. To further investigate this discrepancy we turn to single-cell theory in the following.

4.6.7 Inferring single-cell conditions from population data

The previous experimental results of increasing the flow rate and lowering the amount of DM suggests that increased DM currents lead to lower levels of f (Fig. 4.13). By formulating the simplest reasonable single-cell model which is consistent with our findings, we in the following deduce self-consistently the external conditions experienced by the cells in the different experiments. This idea is exploited in the following using a simple single-cell model to investigate the average near-cell environment.

Single-cell model

The cells exhibit large variation in activation between the different experiments, both in timing and in fraction of active cells: Cells in the same experiment differentiate at different times, and variations in Φ exceeding those of finite statistics are found between repeat experiments. The experimental observations therefore suggest that population behavior should be interpreted as a deterministic behavior convolved with stochastic single-cell variations.

The following model assumes that the decision to differentiate is made by the single cell based on the intracellular concentration of some critical transcription factor g , and that the production rate of g depends on the extracellular concentration of c_f . In light of the uncertainty of whether c_f or J_f is the appropriate parameter determining differentiation, we will in the following rely on the indications from the previous section that it is indeed

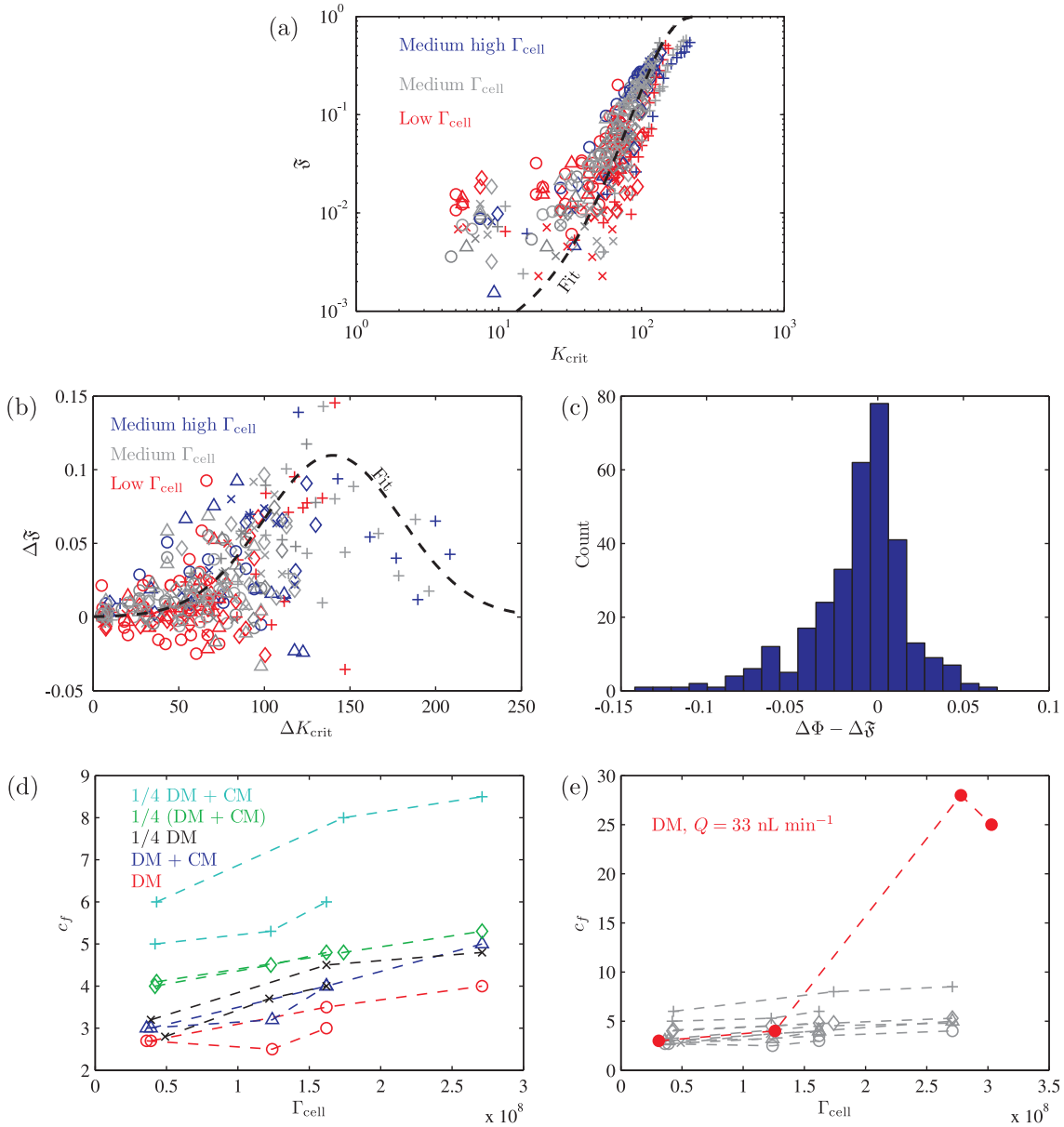


Figure 4.17: Collapsing the experimental $\Phi(t)$ measurements according to a single-cell model. (a) The collapsed experimental data from all five types of experiments, fitted under the assumption that the distribution F is a Gaussian. The color indicates the cell density going from red ($\sim 0.4 \times 10^8 \text{ m}^{-2}$) over gray ($\sim 1.2 \times 10^8 \text{ m}^{-2}$) to blue ($\sim 2.7 \times 10^8 \text{ m}^{-2}$) and the symbols indicating the experimental conditions (see legend in panel (d)). The fit is indicated by the dashed black line. (b) The fit is made to the increments $\Delta\Phi$ since errors in $\Delta\Phi$ are uncorrelated, unlike the “cumulative distribution”-interpretation of Φ . (c) The deviations $\Delta\Phi - \Delta\hat{\Phi}$ of the fit to a normal distribution is itself normally distributed with $\Delta\Phi - \Delta\hat{\Phi} = 0.003 \pm 0.017$ (mean \pm s.d.). The standard deviation of the distribution of deviations is in good agreement with the estimated image analysis detection error of $\sim 2.5\%$, see Sec. 4.3.5. (d) The fitted values of c_f for $Q = 500 \text{ nL min}^{-1}$ agree with the interpretation from the experiments that the c_f level increases from DM, over DM+CM, 1/4 DM, 1/4 (DM+CM) to 1/4 DM + CM. (e) The fitted values of c_f for the one experimental run at $Q = 33 \text{ nL min}^{-1}$ shows the same tendency as $Q = 500 \text{ nL min}^{-1}$, but much higher values of c_f at the higher cell densities. Data from panel (d) is included in gray.

the concentration. However, it is for the current model irrelevant whether it is c_f or J_f . In any given experiment, each cell is assumed to be exposed to the same level of f , and we do not consider further the details of the secretion. Furthermore, g is assumed to decay at a rate proportional to its concentration since transcription factors are known to be unstable [6]. As discussed previously in Sec. 4.1.4 the differentiation depends on the three-level signaling cascade (Fig. 4.1(c)), so the premise that differentiation depends on the level of some intracellular signaling molecule is well established. However, the exact nature of g is not further specified, it is only assumed to be a critical signaling molecule whose concentration is the limiting factor in the differentiation pathway. The simplest model for g based on these assumptions is

$$\frac{dg(t)}{dt} = k \frac{c_f}{c_f + K_d} - Wg(t), \quad (4.15)$$

where in the production term (first term on the right hand side) we assume that the dependence on c_f is Michaelian (see Appendix C.4, p. 153) with an activation level given by K_d , since hints of threshold values of c_f was observed in the experiments. Solving this equation while requiring that $g(0) = 0$ (i.e. assuming that c_f is supplied at $t = 0$ so $g(t \leq 0) = 0$) yields

$$g(t) = \frac{k}{W} \frac{c_f}{c_f + K_d} (1 - e^{-Wt}). \quad (4.16)$$

Each cell can be in one of two states — undifferentiated or differentiated — and the differentiation procedure is irreversible. Representing the undifferentiated state by 0 and the differentiated state by 1, and making the definition that each cell is either differentiated or not⁷, the state \mathcal{S} of a cell can therefore formally be given by

$$\mathcal{S}(t) = \Theta(g(t) - g_{\text{crit}}), \quad (4.17)$$

where Θ is the Heaviside step function and g_{crit} is the concentration at which this cell differentiates⁸.

A final — and critical — input to the model is the assumption that the critical activation level (the value of K_d) varies between the individual cells with some probability distribution density f . This distribution is the same for all experiments since all cells were taken from the same pool. Thus, while each cell is exposed to the same concentration of c_f , these variations in single-cell K_d -values means that the single cells in each experiment will differentiate at different times, with lower levels of K_d corresponding to faster differentiation. Since furthermore only cells which at some point satisfy $g(t) \geq g_{\text{crit}}$ will differentiate a larger fraction of cells will differentiate at higher c_f -concentrations. That the critical concentration level K_d is allowed to vary between the cells is no coincidence: typically this

⁷The details of the differentiation process are ignored since the data is not of a suitable quality, and it is furthermore assumed that a cell cannot be fractionally differentiated, i.e. that a cell cannot be e.g. 37 % differentiated.

⁸Exactly what happens when this level is exceeded remains unspecified; it could be the level where the positive feedback loops are activated, or it could correspond to the concentration where adipocyte-specific genes are active to an extent that allows the first vacuoles to form.

critical concentration is the result of a number of chemical reactions of a limited amount of complex molecules whose binding affinities, copy numbers etc. will vary in addition to any molecular fluctuations.

Applying the model to experimental population data

The fraction of differentiated cells Φ for an experiment of N cells is given by the average over all cell states $\mathcal{S}(t)$ at each time step,

$$\Phi(t) = \langle \mathcal{S} \rangle(t) = \sum_{n=1}^N \mathcal{S}_n(t) \frac{1}{N}, \quad (4.18)$$

where $\langle \mathcal{S} \rangle(t)$ denotes the ensemble average at time t .

In the limit of infinitely many cells, this average of cell states is equivalent to an average over the distribution $\mathfrak{f}(K_d)$ of single-cell activation levels

$$\Phi(t) = \langle \mathcal{S}_n \rangle(t) = \int_0^\infty \mathcal{S}(t, K_d) \mathfrak{f}(K_d) dK_d. \quad (4.19)$$

Performing the integration yields

$$\Phi(t) = \begin{cases} \mathfrak{F}(K_{\text{crit}}(c_f, G, W, t)), & K_{\text{crit}} > 0 \\ 0, & \text{otherwise} \end{cases}, \quad (4.20)$$

where $\mathfrak{F}(x) = \int \mathfrak{f}(x) dx$ is the cumulative distribution function associated with \mathfrak{f} , $G = k/g_{\text{crit}}$ and

$$K_{\text{crit}}(c_f, G, W, t) = \left[\frac{G}{W} (1 - e^{-Wt}) - 1 \right] c_f. \quad (4.21)$$

Thus, by rescaling time according to Eq. (4.21), all experimentally measured curves of $\Phi(t)$ should collapse onto a single curve, and this curve will be the cumulative distribution function of the single-cell activation level K_d . Essentially, the model converts measured time to intracellular level of g , and compares the level of g in each cell to the critical level. Then because of the variations in single-cell K_d not all cells in a given experiment can differentiate; this is only possible for cells with $G/W \times c_f/(c_f + K_d) > 1$.

4.6.8 Details of fitting to population data

Equation (4.20) postulates a relationship between the population data and an unknown distribution \mathfrak{F} , but does not provide any clues to the functional form of \mathfrak{F} . Attempts to invert the equation have been unsuccessful, as have additional attempts to derive an equation that could determine the distribution by other means.

The most natural assumption is then that K_d is normally distributed with mean μ_{K_d} and variance $\sigma_{K_d}^2$. By making such an assumption, any fitting procedure is naturally biased. While this is not optimal, it provides the best means of progress.

In fitting the experimental population data of the Φ time series to \mathfrak{F} using the rescaling of Eq. (4.21), $G = k/g_{\text{crit}}$ and W were assumed to be the same for all time series (across

all experimental conditions) while the concentration level c_f was allowed to vary for each time series. In addition, the parameters μ_{K_d} and $\sigma_{K_d}^2$ of the distribution were also allowed to vary.

The experimental values of Φ are convoluted with noise stemming from uncertainties in the image analysis, and to a lesser extent, errors from finite statistics. Furthermore, each point in a cumulative distribution function is correlated with the previous values (the final points when the function reaches unity are completely correlated), so fitting to a cumulative distribution function carries a substantial risk of introducing correlation bias. The population data was therefore fitted using the increments $\Delta\Phi(t_i) = \Phi(t_i) - \Phi(t_{i-1})$ and the associated increments in \mathfrak{F} , $\Delta\mathfrak{F}(K_{\text{crit}}(t_i)) = \mathfrak{F}(K_{\text{crit}}(t_i)) - \mathfrak{F}(K_{\text{crit}}(t_{i-1}))$, since the error in the increments is uncorrelated. For noisy data like ours, we will expect (and show) that the deviations between the increments and the fit are normally distributed. The values of all free parameters were initially tuned manually before a least-squares fitting routine finalized the simultaneously fit of all free parameters (MATLAB's `lsqcurvefit`).

4.6.9 Results from fitting the single-cell model

Figure 4.17(a) shows the data collapse (points) and the distribution \mathfrak{F} (dashed black line), with the color indicating the cell density going from red ($\sim 0.4 \times 10^8 \text{ m}^{-2}$) over gray ($\sim 1.2 \times 10^8 \text{ m}^{-2}$) to blue ($\sim 2.7 \times 10^8 \text{ m}^{-2}$) and the symbols indicating the experimental conditions (see legend in panel (d)). The parameters of the normal distribution fit are $\mu_{K_d} = 140$ and $\sigma_{K_d} = 40$, while the values of the population-fixed variables were found to $G = k/g_{\text{crit}} = 3.0$ and $W = 0.1$.

While the data does collapse onto the normal distribution fit, there remains notable variations about \mathfrak{F} . These variations are more visible in Fig. 4.17(b), which shows the increments used for the fit. In addition to these large fluctuations, the data unfortunately mostly samples the lower tail (values of K_d below the mean μ_{K_d}). Examining the fluctuations of the experimental data about \mathfrak{F} (Fig. 4.17(c)), these are found to be normally distributed with $\Delta\Phi - \Delta F = 0.003 \pm 0.017$ (mean \pm s.d.). Uncorrelated errors stemming from e.g. image analysis are expected to follow a normal distribution, and since furthermore the standard deviation of 0.017 is in good agreement with the estimated error of 0.025 presented previously (Sec. 4.3.5), the image analysis tools is a likely source of this measurement error. The overall agreement between the model and the data suggests that this model captures the basics of the single-cell behavior, even if the normal distribution of \mathfrak{F} is not thoroughly proved⁹. This verifies that the observed single-cell variations in timing and level of the population response are both caused by distributed single-cell activation levels (K_d -levels) with lower K_d resulting in faster response.

External conditions inferred from the model confirm experimental analysis

The fitted values of c_f presented in Fig. 4.17(d) for all experiments at $Q = 500 \text{ nL min}^{-1}$ corroborate the interpretations of the experimental data. Firstly, c_f -levels are observed

⁹The quality of the data rendered indecisive all performed statistical tests, such as the F-test, to infer how well the data is fitted by the model.

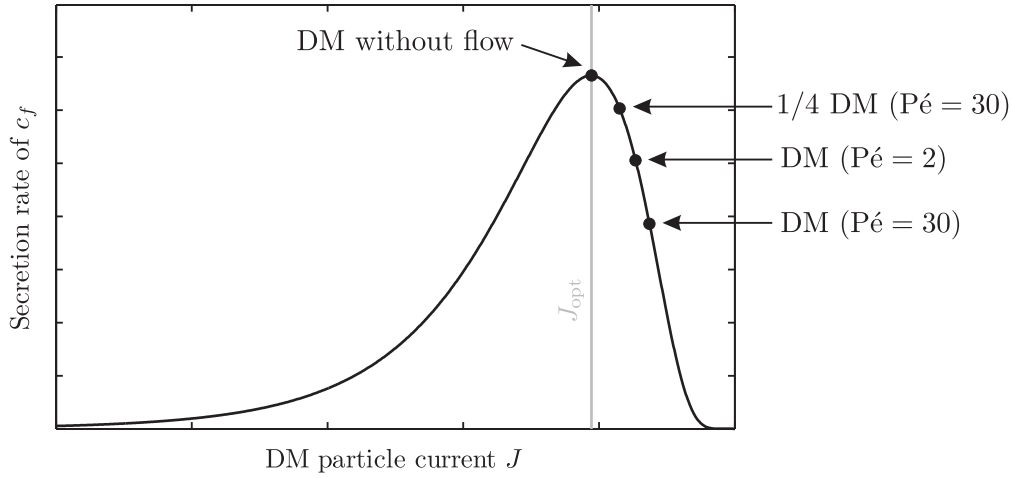


Figure 4.18: Schematic of hypothesized secretion rate dependence on the particle current J of differentiation medium reagents. The rate is characterized by a maximum secretion at the current J_{opt} . The marks indicate the secretion rates under the different experimental conditions.

to increase with the cell density in most cases. Secondly, the values of c_f are found to increase in a manner consistent with the interpretations of the experimental data: c_f is lowest when only DM is supplied (red), increases a little when DM+CM is supplied (blue), increases further for the cases of 1/4 DM (black), shows another increase at 1/4 (DM + CM) (green) and is largest at 1/4 DM + CM (cyan). The layering of the c_f values in the figure are somewhat fortuitous since the variations between repeat experiments show noticeable variation for both 1/4 AM (black) and especially for 1/4 DM + CM (cyan), however the general trend agrees with the interpretations of the experimental data discussed in Sec. 4.6.1. Hence, using the model, which incorporates knowledge about the single-cell differentiation machinery along with the experimental observations, the non-trivial secretion dynamics suggested by the experiments and the continuum models are confirmed.

The results for DM at $Q = 33 \text{ nL min}^{-1}$ in Fig. 4.17(e) show a somewhat different dynamics where c_f jumps to large values of $c_f \approx 25$ at the higher cell densities. Taken at face value, this indicates a further feature of the secretion rate, namely a very strong negative dependence of the secretion on received DM particle current. However, the values of $c_f \approx 25$ are an order of magnitude greater than at $Q = 500 \text{ nL min}^{-1}$, and since unfortunately the experiments were not repeated, and time has not permitted further investigation of this issue, it remains unclear whether these results should be trusted. Nonetheless, they do provide an intriguing prediction for future work.

4.6.10 A single hypothesis reconciles all results

Both the experimental results of lowering the DM concentration (Sec. 4.6.1) and the theoretical investigation of the concentration levels sensed by the cells (Sec. 4.6.7) indicate higher levels of the differentiation-inducing secreted signal at lower DM concentrations, yet

an increased current of DM was found in the continuum-model investigation of particle-current-based chemosensing. These observations can all be reconciled by hypothesizing that the secretion rate is a non-monotone function of the DM current with a maximum at some current J_{opt} , as suggested in the schematic in Fig. 4.18.

The added glucocorticoid reagent dexamethasone (added at 1 μM in our experiments) is a possible candidate for the DM component limiting secretion, since previous reports from static culture have indicated maximum differentiation when glucocorticoids are supplied in the range $10^{-7} - 10^{-6}$ M [88]. Unfortunately dexamethasone was not probed in that study, but an additional static culture study focusing specifically on dexamethasone did find increased long term differentiation when the reagent was used at concentrations below 1 μM [65]. Hence, the concentration 1 μM results in a particle current that is close to the optimum *for static conditions* but will in perfusion bring the current away from the optimum, see Fig. 4.18.

Looking for the mathematical form of this secretion rate is irrelevant in light of the accuracy of the current data and has not been pursued further, but it does offer an interesting opening for future research.

4.7 Conclusions

In this chapter, we have studied the differentiation of preadipocytic stem cells into fully differentiated adipocytes using microfluidic perfusion experiments and theoretical analysis. Surprisingly, and contrary to the current beliefs, our results strongly indicate that the decision to differentiate is made by the single cell in response to a chemical signal secreted by both differentiated and undifferentiated cells, which, in addition, secrete at indistinguishable rates. While the identity of this secreted chemical remains unknown, gene expression measurements revealed that it acts at the first level of the differentiation-signaling cascade and thus is required for initiating the differentiation. Furthermore, it therefore cannot be one of the already known secreted signals, since these act at the second level of the differentiation cascade. The requirement of a cell-secreted signal in turn implies that adipocyte stem cell differentiation is a systemic response.

The differentiation-inducing signal is secreted in response to the differentiation medium, but the experimental results indicated an increased response at lower doses of differentiation medium. These indications were confirmed from a simple single-cell physics model based on very basic assumptions. However, while a theoretical analysis of the physics of chemosensing revealed that in perfusion experiments secretion depends on the particle current to a cell — and not the external concentration — the same analysis found an *increased* secretion at higher flow rates, which is contrary to the experimental findings. To reconcile these observations, it was hypothesized that the secretion rate is a non-monotone function of the particle current of differentiation medium, so increasing the flow rate or the concentration of differentiation medium would therefore lower the secretion rate. A dependence of differentiation on the glucocorticoid reagents of the differentiation medium has previously been reported.

4.8 Outlook

The explanations and interpretations presented in this chapter all focus on single-cell dynamics, yet the resolution of the experimental data is very noisy at this level. Moreover, the nature of the secreted chemical remains unknown. Obtaining quantitative single-cell data with low errors to shed light on these issues should be the primary focus of subsequent research. Such data could be used to test the predictions of the theoretical models and further probe the experimental interpretations presented here. Furthermore, testing the predictions of the models provides interesting starting points for deeper understanding of the details and underlying mechanisms of the differentiation.

Optical tags

Single-cell optical tags would greatly ease the image analysis and thereby reduce the error. One tag for the cytosol and a second for the nucleus would be optimal for both cell tracking and assignment of the vacuoles to the correct cells. However, since the cells used here are primary human stem cells, it is not feasible to incorporate a fluorescent tag into their genomes. This is typically done by transfecting a single cell followed by cloning, so the fluorescent cells will no longer be primary stem cells when enough of them have been cloned to do the experiments.

Optical tags on key intracellular transcription factors would also allow for true single-cell study of the response. This would test the hypothesis of variable single-cell response. However, such tagging is equally difficult to achieve experimentally.

Using cell lines such as 3T3-L1, one could construct such fluorescent tags. Although these are not primary cells, studying them would provide valuable information with the sought high resolution.

Detailed investigation of the role of each DM reagent

Selectively removing the different reagents of the DM and using a large experimental matrix is likely to shed light on the role of each DM reagent in the differentiation, and might lead to further clues about the identity of the secreted differentiation-inducing signal. Furthermore, experiments with pulsed stimulation could be used to detect the frequency-dependence of the response, and therefore possibly provide insight into the core signaling network responsible for the differentiation: by comparing these results to the three-level signaling cascade, one could identify further details about the roles played by each cascade level.

Investigation of the identity of the secreted signal

Spatio-temporal investigations of single-cell secretion dynamics are also needed. However, this is another problem for which there exist no strong experimental techniques. Secretomic analyses could be applied to probe the identity of the secreted chemical, however, such attempts would likely be futile without additional clues.

Chapter 5

Conclusions and outlook

General conclusions

The present thesis has been devoted to (i) the theoretical study of a collection of advection-diffusion-reaction phenomena, focusing on how these basic mechanisms combine to form complex macroscopic effects and furthermore (ii) on how this affects biological function.

While complex and non-trivial macroscopic phenomena were found in all three projects, the key to understanding each project was a simple physical picture of competing processes. Hence, the concentration dispersion studied in Chapter 2 could be qualitatively predicted once the basic processes of concentration field diffusion, momentum diffusion and local velocity variations were observed. Similarly, pseudopod formation biases by secreted chemokine and the current direction of motion were found to explain the great variability in single-cell migration, while secretion with non-trivial rate could explain all experimental findings of adipose-derived stem cell differentiation into adipocytes. This emphasizes the criticality of seeking the simplest, physically plausible explanation. Furthermore, its success in the biological projects illustrates how powerful it really is when working with such very open problems.

Finally, the work in this thesis illustrates how the concepts of physics can be used to make fundamental contributions to biology, and furthermore illustrates the importance of high-resolution and well-controlled data as the first step in understanding such complex problems. The basic limits and internal consistency imposed by physics provides a strong starting point for analyzing biological phenomena, which together with biological insight can peek further into how life works.

Outlook

Living matter has “a mind of its own”: it regenerates, it reproduces, it senses and adapts to its surroundings. These are all in stark contrasts to the capabilities of “normal” matter and artificially produced objects, and it is the author’s belief that understanding these things is the single most important problem in physics. In the words of Erwin Schrödinger, from his famous 1944 book *What is life?*: “...*living matter, while not eluding the "laws of physics" as established up to date, is likely to involve "other laws of physics" hitherto unknown,*

which however, once they have been revealed, will form just as integral a part of science as the former” [115]. Physicists should therefore be throwing themselves onto biology!

As exemplified over and over in the literature — and by the two biological studies in this thesis — interesting self-organization and emergent collective phenomena resulting from the interaction of ignorant individuals currently beyond our understanding (such as swarming, quorum sensing, adipocyte stem cell differentiation), appear to be routinely exploited by nature to achieve multi-agent biological function. The single cell performs a simple and mostly predictable functions, yet these non-trivial multicellular responses emerge at the population level. Unraveling the details and limits of coordinated multicellular response resulting from the interaction of ignorant individuals is a fascinating subject for future study. While the discovery of such multi-agent emergent properties across many length scales and organisms could suggest that such behavior is a universal “attractor” in a dynamical system’s sense, our results on social cell migration reveal that e.g. swarming is not such an attractor, but requires a certain type of interaction. It is therefore more likely that different kinds of cell-cell interactions each contain different phases, so swarming and the sustained single-cell behavior in our study arises in different parts of the phase space¹. This points to the extension of the physical notion of phases to non-equilibrium systems in general, as has in fact previously been suggested for collective migration [141].

A second and interrelated problem of similar importance revolves around understanding the role of single-cell variability in shaping these multicellular functions. Single-cell responses are rarely identical, yet macroscopic responses are. Determining the correct way to theoretically deal with these variabilities and their consequences is likely to shed more light onto the underpinnings of biology and how life works. Thus, revealing the biological equivalent to the Boltzmann factor assigned to the individual states of a system should provide a major breakthrough in making biology a truly quantitative, predictive science. The result would be statistical laws, which nonetheless are laws of nature in the same way as the laws of “normal” statistical physics.

In addition to providing a great step forward for biology, understanding these effects may have a profound impact on medical science, automated production optimization and perhaps society as a whole.

¹Contrary to thermodynamic phases, these single-cell parameters may not depend on external variables such as temperature.

Appendix A

Mathematical and numerical details for Taylor–Aris dispersion

Many of the mathematical details in deriving the theoretical results in Chapter 2 were omitted from the main text to enhance readability. These are presented in the present appendix for completeness.

A.1 Detailed derivation of D_{eff} for transversely uniform initial solute distribution

The transverse uniformity of the solute means that $|\tilde{c}_0\rangle = |1\rangle$ and $|\tilde{c}_1\rangle = 0$ as mentioned in Eq. (2.42), and a_{0n} , β_{j0}^ℓ and a_{1n} therefore reduce to

$$a_{0n} = \delta_{n,0} \tag{A.1a}$$

$$\beta_{j0}^\ell = (1 - \delta_{\ell,0}\delta_{j,0}) \frac{\langle f_j | u_\ell \rangle}{\lambda_j + i\ell\omega_o}, \tag{A.1b}$$

$$a_{1n} = - \sum_{\ell=-\infty}^{\infty} (1 - \delta_{\ell,0}\delta_{n,0}) \frac{\langle f_n | u_\ell \rangle}{\lambda_n + i\ell\omega_o}, \tag{A.1c}$$

where the relation $\langle f_j | u_\ell | f_0 \rangle = \langle f_j | u_\ell | 1 \rangle = \langle f_j | u_\ell \rangle$ has been used. Using these simplifications and the definitions of the $p = 1$ full moment $M_1(t)$ and its time derivative dM_1/dt Eqs. (2.41a) and (2.41b) one directly finds

$$\frac{dM_1}{dt} = \text{Pé} \sum_{k=-\infty}^{\infty} \langle u_k | 1 \rangle e^{-ik\omega_o t}, \tag{A.2a}$$

$$M_1 = \text{Pé} \sum_{\ell=-\infty}^{\infty} \langle u_\ell | 1 \rangle \frac{1 - e^{-i\ell\omega_o t}}{i\ell\omega_o}, \tag{A.2b}$$

where as usual $\lim_{\ell \rightarrow 0} \frac{1 - e^{i\ell\omega_o t}}{i\ell\omega_o} = t$. Since the effective diffusivity is defined by $D_{\text{eff}} = \frac{1}{2} \frac{dM_2}{dt} - M_1 \frac{dM_1}{dt}$ it is convenient to explicitly state the product $M_1 \frac{dM_1}{dt}$,

$$M_1 \frac{dM_1}{dt} = \text{Pe}^2 \sum_{k=-\infty}^{\infty} \sum_{\ell=-\infty}^{\infty} \langle u_k | 1 \rangle e^{-ik\omega_o t} \langle u_\ell | 1 \rangle \frac{1 - e^{-i\ell\omega_o t}}{i\ell\omega_o} \quad (\text{A.3a})$$

$$= \text{Pe}^2 \left[\sum_{k=-\infty}^{\infty} \langle u_k | 1 \rangle \langle u_0 | 1 \rangle t e^{-ik\omega_o t} + \sum_{k=-\infty}^{\infty} \sum_{\ell=-\infty}^{\infty} (1 - \delta_{\ell,0}) \langle u_k | 1 \rangle \langle 1 | u_\ell \rangle \frac{e^{i\ell\omega_o t} - 1}{i\ell\omega_o} e^{-ik\omega_o t} \right], \quad (\text{A.3b})$$

where the identity $\langle u_\ell | 1 \rangle \frac{1 - e^{-i\ell\omega_o t}}{i\ell\omega_o} = \langle 1 | u_\ell \rangle \frac{e^{i\ell\omega_o t} - 1}{i\ell\omega_o}$ was exploited.

Applying the simplifications Eq. (A.1) to the definition of dM_2/dt (Eq. (2.41c)) is most transparent when working with the expanded version of the equation

$$\frac{1}{2} \frac{dM_2}{dt} = 1 + \text{Pe}^2 \left[\sum_{k=-\infty}^{\infty} \langle u_k | 1 \rangle e^{-ik\omega_o t} \gamma_{10} t + \sum_{m=0}^{\infty} \sum_{k=-\infty}^{\infty} a_{1m} \langle u_k | f_m \rangle e^{-(\lambda_m + ik\omega_o)t} \right. \\ \left. + \sum_{m=0}^{\infty} \sum_{k=-\infty}^{\infty} \sum_{\ell=-\infty}^{\infty} \langle u_k | f_m \rangle e^{-ik\omega_o t} \beta_{m0}^\ell e^{i\ell\omega_o t} \right]. \quad (\text{A.4})$$

Inserting the simplifications Eqs. (A.1b) and (A.1c) and using that $\gamma_{10} = \langle 1 | u_0 | 1 \rangle = \langle 1 | u_0 \rangle = \langle u_0 | 1 \rangle$ since $u_0(\mathbf{r}_\perp)$ is real yields

$$\frac{1}{2} \frac{dM_2}{dt} = 1 + \text{Pe}^2 \left[\sum_{\ell=-\infty}^{\infty} \langle u_\ell | 1 \rangle \langle u_0 | 1 \rangle t e^{-i\ell\omega_o t} + \sum_{m=0}^{\infty} \sum_{\ell=-\infty}^{\infty} \sum_{k=-\infty}^{\infty} \frac{\langle u_k | f_m \rangle \langle f_m | u_\ell \rangle}{\lambda_m + i\ell\omega_o} \right. \\ \left. \times (1 - \delta_{m,0} \delta_{\ell,0}) \left\{ e^{i\ell\omega_o t} - e^{-\lambda_m t} \right\} e^{-ik\omega_o t} \right]. \quad (\text{A.5})$$

When computing the effective diffusivity $D_{\text{eff}} = \frac{1}{2} \frac{dM_2}{dt} - M_1 \frac{dM_1}{dt}$ the first single sum in the above equation is identically canceled by a similar sum from $M_1 \frac{dM_1}{dt}$, see Eq. (A.3). This leaves the following expression

$$D_{\text{eff}} = 1 + \text{Pe}^2 \left[\sum_{m=0}^{\infty} \sum_{k=-\infty}^{\infty} \sum_{\ell=-\infty}^{\infty} (1 - \delta_{\ell,0} \delta_{m,0}) \frac{\langle u_k | f_m \rangle \langle f_m | u_\ell \rangle}{\lambda_m + i\ell\omega_o} \left\{ e^{i(\ell-k)\omega_o t} - e^{-(\lambda_m + ik\omega_o)t} \right\} \right. \\ \left. - \sum_{k=-\infty}^{\infty} \sum_{\ell=-\infty}^{\infty} (1 - \delta_{\ell,0}) \frac{\langle u_k | 1 \rangle \langle 1 | u_\ell \rangle}{i\ell\omega_o} \left\{ e^{i(\ell-k)\omega_o t} - e^{-ik\omega_o t} \right\} \right]. \quad (\text{A.6})$$

Now, the second double sum is recognized as being identical to the triple sum for $m = 0$ with an opposite sign. This double sum therefore removes all contributions from the triple sum for $m = 0, \ell \neq 0$, with the net effect that only terms of $m \geq 1$ survive. Invoking

this and a final index change of m to n , we arrive at the formula for $D_{\text{eff}}(t)$ presented in Eq. (2.45):

$$D_{\text{eff}}(t) = 1 + \text{Pe}^2 \sum_{n=1}^{\infty} \sum_{\ell=-\infty}^{\infty} \sum_{k=-\infty}^{\infty} \frac{\langle u_k | f_n \rangle \langle f_n | u_\ell \rangle}{\lambda_n + i\ell\omega_o} \left[e^{i(\ell-k)\omega_o t} - e^{-(\lambda_n + i k \omega_o)t} \right]. \quad (\text{A.7})$$

A.2 Simplifying $\frac{1}{2} \frac{dM_2}{dt}$ for an initial point concentration

The expression for $\frac{1}{2} \frac{dM_2}{dt}$ given by Eq. (2.57a) is immediately simplified by invoking the delta function and changing index q to m . This gives

$$\begin{aligned} \frac{1}{2} \frac{dM_2}{dt} = 1 + \text{Pe}^2 \Bigg\{ & \sum_{n=0}^{\infty} \sum_{k=-\infty}^{\infty} \langle u_k | f_n \rangle e^{-(\lambda_n + i k \omega_o)t} f_n(\mathbf{r}_\perp^o) \langle f_n | u_0 | f_n \rangle t \\ & - \sum_{n=0}^{\infty} \sum_{m=0}^{\infty} \sum_{k=-\infty}^{\infty} \sum_{\ell=-\infty}^{\infty} f_m(\mathbf{r}_\perp^o) \langle u_k | f_n \rangle \beta_{nm}^\ell e^{-(\lambda_n + i k \omega_o)t} \\ & + \sum_{n=0}^{\infty} \sum_{m=0}^{\infty} \sum_{k=-\infty}^{\infty} \sum_{\ell=-\infty}^{\infty} f_n(\mathbf{r}_\perp^o) \langle u_k | f_m \rangle \beta_{mn}^\ell e^{-(\lambda_n + i k \omega_o)t} e^{i\ell\omega_o t} \Bigg\}. \quad (\text{A.8}) \end{aligned}$$

By swapping indices m and n in the second line, using the definition of β_{mn}^ℓ in Eq. (2.38), combining the two quadruple sums to one, and pulling out a factor of $e^{-(\lambda_m + i k \omega_o)t}$ in this single remaining quadruple sum, one finds

$$\begin{aligned} \frac{1}{2} \frac{dM_2}{dt} = 1 + \text{Pe}^2 \Bigg\{ & \sum_{n=0}^{\infty} \sum_{k=-\infty}^{\infty} \langle u_k | f_n \rangle e^{-(\lambda_n + i k \omega_o)t} f_n(\mathbf{r}_\perp^o) \langle f_n | u_0 | f_n \rangle t \\ & + \sum_{n=0}^{\infty} \sum_{m=0}^{\infty} \sum_{k=-\infty}^{\infty} \sum_{\ell=-\infty}^{\infty} f_n(\mathbf{r}_\perp^o) \langle u_k | f_m \rangle (1 - \delta_{\ell,0} \delta_{n,m}) \frac{\langle f_m | u_\ell | f_n \rangle}{\lambda_m - \lambda_n + i\ell\omega_o} \\ & \times \left[e^{(\lambda_m - \lambda_n + i\ell\omega_o)t} - 1 \right] e^{-(\lambda_m + i k \omega_o)t} \Bigg\}. \quad (\text{A.9}) \end{aligned}$$

We note now that the double sum handles exactly the cases for which the quadruple sum gives zero. Thus, taking $\frac{e^{(\lambda_m - \lambda_n + i\ell\omega_o)t} - 1}{\lambda_m - \lambda_n + i\ell\omega_o}$ to be equal to t for $(m, n, \ell) = (0, 0, 0)$ (which indeed is the limit and coincidentally is the useful interpretation of the special case of zero-valued indices) the double sum will emerge from the quadruple sum whenever $\ell = 0$, $m = n$. We can thus drop the factor $(1 - \delta_{\ell,0} \delta_{n,m})$ along with the double sum, whereby we arrive at the result presented in Eq. (2.57b):

$$\begin{aligned} \frac{1}{2} \frac{dM_2}{dt} = 1 + \text{Pe}^2 \sum_{n=0}^{\infty} \sum_{m=0}^{\infty} \sum_{\ell=-\infty}^{\infty} \sum_{k=-\infty}^{\infty} f_n(\mathbf{r}_\perp^o) \frac{\langle u_k | f_m \rangle \langle f_m | u_\ell | f_m \rangle}{\lambda_m - \lambda_n + i\ell\omega_o} \\ \times \left[e^{(\lambda_m - \lambda_n + i\ell\omega_o)t} - 1 \right] e^{-(\lambda_m + i k \omega_o)t}. \quad (\text{A.10a}) \end{aligned}$$

A.3 The long-time limit of $D_{\text{eff}}^{\text{point}}$ for steady flows

The equation for the effective diffusivity in steady flow Eq. (2.59) does not have a contribution for $(m, n) = (0, 0)$ since the terms inside the square bracket cancel each other out. Removing this term and writing the remaining double sum $\sum_{n=0}^{\infty} \sum_{\substack{m=0 \\ (m,n) \neq (0,0)}}^{\infty}$ as $\sum_{n=1}^{\infty} + \sum_{m=1}^{\infty} + \sum_{n=m=1}^{\infty} + \sum_{n=1}^{\infty} \sum_{\substack{m=1 \\ m \neq n}}^{\infty}$ one finds

$$D_{\text{eff}}^{\text{point}} = 1 + \text{Pé}^2 \left\{ \sum_{n=1}^{\infty} f_n(\mathbf{r}_{\perp}^o) \langle u_0 | 1 \rangle \left[\langle u_0 | f_n \rangle \frac{1 - e^{-\lambda_n t}}{\lambda_n} + \langle u_0 | f_n \rangle \frac{e^{-\lambda_n t} - 1}{\lambda_n} \right] \right. \\ + \sum_{m=1}^{\infty} \langle u_0 | f_m \rangle \left[\langle f_m | u_0 \rangle \frac{1 - e^{-\lambda_m t}}{\lambda_m} - f_m(\mathbf{r}_{\perp}^o) \langle u_0 | 1 \rangle t e^{-\lambda_m t} \right] \\ + \sum_{n=1}^{\infty} f_n(\mathbf{r}_{\perp}^o) \langle u_0 | f_n \rangle \left[\langle f_n | u_0 | f_n \rangle t e^{-\lambda_n t} + f_m(\mathbf{r}_{\perp}^o) \langle u_0 | f_n \rangle \frac{e^{-2\lambda_n t} - e^{-\lambda_n t}}{\lambda_n} \right] \\ + \sum_{n=1}^{\infty} \sum_{\substack{m=1 \\ m \neq n}}^{\infty} f_n(\mathbf{r}_{\perp}^o) \langle u_0 | f_m \rangle \left[\langle f_m | u_0 | f_n \rangle \frac{e^{-\lambda_n t} - e^{-\lambda_m t}}{\lambda_m - \lambda_n} \right. \\ \left. \left. + f_m(\mathbf{r}_{\perp}^o) \langle u_0 | f_n \rangle \frac{e^{-2\lambda_n t} - e^{-\lambda_n t}}{\lambda_n} \right] \right\}. \quad (\text{A.11})$$

The terms inside the square bracket of the first single-sum cancel identically, so this sum does not contribute to the final result. Combining the two single sums to one and rearranging we arrive at

$$D_{\text{eff}}^{\text{point}} = 1 + \text{Pé}^2 \left\{ \sum_{n=1}^{\infty} \langle u_0 | f_n \rangle \left[f_n(\mathbf{r}_{\perp}^o) (\langle f_n | u_0 | f_n \rangle - \langle u_0 | 1 \rangle) t e^{-\lambda_n t} \right. \right. \\ \left. \left. + \langle f_n | u_0 \rangle \frac{1 - e^{-\lambda_n t}}{\lambda_n} + f_n(\mathbf{r}_{\perp}^o) \langle u_0 | f_n \rangle \frac{e^{-2\lambda_n t} - e^{-\lambda_n t}}{\lambda_n} \right] \right. \\ + \sum_{n=1}^{\infty} \sum_{\substack{m=1 \\ m \neq n}}^{\infty} f_n(\mathbf{r}_{\perp}^o) \langle u_0 | f_m \rangle \left[\langle f_m | u_0 | f_n \rangle \frac{e^{-\lambda_n t} - e^{-\lambda_m t}}{\lambda_m - \lambda_n} \right. \\ \left. \left. + f_m(\mathbf{r}_{\perp}^o) \langle u_0 | f_n \rangle \frac{e^{-(\lambda_m + \lambda_n)t} - e^{-\lambda_m t}}{\lambda_n} \right] \right\}. \quad (\text{A.12})$$

Note that the terms depending on $t e^{-\lambda_n t}$ arise from both the first and second single sum in Eq. (A.11). Taking the long-time limit $t \gg 1/\lambda_1$ of this equation, and noting that $\langle u_0 | f_n \rangle = \langle f_n | u_0 \rangle$ since we consider only steady flow so both u_0 and f_n are real, we arrive at

$$D_{\text{eff}}^{\text{point}} = 1 + \text{Pé}^2 \sum_{n=1}^{\infty} \frac{|\langle u_0 | f_n \rangle|^2}{\lambda_n}, \quad (\text{A.13})$$

which is the well-known result for transverse uniform initial distributions (the Taylor–Aris limit) see Eq. (2.50). This convergence in the long-time limit of the effective diffusivity for a point concentration confirms that the solute eventually will fill the entire channel, as we would expect on physical grounds.

A.4 Short-time dispersion of an initially transverse uniform distribution

We show here that $D_{\text{eff}}(t)$ is positive for short times $t \ll 1/\lambda_1, 1/(2\ell_{\text{max}}\omega_o)$. In this limit we have

$$e^{i(\ell-k)\omega_o t} - e^{-(\lambda_n + i k \omega_o)t} = (\lambda_n + i \ell \omega_o)t + \mathcal{O}(t^2), \quad (\text{A.14})$$

thus reducing Eq. (2.45) for $D_{\text{eff}}(t)$ to

$$\begin{aligned} D_{\text{eff}}(t) &\approx 1 + \text{Pé}^2 \sum_{n=1}^{\infty} \sum_{\ell=-\ell_{\text{max}}}^{\ell_{\text{max}}} \sum_{k=-\ell_{\text{max}}}^{\ell_{\text{max}}} \langle u_k | f_n \rangle \langle f_n | u_\ell \rangle t \\ &= 1 + t \text{Pé}^2 \sum_{n=1}^{\infty} \left\langle \sum_{k=-\ell_{\text{max}}}^{\ell_{\text{max}}} u_k | f_n \right\rangle \langle f_n | \sum_{\ell=-\ell_{\text{max}}}^{\ell_{\text{max}}} u_\ell \rangle \\ &= 1 + t \text{Pé}^2 \sum_{n=1}^{\infty} \left| \langle f_n | u(0) \rangle \right|^2, \quad t \ll \frac{1}{\lambda_1}, \frac{1}{2\ell_{\text{max}}\omega_o}. \end{aligned} \quad (\text{A.15})$$

Here $u(0)$ is the total velocity field $u(t)$ evaluated at time $t = 0$. This expression becomes problematic to apply in the case where infinitely many harmonics of the velocity field is present at $t = 0$ as for the startup of the Poiseuille flow, but for flows with a maximum frequency we have shown $D_{\text{eff}}(t) > 0$.

A.5 Numerics

A.5.1 Evaluation of the theoretical formulae

Our theoretical expressions (e.g. Eq. (2.45)) for $D_{\text{eff}}(t)$ involves infinite sums, which fortunately converge quickly. We therefore truncated the sums after the first fifty terms unless stated otherwise in the text.

Many of the expressions for $D_{\text{eff}}(t)$ involve more than one nested summation, whose numerical evaluation can be time consuming. To remedy this, we therefore reduced the number of terms needed to be calculated by separating the ℓ - and k -sums and collecting complex conjugated pairs of index $\{\ell, -\ell\}$ and $\{k, -k\}$. For $D_{\text{eff}}(t)$ for an initially

transversely uniform distribution Eq. (2.45) this leads to

$$D_{\text{eff}}(t) = 1 + \text{Pé}^2 \sum_{n=1}^{\infty} \left\{ \frac{\langle f_n | u_0 \rangle}{\lambda_n} \left[1 - e^{-\lambda_n t} \right] + 2 \sum_{\ell=1}^{\infty} \text{Re} \left[\frac{\langle f_n | u_{\ell} \rangle}{\lambda_n + i\ell\omega_o} \left(e^{i\ell\omega_o t} - e^{-\lambda_n t} \right) \right] \right\} \\ \times \left\{ \langle f_n | u_0 \rangle + 2 \sum_{k=1}^{\infty} \text{Re} \left[\langle f_n | u_k \rangle e^{ik\omega_o t} \right] \right\}. \quad (\text{A.16})$$

Furthermore, The involved n -, ℓ -, and k -dependent terms are calculated and placed in lists before evaluating the truncated sums.

A.5.2 Brute-force numerics for transverse uniform initial distributions

Using the commercial finite element package COMSOL MULTIPHYSICS version 3.5a, we calculated $D_{\text{eff}}(t)$ numerically directly from the definition Eq. (2.23) by solving for the concentration field c in the governing advection-diffusion equation (2.14) using the analytical solutions for the velocity field as input. From the obtained $c(\mathbf{r}, t)$ -field we determined $M_1(t)$, $dM_1(t)/dt$ and $dM_2(t)/dt$, and from these $D_{\text{eff}}(t)$. To ensure mass conservation, the number of mesh elements was chosen so that the local Péclet number in each cell (as given by the velocity in the mesh element, the mesh element length and the global diffusivity) was approximately 0.5.

Where possible, the available symmetries were exploited for computational efficiency. To this end the solutions of the flow problems in channels of circular cross-section took advantage of the azimuthal symmetry and the solution was furthermore computed in a frame of reference traveling with the mean speed of the flow. Even with these simplifications each simulation took at least 24 h to complete on a dedicated 12 core, 48 GB RAM computer, and the solution was furthermore limited to $\text{Pé} \lesssim 25$ for time-dependent flows.

For rectangular cross sections, the problem was only solved for one quarter of the cross section in a frame of reference moving with the flow mean speed. However, due to memory limitations even these simplifications proved unfeasible for Péclet numbers exceeding ~ 2 and aspect ratios above 2, $R \gtrsim 2$. Thus, for the results presented in Fig. 2.5(a) we numerically solved the axial moment equation Eq. (2.16a) for c_o and c_1 , and from these obtained $M_1(t)$, $dM_1(t)/dt$, and $dM_2(t)/dt$, as well as $D_{\text{eff}}(t)$. Time-averages of the numerical simulation results were computed by running the simulation for a full period of the base frequency after the decay of all transients, followed by numerical integration of $D_{\text{eff}}(t)$ over the period. These simulations took between 12 h and 5 days on the dedicated computer, so using our theory provides a speed up of a factor of $\sim 10^5$.

A.5.3 Brute-force numerics for initial point distributions

Because of the severe limitations on the numerical solutions presented above, brute-force numerical solutions to the problem of an initial point concentration are only feasible for an initial placement at the centerline of the circular cross-section (see Fig. 2.7(b), p. 39). Any other placement would require very time consuming full three-dimensional solutions, which in turn necessitates the need for more computing power. Using all the simplifications listed

above, the mesh resolution in a region around the initial position was increased, leading to a limitation of $\text{Pé} \lesssim 12$ on the dedicated computed mentioned before. We used a Gaussian initial distribution with variance corresponding to an elapsed time of $t = 10^{-4}$ since release (non-dimensional units), which is much lower than $t \approx 10^{-2}$ where the distribution begins to deviate from the Gaussian, see Fig. 2.7.

A.6 Pulsatile flow in a rectangular channel

Analytical solutions for the pulsatile flow in a channel of rectangular cross section have been presented elsewhere, most recently by Morris & Forster [96]. However, their solution predicts the very unphysical result of infinite $D_{\text{eff}}^{\text{avr}}(\infty)$ in the limit of Wo going to zero. We have found another solution to the problem, that predicts finite values of D_{eff} for all frequencies and in addition has a much simpler mathematical form. Furthermore, this solution retrieves the analytical solution for steady Poiseuille flow in the limit of infinitely slow driving frequency, as must be required on physical grounds, and which is not the case for the solution of [96].

We take the pressure of the ℓ th harmonic to be $\Delta p_\ell \cos(\ell \tilde{\omega}_o t) = \varepsilon_\ell \Delta p_0 (e^{i\tilde{\omega}_o t} + e^{-i\tilde{\omega}_o t})/2$ as usual, and assume the same time-dependence of the velocity field. Normalizing the length scales by L_o and taking the velocity scale to be the mean velocity for the steady flow in a rectangular channel Eq. (2.75b), the (Navier-)Stokes equation Eq. (2.13) for $-R \leq y \leq R$, $-1 \leq z \leq 1$ becomes

$$i\ell \text{Wo}^2 u_\ell(y, z) = \varepsilon_\ell \frac{3}{2\Gamma(R)} + (\partial_y^2 + \partial_z^2) u_\ell(y, z), \quad (\text{A.17})$$

where $v_\ell(y, z, t) = u_\ell(y, z) e^{i\ell \tilde{\omega}_o t} + u_{-\ell}(y, z) e^{-i\ell \tilde{\omega}_o t}$ and $\varepsilon_\ell = \Delta p_\ell / \Delta p_0$ as usual. Following the solution procedure of the case of steady flow in a channel of rectangular cross section, the constant $\varepsilon_\ell \frac{3}{2\Gamma(R)}$ and the velocity $u_\ell(y, z)$ are Fourier expanded in z

$$\varepsilon_\ell \frac{3}{2\Gamma(R)} = \varepsilon_\ell \frac{3}{2\Gamma(R)} \frac{4}{\pi} \sum_{j, \text{odd}}^{\infty} \frac{1}{j} \sin\left(\frac{j\pi}{2}(z+1)\right), \quad (\text{A.18a})$$

$$u_\ell(y, z) = \sum_{j=0}^{\infty} f_j(y) \sin\left(\frac{j\pi}{2}(z+1)\right). \quad (\text{A.18b})$$

Inserting these expressions into Eq. (A.17) leads to

$$f_j(y) = 0, \quad \text{for } j \text{ even}, \quad (\text{A.19a})$$

$$f_j''(y) - \left(i\text{Wo}^2 \ell + \frac{j^2 \pi^2}{4}\right) f_j(y) = -\frac{\varepsilon_\ell}{\Gamma(R)} \frac{6}{\pi j}, \quad \text{for } j \text{ odd}. \quad (\text{A.19b})$$

The solution to the inhomogeneous differential equation for j odd is the sum of a particular solution and the solution to the corresponding homogeneous problem. A particular solution is

$$f_j^{\text{part}} = \frac{24 \varepsilon_\ell}{\Gamma(R)} \frac{1}{j \pi} \frac{1}{q_{j\ell}(\text{Wo})}, \quad (\text{A.20})$$

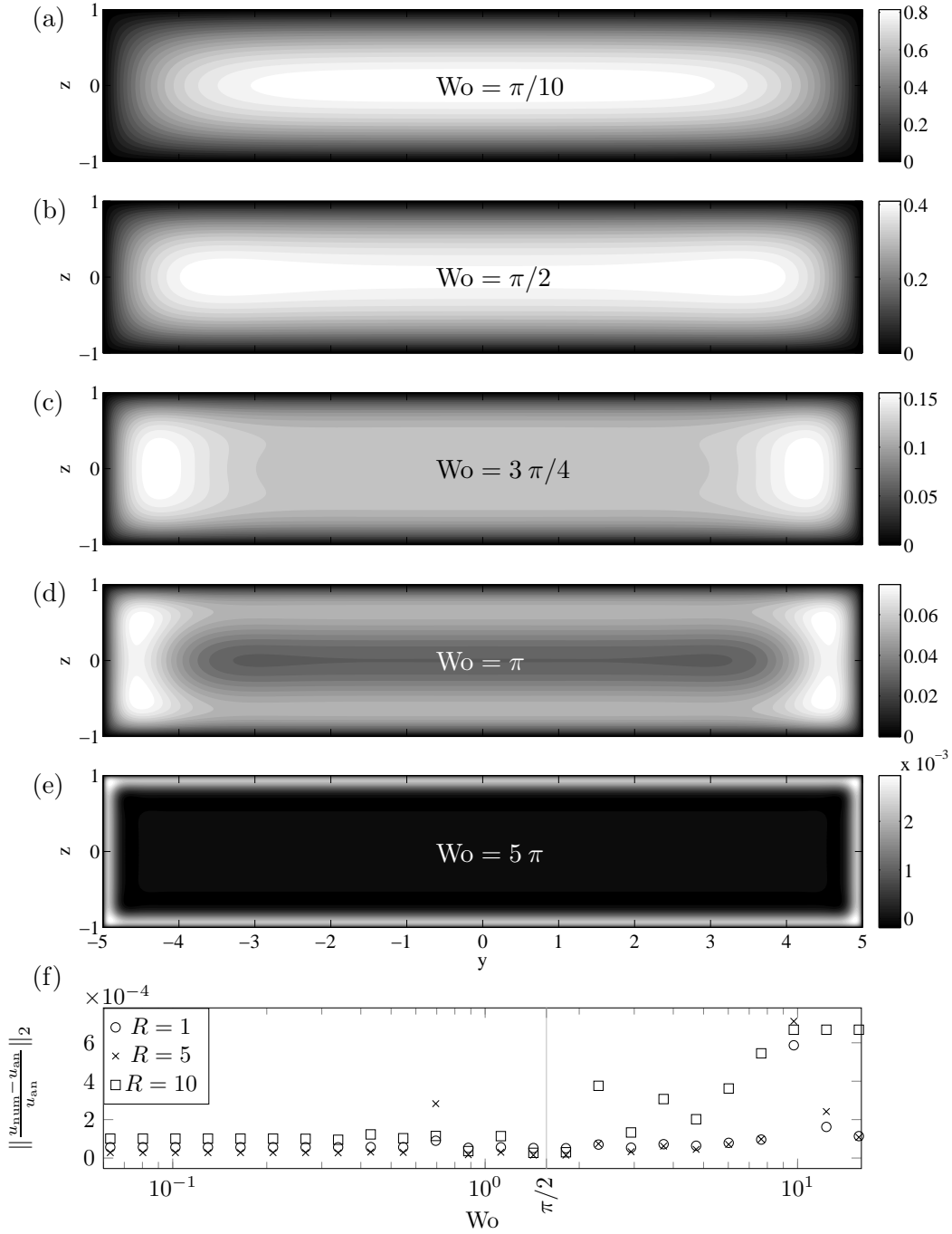


Figure A.1: The pulsatile velocity field in a rectangular channel of $R = 5$, as given by Eq. (A.22). (a)-(e) displays the velocity field at different values of Wo , each taken at the same point in the oscillation cycle. The structure of the velocity field changes rapidly from the regular Poiseuille paraboloid found for $Wo \ll \pi/2$ (panel (a)) to the Womersley regime for $Wo \gg \pi/2$ of panel (e), with narrow wall boundary layers dominating the flow in the latter regime. The first deviations from the paraboloid are visible when the oscillation time balance the momentum diffusion time, i.e. for $Wo = \pi/2$ (panel (b)). Panel (c) illustrates the case where the boundary layers have started to form in the longer y direction but have yet to form in the short z direction, while panel (d) illustrates a cases where the boundary layers have just formed in both transverse directions. (f) The L_2 norm of the relative error between the analytical solution and a numerical simulation of the pulsatile velocity field are on the orders 10^{-4} – 10^{-3} indicating very good agreement. The solutions are computed for $R = 1, 5, 10$ for a range of Wo comprising the transition from the Poiseuille regime ($Wo \ll \pi/2$) to the Womersley regime ($Wo \gg \pi/2$).

where

$$q_{j\ell}(\text{Wo}) = \sqrt{4i\text{Wo}^2\ell + j^2\pi^2}. \quad (\text{A.21})$$

The homogeneous solution is easily found and using the boundary condition $u_\ell(\pm R, z) = 0$ we find the final solution for $u_\ell(y, z)$

$$u_\ell(y, z) = \frac{24\varepsilon_\ell}{\Gamma(R)} \sum_{j,\text{odd}} \frac{1}{j\pi} \frac{1}{q_{j\ell}(\text{Wo})} \left[1 - \frac{\cosh(q_{j\ell}(\text{Wo})\frac{y}{2})}{\cosh(q_{j\ell}(\text{Wo})\frac{R}{2})} \right] \sin\left(\frac{j\pi}{2}(z+1)\right). \quad (\text{A.22})$$

The physical flow is then as usual given by $v_\ell(y, z, t) = u_\ell(y, z) e^{i\ell\tilde{\omega}_0 t} + u_{-\ell}(y, z) e^{-i\ell\tilde{\omega}_0 t}$.

The solution presented in Fig. A.1 exhibits the normal boundary layers found in Womersley's solution for the circular cross-section, see Fig. 2.2 and [146]. These boundary layers arise when the fluid momentum relaxation time scale becomes on the same order as the time scale of the oscillations of the driving pressure, i.e. for $\text{Wo} \gtrsim \pi/2$.

The width of the boundary layers is given by the shortest of the two transverse directions, and is thus independent of the channel aspect ratio R . This is similar to the analytical solution to the steady state Poiseuille flow in a rectangular cross section. However, the solute boundary layer thicknesses in the transverse direction depend on the total channel width in the same direction, and so the boundary layer thickness in the longer of the two transverse directions depends on the aspect ratio.

We note that the found solution in the limit of infinitely slow frequency $\text{Wo} \rightarrow 0$ reduces to the well-known Poiseuille solution for the rectangular channel [25], as is expected on physical grounds.

The analytical solution is compared to a direct numerical simulation in Fig. A.1(f). This solution is found by solving the Navier–Stokes equation with a harmonically oscillating driving pressure in a three dimensional domain of aspect ratio $R = 1, 5, 10$. The problem was solved numerically in COMSOL MULTIPHYSICS version 3.5a by implementing the Navier–Stokes equation in weak formulation with a prescribed time-dependent pressure gradient, using the zero-velocity as initial condition. The simulation was run a fixed time interval which comprised many oscillation cycles thereby exceeding the periods of the initial build-up of the flow. The L_2 norm of the relative error between the analytical and numerical solutions evaluated at each mesh point at the final simulation time point has been used to quantify the difference between the two. We find very low values of this difference for three different aspect ratios, and for the presented range of Wo spanning from the Poiseuille regime ($\text{Wo} \ll \pi/2$) to the Womersley regime ($\text{Wo} \gg \pi/2$). This further confirms the validity of our analytical solution.

Appendix B

Additional material for cell migration study

B.1 Summary of all experiments

The microfluidic cell culture platform allows for independent and isolated experiments to be run in parallel. All cell densities were tested in parallel chambers using different chips, with up to 24 chambers run in parallel in one experimental run. The experiments of each run are summarized in Table B.1, with cell density expressed by the average minimum cell-cell distance of all cells \bar{d}_{\min} in each experiment.

Table B.1: Microfluidic experiments

Chip	Max. \bar{d}_{\min}	Min. \bar{d}_{\min}	Avg. \bar{d}_{\min}	# of exp.
1	142.8 μm	82.0 μm	103.0 μm	16
2	89.7 μm	72.0 μm	80.5 μm	24
3	95.7 μm	76.0 μm	84.8 μm	15
4	143.9 μm	61.8 μm	87.3 μm	22
5	69.7 μm	57.8 μm	63.7 μm	2

B.2 Migration statistics of cells stimulated with tumor necrosis factor α (TNF α)

Upon completing the trajectory analyses of the non-stimulated cells, we compared these results to cells of the same cell line exposed to the inflammatory signaling molecule tumor necrosis factor (TNF)- α . We observed no difference in motility characteristics between non-stimulated cells and cells exposed to TNF α in the range 0.005 ng mL^{-1} to 100 ng mL^{-1} , see Fig. B.1 which plots both the speed distribution and fits of the average directional autocorrelation to the function $\phi e^{-\tau_{\text{ag}}/\tau_p}$ that was also used in the main text (no TNF indicated by blue, high TNF levels by orange). We also compared the results of manual tracking of the pseudopodia of 10 non-stimulated cells to the results obtained from the automated analysis applied to the TNF-exposed data and found no variation. Given the agreement of the motility characteristics and the large range of TNF α investigated, we concluded that TNF α does not influence the motility, and therefore included the cells exposed to TNF α in the analyses.

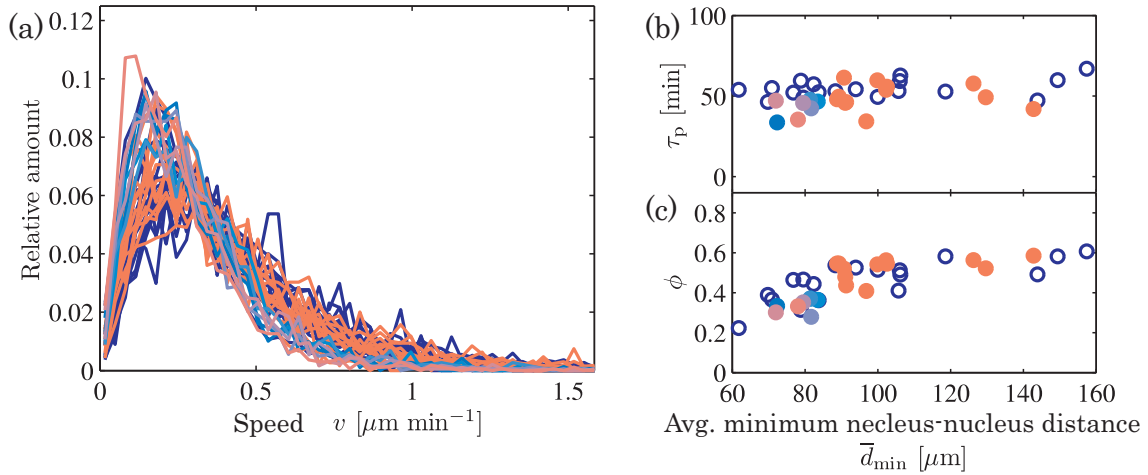


Figure B.1: Comparison between non-stimulated cells and cells exposed to the inflammatory signaling chemical TNF α shows no effect of the chemical. Each line in (a) and each circle in (b)-(c) is the average from one chamber. Non-stimulated cells are given by blue (open circles in (b)-(c)), results from stimulated cells are assigned a color ranging from light blue (lowest dose, 0.005 ng mL^{-1}) to orange (highest dose, 100 ng mL^{-1}) in ten steps ($0.005, 0.01, 0.025, 0.05, 0.1, 0.25, 0.5, 1, 10$ and 100 ng mL^{-1}). (a) Chamber speed distribution. (b)-(c) Persistence time τ_p and weight factor ϕ (see Fig. 3.7).

B.3 Additional data for dependence on cell density

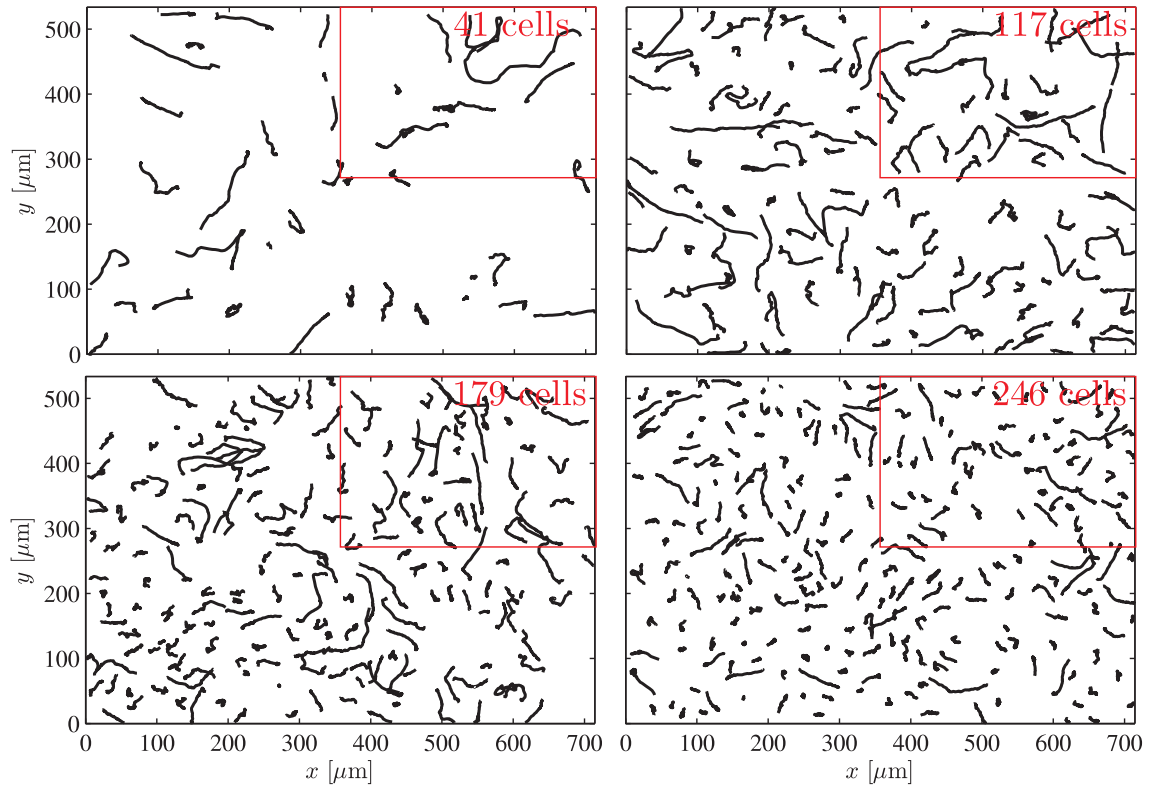


Figure B.2: Whole-chamber cell trajectories at four different densities. Exerts are given in Fig. 2(e) in the main text, with the exerts corresponding to the regions marked by red boxes. The average cell diameter is $41.7 \mu\text{m}$ (supplementary Fig. 3.10(a)), and the average minimum cell-cell distance varies from $149 \mu\text{m}$ at the lowest density to $45 \mu\text{m}$ at the highest.

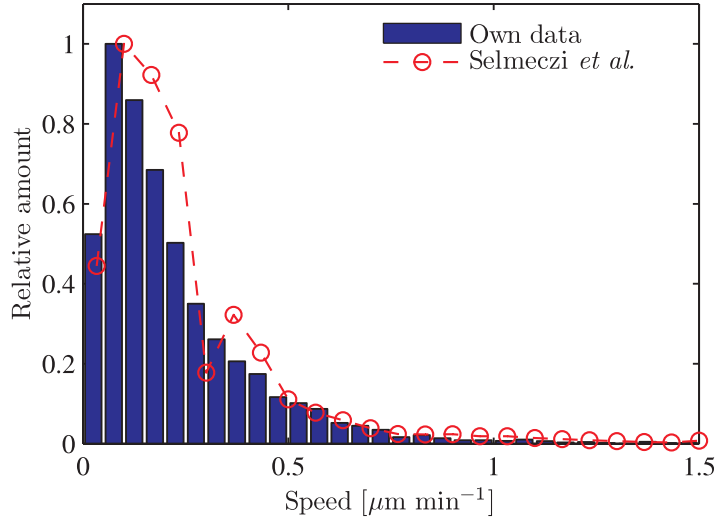


Figure B.3: Comparison of own speed distribution (blue bars) and the speed distribution of isolated human fibroblasts extracted from Selmeczi *et al.* [117]. The two distributions are in agreement.

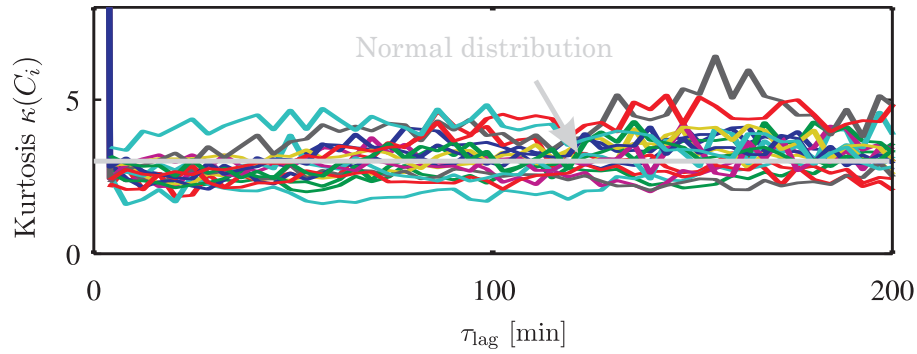


Figure B.4: Kurtosis $\kappa(C_i)$ of the distribution of single-cell directional autocorrelation functions C_i computed at each lag time τ_{lag} . The figure shows the result for 14 separate chambers across densities (colors are reused) and no dependence on cell density was detected. The gray line indicates $\kappa = 3$, the kurtosis of the normal distribution, around which all experimental results fall. Hence, the chamber-mean directional autocorrelation function $\langle C(\tau_{\text{lag}}) \rangle$ is representative of the single cell across densities.

B.4 No pseudopod formation-bias by positions existing pseudopodia

We did not find any dominating dependence of the position of pseudopod formation on the presence of existing pseudopodia, which has otherwise been reported for isolated cells migration in shallow chemokine gradients [7].

To arrive at this result, we computed the angle $\Delta\beta$ between the position of formation and the nearest neighboring pseudopod. For completely random pseudopod formation, we expect a pseudopod to be present on average every $360^\circ/N_p$ where N_p is the current number of pseudopodia of the cell. On the other hand, a strong induction of existing pseudopodia on forming pseudopodia would lead to an angular difference $\Delta\beta$ independent of the number of existing pseudopodia. Grouping the results based on N_p , see Fig. B.5, we find the most occurring positions of pseudopod formation coinciding with the angular difference $\Delta\beta = \pm 360^\circ/(2N_p)$ (indicated by the dashed lines in the figure), indicating that no dominating relationship exists between the positions of established pseudopodia and the positions of formation for new pseudopodia. This emphasizes the differences between being isolated and being in a social context. Since we do find significant positive correlation between pseudopod formation and both current direction of motion and secreted chemokines, we expect the variations are due to these effects and the limits set by finite statistics.

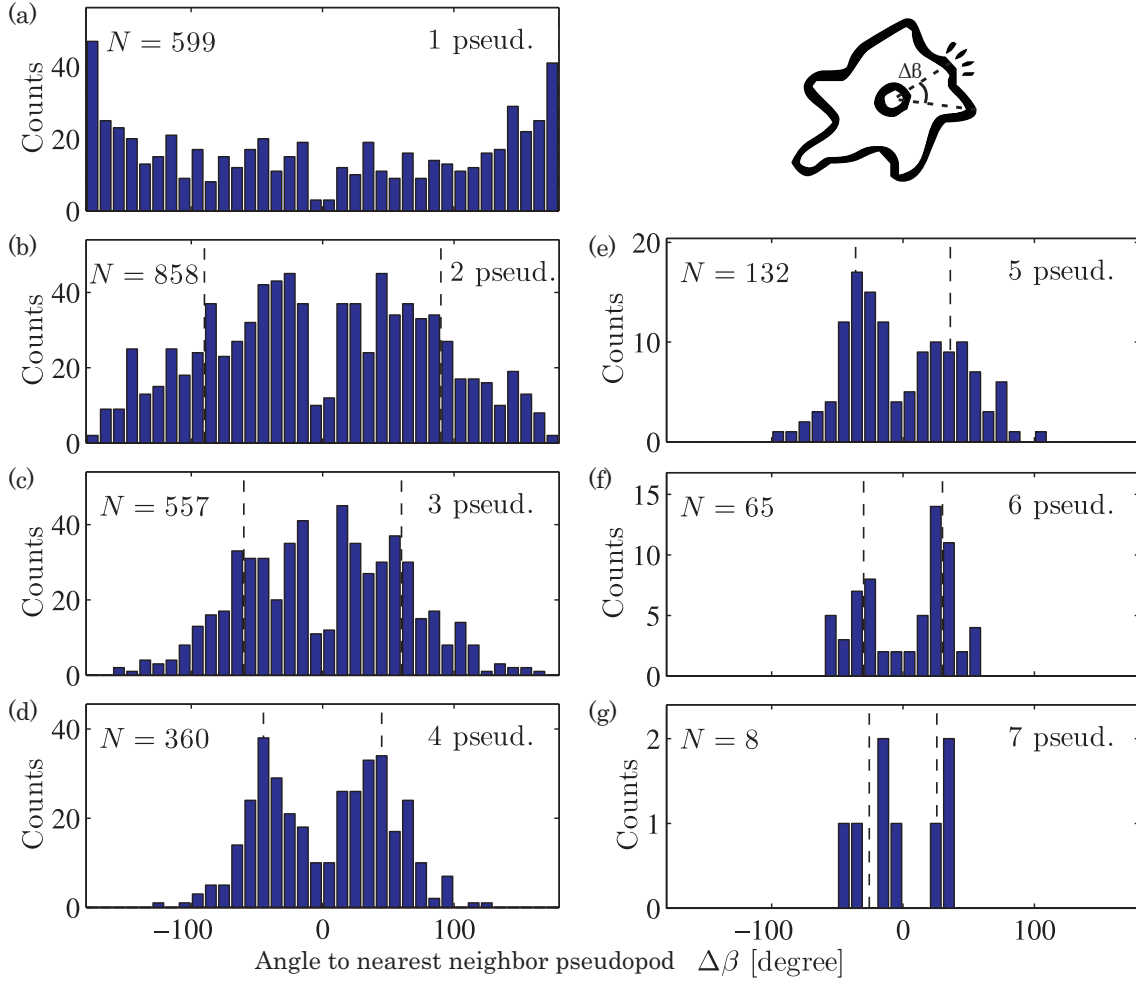


Figure B.5: The angle $\Delta\beta$ between a newly formed pseudopod and the closest neighbor pseudopod, grouped based on the number of pseudopodia of the current cell. The distribution means and peaks correlate with the angular distance $\Delta\beta = \pm 360^\circ / (2N_p)$ expected for pseudopodia randomly distributed along the perimeter and marked by the dashed lines in the figures. In each panel, N gives the number of detected pseudopodia making up the distribution. (a) Cells with $N_p = 1$ existing pseudopod ($360^\circ / 2 = 180^\circ$ and coincide with the figure bounding box), (b) cells with $N_p = 2$, (c) cells with $N_p = 3$, (d) cells with $N_p = 4$, (e) cells with $N_p = 5$, (f) cells with $N_p = 6$ and (g) cells with $N_p = 7$ existing pseudopodia.

B.5 Numerical implementation of the developed cell migration model

The following gives a short overview of the numerical implementation of the model. It is not meant as a manual, but only to provide insight into the details of the implementation.

Our experimental analyses suggest that the pseudopodia of the individual cell are dynamic entities that each have their own lives. Therefore, the model tracks each of the N_m membrane points of the individual cells for all cells. At each time step, membrane points are checked for activation, collision and cessation of activation due to either contact or expiration of life time, before forces are assigned to active membrane points, whole cells are moved, and the time stamps of all counters keeping track of collisions (both which pseudopodia of which cells, and duration), duration of active membrane points, duration of membrane point waiting time since last activation, and simulation time. Finally, the concentration field is updated due to the new positions of the cells.

The flow of the program at each time step is as follows, with each part to be described in detail in Sec. 3.5 starting on p. 68,

1. Activation of membrane points and pseudopod growth for each cell. The time since membrane point activation and pseudopod lengths are updated. This is detailed in Sec. 3.5.2.
2. Handle collisions i.e. contact inhibition of locomotion (Sec. 3.5.5): membrane points of different cells within a distance ϵ of each other are considered to be in collision. Time since initial collision is tracked, and if the experimentally determined collision time τ_c is surpassed, the point is flagged for collapse, in accordance with the experimental observations.
3. Forces are assigned to all active points along the appropriate directions, as described by Eq. (3.12) of Sec. 3.5.2.
4. Move all non-active points by Eq. (3.16) of Sec. 3.5.3. This also includes points which are retracting following activation or collision.
5. Collapse retracting points according to Eq. (3.11) of Sec. 3.5.2. If a membrane point has fully retracted and the waiting time τ_{rest} has passed, the point is transferred to a normal passive point.
6. Update time stamp and concentration field due to the new cell positions, by summing Eq. (3.18) of Sec. 3.5.4 for all cells.

Note that protruding points are moved before the entire cell, while collapsing points first move with the cell center of mass and then retracts. Collapsing points may be activated in later time steps, in which case the point transitions to an activated point and the cycle restarts.

The model has been implemented in MATLAB and this implementation is freely available for download at <http://sourceforge.net/projects/cell-migration/>, with Fig. B.6 giving the flow diagram of the implementation.

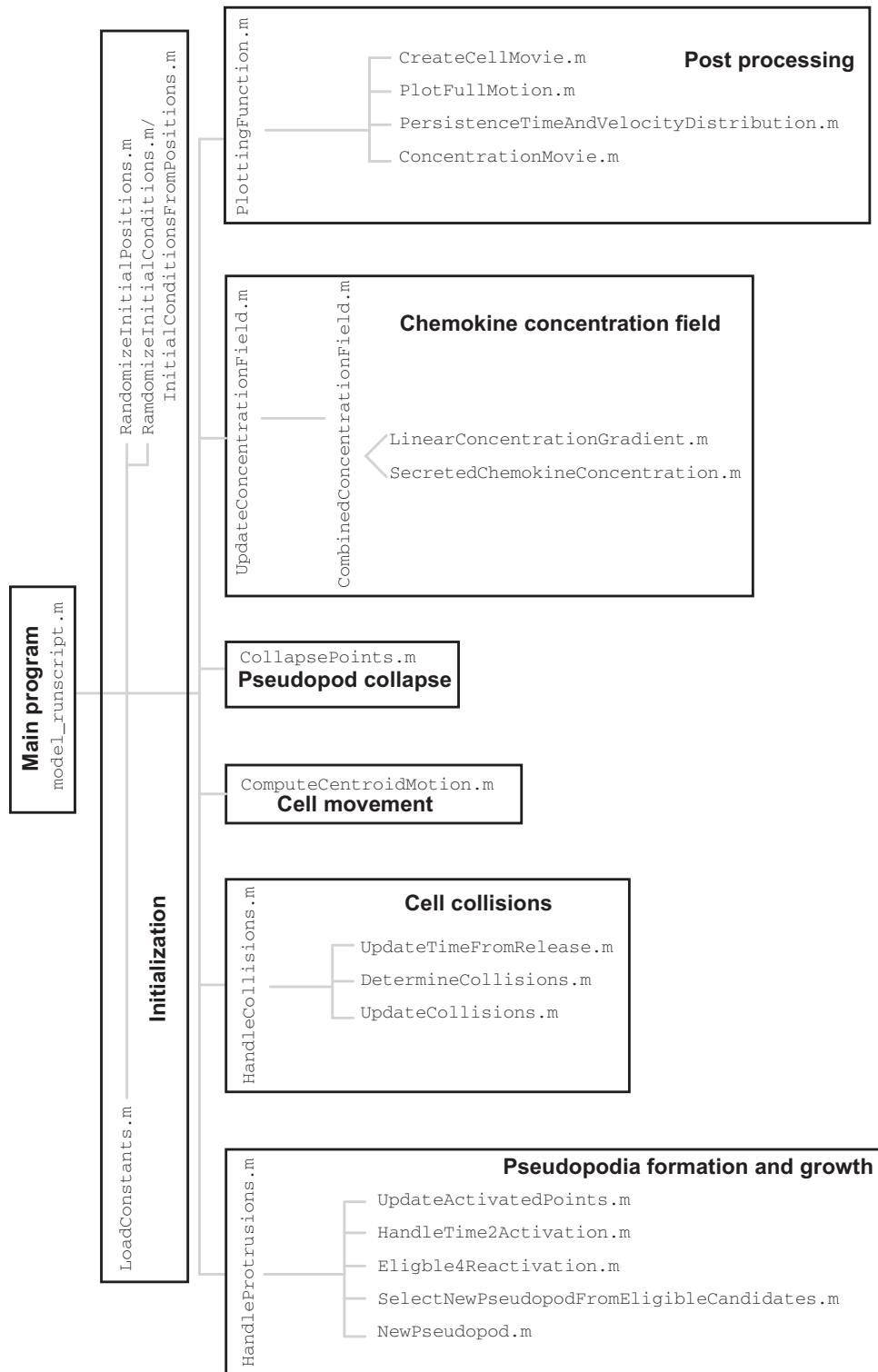


Figure B.6: Flow diagram of the MATLAB implementation of the model. In addition to those listed, each subroutine in the diagram calls several subroutines which are not listed to perform special tasks.

The model is run by executing the driver `model_runscript.m`, which loads all constants, places the model cells onto a computational domain, and simulates their movement for a selected time. Two options for initial cell positioning are provided: random placement on the computational domain or preselected initial positions. These preselected positions can be taken from e.g. an actual experiment or may be specified by the user. All options for initial positions are specified in `LoadConstants.m` and/or the `model_runscript.m`.

The program stores the positions of all membrane points at all times, along with details about the activation time of all currently active membrane points, the contact times of all active membrane points currently in contact, the concentration field at all positions, the run time t , and of course the center-of-mass positions \mathbf{x}_m of all cells. Hence, the output file is replaced after each simulation time step. The option to restart a simulation from a previous output file is under development.

The implementation also allows for the inclusion of external concentration gradients and/or background concentrations. These options may be chosen in the function `LinearConcentrationGradient.m`.

A number of post-processing options have also been developed. `PlotFullMotion.m` plots the trajectories of all cells in the simulation sampled at any specified time interval, while `PersistenceTimeAndVelocityDistribution.m` computes the persistence time and velocity distributions from the model output data sampled at these times. `CreateCellMovie.m` generates a movie of the motion of all the cells at all simulation time points, while `ConcentrationMovie.m` generates a movie of the contours of the concentration field with the cell positions overlaid.

A user-friendly implementation of periodic boundary conditions is included in the next release, which should be available online by late September 2012.

Appendix C

Additional data for adipocyte stem cell differentiation

C.1 Additional genetic marker data

A repeat run of gene expression measurements was completed to verify the findings presented in Fig. 4.6. As in the first experiment, all expression levels are normalized by the expression of the “housekeeping” gene β -actin. The results of this experiment are presented in Figs. C.1 and C.2(b) below; Figure C.2(a) presents the results for the experiment whose temporal expression profiles are given in Fig. 4.6. Data from both panels of Fig. C.2 is included in Fig. 4.11 in the main text.

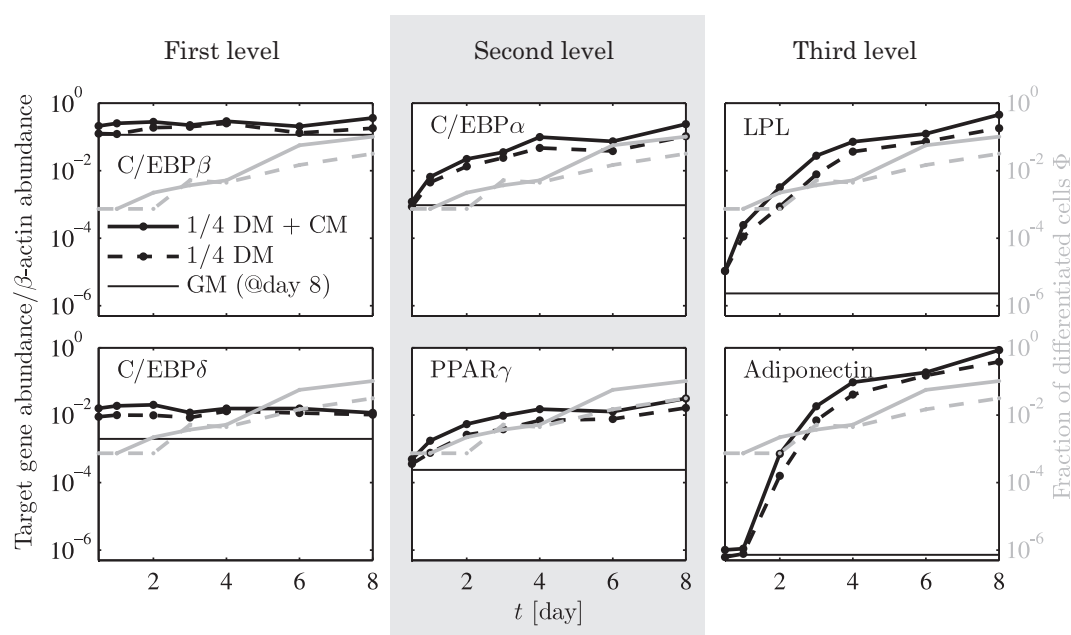


Figure C.1: Temporal expression profiles (black) of the six target genes $C/EBP\delta$ and $C/EBP\beta$ (first level of signaling cascade), $PPAR\gamma$ and $C/EBP\alpha$ (second level) and the adipocyte-specific LDL and $Adiponectin$ (third level) exposed to 1/4 DM (dashed) and 1/4 DM + CM (full lines). Also shown is the fraction of differentiated cells (gray, same line styles). For reference, the expression level of the same genes from experiments exposed only to growth medium (and sampled only at the last day) is also included (thin black line). These temporal profiles confirm the results presented in Fig. 4.6.

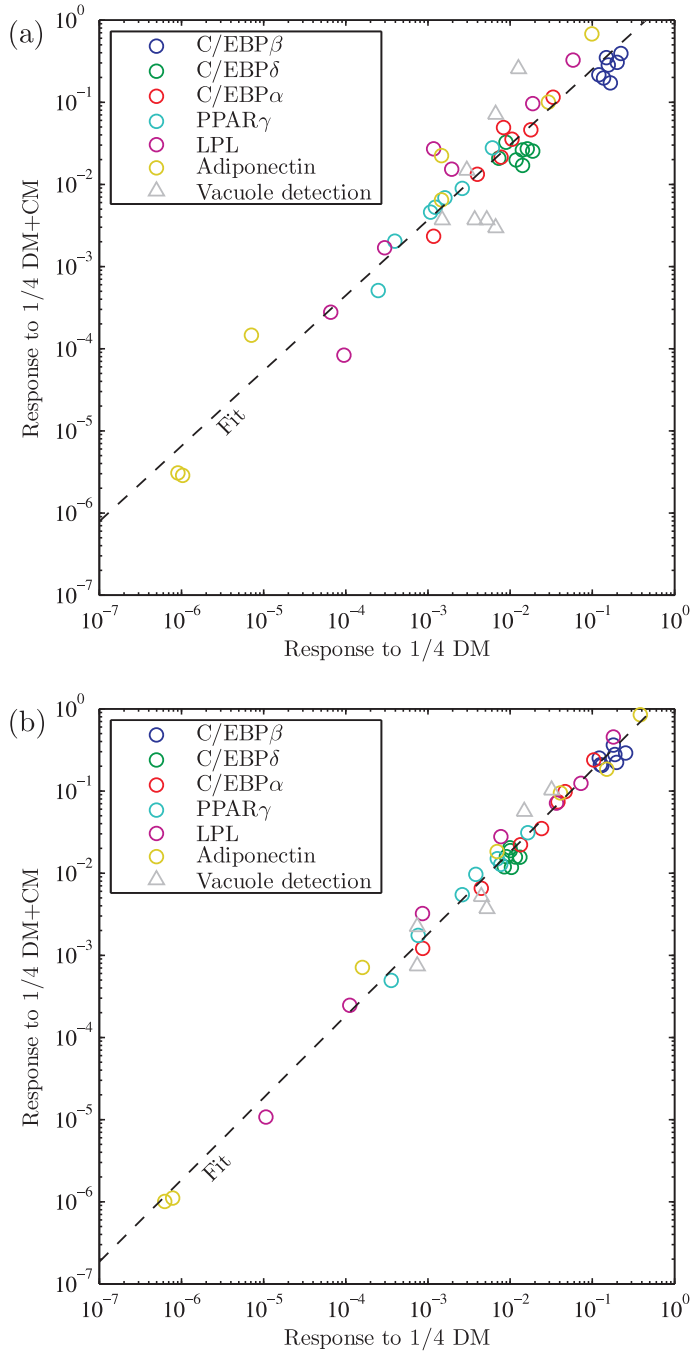


Figure C.2: Relative gene expression abundance (normalized by β -actin expression level) for cells exposed to 1/4 DM and 1/4 DM + CM (circles). Also shown is the fraction of differentiated cells (gray triangles). A linear correlation is found at all levels of the expression, which is replicated by the image analysis. Each panel shows the result of an independent set of experiments conducted on different dates, along with a fit to this data (dashed black lines). (a) Fit: $1/4DM + CM = 2.86(1/4DM)^{0.97}$. (b) Fit: $1/4DM + CM = 1.88(1/4DM)^{0.99}$.

C.2 The irrelevance of fluid shear on stem cell behavior

Cells exposed to a perfusion flow will necessarily also experience a shear stress induced by the fluid. While high levels will directly impart mechanical damage to the cells, some cell types in addition sense the shear and change their behavior when exposed to lower levels. A prominent example is the endothelial cells lining the interior surface of the cardiovascular system which play a major role in sensing the flow conditions and coordinating systemic response. These cells initiate certain chemical signals in response to elevated shear stress levels, and are generally thought to have one of the lower shear-sensing thresholds [41]; the threshold limit activating this shear-dependent signaling has previously been determined to ~ 1 Pa [109].

Contrary to endothelial cells, the adipose-derived stem cells used in this study are not subjected to flow under normal conditions in the body, and it is therefore not certain that they will change their behavior in response to elevated-yet-harmless shear levels; in fact, it would be highly surprising to find such a dependence of differentiation on shear forces. Ensuring that the shear stress experienced by the stem cells is well below the sensing threshold of endothelial cells forms a strong argument against any effects of shear on the observed differentiation behavior.

The shear stress on a half ellipsoid on the chamber floor was computed to estimate the shear stress experienced by the cells. The j th component of the shear stress τ_j on the ellipsoid surface is computed from the fluid stress tensor σ_{ij} using the components of the normal vector n_i at the surface as

$$\tau_j = -n_i \sigma_{ij} = -\eta n_i (\partial_i v_j + \partial_j v_i), \quad (\text{C.1})$$

where η is the fluid viscosity. The ellipsoid of radius (semi-major axis) $10 \mu\text{m}$ and height (semi-minor axis) $5 \mu\text{m}$ was placed at the center of the channel in the geometry used previously (see Fig. 4.14), and the problem was solved numerically in two dimensions using COMSOL MULTIPHYSICS version 3.5a. While this two-dimensional solution ignores the shear contribution from the spanwise velocity gradients close to the chamber side walls, it nonetheless gives an order of magnitude estimate of the shear which applies to most of the cells. In addition, the experimental data does not show a higher fraction of differentiated cells in the regions of higher shear stress close to the chamber side walls, see the image Fig. 4.3 and the previous analysis of spatially isotropic differentiation in the chamber in Sec. 4.4.1. Figure C.3 shows the computed shear stress on the cell (ellipsoid) for a wide range of channel flow rates Q , including the two experimental cases ($Q = 33 \text{ nL min}^{-1}$ and $Q = 500 \text{ nL min}^{-1}$). The largest shear stress experienced in any of the experimental conditions is around 0.01 Pa , which is two orders of magnitude lower than the shear sensing-limit for endothelial cells. Hence, effects of shear stress are very unlikely in the experiments.

Estimating the additional shear from transverse velocity gradients

Finally, the magnitude of the spanwise velocity gradients experienced by a cell close to the wall may be estimated as follows. The velocity field reaches its maximum value in

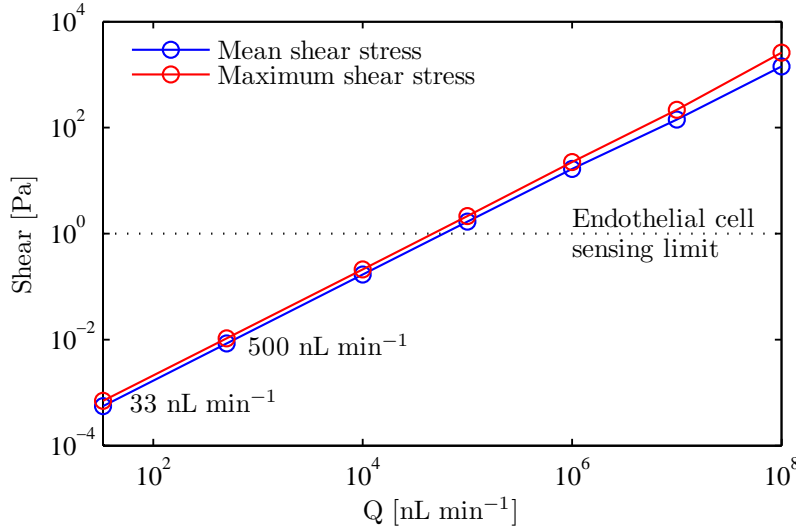


Figure C.3: Computed shear stress experienced by a half ellipsoid of radius (semi-major axis) 10 μm and height (semi-minor axis) 5 μm at the floor of the cell culture chamber as a function of flow rate Q . The shear-stress sensing limit for endothelial cells of ~ 1 Pa is several orders of magnitude greater, and shear stress is therefore very unlikely to have any effect on the differentiation of the stem cells.

the spanwise direction on a length scale of h/π , where h is the shorter channel height (and not the channel width w) [25]. For the cell culture chambers of $h = 500 \mu\text{m}$ this characteristic length scale is $\sim 160 \mu\text{m}$ which is roughly 8 times the average cell diameter. The maximum speed U_o reached in the middle of the chamber at the height of the cells h_c is $U_o(h_c) = 6\bar{U}(1 - h_c/h)h_c/h \approx 0.1\bar{U}$, about one tenth of the average speed $\bar{U} = Q/(hw)$. The maximum shear would be experienced by cells placed directly next to the wall where the velocity gradients have the largest amplitude. Assuming that all variations in velocity happen on the scale of the cell (i.e over the cell diameter of $20 \mu\text{m}$) will severely overestimate the shear, but serves as an absolute upper bound and is

$$\tau_{\text{wall}} = \frac{\Delta v}{\Delta y} = \frac{\bar{U} - 0}{20 \mu\text{m}}. \quad (\text{C.2})$$

With the highest flow rate of $Q = 500 \text{ nL min}^{-1}$ one finds $\tau_{\text{wall}} = 5 \times 10^{-2} \text{ Pa}$ (with $h = 500 \mu\text{m}$ and $w = 1500 \mu\text{m}$), which remains on the order of the numerical calculations presented above and also remains about two orders of magnitude below the critical level.

C.3 Additional data for nearest neighbors and differentiation

This section presents additional data supporting the observation that differentiated cells do not secrete the differentiation-inducing signal at a higher rate. Applying the analyses presented in Sec. 4.6.1, we show here that changing flow rate and density does not compromise the results. Nor does including newly differentiated cells downstream of the previously differentiated cells. Thus, the distribution of cell-cell distances between previously differentiated cells and newly differentiated cells is always biased towards larger distances than the distribution of cell-cell distances between all cells (Figs. C.4 and C.6), and the number of differentiated cells within a distance $\rho = 200 \mu\text{m}$ from an already differentiated cell is also just what one would expect from random differentiation (Figs. C.5 and C.7). The

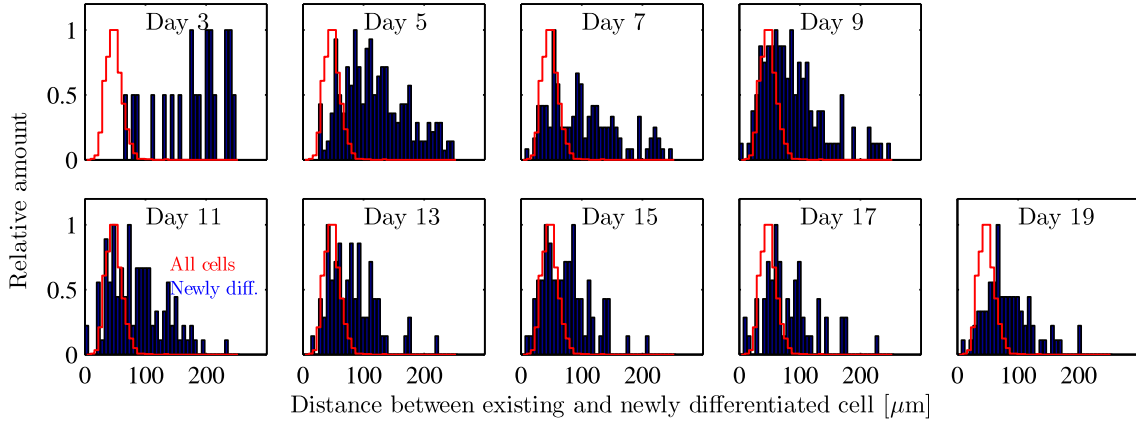


Figure C.4: Same as Fig. 4.9, only here $\Gamma_{\text{cell}} = 2.71 \times 10^8 \text{ m}^{-2}$ and $Q = 33 \text{ nL min}^{-1}$. The cells are exposed to only normal DM.

results look similar for an experiment which includes conditioned medium (CM), as shown in Figs. C.8 and C.9

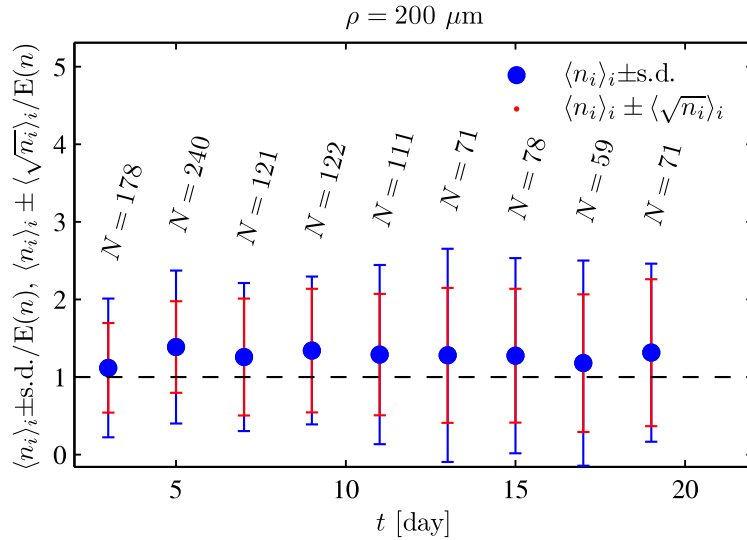


Figure C.5: Same as Fig. 4.10, only here $\Gamma_{\text{cell}} = 2.71 \times 10^8 \text{ m}^{-2}$ and $Q = 33 \text{ nL min}^{-1}$. The cells are exposed to only normal DM.

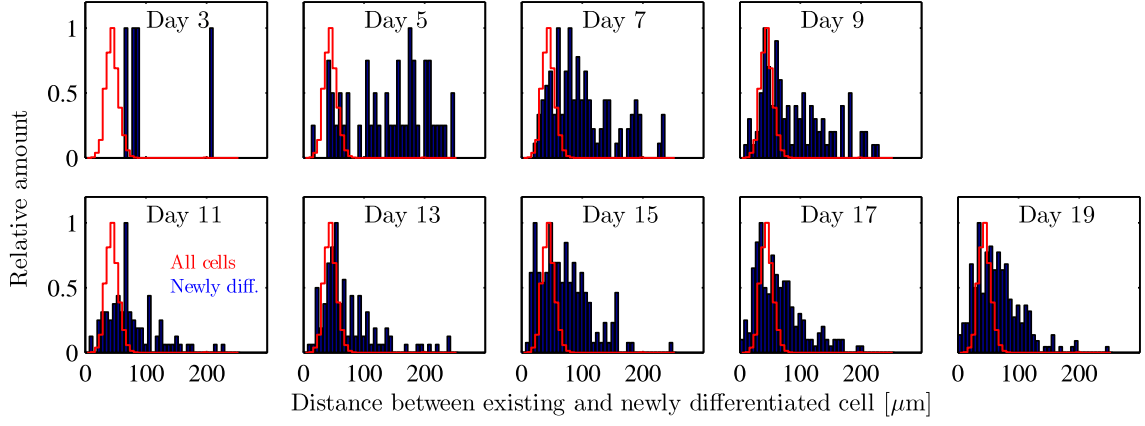


Figure C.6: Same as Fig. 4.9 but including all newly differentiated cells whether upstream or downstream. $\Gamma_{\text{cell}} = 2.71 \times 10^8 \text{ m}^{-2}$ and $Q = 500 \text{ nL min}^{-1}$. The cells are exposed to only normal DM.

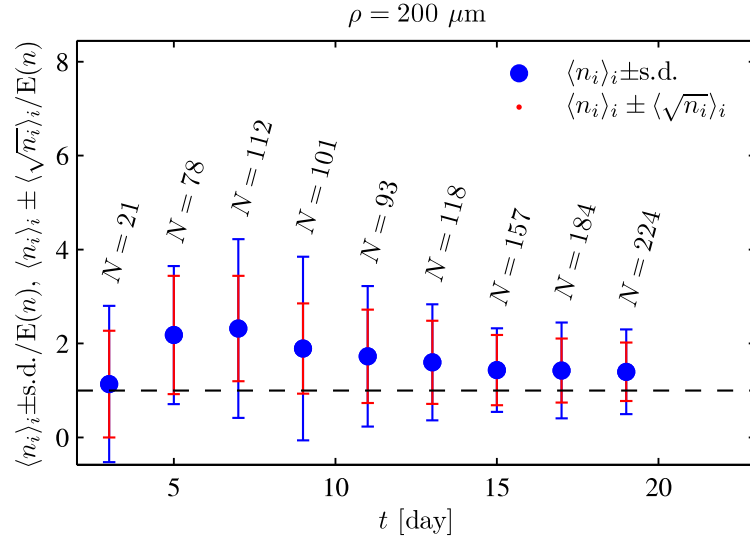


Figure C.7: Same as Fig. 4.10 but including all newly differentiated cells whether upstream or downstream. $\Gamma_{\text{cell}} = 2.71 \times 10^8 \text{ m}^{-2}$ and $Q = 500 \text{ nL min}^{-1}$. The cells are exposed to only normal DM.

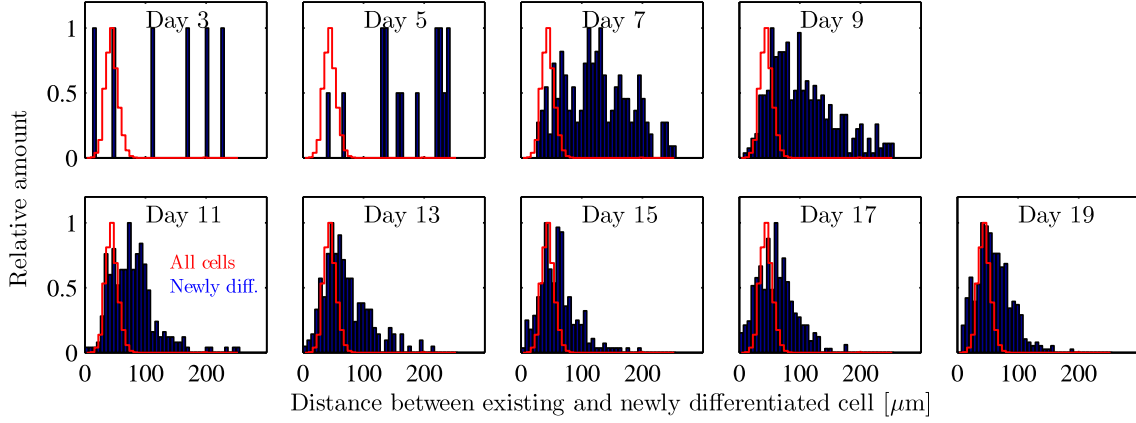


Figure C.8: Same as Fig. 4.9 but for an experiment exposed to differentiation medium and conditioned medium. $\Gamma_{\text{cell}} = 2.71 \times 10^8 \text{ m}^{-2}$ and $Q = 500 \text{ nL min}^{-1}$.

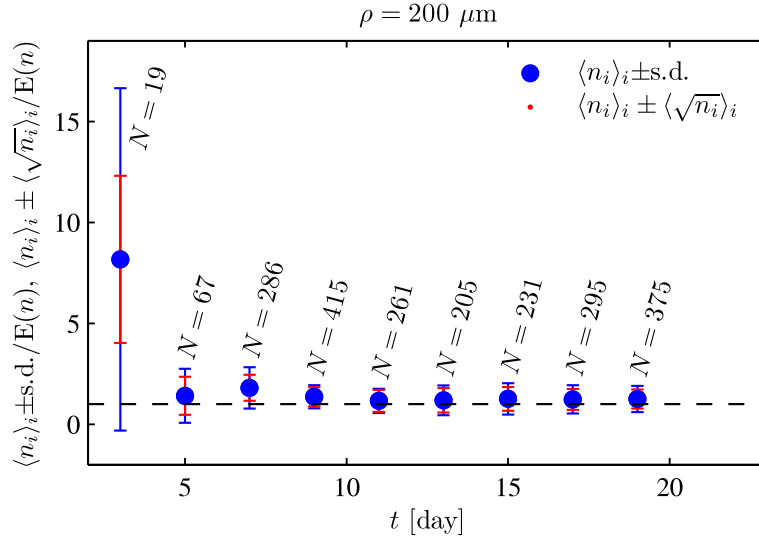


Figure C.9: Same as Fig. 4.10 but for an experiment exposed to differentiation medium and conditioned medium. $\Gamma_{\text{cell}} = 2.71 \times 10^8 \text{ m}^{-2}$ and $Q = 500 \text{ nL min}^{-1}$.

C.4 Traditional biochemistry of ligand-receptor binding

The traditional biochemistry of ligand-receptor binding is recapitulated here to complete the discussion of the role of particle currents in cellular signaling. This is standard material found in most basic text books on biochemistry and biochemical reactions, e.g. [5, 6, 20].

We consider a chemical reaction between a signaling molecule (ligand) L and a receptor R , which together form a bound receptor, denoted by LR . We furthermore allow the ligand-receptor complex to dissociate. The simplest (first-order) reaction describing this is



In chemical equilibrium, standard law-of-mass-action reaction kinetics holds that the forward rate equals the backward rate. Denoting the rate constants of binding and unbinding by k_{on} and k_{off} , respectively, and furthermore using c_x to denote the concentration of substance x , Eq. (C.3) in equilibrium corresponds to

$$k_{\text{on}}c_Rc_L = k_{\text{off}}c_{RL}. \quad (\text{C.4})$$

The number of receptors is limited, so the total amount of receptors c_R^{tot} is simply the sum of free (c_R) and bound (c_{RL}) receptors,

$$c_R^{\text{tot}} = c_R + c_{RL}, \quad (\text{C.5})$$

where the stoichiometry of first-order kinetics assures that one receptor is used per bound ligand. Solving for the bound receptors c_{RL} in Eq. (C.4) and using the condition Eq. (C.5) yields

$$c_{RL} = c_R^{\text{tot}} \frac{c_L}{K_d + c_L}, \quad (\text{C.6})$$

where $K_d = k_{\text{off}}/k_{\text{on}}$ is the so-called dissociation constant. Given a total concentration of receptors c_R^{tot} , we see that the equilibrium probability \bar{p} that a receptor is bound is given by

$$\bar{p} = \frac{c_L}{K_d + c_L}, \quad (\text{C.7})$$

that is, only by the ligand concentration c_L and the dissociation constant K_d of the chemical reaction. This sigmoidal probability function goes from 0 to 1, with the dissociation constant setting the concentration scale where the probability is 1/2.

Reactions of this type abound in biochemistry from the subcellular to cellular levels. For enzymatic reactions, Eq. (C.6) is known as the Michaelis–Menten equation [20].

Appendix D

Paper published in the Journal of Micromechanics and Microengineering

Title: Pulsatile microfluidics as an analytical tool for determining the dynamic characteristics of microfluidic systems

Authors: Søren Vedel, Laurits Højgaard Olesen, and Henrik Bruus.

Reference: Published in the Journal of Micromechanics and Microengineering **20**, 035026 (2010) (11 pages)

Pulsatile microfluidics as an analytical tool for determining the dynamic characteristics of microfluidic systems

Søren Vedel¹, Laurits Højgaard Olesen² and Henrik Bruus¹

¹ Department of Micro- and Nanotechnology, Technical University of Denmark, DTU Nanotech Building 345 East, DK-2800 Kongens Lyngby, Denmark

² Device Research and Technology, Novo Nordisk A/S, Brennum Park, DK-3400 Hillerød, Denmark

E-mail: Henrik.Bruus@nanotech.dtu.dk

Received 28 September 2009, in final form 30 December 2009

Published 2 March 2010

Online at stacks.iop.org/JMM/20/035026

Abstract

An understanding of all fluid dynamic time scales is needed to fully understand and hence exploit the capabilities of fluid flow in microfluidic systems. We propose the use of harmonically oscillating microfluidics as an analytical tool for the deduction of these time scales. Furthermore, we suggest the use of system-level equivalent circuit theory as an adequate theory of the behavior of the system. A novel pressure source capable of operation in the desired frequency range is presented for this generic analysis. As a proof of concept, we study the fairly complex system of water-filled interconnected elastic microfluidic tubes containing a large, trapped air bubble and driven by a pulsatile pressure difference. We demonstrate good agreement between the system-level model and the experimental results, allowing us to determine the dynamic time scales of the system. However, the generic analysis can be applied to all microfluidic systems, both ac and dc.

(Some figures in this article are in colour only in the electronic version)

1. Introduction

The fluid flow of almost all microfluidic systems so far presented in the literature operates in a steady state. Though some of the recently presented highly parallelized systems depend on on-chip dynamics, such as the system of Thorsen *et al* [1] consisting of 256 sub-nanoliter reaction chambers and 2056 microvalves, the flow of liquid is almost exclusively in a steady state. This is because the system is run for enough time that any temporal effects such as fluid inertia and system compliance have died out. In fact, this independence of time is to many one of the attractions of microfluidics. Apart from the inherently time-dependent valves, which have been studied for some time—see e.g. the work of Olsson *et al* [2] or Brask *et al* [3]—few microfluidic systems have been designed to exploit these temporal dependencies. A recent example is the passive on-chip switch of Leslie *et al* [4], which requires an externally applied harmonically oscillating pressure gradient to drive the fluid. Elastic membranes on the chip act as sources of compliance, which are expanded when the fluid pressure inside

the chip increases, and the expanded volume is filled with incoming fluid. This fluid can be thought of as stored in the compliant membrane. The converse happens when the fluid pressure in the system decreases: the membrane contracts and a volume of fluid is pushed out (negative storage). When the oscillation frequency is so fast that this expanding/contracting motion does not have time to occur, the fluid flow will never reach a steady state and very little of it will have time to flow downstream; the volume of fluid that has been moved downstream of the compliant medium is less than would have been the case, had the fluid moved in a steady state. Using two channels of different liquid inertias and tuning the driving frequency, the chip of Leslie *et al* displays a switching behavior where the flow in one channel is amplified while the flow in the other is impeded.

Whether one is designing an ‘ac’ or ‘dc’ system, full exploitation of the system requires the understanding of all transient effects. For the system of Thorsen *et al* the chemical reactions could be compromised if insufficient volumes of fluid are delivered to the chambers as a consequence of long

transient time scales. On the other hand, waiting much longer than needed for the fluid to reach a steady state limits the system throughput. The ac system of Leslie *et al* hinges critically on the correct tuning of the compliance time scales of the two channels of the switch. Clearly, understanding and exploitation of the transient fluidic effects are required to fully realize the potential of lab-on-a-chip systems as a significant improvement to ‘regular’ laboratories.

A common method for studying the dynamics of a physical system is to use harmonically oscillating external fields, which allow for the study of all time scales of the system by sweeping the oscillation frequency. For a typical microfluidic system, pulsatile (harmonically oscillating) driving pressure would be the typical choice of the external field. By studying the frequency response of the microfluidic system, the various time scales are found, and the dominating time scale can be determined. As illustrated above, these time scales set the upper limit for when the system reaches a steady state, and are thus important parameters when more than one operation is to occur on the chip.

An estimate of the typical transient time scales of a microfluidic system can be given by considering the start-up of a pressure driven flow. Such a flow will accelerate and approach the steady state solution of the Hagen–Poiseuille law asymptotically with a characteristic time τ [5]. For a circular cross section, τ is given by

$$\tau = \frac{a^2}{\gamma_1^2 \nu}, \quad (1)$$

where a is the tube radius, ν is the kinematic viscosity of the liquid and $\gamma_1 = 2.4048$ is the first root of the Bessel function of the first kind of order 0 (see table 1 for a list of parameters). For a water-filled tube of $a \sim 100 \mu\text{m}$ this time scale is $\tau \sim 1.7 \text{ ms}$, so in order to use pulsatile microfluidics, a driving mechanism capable of probing frequencies into the low kilohertz range is needed. Secondly, this driving mechanism should deliver characteristic volumes of $\mathcal{V} \sim 0.1 \text{ mm}^3$ per cycle. This is to ensure that a volume sufficiently larger than the characteristic volume of a generic microfluidic system (e.g. [1, 6]) is delivered by each stroke, thus rendering the flow in the system fully pulsatile.

Lumped parameter modeling in microfluidics consists of modeling the system of consideration as a network of ideal hydraulic resistances R_{hyd} , inertances L_{hyd} and compliances C_{hyd} , corresponding respectively to viscous losses, inertial losses and volume storage (departure from rigid confinement) [2, 4, 7–10]. The components depend on various system parameters such as tube radius, fluid viscosity, etc. The method is known as equivalent circuit (EC) theory due to the mathematical equivalency to electric circuits which extends so far that Kirchhoffian network analysis may be applied to the microfluidic network, and it is therefore customary to represent the microfluidic circuit by its equivalent electric circuit, see e.g. figure 9. By direct analogy to electric circuits there are three dynamic time scales in microfluidics: $\tau_{RC} = R_{\text{hyd}}C_{\text{hyd}}$, $\tau_{LR} = L_{\text{hyd}}/R_{\text{hyd}}$ and $\tau_{LC} = \sqrt{L_{\text{hyd}}C_{\text{hyd}}}$. Although derived for components, the linearity of the governing Stokes equation of fluid flow assures the validity of the modeling approach to

Table 1. List of parameters, alphabetized by symbol.

Parameter	Symbol	Unit/value
Area	\mathcal{A}	m^2
Inner radius	a	m
Compliance	C_{hyd}	$\text{m}^3 \text{Pa}^{-1}$
Young’s modulus	E	Pa
Frequency	f	Hz
Wall thickness	h	m
Electric current	I	A
Bessel function the first kind of order n	J_n	—
Membrane spring constant	k	N m^{-1}
Actuator force constant	k_F	N A^{-1}
Electric inductance	L_{el}	V s A^{-1}
Hydraulic inertance	L_{hyd}	$\text{Pa s}^2 \text{m}^{-3}$
Tube length	ℓ	m
Plunger mass	M	kg
Power	P	J s^{-1}
Pressure	p	Pa
Flow rate	Q	$\text{m}^3 \text{s}^{-1}$
Pressure source chamber flow rate	Q_c	$\text{m}^3 \text{s}^{-1}$
Electric resistance	R_{el}	V A^{-1}
Hydraulic resistance	R_{hyd}	Pa s m^{-3}
Radial coordinate	r	m
Period	T	s
Time	t	s
Voltage	U	V
Wall radial displacement	u_r	m
Volume	\mathcal{V}	m^3
Chamber volume	\mathcal{V}_c	m^3
Initial chamber volume	$\mathcal{V}_{\text{init}}$	m^3
Tent volume	$\mathcal{V}_{\text{tent}}$	m^3
Velocity	v	m s^{-1}
Axial fluid velocity	v_x	m s^{-1}
Coil velocity	v_{coil}	m s^{-1}
Plunger coordinate	x	m
Bubble relative coordinate	x_{rel}	m
Hydraulic impedance	Z_{hyd}	Pa s m^{-3}
Womersley number	α	—
Critical Womersley number	α_c	α/γ_1
First root of J_0	γ_1	2.4048
Wall compliance constant	β	—
Dynamic viscosity	η	Pa s
Momentum diffusion length	λ_d	m
Kinematic viscosity	ν	$\text{m}^2 \text{s}^{-1}$
Density	ρ	kg m^{-3}
Poisson’s ratio	σ	—
Dynamic time scale	τ	s
Angular frequency	ω	rad s^{-1}

full system-level analysis [11, 12]. The work of these authors demonstrates the very good level of accuracy attainable by these models for both steady-state and dynamic systems.

In this paper we suggest the use of experimental pulsatile microfluidics in connection with EC theory as an analytical tool for the derivation of the time scales for any microfluidic system. The use of the predictive capabilities of time-dependent EC theory have already been demonstrated for a component by Kim *et al* [9], who derived the compliance of a silicone rubber tube from the characteristic time of the build-up of pressure, and by Leslie *et al* [4], who as previously mentioned generated an on-chip switch by use of rectifying valves and an externally driven ac flow. However,

the use of pulsatile microfluidics allows for the deduction of the time scale of any time-dependent component within any microfluidic system, as long as a valid model of the system is in place. The analysis will allow for the experimental determination of these time scales, while system-level EC analysis will provide a theory to which the experimental results can be compared. The analysis applies to both ac and dc microfluidic systems, since even systems intended for dc operation have inherent dynamic time scales, as mentioned previously. Since the EC elements are given in terms of system parameters, deviations between model results and experimental data will strongly indicate which parameter of the model is incorrect. However, the real strength of the approach lies in the fact that one often has components of unknown compliance in the microfluidic system, such as oddly shaped membranes, valves, trapped gas bubbles etc, which then may be determined using the suggested approach. For example, for many of the bubble-based microfluidic applications such as pumps [13, 14], valves [15, 16], sensors [17, 18] and actuators [19, 20] the approach can be used to verify the bubble size and hence the performance of the system.

As a proof of concept we will in the following expose a full-microfluidic network containing one component of unknown compliance to a pulsatile pressure difference. In addition to the unknown compliance, this ac network consists of interconnected elastic tubing with one large moving air bubble and several stationary compliances of known value. We use system-level EC analysis to model the system in order to derive a numerical value for said compliance while also proving the sufficiency of system-level EC modeling. We note, however, that this generic method of using pulsatile microfluidics is by no means limited to only this purpose. A novel pulsatile pressure source capable of probing the desired low-kilohertz frequencies will be presented and the appropriate EC circuit elements for the proof-of-concept experiment will be derived.

2. The physics of pulsatile flow

The analytical solution to pulsatile flow void of start-up effects is usually credited to Womersley [21], although the problem has been solved independently by several scholars [22–25]. The solution is found by solving the Navier–Stokes equation in cylindrical coordinates and not surprisingly, this solution finds that a harmonically oscillating flow rate arises due to the pulsatile pressure. From a physical standpoint, the fluid flow experiences both viscous resistance and inertia, the latter due to the pulsatility. This is in contrast to the steady-state Poiseuille solution, where only viscous resistance is present.

Womersley's solution depends on the dimensionless Womersley number $\alpha \equiv \sqrt{a^2 \omega / \nu}$, where ω is the angular frequency of the pressure oscillations, i.e. $p(t) = \text{Re}[\Delta \tilde{p} e^{i\omega t}] + p_0$ where the tilde indicates the (in general complex) amplitude and p_0 is a reference pressure. The Womersley number may be interpreted as a non-dimensional measure of the diffusion of momentum: The kinematic viscosity ν is the diffusivity of momentum in the pressure-driven flow [8], while $a^2 \omega$ is the diffusivity required for

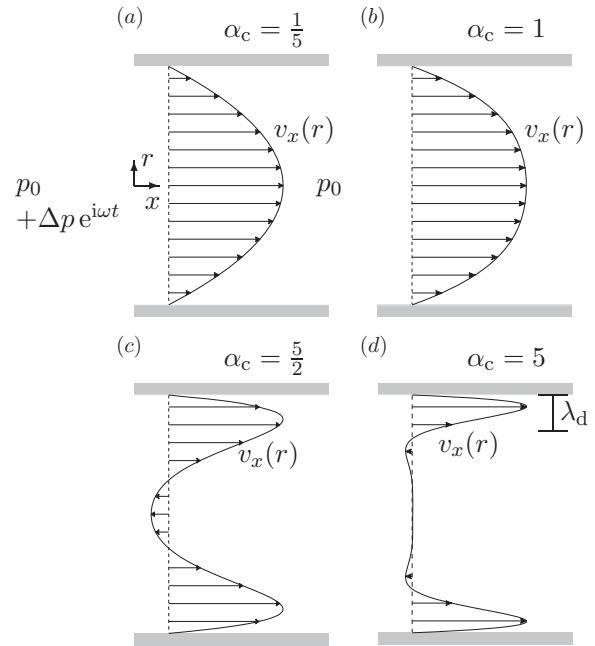


Figure 1. Axial velocity profiles $v_x(r)$ for a liquid with no-slip boundary conditions driven by a pressure difference $\Delta p e^{i\omega t}$ in a tube, calculated using MATLAB. All velocity profiles are computed at the time $t = T$ for four values of α_c , where T is the oscillation period, and α_c is defined in equation (2). The four velocity profiles are not shown to scale. The direction of the pressure difference is indicated in the figure for $\alpha_c = 1/5$ and is the same for all figures. The effects of inertia on the velocity profile are clearly observable for $\alpha_c > 1$ by the deviation from the Poiseuille paraboloid. The momentum diffusion length $\lambda_d = \sqrt{\nu/\omega}$ giving the width of the quasi-steady annular region is indicated for $\alpha_c = 5$.

momentum to diffuse across the channel before the pressure changes. However, a more intuitive measure may be introduced by considering the inertial relaxation time of equation (1), i.e. the time scale on which the fluid reaches the steady state in response to an instantaneous change in the driving pressure. A critical Womersley number α_c for a circular tube may then be defined as

$$\alpha_c \equiv \sqrt{\frac{a^2}{\nu}} \omega = \sqrt{\tau \omega} = \frac{\alpha}{\gamma_1}, \quad (2)$$

which then measures the fluid relaxation time in response to the rate of change of the pressure ω . It is immediately seen that for $\alpha_c < 1$ the fluid at all times reaches a steady state before changes happen to the pressure, and the fluid flow is quasi-steady. For $\alpha_c > 1$ the fluid does not reach a steady state before the pressure changes, and inertia becomes important. Snapshots of the velocity profile computed using MATLAB are given in figure 1. The steady-state Poiseuille paraboloid is retrieved in the quasi-steady limit ($\alpha_c = 1/5$, panel (a)), while for $\alpha_c > 1$ (panels (c) and (d)) increasingly more pronounced deviations from this are seen as the flow becomes increasingly more dominated by inertia.

For $\alpha_c > 1$ the flow still has inertia acting in the opposite direction when the pressure gradient is reversed. Consequently, it will take some time before the pressure

gradient can change the direction of the inertia. This introduces a phase shift between the fluid motion and the pressure gradient. However, at the confinement walls, the no-slip boundary condition enforces very low velocities with correspondingly low inertia, so fluid close to the walls have a smaller phase shift than fluid in the center of the confinement. At $\alpha_c \gtrsim 5$ a full π phase shift is observed between the flow close to the walls and that at the center, forming a ‘fluidic skin effect’ or annular region as documented experimentally by Richardson [26]. The width of this region is given by the momentum diffusion length λ_d which can be found from the diffusivity of momentum and the characteristic time ω^{-1} as $\lambda_d = \sqrt{\nu/\omega}$. The parabolic velocity profile in this annular region observable in figure 1(d) supports the notion that the flow here remains quasi-static for $\alpha_c > 1$.

As previously shown by Morris and Forster [6], one may derive an exact fluidic impedance Z_{hyd} from Womersley’s analytical solution accounting for both inertia and viscous resistance. It relates pressure and flow rate amplitudes as $\Delta\tilde{p} = Z_{\text{hyd}} \tilde{Q}$ with

$$Z_{\text{hyd}} = \frac{\rho\omega\ell}{\pi a^2} i \left[1 - \frac{2 J_1(\alpha i^{\frac{3}{2}})}{\alpha i^{\frac{3}{2}} J_0(\alpha i^{\frac{3}{2}})} \right]^{-1}, \quad (3)$$

where J_n is the Bessel function of the first kind of order n , t is the time and $i = \sqrt{-1}$.

The field of pulsatile microfluidics is largely unexplored and has previously only been used in the study of reciprocating pumps. Olsson *et al* [2] correctly assumed a plug-flow velocity profile in the pump chamber without justifying the assumption. In an experimental study, Sheen *et al* [27] assumed a parabolic velocity profile even though their results extended into the inertially dominated regime where this assumption becomes invalid. One correct treatment of the fluid physics into this regime in connection with micropumps is given by Morris and Forster [6].

2.1. Resistance of pulsatile flow

The hydraulic resistance of a pressure-driven flow is a result of the conversion of kinetic energy into heat through viscous power dissipation P . For a fully developed flow in a tube of circular cross section of radius a and axial length ℓ it is given by [8]

$$P = \eta 2\pi \ell \int_0^a r [\partial_r v_x(r)]^2 dr, \quad (4)$$

where v_x is the axial velocity. In the quasi-steady limit the resistance does not differ from that of Poiseuille flow, but deviations appear in the limit of $\alpha_c > 1$ since the velocity profile gradient changes. These changes are observable in figure 1. The velocity amplitude \tilde{v}_x scales as the acceleration times the characteristic time, where the former is force per mass $A\Delta\tilde{p}/(\rho A\ell)$ and the latter is ω^{-1} , so $\tilde{v}_x \propto \Delta\tilde{p}/\omega$. The integrand $\partial_r v_x \approx \tilde{v}_x/\lambda_d$ differs only significantly from zero within a small annulus of radius a and width $\lambda_d = \sqrt{\nu/\omega}$ so the viscous power dissipation can be estimated as

$$P \propto 2\pi a \lambda_d \frac{\tilde{v}_x^2}{\lambda_d^2} \propto \Delta\tilde{p}^2 \omega^{-\frac{3}{2}}. \quad (5)$$

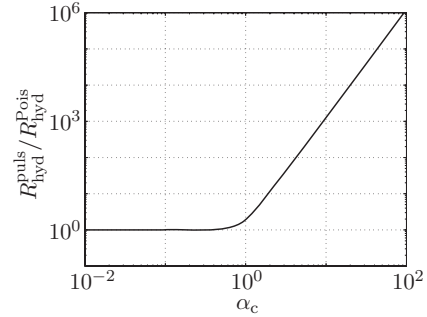


Figure 2. Model calculation of the time-averaged resistance of the pulsatile flow $R_{\text{hyd}}^{\text{puls}}$ normalized by the resistance of the Poiseuille flow $R_{\text{hyd}}^{\text{Pois}}$, plotted as a function of the critical Womersley number α_c . A sharp increase is observed when the flow enters the inertially dominated regime of $\alpha_c \geq 1$, where $R_{\text{hyd}}^{\text{puls}} \propto \alpha_c^3$.

For Poiseuille flow one finds $R_{\text{hyd}}^{\text{Pois}} = 8\eta\ell/(\pi a^4) = (\Delta\tilde{p})^2/P$, so the hydraulic resistance of the pulsatile flow scales as $R_{\text{hyd}}^{\text{puls}} \propto \omega^{\frac{3}{2}} \propto \alpha_c^3$ for high α_c .

This remarkable estimate may be verified from the impedance of equation (3) by considering the time-averaged resistance of the pulsatile flow over one oscillation cycle. The time-averaged power consumption is $\langle P \rangle = \text{Re}[\tilde{Q}^* \Delta\tilde{p}]/2$, where Re and the asterisk indicates the real part and the complex conjugate, respectively. Choosing the pressure amplitude to be real and defining all phases relative to $\Delta\tilde{p}$ while noting that $\tilde{Q} = \Delta\tilde{p}/Z_{\text{hyd}}$ we find

$$\langle P \rangle = \frac{1}{2} \text{Re} \left[\frac{1}{Z_{\text{hyd}}} \right] \Delta\tilde{p}^2. \quad (6)$$

To correctly compare to a Poiseuille flow, the same pressure difference must be used. By direct analogy to voltage in ac electric systems we find $\Delta p_{\text{rms}} = \Delta\tilde{p}/\sqrt{2}$ yielding $P = \Delta\tilde{p}^2/(2R_{\text{hyd}})$, so comparing to equation (6) we then find the time-averaged resistance of the pulsatile flow to

$$R_{\text{hyd}}^{\text{puls}} = \frac{1}{\text{Re} \left[\frac{1}{Z_{\text{hyd}}} \right]}, \quad (7)$$

which exhibits the suggested dependence on α_c^3 , as shown in figure 2 or as seen from equation (3). This result emphasizes the need to use the correct impedance of equation (3) when modeling the pulsatile flow.

3. Pressure source

A thorough survey of micropumps and flow generators, both commercially available and documented in the scientific literature [28, 29], shows that few which operate up to the low-kilohertz range generate very small flow rates. To satisfy the criterion of stroke volumes of $\mathcal{V} \sim 0.1 \text{ mm}^3$ we have developed a novel pressure source to better probe the desired frequency range.

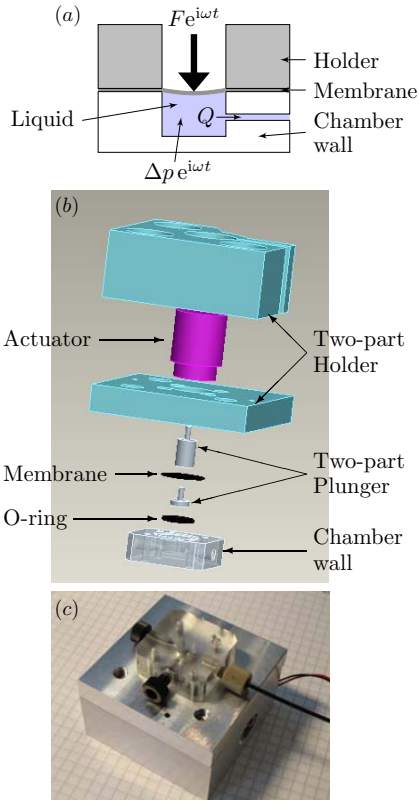


Figure 3. The constructed pressure source. (a) Sketch of the working principle. (b) 3D CAD drawing. (c) The assembled pressure source shown upside-down on a piece of paper with grid lines intersecting every 5 mm.

3.1. Design and fabrication

The pressure source works by applying a harmonically oscillating linear force onto a liquid-filled chamber, see figure 3(a). A linear actuator is used to deliver the force onto a silicone rubber membrane via a plunger, with the membrane separating the liquid system from the surroundings.

A linear voice coil actuator (LA08-10-000A by BEI Kimco Magnetics, San Marcos, CA, USA) was used as the driving mechanism. By virtue of the Lorentz force, this actuator delivers a linear force in response to an electric current in the coil, and it can probe frequencies of up to $f = 0.99$ kHz while still delivering stroke volumes of $V \sim 0.1$ mm³. Power was delivered to the actuator from an electric ac generator.

An aluminum holder is used to fixate the actuator and consists of two parts which are held together by screws. A two-part titanium plunger is fastened into the actuator coil. The membrane is clamped between the two parts of the plunger thereby forcing the thin silicone rubber membrane (0.20 mm thickness) to follow the motion of the plunger during the entire oscillation cycle. To ensure a complete sealing of the liquid in the chamber, the membrane is also clamped between the bottom part of the holder and the chamber wall, with a small rubber O-ring placed in a groove around the edge of the chamber. The chamber (4.50 mm radius and 6.50 mm depth) has three threaded holes for connection to the fluid system. The chamber wall is mounted onto the actuator holder by four

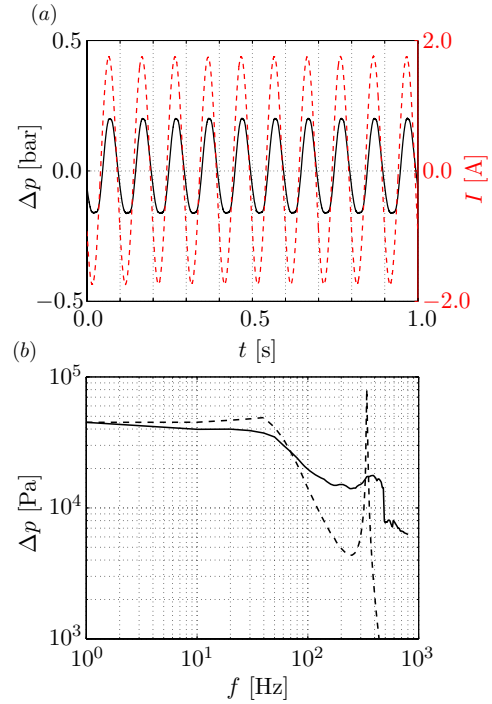


Figure 4. (a) Example of experimentally measured performance of the pressure source at $f = 10$ Hz. The generated pressure p (full line) is clearly pulsatile in response to the applied harmonically oscillating electric current I (dashed line). (b) Experimentally determined (full line) and model predictions (dashed line, see section 3.2) of the pressure amplitude Δp as a function of oscillation frequency f for current amplitude of 1.0 A. The experimental data indicate a resonance around $f = 350$ Hz, which the model predicts to be $f = 340$ Hz. The discrepancy between the model results and the experimental data for high frequencies can be explained by the simplifying assumption that the actuator membrane acts as a linear spring (see equation (8)). It is likely that the membrane does in fact exhibit a viscoelastic behavior which would account for the large value of the experimentally observed damping.

screws. An exploded 3D CAD drawing of the pressure source is given in figure 3(b), while the assembled source is shown in panel (c).

The performance of the pressure source is illustrated in figure 4. Panel (a) shows that the pressure source does in fact deliver a pulsatile pressure when operated with a 10 Hz harmonically oscillating electric current, while panel (b) indicates the attainable pressure amplitude as a function of frequency for a current amplitude of 1.0 A. The capability of the source is thus demonstrated to deliver pressures in the kPa range up to at least $f = 0.8$ kHz, the largest applied frequency in the measurement.

3.2. Pressure source circuit model

In order to couple the pressure source to the EC equations for the microfluidics of the system it acts on, a simple circuit model has been developed to account for the coupled electric, mechanical and microfluidic physics governing the pressure source. Assuming that all fields vary harmonically in time as $g(t) = \tilde{g} e^{i\omega t}$, the derivatives with respect to time simplify as

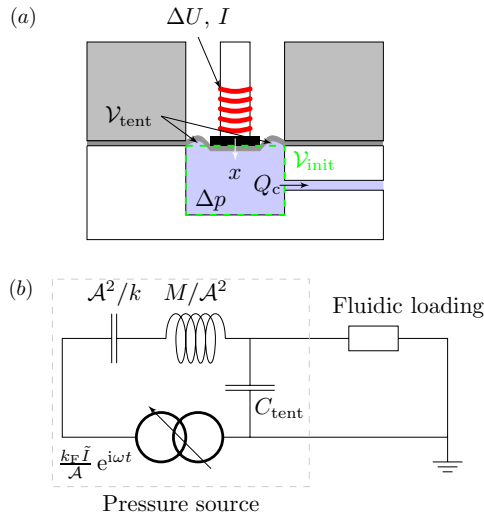


Figure 5. (a) Schematic illustration of the pressure source indicating the coil voltage ΔU and current I , the initial chamber volume V_{init} and membrane 'tent' volume V_{tent} , as well as the fluidic responses: pressure Δp and the chamber flow rate Q_c . (b) Equivalent circuit diagram for the pressure source with a plunger of mass M and area A , a membrane of stiffness k and compliance C_{tent} , and the coil of current amplitude \tilde{I} and back-EMF constant k_F . The fluidic loading is determined by the system the source acts on.

$\partial_t \rightarrow i\omega$. A schematic representation of the pressure source is given in figure 5(a).

The motion of the coil is governed by Newton's second law, where the external forces are the electromagnetic force on the actuator $F_{\text{act}} = k_F I(t)$, the assumed linear spring force of the membrane $F_m = -kx(t)$, and the force arising when a pressure difference exists across the membrane $F_p = -A\Delta p(t)$, where A is the effective area the plunger acts on. The motion of the plunger of mass M is then given by

$$-M\omega^2 \tilde{x} = k_F \tilde{I} - k\tilde{x} - A\Delta \tilde{p}, \quad (8)$$

where \tilde{x} is the plunger displacement amplitude, and the coil velocity \tilde{v}_{coil} is found as

$$\tilde{v}_{\text{coil}} = i\omega \tilde{x}. \quad (9)$$

The coil electric circuit obeys the equation

$$\Delta \tilde{U} = R_{\text{el}} \tilde{I} + i\omega L_{\text{el}} \tilde{I} + k_F \tilde{v}_{\text{coil}}, \quad (10)$$

where k_F is the back-EMF constant.

During operation, the volume of the chamber V_c depends on the position of the plunger and the expansion of the membrane due to the generated over-pressure in the chamber. The plunger radius is 3.53 mm while the chamber radius is 4.50 mm, so a small free-membrane area exists between the plunger and the chamber and holder walls. This part of the membrane will expand when a pressure difference is present across it due to its elastic nature, and the expanded volume will be filled with incoming fluid. Denoting the volume of fluid stored in the expanded membrane V_{tent} —so named due to the resemblance of the expanded membrane to a tent—and noting that the volume displaced by the actuator is $V_{\text{disp}}(t) = Ax(t)$, the chamber volume is given by

$$V_c = V_{\text{tent}} - Ax(t) + V_{\text{init}}. \quad (11)$$

V_{init} is the volume of the chamber when the system is at rest, and the negative sign arises since a positive displacement of the plunger pushes liquid out of the chamber. The volume V_{tent} is related to the generated over-pressure through a compliance as

$$V_{\text{tent}} = C_{\text{tent}} \Delta p(t). \quad (12)$$

A positive flow rate Q_c exits the chamber when its volume is diminished, so this flow rate is found as the negative time rate of change of equation (11):

$$\tilde{Q}_c = A\tilde{v}_{\text{coil}} - i\omega C_{\text{tent}} \Delta \tilde{p}. \quad (13)$$

Equations (8)–(10) and (13) couple the six unknown amplitudes \tilde{x} , \tilde{v}_{coil} , $\Delta \tilde{U}$, \tilde{I} , $\Delta \tilde{p}$ and \tilde{Q}_c , so two additional equations are required to close the system. These are derived from the 'fluidic loading' on the source, i.e. expressions for the flow rate and total pressure difference of the system driven by the source. However, the following equation relating the generated flow rate and over-pressure may be deduced from equations (8), (9) and (13):

$$\tilde{Q}_c = \frac{k_F \tilde{I}}{A \left(\frac{k}{A^2} \frac{1}{i\omega} + \frac{M}{A^2} i\omega \right)} - \Delta \tilde{p} \left[\left(\frac{k}{A^2} \frac{1}{i\omega} + \frac{M}{A^2} i\omega \right) i\omega C_{\text{tent}} + 1 \right]. \quad (14)$$

An expression for the pressure amplitude as a function of the electric current amplitude and plunger velocity can also be derived from equations (8) and (13):

$$\Delta \tilde{p} = \frac{k_F \tilde{I}}{A} - \left(\frac{k}{A^2} \frac{1}{i\omega} + \frac{M}{A^2} i\omega \right) \tilde{v}_{\text{coil}} A. \quad (15)$$

Equations (14) and (15) reveal that the pressure source does deliver a pressure, which can maximally be $\Delta p_{\text{max}} = k_F \tilde{I} / A$. However, not all of the actuator force is deposited as pressure in the fluid, as some is used to accelerate the plunger and membrane. These time-dependent losses are observed to enter the fluid equations as a hydraulic inductance M/A^2 and compliance A^2/k , which are both given in terms of the known quantities M , k and A . This compliance is a consequence of the spring behavior of the membrane, which arises because some of the coil force is required to elongate the membrane. Hence, the flow rate leaving the chamber is less than what would have been the case if no force were required to deflect the membrane. This, in the view of the microfluidics, is the same as a storage of volume inside the chamber, and it is therefore not surprising to find the membrane elasticity enter into the equations as another compliance in addition to C_{tent} .

The circuit diagram for the EC model of the pressure source is given in figure 5(b), and table 2 lists the values of the physical parameters. The membrane spring constant k was determined experimentally by fitting the model results to the experimental data in figure 4(b), and fair agreement is found. However, the width of the resonance peak in the experimental data around 350 Hz and the weak amplitude decrease above 50 Hz are not well reproduced by the model. These deviations can be explained by the simplifying assumption that the actuator membrane acts as a Hookean spring, but it is likely that it does in fact display a viscoelastic behavior, which would account for the large value of the observed damping.

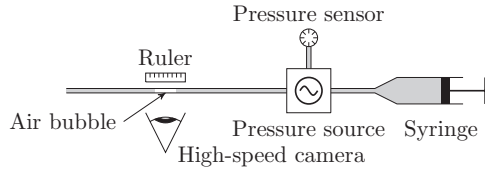


Figure 6. Schematic illustration of the experimental setup used for the proof of concept experiment.

Table 2. Physical parameters for the pressure source circuit model.

Symbol	Value
A	$7.61 \times 10^{-5} \text{ m}^2$
C_{tent}	$2.0 \times 10^{-13} \text{ m}^3 \text{ Pa}^{-1}$
k	$1.1 \times 10^4 \text{ N m}^{-1}$
k_F	2.7 V s m^{-1}
L_{el}	$2.1 \times 10^{-4} \text{ H}$
M	$8.64 \times 10^{-3} \text{ kg}$
R_{el}	2.4Ω

4. Experimental considerations

The proposed method is generic and thus applies to all systems exhibiting temporal dependence. For illustration, we study in the following the fairly complex physical system of a full water-filled system of interconnected elastic microfluidic tubes with a trapped air bubble driven by a pulsatile pressure difference. A schematic drawing of the system is given in figure 6. We will compare the experimental results to the predictions of a system-level EC model, with one unknown parameter, see section 7. We emphasize that even though the proof of concept study presented here involves an ac system, no such limitations apply to the method of using the pulsatile pressure source to deduce the time scales of a system.

The motion of gas bubbles in liquids has been studied extensively in the literature, see e.g. [30–35], but very few accounts using the EC approach have been found, e.g. Fuerstman *et al* [36].

4.1. Setup and method

A schematic illustration of the setup is shown in figure 6. A differential pressure sensor (Honeywell 40PC by Honeywell International Ltd, Morristown, NJ, USA) was connected to one of the three chamber outlets through a teflon tube ($\ell_{\text{sen}} = 4.1 \text{ cm}$, $a_{\text{sen}} = 0.125 \text{ mm}$, $h_{\text{sen}} = 0.669 \text{ mm}$) and a milli-Q water-filled 10 mL syringe (filled to 8.1 mL) to another of the outlets via a teflon tube of dimensions $\ell_{\text{syr}} = 17.5 \text{ cm}$, $a_{\text{syr}} = 0.125 \text{ mm}$ and $h_{\text{syr}} = 0.669 \text{ mm}$. A long transparent tube ($\ell = 42.9 \text{ cm}$, $a = 0.254 \text{ mm}$, $h = 0.540 \text{ mm}$) was connected to the last chamber outlet, allowing the tube to exit into an open reservoir. The bubble (relaxed axial length $\ell_{\text{bub}} = 1.35 \text{ cm}$) was placed in this tube, roughly halfway between the chamber and the tube outlet. A metric ruler was placed next to the tube and just above the bubble for scale.

The bubble motion was detected using a Photron Fastcam APX RS high-speed camera (Photron USA Inc., San Diego,

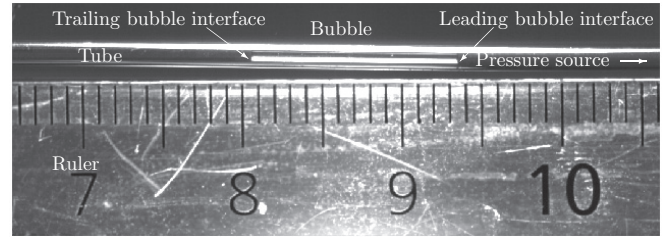


Figure 7. Example of a raw bubble image from the camera showing part of the tube exiting the pressure source chamber. The right end of the tube is connected to the pressure source while the left end exits into atmospheric conditions. The bubble is found roughly in the middle of the tube. A mm-scale ruler (numbers indicate centimeter) is positioned below the tube for scale.

CA, USA) fitted with a 1:2.8D lens (AF Micro Nikkor by Nikon Corp., Imaging Company, Tokyo, Japan), with dedicated Photron software used for storage. Individual gray scale images were framed at 1 kHz sampling rate and stored in tiff format, for a time interval comprising several oscillation periods. An example of an image is given in figure 7, where the pressure source found to the right of the photo. The bubble interface closest to the pressure source—the right-most interface in the photo—is termed the ‘leading interface’ while the interface the furthest away from the source is referred to as the ‘trailing bubble interface’.

The bubble position was adjusted using the syringe. Once in place and with a specified pressure frequency, the ac generator and camera were activated simultaneously. Images were taken for 6 s, after which the supply voltage to the pressure source was turned off. The experiment was conducted at the frequencies of 1 Hz, 30 Hz, 50 Hz and 100 Hz, and for each experiment, the pressure and the electric current driving the actuator were recorded.

4.2. Image processing

An image-processing routine has been developed in MATLAB to deduce the motion of the air–water interfaces of the bubble. Upon loading the raw tiff image and converting it to black/white (represented as 0 and 1, respectively), the routine searches for the first white pixel in a specified region by searching for the first pixel with value above 0.5. This first pixel of the bubble is approximately the position of the boundary. The position of this pixel is stored and the routine continues to the next image in the set. This analysis is done for both left and right bubble interface, and the positions of both interfaces are plotted versus time. A scale is found as the horizontal distance between 2 mm marks on the ruler in the first image of the set.

5. Experimental results

A bubble-relative reference frame, denoted by a subscript ‘rel’, is placed with the x -axis along the axis of the tube and with the origin at the bubble equilibrium position. The motion of the two bubble interfaces about this equilibrium position as

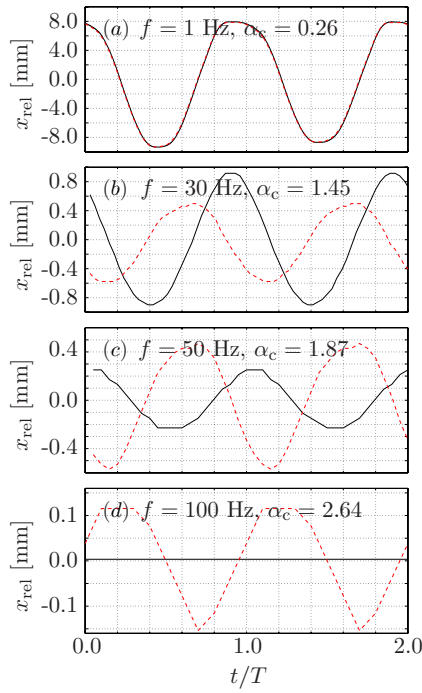


Figure 8. The measured motion of the leading (dashed line) and trailing (full line) air bubble boundaries about an equilibrium position as picked out by the image-processing routine at four different frequencies. The time axis has been normalized by the oscillation period T . Resistance dominates the pulsatile flow of liquid for $\alpha_c < 1$ while inertia dominates for $\alpha_c > 1$. The resonance indicated by the data is likely caused by the interplay of the compliance of the bubble and the inertia of the liquid.

picked out by the image-processing routine is given in figure 8 for all four frequencies. The critical Womersley number for the milli- Q water is given for all frequencies and it is observed that inertia dominates the water for all but the case of 1 Hz since $\alpha_c > 1$ for the former and $\alpha_c < 1$ for the latter.

The motion of both interfaces is approximately sinusoidal in the entire frequency range, and clearly so at the intermediate frequencies of $f = 30$ Hz and $f = 50$ Hz. The deviations at $f = 1$ Hz may be attributed to the fact that the plunger displacement at this frequency vastly exceeds the displacements at the following frequencies, so the assumed linear spring behavior of the membrane is no longer valid. At $f = 100$ Hz noticeable pixelation makes it somewhat difficult to see the sinusoidal motion of the interfaces.

The two interfaces move completely in phase at $f = 1$ Hz (hence the dashed line cannot be seen), but shifts in both phase and amplitude are found for all subsequent frequencies. At 30 Hz the trailing bubble interface has a larger amplitude than the leading interface, which is reversed at 50 Hz. At $f = 100$ Hz there is no motion of the trailing bubble interface. This sudden increase followed by a rapid decrease in amplitude coupled with a simultaneous change in phase lag from 0 through $\pi/2$ to π indicates a resonance near 30 Hz.

The pressure source stroke volumes can also be verified deduced from this simple experiment. The displacement of the air bubble ℓ_{disp} in either direction about its equilibrium position is due to the displacement of liquid. Thus, the stroke

Table 3. Elastic wave speeds for common tube materials used in experimental microfluidics, and stainless steel for comparison.

Material	Young's modulus (GPa)	Wave speed (m s^{-1})
Silicone rubber	0.002	1.75×10^2
Teflon	0.50	9.41×10^2
PEEK	3.60	2.38×10^3
Stainless steel	210	6.04×10^3

volume is $\mathcal{V} = \ell_{\text{disp}} \pi a_{\text{bub}}^2$. With $a_{\text{bub}} = 0.254$ mm, the stroke volume varies from about 2 mm^3 at $f = 1$ Hz to $\sim 0.03 \text{ mm}^3$ at $f = 100$ Hz. The stroke volume is above or close to the desired 0.1 mm^3 during the entire probed interval, and higher volumes can easily be achieved by increasing the electric power to the actuator.

5.1. EC interpretation of the observations

To interpret the observed resonance frequency at $f = 30$ Hz, the physical system of the bubble in the long, water-filled tube is analyzed as an electric RCL -circuit. Since inertia in the liquid dominates at 30 Hz ($\alpha_c = 1.45$) the observed resonance is believed to be of the LC -type with the dominating compliance stemming from the bubble. Using the regular expressions for inductance $L_{\text{hyd}} = \rho \ell / (\pi a^2)$ and isothermal compliance of an air bubble $C_{\text{hyd}} = \mathcal{V}_0 / p_0$ [8] where the subscript '0' indicates a reference state and $\mathcal{V}_0 = \ell_{\text{bub}} \pi a_{\text{bub}}^2$, we find

$$f = \frac{1}{2\pi \sqrt{L_{\text{hyd}} C_{\text{bub}}}} = 30.86 \text{ Hz.} \quad (16)$$

This is in good agreement with the experimental observation of $f \approx 30$ Hz, so the resonance is likely caused by the interplay of liquid inertia and bubble compliance. Also, this simple analysis indicates the strength of EC modeling in predicting system dynamics.

6. Compliance of elastic tubing

The system under consideration consists of interconnected elastic tubes of the circular cross section with sub-millimeter inner radius. To account for all temporal effects of the system in a system-level EC model, an expression for this elastic tube wall compliance is needed. This may be derived from the definition of compliance $C_{\text{hyd}} = d\mathcal{V}/dp$ [8], and the elastodynamic equation, see e.g. [37]. Under the assumption of radial displacements only, the elastic wave speeds of the wall displacements for common tube materials from experimental microfluidics are listed in table 3 based on data from [38, 39]. A typical tube has the wall thickness $h \sim 0.5$ mm, so changes in the pressure inside the tube will traverse the wall in $t \sim 3 \mu\text{s}$ for a silicone rubber tube, and faster for all other materials listed due to their higher wave speeds, so the wall can be considered quasi-static even for pressure oscillations in the kilohertz regime.

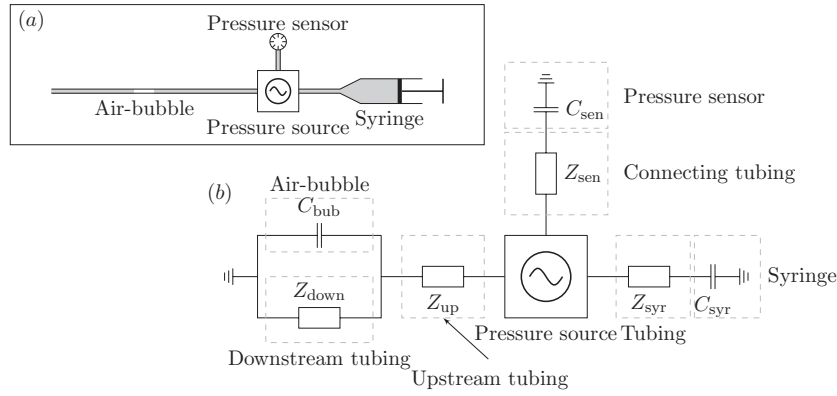


Figure 9. System-level EC model for the experiment. (a) The schematic representation of the setup shown for convenience. (b) The EC model of the full system.

The steady state tube wall displacement is [37]

$$u_r(r) = (1 + \sigma) \left[(1 - \sigma) + \frac{(a + h)^2}{r^2} \right] \frac{a^2}{(a + h)^2 - a^2} \frac{p}{E} r, \quad (17)$$

where E is Young's modulus and σ is Poisson's ratio. The volume increase associated with the displaced wall is $\mathcal{V} = 2\pi a \ell u_r(a)$. The compliance is then found as

$$C_{hyd} = \beta \frac{2\pi a^3 \ell}{Eh}, \quad (18)$$

with the non-dimensional constant β given by

$$\beta = \frac{a}{h + 2a} (1 + \sigma) \left[2(1 - \sigma) + 2\frac{h}{a} + \frac{h^2}{a^2} \right]. \quad (19)$$

The compliance of equation (18) applies to all anisotropic materials of all wall thicknesses. In the limit $h \ll a$ we find $\beta \approx 1 - \sigma^2$ with $\sigma^2 \approx 0$ since $0 \leq \sigma \leq 0.5$, so the wall compliance becomes $C_{hyd} = 2\pi a^3 \ell / (Eh)$. This is a well-known result used in several cases to model the arterial wall [40–44]. In the other limit of $h \gg a$, usually found in experimental microfluidics, the compliance becomes $C_{hyd} = 2\pi a^2 \ell (1 + \sigma) / E$, which is independent of the wall thickness h .

A typical teflon tube segment has the dimensions $\ell \sim 10^2$ mm, $h \sim 0.5$ mm and $a \sim 0.2$ mm, and since the Poisson ratio is $\sigma = 0.45$ the compliance of the tube is $C_{hyd} \sim 3 \times 10^{-17}$ m³ Pa⁻¹. The air bubble for this experiment has the rest volume $\mathcal{V}_0 = \ell_{bub} \pi a_{bub}^2$ which is $\mathcal{V}_{bub} \sim 3$ mm³ since $a_{bub} = 0.254$ mm, and the experiment was done at standard atmospheric conditions, so $p_0 \sim 10^5$ Pa. The compliance of this air bubble is then $C_{hyd} \sim 3 \times 10^{-14}$ m³ Pa⁻¹, which is three orders of magnitude greater than the compliance of the elastic wall. This latter may therefore be neglected when modeling the experiment.

7. System-level EC model

The full system-level model is summarized in figure 9, where the elastic walls have been neglected as just described. The numerical values of the circuit elements are easily obtained from equation (3) and $C_{hyd} = p_0 / \mathcal{V}_0$, but the compliance of

Table 4. Values for the EC elements of the model of the full system at $f = 1$ Hz.

Element	Value
C_{bub}	2.70×10^{-14} m ³ Pa ⁻¹
C_{syr}	3.61×10^{-13} m ³ Pa ⁻¹
Z_{down}	$1.23 \times 10^{12} + i 8.26 \times 10^9$ Pa s m ⁻³
Z_{sen}	$6.80 \times 10^{11} + i 1.11 \times 10^{11}$ Pa s m ⁻³
Z_{syr}	$1.83 \times 10^{12} + i 2.98 \times 10^{10}$ Pa s m ⁻³
Z_{up}	$1.36 \times 10^{12} + i 8.86 \times 10^9$ Pa s m ⁻³

the pressure sensor is difficult to determine from theoretical considerations. This compliance arises since the sensor detects pressure through the deflection of a silicon membrane. Hence, we choose to determine this compliance from the experiment by measuring both pressure in the sensor and actuator electric current, and fitting C_{sen} . In turn, this approach proves the applicability of the method to any undetermined compliance in a microfluidic system.

The syringe is connected to the pressure source chamber using the same teflon tubing as for the pressure sensor. In theory, the connecting tubing and the syringe should each be modeled using individual impedances and compliances; however, the syringe itself has a much larger radius than the tubing, so the syringe impedance may be neglected to a good approximation since $Z_{hyd} \propto a^{-2}$, but its compliance cannot since C_{hyd} of equation (18) depends on a^3 .

The imaged bubble is modeled as previously mentioned with $C_{bub} = \mathcal{V}_0 / p_0$ using $\mathcal{V}_0 = \ell_{bub} \pi a_{bub}^2$ for simplicity, although the axial length of the bubble is observed to change during experimentation for 30 Hz and 50 Hz. Given the level of approximation otherwise employed the deviations introduced by this simplification are negligible. The values of the circuit elements for $f = 1$ Hz are listed in table 4; the impedances of course change as they are frequency dependent.

The motion of the bubble interfaces are derived from the flow rates up and downstream of the bubble by noting that the volume and flow rate are related as $\mathcal{V} = \int Q(t) dt$ with $\mathcal{V} = x_{rel} \pi a^2$ using x_{rel} of section 5. The bubble-interface displacement amplitudes x_{rel}^{LI} (leading interface) and x_{rel}^{TI} (trailing interface) are given in terms of the applied electric

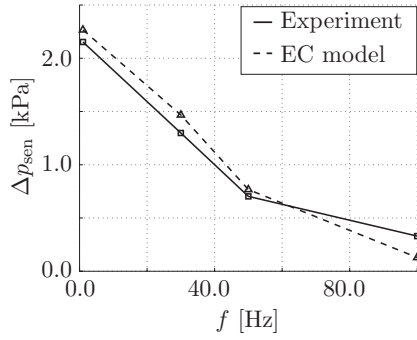


Figure 10. Sensor pressure difference used for determining the correct value of the sensor compliance by comparison of experimental and system-level EC model results. The figure shows the best fit which is found for the value $C_{\text{sen}} = 2.50 \times 10^{-14} \text{ m}^3 \text{ Pa}^{-1}$.

current amplitude \tilde{I} by

$$\tilde{x}_{\text{rel}}^{\text{LI}} = \frac{\frac{k}{i\omega A^2} + i\omega \frac{M}{A^2}}{Z_{\text{tot}}} \frac{1}{i\omega \pi a_{\text{bub}}^2} \frac{1}{Z_{\text{up}}} \frac{k_F \tilde{I}}{A}, \quad (20)$$

$$\begin{aligned} \tilde{x}_{\text{rel}}^{\text{TI}} &= \frac{\frac{k}{i\omega A^2} + i\omega \frac{M}{A^2}}{Z_{\text{tot}}} \frac{1}{i\omega \pi a_{\text{bub}}^2} \\ &\times \frac{1}{Z_{\text{down}} + Z_{\text{up}} + i\omega C_{\text{bub}} Z_{\text{down}} Z_{\text{up}}} \frac{k_F \tilde{I}}{A}, \end{aligned} \quad (21)$$

where the total system impedance Z_{tot} is

$$\begin{aligned} Z_{\text{tot}} &= \frac{k}{i\omega A^2} + i\omega \frac{M}{A^2} + \{i\omega C_{\text{tent}} \\ &+ [Z_{\text{syrr}} + (i\omega C_{\text{syrr}})^{-1}]^{-1} + [Z_{\text{sen}} + (i\omega C_{\text{sen}})^{-1}]^{-1} \\ &+ [Z_{\text{up}} + (i\omega C_{\text{bub}} + Z_{\text{down}}^{-1})^{-1}]^{-1}\}^{-1}. \end{aligned} \quad (22)$$

8. Comparison of system-level EC model and experiment

In order to compare the model and experimental results, the undetermined value of the pressure sensor compliance is first determined as follows: the pressure in the sensor is computed from the system-level model using the measured electric coil current as input, and then compared to the measured pressure in the same location. C_{sen} is tuned until the best agreement between experimental and model data is found at all probed frequencies, which turns out to be for $C_{\text{sen}} = 2.50 \times 10^{-14} \text{ m}^3 \text{ Pa}^{-1}$, see figure 10.

The results of the system-level EC model, given in figure 11, shows that the model correctly predicts the observed dynamics for all probed frequencies, while also giving the correct amplitudes and phase shift between the leading and trailing interfaces. The complex microfluidic system can thus be adequately modeled by EC theory.

The model captures the amplitudes of the oscillations of the leading interface better than the trailing interface, with some of the discrepancy at 1 Hz and 30 Hz attributed to the assumption of constant bubble length in the model although the experimental data suggests otherwise. The resolution of the images is $40.0 \mu\text{m}$ per pixel, so the discrepancy of

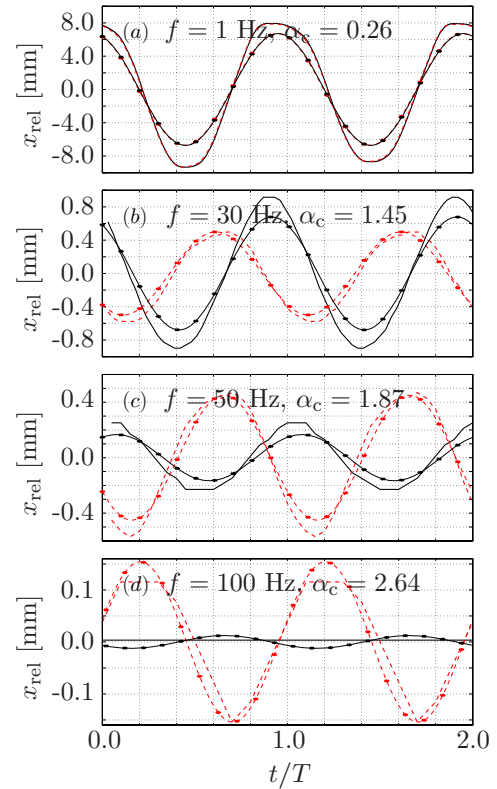


Figure 11. Comparison of experimental and model results for the motion of the leading (dashed) and trailing (solid) air bubble interfaces at four frequencies. The time axis is normalized by the oscillation period T . The experimental results (thick lines) and model results (thin and starred lines) show very good agreement for all four frequencies.

the trailing interface at 100 Hz is below this threshold and the motion predicted by the model cannot be ruled out. Furthermore, the existence of a resonance around 30 Hz observed experimentally and further suggested from the simplest circuit analysis is also captured by the system-level model.

9. Concluding remarks

In conclusion, we have proposed the use of pulsatile microfluidics as an analytical tool leading to understanding and determination of the transient time scales of any microfluidic system. A novel pressure source has been fabricated and tested. It resolves the appropriate frequency range for most such systems, while still delivering stroke volumes of $\mathcal{V} \sim 0.1 \text{ mm}^3$.

As a proof of concept, pulsatile kilohertz microfluidics has been applied to a full system of interconnected and milli- Q water-filled elastic tubes of sub-millimeter radius containing a trapped air bubble, and good agreement between an equivalent circuit theory model and the experimental results have been found. Moreover, the predictive capabilities of the equivalent circuit model have been demonstrated by deducing an unknown compliance from the comparison of model results and experimental data.

Although the method suggested in this paper is directly analogous to the approaches of experimental electric circuit analysis, its realization is substantially more cumbersome. This is due to the scaling of fluid inertia and the (unexpected) scaling of fluid resistance with driving frequency, which combine to make pulsatile microfluidics into the low-kilohertz range with stroke volumes of $V \sim 0.1 \text{ mm}^3$ very difficult to produce. However, the prospect of microfluidic systems with application-tuned dynamic time scales and the just mentioned difficulties of experimentally conducting system-level circuit analysis only emphasize the need for analytical tools like the one presented here.

Acknowledgments

The help of Henrik Ljunggren is recognized with the design and fabrication of the pressure source, and the help of Ulrik Ullum is recognized with the photographic setup of section 4.1. Both are of Novo Nordisk A/S, Hillerød, Denmark. SV was supported by Novo Nordisk A/S and grant no 2106-08-0018 'ProCell', under the Programme Commission on Strategic Growth Technologies, the Danish Agency for Science, Technology and Innovation.

References

- [1] Thorsen T, Maerkl S and Quake S R 2002 *Science* **298** 580
- [2] Olsson A, Stemme G and Stemme E 1999 *J. Micromech. Microeng.* **9** 34
- [3] Brask A, Snackenborg D, Kutter J P and Bruus H 2006 *Lab Chip* **6** 280
- [4] Leslie D L, Easley C J, Seker E, Karlinsey J M, Utz M, Begley M R and Landers J P 2009 *Nat. Phys.* **5** 231
- [5] Mortensen N A and Bruus H 2006 *Phys. Rev. E* **74** 017301
- [6] Morris C J and Forster F K 2004 *Exp. Fluids* **36** 928
- [7] Bourouina T and Grandchamp J-P 1996 *J. Micromech. Microeng.* **6** 398
- [8] Bruus H 2008 *Theoretical Microfluidics* (Oxford: Oxford University Press)
- [9] Kim D, Chesler N C and Beebe D J 2006 *Lab Chip* **6** 639
- [10] Zengerle R and Richter M 1994 *J. Micromech. Microeng.* **4** 192
- [11] Brask A, Goranović G and Bruus H 2003 *Sensors Actuators B* **92** 127
- [12] Vedel S 2009 *Master's Thesis* Technical University of Denmark available online at www.nanotech.dtu.dk/microfluidics
- [13] Geng X, Yuan H, Oğuz H N and Prosperetti A 2001 *J. Micromech. Microeng.* **11** 270
- [14] Tsai J H and Lin L 2002 *J. Microelectromech. Syst.* **11** 665
- [15] van der Wijngaart W, Chugh D, Man E, Melin J and Stemme G 2007 *J. Microelectromech. Syst.* **16** 765
- [16] Xu W, Wu L L, Zhang Y, Xue H, Li G P and Bachman M 2009 *Sensors Actuators B* **142** 355
- [17] de Jong J, de Bruin G, Reinten H, van der Berg M, Wijshoff H, Versluis M and Lohse D 2006 *J. Acoust. Soc. Am.* **120** 1257
- [18] Satoh W, Shimizu Y, Kaneto T and Suzuki H 2006 *Sensors Actuators B* **123** 1153
- [19] Maxwell R B, Gerhardt A L, Toner M, Gray M L and Schmidt M A 2003 *J. Microelectromech. Syst.* **12** 630
- [20] Hua S Z, Sachs F, Yang D X and Chopra H P 2002 *Anal. Chem.* **74** 6392
- [21] Womersley J R 1955 *J. Physiol.* **127** 553
- [22] Crandall I B 1926 *Theory of Vibrating Systems and Sound* (New York: D Van Nostrand Comp., Inc.)
- [23] Sexl T 1930 *Z. Phys.* **61** 349
- [24] Lambossy P 1952 *Helv. Phys. Acta* **25** 371
- [25] Uchida S 1956 *Z. Angew. Math. Phys.* **7** 403
- [26] Richardson E G 1928 *Proc. Phys. Soc. Lond.* **40** 206
- [27] Sheen H J, Hsu C J, Wu T W, Chang C C, Chu H C, Yang C Y and Lei U 2008 *Microfluid. Nanofluid.* **4** 331
- [28] Gilbertson R G and Busch J D 1996 *J. Br. Interplanet. Soc.* **49** 129
- [29] Laser D J and Santiago J G 2004 *J. Micromech. Microeng.* **14** R35
- [30] Bretherton F 1961 *J. Fluid Mech.* **10** 166
- [31] Park C-W and Homsy G M 1984 *J. Fluid Mech.* **139** 291
- [32] Schwartz L W, Princen H M and Kiss A D 1986 *J. Fluid Mech.* **172** 259
- [33] Ratulowski J and Chang H-C 1989 *Phys. Fluids A* **1** 1642
- [34] Chio H, Jensen M J, Wang X, Bruus H and Attinger D 2006 *J. Micromech. Microeng.* **16** 143
- [35] Brennen C E 1995 *Cavitation and Bubble Dynamics* (New York: Oxford University Press)
- [36] Fuerstman M J, Lai A, Thurlow M E, Shevkoplyas S S, Stone H A and Whitesides G M 2007 *Lab Chip* **7** 1479
- [37] Landau L D and Lifshitz E M 1986 *Theory of Elasticity (A Course of Theoretical Physics vol 7)* 3rd edn (Oxford: Pergamon)
- [38] Sundström B (ed) 1999 *Handbok och formelsamling i Hållfasthetslära* 2nd edn (Stockholm: Institutionen för hållfasthetslära, KTH)
- [39] Osswald T A, Baur E, Brinkmann S, Oberbach K and Schmachtenberg E 2006 *International Plastics Handbook* (Munich: Carl Hanser)
- [40] Womersley J R 1957 *Tech. Rep.* Wright Air Development Center 56-614
- [41] Morgan G W and Kiely J P 1954 *J. Acoust. Soc. Am.* **26** 323
- [42] Morgan G W and Ferrante W R 1955 *J. Acoust. Soc. Am.* **27** 715
- [43] Moens A I 1878 *Die Pulscurve* (Leiden: Brill)
- [44] Korteweg D J 1878 *Ann. Phys. Chem. (NS)* **5** 52

Appendix E

Paper published in the Journal of Fluid Mechanics

Title: Transient Taylor–Aris dispersion of time-dependent flows in straight channels

Authors: Søren Vedel and Henrik Bruus.

Reference: Published in the Journal of Fluid Mechanics **691**, 95-122 (2012) (28 pages)

Transient Taylor–Aris dispersion for time-dependent flows in straight channels

Søren Vedel[†] and Henrik Bruus

Department of Micro- and Nanotechnology, Technical University of Denmark,
DTU Nanotech Building 345 B, DK-2800 Kongens Lyngby, Denmark

(Received 23 December 2010; revised 1 July 2011; accepted 6 October 2011;
first published online 2 December 2011)

Taylor–Aris dispersion, the shear-induced enhancement of solute diffusion in the flow direction of the solvent, has been studied intensely in the past half century for the case of steady flow and single-frequency pulsating flows. Here, combining Aris’s method of moments with Dirac’s bra–ket formalism, we derive an expression for the effective solute diffusivity valid for transient Taylor–Aris dispersion in any given time-dependent, multi-frequency solvent flow through straight channels. Our theory shows that the solute dispersion may be greatly enhanced by the time-dependent parts of the flow, and it explicitly reveals how the dispersion coefficient depends on the external driving frequencies of the velocity field and the internal relaxation rates for mass and momentum diffusion. Although applicable to any type of fluid, we restrict the examples of our theory to Newtonian fluids, for which we both recover the known results for steady and single-frequency pulsating flows, and find new, richer structure of the dispersion as function of system parameters in multi-frequency systems. We show that the effective diffusivity is enhanced significantly by those parts of the time-dependent velocity field that have frequencies smaller than the fluid momentum diffusion rate and the solute diffusion rate.

Key words: general fluid mechanics, particle/fluid flows

1. Introduction

In his seminal work Taylor (1953) clarified the basic physical principles for the dispersion of the concentration profiles of solutes in a steady Poiseuille flow: the shear from the solvent flow acts to increase the dispersion, or effective diffusivity, of the solute in the direction of the flow. For a channel with a circular cross-section of radius a , he derived the now classical expression for the effective diffusivity $D_{\text{eff}} = (1 + Péc^2/48)D$, where $Péc = aU_o/D$ is the Péclet number for the system, U_o being the average solvent flow speed and D the solute molecular diffusivity. This work was extended to a wider range of Péclet numbers and geometries by Aris (1956) using the elegant method of statistical moments. Many other aspects of shear-enhanced solute dispersion in steady flows have since been studied in the literature, including buoyancy and channel curvature (Erdogan & Chatwin 1967), interphase mass transfer (Sankarasubramanian & Gill 1973), transient phenomena (Chatwin 1977), effects of walls in three-dimensional dispersion (Doshi, Daiya &

[†] Email address for correspondence: soren.vedel@nanotech.dtu.dk

Gill 1978), a stochastic description (van den Broeck 1982), influence of channel aspect ratio (Chatwin & Sullivan 1982), and generalized dispersion of mass, energy and momentum in unbounded systems (Brenner & Edwards 1993; Goddard 1993). Taylor dispersion is now textbook material (Brenner & Edwards 1993; Probstein 1994; Bird, Stewart & Lightfoot 2006).

Even today shear-flow-enhanced dispersion is studied actively as illustrated by the recent analyses of D_{eff} in transient anomalous diffusion of point discharges (Latini & Bernoff 2001), in electro-osmotic flow with random zeta potentials (Gleeson 2002), in steady flows in a wide class of channel cross-sections (Ajdari, Bontoux & Stone 2006; Bontoux *et al.* 2006; Dutta, Ramachandran & Leighton 2006), in harmonically oscillating Couette–Poiseuille flows (Paul & Mazumder 2008), in steady Poiseuille flows using a Brownian-motion approach (Camassa, Lin & McLaughlin 2010) and in steady, non-Newtonian fluid flow (Vikhansky & Wang 2011).

In many practical applications (Skafte-Pedersen *et al.* 2009; Vedel, Olesen & Bruus 2010) flows are unsteady and therefore typically generate more shear than their steady counterparts. The chemical engineering community has long recognized that increased mass transfer can be achieved by pulsating the flow, see e.g. Taylor & Leonard (1965) and Molloy & Leighton (1998), but many physical interpretations and quantitative aspects of this additional shear remains to be investigated theoretically. This is surprising given that the first investigation of Taylor dispersion in time-dependent flows dates back to Aris (1960) and its generalization by Brenner & Edwards (1993), and also given the large volume of studies dedicated to steady flows. Time-dependent phenomena that have been studied are non-transient, single-frequency pulsating flows (Harris & Goren 1967; Chatwin 1975; Watson 1983; Thomas & Narayanan 2001; Jansons 2006), the first examples of transient-flow analysis of single-frequency flows by Mazumder and coworkers (Mukherjee & Mazumder 1988; Bandyopadhyay & Mazumder 1999), and dispersion in a time-dependent flow in an unbounded system (Leighton 1989).

Here, we go beyond the previous results on dispersion in single-frequency flows and study any given time-dependent laminar flow in a straight channel of any constant cross-sectional shape, in particular relevant for microfluidic systems. Based on Aris's scheme we derive a general and compact expression for the transient, effective Taylor–Aris diffusivity $D_{eff}(t)$ with explicit dependence on the externally applied flow frequencies $\ell\omega_o$ and the internal relaxation rates λ_1 and α_{fl} for solute mass diffusion and solvent momentum diffusion, respectively. We show that D_{eff} is enhanced significantly by those frequency-components of the time-dependent velocity field which have an oscillation frequency smaller than any relaxation rate of the system, and thus provide enough time for the solute to equilibrate. We further show how this enhancement is diminished each time a frequency is increased and becomes larger than a given relaxation rate. Moreover, for the start-up of a Poiseuille flow, which includes any flow frequency, we find that the transient time of D_{eff} is determined by the slowest of the relaxation processes, i.e. the maximum of $1/\lambda_1$ and $1/\alpha_{fl}$. Finally, we demonstrate the practical usefulness of our theory as a design tool by characterizing the dispersion generated by a microfluidic, peristaltic pump.

2. The physical model and Aris's method of moments

In the following we establish our physical model together with our notation and present the well-known method of moments for calculating the dispersion coefficient D_{eff} . We consider a long, straight channel parallel to the x -axis, and assume that it is

translational invariant along this axis with an arbitrary, but constant, cross-section Ω . The coordinates in the transverse yz -plane are denoted $\mathbf{r}_\perp = (y, z)$, so that the full coordinates are written as $\mathbf{r} = (x, \mathbf{r}_\perp)$, and likewise for the gradient operator ∇ and the Laplace operator ∇^2 ,

$$\mathbf{r} = (x, \mathbf{r}_\perp) \quad \text{with } \mathbf{r}_\perp = (y, z), \quad (2.1a)$$

$$\nabla = \mathbf{e}_x \partial_x + \nabla_\perp \quad \text{with } \nabla_\perp = \mathbf{e}_y \partial_y + \mathbf{e}_z \partial_z, \quad (2.1b)$$

$$\nabla^2 = \partial_x^2 + \nabla_\perp^2 \quad \text{with } \nabla_\perp^2 = \partial_y^2 + \partial_z^2. \quad (2.1c)$$

The channel has length \mathcal{L} , cross-sectional area $\mathcal{A} = \int_\Omega d\mathbf{r}_\perp$ and volume $\mathcal{V} = \mathcal{L}\mathcal{A}$. Our analysis involves expansion of the spatial dependence of functions into linear combinations of suitably chosen basis functions. For notational convenience we shall therefore rely on a Hilbert-space representation using the compact Dirac bra–ket notation, employed more often in quantum mechanics (Dirac 1981) than in fluid mechanics (Bruus 2008; Mortensen, Olesen & Bruus 2006; Mortensen & Bruus 2006). For any pair of functions $f(x, \mathbf{r}_\perp, t)$ and $g(x, \mathbf{r}_\perp, t)$ represented by the bra $\langle f|$ and the ket $|g\rangle$, the inner product $\langle f|g\rangle$, is defined by the integral, where the asterisk indicates complex conjugation,

$$\langle f|g\rangle = \frac{1}{\mathcal{V}} \int_{-\mathcal{L}/2}^{\mathcal{L}/2} dx \int_\Omega d\mathbf{r}_\perp f^*(x, \mathbf{r}_\perp, t) g(x, \mathbf{r}_\perp, t). \quad (2.2)$$

This definition also includes the case where the involved functions only depend on the transverse coordinates \mathbf{r}_\perp . For $f_\perp(\mathbf{r}_\perp, t)$ and $g_\perp(\mathbf{r}_\perp, t)$ we obtain

$$\langle f_\perp|g_\perp\rangle = \frac{1}{\mathcal{A}} \int_\Omega d\mathbf{r}_\perp f_\perp^*(\mathbf{r}_\perp, t) g_\perp(\mathbf{r}_\perp, t), \quad (2.3)$$

as the x -integration trivially gives unity. Details and useful properties of the bra–ket notation are given in [Appendix](#).

From now on we use dimensionless quantities defined in terms of the characteristic transverse length L_o , often the shortest distance a from the centre line of the channel to the wall, the diffusion time T_o from the molecular diffusivity D of the solute, the advection velocity U_o from a scale U_{char} in the time-dependent flow, and the average solute concentration C_o of the solute concentration field $c(x, \mathbf{r}_\perp, t)$,

$$L_o = a, \quad T_o = \frac{L_o^2}{D}, \quad U_o = U_{char}, \quad C_o = \langle 1|c(x, \mathbf{r}_\perp, 0)\rangle. \quad (2.4)$$

The specific choice of U_{char} in (2.4) is not unique: for a steady flow it could be taken as the mean velocity; for a single-frequency oscillating flow as the root mean square (r.m.s.) velocity. See [Appendix](#) for a list of symbols.

Denoting the base angular frequency of the solvent flow $\tilde{\omega}_o$ (rad s^{−1}), the system is characterized by three dimensionless numbers: the Péclet number $Pé$ (the ratio of advection speed to mass diffusion speed), the Schmidt number Sc (the ratio of momentum diffusion speed to mass diffusion speed) and the Womersley number Wo (the square root of the ratio of oscillation speed at frequency $\tilde{\omega}_o$ to momentum diffusion speed for a Newtonian fluid of kinematic viscosity ν),

$$Pé = \frac{L_o U_o}{D}, \quad Sc = \frac{\nu}{D}, \quad Wo = \sqrt{\frac{L_o^2 \tilde{\omega}_o}{\nu}}. \quad (2.5)$$

For non-Newtonian fluids with an internal molecular stress relaxation time τ_{mol} , the Deborah number $De = \tau_{mol}\omega_o$ would appear, but this is not treated in this work.

2.1. The time-dependent velocity field

We take the velocity field to be any axis-parallel channel flow $\mathbf{v} = u(\mathbf{r}_\perp, t)\mathbf{e}_x$, and represent $u(\mathbf{r}_\perp, t)$ by a standard Fourier series with components u_ℓ for each higher harmonic $\ell\omega_o$ (ℓ being an integer) in the dimensionless base frequency $\omega_o = \tilde{\omega}_o T_o = Wo^2 Sc$,

$$u(\mathbf{r}_\perp, t) = \sum_{\ell=-\infty}^{\infty} u_\ell(\mathbf{r}_\perp) e^{i\ell\omega_o t}, \quad (2.6)$$

where complex notation is introduced for the time with $i = \sqrt{-1}$. By demanding that $u_{-\ell}(\mathbf{r}_\perp) = u_\ell^*(\mathbf{r}_\perp)$, we ensure that the velocity field is real (Brenner & Edwards 1993).

The fluid responds to changes in external conditions on a time scale which depends on its internal stress relaxation time, and whether fluid inertia dominates may be estimated by the product of the driving frequency $\tilde{\omega}_o$ and this internal time scale. For Newtonian fluids the stress relaxation time scale is given by the momentum diffusion time $1/\alpha_{fl}$, related to the momentum diffusion rate α_{fl} , which is derived from the momentum diffusion equation $\partial_t u = Sc \nabla_\perp^2 u$ and given by

$$\alpha_{fl} \propto Sc \quad (2.7)$$

with a geometry-dependent proportionality factor. Note that since $\alpha_{fl} \propto Sc$, the square of the Womersley number is proportional to the ratio of the dimensionless driving frequency ω_o and the momentum diffusion equilibration rate,

$$Wo^2 = \frac{\omega_o}{Sc} \propto \frac{\omega_o}{\alpha_{fl}}. \quad (2.8)$$

2.2. Dispersion and the advection–diffusion equation

The transport of the diffusive solute concentration c in the above-mentioned velocity field is given by the dimensionless advection–diffusion equation,

$$\partial_t c(x, \mathbf{r}_\perp, t) + P\acute{e} u(\mathbf{r}_\perp, t) \partial_x c(x, \mathbf{r}_\perp, t) = (\partial_x^2 + \nabla_\perp^2) c(x, \mathbf{r}_\perp, t). \quad (2.9)$$

The corresponding boundary conditions are

$$\mathbf{n} \cdot \nabla_\perp c = 0, \text{ on all walls,} \quad (2.10a)$$

$$c(x, \mathbf{r}_\perp, 0) = \tilde{c}(x, \mathbf{r}_\perp), \quad (2.10b)$$

$$x^s \partial_x^q c \rightarrow 0, \quad \text{for } |x| \rightarrow \frac{\mathcal{L}}{2} \text{ and } s, q = 0, 1, 2, \dots, \quad (2.10c)$$

where \mathbf{n} is the surface normal and \tilde{c} is a given initial concentration field, and condition (2.10c) states that all spatial gradients in c as well as c itself vanish far away along the axis of the channel.

Using Aris's method of moments the effective diffusivity $D_{eff}(t)$ is defined by the time derivative of the axial variance $\mu_2(t) = \langle (x - \bar{x})^2 | c \rangle$ of the solute distribution, $\bar{x}(t) = M_1(t)$ being the centre of mass (A 5b), and may be computed as (Aris 1956, 1960; Chatwin 1975; Barton 1983; Mukherjee & Mazumder 1988; Brenner

& Edwards 1993)

$$D_{\text{eff}}(t) = \frac{1}{2} \frac{d\mu_2(t)}{dt} = \frac{1}{2} \frac{dM_2}{dt} - M_1 \frac{dM_1}{dt}, \quad (2.11)$$

where the p th full moment $M_p(t)$ of the solute concentration field $c(x, \mathbf{r}_\perp, t)$ and the associated axial moment $c_p(\mathbf{r}_\perp, t)$ are defined by

$$M_p(t) = \langle x^p | c \rangle = \frac{1}{\mathcal{A}} \int_{\Omega} d\mathbf{r}_\perp c_p(\mathbf{r}_\perp, t), \quad p = 0, 1, 2, \dots, \quad (2.12a)$$

$$c_p(\mathbf{r}_\perp, t) = \frac{1}{\mathcal{L}} \int_{-\mathcal{L}/2}^{\mathcal{L}/2} dx x^p c(x, \mathbf{r}_\perp, t), \quad p = 0, 1, 2, \dots \quad (2.12b)$$

The derivation of (2.11) is sketched in Appendix, where we also show that the moments $c_p(\mathbf{r}_\perp, t)$ and $M_p(t)$ evolve according to the recursive equations of motion,

$$\partial_t c_p(\mathbf{r}_\perp, t) - \nabla_\perp^2 c_p(\mathbf{r}_\perp, t) = p(p-1) c_{p-2}(\mathbf{r}_\perp, t) + P\acute{e} u(\mathbf{r}_\perp, t) p c_{p-1}(\mathbf{r}_\perp, t), \quad p = 0, 1, 2, \dots, \quad (2.13a)$$

$$\frac{dM_p(t)}{dt} = p(p-1) \langle 1 | c_{p-2} \rangle + P\acute{e} p \langle u | c_{p-1} \rangle, \quad p = 0, 1, 2, \dots, \quad (2.13b)$$

with the boundary and initial conditions

$$\mathbf{n} \cdot \nabla_\perp c_p = 0 \quad \text{on all walls}, \quad (2.14a)$$

$$c_p(\mathbf{r}_\perp, t) < \infty, \quad (2.14b)$$

$$c_p(\mathbf{r}_\perp, 0) = \tilde{c}_p(\mathbf{r}_\perp), \quad (2.14c)$$

$$M_p(0) = \langle x^p | \tilde{c} \rangle. \quad (2.14d)$$

The main goal of this paper is to solve (2.11) for general time-dependent flows in straight channels of arbitrary, constant cross-section, and to study how D_{eff} depends on the physical frequencies and relaxation rates of the systems.

3. Dispersion for multiple-frequency flow

The solution procedure of the problem was introduced by Barton (1983) for steady flows and later extended to also include single-frequency harmonic pulsatile flows by Mukherjee & Mazumder (1988). The expressions presented in this section generalize their results to any given time-dependent flow. We derive them using the more compact bra–ket formalism as follows: from (2.13a) with $p = 0$ and 1 we determine the axial moment $c_o(\mathbf{r}_\perp, t)$ and subsequently $c_1(\mathbf{r}_\perp, t)$. With these at hand, the full moment M_1 as well as the time derivatives dM_1/dt and dM_2/dt can be obtained from (2.13b) with $p = 1$ and 2, which then are fed into (2.11) to determine D_{eff} .

3.1. The zeroth axial moment and basis functions

We begin by analysing the $p = 0$ axial moment (2.13a) for $c_o(\mathbf{r}_\perp, t)$,

$$(\partial_t - \nabla_\perp^2) | c_o(\mathbf{r}_\perp, t) \rangle = 0. \quad (3.1)$$

This moment fulfills the Neumann boundary condition

$$\mathbf{n} \cdot \nabla_\perp c_o = 0 \quad \text{on all walls}, \quad (3.2)$$

and has the initial condition

$$c_o(\mathbf{r}_\perp, 0) = \tilde{c}_0(\mathbf{r}_\perp) = \int_{-\mathcal{L}/2}^{\mathcal{L}/2} dx \tilde{c}(x, \mathbf{r}_\perp). \quad (3.3)$$

Using separation of variables, the solution for $c_o(\mathbf{r}_\perp, t)$ can be written as the expansion

$$|c_o(\mathbf{r}_\perp, t)\rangle = \sum_{n=0}^{\infty} a_{0n} e^{-\lambda_n t} |f_n(\mathbf{r}_\perp)\rangle, \quad (3.4)$$

where the time-independent eigenfunctions $f_n(\mathbf{r}_\perp)$ with eigenvalues λ_n are defined by

$$(\lambda_n + \nabla_\perp^2) |f_n(\mathbf{r}_\perp)\rangle = 0, \quad n = 0, 1, 2, \dots, \quad (3.5a)$$

$$\mathbf{n} \cdot \nabla_\perp |f_n(\mathbf{r}_\perp)\rangle = 0 \quad \text{on all walls}, \quad (3.5b)$$

and form a complete orthonormal basis in the sense of (A 3). Note that the lowest $n = 0$ eigenvalue is zero, $\lambda_0 = 0$, with eigenfunction unity, $f_0(\mathbf{r}_\perp) = 1$, while for $n > 0$ the eigenvalues are positive, $\lambda_n > 0$. We remark that although the general advection–diffusion problem (2.9) is non-Hermitian, the reduced, transverse problem (3.5) is Hermitian, and we can take full advantage of the Dirac Hilbert-space formulation.

The expansion coefficients a_{0m} are found by multiplying (3.4) at $t = 0$ by $\langle f_m |$,

$$a_{0m} = \langle f_m | \tilde{c}_0 \rangle, \quad m = 0, 1, 2, \dots \quad (3.6)$$

For infinite time, all terms in (3.4) except $n = 0$ decay exponentially, and we obtain

$$|c_o(\mathbf{r}_\perp, \infty)\rangle = a_{00} |f_0(\mathbf{r}_\perp)\rangle = \langle 1 | \tilde{c}_0 \rangle |1\rangle = |1\rangle, \quad (3.7)$$

representing the state where, by diffusion, the solute concentration has spread out uniformly in space.

3.2. The first axial moment and basis functions

The $p = 1$ axial moment equation (2.13a) for $c_1(\mathbf{r}_\perp, t)$ is analysed in a similar manner. Using that $c_o(\mathbf{r}_\perp, t)$ is now a known function, we have

$$(\partial_t - \nabla_\perp^2) |c_1(\mathbf{r}_\perp, t)\rangle = P \acute{e} u(\mathbf{r}_\perp, t) |c_o(\mathbf{r}_\perp, t)\rangle = P \acute{e} u(\mathbf{r}_\perp, t) \sum_{n=0}^{\infty} a_{0n} e^{-\lambda_n t} |f_n(\mathbf{r}_\perp)\rangle, \quad (3.8a)$$

where c_1 fulfills the Neumann boundary condition

$$\mathbf{n} \cdot \nabla_\perp c_1 = 0 \quad \text{on all walls}, \quad (3.8b)$$

and the initial condition

$$c_1(\mathbf{r}_\perp, 0) = \tilde{c}_1(\mathbf{r}_\perp) = \int_{-\mathcal{L}/2}^{\mathcal{L}/2} dx x \tilde{c}(x, \mathbf{r}_\perp). \quad (3.8c)$$

As pointed out by Barton (1983), solving the inhomogeneous partial differential equation (3.8a) for c_1 requires some care regarding the null space of the differential operator $(\partial_t - \nabla_\perp^2)$. Using the time Fourier expansion equation (2.6) of the velocity field $u(\mathbf{r}_\perp, t)$, we see that, due to the time-independent $\ell = 0$ component of u , the right-hand side of (3.8a) contains terms of the form $P \acute{e} a_{0n} u_0(\mathbf{r}_\perp) e^{-\lambda_n t} |f_n\rangle$, which have

non-zero overlap with kets of the form $e^{-\lambda_n t}|f_n\rangle$. Noting that

$$(\partial_t - \nabla_\perp^2)[e^{-\lambda_n t}|f_n\rangle] = 0, \quad (3.9a)$$

$$(\partial_t - \nabla_\perp^2)[te^{-\lambda_n t}|f_n\rangle] = e^{-\lambda_n t}|f_n\rangle, \quad (3.9b)$$

we thus expand $c_1(\mathbf{r}_\perp, t)$ in terms of both $e^{-\lambda_n t}|f_n\rangle$ and $te^{-\lambda_n t}|f_n\rangle$, and seek solutions of $|c_1(\mathbf{r}_\perp, t)\rangle$ of the form

$$|c_1\rangle = P\dot{e} \sum_{n=0}^{\infty} [(\gamma_{1n}a_{0n}t + a_{1n})|f_n\rangle + a_{0n}|\phi_n\rangle]e^{-\lambda_n t}, \quad (3.10)$$

where the unknown coefficients, γ_{1n} and a_{1n} , as well as the unknown time-dependent ket $|\phi_n(\mathbf{r}_\perp, t)\rangle$ are determined in the following. Inserting this trial expansion of $|c_1(\mathbf{r}_\perp, t)\rangle$ into the equation of motion (3.8a) leads to

$$(\partial_t - \nabla_\perp^2 - \lambda_n)|\phi_n(\mathbf{r}_\perp, t)\rangle = [u(\mathbf{r}_\perp, t) - \gamma_{1n}]|f_n(\mathbf{r}_\perp)\rangle. \quad (3.11)$$

The unknown ket $|\phi_n(\mathbf{r}_\perp, t)\rangle$ is now expanded in a Fourier series in time and a $|f_m(\mathbf{r}_\perp)\rangle$ series in space,

$$|\phi_n(\mathbf{r}_\perp, t)\rangle = \sum_{\ell=-\infty}^{\infty} \sum_{m=0}^{\infty} \beta_{mn}^\ell e^{i\ell\omega_o t} |f_m(\mathbf{r}_\perp)\rangle, \quad (3.12)$$

which upon insertion into (3.11) followed by multiplication by $\langle f_k|$ results in the following matrix equation for the coefficients β_{kn}^ℓ ,

$$(\lambda_k - \lambda_n + i\ell\omega_o)\beta_{kn}^\ell = \langle f_k|u_\ell|f_n\rangle - \gamma_{1n}\delta_{\ell,0}\delta_{k,n}. \quad (3.13)$$

Here, we see that the special case of the time-independent term $\ell = 0$, together with the diagonal term $k = n$, only allows a solution if we choose

$$\gamma_{1n} = \langle f_n|u_0(\mathbf{r}_\perp)|f_n\rangle, \quad (3.14)$$

while the β coefficients are given by

$$\beta_{kn}^\ell = (1 - \delta_{\ell,0}\delta_{k,n}) \frac{\langle f_k|u_\ell(\mathbf{r}_\perp)|f_n\rangle}{\lambda_k - \lambda_n + i\ell\omega_o}. \quad (3.15)$$

Note that any value of β_{nn}^0 is allowed, so for convenience we set it to zero. Moreover, $\beta_{kn}^{-\ell} = (\beta_{kn}^\ell)^*$ ensures real values of the resulting fields.

Finally, the coefficients a_{1n} are found using the initial condition (3.8c) in (3.10) at $t = 0$, multiplying by $\langle f_k|$, and finally exchanging the indices n and k ,

$$a_{1n} = \frac{1}{P\dot{e}} \langle f_n|\tilde{c}_1(\mathbf{r}_\perp)\rangle - \sum_{k=0}^{\infty} a_{0k} \sum_{l=-\infty}^{\infty} \beta_{nk}^l. \quad (3.16)$$

Collecting all terms, we write the formal solution as

$$|c_1(\mathbf{r}_\perp, t)\rangle = P\dot{e} \sum_{m=0}^{\infty} \sum_{n=0}^{\infty} \left[(a_{0n}\gamma_{1n}t + a_{1n})\delta_{n,m} + a_{0n} \left(\sum_{\ell=-\infty}^{\infty} \beta_{mn}^\ell e^{i\ell\omega_o t} \right) \right] e^{-\lambda_n t} |f_m\rangle. \quad (3.17)$$

3.3. Expressions for the effective diffusivity

The effective diffusivity $D_{\text{eff}} = (1/2)(dM_2/dt) - M_1(dM_1/dt)$ can now be expressed in terms of a basis function expansion. The time derivative $dM_1/dt = P\acute{e} \langle u|c_o \rangle$ of the full moment M_1 in (2.13b) becomes

$$\frac{dM_1}{dt} = P\acute{e} \sum_{n=0}^{\infty} \sum_{\ell=-\infty}^{\infty} a_{0n} \langle u_{\ell}|f_n \rangle e^{-(\lambda_n + i\ell\omega_o)t}, \quad (3.18a)$$

where we have used (A 2b) for the phase factor. By proper choice of the coordinate system, the initial centroid $\bar{x}(0)$ of the distribution is zero. This, combined with (A 5b), determines the initial value $M_1(0) = \bar{x}(0) = 0$, and time integration of (3.18a) gives

$$M_1 = P\acute{e} \sum_{n=0}^{\infty} \sum_{\ell=-\infty}^{\infty} a_{0n} \langle u_{\ell}|f_n \rangle \frac{1 - e^{-(\lambda_n + i\ell\omega_o)t}}{\lambda_n + i\ell\omega_o}. \quad (3.18b)$$

Here, the term $(n, \ell) = (0, 0)$ depends linearly on time because $\lim_{q \rightarrow 0} [(1 - e^{-qt})/q] = t$. Similarly, for the time derivative $(1/2)(dM_2/dt) = \langle 1|c_o \rangle + P\acute{e} \langle u|c_1 \rangle$ of the full moment M_2 , (2.13b), we obtain

$$\begin{aligned} \frac{1}{2} \frac{dM_2}{dt} &= 1 + P\acute{e}^2 \sum_{m=0}^{\infty} \sum_{n=0}^{\infty} \sum_{k=-\infty}^{\infty} \langle u_k|f_m \rangle e^{-(\lambda_n + ik\omega_o)t} \\ &\quad \times \left[(a_{0n}\gamma_{1n}t + a_{1n})\delta_{n,m} + a_{0n} \sum_{\ell=-\infty}^{\infty} \beta_{mn}^{\ell} e^{i\ell\omega_o t} \right]. \end{aligned} \quad (3.18c)$$

All expressions derived so far are explicitly real because of the pairwise summation of complex conjugate terms with index ℓ and $-\ell$. Furthermore, they apply to any initial solute distributions, such as the non-uniform distributions recently studied by Camassa *et al.* (2010), as well as any given velocity field, which can be represented by (2.6).

We now study the special case of an initial solute distribution \tilde{c} being uniform in the cross-sectional plane. This introduces significant simplifications in D_{eff} , which otherwise depends on the channel cross-section, the flow profile u , and the initial solute distribution \tilde{c} through the coefficients u_{ℓ} , a_{0n} , a_{1n} , γ_{1n} , and β_{kn}^{ℓ} . Transverse uniformity leads to

$$|\tilde{c}_0\rangle = |1\rangle \quad \text{and} \quad |\tilde{c}_1\rangle = 0, \quad (3.19)$$

and a_{0n} , β_{j0}^{ℓ} and a_{1n} therefore reduce to

$$a_{0n} = \delta_{n,0} \quad (3.20a)$$

$$\beta_{j0}^{\ell} = (1 - \delta_{\ell,0}\delta_{j,0}) \frac{\langle f_j|u_{\ell} \rangle}{\lambda_j + i\ell\omega_o}, \quad (3.20b)$$

$$a_{1n} = - \sum_{\ell=-\infty}^{\infty} (1 - \delta_{\ell,0}\delta_{n,0}) \frac{\langle f_n|u_{\ell} \rangle}{\lambda_n + i\ell\omega_o}, \quad (3.20c)$$

where $\langle f_j|u_{\ell}|f_0 \rangle = \langle f_j|u_{\ell}|1 \rangle = \langle f_j|u_{\ell} \rangle$ has been used. Hence, (3.18) becomes

$$\frac{dM_1}{dt} = P\acute{e} \sum_{k=-\infty}^{\infty} \langle u_k|1 \rangle e^{-ik\omega_o t}, \quad (3.21a)$$

$$\begin{aligned}
 M_1 &= P\acute{e} \sum_{\ell=-\infty}^{\infty} \langle u_\ell | 1 \rangle \frac{1 - e^{-i\ell\omega_o t}}{i\ell\omega_o} \\
 &= P\acute{e} \left\{ \langle u_0 | 1 \rangle t + \sum_{\ell=-\infty}^{\infty} (1 - \delta_{\ell,0}) \langle 1 | u_\ell \rangle \frac{e^{i\ell\omega_o t} - 1}{i\ell\omega_o} \right\}, \quad (3.21b)
 \end{aligned}$$

$$\begin{aligned}
 \frac{1}{2} \frac{dM_2}{dt} &= 1 + P\acute{e}^2 \left\{ \sum_{\ell=-\infty}^{\infty} \langle u_\ell | 1 \rangle \langle u_0 | 1 \rangle t e^{-i\ell\omega_o t} + \sum_{m=0}^{\infty} \sum_{\ell=-\infty}^{\infty} \sum_{k=-\infty}^{\infty} \frac{\langle u_k | f_m \rangle \langle f_m | u_\ell \rangle}{\lambda_m + i\ell\omega_o} \right. \\
 &\quad \times (1 - \delta_{m,0} \delta_{\ell,0}) [e^{i\ell\omega_o t} - e^{-\lambda_m t}] e^{-ik\omega_o t} \Big\}, \quad (3.21c)
 \end{aligned}$$

and after a final index change of m to n we arrive at

$$D_{eff}(t) = 1 + P\acute{e}^2 \sum_{n=1}^{\infty} \sum_{\ell=-\infty}^{\infty} \sum_{k=-\infty}^{\infty} \frac{\langle u_k | f_n \rangle \langle f_n | u_\ell \rangle}{\lambda_n + i\ell\omega_o} [e^{i(\ell-k)\omega_o t} - e^{-(\lambda_n + i k \omega_o) t}]. \quad (3.22)$$

This is the main theoretical result of our work: a closed expression for the transient Taylor–Aris dispersion $D_{eff}(t)$ for any given time-dependent, axial flow field $u(\mathbf{r}_\perp, t)$ in the case of complete transverse diffusion. The flow frequencies $\ell\omega_o$ and solute diffusion relaxation rates λ_n appears explicitly, while the momentum relaxation rates α_{fl} are implicit in $\langle f_n | u_\ell \rangle$. The result (3.22), which generalizes previous steady and single-frequency results, is particularly relevant in the field of microfluidics characterized by laminar flow in channels of small cross-sectional dimensions compared with the channel lengths.

The time-averaged diffusivity $D_{eff}^{avr}(t)$ over one oscillation period $\tau_0 = 2\pi/\omega_o$ is

$$D_{eff}^{avr}(t) = \frac{1}{\tau_0} \int_t^{t+\tau_0} D_{eff}(t) dt \quad (3.23a)$$

$$\begin{aligned}
 &= 1 + P\acute{e}^2 \sum_{n=1}^{\infty} \sum_{\ell=-\infty}^{\infty} \sum_{k=-\infty}^{\infty} \frac{\langle u_k | f_n \rangle \langle f_n | u_\ell \rangle}{\lambda_n + i\ell\omega_o} \\
 &\quad \times \left[\delta_{\ell,k} - \frac{1 - e^{-\lambda_n \tau_0}}{(\lambda_n + i k \omega_o) \tau_0} e^{-(\lambda_n + i k \omega_o) t} \right], \quad (3.23b)
 \end{aligned}$$

which in the long-time limit $t \gg 1/\lambda_1$ reduces to

$$D_{eff}^{avr}(\infty) = 1 + P\acute{e}^2 \sum_{n=1}^{\infty} \left[\frac{|\langle u_0 | f_n \rangle|^2}{\lambda_n} + \sum_{\ell=1}^{\infty} \frac{2\lambda_n |\langle u_\ell | f_n \rangle|^2}{\lambda_n^2 + \ell^2 \omega_o^2} \right]. \quad (3.24)$$

Note that the ℓ -sum only runs over positive integers and not as previously over all integers.

Finally, in the case of a steady flow given by

$$|u_\ell\rangle = \delta_{\ell,0} |u_0\rangle, \quad (3.25)$$

expression (3.22) for the effective diffusivity reduces to

$$D_{eff}^{steady}(t) = 1 + P\acute{e}^2 \sum_{n=1}^{\infty} \frac{|\langle u_0 | f_n \rangle|^2}{\lambda_n} (1 - e^{-\lambda_n t}), \quad (3.26)$$

and hence we recover the steady-flow, transient-solute result of Barton (1983).

4. General aspects of dispersion and relaxation rates

Our main result (3.22) implies directly that for all time-dependent flows the effective diffusivity depends on the velocity squared, $D_{eff} \propto P\dot{\epsilon}^2 \propto U_o^2$. However, the specific form of D_{eff} depends on the magnitude of the amplitude $\|u_\ell\|$, of a given velocity component with frequency $\ell\omega_o$, relative to the amplitude $\|u_0\|$ of the steady component.

For small oscillation amplitudes $\|u_\ell\| \ll \|u_0\|$, the velocity field remains unidirectional, but its magnitude, and hence the shear gradients in the velocity, oscillates with frequency $\ell\omega_o$ around the steady value. Consequently, $D_{eff}(t)$ oscillates with frequency $\ell\omega_o$ around its time-averaged value $D_{eff}^{avr}(\infty)$. For sufficiently large amplitudes $\|u_\ell\| \gg \|u_0\|$ (the exact limit depends on the channel cross-section geometry), the direction of the velocity field changes sign with frequency $2\ell\omega_o$. As a result, due to the terms with $k = -\ell$ in (3.23b), $D_{eff}(t)$ also oscillates with the double frequency $2\ell\omega_o$. Moreover, because this frequency doubling ensures a non-zero, time-averaged effective diffusivity $D_{eff}^{avr} \propto \|u_\ell\|^2 P\dot{\epsilon}^2$, D_{eff}^{avr} increases above D_{eff}^{steady} . This reflects that now $\|u_\ell\|U_o$ and not U_o should be chosen as U_{char} in (2.4), thus quantifying the observations made in the chemical engineering community that pulsating flows lead to increased mass transfer (Taylor & Leonard 1965).

By definition, the variance of the solute distribution $\mu_2(t)$ is positive at all times, but this does not imply that the differential variance $D_{eff}(t) = (1/2)(d\mu_2/dt)$ also remains positive; in fact, negative values of $D_{eff}(t)$ are often encountered. In general, for short times $t \ll 1/\lambda_1, 1/(2\ell_{max}\omega_o)$, we find $D_{eff}(t) = 1 + tP\dot{\epsilon}^2 \sum_{n=1}^{\infty} |\langle f_n u(0) \rangle|^2 > 0$, see Appendix, while for steady-flow oscillations of large amplitudes $\|u_\ell\| \gg \|u_0\|$ the transient contraction of the solute concentration field associated with each reversal of the solvent flow direction leads to negative values of $D_{eff}(t)$. The cross-over point to negative values of $D_{eff}(t)$ depends on the relative amplitudes of all components of the velocity field, and is therefore not easily estimated in the general case. However, for the simple case of a single-frequency flow the cross-over point can be identified from (3.24). The time-averaged (positive) level is set by the diagonal terms $\ell = k$ for $-1, 0$ and 1 in the n -sum given by $|\langle u_0 f_n \rangle|^2 / \lambda_n + |\langle u_1 f_n \rangle|^2 2\lambda_n / (\lambda_n^2 + \omega_o^2)$, while the cross-terms $\ell = -k$ for -1 and 1 gives the oscillating terms $2\text{Re}[(\langle u_1 f_n \rangle e^{i\omega_o t})^2 / (\lambda_1 + i\omega_o)]$. For the dominant $n = 1$ term at the intermediate frequency $\lambda_1 \ll \omega_o \lesssim Sc$, we can neglect λ_1 in the denominators, and since $Wo = \sqrt{\omega_o / Sc} \lesssim 1$ we have $\langle u_1 f_n \rangle \approx \langle u_0 f_n \rangle \|u_1\| / \|u_0\|$, which results in $D_{eff} \propto 1 + 2(\|u_1\|^2 / \|u_0\|^2)(\lambda_1 / \omega_o)[(\lambda_1 / \omega_o) + \sin(2\omega_o t + 2\phi_0)]$, where the phase ϕ_0 is given by $\langle u_1 f_n \rangle = |\langle u_1 f_n \rangle| e^{i\phi_0}$. Negative values of $D_{eff}(t)$ are therefore expected for $\|u_1\| > \|u_0\| \sqrt{\omega_o / (2\lambda_1)}$.

In the absence of a steady component in the velocity field, $u_0 = 0$, the frequency doubling is always present. Thus, for purely oscillating flows one finds a shear-enhanced dispersion above molecular diffusion, even though there is no net flow.

General conclusions for the shape dependence of D_{eff} may be obtained by applying random matrix theory (Mehta 2004) to the geometry-dependent inner product/eigenvalue expressions (3.22), (3.24) and (3.26) following the analysis of the shape-dependent quantum transport through quantum dots (Bruus & Stone 1994). For a non-integrable system the values of the inner products in (3.26) can be regarded as a random distribution with an average of the order unity. We therefore expect the sum to be dominated by the lowest eigenvalues, for which $\lambda_n \propto 1/R^2$, where R is the aspect ratio of the characteristic length scales of the two cross-section directions ($R \geq 1$), which for a rectangle is the wide ‘width’ divided by the short ‘height’. Consequently

$(D_{\text{eff}}^{\text{steady}} - 1) \propto P\hat{e}^2 R^2$, indicating that the dominating length scale no longer is the short ‘height’ but the wide ‘width’. This is in agreement with the analysis of the shallow, slowly varying cross-sections studied by Ajdari *et al.* (2006) and Dutta *et al.* (2006).

The solute dispersion can be calculated from (3.22), if the Fourier series of the flow velocity is known, e.g. the single-frequency flow in a Newtonian fluids (Womersley 1955) or steady non-Newtonian fluid flow (Fan & Wang 1966). However, in the rest of the paper we restrict the application of our theory to the case of incompressible Newtonian fluids of kinematic viscosity (or momentum diffusivity) ν in the laminar regime which are governed by the time-dependent Stokes equation,

$$\partial_t u(\mathbf{r}_\perp, t) = Sc \left[\nabla_\perp^2 u(\mathbf{r}_\perp, t) + \frac{1}{\mathcal{L}} \Delta p(t) \right]. \quad (4.1)$$

Here, $\Delta p(t)$ is the time-dependent pressure drop along the channel of length \mathcal{L} , resolved by the components $\varepsilon_\ell \Delta p e^{i\ell\omega_o t}$ (ε_ℓ is a dimensionless amplitude) with the dimensionless base frequency $\omega_o = Wo^2 Sc$, and the dimension-full pressure has been normalized by the shear-induced pressure $P_o = (\eta U_o)/L_o$. The Schmidt number Sc appears since the time scale has been chosen to be the transverse mass diffusion time and not the momentum diffusion time. The linearity of this equation allows us to solve the flow problem analytically and thereby obtain the Fourier coefficients u_ℓ and the momentum diffusion rate α_ℓ . The dispersion $D_{\text{eff}}(t)$ depends on α_ℓ , and thus on Wo by (2.8), implicitly through the velocity components u_ℓ .

The effective diffusivity varies greatly depending on the system parameters. Below, we provide explicit estimates of the relaxation rates of the solute and fluid momentum, by analysing specific time-dependent systems of increasing complexity through the addition of more time scales to both motion of the solvent and diffusion of the solute. We interpret the results for D_{eff} in terms of the relaxation rates and the flow frequencies in agreement with the general considerations just outlined.

5. Multiple-frequency flow in one-length-scale cross-sections

We begin by analysing channel cross-sections with only one inherent length scale, such as the circular tube or the infinite parallel-plate slit, and the associated time scale for transverse solute diffusion. All results presented in this section are computed for the circular cross-section, but qualitatively they apply to other single-length cross-sections. We consider a circular tube of unit radius (the radius being $a = L_o$ in dimension-full coordinates) and calculate the velocity field from the Stokes equation, (4.1). Using cylindrical coordinates and a generalized wavenumber k_ℓ , the velocity component u_ℓ fulfilling the boundary conditions $u|_{r=1} = 0$ and $\partial_r u|_{r=0} = 0$ is (Womersley 1955)

$$k_\ell = k_\ell(Wo) = \sqrt{-i\ell Wo^2} = \sqrt{-i\ell\omega_o/Sc}, \quad (5.1a)$$

$$|u_\ell\rangle = \varepsilon_\ell \frac{8}{k_\ell^2} \left[\frac{J_0(k_\ell r)}{J_0(k_\ell)} - 1 \right], \quad (5.1b)$$

where the steady-state Poiseuille solution is $u_0(r) = \lim_{\ell \rightarrow 0} u_\ell(r) = \varepsilon_0 2(1 - r^2)$. The velocity scale is taken to be the average steady state velocity $U_o = \Delta p a^2 / (8\eta\mathcal{L})$ for $\varepsilon_0 = 1$. The eigenfunctions and eigenvalues corresponding to (3.4) are

$$|f_n\rangle = \delta_{n,0} + (1 - \delta_{n,0}) \frac{J_0(\xi_{1,n} r)}{J_0(\xi_{1,n})}, \quad (5.2a)$$

$$\lambda_n = (1 - \delta_{n,0})\xi_{1,n}^2, \quad (5.2b)$$

where $J_s(x)$ is the Bessel function of the first kind of order s , and $\xi_{s,n}$ is the n th root of $J_s(x)$. For cylindrical coordinates (axisymmetric case) $\langle f|g \rangle = \int_0^1 dr 2rf^*(r)g(r)$, so

$$\langle f_n|u_\ell \rangle = -\varepsilon_\ell \frac{16}{(\xi_{1,n}^2 - k_\ell^2)k_\ell} \frac{J_1(k_\ell)}{J_0(k_\ell)} \quad \text{for } n > 0, \quad (5.3)$$

and $\langle f_n|u_0 \rangle = \lim_{\ell \rightarrow 0} \langle f_n|u_\ell \rangle = -8/\xi_{1,n}^2$ for the steady term. Using these $\langle f_n|u_\ell \rangle$ in (3.22) allows us to calculate $D_{\text{eff}}(t)$ for an unsteady flow, and by inserting them in (3.26) we recover $D_{\text{eff}}^{\text{steady}}(t) = 1 + P\acute{e}^2[(1/48) - \sum_{n=1}^{\infty} (64/\xi_{1,n}^6) \exp(-\xi_{1,n}^2 t)]$, the classic result for a transient solute concentration in a steady flow obtained by Barton (1983).

The fluid momentum equilibration rate for the circular cross-section is $\alpha_{fl} = Sc\xi_{0,1}^2$, so the generalized wavenumber $k_\ell = \sqrt{-i\ell Wo^2} = \xi_{0,1}\sqrt{-i\ell\omega_o/\alpha_{fl}}$ and the overlap integrals (5.3) depend explicitly on the fluid inertia through the ratio of the driving frequency ω_o to the fluid momentum equilibration rate α_{fl} .

5.1. A steady-plus-one-frequency flow

We consider now the simple case of a steady flow of fixed amplitude $\varepsilon_0 = 1$ with the addition of one oscillating component of variable amplitude ε_1 . The dispersion in this particular flow has previously been studied to various levels of detail (Aris 1960; Chatwin 1975; Mukherjee & Mazumder 1988). Our theory both recovers, quantifies and provides insight to the underlying physical mechanisms encountered in these previous studies.

$D_{\text{eff}}(t)$ transiently builds towards a steady-oscillation level on the time scale $1/\lambda_1 = 1/\xi_{1,1}^2 = 0.068$, as seen in the example figure 1(a) (black line) for $\varepsilon_1 = 0.05$, $P\acute{e} = 20$, $Sc = 1000$, $\omega_o = 200$ and $Wo = \sqrt{\omega_o/Sc} = 0.447$. As expected from the general observations in §4, $D_{\text{eff}}(t)$ oscillates around $D_{\text{eff}}^{\text{avr}}(t) \approx D_{\text{eff}}^{\text{steady}}(t)$ for $\varepsilon_1^2 \ll \varepsilon_0^2 = 1$ (grey line). The inset shows increasing $D_{\text{eff}}^{\text{avr}}(t)$ for growing oscillation amplitude, $\varepsilon_1 = 0, 3$ and 12 , where $D_{\text{eff}}^{\text{avr}}$ changes from following D_{eff} fairly closely at $\varepsilon_1 = 3$ to being substantially enhanced for $\varepsilon_1 = 12$. In figure 1(b) we zoom in on the two grey zones of (a) to show the excellent agreement between our theory for $D_{\text{eff}}(t) - D_{\text{eff}}^{\text{steady}}(t)$ (full line), numerics (circles, see Appendix for details), and the single-frequency theory of Mukherjee & Mazumder (1988) (stars).

Extending the physical analysis provided by Mukherjee & Mazumder (1988), we have augmented ε_1 by a factor of 1000 to the value 50 in figure 1(c), and the normalized plot $D_{\text{eff}}(t)/D_{\text{eff}}^{\text{avr}}(\infty)$ illustrates that the oscillation-induced enhancement of $D_{\text{eff}}^{\text{avr}}(t)$ shown in the inset of (a) is accompanied by both a frequency doubling in, and negative values of, $D_{\text{eff}}(t)$ as discussed in §4. The onset of this nonlinearity in the dispersion is further investigated in figure 1(d), where $D_{\text{eff}}^{\text{avr}}(\infty)/D_{\text{eff}}^{\text{steady}}(\infty)$ is plotted versus the oscillation amplitude ε_1 : a cross-over from the linear regime, where $D_{\text{eff}}^{\text{avr}}(\infty)/D_{\text{eff}}^{\text{steady}}(\infty) \approx 1$, to the nonlinear regime, where $D_{\text{eff}}^{\text{avr}}(\infty)/D_{\text{eff}}^{\text{steady}}(\infty) \propto \varepsilon_1^2$, happens at a frequency-dependent critical value ε_1^c . We estimate ε_1^c in the low-frequency limit $Wo \lesssim \xi_{0,1} \approx 2.40$ from (3.24) using that in this case $\langle u_1|f_n \rangle \approx \langle u_0|f_n \rangle$, and since

$$\varepsilon_\ell = \delta_{\ell,0} + \varepsilon_1(\delta_{\ell,-1} + \delta_{\ell,1}), \quad (5.4)$$

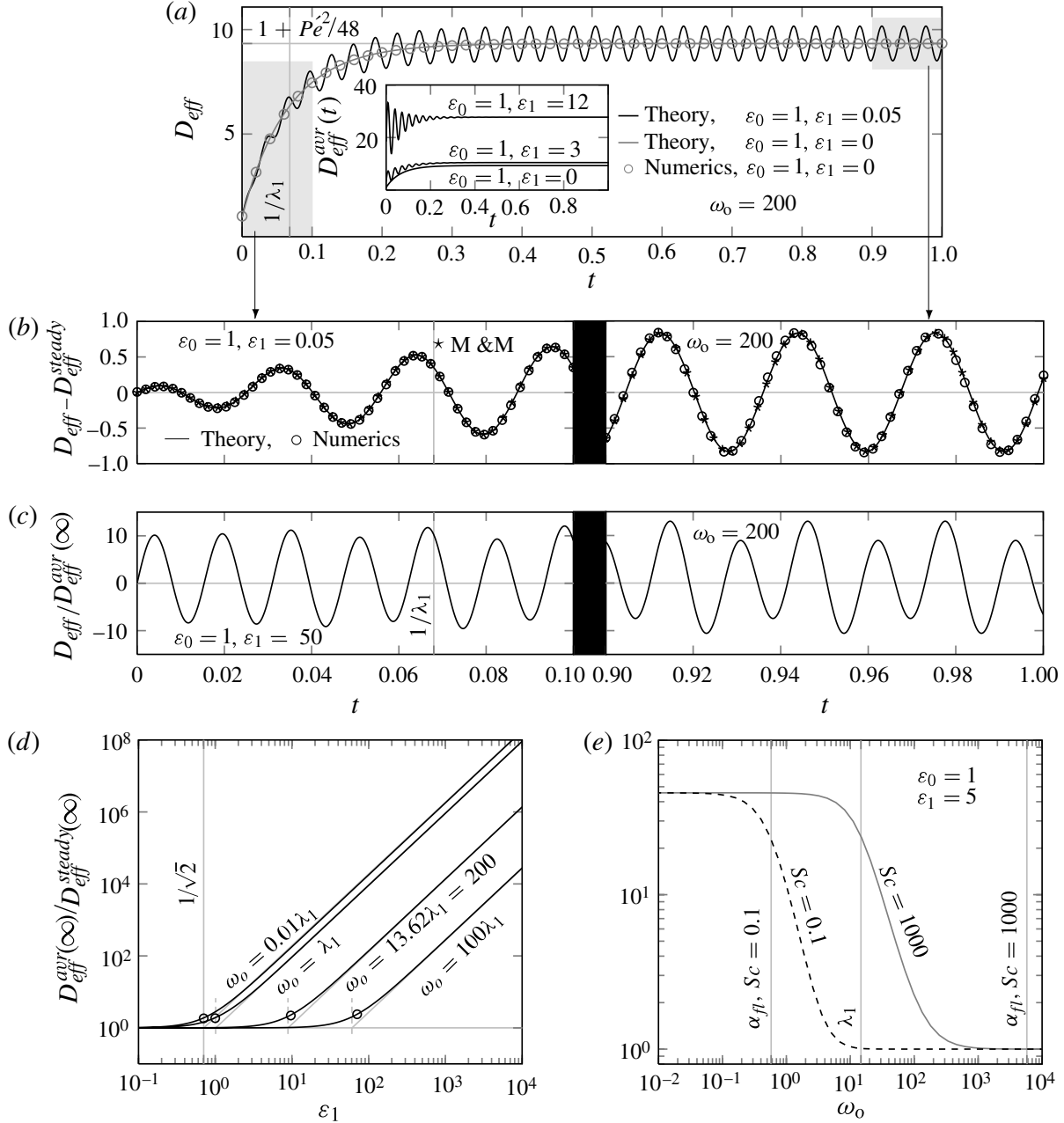


FIGURE 1. $D_{eff}(t)$ calculated by (3.22) in a tube of circular cross-section for a harmonically oscillating flow of frequency ω_o superimposed on a steady flow, $Pe = 20$. (a) $D_{eff}(t)$ for $\omega_0 = 200$, $Wo = 0.447$ and velocity amplitudes $\varepsilon_1 = 0.05 \ll \varepsilon_0 = 1$ (black line) oscillating around $D_{eff}^{steady}(t)$ determined by theory (3.26) (grey line) and by direct numerical simulation (grey circles). The inset shows $D_{eff}^{avr}(t)$ for $\varepsilon_1 = 0, 3$ and 12 , (3.23b). (b) Zoom-in on $D_{eff}(t)$ for the initial transient period $0 < t < 0.1$ (left) and the steady regime $0.9 < t < 1$ (right) showing agreement between our theory (black line), our numerics (circles) and the theory of Mukherjee & Mazumder (1988) (M & M). (c) Normalized effective diffusivity $D_{eff}(t)/D_{eff}^{avr}(\infty)$ showing frequency doubling; parameters as in (b) except now $\varepsilon_1 = 50$. (d) $D_{eff}^{avr}(\infty)/D_{eff}^{steady}(\infty)$, (5.5), versus ε_1 for four different frequencies ω_o . The cross-over point ε_1^c (open circles) from the linear regime ($D_{eff}^{avr}/D_{eff}^{steady} \approx 1$) to the nonlinear one ($D_{eff}^{avr}/D_{eff}^{steady} \propto \varepsilon_1^2$) increases for increasing ω_o , as described by (5.6). (e) $D_{eff}^{avr}(\infty)/D_{eff}^{steady}(\infty)$ versus ω_o for two fluids. For $Sc = 0.1$ (gas-like, dashed line) it decreases to 1 once $\omega_o > \alpha_{fl}$ (solvent-momentum-diffusion limited), while for $Sc = 1000$ (water-like, grey line), it decreases to 1 when $\omega_o > \lambda_1$ (solute-diffusion limited).

it follows that

$$D_{eff}^{avr}(\infty) \approx 1 + P\acute{e}^2 \sum_{n=1}^{\infty} \left[1 + \frac{2\varepsilon_1^2}{1 + (\omega_o/\lambda_n)^2} \right] \frac{|\langle u_0 | f_n \rangle|^2}{\lambda_n}. \quad (5.5)$$

Thus, the cross-over to period-doubled behaviour (dominance of the ε_1^2 term) happens when ε_1 equals

$$\varepsilon_1^c = \frac{1}{\sqrt{2}} \sqrt{1 + \frac{\omega_o^2}{\lambda_1^2}} = \begin{cases} \frac{1}{\sqrt{2}} & \text{for } \omega_o \ll \lambda_1, \\ \frac{\omega_o}{\sqrt{2}\lambda_1} & \text{for } \omega_o \gg \lambda_1. \end{cases} \quad (5.6)$$

When $\omega_o \ll \lambda_1$, the solute fully equilibrates by diffusion (λ_1 is the solute diffusion equilibration rate) and thereby exploits all velocity gradients, so the cross-over to frequency-doubled behaviour happens as soon as the amplitude of the sinusoidal part of the velocity field exceeds that of the steady component, i.e. at the r.m.s. value $\varepsilon_1^c = 1/\sqrt{2}$ for $\varepsilon_0 = 1$. In contrast, for $\omega_o \gg \lambda_1$ the solute diffusion cannot fully follow the solvent oscillations, and only by increasing the amplitude significantly will the oscillation component contribute to D_{eff} , and as a consequence the cross-over amplitude scales as $\varepsilon_1^c \propto \omega_o/\lambda_1$. In figure 1(d) is shown that the estimates of (5.6) are correct. This result further agrees with, and quantifies, the observations of Chatwin (1975) and Watson (1983), but disagrees with Aris (1960), who based on cases with $\varepsilon_1 \leq 1$ predicted that the pulsatile contribution to $D_{eff}^{avr}(\infty)$ is less than 1 %, which is clearly incorrect for large values of ε_1 . For $\varepsilon_1 > \varepsilon_1^c$ we have $(D_{eff}^{avr} - 1) \propto \varepsilon_1^2 P\acute{e}^2$ signalling the change of characteristic velocity scale discussed in § 4.

In addition to these limitations set by the equilibration of the solute, the dispersion may also be limited by fluid inertia, which similarly to the solute diffusion equilibration rate is characterized by a solvent-momentum equilibration rate α_{fl} . All time scales can be resolved by the solute when the driving frequency is much lower than the two equilibration rates, allowing time enough to establish the time-dependent velocity gradients and for the solute to diffuse in them, see figure 1(e). However, D_{eff} decreases if ω_o exceeds either of these equilibration rates.

The behaviour of D_{eff} seems quantitatively similar whether the limiting factor is solute diffusion or solvent momentum diffusion, but the underlying physical mechanisms are different. For solute/solvent combinations which are limited by solute diffusion, $\lambda_1 \ll \alpha_{fl}$ (full grey line in figure 1e), the solute is constantly oscillating back and forth in addition to the steady motion as caused by the velocity field. This is still the case when $\omega_o > \lambda_1$, but here the solute only has time to diffuse by the gradients created by the steady velocity; new solute gradients are created by the oscillating part faster than the old gradients are smoothed out by diffusion. This corresponds to the case where the fluid is water.

In the other limit of solute/solvent configuration, $\alpha_{fl} \ll \lambda_1$, the limiting factor is the diffusion of fluid momentum (inertia): the fluid momentum does not have time to react to the pressure oscillations at the driving frequency, so the fluid will only be moved by the steady part of the pressure. Thus, only the steady velocity field will shear the solute distribution resulting in the dispersion of only the steady flow. This effect is seen in the dashed black line in figure 1(e), which corresponds to the case where channel radius is the same as for the water case above (thus keeping λ_1 fixed) but the fluid is air (Lide 1995).

5.2. A steady-plus-two-frequencies flow

Through the driving pressure, we now add a second time scale to the flow so it consists of a steady component, and the two frequencies ω_o and $\tilde{\ell}\omega_o$, $\tilde{\ell}$ being an integer. The effects in D_{eff} of the previous section extend to the second frequency, and we continue to find good agreement between theory and numerics, see figure 2. We first take $\tilde{\ell} = 2$. As expected from the general observations in §4, $D_{eff}(t)$ oscillates around D_{eff}^{steady} with the frequencies of the velocity field when the oscillation amplitudes ε_1 and ε_2 are sufficiently small (limits given below), see figure 2(a), while frequency doubling and negative values appear when ε_1 and ε_2 become large, see figure 2(b). As for the single-frequency case, there is substantial increase of $D_{eff}^{avr}(\infty)/D_{eff}^{steady}(\infty)$ for large values of ε_1 and ε_2 and the cross-over to nonlinearity for $\tilde{\ell} = 2$ may be predicted from simple estimates for $Wo \lesssim \xi_{0,1}$ as follows. Since

$$\varepsilon_\ell = \delta_{\ell,0} + \varepsilon_1(\delta_{\ell,-1} + \delta_{\ell,1}) + \varepsilon_2(\delta_{\ell,-2} + \delta_{\ell,2}), \quad (5.7)$$

we distinguish between the three regimes $\varepsilon_2 \ll 1$, $\varepsilon_1 \ll 1$ and $\varepsilon_1 = \varepsilon_2$. In the first case we trivially retrieve the result (5.6), while the second case similarly yields

$$\varepsilon_2^c = \frac{1}{\sqrt{2}} \sqrt{1 + \frac{4\omega_o^2}{\lambda_1^2}} = \begin{cases} \frac{1}{\sqrt{2}} & \text{for } \omega_o \ll \lambda_1, \\ \frac{\sqrt{2}\omega_o}{\lambda_1} & \text{for } \omega_o \gg \lambda_1. \end{cases} \quad (5.8)$$

Hence, the frequency doubling for each of the velocity field frequencies is independent, since a significant nonlinear effect is found when either $\varepsilon_1 > \varepsilon_1^c$ or $\varepsilon_2 > \varepsilon_2^c$. In the third case of $\varepsilon_1 = \varepsilon_2 = \varepsilon$, we find

$$\varepsilon^c = \frac{1}{\sqrt{2}} \sqrt{\frac{1 + \frac{5\omega_o^2}{\lambda_1^2} + \frac{4\omega_o^4}{\lambda_1^4}}{1 + \frac{5\omega_o^2}{\lambda_1^2}}} = \begin{cases} \frac{1}{\sqrt{2}} & \text{for } \omega_o \ll \lambda_1, \\ \sqrt{\frac{2}{5}} \frac{\omega_o}{\lambda_1} & \text{for } \omega_o \gg \lambda_1, \end{cases} \quad (5.9)$$

where the second thresholds is slightly lower than for the single-frequency (5.6).

Our understanding of the behaviour of D_{eff}^{avr} from the involved diffusion processes of fluid momentum and solute, presented in the previous section on single-frequency flow, applies to each of the frequencies of the flow. The addition of a second velocity frequency introduces more shear and hence more gradients to the concentration field and D_{eff}^{avr} therefore increases even further when all velocity frequencies can be resolved, see dashed line in figure 2(c), where solute diffusion is the limiting process ($\lambda_1 \ll \alpha_{fl}$) and where for clarity the second frequency is $30\omega_o$ instead of the $2\omega_o$. Two distinct decreases are found in this curve: the first is when the solute equilibration rate λ_1 surpasses $30\omega_o$ and the second when λ_1 increases past the base frequency. The decreases arise because the gradients created by $30\omega_o$ and ω_o , respectively, can no longer be exploited by the solute. When both frequencies can be resolved D_{eff}^{avr} is almost a factor two greater than the single-frequency case of figure 1(e), here reproduced as the grey line, so the second velocity frequency leads to a large enhancement of D_{eff} . Had we chosen $\alpha_{fl} \ll \lambda_1$ in the figure, the same decreases would have been observed around $30\omega_o \approx \alpha_{fl}$ and $\omega_o \approx \alpha_{fl}$.

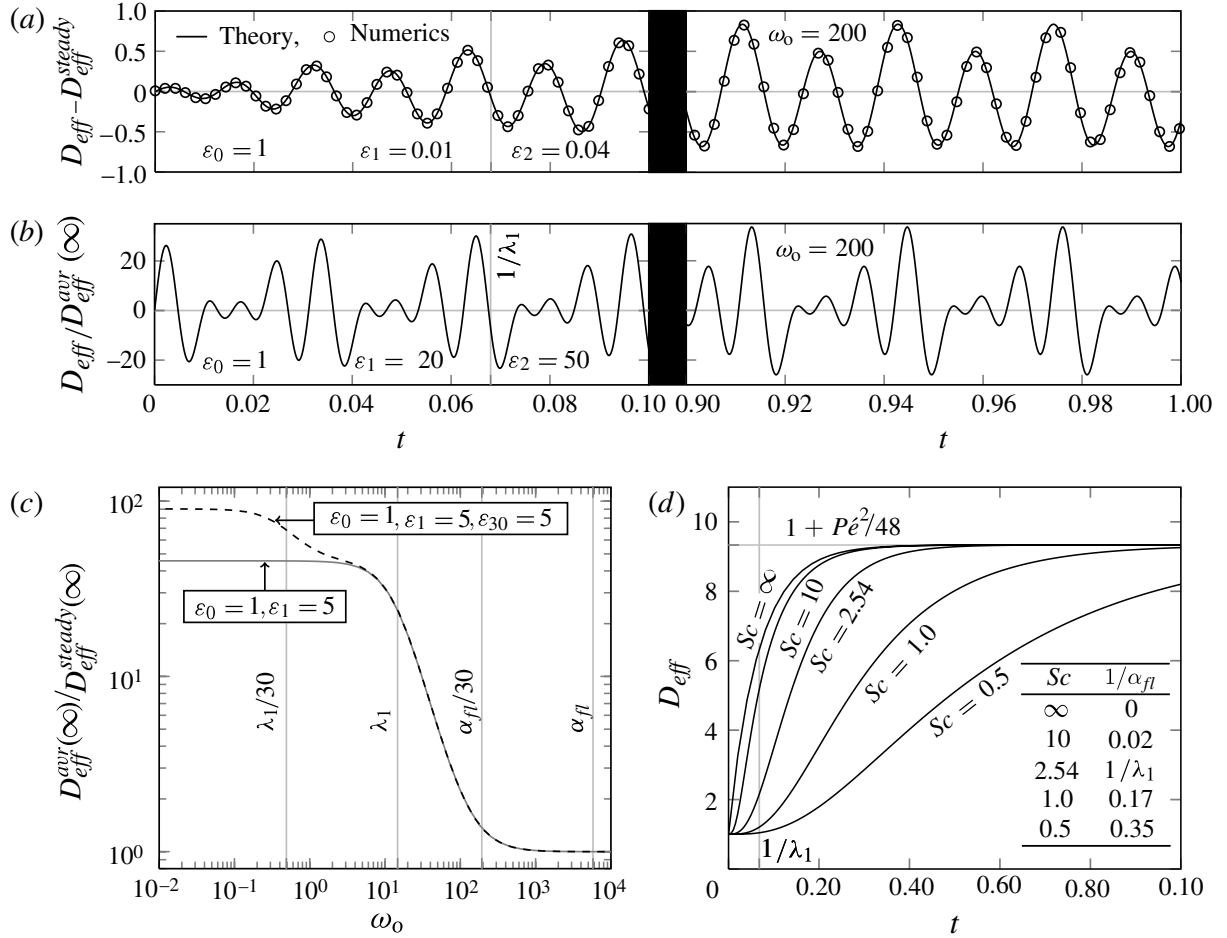


FIGURE 2. Calculated $D_{eff}(t)$ for a circular cross-section as in figure 1, but with a second oscillating velocity component added. (a) $D_{eff}(t) - D_{eff}^{steady}(t)$ from (3.22) (black line) and numerics (circles) the transient period (left) and the steady regime (right) for small amplitudes, $\varepsilon_1 = 0.01$ and $\varepsilon_2 = 0.04$. (b) As in panel (a), but for large amplitudes, $\varepsilon_1 = 20$ and $\varepsilon_2 = 50$, showing frequency doubling for both ω_o and $2\omega_o$. (c) $D_{eff}^{avr}(\infty) / D_{eff}^{steady}(\infty)$ versus ω_o for $Sc = 10^3$ and $\varepsilon_0 = 1$, $\varepsilon_1 = \varepsilon_{30} = 5$ (dashed curve). For clarity $\tilde{\ell} = 30$ is used instead of $\tilde{\ell} = 2$ to better illustrate the effects of each frequency. $D_{eff}^{avr}(\infty)$ decreases in two steps as ω_o crosses $\lambda_1/30$ and λ_1 . The one-frequency case figure 1(e), $Sc = 10^3$ (grey curve), is shown for comparison. (d) Startup of tube flow from rest: calculated $D_{eff}(t)$ versus time for $P\dot{\varepsilon} = 20$. For $Sc \lesssim 1$ the dispersion saturates on the solvent acceleration time scale $1/\alpha_{fl} \approx 1/Sc$, while for $Sc \gg 1$ it saturates on the solute diffusion time $1/\lambda_1 = 1/\xi_{1,1}^2 \approx 0.07$. The Fourier series has $T = 5$ and contains 1000 terms.

5.3. Unsteady, unidirectional flow: startup of Poiseuille flow

In the previous sections we found that fluid inertia limits the solute dispersion because the flow does not equilibrate to a steady state. To further investigate the inertial effects we consider solute in a circular channel where the solvent, after initially being at rest, suddenly at $t = 0$ begins to move due to an instantly applied pressure drop along the channel. The analytical solution of this startup of a Poiseuille flow is found in terms of a Fourier–Bessel expansion in the radial coordinate, where each term is multiplied by an exponential time decay of rate α_m (Batchelor 1967),

$$u(r, t) = 2(r^2 - 1) - \sum_{m=1}^{\infty} \frac{16}{\xi_{0,m}^3} \frac{J_0(\xi_{0,m}r)}{J_1(\xi_{0,m})} e^{-\alpha_m t}, \quad (5.10a)$$

$$\alpha_m = Sc \xi_{0,m}^2 \quad \text{for } m = 1, 2, 3, \dots \quad (5.10b)$$

The smallest of these inertial decay rates, $\alpha_1 = \xi_{0,1}^2 Sc \approx 5.78 Sc = \alpha_{fl}$, sets the characteristic time of the acceleration $1/\alpha_{fl}$ as in (2.7) and in §5.1. To align this solution with the developed theory, the temporal functions are written as Fourier series with a base period T much larger than the acceleration time, $T \gg 1/\alpha_{fl}$. Hence, the flow will reach a steady state significantly faster than the base period T , and the approximation will be the correct solution for $0 < t < T$. We obtain

$$u(r, t) = 2(1 - r^2) - \sum_{m=1}^{\infty} \sum_{\ell=-\infty}^{\infty} \frac{16J_0(\xi_{0,m}r)}{\xi_{0,m}^3 J_1(\xi_{0,m})} A_{\ell m} e^{i\ell\omega_o t}, \quad (5.11a)$$

$$A_{\ell m} = \frac{1 - e^{-\alpha_m T}}{\alpha_m T + i\ell 2\pi}, \quad (5.11b)$$

where $\omega_o = 2\pi/T$ so that $Wo = \sqrt{2\pi/(ScT)} = \xi_{0,1} \sqrt{2\pi/(\alpha_{fl}T)}$. The velocity scale is the same as for a steady flow in a circular tube, so the ℓ th velocity component $u_\ell(r)$ is

$$u_\ell(r) = 2(1 - r^2) \delta_{\ell,0} - \sum_{m=1}^{\infty} \frac{16A_{\ell m} J_0(\xi_{0,m}r)}{\xi_{0,m}^3 J_1(\xi_{0,m})}. \quad (5.12)$$

Combining this with the eigenvalue solution of (5.2), we find for $n > 0$

$$\langle f_n | u_\ell \rangle = -\frac{8\delta_{\ell,0}}{\xi_{1,n}^2} - \sum_{m=1}^{\infty} \frac{32(1 - e^{-\alpha_m T})}{\xi_{0,m}^2 (\xi_{0,m}^2 - \xi_{1,n}^2) (\alpha_m T + i\ell 2\pi)}. \quad (5.13)$$

The two physical processes of fluid acceleration and solute dispersion happens on the two time scales $1/\alpha_{fl}$ and $1/\lambda_1$, respectively, but since fluid motion is required to generate the shear needed for the Taylor–Aris dispersion effect, the dispersion is limited by either the solute diffusion, or solvent inertia. In the first case ($\alpha_{fl} \gg \lambda_1$), the fluid reaches steady state much faster than the solute and the dispersion therefore behaves as in the case of a steady flow. Since $\alpha_{fl} \propto Sc$ this can be thought of as having $Sc = \infty$, so the only transient behaviour observed is that of the solute diffusion; this is the case of water. For the second case ($\alpha_{fl} \propto Sc \ll \lambda_1$) with slower momentum equilibration rates $0.1 < Sc < 10$ found in gases (Lide 1995), the solute dispersion evolves in the slow increase of the velocity shear gradients, which now dominates the transient behaviour, and $D_{eff}(t)$ is thus smaller than $D_{eff}^{steady}(t)$. These inertial effects are illustrated in figure 2(d), where dispersion co-evolves with the transient start-up of a Poiseuille flow in a straight tube at $Pé = 20$, and where the equilibration rates for solute mass diffusion and solvent momentum diffusion are equal for $Sc = \xi_{1,1}^2/\xi_{0,1}^2 = 2.54$. We take $T = 5$, and to diminish unphysical effects of the Gibbs phenomenon close to $t = 0$, we include 1000 terms in the Fourier series.

In conclusion, fluid inertia limits fluid shear and hence the solute dispersion. However, given the characteristic time scale $1/\alpha_{fl} \propto 1/Sc \ll 1/\lambda_1$, inertial effects only become important for Taylor–Aris dispersion in gasses.

6. Multiple-frequency flow in two-length-scale cross-sections

We move on to consider the effects of adding a second length scale to the cross-sectional geometry. We illustrate this case by use of the rectangle, but the presented findings hold quantitatively for other cross-sections with two length scales, e.g. the ellipse.

6.1. The rectangular cross-section

We denote the height of the channel by $2a$ and the width by $2w$, with $w \geq a$ so that the aspect ratio $R = w/a$ satisfies $R \geq 1$. We take the characteristic length scale to be $L_o = a$, so $Pé = U_o a/D$ and $Wo = \sqrt{a^2 \tilde{\omega}_o/\nu}$, and in non-dimensional units we place the rectangular cross-section such that $-R \leq y \leq R$ and $-1 \leq z \leq 1$. The analytical velocity field for the steady Poiseuille flow is well known, see e.g. Bruus (2008), and in analogy with (5.1b) by introducing a generalized wavenumber $q_{j\ell}$, the pulsatile velocity field is found by a trivial extension thereof,

$$q_{j\ell} = q_{j\ell}(Wo) = \sqrt{i4Wo^2\ell + j^2\pi^2}, \quad (6.1a)$$

$$|u_\ell\rangle = \varepsilon_\ell(1 + \delta_{\ell,0}) \frac{24}{\Gamma} \sum_{j,\text{odd}} \frac{1}{j\pi q_{j\ell}^2} \left[1 - \frac{\cosh\left(q_{j\ell} \frac{y}{2}\right)}{\cosh\left(q_{j\ell} \frac{R}{2}\right)} \right] \sin\left(j\pi \frac{z+1}{2}\right), \quad (6.1b)$$

where the prefactor Γ and the velocity scale U_o (chosen as the is the cross-sectional average of the steady flow with $\varepsilon_0 = 1$) are given by

$$\Gamma = \Gamma(R) = 1 - \sum_{j,\text{odd}} \frac{1}{j^5} \frac{192}{\pi^5} \frac{1}{R} \tanh\left(j\pi \frac{R}{2}\right), \quad (6.2a)$$

$$U_o = \frac{\Delta p a^2 \Gamma}{3\eta \mathcal{L}}. \quad (6.2b)$$

The steady flow profile is retrieved from (6.1b) by the limit $u_0(y, z) = \lim_{\ell \rightarrow 0} u_\ell(y, z)$ using $q_{j0} = j\pi$. Similar to the circular cross-section, the generalized wavenumber $q_{j\ell}$ depends explicitly on the fluid momentum equilibration rate $\alpha_{fl} = (1 + 1/R^2)(\pi^2/4)Sc$ since $q_{j\ell} = \pi \sqrt{i\ell(1 + 1/R^2)(\omega_o/\alpha_{fl}) + j^2}$. The corresponding basis functions and eigenvalues are

$$|f_{nm}\rangle = \frac{2 \cos\left(n\pi \frac{y+R}{2R}\right) \cos\left(m\pi \frac{z+1}{2}\right)}{\sqrt{(1 + \delta_{n,0})(1 + \delta_{m,0})}}, \quad (6.3a)$$

$$\lambda_{nm} = \left(\frac{n\pi}{2R}\right)^2 + \left(\frac{m\pi}{2}\right)^2, \quad n, m = 0, 1, 2, \dots, \quad (6.3b)$$

which satisfy the requirement $|f_{00}\rangle = 1$ with $\lambda_{00} = 0$. The single index n of (5.2) is here changed to the double index (n, m) , and $n = 0$ to $(n, m) = (0, 0)$. The inner products $\langle f_n | u_\ell \rangle$ of (3.22) become $\langle f_{nm} | u_\ell \rangle$ given by

$$\langle f_{nm} | u_\ell \rangle = \begin{cases} \frac{\varepsilon_\ell(1 + \delta_{\ell,0})}{\sqrt{(1 + \delta_{n,0})(1 + \delta_{m,0})}} \frac{96R}{\Gamma \pi^2} \\ \quad \times \sum_{j,\text{odd}} \frac{q_{jl} R \delta_{n,0} - 2 \tanh\left(\frac{q_{jl} R}{2}\right)}{q_{jl}(j^2 - m^2)(n^2 \pi^2 + q_{jl}^2 R^2)} & n, m \text{ even,} \\ 0 & \text{otherwise,} \end{cases} \quad (6.4)$$

and sums $\sum_{n=1}^{\infty} = \sum_{n \neq 0}^{\infty}$ become $\sum_{\{n,m\} \neq \{0,0\}}^{\infty}$.

The two inherent length scales of this cross-section introduce two diffusion times, one along each coordinate direction, and hence two solute equilibration rates,

$$\lambda_{20}(R) = \frac{\pi^2}{R^2} \quad (\text{width}) \quad \text{and} \quad \lambda_{02} = \pi^2 \quad (\text{height}). \quad (6.5)$$

We have previously described how the behaviour of D_{eff} can be understood in terms of the involved diffusion processes of fluid momentum and solute, and it follows directly that while this obviously extends to the present case, the presence of the additional time scales from the second geometric dimension introduces more structure: for each frequency in the fluid velocity field, the solute dispersion will increase if it has time to equilibrate along either of its transverse directions (i.e. if $\omega_o \lesssim \lambda_{20}$ or $\omega_o \lesssim \lambda_{02}$), with more dispersivity when the frequency allows equilibration along both directions. Thus, for a velocity field with two frequency scales there will be four critical frequencies: the two solute equilibration rates for each of the two fluid time scales. This is illustrated in figure 3(a) for the case of $\varepsilon_0 = \varepsilon_1 = \varepsilon_{30} = 1$ with $Pé = 20$ and $R = 100$, and for a solvent/solute composition such that the equilibration rate of the solvent momentum $\alpha_{\mathcal{F}} = (1 + 1/R^2)(\pi^2/4)Sc$ is much greater than those of the solute diffusion, λ_{20} and λ_{02} . As function of driving frequency ω_o , D_{eff}^{avr} decreases in four steps: the first two and most significant drops happen near $\lambda_{20}/30$ and λ_{20} , where the diffusion across the width no longer can exploit the gradients of first the $30\omega_o$ -harmonic and then the ω_o -harmonic. The last two (minor) drops happen near $\lambda_{02}/30$ and finally λ_{02} , where the height diffusion ceases to be able to follow the $30\omega_o$ -harmonic and lastly the ω_o -harmonic. The substantial increases in time-averaged dispersion found for the two-frequency flow of the previous section is again found in this case: for low frequencies ω_o which allow complete solute equilibration, D_{eff}^{avr} is almost a factor of two greater than when only the steady velocity contributes to the solute dispersion ($D_{eff}^{avr}(\infty) = 120.41$ at $\omega_o = 10^{-8}$ compared with $D_{eff}^{avr}(\infty) = 60.70$ at $\omega_o = 10^4$). For comparison we have also included the special case of $R = 1$, a one-length-scale cross-section, where the two solute diffusion equilibration rates λ_{20} and λ_{02} are identical, and where we consequently find only two decreasing steps. We have also validated our theory against numerics for the case $R = 1$ (details given in [Appendix](#)), and find excellent agreement.

Since the solute equilibration rate λ_{20} depends on the aspect ratio R , (6.5), the same frequency ω_o and velocity component amplitudes ε_ℓ will give rise to different behaviours of D_{eff} in channels of different R . This is plotted in figure 3(b) for $\omega_o = 10^4$ and $\omega_o = 10^{-7}$ with the flow chosen as in (a) to be a two-frequency flow with amplitudes $\varepsilon_0 = \varepsilon_1 = \varepsilon_{30} = 1$. For reference we have also plotted the dependence of D_{eff}^{steady} in the limit $R \rightarrow \infty$ where we retrieve the well-known result (Doshi *et al.* 1978; Chatwin & Sullivan 1982) $D_{eff}^{steady}(\infty) = 1 + \chi_{rect}Pé^2$ with $\chi_{rect} = 2/105 + 11532\zeta(5)^2/\pi^{10}$ where $\zeta(x) = \sum_{j=1}^{\infty} j^{-x}$ is the Riemann zeta function. For sufficiently fast oscillation, here $\omega_o = 10^4$ (lower black line), we have $\omega_o \gg \lambda_{02}$, and as in figure 2(b) this is too fast for the solute diffusion to follow, and we recover the steady-flow case (triangles) and $D_{eff}^{avr}(\infty) = D_{eff}^{steady}(\infty)$. Had we chosen larger oscillation amplitudes ε_ℓ the nonlinear effect discussed in §4 would have set in and increased D_{eff}^{avr} . For the fixed slow oscillation frequency $\omega_o = 10^{-7}$ (top black line), D_{eff}^{avr} initially increases with R , as the solute diffusion now is able to follow the fluid movement. However, due to the R -dependence of λ_{20} in (6.5), a point is reached beyond which $\lambda_{20}(R)/30 < \omega_o$, and D_{eff}^{avr} decreases to a lower value. Later, when $\lambda_{20}(R)$ falls below ω_o , a second decrease occurs, after which D_{eff}^{avr} settles

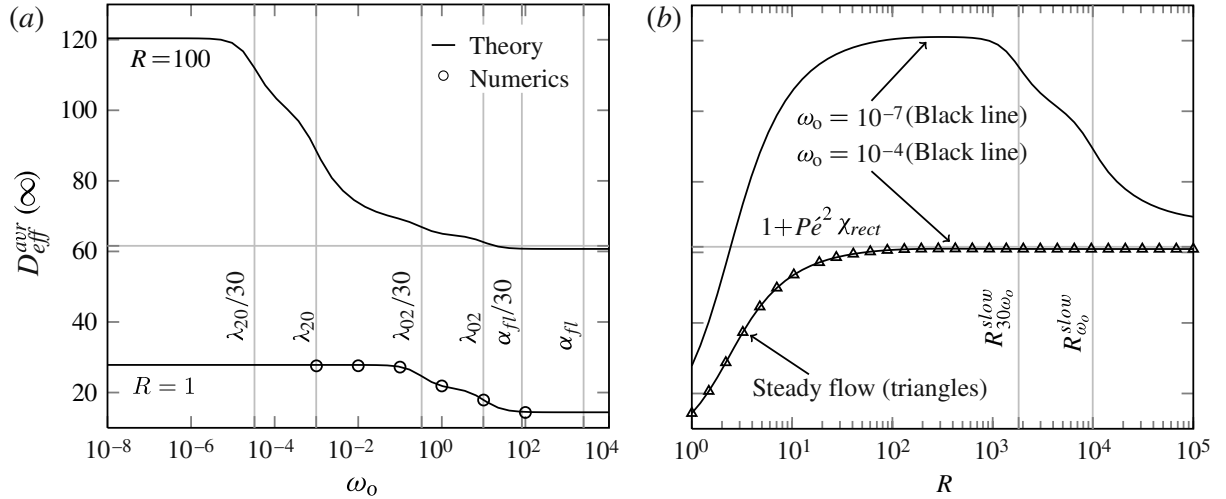


FIGURE 3. $D_{eff}^{avr}(\infty)$ for a two-frequency flow $\varepsilon_0 = \varepsilon_1 = \varepsilon_{30} = 1$ in rectangular channels of aspect ratio R . (a) $D_{eff}^{avr}(\infty)$ versus base frequency ω_o for $R = 1$ and $R = 100$ at $Pé = 20$, and with the agreement with numerics (circles) illustrated at $R = 1$ (details given in [Appendix](#)). As ω_o increases D_{eff}^{avr} decreases in four steps, namely when ω_o crosses $\lambda_{20}/30$, λ_{20} , $\lambda_{02}/30$, and λ_{02} (for $R = 100$). For $R = 1$ there are only two steps, namely when ω_o crosses $\lambda_{02}/30$ and λ_{02} this rate being the same for $R = 1$ and $R = 100$. (b) $D_{eff}^{avr}(\infty)$ versus R for fast oscillation ($\omega_o = 10^4$) and steady flow, both recovering the behaviour of figure 1(a), and for slow oscillation ($\omega_o = 10^{-7}$), for which $D_{eff}(\infty)$ reaches a maximum before decreasing in two steps at $\lambda_{20}(R) = 30 \times 10^{-7}$ and $\lambda_{20}(R) = 10^{-7}$, marked by the aspect ratios $R_{30\omega_o}^{slow}$ and $R_{\omega_o}^{slow}$, respectively.

at $D_{eff}^{steady}(\infty) = 1 + \chi_{rect} P_e^2$, since none of the added shear of the time-dependent velocity components contribute to D_{eff}^{avr} .

The highest value of D_{eff}^{avr} achievable for a fixed velocity field with fixed frequency ω_o is found in a region with the upper limit set by $3 \ell_{max} \omega_o \approx \lambda_{20} = \pi^2/R^2$, where ℓ_{max} is the maximum frequency component in the velocity field, and the lower limit is set by the value of R which ensures that the steady part of the velocity field reaches the maximum dispersion of $D_{eff}^{steady}(\infty) = 1 + P_e^2 \chi_{rect}$, $R \lesssim 100$.

Finally, a brief discussion is in order regarding the behaviour of $D_{eff}^{steady}(\infty)$ in the limit $R \rightarrow \infty$. It is well known that $\chi_{rect} = 2/105 + 11532 \zeta(5)^2/\pi^{10} \approx 7.95 \chi_{plate}$ where $\chi_{plate} = 2/105$ is the coefficient for infinite parallel plates (no sidewalls), which might seem to contradict the general scaling of $(D_{eff} - 1) \propto P_e^2/R^2$ described in §4. However, the rectangular cross-section is integrable, and the inner products $\langle f_{n0} | u_0 \rangle \propto 1/R$, because as function of the width coordinate y , u_0 is constant except for the ends covering a fraction $1/R$ of the width, while f_{n0} oscillates, see (6.1b) and (6.3a). As a result, the factor R^2 from $1/\lambda_{nm}$ is cancelled by the factor $1/R^2$ from the inner product, and $(D_{eff}^{steady} - 1) \propto P_e^2$, making the small height the dominant length scale. This explains why in $\chi_{rect} \approx \chi_{plate}$ instead of $\chi_{rect} \approx \chi_{plate} R^2$. Physically, the steady flow in high-aspect-ratio rectangular channels is independent of the channel width except for boundary layers of width unity near the sidewalls, while it remains parabolic in the height. Compared with the infinite parallel plate channel, the sidewalls therefore increase both the mean velocity and the created gradients in the concentration field along the height, causing an increase of $D_{eff}(\infty)$, which none the less remains on the order of $D_{eff}(\infty)$ from the parallel plates. For channel

R	2.67	ε_0	1.000	α_{fl}	2810
$Pé$	6.92	ε_1	$0.352 \exp(-2.19i)$	ω_o	2.94
Wo	0.05	ε_2	$0.203 \exp(-2.24i)$	λ_{20}	1.39
Sc	1000	ε_3	$0.059 \exp(+1.54i)$	λ_{02}	9.87

TABLE 1. Dimensionless parameters of the flow generated by the peristaltic pump of Skaft-Pedersen *et al.* (2009), see § 6.2.

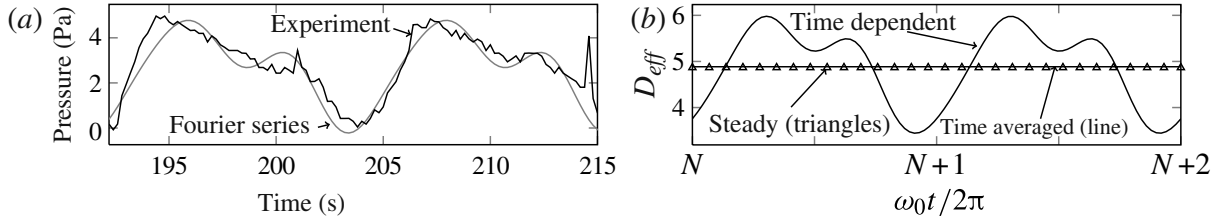


FIGURE 4. (a) Two periods of the measured time-dependent pressure delivered by the peristaltic pump (black) by Skaft-Pedersen *et al.* (2009) and of the approximate Fourier series ($|\ell| \leq 3$) used in the analysis (grey). (b) Calculated $D_{eff}(t)$ for the two cycles of the peristaltic pump following period $N = 10^4$ after the decay of all transients: the Fourier series (black), only the steady component (dashed) and the time-averaged Fourier series (grey).

cross-sections which vary continuously along both cross-section directions (e.g. elliptic), the characteristic length scale of velocity variations is of order R , resulting in shear along all of R and the scaling $(D_{eff}^{steady} - 1) \propto Pé^2 R^2$ as described in § 4.

6.2. Analysis of a peristaltic micropump

To illustrate the practical usefulness of the developed theory, we here shortly describe dispersion limiting of a micropump. The pressure delivered by the novel 12-channel, 8-roller, peristaltic pump for microfluidics of Skaft-Pedersen *et al.* (2009) is pulsating with the operating base frequency $\tilde{\omega}_o = 0.52 \text{ rad s}^{-1}$, as measured in a rectangular channel of $R = 2.67$ ($a = 75 \text{ } \mu\text{m}$, $w = 200 \text{ } \mu\text{m}$), and shown by the black line in figure 4(a). To analyse the influence of this time-dependent flow on the dispersion of a solute with typical molecular diffusivity $D = 10^{-9} \text{ m}^2 \text{ s}^{-1}$, we approximate the pressure by a Fourier series with $|\ell| \leq 3$ (grey line). The discrepancy between the approximation and the actual signal fluctuates faster than the highest harmonic and is not resolved by the solute. The velocity scale U_o is taken as the (dominating) steady component and the dimensionless parameters of the system are listed in table 1.

The pump is designed to have minimal dispersion, which follows from our theory: it is normally operated at $\omega_o = 2.94$, which is faster than the solute equilibration rate $\lambda_{20} = 1.39$ of the width, so only the diffusion in the height direction with $\lambda_{02} = 9.87$ is resolved. Furthermore, because the square of all oscillation amplitudes are small, $|\varepsilon_\ell| < 0.12$, their contribution to D_{eff} is minute, and $D_{eff}^{avr}(\infty) = 1.004 D_{eff}^{steady}(\infty)$, see figure 4(b). The dispersion may be increased by running the pump at lower frequency, e.g. $D_{eff}^{avr}(\infty) = 1.17 D_{eff}^{steady}(\infty)$ changing ω_o to $0.1 \omega_o$, or with higher oscillation amplitudes, $D_{eff}^{avr}(\infty) = 1.39 D_{eff}^{steady}(\infty)$ changing ε_ℓ to $10 \varepsilon_\ell$ for $\ell \neq 0$. If these changes are made simultaneously, we find $D_{eff}^{avr}(\infty) = 2.76 D_{eff}^{steady}(\infty)$.

7. Concluding remarks

By combining Aris's method of moments and Dirac's bra-ket formalism, we have derived the compact, closed form (3.22) for the transient Taylor–Aris dispersion or effective diffusivity $D_{eff}(t)$ valid for any time-dependent flow in a long, straight channel of arbitrary but constant cross-section. For a general time-dependent flow and as a function of system parameters, $D_{eff}(t)$ exhibits a rich and non-trivial structure due to the interplay between internal equilibration rates and external driving frequencies. Our analysis based on (3.22) has led to the following conclusions.

- (i) In general, the effective diffusivity is enhanced significantly by those parts of the time-dependent velocity field that have frequencies $\ell\omega_o$ lower than the fluid momentum diffusion rate α_η and the solute diffusion rate λ_1 , in which case the dispersive effect has sufficient time to fully evolve.
- (ii) We have explained why sufficiently large oscillation amplitudes $\|u_\ell\|$ lead to negative values of the instantaneous effective diffusivity $D_{eff}(t)$. In § 4 an amplitude threshold value for this transition has been derived for a steady-plus-one-frequency flow. This threshold depends on the ratio $\sqrt{\omega_o/(2\lambda_1)}$.
- (iii) As function of the normalized amplitudes ε_ℓ of the oscillatory flow components, scaling laws have been derived for the cross-over ε^c of the time-averaged effective diffusivity $D_{eff}^{avr}(t)$ from the linear regime of small oscillatory flow components superimposed on a large steady-flow component of normalized amplitude ε_0 , to the nonlinear, frequency-doubled regime of large oscillation amplitudes. Specific examples are shown in §§ 5.1 and 5.2 for steady-plus-one-frequency and steady-plus-two-frequencies flows.
- (iv) Our formulation of D_{eff} in terms of inner products (overlap integrals) and eigenvalues facilitates general analyses in terms of random matrix theory. As an example of such an analysis we have sketched an explanation for the well-known fact that the relevant Péclet number for the Taylor–Aris dispersion in a channel of rectangular cross-section involves the short height and not as expected on general grounds, the wide width.
- (v) For Newtonian solvents we have validated our theory by comparing it with the special cases of dispersion in steady flow and single-frequency pulsating flow treated in the literature, and by direct numerical simulations of single- and multiple-frequency flows in circular (figures 1(b) and 2(a)) and rectangular cross-sections (figure 3(a)).
- (vi) For Newtonian solvents in the cases of one-length scale and steady-plus-one-frequency flow, figure 1(e), one-length scale and steady-plus-two-frequency flow, figure 2(c), and two-length scale and steady-plus-two-frequency flows, figure 3(a), we have characterized the explicit suppression of the oscillatory enhancement of $D_{eff}^{avr}(\omega_o)$ each time a driving frequency $\ell\omega_o$ becomes larger than the internal diffusion relaxation rate λ_1 or the momentum relaxation rate α_η . In particular in figures 1(e) and 2(d), we found that this suppression is controlled by the solute mass diffusion in liquids and by the solvent momentum diffusion (or inertia) in gasses.
- (vii) In § 6.2 we have illustrated the practical usefulness of the developed theory as a design tool for dispersion-control in microfluidic systems.

Our work has resulted in a compact, transparent, and efficient theoretical method for analysing transient Taylor–Aris dispersion in straight channels. Using it, we have

gained physical insight in, and made explicit predictions of, the effects of general time-dependent flows on dispersion. The theory opens up for further generalizations such as including the effects of non-Newtonian solvents and non-trivial channel topologies.

Acknowledgements

We thank P. Skafte-Pedersen for supplying the experimental pump data of § 6.2, R. Barnkob for assisting with the 64-bit computer used for the numerical part of this work, and H. A. Stone, R. Camassa and R. M. McLaughlin for stimulating discussions on the background literature. This research was supported by grant number 2106-08-0018 ‘ProCell’, under the Programme Commission on Strategic Growth Technologies, the Danish Agency for Science, Technology and Innovation.

Appendix. Mathematical and numerical details; list of symbols

A list of quantities used in this work alphabetized by symbol (Latin before Greek) is given in table 2.

A.1. The Dirac bra–ket notation for spatial dependence

The basic concept of the bra–ket notation is the inner product of functions, defined by (2.2). It is linear

$$\langle f | A_1 g_1 + A_2 g_2 \rangle = A_1 \langle f | g_1 \rangle + A_2 \langle f | g_2 \rangle, \quad (\text{A } 1)$$

and given the complex representation (2.6) of the velocity field, we often use that

$$\langle u_\ell | g \rangle = \langle g | u_\ell \rangle^* = \langle g^* | u_{-\ell} \rangle, \quad (\text{A } 2a)$$

$$\langle u_\ell e^{i\ell\omega_o t} | g \rangle = e^{-i\ell\omega_o t} \langle u_\ell | g \rangle. \quad (\text{A } 2b)$$

The bra–ket notation is particularly compact when working with basis function expansions. A set of functions $|f_n\rangle$, $n = 0, 1, 2, \dots$, is said to form an orthonormal basis when it fulfills the so-called completeness and orthonormal conditions given by

$$\sum_{n=0}^{\infty} |f_n\rangle \langle f_n| = 1 \quad \text{and} \quad \langle f_m | f_n \rangle = \delta_{m,n}, \quad (\text{A } 3)$$

respectively, where by definition $\delta_{m,n} = 1$ for $m = n$, and 0 for $m \neq n$. Any function $|g\rangle$ can formally be expressed by an expansion in this basis as

$$|g\rangle = \sum_{n=0}^{\infty} a_n |f_n\rangle, \quad (\text{A } 4a)$$

$$a_m = \langle f_m | g \rangle \quad m = 0, 1, 2, \dots \quad (\text{A } 4b)$$

Here (A 4b) follows from multiplication of (A 4a) from the left by $\langle f_m |$ and using (A 3). Since the functions f and g in general depend on time, the inner product may also depend on time. We find that the bra–ket notion allows for a better overview during formal manipulations and lets the underlying structure of the theory stand out more clearly without the clutter of voluminous expressions of integrals. The formalism is particularly convenient for problems involving the Laplace operator, like the present case, because often the corresponding basis functions and eigenvalues are known.

A.2. Method of statistical moments

The great insight of Aris was to realize that the advection–diffusion problem can be rewritten as a series of equations for statistical moments of the solute distribution,

Quantity	Symbol
Cross-sectional part of the ∇ operator	$\nabla_{\perp} = \mathbf{e}_y \partial_y + \mathbf{e}_z \partial_z$
Bra of \bullet , and ket of \bullet	$\langle \bullet $, and $ \bullet\rangle$
Complex conjugation	$*$
Cross-sectional area	\mathcal{A}
Channel radius/half-height	a
Concentration field of solute	c
p th axial moment of concentration	c_p
Initial value for $c(x, \mathbf{r}_{\perp}, t)$	$\tilde{c}(x, \mathbf{r}_{\perp})$
Characteristic concentration	C_o
Molecular diffusivity	D
Effective diffusivity	D_{eff}
Effective diffusivity, time averaged	D_{eff}^{avr}
Effective diffusivity, steady flow	D_{eff}^{steady}
Cartesian basis vectors	$\mathbf{e}_x, \mathbf{e}_y, \mathbf{e}_z$
n th basis function	f_n
Bessel function, first kind of order s	J_s
Generalized wavenumber, (5.1a)	k_{ℓ}
Channel length	\mathcal{L}
Characteristic length	L_o
p th full moment of concentration	M_p
Surface normal vector	\mathbf{n}
Pressure	p
Characteristic pressure	P_o
Péclet number	$Pe = U_o L_o / D$
Generalized wavenumber, (6.1a)	$q_{j\ell}$
Channel aspect ratio	$R = w/a$
Position vector	\mathbf{r}
Cross-sectional position vector	$\mathbf{r}_{\perp} = (y, z)$
Schmidt number	$Sc = \nu/D$
Characteristic time	T_o
Time	t
Characteristic velocity	U_o
Axial velocity component of solvent	u
Volume	\mathcal{V}
Velocity field of solvent	\mathbf{v}
Channel half-width	w
Womersley number	$Wo = \sqrt{L_o^2 \tilde{\omega}_o / \nu}$
Solute centre of mass	\bar{x}
Cylindrical coordinates	x, r, φ
Cartesian coordinates	x, y, z
Fluid momentum equilibration rate	α_m, α_{fl}
Prefactor (6.2a)	Γ
Kronecker delta	$\delta_{n,m}$
ℓ th velocity component amplitude	ε_{ℓ}
Dynamic viscosity	η
n th root of Bessel function J_s	$\xi_{s,n}$

TABLE 2. (Continued on next page)

Quantity	Symbol
n th diffusion rate eigenvalue	λ_n
p th moment of concentration about the mean	μ_p
Kinematic viscosity of solvent	ν
Density of solvent	ρ
Diffusivity enhancement	$\chi_{plate}, \chi_{rect}$
Cross-section	Ω
Base frequency, non-dimensionalized	$\omega_o = Wo^2 Sc$
Base frequency, dimension-full	$\tilde{\omega}_o$
Oscillation period	$\tau_0 = 2\pi/\omega_o$

TABLE 2. (cntd) List of quantities used in this work alphabetized by symbol (Latin before Greek).

which then can be solved sequentially (Aris 1956). Each additional moment adds new information about the distribution, and some of the lower moments have direct physical interpretations. We here give Aris’s definitions and resulting equations of motion for the statistical moments reformulated in the bra–ket notation.

The p th axial moment $c_p(\mathbf{r}_\perp, t)$ of the solute concentration field $c(x, \mathbf{r}_\perp, t)$ and the associated full moment $M_p(t)$ are defined by (2.12b) and (2.12a) in the main text. Taking the time derivative of these equations and using the advection–diffusion equation (2.9), we obtain the recursive equations of motion (2.13a) and (2.13b) for c_p and M_p as well as their boundary conditions, (2.14). M_0 corresponds to the unit norm of c , while M_1 is the time-dependent, axial centre of mass \bar{x} of c ,

$$M_0 = \langle 1 | c \rangle = 1, \quad (\text{A } 5a)$$

$$M_1 = \langle x | c \rangle = \bar{x}(t). \quad (\text{A } 5b)$$

The p th moment μ_p about the centre of mass is defined by

$$\mu_p(t) = \langle (x - \bar{x})^p | c \rangle, \quad (\text{A } 6)$$

and by the linearity of the inner product, (A 1), we find for $p = 0, 1$ and 2 ,

$$\mu_0(t) = \langle 1 | c \rangle = 1, \quad (\text{A } 7a)$$

$$\mu_1(t) = \langle (x - \bar{x}) | c \rangle = 0, \quad (\text{A } 7b)$$

$$\mu_2(t) = \langle (x - \bar{x})^2 | c \rangle = M_2(t) - M_1(t)^2. \quad (\text{A } 7c)$$

In particular the time-dependent spatial variance μ_2 of the solute concentration is of key interest as it relates the to the solute molecular diffusivity and the effective diffusivity D_{eff} . For a vanishing velocity field, $u = 0$, μ_2 relates to the diffusivity D of the solute by $d\mu_2/dt = 2D$, or in dimensionless form, $d\mu_2/dt = 2$, since:

$$\begin{aligned} \frac{d\mu_2}{dt} &= \langle (x - \bar{x})^2 | \partial_t c \rangle - 2 \langle (x - \bar{x}) | c \rangle \frac{d\bar{x}}{dt} \\ &= \langle (x - \bar{x})^2 | \nabla^2 c \rangle - 2\mu_1 \frac{d\bar{x}}{dt} = 2 \langle 1 | c \rangle = 2, \end{aligned} \quad (\text{A } 8)$$

where in the last term we have integrated by parts twice and used the boundary conditions (2.10a) and (2.10c). This corresponds to the well-known result for diffusion in one dimension, $(\Delta x)^2 = 2Dt$, with $\mu_2 \sim (\Delta x)^2$.

When the solvent velocity field u is non-zero the time-dependence of the variance is no longer linear. However, by a traditional generalization (Aris 1956, 1960; Chatwin 1975; Barton 1983; Mukherjee & Mazumder 1988; Brenner & Edwards 1993) the dispersion or effective diffusivity $D_{\text{eff}}(t)$ is defined as done in (2.11) in the main text $D_{\text{eff}}(t) = (1/2)(d\mu_2/dt) = (1/2)(dM_2/dt) - M_1(dM_1/dt)$. Other works have been concerned with the skewness μ_3 of the solute distribution (Barton 1983; Camassa *et al.* 2010). More information about the distribution of c is added with each moment, however, the information contained in each moment remains valid no matter how many moments have been determined.

A.3. The dispersion for short times

We show here that $D_{\text{eff}}(t)$ is positive for short times $t \ll 1/\lambda_1, 1/(2\ell_{\text{max}}\omega_o)$. In this limit we have

$$e^{i(\ell-k)\omega_o t} - e^{-(\lambda_n + i\ell\omega_o)t} = (\lambda_n + i\ell\omega_o)t + O(t^2), \quad (\text{A } 9)$$

thus reducing (3.22) for $D_{\text{eff}}(t)$ to

$$\begin{aligned} D_{\text{eff}}(t) &\approx 1 + P\acute{e}^2 \sum_{n=1}^{\infty} \sum_{\ell=-\ell_{\text{max}}}^{\ell_{\text{max}}} \sum_{k=-\ell_{\text{max}}}^{\ell_{\text{max}}} \langle u_k | f_n \rangle \langle f_n | u_\ell \rangle t \\ &= 1 + tP\acute{e}^2 \sum_{n=1}^{\infty} \left\langle \sum_{k=-\ell_{\text{max}}}^{\ell_{\text{max}}} u_k | f_n \right\rangle \left\langle f_n | \sum_{\ell=-\ell_{\text{max}}}^{\ell_{\text{max}}} u_\ell \right\rangle \\ &= 1 + tP\acute{e}^2 \sum_{n=1}^{\infty} | \langle f_n | u(0) \rangle |^2, \quad t \ll \frac{1}{\lambda_1}, \frac{1}{2\ell_{\text{max}}\omega_o}. \end{aligned} \quad (\text{A } 10)$$

Here $u(0)$ is the total velocity field $u(t)$ evaluated at time $t = 0$. This expression becomes problematic to apply in the case where infinitely many harmonics of the velocity field is present at $t = 0$ as for the startup of the Poiseuille flow, but for flows with a maximum frequency we have shown $D_{\text{eff}}(t) > 0$.

A.4. Numerics

For numerical evaluations of the effective diffusivity $D_{\text{eff}}(t)$ we relied on three methods. First, using the commercial finite element package COMSOL MULTIPHYSICS version 3.5a, we calculated $D_{\text{eff}}(t)$ numerically directly from the definition (2.11) by solving for the concentration field c in the governing advection–diffusion equation (2.9) using the analytical solutions for the velocity field as input. From the obtained $c(\mathbf{r}, t)$ we determined $M_1(t)$, $dM_1(t)/dt$ and $dM_2(t)/dt$, and from these $D_{\text{eff}}(t)$. To ensure mass conservation the number of mesh elements was chosen so that the local Péclet number in each cell (as given by the velocity in the mesh element, the mesh element length and the global diffusivity) was approximately 0.5. Where possible, the available symmetries were exploited for computational efficiency. To this end the solutions of the flow problems in channels of circular cross-section took advantage of the azimuthal symmetry and the solution was computed in a frame of reference travelling with the mean speed of the flow.

Second, for rectangular cross-sections the problem was only solved for one quarter of the cross-section in a frame of reference moving with the flow mean speed. However, due to memory limitations even these simplifications proved unfeasible for Péclet numbers exceeding ~ 2 and aspect ratios above ~ 2 . Thus, for the results presented in figure 3(a) we numerically solved the axial moment equation (2.12b)

for c_o and c_1 , and from these obtained $M_1(t)$, $dM_1(t)/dt$, and $dM_2(t)/dt$, as well as $D_{eff}(t)$. Time averages of the numerical simulation results were computed by running the simulation for a full period of the base frequency after the decay of all transients, followed by numerical integration of $D_{eff}(t)$ over the period.

Third, we calculated $D_{eff}(t)$ based on our theoretical expression (3.22), but reduced the number of terms needed to be calculated by separating the ℓ - and k -sums and collecting complex conjugated pairs of index $\{\ell, -\ell\}$ and $\{k, -k\}$,

$$D_{eff}(t) = 1 + Pe^2 \sum_{n=1}^{\infty} \left\{ \frac{\langle f_n | u_0 \rangle}{\lambda_n} [1 - e^{-\lambda_n t}] + 2 \sum_{\ell=1}^{\infty} \operatorname{Re} \left[\frac{\langle f_n | u_{\ell} \rangle}{\lambda_n + i\ell\omega_o} (e^{i\ell\omega_o t} - e^{-\lambda_n t}) \right] \right\} \\ \times \left\{ \langle f_n | u_0 \rangle + 2 \sum_{k=1}^{\infty} \operatorname{Re}[\langle f_n | u_k \rangle e^{ik\omega_o t}] \right\}. \quad (\text{A } 11)$$

Furthermore, the involved n -, ℓ - and k -dependent terms are calculated and placed in lists before evaluating the sums. The latter converge quickly, and we have therefore truncated them after the first 50 terms unless stated otherwise in the text.

REFERENCES

- AJDARI, A., BONToux, N. & STONE, H. A. 2006 Hydrodynamic dispersion in shallow microchannels: the effect of cross-sectional shape. *Analyt. Chem.* **78**, 387–392.
- ARIS, R. 1956 On the dispersion of a solute in a fluid flowing through a tube. *Proc. R. Soc. Lond. A Mat.* **235** (1200), 67–77.
- ARIS, R. 1960 On the dispersion of solute in pulsating flow through a tube. *Proc. R. Soc. Lond. A Mat.* **259** (1298), 370–376.
- BANDYOPADHYAY, S. & MAZUMDER, B. S. 1999 Unsteady convective diffusion in a pulsatile flow through a channel. *Acta Mechanica* **134**, 1–16.
- BARTON, N. G. 1983 On the method of moments for solute dispersion. *J. Fluid Mech.* **126**, 205–218.
- BATCHELOR, G. K. 1967 *An Introduction to Fluid Dynamics*. Cambridge University Press.
- BIRD, R. B., STEWART, W. E. & LIGHTFOOT, E. N. 2006 *Transport Phenomena*, 2nd edn. John Wiley and Sons.
- BONToux, N., PÉPIN, A., CHEN, Y., AJDARI, A. & STONE, H. A. 2006 Experimental characterization of hydrodynamic dispersion in shallow microchannels. *Lab on a Chip* **6**, 930–935.
- BRENNER, H. & EDWARDS, D. A. 1993 *Macrotransport Processes*. Butterworth–Heinemann.
- BRUUS, H. 2008 *Theoretical Microfluidics*. Oxford University Press.
- BRUUS, H. & STONE, A. D. 1994 Quantum chaos in a deformable billiard: applications to quantum dots. *Phys. Rev. B* **50** (24), 18275–18287.
- CAMASSA, R., LIN, Z. & MCLAUGHLIN, R. 2010 The exact evolution of scalar variance in pipe and channel flow. *Commun. Math. Sci.* **8** (2), 601–626.
- CHATWIN, P. C. 1975 On the longitudinal dispersion of passive contaminant in oscillatory flows in tubes. *J. Fluid Mech.* **71**, 513–527.
- CHATWIN, P. C. 1977 Initial development of longitudinal dispersion in straight tubes. *J. Fluid Mech.* **80**, 33–48.
- CHATWIN, P. C. & SULLIVAN, P. J. 1982 The effects of aspect ratio on longitudinal diffusivity in rectangular channels. *J. Fluid Mech.* **120**, 347–358.
- DIRAC, P. A. M. 1981 *The Principles of Quantum Mechanics*, 4th edn. Oxford University Press.
- DOSHI, M. R., DAIYA, P. M. & GILL, W. N. 1978 Three dimensional laminar dispersion in open and closed rectangular conduits. *Chem. Engng Sci.* **33**, 795–804.
- DUTTA, D., RAMACHANDRAN, A & LEIGHTON, D. T. 2006 Effect of channel geometry on solute dispersion in pressure-driven microfluidic systems. *Microfluid Nanofluid* **2**, 275–290.

- ERDOGAN, M. E. & CHATWIN, P. C. 1967 Effects of curvature and buoyancy on laminar dispersion of solute in a horizontal tube. *J. Fluid Mech.* **29** (3), 465–484.
- FAN, L. T. & WANG, C. B. 1966 Dispersion of matter in non-Newtonian laminar flow through a circular tube. *Proc. R. Soc. Lond. A Mat.* **292** (1429), 203–208.
- GLEESON, J. P. 2002 Electroosmotic flows with random zeta potential. *J. Colloid Interface Sci.* **249** (1), 217–226.
- GODDARD, J. D. 1993 The Green's function for passive scalar diffusion in a homogeneously sheared continuum. *Phys. Fluids A* **5**, 2295–2297.
- HARRIS, H. G. & GOREN, S. L. 1967 Axial diffusion in a cylinder with pulsed flow. *Chem. Engng Sci.* **22**, 1571–1576.
- JANSONS, K. M. 2006 On Taylor dispersion in oscillatory channel flows. *Proc. R. Soc. Lond. A Mat.* **462**, 3501–3509.
- LATINI, M & BERNOFF, AJ 2001 Transient anomalous diffusion in Poiseuille flow. *J. Fluid Mech.* **441**, 399–411.
- LEIGHTON, D. T. 1989 Diffusion from an initial point distribution in an unbounded oscillating simple shear flow. *Physico-Chem. Hydrodyn.* **11**, 377–386.
- LIDE (EDITOR-IN-CHIEF), D. R. 1995 *CRC Handbook of Chemistry and Physics*, 75th edn. CRC Press.
- MEHTA, M. L. 2004 *Random Matrices*, 3rd edn. *Pure and Applied Mathematics*, vol. 142. Elsevier/Academic Press.
- MOLLOY, R. F. & LEIGHTON, D. T. 1998 Binary oscillatory cross-flow electrophoresis: theory and experiments. *J. Pharma. Sci.* **87**, 1270–1281.
- MORTENSEN, N. A. & BRUUS, H. 2006 Universal dynamics in the onset of a Hagen–Poiseuille flow. *Phys. Rev. E* **74** (1), 017301.
- MORTENSEN, N. A., OLESEN, L. H. & BRUUS, H. 2006 Transport coefficients for electrolytes in arbitrarily shaped nano and micro-fluidic channels. *New J. Phys.* **8**, 37–51.
- MUKHERJEE, A. & MAZUMDER, B. S. 1988 Dispersion of contaminant in oscillatory flows. *Acta Mechanica* **74**, 107.
- PAUL, S. & MAZUMDER, B. S. 2008 Dispersion in unsteady Couette–Poiseuille flows. *Intl J. Engng Sci.* **46**, 1203–1217.
- PROBSTEN, R. F. 1994 *Physicochemical Hydrodynamics. An Introduction*, 2nd edn. John Wiley and Sons.
- SANKARASUBRAMANIAN, R. & GILL, W. N. 1973 Unsteady convective diffusion with interphase mass-transfer. *Proc. R. Soc. Lond. A Mat.* **333** (1592), 115–132.
- SKAFTE-PEDERSEN, P., SABOURIN, D., DUFVA, M. & SNAKENBORG, D. 2009 Multi-channel peristaltic pump for microfluidic applications featuring monolithic PDMS inlay. *Lab on a Chip* **9**, 3003–3006.
- TAYLOR, G. I. 1953 Dispersion of soluble matter in solvent flowing slowly through a tube. *Proc. R. Soc. Lond. A Mat.* **219** (1137), 186.
- TAYLOR, H. M. & LEONARD, E. F. 1965 Axial dispersion during pulsating pipe flow. *AIChE J.* **11** (4), 686–689.
- THOMAS, A. M. & NARAYANAN, R. 2001 Physics of oscillatory flow and its effect on the mass transfer and separation of species. *Phys. Fluids* **13** (4), 859–866.
- VAN DEN BROECK, C. 1982 A stochastic description of longitudinal dispersion in uniaxial flows. *Physica A* **112**, 343–352.
- VEDEL, S., OLESEN, L. H. & BRUUS, H. 2010 Pulsatile microfluidics as an analytical tool for determining the dynamic characteristics of microfluidic systems. *J. Micromech. Microengng* **20**, 035026.
- VIKHANSKY, A. & WANG, W. 2011 Taylor dispersion in finite-length capillaries. *Chem. Engng Sci.* **66** (4), 642–649.
- WATSON, E. J. 1983 Diffusion in oscillatory pipe flow. *J. Fluid Mech.* **133**, 233–244.
- WOMERSLEY, J. R. 1955 Method for the calculation of velocity, rate of flow and viscous drag in arteries when the pressure gradient is known. *J. Physiol.* **127**, 553–563.

Appendix F

Paper published in the Proceedings of the National Academy of Sciences of the USA

Title: Migration of cells in a social context

Authors: Søren Vedel, Savaş Tay, Darius M. Johnston, Henrik Bruus and Stephen R. Quake.

Migration of cells in a social context

Søren Vedel^{a,1}, Savaş Tay^{b,1}, Darius M. Johnston^{c,d,e}, Henrik Bruus^a, and Stephen R. Quake^{c,d,e,2}

^aDepartment of Micro- and Nanotechnology, Technical University of Denmark, DK-2800 Kongens Lyngby, Denmark; ^bDepartment of Biosystems Science and Engineering, ETH Zurich, 4058 Basel, Switzerland; and Departments of ^cApplied Physics and ^dBioengineering and ^eHoward Hughes Medical Institute, Stanford University, Stanford, CA 94305

Edited by Robert H. Austin, Princeton University, Princeton, NJ, and approved November 15, 2012 (received for review March 13, 2012)

In multicellular organisms and complex ecosystems, cells migrate in a social context. Whereas this is essential for the basic processes of life, the influence of neighboring cells on the individual remains poorly understood. Previous work on isolated cells has observed a stereotypical migratory behavior characterized by short-time directional persistence with long-time random movement. We discovered a much richer dynamic in the social context, with significant variations in directionality, displacement, and speed, which are all modulated by local cell density. We developed a mathematical model based on the experimentally identified “cellular traffic rules” and basic physics that revealed that these emergent behaviors are caused by the interplay of single-cell properties and intercellular interactions, the latter being dominated by a pseudopod formation bias mediated by secreted chemicals and pseudopod collapse following collisions. The model demonstrates how aspects of complex biology can be explained by simple rules of physics and constitutes a rapid test bed for future studies of collective migration of individual cells.

cell migration | single-cell analysis | physical modeling | microfluidics

Collective migration, from migrating cells in tissue (1–3) to swarming insects (4) to flocks of birds (5) and pedestrians in heavy traffic (6), constitutes one of the most fascinating spectacles in nature. In addition to its aesthetic qualities, social cell migration is involved in embryonic development (7), wound healing (8), and immune response (9), and unregulated migration leads to disease, including cancer metastasis (10). Previous work on single-cell migration has focused on isolated (11–20) or strongly polarized and aligning (21, 22) cell types, mostly using population-averaged bulk assays (23) or simple observations in a social context (2, 3). However, strongly cross-correlated cell motion and collective substrate deformation has been found to arise in mechanically interlinked cells transmitting forces through both cell–cell linkages and the substrate (24–29). These studies revealed useful information on cell migration, but because in general the relevant interactions in a social context and their relative importance are not established, migratory behavior of cells in a social context remains as one of the major unresolved problems in biology (30). Furthermore, striking social effects such as highly sensitive collective responses in a number of sensing systems [e.g., quorum sensing (31, 32) and onset of collective behavior in *Dictyostelium discoideum* (33)] mediated by increased levels of cell-secreted signals in higher cell density indicate that mechanical links are not necessary for collective behavior. At the subcellular level, many types of nonswimming motile cells involved in multicellular biology [e.g., fibroblasts, *Dictyostelium*, and neutrophils (13, 14, 16–18)] have been found to transmit traction force to the substrate by intracellularly polymerizing their cytoskeletons in dynamically formed membrane protrusions known as pseudopodia. However, whether the social context changes this, mechanisms by which the social context manifests itself, and the implications of being close to neighboring cells all remain unexplored.

Here we shed light on these fundamental questions using a combination of high-throughput microfluidic cell culture (34) of 3T3 fibroblast cells expressing fluorescent fusion proteins, time-lapse microscopy with subcellular resolution, and physical modeling (*SI Appendix, Materials and Methods and Model Details*). Contrary to previous work (22, 24–26, 29), these cells form neither

2D sheets nor 3D structures, nor are they highly polarized, and their single-cell migratory behavior is established (13, 14, 16). The microfluidic cell culture platform hosts independent and isolated culture conditions in each of the isolated 96 polymethylsiloxane (PDMS) chambers (34-nL volume) that mimic physiological conditions more plausibly than traditional cell-culture environments in which concentrations of, for instance, secreted signaling molecules are diluted into large volumes of surrounding fluid. Using only freshly thawed cells, we cultured them at densities ranging from 15 to ~100% confluence in up to 24 parallel chambers at a time; more than 8,000 cells were quantified, yielding hundreds of thousands of data points from a total of only five experimental runs. Experiments on any given density were repeated at least once on different chips, and we studied different densities in parallel on each chip (*SI Appendix, Table S1*). We replaced the chamber volume at time $t = 0$, sealed the chamber using the microfluidic membrane valves, and imaged the cells every 4–6 min for 5–6 h, focusing on a region of ~500 $\mu\text{m} \times 700 \mu\text{m}$ in the center of the chamber to avoid edge effects, which contained a population consisting of between 36 and 246 cells [corresponding to an average minimum nucleus–nucleus distance \bar{d}_{\min} in the range of approximately one to three cell diameters, which on average is 41.7 μm (*SI Appendix, Fig. S124*)]. Using different fluorescent fusion proteins to image the nuclei (green) and cytosols (red) (Fig. 1*A*) coupled with high imaging resolution allowed us to track single-cell migration behavior and pseudopodia, producing a very comprehensive dataset; such detailed quantitative measurements of single-cell behavior are emerging as a strong tool for studying biological systems, as recently exemplified for cell cycle stability (35) and inflammatory signaling (36).

Results

Quantitative Cell Migration Characteristics. Our measurements reveal the migration characteristics of cells at different densities. Although all cells move (Fig. 1*A* and *SI Appendix, Fig. S2* and *Table S2* and *Movie S1*) with no preferred overall direction (*SI Appendix, Fig. S3*), we find large diversity with negligible cross-correlation in the migratory behavior of the cells at the same density (Figs. 1 and 2*E* and *SI Appendix, Fig. S2*): Some cells move along almost straight lines, other follow curved paths, and yet others traverse very short distances with little apparent directionality (Fig. 1*B*). This continuum of different migratory behaviors, which is very different from the stereotyped single-cell behavior found for isolated cells (11, 13, 14), suggests that there is a strong effect of the

Author contributions: S.V., S.T., H.B., and S.R.Q. designed research; S.V., S.T., and D.M.J. performed research; S.V., S.T., H.B., and S.R.Q. analyzed data; and S.V., S.T., H.B., and S.R.Q. wrote the paper.

The authors declare no conflict of interest.

This article is a PNAS Direct Submission.

Freely available online through the PNAS open access option.

Data deposition: A MATLAB implementation of the model presented in the paper has been deposited at [SourceForge.net](http://sourceforge.net/projects/cell-migration/), <http://sourceforge.net/projects/cell-migration/>.

¹S.V. and S.T. contributed equally to this work.

²To whom correspondence should be addressed. E-mail: quake@stanford.edu.

This article contains supporting information online at www.pnas.org/lookup/suppl/doi:10.1073/pnas.1204291110/-/DCSupplemental.

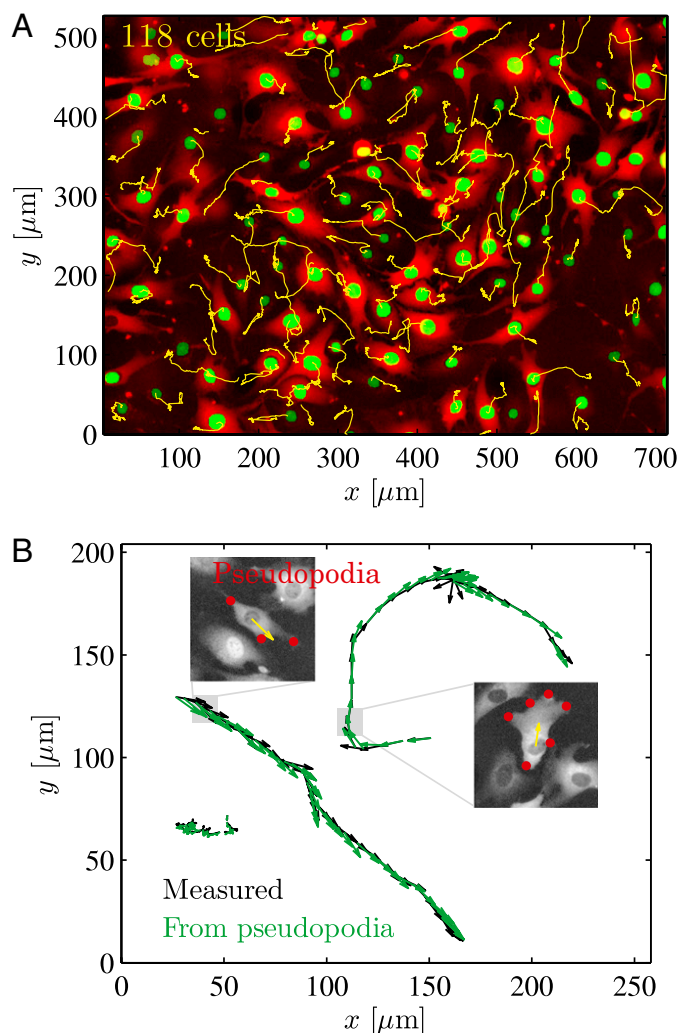


Fig. 1. Trajectories of the cells generated during the first 200 min of an experiment. (A) Trajectories (yellow) displayed on top of the fluorescence image illustrating the different fusion proteins used for the cytosols (red) and nuclei (green). (B) Trajectories can be nominally straight, curve, or display little apparent directionality. The vectorial sum of the pseudopodia of the cell (marked by red in insets) predicts the observed movement, because each pseudopod applies nominally the same force (20).

social context on the migration of the individual, even in the absence of cell–cell linkages (24–26). To fully understand this effect, including whether it is due to inherent cell–cell motility variations or is an emergent group property, we quantified all aspects of the migration using a number of cooperating statistical measures that together fully characterize the migration.

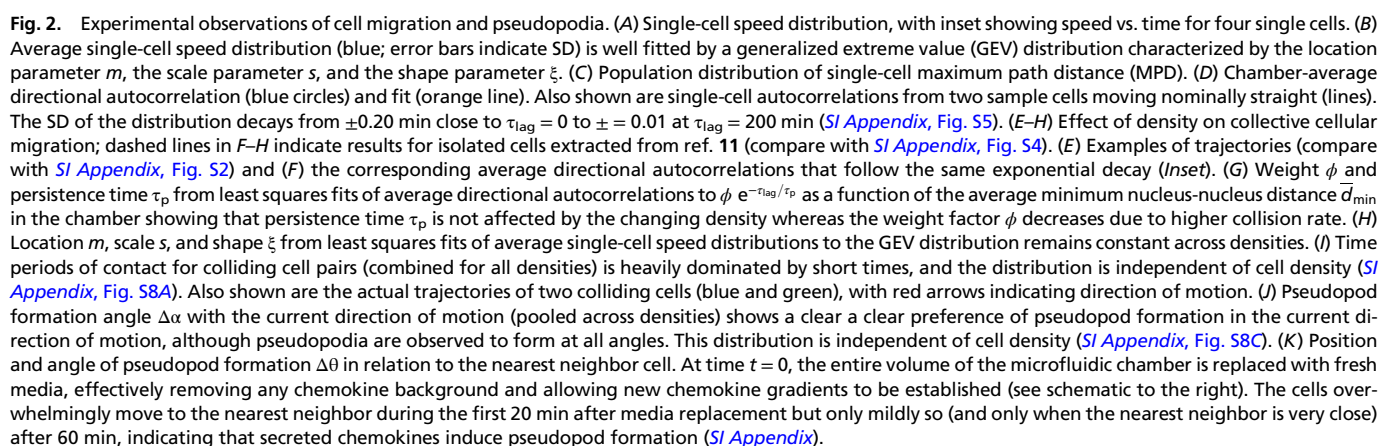
We first focus on an experiment at intermediate cell density ($\bar{d}_{\min} = 91.1 \mu\text{m}$) to introduce our statistical measures and illustrate our key findings. The speed of the individual cell fluctuates substantially as a function of time (Fig. 2*A Inset*) with similar single-cell speed distributions (Fig. 2*A*), and the average single-cell distribution from one experiment displays a distinct non-Gaussian tail (Fig. 2*B*) that has previously been shown to be a general feature of non-sheet-forming motile cells (37). The existence of similar non-Gaussian single-cell speed distributions suggests by the central limit theorem that each cell does not have an inherent velocity scale, but rather that cell speed is a dependent variable. The simultaneous observations of fluctuating single-cell speed and cell velocity being a dependent variable is consistent with pseudopodia-driven motility (*SI Appendix*).

To quantify the variations in total space sampled by the individuals we introduce the “maximum path distance” (MPD), defined as the maximum distance between any two points on the trajectory of the individual cell. This measure, which is equivalent to the span dimension of polymer physics (38), displayed large variations across the population, with large and small MPD values corresponding to cells moving nominally straight and cells that displace themselves small distances, respectively (MPD is nontrivially related to variations in single-cell trajectory curvature).

The observed variations in trajectories could be caused by a relative lack of collisions; however, we observed cells moving nominally straight even though they were in direct contact with other cells, as well as cells without direct contact with other cells displaying little long-term directionality (*Movie S1*). This indicates that collisions are not solely responsible for the variations in migratory behavior, and so to further investigate this single-cell directionality, we compute the directional autocorrelation of the cellular trajectories using the unit vectors in the direction of instantaneous velocity (*SI Appendix*, Eq. S3 and Fig. 2*D*). This measure describes the average alignment of the direction of motion of the same cell over time and therefore measures the persistence of the direction of motion. Using the unit vectors in the direction of instantaneous velocity as opposed to the velocity vectors themselves removes any bias from the fluctuating speed and sets the range from 0 (no correlation) to 1 (complete correlation). The chamber-mean directional autocorrelation, which is representative of the majority of the cells (outliers only nominally affect the mean because the kurtosis is everywhere low; *SI Appendix*, Fig. S5), shows that the instantaneous step taken by each cell is positively correlated with the previous steps (Fig. 2*D*). The first sharp drop-off between the first and second time points occurs because changes in directionality are measured only every 4–6 min, and the rest of the data are well described by a decaying exponential $\phi e^{-\tau_{\text{lag}}/\tau_p}$. Here, the persistence time of directionality τ_p and the weight ϕ (varying from 0 to 1) describe, respectively, the time for the average cell to randomize its direction and the extent of directional motion in the chamber, with higher values of ϕ indicating a larger fraction of directionally persistent cells. For the present experiment we found $\phi = 0.46$ and $\tau_p = 69$ min.

Varying the cell density, we continue to observe straight-moving cells at all densities (Fig. 2*E*) even though each cell at intermediate and high densities experiences many collisions (and the ratio of cell surface area to total available chamber area is around 0.8 at all times; *SI Appendix*). The fraction of directionally persistent cells decreases at higher densities, but the persistence time of the individual cells remains essentially constant. This is illustrated by the decrease of the weight ϕ and the constancy of persistence time of directionality τ_p in Fig. 2*F* and *G*. The average single-cell speed distribution is also independent of density, and this is well-fitted by generalized extreme value (GEV) distribution, which forms a natural parameterization (Fig. 2*H*; example fit shown in Fig. 2*B*). Both our measurements of speed distribution and the low-density limit of the directional autocorrelation agree with previous results for human fibroblasts (11) (the latter indicated by dashed lines in Fig. 2*F–H*; compare with *SI Appendix*, Fig. S4). These findings indicate that the observed directionality does not depend on the fluctuating speed of the single cell, and the small variations in τ_p both within and across densities suggests that the directional persistence of motion, unlike cell speed and trajectory, is an inherent property of the cell’s motility apparatus (i.e., internal polarization). Furthermore, the convergence of all our statistical measures to the level of isolated cells at $\bar{d}_{\min} \approx 120 \mu\text{m}$ determines the critical density where the social context becomes important.

Pseudopod Formation and Lifetime Is Affected by Social Context. We verified that the cell migration in the social context is also mediated by pseudopodia (Fig. 1*B* and *Movie S2*), and so to probe the origin of the diverse cellular migratory behavior we therefore next



and exhibits no dependence of density (Fig. 2I and *SI Appendix*, Fig. S84). We found a distribution of pseudopod lifetimes with a mean of 11.8 min (*SI Appendix*, Fig. S64), so the directional persistence of ~ 50 min indicated by the autocorrelation analysis (Fig. 2D and G) can only be maintained by the cells through ordered pseudopod formation. Further investigations indicated that

pseudopod formation is dominated by independent biases by the current direction of motion (Fig. 2*J*) and chemicals (chemokine) secreted by the cells (Fig. 2*K* and *SI Appendix, Table S2*). Evidence of the former was found by computing the angle between the current cellular direction of motion and the position of pseudopod formation (Fig. 2*J*), which displayed a clear bias for the present direction of motion that is probably mediated by an internal polarization of key molecules (40), whereas evidence for the latter was found by studying the influence of neighbor cells in biasing pseudopod formation: Pseudopodia formed exclusively toward the nearest neighbor cell during the first 20 min after medium replacement (Fig. 2*K Upper*), but much less so when the analysis was redone starting 60 min after replacement (except when the neighbor is very close; Fig. 2*K Lower*). The effect was reproduced following additional media replacements in separate control experiments (*SI Appendix, Fig. S9*). Because these cells both possess chemotactic ability and furthermore are known to secrete some chemokines (*SI Appendix*), this effect is most likely caused by one or several secreted chemokine(s), as evidenced by the decrease of the response at later times except very close to neighbors and corroborated by the fact that most chemokine molecules have diffusivities on the order $10^{-10} \text{ m}^2 \cdot \text{s}^{-1}$, which sets the time scale for chamber filling to ~ 40 min. In other words, the secreted chemokines will have saturated the chamber by 40 min, effectively reducing chemokine gradient depths and the signal-to-noise ratio of chemokine receptor activity. Moreover, the constant base level of pseudopod formation observed in our investigation of directional bias (Fig. 2*J*) further illustrates the existence of an additional and independent pseudopod formation biasing system that on average is independent of the current direction of motion, and therefore is likely achieved by the chemokine bias. Although we did observe new pseudopods arising from splitting of existing pseudopodia, similar to the predominant origin of pseudopods observed in isolated cells (14), this was found to be secondary to the biased de novo formation of pseudopods just described (*SI Appendix, Fig. S7*). These observations indicate that the motile apparatus of the individual cell is centered around maintaining a certain direction through an internally controlled pseudopod formation bias (polarization), and that being in a social context introduces a second mechanism based on chemokine-mediated biasing, similar to findings in a previous report for *Dictyostelium* cells (41), as well as a higher frequency of pseudopod formation due to collisions.

Physical Model. To investigate whether these observed traffic rules on the individual cell level indeed do cause the very varied collective motion we observed, we formulated an agent-based mathematical model using the simplest physically reasonable assumptions for the motion of the individual cell based on three types of input: (i) our own pseudopod observations, (ii) previous experimental studies on chemotaxis of isolated cells, and (iii) Newton's second law of particle motion (*SI Appendix, Model Details*). This model, which can be considered an extension of the Vicsek model (21, 22, 42), exploits known cellular biophysics to simulate our experiments with a few hundred cells, a regime that is inaccessible to continuum modeling (43, 44). Model cells (Fig. 3*A*) dynamically form pseudopodia that each apply a force \mathbf{F}_i of constant magnitude F_0 radially away from the nucleus. In a time interval Δt the resultant force moves the cell a distance Δx , or equivalently imparts a velocity $\mathbf{v} = \Delta x / \Delta t$ given by

$$\gamma \mathbf{v} = \sum_i \mathbf{F}_i, \quad [1]$$

where γ is a friction coefficient assumed to be identical for all model cells. Pseudopod formation is biased by the current direction of motion and a spatiotemporal field of chemokine

concentration secreted by all cells. We use biased stochastic pseudopod activation because of the large thermal fluctuations in the low concentrations of intra- and extracellular chemicals. Touching pseudopodia of colliding cells collapse, and their local forces stop because of contact inhibition of locomotion. We furthermore assume chemokine secretion is identical for all cells; that force, collision times, and chemokine response function is the same for all pseudopodia; and that this function is a Hill function of the local relative chemokine concentration (Fig. 3*C*). All model parameters are determined either directly from the data (such as Fig. 2*I* and *J*) or from reported literature results, except for the cell friction coefficient γ , of which no reliable measurements exist. We determined γ from the ensemble average of velocity distribution data by fitting one simulation to one experiment; having determined this single parameter the model predicts all statistical aspects of the collective motion. This is shown below through a number of statistical tests. Although simpler theoretical models have been presented in the past with the objective of investigating certain traits of the collective migration phenomena (21, 22, 37, 42–45), none of these models is able to simultaneously account for a wide variety of the migration data such as ours, and our model thus provides one of the simplest ways of incorporating all of our observations in a physically transparent formulation.

Comparison with Experiments. The model results are summarized in Fig. 3 and demonstrate quantitative agreement with the experiments in terms of single-cell speeds (Fig. 3*D* and *E*), trajectories (Fig. 3*B* and *G*), and directionality (Fig. 3*F*), thereby verifying our experimentally derived hypotheses of the role of the social interactions on motility (*SI Appendix, Fig. S10* and *Movie S4*). The model quantitatively reproduces across cell densities—with a single value of γ —that the individual cells have the same nonnormal speed distribution (Fig. 3*D*) with an average that is similar to the experimental average (Fig. 3*E*); the exponentially decaying autocorrelation (Fig. 3*F*) including the changes in the weight factor ϕ , indicating the importance of the social interactions; and both the shape and range of the distribution of maximum path distances (Fig. 3*G*). The model also predicts the existence of cells moving along almost straight lines for the entire experiment (Fig. 3*B*) and the maximum path distance for these cells [largest single-cell measurements of maximum path distances are the same for model and experiment Fig. 3*G*], but it does underpredict the ratio of these cells, as indicated by smaller tail of model predictions in Fig. 3*G*. In addition, the model value of $\gamma = 39 \text{ kg} \cdot \text{s}^{-1}$ is in fair agreement with an estimate of $\gamma \approx 29 \text{ kg} \cdot \text{s}^{-1}$ extracted from ref. 20 but is roughly one order of magnitude greater than an estimate from endothelial cells and a *Dictyostelium* slug (46) (*SI Appendix*). Although the model captures many features of our single-cell microscopy data, it falls short of perfectly reproducing the tail of the speed distribution (Fig. 3*D* and *E* and *SI Appendix, Fig. S11*), likely because of the assumption of identical and time-independent pseudopod forces (*SI Appendix*). The model furthermore also does not precisely capture the exact shape of the average directional autocorrelations (Fig. 3*F*), indicating that directional persistence is likely achieved through a more complex machinery than is assumed in the model.

Discussion

The agreement of model predictions with experimental data for all of the emergent properties presented in Fig. 3 suggests that the subprocesses included in the model govern the motility. We therefore arrive at the following explanations for our observations: The dynamically changing positions of pseudopodia cause large fluctuations in speed at all densities, whereas directional persistence is achieved primarily by the directional bias of pseudopod formation but heavily influenced by both collisions and the secreted chemokine. The cells at low density are effectively isolated as they rarely collide and the nominally isotropic chemokine field

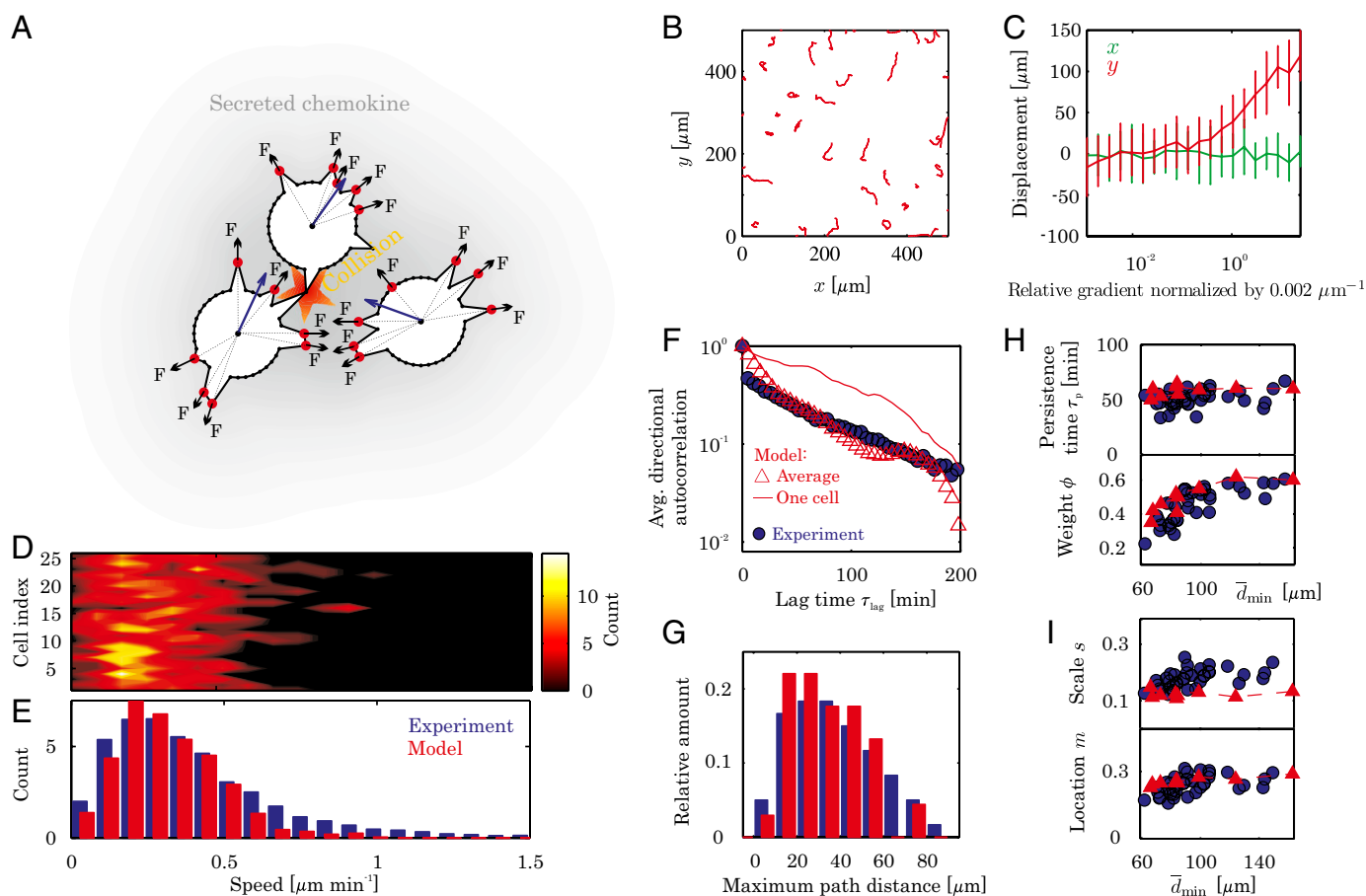


Fig. 3. Model formulation and predictions (model, red; experiments, blue). Experimental data are the same as in Fig. 2. (A) Single cells move by dynamically and stochastically forming pseudopodia (red) while they secrete chemokine, with each pseudopod providing a force, and colliding pseudopodia collapse. (B) Example model trajectories. (C) Average displacement in a 300-min simulation for different relative gradients (the gradient is applied only in the y direction) illustrate that model cells reliably respond to gradients above $0.002 \mu\text{m}^{-1}$, as experimentally observed by Melvin et al. (16). The simulation was repeated 20 times for a single cell at each gradient level and error bars indicate SD. (D) Single-cell speed distributions (compare with Fig. 2A). (E) Average single-cell speed distribution, showing excellent agreement with experiments. (F) Chamber-averaged directional autocorrelation and one single-cell autocorrelation from a cell moving nominally straight (compare with Fig. 2D; compare with [SI Appendix, Fig. S5](#)). (G) Population distribution of maximum path distance (blue, experiment; red, model). (H and I) Model results across densities with the latter expressed by the average minimum cell-cell distance \bar{d}_{\min} (red, model; blue, experiment). (H) Weight ϕ and persistence time τ_p for the fit to $\phi e^{-t/\tau_p}$. (I) Location parameter m and scale parameter s in fit of average speed distribution to a GEV distribution. The shape parameter ξ ([SI Appendix, Fig. S11](#)), describing the tail of the distribution, is not well captured by the model because it underpredicts this part of the speed distribution, as seen in E.

therefore has little influence on the positions of new pseudopodia, whereas high collision rates at high densities lead to constant randomization of pseudopodia positions and low ϕ . At any density, straight-moving cells execute this motile behavior because their lateral pseudopodia are more often suppressed by lateral collisions with other cells or abruptly changing, large chemokine gradients. Cells displaying little overall directionality constantly have their direction of motion cut off, leading to many collisions, whereas curling cells experience few collisions and/or a clear and slowly moving chemokine bias. The observed continuum of different trajectories is therefore a direct consequence of the fluctuating near-cell environment and is no more surprising than similar observations of very varied trajectories of many interacting bodies obeying Newtonian mechanics. The model thus provides a comprehensible description of social cell migration that captures all of the complexity formulated in terms of biophysically well-defined single-cell quantities and, furthermore, illustrates how very complex biological behavior emerges from simple interaction rules.

Contrary to several other cell types, such as keratocytes (22), 3T3 fibroblast cells do not exhibit large-scale multicellular organization such as flocking (21). Fibroblasts deviate from these flocking cell types by not having strong local alignment of the

neighbors, which therefore must be considered critical in achieving flocking. We nonetheless hypothesize that the observed effects of the neighboring cells on single-cell migration is highly relevant at physiological conditions. Within a population, the high collision rate continuously randomizes the directionality of the individual cells, so that on average there will always be cells moving away from the population. In the presence of an external signal, some of these boundary cells will be correctly aligned with this signal and will reliably move up the gradient, with the directional persistence providing the initial stabilization of the movement away from the population. This mechanism provides a directionally isotropic and fast sensor of external signals for the population, even though the single-cell polarizations vary and single-cell realignment with the external signal would occur on the time scale of directional persistence (τ_p). Whereas this social effect is fundamentally different from flocking and other social effects such as quorum sensing, it is another example of how nature achieves group-level dynamics of ignorant individuals for biological function beyond the control of the individuals by simply modulating the signal at the level of the individual through increased cell density. This mechanism could be a general biological principle underlying emerging population

behavior, yet the underpinnings, limits, and consequences remain to be investigated.

In summary, our investigations of social cell migration for thousands of cells at different densities have revealed a diverse migratory behavior that is largely controlled by the changing environment: Whereas the single cell tries to maintain its current direction of motion through preferentially forming pseudopodia in this direction, secreted chemokine-induced pseudopod formation along with collisions lead to pseudopod collapse, resulting in much more complex migratory behaviors than those reported for isolated cells, even in the absence of cell–cell variations. A simple model based on these observations quantitatively reproduces most migration behaviors across densities, including the existence of outliers, illustrating that these are the intercellular rules governing migration. In addition to their biological significance, our findings illustrate how complex biological behavior arises as a physical consequence of noisy single-cell behavior and interactions among the individuals, open a path for the derivation of continuum theory, and illustrate the importance of single-cell data in understanding such behavior.

Materials and Methods

Cell Line and Microfluidic Cell Culture Experiments. We used newly thawed p65^{−/−} mouse fibroblast (3T3) cells expressing the cytosolic fluorescent fusion

protein p65-DsRed under control of the endogenous mouse p65 promoter as well as the nuclear marker H2B-GFP driven by the human ubiquitin C promoter. Cells were seeded at densities from 4,000–40,000 cells cm^{−2} (~40–400 cells per chamber) into microfluidic chambers and the external conditions were set to standard culture conditions [5% (vol/vol) CO₂ and 37 °C external temperature] and maintained at this level. To conduct the experiments we replaced the chamber volume with fresh medium and sealed the chamber (the cells remained in the same media during the entire experiment; some cells were also exposed to TNF-α). The cells were imaged at a constant rate either every 4 or 6 min in both GFP and DsRed fluorescence channels during the entire experiment (5–6 h). Details are given in [SI Appendix, Materials and Methods](#).

Automated Image Analysis. Automated image analysis algorithms used to obtain cell trajectories and pseudopod statistics are detailed in [SI Appendix, Materials and Methods](#).

Model. Details of model development and implementation in MATLAB are given in [SI Appendix, Model Details](#).

ACKNOWLEDGMENTS. The authors thank Tobias Meyer for a critical reading of the manuscript. S.V. thanks Tobias Meyer, Sean Collins, and Feng-Chiao Tsai for stimulating discussions. S.V. was supported by Grant 2106-08-0018 “ProCell,” under the Programme Commission on Strategic Growth Technologies, the Danish Agency for Science, Technology and Innovation.

- Orlic D, et al. (2001) Bone marrow cells regenerate infarcted myocardium. *Nature* 410(6829):701–705.
- Abercrombie M, Heaysman JEM (1953) Observations on the social behaviour of cells in tissue culture. I. Speed of movement of chick heart fibroblasts in relation to their mutual contacts. *Exp Cell Res* 5(1):111–131.
- Abercrombie M, Heaysman JE (1954) Observations on the social behaviour of cells in tissue culture. II. Monolayering of fibroblasts. *Exp Cell Res* 6(2):293–306.
- Yates CA, et al. (2009) Inherent noise can facilitate coherence in collective swarm motion. *Proc Natl Acad Sci USA* 106(14):5464–5469.
- Ballerini M, et al. (2008) Interaction ruling animal collective behavior depends on topological rather than metric distance: Evidence from a field study. *Proc Natl Acad Sci USA* 105(4):1232–1237.
- Helbing D, Farkas IJ, Vicsek T (2000) Simulating dynamical features of escape panic. *Nature* 407(6803):487–490.
- Martin P, Parkhurst SM (2004) Parallels between tissue repair and embryo morphogenesis. *Development* 131(13):3021–3034.
- Lecaudey V, Gilmour D (2006) Organizing moving groups during morphogenesis. *Curr Opin Cell Biol* 18(1):102–107.
- Alberts B, et al. (2007) *Molecular Biology of the Cell* (Garland Science, New York), 5th Ed.
- Friedl P, Wolf K (2003) Tumour-cell invasion and migration: Diversity and escape mechanisms. *Nat Rev Cancer* 3(5):362–374.
- Selmeczi D, Mosler S, Hagedorn PH, Larsen NB, Flyvbjerg H (2005) Cell motility as persistent random motion: Theories from experiments. *Biophys J* 89(2):912–931.
- Li L, Cox EC, Flyvbjerg H (2011) ‘Dicty dynamics’: Dictyostelium motility as persistent random motion. *Phys Biol* 8(4):046006.
- Arriemerlou C, Meyer T (2005) A local coupling model and compass parameter for eukaryotic chemotaxis. *Dev Cell* 8(2):215–227.
- Andrew N, Insall RH (2007) Chemotaxis in shallow gradients is mediated independently of PtdIns 3-kinase by biased choices between random protrusions. *Nat Cell Biol* 9(2):193–200.
- Keren K, et al. (2008) Mechanism of shape determination in motile cells. *Nature* 453(7194):475–480.
- Melvin AT, Welf ES, Wang Y, Irvine DJ, Haugh JM (2011) In chemotaxing fibroblasts, both high-fidelity and weakly biased cell movements track the localization of PI3K signaling. *Biophys J* 100(8):1893–1901.
- Lauffenburger DA, Horwitz AF (1996) Cell migration: A physically integrated molecular process. *Cell* 84(3):359–369.
- DiMilla PA, Barbee K, Lauffenburger DA (1991) Mathematical model for the effects of adhesion and mechanics on cell migration speed. *Biophys J* 60(1):15–37.
- Schreiber CH, Stewart M, Duke T (2010) Simulation of cell motility that reproduces the force-velocity relationship. *Proc Natl Acad Sci USA* 107(20):9141–9146.
- Munevar S, Wang Y, Dembo M (2001) Traction force microscopy of migrating normal and H-ras transformed 3T3 fibroblasts. *Biophys J* 80(4):1744–1757.
- Vicsek T, Czirók A, Ben-Jacob E, Cohen I, Shochet O (1995) Novel type of phase transition in a system of self-driven particles. *Phys Rev Lett* 75(6):1226–1229.
- Szabó B, et al. (2006) Phase transition in the collective migration of tissue cells: experiment and model. *Phys Rev E Stat Nonlin Soft Matter Phys* 74(6 Pt 1):061908.
- Gail MH, Boone CW (1970) The locomotion of mouse fibroblasts in tissue culture. *Biophys J* 10(10):980–993.
- Angelini TE, et al. (2011) Glass-like dynamics of collective cell migration. *Proc Natl Acad Sci USA* 108(12):4714–4719.
- Reffay M, et al. (2011) Orientation and polarity in collectively migrating cell structures: Statics and dynamics. *Biophys J* 100(11):2566–2575.
- Vitorino P, Meyer T (2008) Modular control of endothelial sheet migration. *Genes Dev* 22(23):3268–3281.
- Trepat X, et al. (2009) Physical forces during collective cell migration. *Nat Phys* 5:426–430.
- Angelini TE, Hannezo E, Trepat X, Fredberg JJ, Weitz DA (2010) Cell migration driven by cooperative substrate deformation patterns. *Phys Rev Lett* 104(16):168104.
- Tambe DT, et al. (2011) Collective cell guidance by cooperative intercellular forces. *Nat Mater* 10(6):469–475.
- Travis J (2011) Mysteries of the cell: Cell biology’s open cases. *Science* 334(6059):1051.
- Waters CM, Bassler BL (2005) Quorum sensing: Cell-to-cell communication in bacteria. *Annu Rev Cell Dev Biol* 21:319–346.
- Nadell CD, Xavier JB, Levin SA, Foster KR (2008) The evolution of quorum sensing in bacterial biofilms. *PLoS Comp. Biol.* 6:e14.
- Gregor T, Fujimoto K, Masaki N, Sawai S (2010) The onset of collective behavior in social amoebae. *Science* 328(5981):1021–1025.
- Gómez-Sjöberg R, Leyrat AA, Pirone DM, Chen CS, Quake SR (2007) Versatile, fully automated, microfluidic cell culture system. *Anal Chem* 79(22):8557–8563.
- Skotheim JM, Di Talia S, Siggia ED, Cross FR (2008) Positive feedback of G1 cyclins ensures coherent cell cycle entry. *Nature* 454(7202):291–296.
- Tay S, et al. (2010) Single-cell NF-κB dynamics reveal digital activation and analogue information processing. *Nature* 466(7303):267–271.
- Czirók A, Schlett K, Madarász E, Vicsek T (1998) Exponential distribution of locomotion activity in cell cultures. *Phys Rev Lett* 81:3038–3041.
- Wang Y, Teraoka I, Hansen FY, Peters GH, Hassager O (2010) Mean span dimensions of ideal polymer chains containing branches and rings. *Macromolecules* 44:403–412.
- Carmona-Fontaine C, et al. (2008) Contact inhibition of locomotion in vivo controls neural crest directional migration. *Nature* 456(7224):957–961.
- King SJ, et al. (2011) β1 integrins regulate fibroblast chemotaxis through control of N-WASP stability. *EMBO J* 30(9):1705–1718.
- Samadani A, Mettetal J, van Oudenaarden A (2006) Cellular asymmetry and individuality in directional sensing. *Proc Natl Acad Sci USA* 103(31):11549–11554.
- Yamao M, Naoki H, Ishii S (2011) Multi-cellular logistics of collective cell migration. *PLoS ONE* 6(12):e27950.
- Saintillan D, Shelley MJ (2008) Instabilities and pattern formation in active particle suspensions: kinetic theory and continuum simulations. *Phys Rev Lett* 100(17):178103.
- Lambert G, Liao D, Austin RH (2010) Collective escape of chemotactic swimmers through microscopic ratchets. *Phys Rev Lett* 104(16):168102.
- Graner F, Glazier JA (1992) Simulation of biological cell sorting using a two-dimensional extended Potts model. *Phys Rev Lett* 69(13):2013–2016.
- Larripa K, Mogilner A (2006) Transport of a 1D viscoelastic actin-myosin strip of gel as a model of a crawling cell. *Physica A* 372(1):113–123.

Migration of cells in a social context

Supplementary Information Appendix

Søren Vedel¹, Savaş Tay², Darius M. Johnston³, Henrik Bruus¹, and Stephen R. Quake³

¹*Department of Micro- and Nanotechnology, Technical University of Denmark,
DTU Nanotech building 345 B, DK-2800 Kongens Lyngby, Denmark*

²*Department of Biosystems Science and Engineering, Swiss Federal Institute of Technology, ETH Zürich,
Mattenstrasse 26, Basel, Switzerland*

³*Departments of Applied Physics and Bioengineering, Stanford University and Howard Hughes Medical Institute,
Stanford, California 94305, USA*

I. MATERIALS AND METHODS

A. Cell lines

We used p65^{-/-} mouse fibroblast (3T3) cells expressing the cytosolic fluorescent fusion protein p65-DsRed under control of the endogenous mouse p65 promoter as well as the nuclear marker H2B-GFP driven by the human ubiquitin C promoter. Both markers were created using lentiviral systems [1]. After cloning, the cells were frozen and newly thawed cells were used for each experiment to prevent 3T3 cell re-transformation and to minimize heterogeneity. The motility statistics of these cells agree with single-cell statistics found in the literature, e.g. [2].

B. Microfluidic cell culture experiments

Cells were seeded at densities from 4,000–40,000 cells cm⁻² ($\sim 40 - 400$ cells per chamber) into microfluidic chambers and were cultured for one day to reach 15-100% confluence before experiments. The external conditions were set to standard culture conditions (5% CO₂ and 37 °C external temperature) and maintained at this level. During cell growth, 33% of the chamber volume was replaced with fresh media (DMEM) every hour using the nanolitre microfluidic pump, which resulted in vigorous proliferation of 3T3 cells. We made sure that cells were healthy, motile and proliferating before experiments.

We varied the cell density by precisely controlling the cell counts in each chamber during automated seeding. The cell counts were recorded at every time point during experiments by taking pictures and counting the number of GFP positive nuclei. This produced a well-controlled cell density in the chambers during the entire experimental duration. In the analyses, we considered only a region away from the chamber walls to avoid edge effects, and the number of cells in this region varies between chambers of purportedly identical density. Nevertheless, the number of cells in each picture is counted using the nuclear GFP signal and thus the numbers are exact. Therefore, instead of binning the data based on expected seeding density, we instead report the density-dependence of the data based on the average minimum cell-cell distance of all cells in a chamber over the entire experiment, \bar{d}_{\min} .

The microfluidic culture chip [3] allows the replacement of the entire culture media in less than a second, which results in a step-like removal of all secreted signaling molecules. Once the media was flowed in, the chambers were sealed and were imaged at a constant rate Δt_{samp} either every 4 or 6 min in both GFP and DsRed fluorescence channels during the entire experiment (5-6 hours). The cells remained in the same media during the entire experiment. All cell densities were tested in parallel chambers, up to 24 different microfluidic chambers at a time.

Upon completing the trajectory analyses of the non-stimulated cells, we compared these results to cells of the same cell line exposed to the inflammatory signaling molecule tumor necrosis factor (TNF)- α . We observed no difference in motility characteristics between non-stimulated cells and cells exposed to TNF α in the range 0.005 ng mL⁻¹ to 100 ng mL⁻¹, see Fig. S1 (no TNF indicated by blue, high TNF by orange) which plots both the speed distribution and fits of the average directional autocorrelation to the function $\phi e^{-\tau_{\text{lag}}/\tau_p}$ that was also used in the main text. Since we furthermore did not observe any variation in pseudopod statistics between the two populations we included the cells exposed to TNF α in the analysis.

In total we analyzed the motility of 8566 cells at various densities in 79 different chambers using five different chips. Each density was repeated at least once (each experiment on different chips) and the majority repeated several times, see Table S1. Small variations in \bar{d}_{\min} between otherwise identical chambers are due to the finite number of cells present in each chamber. We have presented the data according to the measured \bar{d}_{\min} rather than binning, since the actual nearest-neighbor distance is important due to the induction of pseudopods by secreted chemokine.

TABLE S1: Microfluidic experiments

Chip	Max. \bar{d}_{\min}	Min. \bar{d}_{\min}	Avg. \bar{d}_{\min}	# of exp.
1	142.8 μm	82.0 μm	103.0 μm	16
2	89.7 μm	72.0 μm	80.5 μm	24
3	95.7 μm	76.0 μm	84.8 μm	15
4	143.9 μm	61.8 μm	87.3 μm	22
5	69.7 μm	57.8 μm	63.7 μm	2

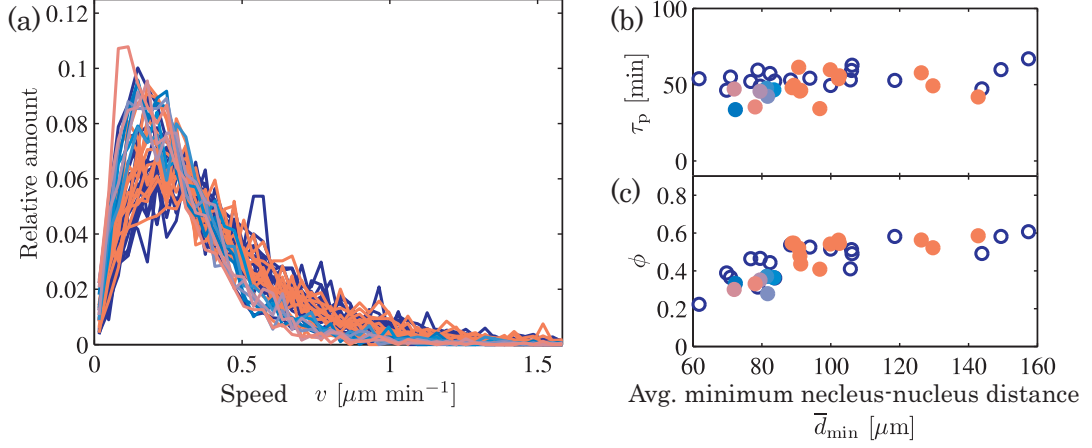


FIG. S1: Comparison between non-stimulated cells and cells exposed to the inflammatory signaling chemical TNF α shows no effect of the chemical. Each line in (a) and each circle in (b)-(c) is the average from one chamber. Non-stimulated cells are given by blue (open circles in (b)-(c)), results from stimulated cells are assigned a color ranging from light blue (lowest dose, 0.005 ng mL $^{-1}$) to orange (highest dose, 100 ng mL $^{-1}$) in ten steps (0.005, 0.01, 0.025, 0.05, 0.1, 0.25, 0.5, 1, 10 and 100 ng mL $^{-1}$). (a) Chamber speed distribution. (b)-(c) Persistence time τ_p and weight factor ϕ (see Fig. 2 in the main text).

Good and unambiguous resolution of the cytosol boundaries are crucial for the correct detection of collisions and pseudopod dynamics (see below). We therefore compared the results of manual analysis of the pseudopodia of 10 non-stimulated cells to the results obtained from the automated analysis (see below) applied to the TNF-exposed data and found no variation. Given the agreement of the motility characteristics and the large range of TNF α investigated, we concluded that TNF α does not influence the motility.

C. Image analysis

To minimize human bias and errors we used automated algorithms to analyze the large experimental data set. Cells were imaged in both the GFP and DsRed channels with a Leica DMI6000B microscope (20 \times air objective) and Retiga-SRV CCD camera (Q Imaging) every 4-6 min for several hours. To generate the coordinates of single cells, custom MATLAB software using the Image Processing Toolbox was used to automatically identify the nuclei centroid from H2B-GFP images as previously described [4]. To identify nuclear regions, H2B-GFP images were local range contrast filtered with a neighborhood of three pixels and then thresholded, where the threshold level was automatically determined by k -means clustering pixel intensities with $k = 3$. Touching or merged nuclei (determined by solidity < 0.925) were then separated by a watershed transform with markers seeded at k -means clustered centroids. Nuclei were then linked to the nearest nuclei in the next time point and preliminary quality control checked for constant nuclear area through tracking. Cytoplasmic regions and p65-DsRed intensities were extracted through a combination of local threshold-

ing and watershed transforms with the nuclei as marker seeds. All cell tracking was manually checked to eliminate mistakes by the automated analysis.

1. Cell trajectories and velocities

The centroid of the nucleus $\mathbf{x}^i(t_j) = (x^i, y^i)_{t_j}$ was used as the position of cell i at time $t_j = \Delta t_{\text{samp}} j$, $j = 0, 1, 2, \dots$. Displacements $\Delta \mathbf{x}^i(t_j)$ and velocities $\mathbf{v}^i(t_j)$ were computed as

$$\Delta \mathbf{x}^i(t_j) = \mathbf{x}^i(t_{j+1}) - \mathbf{x}^i(t_j) \quad \text{and} \quad \mathbf{v}^i(t_j) = \frac{\Delta \mathbf{x}^i(t_j)}{\Delta t_{\text{samp}}} \quad (\text{S1})$$

The experimental noise in determining cellular position was estimated to ~ 20 nm following the arguments in [5], with less than 0.2% of all recorded steps being below this limit (mean displacement between images was ~ 25 times this limit). These small displacements were found dispersed between larger, admissible displacements for individual cells, with no correlation in time. Since the auto-correlation series of the cells that occasionally recorded displacements close to the level of positional noise did not show significant deviations from cells with only admissible displacements, taken from the same chambers, we concluded that all cell trajectories could be used without corrupting the conclusions.

2. Collision and pseudopod analyses

Cell outline coordinates were obtained from each image as the boundary of the cytosolic (p65-DsRed) region of each cell. Contact was defined as two pixels belonging

to separate cells being within 2 pixel from each other, and neighboring outline pixels in contact with the same cell were grouped into regions and linked in time using custom algorithms. For each region the times of contact $t_j, j, \dots, j + N$ were stored, and the contact time was obtained as $t_{j+N} - t_{j-1}$. Only contacts starting after the first image and contacts ceasing prior to the last image in each series were used to ensure the entire lifetime of the contact was imaged.

Pseudopodia were detected from the cell outlines using a MATLAB implementation of the automated algorithm suggested by Bosgraaf and van Haastert [6], with small modifications. A pseudopod is an outward extension of the cell boundary, so following and edge-preserving smoothing step which removes pixelation noise, the algorithm determines the convexity of each node of each cell outline, with convexity ψ_n of node n defined by

$$\psi_n = \theta_n - 360/n - 180, \quad (\text{S2})$$

where θ_n is the outer angle of the line segments pointing from the node to its two neighbors. $\psi_n > 0$ indicates convex (outward) and $\psi_n < 0$ indicates concave (inward) deflection from the outline. Regions of convexity (neighboring points with $\psi_n > 0$) were for each cell linked in time, and the tip of the region was at each time step identified as the center node.

A pseudopod was defined by at least 2 neighboring convex nodes, with the cumulative convexity of the neighboring nodes $\sum \psi_n$ exceeding 10° and the mean convexity gradient exceeding $4^\circ \mu\text{m}^{-1}$. Single concave nodes were allowed in a convex region, and one time step of slight concavity of a region was allowed if the same pseudopod existed both before and after the concave time point. While the algorithm was good at identifying pseudopodia, we found that it occasionally missed some, so each analyzed cell was manually checked to avoid bias introduced by the algorithm. Pseudopodia protrude and exert force for a period of time, before they collapse while providing little force. We computed the nucleus-tip distance between successive time steps, and included only growing (increasing distance) or stagnant (constant distance) pseudopodia in our analyses (Fig. 2 and Table I). Due to the sampling time of $\Delta t_{\text{samp}} \approx 5$ min, some pseudopodia were present in only one image. Cell collisions locally cause the pseudopodia to retract, so we neglected all pseudopodia arising or dying at the times of collision. Furthermore, to avoid bias in the pseudopod life time analysis presented in Fig. S7(a), we first manually tracked pseudopod life times of ~ 40 cells which did not collide and found no pseudopodia existing for more than 80 min. Next, using the automated analysis, we then obtained pseudopod life times from 154 cells which each went at least 80 min without colliding: within the collision-free interval we measured the life times of all pseudopodia starting at each time step. Finally, angles of pseudopod formation $\Delta\alpha$ in relation to direction of motion (Fig. 2(j) and Fig. S7(b)) were computed between the current vectorial displacement $\Delta\mathbf{x}^i(t_j)$ (see Eq. (S1)) and the vector

connecting the nucleus tip and the pseudopod tip.

D. Directional autocorrelation analysis

The vectorial directional autocorrelation of all cells is computed using the unit vectors in the instantaneous direction of motion. For cell i at the lag τ_{lag} this directional autocorrelation is given by

$$C_i(\tau_{\text{lag}}) = \langle \mathbf{e}_j^i \cdot \mathbf{e}_{j+n}^i \rangle, \quad (\text{S3})$$

where \mathbf{e}_j^i and \mathbf{e}_{j+n}^i are the unit vectors in the direction of motion of cell i (e.g. $\mathbf{e}_j^i = \mathbf{v}^i(t_j)/|\mathbf{v}^i(t_j)|$) at times $j\Delta t_{\text{samp}}$ and $(j+n)\Delta t_{\text{samp}}$, τ_{lag} is related to the sampling time Δt_{samp} by $\tau_{\text{lag}} = n\Delta t_{\text{samp}}$, and the brackets denote average over all times. Since we do not have infinite time series, the results in Figs. 2 and 3 in the main text has been obtained from an unbiased estimate, similar to the one used in [5].

II. SUPPLEMENTARY DATA

We present here additional data to supplement the findings presented in the paper. Table S2 lists all observations and model predictions.

A. Density dependence, isotropic cell movement and convergence to isolated-cell migratory behavior

Figure S2 presents trajectories for four chambers supplementing the one set shown in the main text (Fig. 1(a)). Excerpts of these figures are shown in Fig. 2(e) in the main text. Figure S3 shows that there is no preferred direction of motion of the cells in a chamber, so the direction taken by each cell is random, although the motion of each cell depends on previous times according to Fig. 2(d), (f) and (g) in the main text. Figure S4 presents the speed distribution of isolated human fibroblasts from Selmeczi *et al.* [2] (dashed red line), which has been fitted to the generalized extreme value distribution to obtain the reference values presented as dashed black lines in Fig. 2(h) in the main text; the blue bars in the same figure shows our measurement.

B. Non-Gaussian speed distributions and pseudopodia-driven locomotion

The central limit theorem states that data from a large number of independent and identically distributed random variables will be distributed according to the normal distribution. If the random variables are not independent and/or identically distributed, the result is not a Gaussian distribution. Thus, if we were to assume that each

TABLE S2: Summary of all experimental observations and model predictions.

Experimental observations		
Pseudopodia	Cells dynamically form these protrusions which apply traction force to the substrate	Fig. 1(b)
Pseudopod life times	Distributed with a mean of 11.8 min.	Fig. S6(a)
Pseudopod life time and direction of motion	Same life time distributions found whether pseudopodia form along or against the current direction of motion	Fig. S6(b)
Single-cell number of pseudopodia	Nominally constant over time for the individual cell, but variations among the cells	Fig. S6(c) and (d)
Directional pseudopod bias	Pseudopodia formation is biased in the current direction of motion	Fig. 2(j)
Local pseudopod formation bias by other pseudopodia through pseudopod splitting	No evidence that this is dominating although we do observe it	Fig. S7
Chemokine bias	Neighbor cells induce pseudopod formation by secreting a pseudopod-inducing chemical (chemokine)	Fig. 2(k)
Preferred direction of motion	No preferred direction of motion of the cells in a chamber	Fig. S3
Cell-cell collisions	Colliding cells transiently adhere to each other before the touching pseudopodia collapse, in a process known as contact inhibition of locomotion.	Fig. 2(i)
Single-cell speed	Fluctuating, but with similar distributions among cells indicating that all cells move. The average distribution is well fitted by a GEV distribution. Very similar across densities	Fig. 2(a),(b) and (h)
Single-cell trajectories	Some are almost straight, other curl, yet other exhibit little apparent directionality. Fraction of cells moving nominally straight decays at higher density	Figs. 1 and 2(c) and (e)
Single-cell directionality	Chamber-average directional autocorrelation (which well represents the individual) decays exponentially ($\phi e^{-\tau_{\text{lag}}/\tau_p}$) on a time scale of $\tau_p = 50 \pm 11$ min. The weight factor ϕ decays at higher densities since a smaller fraction of cells move nominally straight	Fig. 2(d), (f) and (g), and Fig. S5
Cells moving nominally straight during whole experiment	Present at all densities	Fig. 2(e) and Fig. S2
Model predictions		
Single-cell speed	Fluctuating with similar distributions among cells and all cells moving. Average model speed distribution quantitatively reproduces experiment	Fig. 3(d) and (e)
Single-cell trajectories	Some are almost straight, other curl, yet other exhibit little apparent directionality. MPD distribution is in quantitative agreement with experiment, but fraction of cells moving nominally straight is lower	Figs. 3(b) and (g)
Single-cell directionality	Chamber-average well represents the individual, and this average agrees with experiment	Fig. 3(f) and Fig. S5
Effect of density	Model quantitatively captures the experimental findings across densities	Fig. 3(h) and (i)

cell had a certain inherent velocity scale, we would expect that a large number of isogenic cells would present a Gaussian speed distribution. However, it is well-known that our cells move by pseudopodia so cell speed is a not independent variable, which is therefore not normally distributed since the conditions of the central limit theorem are violated. Hence, the existence of the non-Gaussian speed distribution illustrates that speed is not an independent variable.

Instead, our observation of fluctuating speed and similar single-cell speed distributions are consistent with cell speed being the result of pseudopodia-driven locomotion with transient pseudopodia: Each time a new pseudo-

pod forms, the cell speed is changed, causing the observed fluctuations (Fig. 1(a) inset), while the fact that pseudopodia “drive” the cell means that cell speed is a dependent variable. The fact that similar average speeds are found among the cells is the result of the relative isotropic near-cell environment experienced on average, and the fact that each cell only produces a limited number of pseudopodia (likely due to limited amounts of the intracellular cytoskeletal components needed to form the pseudopodia; Fig. S6(c)). This argument follows a similar argument regarding non-Gaussian traction force distributions in sheets of mechanically interlinked Madin-Darby canine kidney epithelial cells [7].

C. Influence of outliers in chamber-averaged directional autocorrelation functions

The directional autocorrelation series of the individual cells in a chamber are not completely identical and consequently exhibit some variation, as shown by the non-negligible standard deviation of the distribution of directional autocorrelations (Fig. S5(a)). The data is for the experiment of Fig. 2(a)-(d) in the main text. Variations are expected for any biological system, but the decisive question is whether the outliers of the distribution significantly affect the mean, i.e. whether the population mean well represents the individual cell.

To investigate whether the chamber-average directional autocorrelation well represents the individual C_i we computed the kurtosis $\kappa(C_i)$ of the distribution of C_i at each lag time. The kurtosis measures the influence of the outliers in defining the mean, and the kurtosis of the normal distribution is 3. We find that the kurtosis of the distribution of single-cell directional autocorrelations is well described by the mean, since it is everywhere close to 3, see lower panel in Fig. S5(b) where the dashed line indicates $\kappa = 3$, the kurtosis of normal distribution.

D. Relevance of “straight” trajectories: coverage fraction of cell area to total chamber area

The straight trajectories found at all densities (see Fig. 2(e), (f) and (h) as well as Fig. S2) are not just a mere coincidence, but represent features of the dynamics of the cells’ migratory behavior. To support this, we compute the coverage fraction of total cell surface area to total chamber area.

The total area of investigation in a cell culture chamber is

$$A_t = 500 \mu\text{m} \times 700 \mu\text{m} = 3.5 \times 10^{-7} \text{ m}^2, \quad (\text{S4})$$

while the projected surface area of one cell ($\sim 20 \mu\text{m}$ radius) is

$$A_c = \pi \times (20 \mu\text{m})^2 = 1.2 \times 10^{-9} \text{ m}^2. \quad (\text{S5})$$

We define the coverage fraction F_N of N cells as

$$F_N = \frac{N A_c}{A_t}, \quad (\text{S6})$$

so since we have between 36 and 246 cells in the chambers, the coverage fraction varies from 0.12 (36 cells) to 0.84 (246 cells), while $F_N = 0.67$ is found for 100 cells. The fraction of available space for the cells to move on is at any instant $1 - F_N$. Since all the cells move, and we observe them over prolonged periods of time, it is very unlikely by pure chance to find the straight paths as simply just a consequence of a relative lack of collisions. Furthermore, one finds several cells in Supplementary Movie 1 moving along nominally straight lines

even though they collide with other cells (even for some head-on collisions). The existence of straight trajectories at all densities emphasize that these trajectories do not arise out of pure chance, but indeed reflect features of the cell-cell interaction dynamics.

E. Supplementary pseudopod statistics

1. Pseudopod life times

Pseudopod life times are distributed with a mean of $\langle \tau_{\text{pseud}} \rangle = 11.8 \text{ min}$ (Fig. S6(a)), and we find no dependence on pseudopod life time on whether they form along or against the current direction of motion (Fig. S6(b)), expressed by the angle $\Delta\alpha$ between the position of pseudopod formation and the current direction of motion (see also the schematic in Fig. 2(j)).

2. Single-cell number of pseudopodia

For the single cell, the number of pseudopodia as a function of time (ν) exhibits only small variations about a certain number (Fig. S6(c) inset), presumably due to a limited amount of intracellular actin. For each cell we take the mode number ν_m over time as the representative single-cell number of pseudopodia, and the distribution of these mode numbers varies between 1 and 7 (Fig. S6(c)). To quantify the variations about these mode numbers we define the standard variation about the mode number,

$$\sigma = \sqrt{\frac{1}{n-1} \sum_{i=1}^n (\nu_i - \nu_m)^2}. \quad (\text{S7})$$

This measure is similar to the standard deviation, but while the latter is computed with reference to the mean, our measure is computed with reference to the mode number. We show in Fig. S6(d) that for all cells the standard variation about the cell-specific mode number is small, with a mean variation of $\langle \sigma \rangle = 1.35$ for the 154 cells presented in the figure.

3. No local pseudopod formation bias by existing pseudopodia

We did not find any dominating dependence of the position of pseudopod formation on the presence of existing pseudopodia, as reported for isolated cells [8]. To arrive at this result, we computed the angle $\Delta\beta$ between the position of formation and the nearest neighboring pseudopod. For completely random pseudopod formation, we expect a pseudopod to be present on average every $360^\circ/\nu$ where ν is the current number of pseudopodia of the cell, while a strong induction of existing pseudopodia

on forming pseudopodia would lead to an angular difference independent of the number of existing pseudopodia. Grouping the results based on ν , see Fig. S7, we find the most occurring positions of pseudopod formation coinciding with the angular distance $\pm 360^\circ/(2\nu)$ (indicated by the dashed lines in the figure), indicating that no dominating relationship exists between the positions of established pseudopodia and the positions of formation for new pseudopodia. This emphasizes the differences between being isolated and being in a social context. Since we do find significant positive correlation between pseudopod formation and both current direction of motion and secreted chemokines, we expect the variations are due to these effects and the limits set by finite statistics.

4. Pseudopod statistics are independent of cell density

The variations across cell densities (mean \pm s.d.) of pseudopod contact times during collisions (Fig. S8(a)), pseudopod life times (Fig. S8(b)) and pseudopod formation relative to the current direction of motion (Fig. S8(c)) suggests that these statistics are independent of cell density. In all three cases, the normalized pooled data across cell densities agrees with the averages taken over these densities, and the standard deviation is low. We therefore conclude that these statistics are independent of cell density.

F. Supporting information for the hypothesis of chemokine bias of pseudopod formation

We present here three independent lines of supporting information for the hypothesis based on Fig. 2(k) that one or more secreted chemokines induce pseudopod formation.

First, there is a large body of previous work documenting the chemotactic ability of fibroblasts to several chemokines, e.g. [9–13], and another large body of previous work establishing that the same cells secrete various chemokines e.g. [14–17], which together support the notion that these cells could secrete a chemoattractant. Taken together with the previous observations that higher local levels of chemoattractant favor pseudopod formation [9], this suggests that cell-secreted chemoattractants induce pseudopod formation.

Second, assuming that secreted chemokines do not contribute to pseudopod formation, in spite of this vast body of literature, the most obvious other candidates for the observations of preferred pseudopod-formation towards the nearest neighbor cell presented in Fig. 2(k) in the main text are [18]

- (i) mechanical tension in the substrate applied by the cells (mechanotaxis), or
- (ii) the attachment of pseudopod-inducing molecules to the substrate by either the cells themselves or as a

result of the microfabrication procedures (haptotaxis).

The cells are incubated in the chamber for one day prior to media exchange and image acquisition, so the stress field in the substrate, which is sensed by cells in mechanotaxis, would not be expected to vary around flushing; our results in Fig. 2(k) therefore refute (i) as a possible explanation. Regarding (ii), if this was achieved by cells attaching pseudopod-inducing molecules to the substrate, this alternative would imply that cells either preferentially follow each other, or that pseudopods more often form where another cell previously was. This is contrary to our observations. If it was achieved by signaling molecules trapped during the fabrication procedure, we would expect that cells either move along certain paths in the chamber, or that they form pseudopods in specific directions when they are in specific positions in the chamber. These options are also both contrary to our observations. Finally, we would not expect any temporal dependence of a haptotactic response around flushing, which is of course contrary to our findings of Fig. 2(k). Thus, we can safely disregard haptotaxis and mechanotaxis as significant inducers of pseudopodia.

Third, we investigated the positions of pseudopod formation relative to the nearest neighbor cell for two independent experiments with complete media replacement every 2 h. Focusing only on the first 20 min following the first and second media replacement, we redid the analysis presented in Fig. 2(k). If our chemokine hypothesis is true, we would expect new pseudopodia forming in any 20 min segment following any media replacement to have small angle differences ($\Delta\theta \approx 0$) irrespective of whether this was the first or second replacement. We show in Fig. S9 that this is indeed the case for the two independent experiments (see also explanatory schematic in Fig. 2(k)), with each column in the figure corresponding to a different experiment.

Taken together, these previously reported observations and our own experimental findings strongly suggest that a cell-secreted chemokine induce the formation of pseudopodia in the cells.

G. Examples of model-predicted chemokine fields

Chemokine concentration field predicted by the model are given in Fig. S10, with panel (a) showing the chemokine concentration field for a low-density simulation and Fig. S10(b) taken from the same numerical experiment as shown in Fig. 3(b) and (d)-(g) in the main text.

H. Interpreting γ

The cell friction coefficient γ is related to the energy dissipated by the making and breaking of cell-substrate

chemical bonds as the cell moves. Contrary to measurements of the strength of these bonds, the friction is rarely determined experimentally, and the irregularity, softness and general ignorance of the significant molecular contributors of the cell attachment during migration makes first-principles theoretical analysis difficult. A value of $\gamma \approx 29 \text{ kg s}^{-1}$ can be deduced from Munevar *et al.* [19] by estimating the forward traction force from a traction force map and using the stated average velocity. Similarly, and an order-of-magnitude estimate of the friction per unit cell surface area of $10^9 \text{ kg s}^{-1} \text{ m}^{-2}$ by Larripa and Mogilner [20] yields $\gamma \approx 1 \text{ kg s}^{-1}$ for a cell of radius $20 \text{ }\mu\text{m}$. This is an order of magnitude lower than our value of $\gamma = 39 \text{ kg s}^{-1}$, but it should be borne in mind that the value in [20] was estimated from the reported work of others on endothelial cells and a *Dictyostelium* slug.

However, these numbers are many orders of magnitude greater than the viscous Stokes friction with the medium

$$\gamma_{\text{Stokes}} = 6\pi\eta r \quad (\text{S8})$$

of $\gamma_{\text{Stokes}} \approx 4 \times 10^{-7} \text{ kg s}^{-1}$, where $\eta = 1.002 \times 10^{-3} \text{ Pa s}$ is the viscosity of the liquid (assumed to be water) and $r \approx 20 \text{ }\mu\text{m}$ is the cell radius (Table S4). This is not surprising since the molecular interactions with liquid molecules is weaker than the interactions with attaching polymers used by the cells.

I. The tail of the speed distribution

Model speed distributions are fitted to the generalized extreme value (GEV) distribution in Fig. 3 of the main text, and Fig. S11 gives the fitted shape parameter ξ across densities. The shape parameter indicates the significance of the tail in the GEV fit of the speed distribution, and Fig. S11 shows that the model underpredicts the value of ξ . Physically, this implies that the model does not well capture the short burst of very high speeds produced with low probability by the cells. The overall agreement of the rest of the statistical measures for both speed, directionality and total sampled space, suggests that the model is nonetheless very capable of describing the overall dynamics, and since furthermore the model uses the experimental pseudopod statistics as input, a misrepresentation of these statistics can also be disregarded the source of the tail. Together, this suggests that the disagreement is likely due to the model assumption of constant force over time of identical magnitude F_0 applied by each pseudopod, which indeed is a very naive picture of the dynamics of the molecular interactions causing the locomotion. Our model therefore indicates that speed time-dependent and perhaps graded pseudopod forces are found in real cells, but that these subtleties only have nominal influence on the overall dynamics.

J. Movies

Movie 1 The movement of cells at medium density in a chamber during 200 min. The trajectories are given by the yellow lines.

Movie 2 The positions and life times of the pseudopodia change dynamically during the course of an experiment, as illustrated for two cells. Pseudopodia are marked by red circles, with arrows indicating the actual direction of motion (green) and the direction of movement predicted from the pseudopodia (red).

Movie 3 The cells exhibit contact inhibition of locomotion. Colliding cells (marked by green) transiently remain in contact (for roughly 5.5 min, see Fig. 2(i)), before they move away from each other, followed by collapse of the touching pseudopodia of different cells.

Movie 4 Illustration of model cell migration behavior. Active membrane points are indicated by red dots, and the trajectories of the cells are indicated by the blue lines.

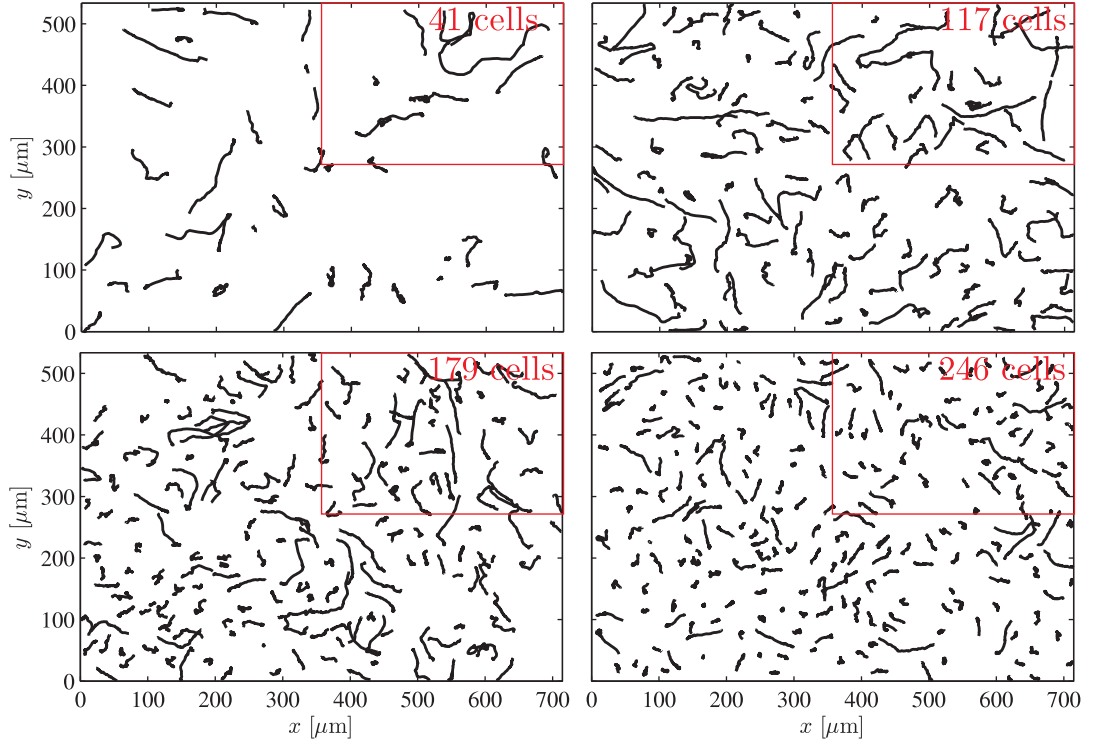


FIG. S2: Whole-chamber cell trajectories at four different densities. Exerts are given in Fig. 2(e) in the main text, with the exerts corresponding to the regions marked by red boxes. The average cell diameter is $41.7 \mu\text{m}$ (supplementary Fig. S12(a)), and the average minimum cell-cell distance varies from $149 \mu\text{m}$ at the lowest density to $45 \mu\text{m}$ at the highest.

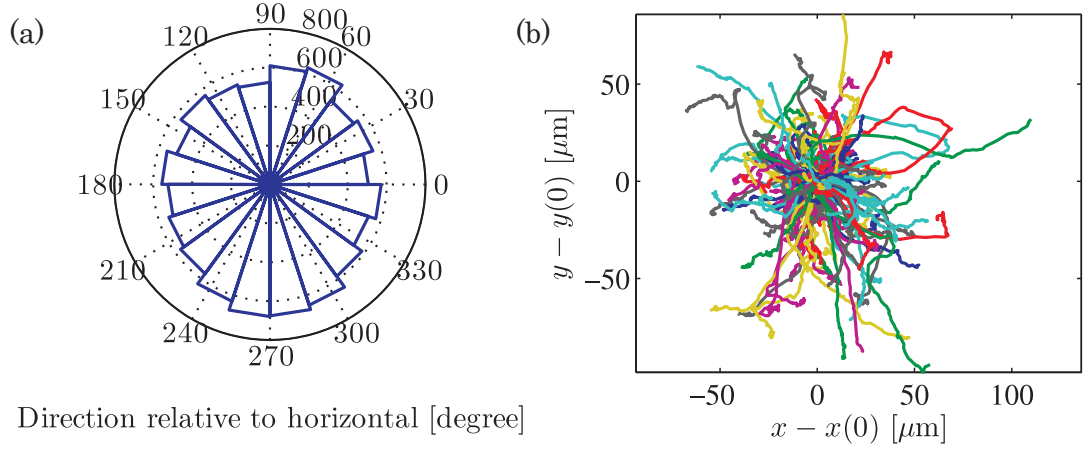


FIG. S3: The cell direction of motion is random, here illustrated by two different means for a single chamber. (a) Histogram of the instantaneous angle of motion relative to horizontal and (b) all trajectories shifted to the same starting position (initial position $\mathbf{x}(t=0)$ has been subtracted, each trajectory is randomly given one of ten different colors) both confirm the absence of a preferred average direction of motion, within the limits of finite statistics.

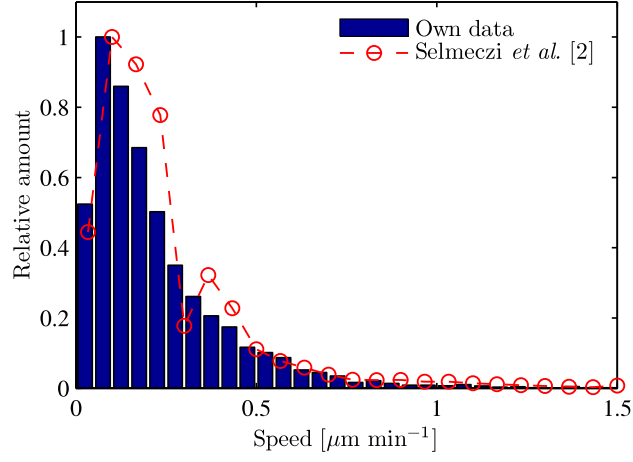


FIG. S4: Comparison of own speed distribution (blue bars) and the speed distribution of isolated human fibroblasts extracted from Selmeczi *et al.* [2]. The two distributions are in agreement.

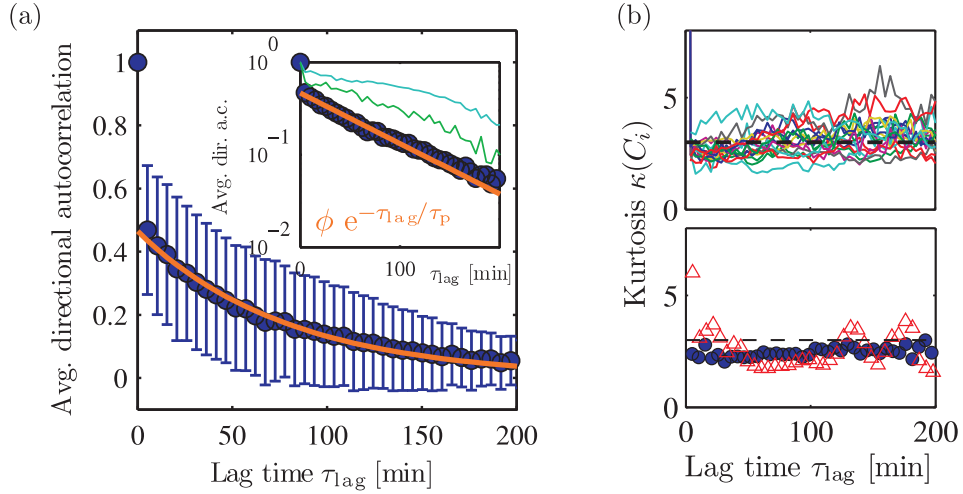


FIG. S5: Distribution of single-cell directional autocorrelations in an experiment. (a) Standard deviation of the distribution of single-cell directional autocorrelation functions shows some variation between the individual cells. The figure shows the result for a representative experiment (same as in Fig. 2(a)-(d) in the main text, lin-log version given in the inset) where the standard deviation decays from ± 0.20 close to $\tau_{\text{lag}} = 0$ min to ± 0.01 at $\tau_{\text{lag}} = 200$ min. (b) Kurtosis of the distribution of single-cell directional autocorrelation functions. Top panel illustrate individual experimental chambers, while the bottom panel illustrates the distribution for both model and experiment for the chamber presented in Figs. 2 and 3 in the main text. Dashed black lines indicate 3, the kurtosis of the normal distribution.

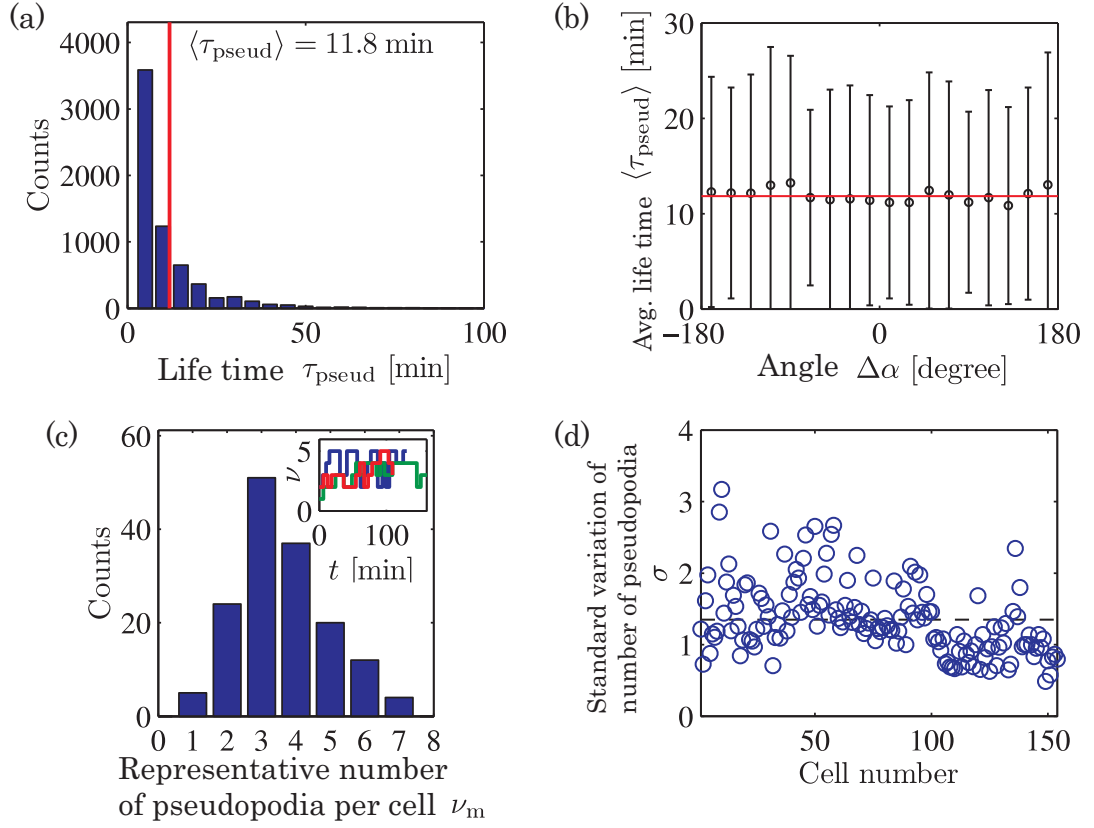


FIG. S6: Supplementary pseudopod statistics. (a) Pseudopod life times with red line indicating mean. (b) Pseudopod life times as function of the angle between the position of pseudopod formation and the current direction of motion. Red line indicates the mean life time for all pseudopodia (it is the same red line as in (a)). (c) Number of pseudopodia per cell is roughly conserved over time. Inset shows single-cell number of pseudopodia versus time and main panel gives the distribution of single-cell mode numbers over time of pseudopodia. (d) The standard variation σ , see Eq. (S7), of the instantaneous number of pseudopodia about the mode number of pseudopodia ν_m , computed for each cell, shows that the mode number is a representative measure of the cell's number of pseudopodia. The dashed black line gives the average for all cells in the figure, $\langle \sigma \rangle = 1.35$.

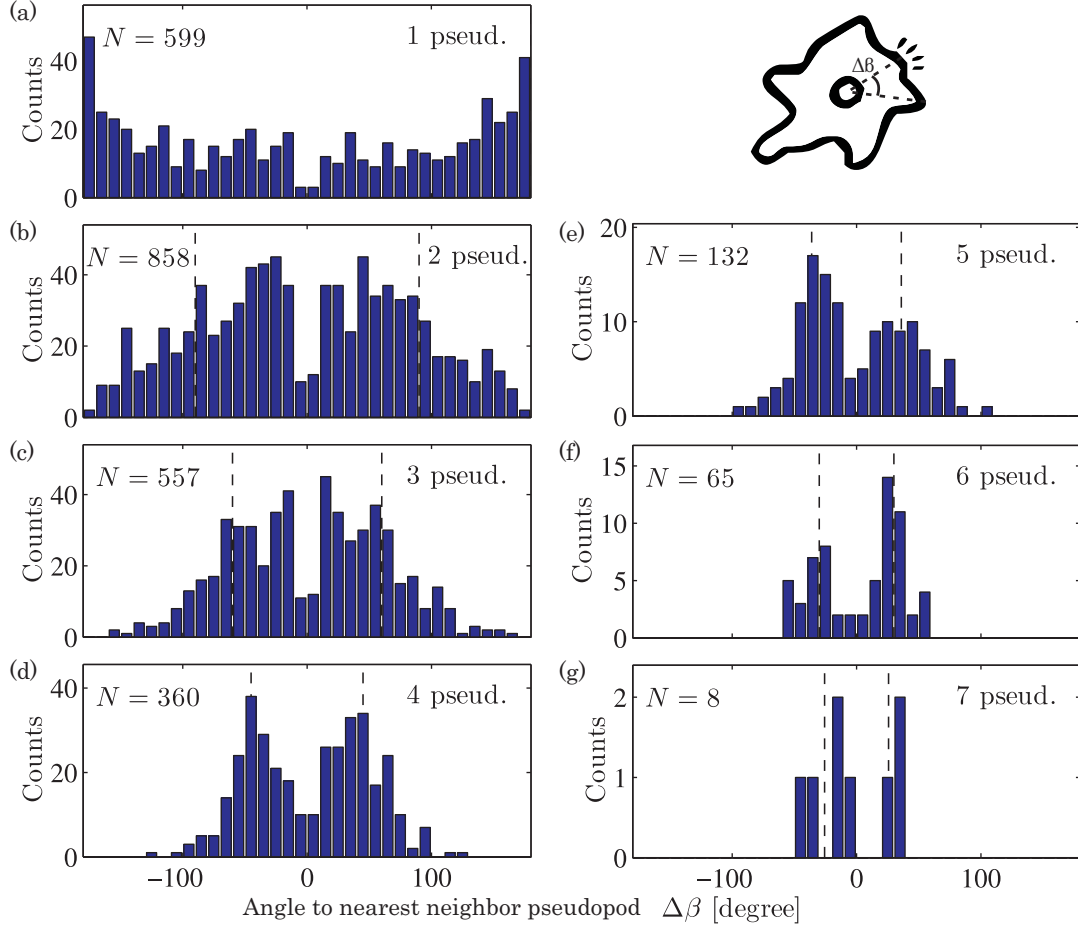


FIG. S7: The angle $\Delta\beta$ between a newly formed pseudopod and the closest neighbor pseudopod, grouped based on the number of pseudopodia of the current cell. The distribution means and peaks correlate with the angular distance $\pm 360^\circ/(2\nu)$ expected for pseudopodia randomly distributed along the perimeter and marked by the dashed lines in the figures. In each panel, N marks the number of pseudopodia making up the distribution. (a) Cells with $\nu = 1$ existing pseudopod ($360^\circ/2 = 180^\circ$ and coincide with the figure bounding box), (b) cells with $\nu = 2$, (c) cells with $\nu = 3$, (d) cells with $\nu = 4$, (e) cells with $\nu = 5$, (f) cells with $\nu = 6$ and (g) cells with $\nu = 7$ existing pseudopodia.

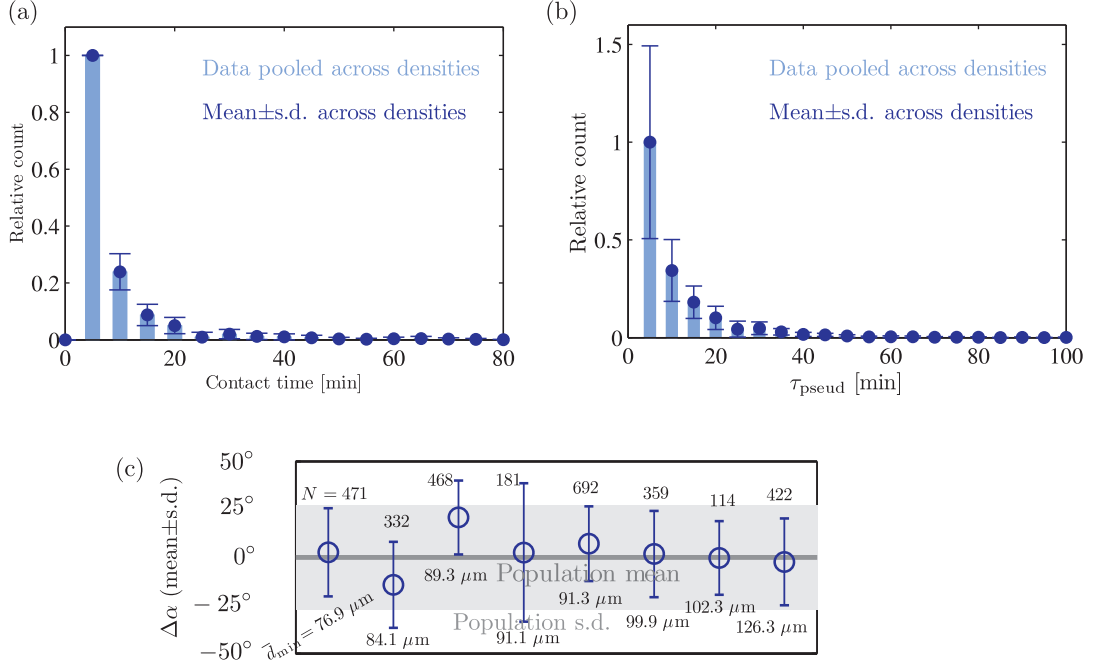


FIG. S8: Key pseudopod statistics are independent of cell density. (a) Duration of cell-cell contact time during collision. The light blue shows the pooled data given in Fig. 2(i) normalized by the largest bin count, and the darker blue filled circles are the averages across 34 independent experiments across densities (mean \pm s.d.). The very good agreement between the mean across densities and the pooled data, along with the small standard deviations, indicate the independence of cell density. (b) Distribution of pseudopod life times (compare to Fig. S6(a)) normalized similar to panel (a) and with light blue corresponding to pooled data across densities and darker blue to averages (mean \pm s.d.) from 8 independent experiments across densities. The agreement between the averages across densities and the pooled data, and the small errors again indicate an independence of this statistics on cell density. (c) Dependence on cell density of the angle $\Delta\alpha$ (compare to Fig. 2(j)) of pseudopod formation relative to the current direction of motion. The chamber density (expressed in terms of \bar{d}_{min}) and the number of investigated pseudopodia N is listed for each data point. A symmetric distribution favoring small angles is found at all densities (see Fig. 2(j) in the main text) which at all instants is well fitted by a Gaussian plus a constant baseline. This figure illustrates the mean and standard deviation of the Gaussian term across cell densities, and illustrates that there is no dependence of cell density. The dark grey line is the population mean across densities and the light grey region indicates the corresponding standard deviation (taken from a similar fit to the data in the main panel of Fig. 2(j)).

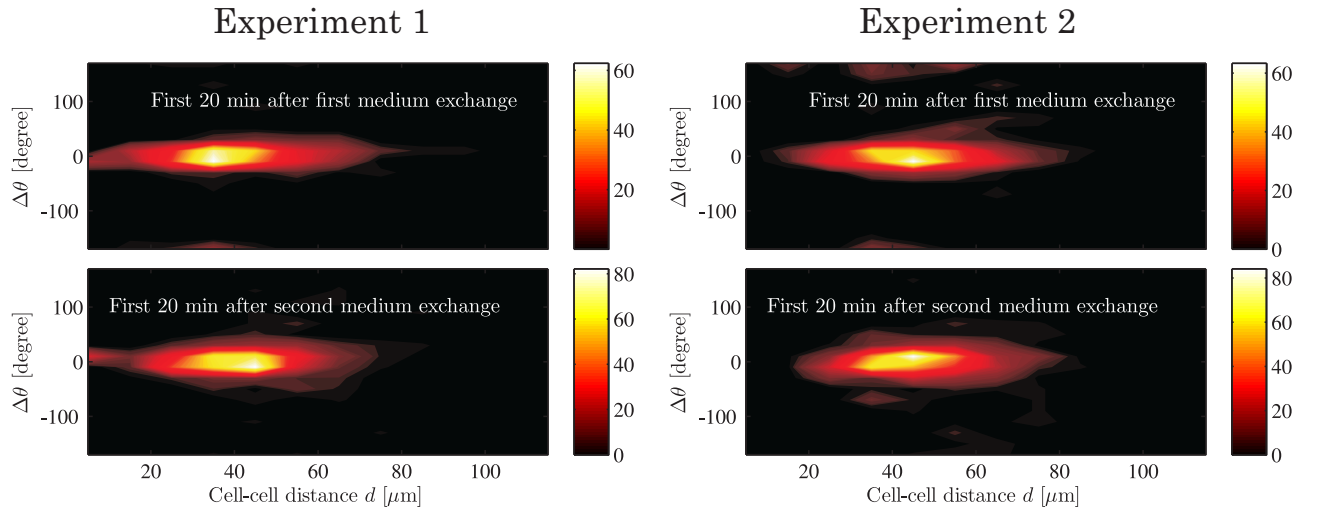


FIG. S9: Supporting experimental evidence for the existence of a cell-secreted pseudopod-inducing chemokine. The heat maps show histograms of the distances d and angle of pseudopod formation $\Delta\theta$ relative to the nearest neighbor cell (see explanatory schematic in Fig. 2(k)) during 20 min segments following media replacement for two independent experiments (shown in separate columns) with complete media replacement every two hours, with light colors corresponding to high counts and dark colors to low counts. The top row shows the result for following the first media replacement, and the bottom row the results following the second replacement, and for all cases the pseudopodia are distributed about $\Delta\theta = 0$ (similar to Fig. 2(k)), as we would expect for a cell-secreted pseudopod-inducing chemokine.

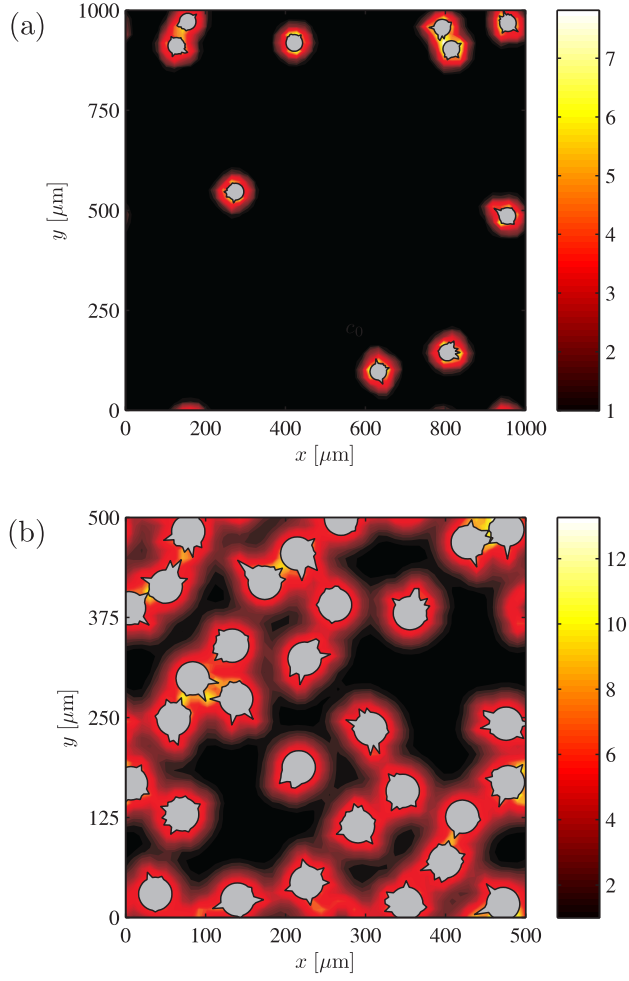


FIG. S10: Supplementary model predicted instantaneous chemokine results not shown in the main text. (a) Instantaneous chemokine concentration field from a low-density simulation. (b) Predicted chemokine concentration field taken from the same numerical experiment as shown in Fig. 3(b) and (d)-(g) in the main text.

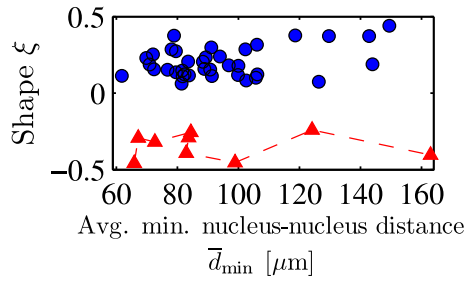


FIG. S11: Supplementary model speed distribution fit (red triangles) to experimental data (blue circles) of the shape parameter ξ of a generalized extreme value distribution across densities. Location parameter m and scale parameter s of the same fits are given in Fig. 3(i) in the main text.

III. MODEL DETAILS

The model was developed to aid in the interpretation of our experimental findings, and it was therefore crucial to construct a physically transparent model. The basic premise of the model is therefore, that each cell can be evaluated by Newtonian mechanics, as long as one is careful in the implementation of the collisions and pseudopodia traction forces. Thus our model, which can be considered as an extension of the Vicsek model [21–23], not only exploits known cellular biophysics in a direct and intuitive way contrary to the abstract thermodynamic ensemble averages of cellular Potts-type models [24, 25], but also enables handling of the few hundreds of cells per experiments - a mesoscale not suitable for continuum modeling theory [26–28].

The model cells are two-dimensional idealizations consisting of a set of N_m points discretizing the cell membrane, which are connected through a center of mass. The motion of this center of mass is taken as the motion of the cell, with the membrane points each being allowed to move in relation to the center of mass, in response to pseudopod formation or collapse, cell-cell contact, etc., as detailed in the following. The model assumes that each cell secretes chemokines, which all other cells react to. Cellular force transduction is achieved by forming pseudopodia through membrane point activation, and these form preferentially in regions of high chemokine concentration and in the current direction of motion; the former is achieved by biasing the probability of formation with the local chemokine concentration.

The model contains a list of parameters, which in most cases are determined directly from the experimental data (parameters summarized in Table S4). Whenever possible, the simplest reasonable approach has been applied, and Table S3 lists all assumptions underlying the model. The model has been implemented in MATLAB and this implementation is freely available for download at <http://sourceforge.net/projects/cell-migration/>. The flow of the program at each time step is as follows, with each part to be described in detail in the following

1. Activation of membrane points and pseudopod growth for each cell. The time since membrane point activation and pseudopod lengths are updated. This is detailed in Sec. IIIB.
2. Handle collisions (Sec. IIIE): membrane points of different cells within a distance ϵ of each other are considered to be in collision. Time since initial collision is tracked, and if the experimentally determined collision time τ_c is surpassed, the point is flagged for collapse.
3. Forces are assigned to all active points along the appropriate directions, as described by Eq. (S13) of Sec. IIIB 4.
4. Move all non-active points by Eq. (S17) of

Sec. IIIC. This also includes points which are retracting following activation or collision.

5. Collapse retracting points according to Eq. (S12) of Sec. IIIB 3. If a membrane point has fully retracted and the waiting time τ_{rest} has passed, the point is transferred to a normal passive point.
6. Update time stamp and concentration field due to the new cell positions, by summing Eq. (S18) of Sec. IIID for all cells.

Note that protruding points are moved before the entire cell, while retracting points first move with the cell center of mass and then retract.

The simulation time step Δt must be smaller than all the model time scales. In addition, the time scale must also allow for colliding cells to be within ϵ of each other before the unphysical process of crossing into each other. To satisfy these criteria we have taken $\Delta t = 0.25$ min.

A. Model cell

Each cell is modeled as a set of N_m points along the cell membrane, see Fig. 3(a) in the main text, some being active and the rest passive. In a given time step, a number of the points are selected (see below) to be active and are moved outwards from the otherwise circular cell. These points thereby form pseudopodia, and their positions dictate the direction of the cell motion.

The membrane points are connected through a “cell center” with position \mathbf{x}_c : A constant force of magnitude F_o is assigned to each active point (described below), and the cell center is displaced a distance $\Delta \mathbf{x}$ in response to the resultant force on all membrane points, see Eq. (S17). All passive points undergo the same displacement $\Delta \mathbf{x}$ (active points have already been moved). Hence, the cell motion is not an independent variable.

The cell is initially modeled as a sphere with radius $r = 20.9 \mu\text{m}$ corresponding to the mean radius of the cells in the experiments, see Fig. S12(a). The real cells are obviously not circular, but as time passes, the formation and collapse of pseudopodia make the model cell shape a dynamic and dependent entity, in agreement with experimental observation. The pseudopod width w is taken from the data to be $8 \mu\text{m}$ (Fig. S12(b)), which agrees with the report of pseudopod width of $\sim 5 \mu\text{m}$ in [9]. The number of membrane points per cell N_m is therefore taken as the cell circumference divided by twice the pseudopod width (by extending a membrane point, the model base pseudopod width is roughly twice the distance between two membrane points),

$$N_m = \frac{2\pi r}{2w} \approx 36. \quad (\text{S9})$$

If two neighboring points are activated at the same time, the width of the pseudopod becomes larger and the force in this direction increases, since each of the

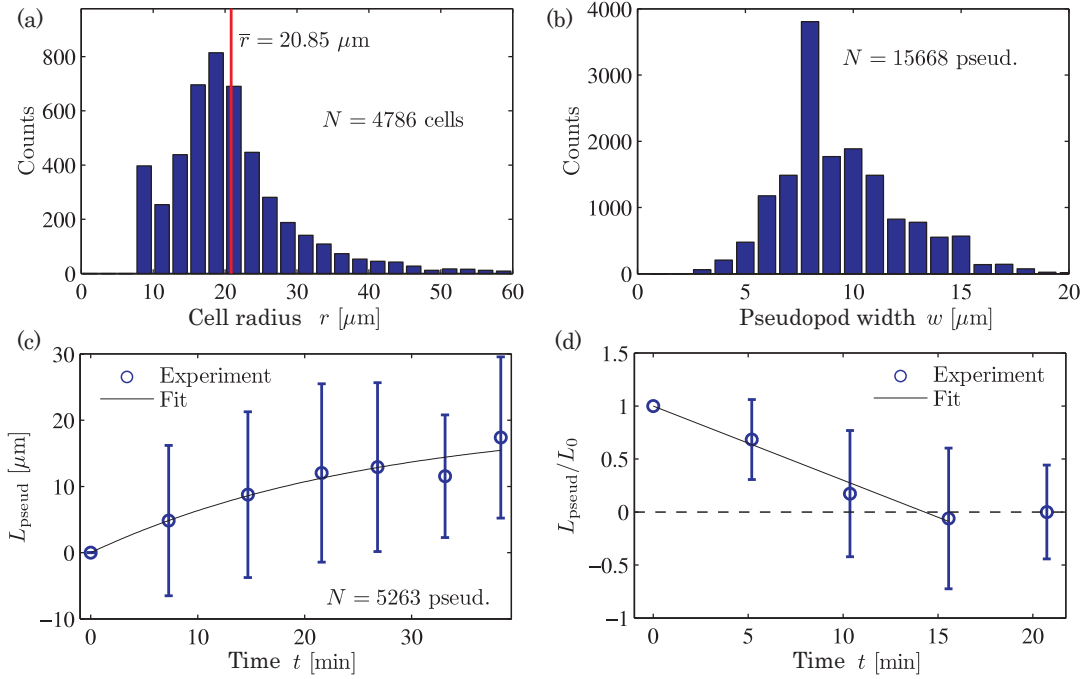


FIG. S12: Experimental determination of model parameters. (a) Cell radius is computed as the average distance between the nucleus and the cell outline. (b) Pseudopod width has been measured at the base of the protrusion. (c) Pseudopod growth obtained from 5263 pseudopodia is approximated by an exponential function (Eq. (S10)). (d) Pseudopod collapse following cessation of a pseudopod from either age or contact with other cells occurs at a constant rate depending on the initial length. Pseudopodia do not collapse between the second to last and final data points (at $t = 16$ min and $t = 22$ min).

two activated points of course pull with the same force F_o . This is in agreement with experimental work on the distribution of a cytosolic kinase (PI3K) known to be involved in the polymerization of actin, which has revealed localized and independent signaling domains of the size of small pseudopodia in the wider pseudopodia known as lamellipodia [9].

It was found experimentally that the number of pseudopodia per cell varies about a constant value, ν_m , which was found to be in the range 1 – 7 (see Fig. 2(c) in the main text). To account for this in the model, each cell is assumed to have a constant number of pseudopodia N_p , so a pseudopod cannot form before an old one stops due to either age or contact with another cell (detailed below). However, since it takes some time for a former pseudopod to retract back into the cell, there will be times where the model cell will appear to have more pseudopodia than N_p ; likewise, cells which often collide with other cells will at some instances appear to have fewer pseudopodia. Each model cell is a random number of pseudopodia N_p ranging from 1 to 7 which does not change. We find no difference whether each cell is assigned N_p according to the distribution shown in Fig. 2(c) in the main text or from a uniform distribution, so to limit the number of variables we have drawn N_p from a uniform distribution for all results.

Experimental studies of isolated migrating cells have

revealed that they have a protrusion opposite the direction of motion in addition to their pseudopodia. This protrusion, also known as the uropod, is pulled towards the cell center by intracellular myosin, while applying less traction force than pseudopodia [29]. Contrary to these findings, most cells in our experiments did not exhibit an observable morphological polarity as they formed pseudopodia in almost any direction, and consequently uropodia could rarely be unambiguously identified. In addition, the dynamics of uropod formation and maintenance for a cell which is constantly changing direction of motion is not well understood, and fibroblasts in particular have lower levels of uropodial myosin compared to e.g. *Dictyostelium* cells. In the experimental observations on which we base our model we therefore neglected cell uropodia, and all experimentally observed protrusions were treated as pseudopodia. Due to the comparatively small traction forces applied by the uropodia and their low numbers, this is a reasonable first approximation, and the good agreement between model and experiment further justify these assumptions.

B. Pseudopod dynamics

Pseudopod growth and collapse are complex processes at the molecular level which have been investigated for

decades [29–31]. The focus of the current work is on modeling the motile behavior at the cell-level, so pseudopod growth and collapse are measured from the data and used as input to the model.

1. Life of a pseudopod

We found experimentally that the number of pseudopodia is roughly constant per cell during an experiment, but with a varying life times (Fig. S6(a)). In the model each pseudopod is assigned a life time drawn from the distribution given in Fig. S6(c). Since we find that the variation in the number of pseudopodia about ν_m is low, a new point is activated only when an old one exists longer than the prescribed life time. When this happens, all non-active and non-collided points are assigned a probability of pseudopod formation (details given below), and for each ending pseudopod a new is picked randomly from the pool of available membrane points. Hence, the number of activated points is conserved but the number of pseudopodia will change as new pseudopodia form while ending pseudopodia retract (pseudopod collapse described in detail below).

Following collision of a pseudopod with another cell, it is observed that a new pseudopod does not form at the position of the old pseudopod immediately after the release. This is in line with biochemical investigations which indicate that contact inhibition of locomotion is caused by a local inhibition of actin polymerization in the region of contact [32]. This is implemented in the model by including a resting time τ_{rest} following the release of the collided points, where said point cannot be reactivated. Following the data, we pick $\tau_{\text{rest}} = 5.5$ min, the mean time difference between two frames.

2. Protrusion

For each activated point, pseudopod protrusion is modeled by moving the point radially outward. We followed the tip of 5263 pseudopodia experimentally to obtain data on the growth of the pseudopodia. The data shows (Fig. S12(c)) that the protrusion (pseudopod) length $L_{\text{pseud}}(t)$ as a function of time can be approximated by

$$L_{\text{pseud}}(t) = L_0 \left(1 - e^{-t/\tau_{\text{pseud}}^{\text{growth}}} \right), \quad (\text{S10})$$

with $L_0 = 26.7 \mu\text{m}$ and $\tau_{\text{pseud}}^{\text{growth}} = 20.2$ min.

There are large variations in pseudopod lengths (hence the large errorbars in Fig. S12(c)), but aiming for simplicity only the mean is used in the model.

The mathematical formulation for the protrusion of an activated point at position \mathbf{x}_i at a time t during the growth of the pseudopod is

$$\mathbf{x}_i + L_{\text{pseud}}(t) \frac{\mathbf{x}_i + \mathbf{x}_c}{|\mathbf{x}_i + \mathbf{x}_c|}, \quad (\text{S11})$$

where \mathbf{x}_c is the position of the cell center.

3. Collapse

After the prescribed pseudopod life time has passed since activation, pseudopodia collapse back into the cell. Biophysically this occurs since the cell-substrate adhesion is broken and the cell degrades the polymerized actin, so pseudopod retraction is caused by the elastic force of the membrane. The data shows (Fig. S12(d)) that the collapse rate depends on pseudopod length, since the normalized pseudopod length may be fitted by

$$\frac{L_{\text{pseud}}(t)}{L_0} = -K t, \quad (\text{S12})$$

with collapse rate $K = 0.07 \text{ min}^{-1}$. Hence, in the model each collapsing membrane point does so an amount $K L_0 \Delta t$ per time step, where L_0 is the full length of the pseudopod from Eq. (S10) and Δt is the duration of the time step. Similar to pseudopod extension, collapse of a point occurs along the direction from the nucleus to the point. As shown in Fig. S12(d), the average pseudopod has completely retracted after ~ 16 min, and therefore does not retract any further; hence the second to last and last data points have about the same length. The fit presented by Eq. (S12) only applies until the pseudopod has collapsed, so in the model we retract pseudopodia only until the reach the radius \bar{r} of the unperturbed cell.

A collapsing point is first moved along with the rest of the cell before the collapse is invoked. Collapsing points may be activated in later time steps, in which case the point transitions to an activated point and the cycle restarts.

4. Pseudopod force

The force assigned to each activated point is a consequence of the attachment and subsequent pulling of microtubules on the adhesion made by the cell with the substrate at the base of the pseudopod. Microtubules constantly “feel out” the inside of the cell but the formation of the attachment depends on the proximity of the nearest microtubule and the pulling force obviously scales with the number of microtubules that attach to each adhesion. However, the microtubules emanate from the centrosome, which is found right in front of the nucleus even for migrating cells, so the direction of the force can be approximated by the pseudopod-nucleus direction [18, 33]. Furthermore, relative variations of the pseudopod point forces are on the order ~ 2 both within the individual cell and between cells [19], and locally the force is more likely to be applied in short bursts of much smaller spatial extent than the width of the pseudopod [9].

Due to their relative small size and aiming for simplicity, these variations are ignored, so each active point is

assigned a force of magnitude F_o along the direction from the cell center to the activated point i

$$\mathbf{F}_i = F_o \frac{\mathbf{x}_i + \mathbf{x}_c}{|\mathbf{x}_i + \mathbf{x}_c|}, \quad (\text{S13})$$

where as in Eq. (S11) \mathbf{x}_i is the position of the i th point and \mathbf{x}_c is the position of the cell center. The point force at the base of each pseudopod is estimated to $F_o \approx 1.1 \times 10^{-7}$ N from Munevar *et al.* [19] who showed experimentally that traction forces can be well approximated by point forces at the pseudopodia in NIH 3T3 fibroblasts.

5. Pseudopod formation bias

A new membrane point is activated after an already active point exceeds its life time or collides with another cell. The stochastic selection of this new point i is biased by secreted chemokine with factor Π_i^c and the current direction of motion with factor Π_i^d , so the probability that this point is activated out of the total N_m points of the cell is

$$p_i = \frac{\Pi_i^c + \Pi_i^d}{\sum_{i=1}^{N_m} (\Pi_i^c + \Pi_i^d)}. \quad (\text{S14})$$

A biased stochastic activation was used due to the low number of involved intra- and extracellular signaling molecules (at typical extracellular chemokine concentrations in the nanomolar range [34, 35] there are large relative fluctuations of as much as 100 % [36]).

The directional bias is determined from a fit to the experimental data in Fig. 2(j) using the angle $\Delta\alpha$ between the current direction of motion and the line connecting the center-of-mass \vec{x}_c and the current membrane point. A Gaussian fit to the normalized experimental data $\Pi_i^d(\Delta\alpha) = A e^{\frac{-\Delta\alpha^2}{2a^2}}$ with mean 0° , standard deviation $a = 29.7^\circ$, and amplitude $A = 0.05$ was used.

Our experimental observations only imply the existence of a pseudopod formation bias by cell-secreted chemokines, not the exact form. To implement this crucial feature in the model, we therefore used previously published results on single-cell chemotaxis. Firstly, the results of Arriemerlou and Meyer implied that pseudopods are more likely to form in the regions of higher chemokine concentration [9]. Secondly, the previously mentioned results from single-cell experiments on NIH 3T3 fibroblasts by Melvin *et al.* had revealed that relative concentration gradients $(\Delta c/\Delta x)/c_0$ of $0.002 \mu\text{m}^{-1}$ are required for unambiguous chemotactic response, and that the response saturates at higher concentrations, while relative concentrations lower than the aforementioned limit do not produce reliable chemotaxis [10]. Furthermore, it has been demonstrated that the local gradient across the cell relative to the average concentration of the cell is the decisive parameter [34]. All this points to a sigmoidal activation function based on local relative

TABLE S3: Model assumptions

– Cell motion is quasi-static
– The scale of secreted concentration is the same for all cells, c_0
– All pseudopodia apply a force of the same magnitude, F_o
– All collisions last the same time, τ_c
– Chemokine activation of membrane points is biased by a Hill function of the relative concentration. This function is the same for all membrane points and all cells.
– All cells have the same friction parameter γ
– All pseudopodia grow and collapse according to the same relations, Eqs. (SS10) and (SS12)
– All cells are circular with the same radius \bar{r}
– Each cell has a fixed number of pseudopods at each time, but different cells have different numbers

chemokine concentration. We use a Hill function based on the local relative chemokine concentration of the cell at membrane point i , c_i/\bar{c} , where $\bar{c} = \sum_{i=1}^{N_m} c_i/N_m$ is the instantaneous average concentration experienced by the cell, as sigmoidal functions of this type are ubiquitous in biochemical signaling activation including gradient sensing in bacterial chemotaxis [37]. The biasing function is

$$\Pi_i^c = \frac{\left(\frac{c_i}{\bar{c}}\right)^h}{1 + \left(\frac{c_i}{\bar{c}}\right)^h}, \quad (\text{S15})$$

where h is the Hill coefficient.

Running our model for isolated cells, we found we could reproduce the experimental results of [10] using $h = 20$ in Eq. (S15), see Fig. 3(c) where each data point represents the average over 20 single-cell simulations each run for 300 min at each concentration. Biochemically, the Hill coefficient h is an expression of cooperativity among the chemical receptors mediating the chemotactic signal, with the coefficient corresponding to the number of cooperating receptors, and it has been shown that improved gradient sensing is achieved by increasing the cooperativity [38]. While the value $h = 50$ used in the model is unrealistically high — the reference value is $h \approx 3$ found for haemoglobin [39] — Hill coefficients of ~ 10 have been reported for bacterial chemotaxis [37], and Hill-like behavior with apparent Hill coefficients of $h \approx 42$ have furthermore been demonstrated to arise from more complex interlinked signaling networks in the maturation of *Xenopus laevis* oocytes [40].

C. Cell motion

Having activated and protruded the appropriate points and assigned forces to them, the resulting force on the cell is used to compute the cell velocity. Due to the time-scales and small masses involved, cell inertia is negligible

TABLE S4: Model assumptions and values assigned to model parameters.

Parameter	Symbol	Value and unit	Source
Cell friction	γ	39.0 kg s^{-1}	Global fit
Pseudopod force	F_o	$1.1 \times 10^{-7} \text{ N}$	Extracted from Munevar <i>et al.</i> [19]
Number of membrane points per cell	N_m	36	Eq. S9 and Fig. S12(a)
Number of pseudopodia per cell	N_p	1 – 7	Fig. 3(c) in the main text
Full pseudopod length	L_0	$26.7 \text{ }\mu\text{m}$	Eq. (S10) and Fig. S12(c)
Pseudopod collapse rate	K	0.07 min^{-1}	Eq. (S12) and Fig. S12(d)
Hill coefficient	h	20	Fig. 3(c) in the main text and Melvin <i>et al.</i> [10]
Decay length scale of secreted chemokines	ℓ_{diff}	$340 \text{ }\mu\text{m}$	Fig. S12(a), combined with Francis and Palsson [41]
Cell radius	r	$20.9 \text{ }\mu\text{m}$	Fig. S12(a)
Collision tolerance distance	ϵ	$3 \text{ }\mu\text{m}$	Chosen to best capture the dynamics, no observable changes choosing ϵ in the range $1 \text{ }\mu\text{m} - 5 \text{ }\mu\text{m}$
Cell-cell contact time	τ_c	5.5 min	Fig. S12(e)
Time between successive activations of the same membrane point	τ_{rest}	5.5 min	Own data
Characteristic pseudopod growth time	$\tau_{\text{pseud}}^{\text{growth}}$	20.7 min	Eq. (S10) and Fig. S12(c)

and the following relationship is postulated

$$\sum_i \mathbf{F}_i = \gamma \mathbf{v}, \quad (\text{S16})$$

where γ is a constant and \mathbf{v} is the velocity of the cell. Physically, γ accounts for the Stokes drag from the fluid and the cell friction force with the substrate, which also scales linearly with the velocity. γ is the same for all cells and is fitted from the data at the value $\gamma = 39.0 \text{ kg s}^{-1}$, which compares reasonably well with an estimated friction coefficient of $\gamma \approx 29 \text{ kg s}^{-1}$ from Munevar *et al.* [19] and an order-of-magnitude estimate of the friction per unit cell surface area of $10^9 \text{ kg s}^{-1} \text{ m}^{-2}$ by Larripa and Mogilner [20]. The displacement of the model cell center $\Delta \mathbf{x}$ is then given by

$$\Delta \mathbf{x} = \mathbf{v} \Delta t, \quad (\text{S17})$$

where Δt is the time step. It has been shown in the literature that NIH 3T3 fibroblasts move along the direction of the resulting traction force [19], which essentially is the postulate of Eqs. (S16) and (S17). All points not activated are moved similarly to the cell center (the activated points have already been moved).

D. Secretion of signaling molecules

To mediate the chemotactic response of Fig. 3(e), model cells secrete chemokines. We assume that each model cell secretes at a constant rate Γ from the entire perimeter and the concentration field from each cell is thus approximated by the analytical solution for a con-

stant source (see e.g. [41])

$$c(d) = G \frac{r}{d-r} \frac{\ell_{\text{diff}}}{\sqrt{\pi}} \left[e^{-\frac{(d-2r)^2}{\ell_{\text{diff}}^2}} - e^{-\frac{d^2}{\ell_{\text{diff}}^2}} - \frac{|d-2r|}{\frac{\ell_{\text{diff}}}{\sqrt{\pi}}} \text{erfc}\left(\frac{|d-2r|}{\ell_{\text{diff}}}\right) + \frac{d}{\frac{\ell_{\text{diff}}}{\sqrt{\pi}}} \text{erfc}\left(\frac{d}{\ell_{\text{diff}}}\right) \right], \quad (\text{S18})$$

where $\text{erfc}(x)$ is the complementary error function, d is the distance from an extracellular point to the cell membrane, r is the cell radius, $G = \Gamma/(2D)$ is the concentration gradient at the cell membrane (taken to be the same for all cells; D is the diffusivity of the chemokine) and ℓ_{diff} is the length scale the concentration field decays on. Due to dilution and degradation, the effective signaling distance of a cell is estimated to 50 times the cell radius by Francis and Paulsson [41], and the length scale ℓ_{diff} is therefore taken to be 1/3 of the effective signaling distance of a cell of radius $r \approx 20 \mu\text{m}$, i.e. $\ell_{\text{diff}} = 340 \mu\text{m}$. Assuming the rate of chemokine secretion is one order of magnitude lower than the rate of antibody production we pick $\Gamma = 100 \text{ molecule per cell per second}$ [42] and since furthermore $D = 10^{-10} \text{ m}^2 \text{ s}^{-1}$ we find $G = 6.6 \times 10^{-4} \text{ mol m}^{-4}$.

E. Cell-cell contact

The contact inhibition of locomotion is characterized by the time of contact τ_c (Fig. 2(i) in the main text). Aiming for simplicity we assume in the model that the force is applied until the contact stops. The contact time τ_c is taken as the most frequent experimentally observed

contact time of pseudopodia in contact with other cells from the data, which unfortunately is identical to the mean sampling time Δt_{samp} ,

$$\tau_c = 5.5 \text{ min.} \quad (\text{S19})$$

The contact inhibition is implemented at the activation point level. If a point comes within a distance ϵ of any point of any other cell (does not need to be an activated point) the two points are deemed to be in contact. This continues until a total of τ_c has passed since the initial contact, and the local force is stopped. Hereafter the points transition to the normal collapse routine, in accordance with the experimental observations. The exact value of ϵ does not influence the behavior of the model cells for the range $1 - 5 \mu\text{m}$.

F. Summary of model parameters

The parameters of the model are summarized in Table S4. There is one fit (the friction coefficient γ , a global fit) while the rest of the parameters are obtained directly from the data or the literature.

G. Boundary conditions

In the experiments we only track cells in the middle of the chamber, neglecting cells close to the wall. In the model we imposed these boundary conditions in two different ways: (i) applying periodic boundary conditions on the secreted chemokine fields and cell motion, or (ii) including cells around the cells on interest (in a band of 4-5 cells) and include a density-specific background chemokine concentration representing the almost constant concentration field experienced by the cells. We found no detectable difference in the outcome, but using periodic boundary conditions saves computational time and therefore speeds up the numerical analysis. Consequently, all results presented in the paper have been computed using these boundary conditions.

H. Model output and comparison to experiment

We initiate the model by seeding cells at a desired concentration, using either the known starting positions from an experiment or random placement. We store the positions of the model cells and the concentration field at

each time step, yielding trajectories as shown in Fig. 3(b) in the main text and concentration fields as shown in Fig. S10. For true comparison between model and experimental data, the model trajectories are sampled at the experimental sampling rate, and motility statistics are computed from these resampled data. Furthermore, the first 20 min of the experimental data is discarded for these comparisons due to the significant chemotactic response caused by the low background level during these times. The model predictions are compared to experiments in Fig. 3 in the main text.

The numerical implementation of the model is not parallelized, so running the program becomes increasingly time consuming with the addition of more cells. To circumvent this issue, we ran several numerical experiments at the same cell density in parallel using ~ 30 cells in each, and then averaged over all cells in all experiments to extract distributions of single-cell speed, directional autocorrelation and maximum path distance. The outcome of this cost and time-reduced simulation scheme was compared to simulations using ~ 100 cells in two cases, where no variations exceeding those of finite statistics were detected.

I. Model outlook

Our statistical results combined with the model could be used to derive a continuum theory of the collective migration. While the number of cells in our experiment (a few hundred) is typically too low for a continuum description, it would be of great interest to derive such a theory for future macroscale studies. Such continuum theories have successfully been applied to collective behavior of both swimming and migrating cells [26–28]. Our experimentally validated model could be used to derive a continuum theory of the collective migration, which we would expect to include pair correlations due to the importance of cell-cell interactions in shaping local dynamics, much like the Zimm theory of polymers in dilute solutions [43]. Specifically, obtaining a sound description of the “collision” term of the continuum theory based on the microscopic (subcellular) dynamics described in our paper would not only contribute to the identification of the correct continuum model (in contrast to ad-hoc arguments and empirical data fitting), but would also lead to a deeper understanding of collective dynamics and rheology.

-
- [1] Lee, T. K, Denny, E. M, Sanghvi, J. C, Gaston, J. E, Maynard, N. D, Hughey, J. J, & Covert, M. W. (2009) A noisy paracrine signal determines the cellular NF- κ B response to lipopolysaccharide. *Sci. Signal.* **2**, 93.
 - [2] Selmeczi, D, Mosler, S, Hagedorn, P. H, Larsen, N. B, &

Flyvbjerg, H. (2005) Cell motility as persistent random motion: Theories from experiments. *Biophys. J.* **89**, 912–931.

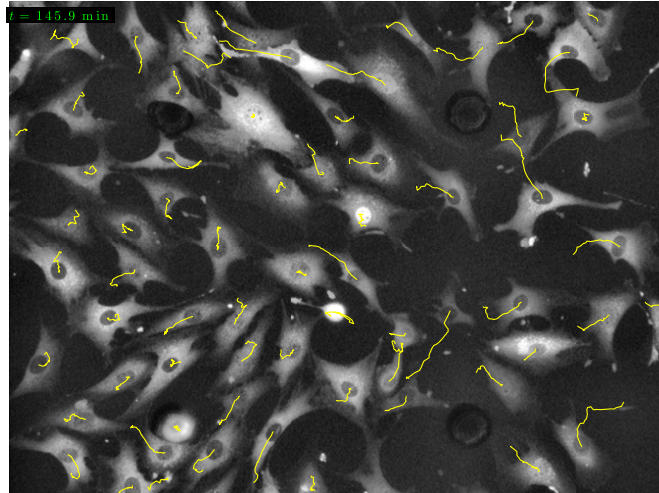
- [3] Gómez-Sjöberg, R, Leyrat, A. A, Pirone, D. M, Chen, C. S, & Quake, S. R. (2007) Versatile, fully automated,

- microfluidic cell culture system. *Anal. Chem.* **79**, 8557–8563.
- [4] Tay, S, Hughey, J. J, Lee, T. K, Lipniacki, T, Quake, S. R, & Covert, M. W. (2010) Single-cell NF- κ B dynamics reveal digital activation and analogue information processing. *Nature* **466**, 267–271.
 - [5] Li, L, Cox, E. C, & Flyvbjerg, H. (2011) “Dicty dynamics”: Dictyostelium motility as persistent random motion. *Phys. Biol.* **8**, 046006.
 - [6] Bosgraaf, L & van Haastert, P. J. M. (2010) Quimp3, an automated pseudopod-tracking algorithm. *Cell Adh. Migr.* **4**, 46–55.
 - [7] Trepap, X, Wasserman, M. R, Angelini, T. E, Millet, E, Weitz, D. A, Butler, J. P, & Fredberg, J. J. (2009) Physical forces during collective cell migration. *Nat. Phys.* **5**, 426–430.
 - [8] Andrew, N & Insall, R. H. (2007) Chemotaxis in shallow gradients is mediated independently of PtdIns 3-kinase by biased choices between random protrusions. *Nature Cell Bio.* **9**, 193–200.
 - [9] Arriemerlou, C & Meyer, T. (2005) A local coupling model and compass parameter for chemotaxis. *Dev. Cell* **8**, 215–227.
 - [10] Melvin, A. T, Welf, E. S, Wang, Y, Irvine, D. J, & Haugh, J. M. (2011) In chemotaxing fibroblasts, both high-fidelity and weakly biased cell movements track the localization of PI3K signaling. *Biophys. J.* **100**, 1893–1901.
 - [11] Seppä, H, Grotendorst, G, Seppä, S, Schiffmann, E, & Martin, G. R. (1982) Platelet-derived growth factor is chemotactic for fibroblasts. *J. Cell Bio.* **92**, 584–588.
 - [12] Postlethwaite, A. E, Keski-Oja, J, Moses, H. L, & Kang, A. H. (1987) Stimulation of the chemotactic migration of human fibroblasts by transforming growth factor β . *J. Exp. Med.* **165**, 251–256.
 - [13] Kanazawa, S, Fujiwara, T, Matsuzaki, S, Shingaki, K, Taniguchi, M, Miyata, S, Tohyama, M, Sakai, Y, Yano, K, Hosokawa, K, & Kubo, T. (2010) bFGF regulates PI3-kinase-Rac1-JNK pathway and promotes fibroblast migration in wound healing. *PLoS One* **5**, e12228.
 - [14] Silzle, T, Kreutz, M, Dobler, M. A, Brockhoff, G, Knuechel, R, & Kunz-Schughart, L. A. (2003) Tumor-associated fibroblasts recruit blood monocytes into tumor tissue. *Eur. J. Immunol.* **33**, 1311–1320.
 - [15] Rojas-Valencia, L, Montiel, F, no, M. M, Selman, M, & Pardo, A. (1995) Expression of a 2.8-kb PDGF-B/c-sis transcript and synthesis of PDGF-like protein by human lung fibroblasts. *Chest* **108**, 240–245.
 - [16] Mansbridge, J. N, Liu, K, Pinney, R. E, Patch, R, Ratcliffe, A, & Naughton, G. K. (1999) Growth factors secreted by fibroblasts: role in healing diabetic foot ulcers. *Diabetes, Obesity and Metabolism* **1**, 265–279.
 - [17] Smith, R. S, Smith, T. J, Blieden, T. M, & Phipps, R. P. (1997) Fibroblasts as sentinel cells. Synthesis of chemokines and regulation of inflammation. *Am. J. Pathol.* **151**, 317–322.
 - [18] Alberts, B, Johnson, A, Lewis, J, Raff, M, Roberts, K, & Walter, P. (2007) *Molecular biology of the cell*. (Garland Science, New York), 5th edition.
 - [19] Munevar, S, Wang, Y, & Dembo, M. (2001) Traction force microscopy of migrating normal and H-ras transformed 3T3 fibroblasts. *Biophys. J.* **80**, 1744–1757.
 - [20] Larripa, K & Mogilner, A. (2006) Transport of a 1D viscoelastic actin-myosin strip of gel as a model of a crawling cell. *Physica A* **372**, 113–123.
 - [21] Vicsek, T, Czirók, A, Ben-Jacob, E, Cohen, I, & Shochet, O. (1995) Novel type of phase transition in a system of self-driven particles. *Phys. Rev. Lett.* **75**, 1226–1229.
 - [22] Szabó, B, Szöllösi, G. J, Gönci, B, Jurányi, Z, Selmeczi, D, & Vicsek, T. (2006) Phase transition in the collective migration of tissue cells: Experiment and model. *Phys. Rev. E* **74**, 061908.
 - [23] Yamao, M, Naoki, H, & Ishii, S. (2011) Multi-cellular logistics of collective cell migration. *PLoS One* **6**, e27950.
 - [24] Graner, F & Glazier, J. A. (1992) Simulation of biological cell sorting using a two-dimensional extended Potts model. *Phys. Rev. Lett.* **69**, 2031–2036.
 - [25] Szabó, A, Ünneper, R, Méhes, E, Twaal, W. O, Argraves, W. S, Cao, Y, & Czirók, A. (2010) Collective cell motion in endothelial monolayers. *Phys. Biol.* **7**, 046007.
 - [26] Saintillian, D & Shelley, M. J. (2008) Instabilities and pattern formation in active particle suspensions: kinetic theory and continuum simulations. *Phys. Rev. Lett.* **100**, 178103.
 - [27] Lambert, G, Liao, D, & Austin, R. H. (2010) Collective escape of chemotactic swimmers through microscopic ratchets. *Phys. Rev. Lett.* **104**, 168102.
 - [28] Basan, M, Joanny, J.-F, Prost, J, & Risler, T. (2011) Undulation instability of epithelial tissue. *Phys. Rev. Lett.* **106**, 158101.
 - [29] Lauffenberger, D. A & Horwitz, A. F. (1996) Cell migration: A physically integrated molecular process. *Cell* **84**, 359–369.
 - [30] DiMilla, P. A, Barbee, K, & Lauffenburger, D. A. (1991) Mathematical model for the effects of adhesion and mechanics on cell migration speed. *Biophys. J.* **60**, 15–37.
 - [31] Schreiber, C. H, Stewart, M, & Duke, T. (2010) Simulation of cell motility that reproduces the force-velocity relationship. *Proc. Natl. Acad. Sci. USA* **107**, 9141–9146.
 - [32] Carmona-Fontaine, C, Matthews, H. K, Kuriyama, S, Moreno, M, Dunn, G. A, Parsons, M, Stern, C. D, & Mayor, R. (2008) Contact inhibition of locomotion *in vivo* controls neural crest directional migration. *Nature* **456**, 957–961.
 - [33] Ueda, M, Gräf, R, MacWilliams, H. K, Schliwa, M, & Euteneuer, U. (1997) Centrosome positioning and directionality of cell movements. *Proc. Natl. Acad. Sci. USA* **94**, 9674–9678.
 - [34] Fuller, D, Chen, W, Adler, M, Groisman, A, Levine, H, Rappel, W.-J, & Loomis, W. F. (2010) External and internal constraints on eukaryotic chemotaxis. *Proc. Natl. Acad. Sci. USA* **107**, 9656–9659.
 - [35] Haessler, U, Pisano, M, Wu, M, & Swartz, M. A. (2011) Dendritic cell chemotaxis in 3D under defined chemokine gradients reveals differential response to ligands CCL21 and CCL19. *Proc. Natl. Acad. Sci. USA* **108**, 5614–5619.
 - [36] Landau, L. D & Lifshitz, E. M. (1980) *Statistical Physics, Part I*. (Butterworth-Heinemann), 3rd edition.
 - [37] Li, G & Weis, R. M. (2000) Covalent modification regulates ligand binding to receptor complexes in the chemosensory system of *Escherichia coli*. *Cell* **100**, 357–365.
 - [38] Hu, B, Chen, W, Rappel, W.-J, & Levine, H. (2010) Physical limits to cellular sensing of spatial gradients. *Phys. Rev. Lett.* **105**, 048104.
 - [39] Stryer, L. (1995) *Biochemistry*. (Freeman, New York), 4th edition.
 - [40] Ferrell, J. E & Machleder, E. M. (1998) The biochem-

- ical basis of an all-or-none cell fate switch in *Xenopus* oocytes. *Science* **280**, 895–898.
- [41] Francis, K & Palsson, B. O. (1997) Effective intercellular communication distances are determined by the relative time constants for cyto/chemokine secretion and diffusion. *Proc. Natl. Acad. Sci. USA* **94**, 12258–12262.
- [42] Savinell, J. M, Lee, G. M, & Palsson, B. O. (1989) On the orders of magnitude of epigenic dynamics and monoclonal antibody production. *Bioprocess Eng.* **4**, 231–234.
- [43] Doi, M. (1995) *Introduction to polymer physics*. (Oxford University Press).

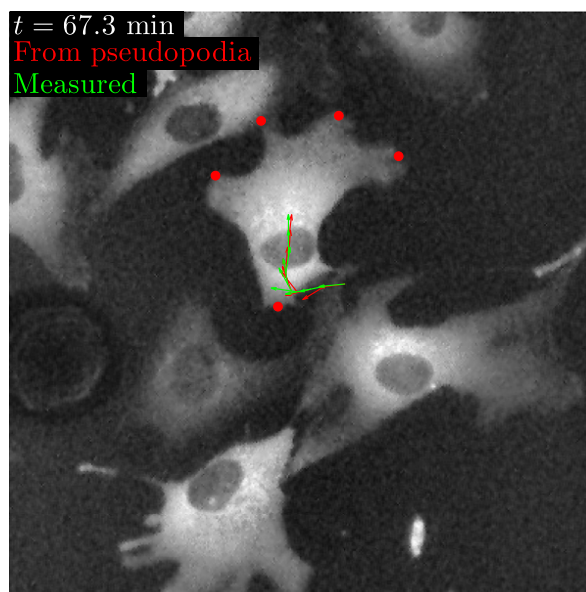
Supporting Information

Vedel et al. 10.1073/pnas.1204291110



Movie S1. The movement of cells at medium density in a chamber during 200 min. The trajectories are given by yellow lines.

[Movie S1](#)

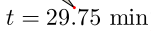


Movie S2. The positions and life times of the pseudopodia change dynamically during the course of an experiment, as illustrated for two cells. Pseudopodia are marked by red circles, with arrows indicating the actual direction of motion (green) and the direction of movement predicted from the pseudopodia (red).

[Movie S2](#)



[Movie S3](#)



[Movie S4](#)

[SI Appendix \(PDF\)](#)

Bibliography

- [1] *Cell biology's open cases*, Science **334** (2011), 1051.
- [2] M. Abercrombie and J. E. M. Heaysman, *Observations on the social behavior of cells in tissue culture I: Speed of movement of chick heart fibroblasts in relation to their mutual contacts*, Exp. Cell Res. **5** (1953), 111–131.
- [3] ———, *Observations on the social behavior of cells in tissue culture: II. “Monolayering” of fibroblasts*, Exp. Cell Res. **6** (1954), 293–306.
- [4] A. Ajdari, N. Bontoux, and H. A. Stone, *Hydrodynamic dispersion in shallow microchannels: the effect of cross-sectional shape*, Anal. Chem. **78** (2006), 387–392.
- [5] B. Alberts, A. Johnson, J. Lewis, M. Raff, K. Roberts, and P. Walter, *Molecular biology of the cell*, 5th ed., Garland Science, New York, 2008.
- [6] U. Alon, *An introduction to systems biology — design principles of biological circuits*, Chapman & Hall/CRC, Boca Raton, FL, 2007.
- [7] N. Andrew and R. H. Insall, *Chemotaxis in shallow gradients is mediated independently of PtdIns 3-kinase by biased choices between random protrusions*, Nat. Cell Bio. **9** (2007), 193–200.
- [8] T. E. Angelini, E. Hannezo, X. Trepate, J. J. Fredberg, and D. A. Weitz, *Cell migration driven by cooperative substrate deformation patterns*, Phys. Rev. Lett. **104** (2010), 168104.
- [9] T. E. Angelini, E. Hannezo, X. Trepate, M. Marquez, J. J. Fredberg, and D. A. Weitz, *Glass-like dynamics of collective cell migration*, Proc. Natl. Acad. Sci. USA **108** (2011), 4714–4719.
- [10] R. Aris, *On the dispersion of a solute in a fluid flowing through a tube*, P Roy Soc Lond A Mat **235** (1956), 67–77.
- [11] ———, *On the dispersion of solute in pulsating flow through a tube*, P Roy Soc Lond A Mat **259** (1960), 370–376.
- [12] C. Arriumerlou and T. Meyer, *A local coupling model and compass parameter for chemotaxis*, Dev. Cell **8** (2005), 215–227.

- [13] T. Arsenijevic, F. Grégoire, V. Delforge, C. Delporte, and J. Perret, *Murine 3T3-L1 adipocyte cell differentiation model: Validated reference genes for qPCR gene expression analysis*, PLoS ONE **7** (2012), e37517.
- [14] M. Ballerini, N. Cabibbo, R. Candelier, A. Cavagna, E. Cisbani, I. Giardina, V. Lecomte, A. Orlandi, G. Parisi, A. Procaccini, M. Viale, and V. Zdravkovic, *Interaction ruling animal collective behavior depends on topological rather than metric distance: Evidence from a field study*, Proc. Natl. Acad. Sci. USA **105** (2008), 1232–1237.
- [15] S. Bandyopadhyay and B. S. Mazumder, *Unsteady convective diffusion in a pulsatile flow through a channel*, Acta Mech **134** (1999), 1–16.
- [16] N. G. Barton, *On the method of moments for solute dispersion*, J Fluid Mech **126** (1983), 205–218.
- [17] M. Basan, J.-F. Joanny, J. Prost, and T. Risler, *Undulation instability of epithelial tissue*, Phys. Rev. Lett. **106** (2011), 158101.
- [18] G. K. Batchelor, *An introduction to fluid dynamics*, Cambridge University Press, Cambridge, 1967.
- [19] H. C. Berg and E. M. Purcell, *Physics of chemoreception*, Biophys. J. **20** (1977), 193–219.
- [20] J. Berthier and P. Silberzan, *Microfluidics for biotechnology*, Artech House, Norwood, MA, 2005.
- [21] K. Blagovic, L. Y. Kim, and J. Voldman, *Microfluidic perfusion for regulating diffusible signaling in stem cells*, PLoS ONE **6** (2011), e22892.
- [22] N. Bontoux, A. Pépin, Y. Chen, A. Ajdari, and H. A. Stone, *Experimental characterization of hydrodynamic dispersion in shallow microchannels*, Lab Chip **6** (2006), 930–935.
- [23] L. Bosgraaf and P. J. M. van Haastert, *Qimp3, an automated pseudopod-tracking algorithm*, Cell Adh. Migr. **4** (2010), 46–55.
- [24] H. Brenner and D. A. Edwards, *Macrotransport processes*, Butterworth–Heinemann, Boston, 1993.
- [25] H. Bruus, *Theoretical microfluidics*, Oxford University Press, Oxford, 2008.
- [26] H. Bruus and A. D. Stone, *Quantum chaos in a deformable billiard: Applications to quantum dots*, Phys. Rev. B **50** (1994), 18275–18287.
- [27] R. Camassa, Z. Lin, and R. McLaughlin, *The exact evolution of scalar variance in pipe and channel flow*, Commun Math Sci **8** (2010), 601–626.

- [28] Z. Cao, R. M. Umek, and S. L. McKnight, *Regulated expression of three C/EBP isoforms during adipose conversion of 3T3-L1 cells*, Genes Dev. **5** (1991), 1538–1552.
- [29] C. Carmona-Fontaine, H. K. Matthews, S. Kuriyama, M. Moreno, G. A. Dunn, M. Parsons, C. D. Stern, and R. Mayor, *Contact inhibition of locomotion in vivo controls neural crest directional migration*, Nature **456** (2008), 957–961.
- [30] W. P. Cawthorn, A. J Bree, Y. Yao, B. Du, N. Hemati, G. Martinez-Santibañez, and O. A. MacDougald, *Wnt6, Wnt10a and Wnt10b inhibit adipogenesis and stimulate osteoblastogenesis through a β -catenin-dependent mechanisms*, Bone **50** (2012), 477–489.
- [31] E. M. Chandler, B. R. Seo, J. P. Califano, R. C. Andresen Eguiluz, J. S. Lee, C. J. Yoon, D. T. Tims, J. X. Wang, L. Cheng, S. Mohanan, M. R. Buckley, I. Cohen, A. Y. Nikitin, R. M. Williams, D. Gourdon, C. A. Reinhart-King, and C. Fischbach, *Implanted adipose progenitor cells as physicochemical regulators of breast cancer*, Proc. Natl. Acad. Sci. USA **109** (2012), 9786–9791.
- [32] P. C. Chatwin, *On the longitudinal dispersion of passive contaminant in oscillatory flows in tubes*, J. Fluid Mech. **71** (1975), 513–527.
- [33] ———, *Initial development of longitudinal dispersion in straight tubes*, J Fluid Mech **80** (1977), 33–48.
- [34] P. C. Chatwin and P. J. Sullivan, *The effects of aspect ratio on longitudinal diffusivity in rectangular channels*, J Fluid Mech **120** (1982), 347–358.
- [35] C. Christodoulides, C. Lagathu, J. K. Sethi, and A. Vidal-Puig, *Adipogenesis and WNT signalling*, Trends Endocrinol. Metab. **20** (2008), 16–24.
- [36] F. Crick, *Central dogma of molecular biology*, Nature **227** (1970), 5258.
- [37] A. G. Cristancho and M. A. Lazar, *Forming functional fat: a growing understanding of adipocyte differentiation*, Nature Rev. Mol. Cell Bio. **12** (2011), 722–734.
- [38] A. Czirók, A.-L. Barabási, and T. Vicsek, *Collective motion of self-propelled particles: Kinetic phase transition in one dimension*, Phys. Rev. Lett. **82** (1999), 209–212.
- [39] A. Czirók, K. Schlett, E. Madarász, and T. Vicsek, *Exponential distribution of locomotion activity in cell cultures*, Phys. Rev. Lett. **81** (1998), 3038–3041.
- [40] D. R. Lide (editor-in-chief), *CRC handbook of chemistry and physics*, 75th ed., CRC Press, New York, NY, 1995.
- [41] P. F. Davies, *Flow-mediated endothelial mechanotransduction*, Physiol. Rev. **75** (1995), 519–560.
- [42] P. A. DiMilla, K. Barbee, and D. A. Lauffenburger, *Mathematical model for the effects of adhesion and mechanics on cell migration speed*, Biophys. J. **60** (1991), 15–37.

- [43] P. A. M. Dirac, *The principles of quantum mechanics*, 4th ed., Oxford University Press, Oxford, 1981.
- [44] M. Doi, *Introduction to polymer physics*, Oxford University Press, 1995.
- [45] M. R. Doshi, P. M. Daiya, and W. N. Gill, *Three dimensional laminar dispersion in open and closed rectangular conduits*, Chem Eng Sci **33** (1978), 795–804.
- [46] D. Dutta, A Ramachandran, and D. T. Leighton, *Effect of channel geometry on solute dispersion in pressure-driven microfluidic systems*, Microfluid Nanofluid **2** (2006), 275–290.
- [47] A. Eldar and M. B. Elowitz, *Functional roles for noise in genetic circuits*, Nature **467** (2010), 167–173.
- [48] M. E. Erdogan and P. C. Chatwin, *Effects of curvature and buoyancy on laminar dispersion of solute in a horizontal tube*, J. Fluid Mech. **29** (1967), 465–484.
- [49] D. F. Escande and F. Sattin, *When can the Fokker–Planck equation describe anomalous or chaotic transport?*, Phys. Rev. Lett. **99** (2007), 185005.
- [50] S. Etienne-Manneville, *Actin and microtubules in cell motility: which one is in control?*, Traffic **5** (2004), 470–477.
- [51] M. S. Fallon, B. A. Howell, and A. Chauhan, *Importance of Taylor dispersion in pharmacokinetic and multiple indicator dilution modeling*, Math. Med. Biol. **26** (2009), 263–296.
- [52] J. E. Ferrell and E. M. Machleder, *The biochemical basis of an all-or-none cell fate switch in *Xenopus* oocytes*, Science **280** (1998), 895–898.
- [53] R. T. Foister and T. G. M. van de Ven, *Diffusion of Brownian particles in shear flows*, J. Fluid Mech. **96** (1980), 105–132.
- [54] K. Francis and B. O. Palsson, *Effective intercellular communication distances are determined by the relative time constants for cyto/chemokine secretion and diffusion*, Proc. Natl. Acad. Sci. USA **94** (1997), 12258–12262.
- [55] P. Friedl and K. Wolf, *Tumour-cell invasion and migration: Diversity and escape mechanisms*, Nat. Rev. Cancer **3** (2003), 362–374.
- [56] D. Fuller, W. Chen, M. Adler, A. Groisman, H. Levine, W.-J. Rappel, and W. F. Loomis, *External and internal constraints on eukaryotic chemotaxis*, Proc. Natl. Acad. Sci. USA **107** (2010), 9656–9659.
- [57] M. H. Gail and C. W. Boone, *The locomotion of mouse fibroblasts in tissue culture*, Biophys. J. **10** (1970), 980–993.
- [58] S. Galic, J. S. Oakhill, and G. R. Steinberg, *Adipose tissue as an endocrine organ*, Mol. Cell. Endocrinol. **316** (2010), 129–139.

- [59] S. Gesta, Y.-H. Tseng, and C. R. Kahn, *Developmental origin of fat: Tracking obesity to its source*, Cell **131** (2007), 242–256.
- [60] J. P. Gleeson, *Electroosmotic flows with random zeta potential*, J. Colloid Interface Sci. **249** (2002), 217–226.
- [61] J. D. Goddard, *The Green’s function for passive scalar diffusion in a homogeneously sheared continuum*, Phys Fluids A **5** (1993), 2295–2297.
- [62] R. E. Goldstein, M. Polin, and I. Tuval, *Noise and synchronization in pairs of beating eukaryotic flagella*, Phys. Rev. Lett. **103** (2009), 168103.
- [63] R. Gómez-Sjöberg, A. A. Leyrat, D. M. Pirone, C. S. Chen, and S. R. Quake, *Versatile, fully automated, microfluidic cell culture system*, Anal. Chem. **79** (2007), 8557–8563.
- [64] F. Graner and J. A. Glazier, *Simulation of biological cell sorting using a two-dimensional extended Potts model*, Phys. Rev. Lett. **69** (1992), 2033–2036.
- [65] A. E. Grigoriadis, J. N. Heersche, and J. E. Aubin, *Differentiation of muscle, fat, cartilage, and bone from progenitor cells present in a bone-derived clonal cell population: effect of dexamethasone*, J. Cell Biol. **106** (1988), 2139–2151.
- [66] U. Haessler, M. Pisano, M. Wu, and M. A. Swartz, *Dendritic cell chemotaxis in 3D under defined chemokine gradients reveals differential response to ligands CCL21 and CCL19*, Proc. Natl. Acad. Sci. USA **108** (2011), 5614–5619.
- [67] H. G. Harris and S. L. Goren, *Axial diffusion in a cylinder with pulsed flow*, Chem Eng Sci **22** (1967), 1571–1576.
- [68] D. Helbing, I. J. Farkas, and T. Vicsek, *Simulating dynamical features of escape panic*, Nature **407** (2000), 487–490.
- [69] M. Hemmingsen, *Usability and applicability of microfluidic cell culture systems*, Ph.D. thesis, Technical University of Denmark, 2012, available online at <http://web-files.ait.dtu.dk/sove/PhDMH.pdf>.
- [70] E. Hovad, *Taylor dispersion in time dependent flow*, Master’s thesis, Technical University of Denmark, 2011, available online at www.nanotech.dtu.dk/microfluidics.
- [71] B. Hu, W. Chen, W.-J. Rappel, and H. Levine, *Physical limits to cellular sensing of spatial gradients*, Phys. Rev. Lett. **105** (2010), 048104.
- [72] K. M. Jansons, *On Taylor dispersion in oscillatory channel flows*, P Roy Soc Lond A Mat **462** (2006), 3501–3509.
- [73] J. R. Karr, J. C. Sanghvi, D. N. Macklin, M. V. Gutschow, J. M. Jacobs, B. Bolival, Jr., N. Assad-Garcia, J. I. Glass, and M. W. Covert, *A whole-cell computational model predicts phenotype from genotype*, Cell **150** (2012), 389–401.

- [74] M. Kawai and C. J. Rosen, *PPAR γ : A circadian transcription factor in adipogenesis and osteogenesis*, Nat. Rev. Endocrinol. **6** (2010), 629–636.
- [75] K. Keren, Z. Pincus, G. M. Allen, E. L. Barnhart, G. Marriott, A. Mogilner, and J. A. Theriot, *Mechanism and shape determination in motile cells*, Nature **453** (2008), 475–480.
- [76] K. A. Kilian, B. Bugarija, B. T. Lahn, and M. Mrksich, *Geometric cues for directing the differentiation of mesenchymal stem cells*, Proc. Natl. Acad. Sci. USA **107** (2010), 4872–4877.
- [77] S. J. King, D. C. Worth, T. M. E. Scales, J. Monypenny, G. E. Jones, and M. Parsons, *$\beta 1$ integrins regulate fibroblast chemotaxis through control of N-WASP stability*, EMBO J. **30** (2011), 1705–1718.
- [78] A. Koppen and E. Kalkhoven, *Brown vs white adipocytes: The PPAR γ coregulator story*, FEBS Lett. **584** (2010), 3250–3259.
- [79] G. Lambert, D. Liao, and R. H. Austin, *Collective escape of chemotactic swimmers through microscopic ratchets*, Phys. Rev. Lett. **104** (2010), 168102.
- [80] L. D. Landau and E. M. Lifshitz, *Statistical physics, Part I*, 3rd ed., Butterworth–Heinemann, 1980.
- [81] K. Larripa and A. Mogilner, *Transport of a 1D viscoelastic actin-myosin strip of gel as a model of a crawling cell*, Physica A **372** (2006), 113–123.
- [82] M. Latini and A. J. Bernoff, *Transient anomalous diffusion in Poiseuille flow*, J. Fluid Mech. **441** (2001), 399–411.
- [83] D. A. Lauffenberger and A. F. Horwitz, *Cell migration: A physically integrated molecular process*, Cell **84** (1996), 359–369.
- [84] V. Lecaudey and D. Gilmour, *Organizing moving groups during morphogenesis*, Curr. Opin. Cell Biol. **18** (2006), 102–107.
- [85] M. I. Lefterova and M. A. Lazar, *New developments in adipogenesis*, Trends Endocrinol. Metab. **20** (2009), 107–104.
- [86] M. I. Lefterova, Y. Zhang, D. J. Steger, M. Schupp, J. Schug, A. Cristancho, D. Feng, D. Zhuo, C. J. Stoeckert, Jr., X. S. Liu, and M. A. Lazar, *PPAR γ and C/EBP factors orchestrate adipocyte biology via adjacent binding on a genome-wide scale*, Genes Dev. **22** (2008), 2941–2952.
- [87] D. T. Leighton, *Diffusion from an initial point distribution in an unbounded oscillating simple shear flow*, PhysicoChem Hydrodyn **11** (1989), 377–386.
- [88] G. Löffler and H. Hauner, *Adipose tissue development: The role of precursor cells and adipogenic factors. Part II: The regulation of the adipogenic conversion by hormones and serum factors*, Klin. Wochenschr. **65** (1987), 812–817.

- [89] G. Li and R. M. Weis, *Covalent modification regulates ligand binding to receptor complexes in the chemosensory system of Escherichia coli*, Cell **100** (2000), 357–365.
- [90] L. Li, E. C. Cox, and H. Flyvbjerg, “*Dicty dynamics*”: *Dictyostelium* motility as persistent random motion, Phys. Biol. **8** (2011), 046006.
- [91] K. W. Lipsø, *Modeling of cell reactions and advection-diffusion processes in microfluidic biochips*, Master’s thesis, Technical University of Denmark, 2012.
- [92] R. McBeath, D. M. Pirone, C. M. Nelson, K. Bhadriraju, and C. S. Chen, *Cell shape, cytoskeletal tension, and RhoA regulate stem cell lineage commitment*, Dev. Cell **6** (2004), 483–495.
- [93] M. L. Mehta, *Random matrices*, 3rd ed., Pure and Applied Mathematics, vol. 142, Elsevier/Academic Press, Amsterdam, 2004.
- [94] A. T. Melvin, E. S. Welf, Y. Wang, D. J. Irvine, and J. M. Haugh, *In chemotaxing fibroblasts, both high-fidelity and weakly biased cell movements track the localization of PI3K signaling*, Biophys. J. **100** (2011), 1893–1901.
- [95] R. F. Molloy and D. T. Leighton, *Binary oscillatory cross-flow electrophoresis: Theory and experiments*, J Pharma Sci **87** (1998), 1270–1281.
- [96] C. J. Morris and F. K. Forster, *Oscillatory flow in microchannels - Comparison of exact and approximate impedance models with experiments*, Exp Fluids **36** (2004), 928–937.
- [97] N. A. Mortensen and H. Bruus, *Universal dynamics in the onset of a Hagen-Poiseuille flow*, Phys. Rev. E **74** (2006), 017301.
- [98] N. A. Mortensen, L.H. Olesen, and H. Bruus, *Transport coefficients for electrolytes in arbitrarily shaped nano and micro-fluidic channels*, New J Phys **8** (2006), 37–51.
- [99] A. Mukherjee and B. S. Mazumder, *Dispersion of contaminant in oscillatory flows*, Acta Mech **74** (1988), 107.
- [100] S. Munevar, Y.-l. Wang, and M. Dembo, *Traction force microscopy of migrating normal and H-ras transformed 3T3 fibroblasts*, Biophys. J. **80** (2001), 1744–1757.
- [101] W. Ostwald, *On the arithmetical representation of viscosity structural fields*, Kolloid-Zeitschrift **47** (1929), 176–187.
- [102] S. Paul and B.S. Mazumder, *Dispersion in unsteady Couette-Poiseuille flows*, Int J Eng Sci **46** (2008), 1203–1217.
- [103] J. Paulsson, *Summing up the noise in gene networks*, Nature **427** (2004), 415–418.
- [104] M. Polin, I. Tuval, K. Drescher, J. P. Gollub, and R. E. Goldstein, *Chlamydomonas swims with two “gears” in a eukaryotic version of run-and-tumble locomotion*, Science **325** (2009), 487–490.

- [105] M. Poujade, E. Grasland-Mongrain, A. Hertzog, J. Jouanneau, P. Chavrier, B. Ladoux, A. Buguin, and P. Silberzan, *Collective migration of an epithelial monolayer in response to a model wound*, Proc. Natl. Acad. Sci. USA **104** (2007), 15988–15993.
- [106] M. Reffay, L. Petitjean, S. Coscoy, E. Grasland-Mongrain, F. Amblard, A. Buguin, and P. Silberzan, *Orientation and polarity in collectively migrating cell structures: Statics and dynamics*, Biophys. J. **100** (2011), 2566–2575.
- [107] P. B. Rhines and W. R. Young, *How rapidly is a passive scalar mixed within closed streamlines?*, J. Fluid Mech. **133** (1983), 133–145.
- [108] E.D. Rosen and B.M. Spiegelman, *Adipocytes as regulators of energy balance and glucose homeostasis*, Nature **444** (2006), 847–853.
- [109] M. Rossi, R. Lindken, B. P. Hierck, and J. Westerweel, *Tapered microfluidic chip for the study of biochemical and mechanical response at subcellular level of endothelial cells to shear flow*, Lab Chip **9** (2009), 1403–1411.
- [110] D. Saintillian and M. J. Shelley, *Instabilities and pattern formation in active particle suspensions: kinetic theory and continuum simulations*, Phys. Rev. Lett. **100** (2008), 178103.
- [111] A. J. Salgado, R. L. Reis, N. Sousa, and J. M. Gimle, *Adipose tissue derived stem cells secretome: Soluble factors and their roles in regenerative medicine*, Curr. Stem Cell Res. & Ther. **5** (2010), 103–110.
- [112] A. Samadani, J. Mettetal, and A. van Oudenaarden, *Cellular asymmetry and individuality in directional sensing*, Proc. Natl. Acad. Sci. USA **103** (2006), 11549–11554.
- [113] R. Sankarasubramanian and W. N. Gill, *Unsteady convective diffusion with inter-phase mass-transfer*, P Roy Soc Lond A Mat **333** (1973), 115–132.
- [114] B. Schoeberl, C. Eichler-Jonsson, E. Gilles, and G. Müller, *Computational modeling of the dynamics of the MAP kinase cascade activated by surface and internalized EGF receptors*, Nat. Biotechnol. **20** (2002), 370–375.
- [115] E. Schrödinger, *What is life?*, Cambridge University Press, Cambridge, 1944.
- [116] C. H. Schreiber, M. Stewart, and T. Duke, *Simulation of cell motility that reproduces the force-velocity relationship*, Proc. Natl. Acad. Sci. USA **107** (2010), 9141–9146.
- [117] D. Selmeczi, S. Mosler, P. H. Hagedorn, N. B. Larsen, and H. Flyvbjerg, *Cell motility as persistent random motion: Theories from experiments*, Biophys. J. **89** (2005), 912–931.
- [118] X. Serra-Picamal, V. Conte, R. Vincent, E. Anon, D. T. Tambe, E. Bazellieres, J. P. Butler, J. J. Fredberg, and X. Trepat, *Mechanical waves during tissue expansion*, Nat. Phys. (2012), Advance online publication July 8, 2012 (DOI: 10.1038/nphys2355).

- [119] D. Shao, H. Levine, and W.-J. Rappel, *Coupling actin flow, adhesion, and morphology in a computational cell motility model*, Proc. Natl. Acad. Sci. USA **109** (2012), 6851–6856.
- [120] D. Shao, W.-J. Rappel, and H. Levine, *Computational model for cell morphodynamics*, Phys. Rev. Lett. **105** (2010), 108104.
- [121] P. Skafte-Pedersen, M. Hemmingsen, D. Sabourin, F. S. Blaga, H. Bruus, and M. Dufva, *A self-contained, programmable microfluidic cell culture system with real-time microscopy access*, Biomedical Microdevices **14** (2012), 385–399, See also www.nanotech.dtu.dk/procell.
- [122] P. Skafte-Pedersen, D. Sabourin, M. Dufva, and D. Snakenborg, *Multi-channel peristaltic pump for microfluidic applications featuring monolithic PDMS inlay*, Lab Chip **9** (2009), 3003–3006.
- [123] F. Sánchez-Madrid and J. M. Serrador, *Bringing up the rear: defining the roles of the uropod*, Nat. Rev. Mol. Cell Bio. **10** (2009), 353–359.
- [124] L. Stryer, *Biochemistry*, 4th ed., Freeman, New York, 1995.
- [125] A. Szabó, R. Ünneper, E. Méhes, W. O. Twaal, W. S. Argraves, Y. Cao, and A. Czirók, *Collective cell motion in endothelial monolayers*, Phys. Biol. **7** (2010), 046007.
- [126] B. Szabó, G. J. Szöllösi, B. Gönci, Zs. Jurányi, D. Selmeczi, and T. Vicsek, *Phase transition in the collective migration of tissue cells: Experiment and model*, Phys. Rev. E **74** (2006), 061908.
- [127] D. J. Tampe, C. C. Hardin, T. E. Angelini, K. Rajendran, C. Y. Park, X. Serra-Picamal, E. H. Zhou, M. H. Zaman, J. P. Butler, D. A. Weitz, J. J. Fredberg, and X. Trepap, *Collective cell guidance by cooperative intercellular forces*, Nat. Mat. **10** (2011), 469–475.
- [128] S. Tay, J. J. Hughey, T. K. Lee, T. Lipniacki, S. R. Quake, and M. W. Covert, *Single-cell NF- κ B dynamics reveal digital activation and analogue information processing*, Nature **466** (2010), 267–271.
- [129] G. I. Taylor, *Dispersion of soluble matter in solvent flowing slowly through a tube*, P Roy Soc Lond A Mat **219** (1953), 186.
- [130] H. M. Taylor and E. F. Leonard, *Axial dispersion during pulsating pipe flow*, A I Ch E Journal **11** (1965), 686–689.
- [131] A. M. Thomas and R. Narayanan, *Physics of oscillatory flow and its effect on the mass transfer and separation of species*, Phys Fluids **13** (2001), 859–866.
- [132] D. W. Thompson, *On growth and form*, Cambridge University Press, Cambridge, 1992, abridged edition by John Tyler Bonner of the 1917 1st ed.

- [133] P. Trayhurn, *Endocrine and signalling role of adipose tissue: new perspectives on fat*, Acta Physiol. Scand. **184** (2005), 285–293.
- [134] X. Trepap, M. R. Wasserman, T. E. Angelini, E. Millet, D. A. Weitz, J. P. Butler, and J. J. Fredberg, *Physical forces during collective cell migration*, Nat. Phys. **5** (2009), 426–430.
- [135] M. Ueda, R. Gräf, H. K. MacWilliams, M. Schliwa, and U. Euteneuer, *Centrosome positioning and directionality of cell movements*, Proc. Natl. Acad. Sci. USA **94** (1997), 9674–9678.
- [136] G. E. Uhlenbeck and L. S. Ornstein, *On the theory of Brownian motion*, Phys. Rev. **36** (1930), 823–841.
- [137] C. van den Broeck, *A stochastic description of longitudinal dispersion in uniaxial flows*, Physica A **112** (1982), 343–352.
- [138] P. J. M. van Haastert, *A model for a correlated random walk based on the ordered extension of pseudopodia*, PLoS Comp. Biol. **6** (2010), e1000874.
- [139] S. Vedel and H. Bruus, *Transient Taylor–Aris dispersion for time-dependent flows in straight channels*, J Fluid Mech **691** (2012), 95–122.
- [140] S. Vedel, L. H. Olesen, and H. Bruus, *Pulsatile microfluidics as an analytical tool for determining the dynamic characteristics of microfluidic systems*, J Micromech Microeng **20** (2010), 035026.
- [141] T. Vicsek, A. Czirók, E. Ben-Jacob, I. Cohen, and O. Shochet, *Novel type of phase transition in a system of self-driven particles*, Phys. Rev. Lett. **75** (1995), 1226–1229.
- [142] A. Vikhansky and W. Wang, *Taylor dispersion in finite-length capillaries*, Chem. Eng. Sci. **66** (2011), 642–649.
- [143] P. Vitorino and T. Meyer, *Modular control of endothelial sheet migration*, Genes Dev. **8** (2008), 3268–3281.
- [144] Y. Wang, I. Teraoka, F. Y. Hansen, G. H. Peters, and O. Hassager, *Mean span dimensions of ideal polymer chains containing branches and rings*, Macromolecules **44** (2010), 403–412.
- [145] E. J. Watson, *Diffusion in oscillatory pipe flow*, J Fluid Mech **133** (1983), 233–244.
- [146] J. R. Womersley, *Method for the calculation of velocity, rate of flow and viscous drag in arteries when the pressure gradient is known*, J. Physiol. **127** (1955), 553–563.
- [147] M. Yamao, H. Naoki, and S. Ishii, *Multi-cellular logistics of collective cell migration*, PLoS ONE **6** (2011), e27950.

- [148] C. A. Yates, R. Erban, C. Escudero, I. D. Couzin, J. Buhl, I. G. Kevrekidis, P. K. Maini, and D. J. T. Sumpter, *Inherent noise can facilitate coherence in collective swarm motion*, Proc. Natl. Acad. Sci. USA **106** (2008), 5464–5469.
- [149] W.-C. Yeh, Z. Cao, M. Classon, and S. L. McKnight, *Cascade regulation of terminal adipocyte differentiation by three members of the C/EBP family of leucine zipper proteins*, Genes Dev. **9** (1995), 168–181.
- [150] P. I. Zhuravlev and G. A. Papoian, *Molecular noise of capping protein binding induces macroscopic instability in filopodial dynamics*, Proc. Natl. Acad. Sci. USA **106** (2009), 11570–11575.
- [151] P. A. Zuk, M. Zhu, P. Ashjian, D. A. De Ugarte, J. I. Huang, H. Mizuno, Z. C. Alfonso, J. K. Fraser, P. Benhaim, and M. H. Hedrick, *Human adipose tissue is a source of multipotent stem cells*, Mol. Bio. Cell **13** (2002), 4279–4295.
- [152] P. A. Zuk, M. Zhu, H. Mizuno, J. Huang, J. W. Futrell, A. J. Katz, P. Benhaim, H. P. Lorenz, and M. H. Hedrick, *Multilineage cells from human adipose tissue: Implications for cell-based therapies*, Tissue Eng. **7** (2001), 211–228.